Teodor Burghelea
Volfango Bertola *Editors*

Transport Phenomena in Complex Fluids

Springer

CISM International Centre for Mechanical Sciences

Courses and Lectures

Volume 598

For more than 40 years the book series edited by CISM, "International Centre for Mechanical Sciences: Courses and Lectures", has presented groundbreaking developments in mechanics and computational engineering methods. It covers such fields as solid and fluid mechanics, mechanics of materials, micro- and nanomechanics, biomechanics, and mechatronics. The papers are written by international authorities in the field. The books are at graduate level but may include some introductory material.

More information about this series at http://www.springer.com/series/76

Teodor Burghelea · Volfango Bertola
Editors

Transport Phenomena in Complex Fluids

 Springer

Editors
Teodor Burghelea
Laboratoire de Thermique
et Energie de Nantes
University of Nantes
Nantes, France

Volfango Bertola
School of Engineering
University of Liverpool
Liverpool, UK

Preface

Complex fluids refer to a broad class of liquids and soft materials with complex microstructure, which is characterised by length and timescales spanning over very large ranges. Examples include polymer solutions and melts, particle suspensions, colloidal gels, foams and emulsions. Unlike simple liquids, such as water, complex fluids exhibit a strongly nonlinear response to external forcing, which can be described by constitutive models where the stress tensor is a nonlinear function of the deformation rate tensor. This has dramatic consequences on the dynamics of complex fluids, at both microscopic and macroscopic levels, and on their ability to transfer or exchange mass, momentum and energy.

The practical importance of complex fluids is rapidly growing in industrial, pharmaceutical and life sciences applications as well as in everyday life. Whether we spread mayonnaise on a sandwich, rinse off the shower gel, blow our nose or sip a thick hot chocolate, we deal with complex fluids on a daily basis. Viscoplastic or viscoelastic gels and dense particle suspensions constitute most foods and pharmaceutical preparations, from pizza dough to painkiller tablets. Moreover, with a better understanding of liquid microstructures, industries have realised that working fluids can be tailored specifically to optimise existing processes, by altering their formulation (e.g. by means of chemical additives) in such a way as to change their dynamic behaviour and/or their properties.

This volume is based on the lectures delivered during the CISM Advanced Course 'Transport Phenomena in Complex Fluids' (Udine, Italy, 7–11 May 2018), which provide a thorough (although not exhaustive) overview of the topic, based on the most recent research results and the most updated methods for their analytical prediction and numerical simulation. The first chapter introduces the fundamental transport equations and gives and the main features of the most common constituents of complex fluids (polymers, surfactants and colloids), while the second chapter reviews the main nonlinear constitutive models; Chap. 3 presents an overview of the experimental methods to characterise the rheological and the interfacial behaviour. Chapters 4 and 5 provide an extensive description of transport phenomena in viscoelastic and viscoplastic fluids, respectively, with focus on the transport of momentum and energy. In Chap. 6, the dynamics of colloidal particles

suspended in a liquid medium is reviewed, while Chap. 7 provides an overview of the phenomenology of complex fluids with free surfaces. Finally, Chap. 8 introduces advanced, mesh-free numerical methods particularly suitable to model complex fluids from the macro- to the meso-scale.

The book is addressed to research scientists and professionals, engineers, R&D managers and graduate students in the fields of Engineering, Chemistry, Biology, Medicine, Applied and Fundamental Sciences, and can be used as support textbook in graduate and postgraduate courses in complex fluids or non-Newtonian fluid dynamics.

This book is dedicated to our lovely Mothers.

Liverpool, UK   Volfango Bertola
Nantes, France   Teodor Burghelea

Contents

Introduction to Transport Phenomena in Complex Fluids

Volfango Bertola

Abstract This chapter provides an overview of transport phenomena in fluids with complex microstructure. The first section reviews the general conservation equations, with focus on the issues arising when they are applied to complex fluids. The second section introduces different types of elementary constituents of complex fluids (polymers, surfactants and colloids).

1 Transport Phenomena

1.1 Advection and Diffusion

Simple transport processes (transport of mass, momentum and thermal energy) are described by the following conservation equation:

$$\alpha \frac{\partial \phi}{\partial t} + \nabla \cdot \mathbf{J}_\phi = 0 \tag{1}$$

where α is a phenomenological coefficient, ϕ is the characteristic potential of the transport process under consideration and $\mathbf{J}_\phi$ is the corresponding flux density. In the case of transport by *advection*, i.e. passive entrainment by the carrying fluid, the flux density is expressed as follows:

$$\mathbf{J}_\phi = \phi \mathbf{u} \tag{2}$$

where $\mathbf{u}$ is the fluid velocity. In the case of transport by *diffusion*, i.e. transport at molecular level, Eq. (1) is usually completed by linear constitutive equations (Fick's law, Newton's law and Fourier's law, respectively), which define the phenomenological relationship between flux densities and the generalized forces expressed in

---

V. Bertola (✉)
School of Engineering, University of Liverpool, Liverpool, UK
e-mail: Volfango.Bertola@liverpool.ac.uk

the form of potential field gradients characteristic of each process, i.e. concentration gradient, velocity gradient and temperature gradient (Bird et al. 2007; Leal 2007):

$$\mathbf{J}_\phi = -\lambda \nabla \phi = \lambda \mathbf{F}_\phi \tag{3}$$

where λ is a phenomenological coefficient and $\mathbf{F}_\phi$ is the generalized force inducing the flow. The combination of Eqs. (1) and (3) leads to the well-known diffusion equation:

$$\alpha \frac{\partial \phi}{\partial t} = \frac{\lambda}{\alpha} \nabla^2 \phi \tag{4}$$

It can be shown that Eq. (4) can be expressed in Liouville's form (i.e. as a continuity equation), after introducing a suitable intrinsic velocity, $\mathbf{u}_\phi$, of the transport process under consideration (Bertola and Cafaro 2010):

$$\begin{aligned} \frac{\partial \phi}{\partial t} + \nabla \cdot (\phi \mathbf{u}_\phi) &= 0 \\ \mathbf{u}_\phi &= -\beta \nabla (\ln \phi) \end{aligned} \tag{5}$$

The introduction of this formalism provides a straightforward proof of the equivalence between the diffusion equation and other well-known equations of mathematical physics, such as the Burgers equation and the Kardar–Parisi–Zhang equation (Bertola and Cafaro 2007).

Linear constitutive equations are particular cases of more general phenomenological relationships between flux densities and forces:

$$\mathbf{J}_\phi = \lambda |\mathbf{F}_\phi|^r \frac{\mathbf{F}_\phi}{|\mathbf{F}_\phi|} \tag{6}$$

Examples of nonlinear phenomenological relationships are the Ostwald–de Waele constitutive equation for non-Newtonian flows, and the constitutive equation derived from the Prandtl–Taylor analogy used in modelling turbulent flows (Bird et al. 2007; Leal 2007).

1.2 Generalized Conservation Equations (Multifield Approach)

Conservation equations state that the evolution in time of a given specific quantity, ρQ, is due to the contributions of its flux, $\mathbf{J}$, and of its generation (or destruction) rate, S, which correspond to a divergence term and to a source term, respectively. Thus, they can be written in compact form (Banerjee and Chan 1980) as follows:

Table 1 Meaning of the symbols Q, $\mathbf{J}$ and S used throughout Eqs. (7)–(14) $\mathbf{u}$ is the velocity, $\mathbf{I}$ is the Kronecker tensor, p is pressure, $\mathbf{\Sigma}$ is the stress tensor, $\mathbf{F}$ is the body force, e_i is the internal energy and q is the heat flux. By replacing Q, $\mathbf{J}$ and S with the appropriate quantities, one obtains the different conservation equations (either local and instantaneous or averaged)

Quantity	Q	$\mathbf{J}$	S
Mass	1	0	0
Momentum	$\mathbf{u}$	$p\mathbf{I} - \mathbf{\Sigma}$	$\mathbf{F}$
Energy	e_i	$q + \mathbf{u} \cdot (p\mathbf{I} - \mathbf{\Sigma})$	$\mathbf{F} \cdot \mathbf{u}$

$$\frac{\partial \rho Q}{\partial t} + \nabla \cdot (\rho \mathbf{u} Q) = -\nabla \cdot \mathbf{J} + \rho S \tag{7}$$

where ρ is density, $\mathbf{u}$ is the fluid velocity and the values for Q, $\mathbf{J}$ and S are given in Table 1.

These equations hold inside each domain V_k, so that one obtains a set of conservation equations in differential form:

$$\frac{\partial \rho_k Q_k}{\partial t} + \nabla \cdot (\rho_k \mathbf{u}_k Q_k) = -\nabla \cdot \mathbf{J}_k + \rho_k S_k \tag{8}$$

In order to put the problem into a treatable form, the local conservation equations are averaged over the control volume and then ensemble averaged; the two operations can be inverted without changing the final result (Delhaye and Achard 1977). Here, averages are performed according to the following standard procedure (Banerjee and Chan 1980), where ensemble (spatial) averaging is denoted by angle brackets, and overbars indicate time-averaged quantities:

$$\frac{1}{V} \int_{V_k} \left\{ \frac{\partial \rho_k Q_k}{\partial t} + \nabla \cdot (\rho_k \mathbf{u}_k Q_k) \right\} dV = \frac{1}{V} \int_{V_k} \{ -\nabla \cdot \mathbf{J}_k + \rho_k S_k \} dV \tag{9}$$

Using the Leibniz rule[1] and to the Gauss theorem,[2] one obtains

---

[1]Leibniz rule:

$$\frac{\partial}{\partial t} \int_{V(\mathbf{x},t)} F dV = \int_{V(\mathbf{x},t)} \frac{\partial F}{\partial t} dV + \int_{\partial V(\mathbf{x},t)} F(\mathbf{u} \cdot \mathbf{n}) dA$$

It is analogous to the Reynolds transport theorem.

[2]Gauss theorem:

$$\int_{V(\mathbf{x},t)} (\nabla \cdot \mathbf{F}) dV = \nabla \cdot \int_{V(\mathbf{x},t)} \mathbf{F} dV + \int_{\partial V(\mathbf{x},t)} (\mathbf{F} \cdot \mathbf{n}) dA$$

If V does not depend explicitly on $\mathbf{x}$, the first term on the r.h.s. vanishes.

Fig. 1 Example of two-field
modelling and notation used
throughout this section
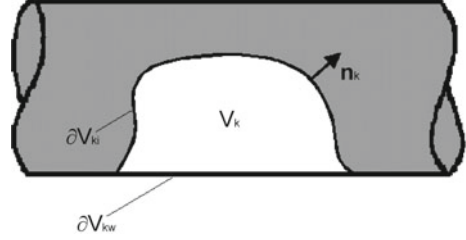
$$\frac{\partial \epsilon_{k,3} \langle \rho_k Q_k \rangle_{V_k}}{\partial t} + \nabla \cdot \epsilon_{k,3} \langle \rho_k \mathbf{u}_k Q_k \rangle_{V_k} = \epsilon_{k,3} \langle \rho_k S_k \rangle_{V_k} +$$
$$- \frac{1}{V} \int_{\partial V_{ki}} \mathbf{n}_k \cdot [(\mathbf{u}_k - \mathbf{u}_i)\rho_k Q_k + \mathbf{J}_k] dA - \frac{1}{V} \int_{\partial V_{kw}} (\mathbf{n}_k \cdot \mathbf{J}_k) dA \qquad (10)$$

where $\epsilon_{k,3}$ is the volume fraction occupied by the k-th domain, $\mathbf{n}_k$ is the outward unit vector normal to the domain boundary, ∂V_{ki} is the part of the domain boundary in contact with other domains (interfacial boundary), ∂V_{kw} is the part of the domain boundary in contact with the wall, $\mathbf{u}_k$ and $\mathbf{u}_i$ are the domain and the interface velocities, respectively; an example of averaging volume containing two domains is shown in Fig. 1. Finally, Eqs. (10) are ensemble averaged:

$$\overline{\frac{\partial \epsilon_{k,3} \langle \rho_k Q_k \rangle_{V_k}}{\partial t} + \nabla \cdot \epsilon_{k,3} \langle \rho_k \mathbf{u}_k Q_k \rangle_{V_k}} = \overline{\epsilon_{k,3} \langle \rho_k S_k \rangle_{V_k}} +$$
$$\overline{- \frac{1}{V} \int_{\partial V_{ki}} \mathbf{n}_k \cdot [(\mathbf{u}_k - \mathbf{u}_i)\rho_k Q_k + \mathbf{J}_k] dA - \frac{1}{V} \int_{\partial V_{kw}} (\mathbf{n}_k \cdot \mathbf{J}_k) dA} \qquad (11)$$

Double averaging ensures the continuity of first derivatives, which otherwise might be discontinuous; this could happen, for instance, in certain regions where field interfaces move in a deterministic manner in time or are stationary, where ensemble averaging alone leads to discontinuities.

Interface conditions Across the domain boundary, it is necessary to impose the conservation of fluxes:

$$\sum_k \frac{1}{V} \int_{\partial V_{ki}} \mathbf{n}_k \cdot [(\mathbf{u}_k - \mathbf{u}_i)\rho_k Q_k + \mathbf{J}_k] dA = 0 \qquad (12)$$

Since the calculation of fluxes at the interface is not easy, sometimes it is preferable to cancel this term by adding up together the conservation equations in adjacent domains, obtaining the so-called mixture models:

$$\sum_k \left\{ \frac{\partial}{\partial t} \left(\overline{\epsilon_{k,3} \langle \rho_k Q_k \rangle_{V_k}} \right) + \nabla \cdot \overline{\epsilon_{k,3} \langle \rho_k \mathbf{u}_k Q_k \rangle_{V_k}} + \nabla \cdot \overline{\epsilon_{k,3} \langle \mathbf{J}_k \rangle_{V_k}} \right\} =$$

$$= \sum_k \left\{ \overline{\epsilon_{k,3} \langle \rho_k S_k \rangle_{V_k}} - \overline{\frac{1}{V} \int_{\partial V_{kw}} (\mathbf{n}_k \cdot \mathbf{J}_k) dA} \right\} \qquad (13)$$

Although Eqs. (13) look simpler than Eqs. (11), all the information regarding the interfaces have been lost. On the other hand, the interface behaviour is essential in describing such phenomena as phase transitions or chemical reactions; thus, it is necessary to reintroduce into the model the lost information, by means of the so-called closure relationships.

Closure relationships The averaged conservation equations alone cannot be solved, even with the appropriate interface and boundary conditions, because their number is smaller than the number of unknowns. This happens because while double averaging the conservation equations allows reducing two-phase flow modelling to a mathematically treatable problem, at the same time it erases the local and instantaneous details, which must be reintroduced into the model by means of the so-called closure relationships or constitutive equations. These relationships provide additional equations in a sufficient number to equal the number of unknowns in order to 'close' the problem; they include equations of state, stress–deformation relationships, etc., and are often empirical or semi-empirical. Most closure relationships are flow-regime dependent, so that the overall accuracy decreases if they are applied to different flow patterns. A discussion on the different ways to solve the closure problem is presented, for instance, in Yadigaroglu and Lahey (1976). Closure relationships are usually sorted into two categories: interface closures, if they relate quantities across the domain boundary, and internal closures, if they relate quantities inside a domain.

Interface closures involve mass, momentum and energy fluxes at the interfaces between contiguous domains and between the domains and the pipe walls (the mass flux and the energy flux vanish for impermeable and adiabatic walls, respectively). For example, in case of evaporation or condensation, the mass flux at the interface is related to the heat flux by the phase transition heat, Δh_{LG}:

$$\left| \frac{1}{V} \int_{\partial V_{ki}} \rho_k \mathbf{n}_k \cdot (\mathbf{u}_k - \mathbf{u}_i) dA \right| = \frac{1}{\Delta h_{LG}} \left| \frac{1}{V} \int_{\partial V_{ki}} \rho_k (\mathbf{n}_k \cdot \mathbf{q}_k) dA \right| \qquad (14)$$

The main problems in developing interface closures arise due to the fact that the interface geometry is generally very complex. As to wall conditions, the problem often reduces to the calculation of shear stresses, for which single-phase flow correlations are used.

Besides interface closures, more equations can be specified inside the domain, such as the equations of state. In particular, relations expressing the average value of the product of fluctuating quantities are required: in fact, in Eq. (10), one can find terms like $\langle \rho_k \mathbf{u}_k \rangle$ and $\langle \rho_k \mathbf{u}_k \mathbf{u}_k \rangle$, which are analogous to Reynolds stresses in turbulent flows. In two-phase flow, these quantities are even more difficult to be described,

because their fluctuations with respect to the mean value depend both on the turbulence inside each domain, and on the distribution of the phases over the averaging volume: although there is a strong reciprocal interaction between turbulence and flow pattern, their length scales are very different, so that modelling Reynolds stress-like quantities is not trivial.

1.3 Complex Fluids Versus Simple Fluids

The solution of the transport equations outlined in Sects. 1.1 and 1.2 strongly depends on the fluid structure, modelled through appropriate constitutive equations, and, in particular, on the *characteristic length*, i.e. the typical size of the fluid elementary constituents, and on the *relaxation time*, which is the time necessary to return to thermodynamic equilibrium after the fluid has been perturbed.

In simple fluids (also called molecular fluids), the characteristic length is of the order of molecular length scales (10^{-10}–10^{-9} m), and the relaxation time is of the order of the timescale of thermal fluctuations ($\approx 10^{-15}$ s). Thus, simple fluids respond almost instantaneously to an external forcing, such as an applied stress or deformation. In complex fluids, both the characteristic length and the relaxation time can range over several orders of magnitude, depending on the size, shape and stiffness of their elementary constituents, and on the short- and long-range interactions arising among them. The qualitative chart displayed in Fig. 2 shows a comparison among fluids with different micro-structures based on these two fundamental parameters.

Whilst the behaviour of simple fluids is adequately described by linear phenomenological models, such as Fick's Law, Newton's Law and Fourier's Law, fluids with complex microstructure often require sophisticated phenomenological models that introduce strong nonlinearities in the conservation equations; in the case

Fig. 2 Characteristic space- and timescales of complex fluids
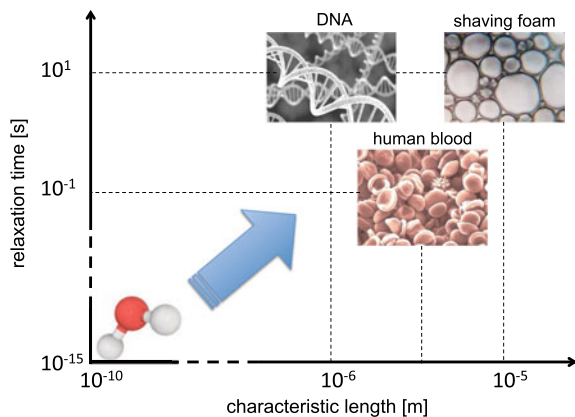
of the equation of motion (momentum equation), these constitutive nonlinearities supplement the inertial nonlinearity characteristic of simple fluids at high Reynolds numbers.

2 Complex Fluids

2.1 Polymers

Polymers are high molecular weight molecules constituted by a large number of units, called monomers, connected by covalent bonds. A common example is polyethylene, $(C_2H_6)_n$, where the basic ethylene unit is repeated n times to form a long linear chain. Other common polymer structures are branched chains and chain networks.

Because of their structure, polymer molecules have a very large number of internal degrees of freedom, corresponding to rotations of C–C bonds[3]; thus, the same molecule can exhibit different instantaneous spatial arrangements, or *conformations*, which can be visualized schematically as a smoothed line segment. The longest sequence of monomers that behaves like a rigid rod defines the persistence length, L_p, which is a function of the backbone stiffness and electric charges distributed along the polymer chain. Thus, a simple way to describe linear chain polymers is to break down the chain into N segments represented by the position vectors of their end points, $\mathbf{a}_i$ $(i = 0...N)$, as shown in Fig. 3.

The end-to-end vector, $\mathbf{R} = \mathbf{a}_N - \mathbf{a}_0$, gives a measure of the actual molecule size; averaging over all molecules yields the root-mean-square end-to-end distance:

$$R_F = \sqrt{\langle \mathbf{R}^2 \rangle} = \sqrt{\langle (\mathbf{a}_N - \mathbf{a}_0)^2 \rangle} \tag{15}$$

A second quantity commonly used to measure the polymer molecule size is the *radius of gyration*, or the root-mean-square distance between the joints between consecutive vectors (Fig. 3) and the centre of mass. If the position of the centre of mass is indicated by vector $\mathbf{a}_G$, the radius of gyration can be calculated as follows:

$$R_g = \sqrt{\left\langle \frac{1}{N+1} \sum_{i=0}^{N} (\mathbf{a}_N - \mathbf{a}_G)^2 \right\rangle} = \sqrt{\frac{1}{N+1} \sum_{i=0}^{N} \langle (\mathbf{a}_N - \mathbf{a}_G)^2 \rangle} \tag{16}$$

In real polymer chains, two monomers cannot overlap, even partially, and occupy the same space; thus, a number of conformations that are ideally possible cannot be realized physically. This effect is known as the *excluded volume*, and has important consequences on the physics of polymer solutions (Strobl 1997; Teraoka 2002).

---

[3]Other internal degrees of freedom correspond to stretching of covalent bonds and oscillations of valence angles; however, their small amplitudes do not affect the molecule shape significantly.
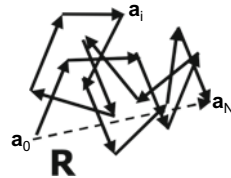
Because of excluded volume, real chains are bigger than ideal chains; in particular, for ideal chains $R_g \propto (N-1)^{1/2}$, while for real chains $R_g \propto (N-1)^{3/5}$ (Flory 1953).

The length of a polymer chain is, of course, proportional to its molecular weight. However, any polymer sample is a mixture of molecules with different degrees of polymerization, and monodisperse polymers (those with a single molecular weight) are exceptions. Polymers are usually polydisperse, and therefore their molecular weight is always the average value of a certain molecular weight distribution. If the polymer consists of n_i chains of exact molecular weight M_i, one can define a number-average molecular weight as

$$M_n = \frac{\sum_i n_i M_i}{\sum_i n_i} \qquad (17)$$

and a weight-average molecular weight as

$$M_w = \frac{\sum_i n_i M_i^2}{\sum_i n_i M_i} \qquad (18)$$

The ratio of Mw to Mn, called polydispersity index (PDI), is often used to express how polydisperse the polymer sample is

$$PDI = \frac{M_w}{M_n} = \frac{\sum_i n_i \sum_i n_i M_i^2}{\left(\sum_i n_i M_i\right)^2} \qquad (19)$$

Many complex fluids are solutions of polymer molecules in a Newtonian solvent. While in the solid state, polymer molecules pack the space either in a regular array (crystalline phase) or at random (amorphous phase), in solutions each polymer molecule interacts with the surrounding solvent molecules, and may exhibit different conformations depending on the concentration.

For a given polymer, there are solvents that dissolve the polymer well (called *good solvents*), solvents that do not dissolve the polymer at all (called *nonsolvents*) and solvents with intermediate properties (called *poor solvents*) which can dissolve the polymer only up to a limited concentration. Tables of solvents and nonsolvents for different polymers can be found in the reference literature (Brandrup et al. 2005). In a good solvent, the solvent molecules impregnate the polymer coil, which swells increasing its volume; the solution remains clear and uniform even at concentrations
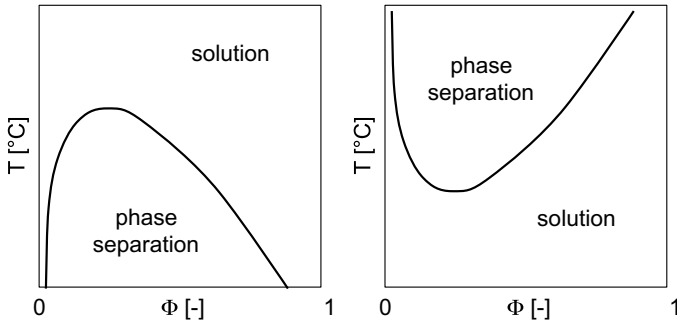
Fig. 4 Examples of phase diagrams of polymer solutions in temperature versus volume fraction coordinates. Left: phase diagram with upper critical temperature; right: phase diagram with lower critical temperature

as high as 100%. In a poor solvent, there is little affinity between the solvent molecules and the polymer coil, which, therefore, crumples reducing its volume. If a small amount of a nonsolvent is added to a polymer solution in a good solvent, the polymer precipitates as the nonsolvent mixes with the good solvent.

The quality of the solvent for a given polymer is strongly dependent on temperature. Thus, one can draw phase diagrams on the temperature versus volume fraction coordinate plane (Fig. 4) to identify the conditions to have a homogeneous solution and those to have phase separation. The qualitative phase diagrams of Fig. 4 indicate that at low volume fractions one has a stable solution over a large range of temperatures. For each polymer solution, there is a particular temperature, called the *theta temperature*, for which the solvent is poor just enough to compensate exactly the increase of the coil size due to the excluded volume effect. In this condition, the solution is called a *theta solution*, and polymer coils behave like ideal chains. For a rigorous thermodynamic analysis of the stability of polymer solutions, one can refer to Teraoka (2002).

A single polymer molecule interacting with the solvent takes a random coil conformation in order to maximize its conformational entropy, which is representative of the number of conformations with equivalent energy that is accessible to the polymer chain at a given temperature, and is defined as $S = k_B \ln(\omega)$, where k_B is Boltzmann's constant and ω is the total possible number of chain conformations. In the case of an ideal chain, one finds (de Gennes 1979)

$$S(\mathbf{R}) = S(0) - \frac{3R^2}{2\langle R^2 \rangle} \tag{20}$$

Equation (20) suggests that the more extended the chain, the lower its entropy, because an extended chain can adopt a fewer number of possible configurations as compared with the numerous possible equivalent conformations of a polymer coil. It can be shown that the variation of conformational entropy is equal to the
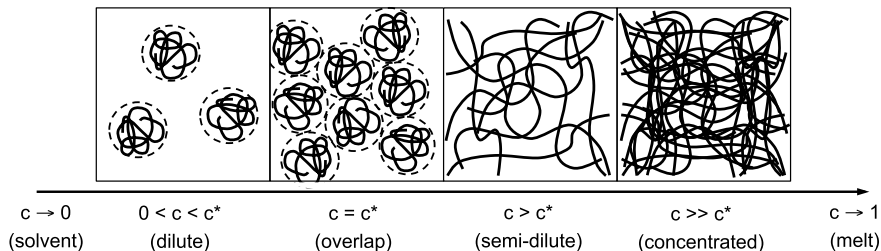
Fig. 5 Schematic illustration of the structure of polymer solutions as a function of the polymer concentration

conventional macroscopic entropy, $dS = \delta Q / T$, where δQ is the heat exchanged between the polymer chain and the environment, and T is temperature (Kittel and Kroemer 1980).[4]

If the polymer coil is stretched, for example, because of an applied stress or deformation, it reduces its conformational entropy, and therefore as soon as the constraint is removed, it will return to a maximum entropy conformation. This physical mechanism results into the viscoelastic behaviour of polymer solutions observed macroscopically, which is discussed in chapter "Transport Phenomena in Viscoelastic Fluids".

Figure 5 shows schematically the structure of polymer solutions as a function of the polymer concentration. At low concentrations, polymer coils are far from one another, i.e. the average distance between two polymer coils is much larger than their size, which defines the so-called *dilute solutions*. Thus, there are no interactions among polymer coils, which can be regarded as particles suspended in the fluid, and the solution viscosity can be estimated using Einstein's relationship for hard sphere suspensions:

$$\eta = \eta_s (1 + 2.5 \Phi + \ldots) \tag{21}$$

where η_s is the viscosity of the pure solvent and Φ is the particle's volume fraction. One can also introduce a *specific viscosity*, or the ratio between the incremental viscosity and the solvent viscosity:

$$\eta_{sp} = \frac{\eta - \eta_s}{\eta_s} \tag{22}$$

and an *intrinsic viscosity*, defined as

$$[\eta]_0 = \lim_{c \to 0} \frac{\eta - \eta_s}{c \eta_s} \tag{23}$$

---

[4]One can verify empirically the equivalence of conformational entropy and macroscopic entropy by stretching an elastic rubber band. If the stretched rubber band is placed above the upper lip, where skin is most sensitive, and the pulling force is released, one feels cold: the stretched polymers return to a coiled conformation, and therefore increase their entropy, absorbing heat.

where c is the polymer mass concentration. The intrinsic viscosity is often calculated using the Mark–Houwink correlation:

$$[\eta]_0 = A \times M^b \tag{24}$$

where M is the molecular weight of the polymer, and A and b are empirical constants.[5]

As the polymer concentration is increased, the average distance between two coils progressively reduces until, at a critical concentration value c^* (the *overlap concentration*), it becomes approximately equal to the average size of coils, and the whole volume of the solution is packed with polymer coils. The overlap concentration can be calculated as follows:

$$c^* = \frac{1}{[\eta]_0} \tag{25}$$

Above the overlap concentration, interactions among polymer coils cannot be neglected, especially for those monomers located on the outer surface of the coil. In particular, electrostatic or hydrogen bonds between monomers belonging to the same macromolecule might break to form new bonds between monomers belonging to different chains. As a result, polymer coils unfold, and the solution structure appears as a network of overlapped and entangled polymer chains, characteristic of *semi-dilute solutions*, as illustrated schematically in Fig. 5. The change in the solution structure corresponds to a significant increase of viscosity, because the chain mobility is greatly reduced compared with the chains in dilute solutions; while in dilute solutions $\eta \propto c$, in semi-dilute solutions $\eta \propto c^2$.

At a higher concentration c^{**}, the solution enters the so-called *concentrated regime* in which each segment of the polymer chain does not have a sufficient space available. Typically, the volume fraction of the polymer at c** is between 0.2 and 0.3.

2.2 Surface-Active Agents (Surfactants)

Surfactants are molecules composed of a hydrophilic head group and a hydrophobic tail group. In other words, this means one side of the surfactant molecule has an affinity for the continuous phase (lyophilic), and the other side is incompatible with the continuous phase (lyophobic); overall, the surfactant molecule is amphiphilic (or amphipathic), i.e. it shows an affinity for different fluids at both ends.

The chemical structures suitable to act as either lyophilic or lyophobic sides of a surfactant molecule vary with the nature of the continuous phase (the solvent). If the solvent is a polar liquid such as water, which represents the most common case in practical applications, the lyophilic (hydrophilic) head is highly polar or ionic, while the lyophobic (hydrophobic) tail can be a hydrocarbon, fluorocarbon,

---

[5]For example, for polyethylene oxide $A = 0.0125$ and $b = 0.78$ (Brandrup et al. 2005).

perfluorocarbon or siloxane chain (Rosen 1978). In particular, the hydrophilic head can have different nature:

- *Cationic*, if the hydrophilic head has a positive charge;
- *Anionic*, if the hydrophilic head has a negative charge;
- *Non-ionic*, if the hydrophilic head has no apparent ionic charge;
- *Zwitterionic*, if the hydrophilic head has both positive and negative charges;
- *Amphoteric*, if the hydrophilic head can have either positive or negative charge depending on the pH of the solvent.

The hydrophobic tail can have a range of different structures; however, differences are less marked than in the case of the hydrophilic group. Usually, one can observe linear or branched hydrocarbon chains, or less frequently double chains or gemini structures where two surfactant molecules are joint in correspondence of their hydrophilic heads.

The relative strength of the hydrophilic and hydrophobic parts of a surfactant molecule is expressed by the hydrophilic to lipophilic balance (HLB), which can be calculated based on the molecular weight (Griffin 1949, 1954):

$$HLB = 20\frac{M_h}{M} \tag{26}$$

where M_h is the molecular weight of the hydrophilic head and M that of the whole surfactant molecule. An alternative approach to calculate the HLB number is to attribute different values to specific chemical groups in the molecule (Davies 1957). Low values of the HLB number indicate the hydrophobic tail outweighs the hydrophilic head, and vice versa high values indicate the surfactant behaviour is dominated by the hydrophilic part. Thus, the HLB number can be used to determine the solubility of a given surfactant in water, and the characteristics of oil–water emulsions containing it (see Table 2). Despite the use of the HLB number as a method to characterize surfactant systems has become common practice in academia as well as in the surfactant industry, one must keep in mind it leads to purely indicative conclusions, because it accounts only for the properties of the surfactant molecule rather than those of the whole system under consideration.

Table 2 Solubility in water and emulsion morphology obtained within different ranges of the HLB number

HLB number	Solubility in water	Emulsion morphology
1–4	Insoluble	Water in oil
4–7	Poor dispersion	Water in oil
7–9	Stable opaque dispersion	–
10–13	Hazy solution	Oil in water
>13	Clear solution	Oil in water
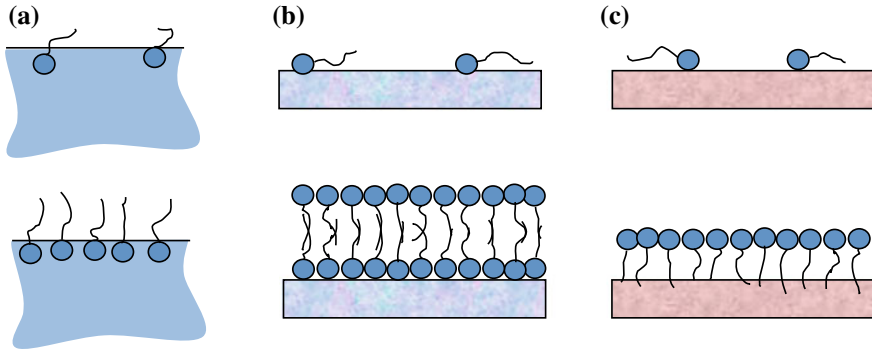
Fig. 6 Schematic picture of surfactant adsorption at fluid–fluid interfaces (**a**), on hydrophilic (**b**), and on hydrophobic surfaces (**c**), for low (top) and high (bottom) bulk concentrations

When surfactants are present in a fluid system at low concentration, they tend to adsorb onto free surfaces or interfaces between any two immiscible phases, oriented according to the affinities of their head and tail groups. When surfactants accumulate at an interface, they reduce its energy level, making it more thermodynamically stable. This makes surfactants essential components in several formulations, including inks, dyes, lubricants, gellants, paints and many others. Figure 6 displays examples of surfactant adsorption at fluid–fluid interfaces, hydrophilic surfaces and hydrophobic surfaces, at both low and high bulk concentrations. Remarkably, on hydrophilic surfaces, one can observe the formation of a double layer to ensure hydrophilic heads are exposed to the solvent.

A relation between the bulk surfactant concentration, C, and the surfactant adsorption, C^S, is provided by the Langmuir adsorption isotherm (Langmuir 1918):

$$C^S = C^S_\infty \frac{C}{C + a} \tag{27}$$

where C^S_∞ is the maximum possible adsorption at the surface when $C \to \infty$ and a is a constant which can be related to the energy of adsorption per molecule. Equation (27) can be generalized to account for the interaction between the adsorbed surfactant molecules and, in case of ionic surfactant, for the electrostatic energy of the surfactant ions (Borwankar and Wasan 1988). Other types of adsorption isotherms can be obtained based on various equations of state (Jho and Burke 1983; van Hunsel et al. 1986; Fainerman and Miller 1995). Figure 7 displays an example of adsorption isotherm as a function of the bulk concentration, together with sketches of typical surfactant distributions observed at different surfactant concentrations.

In general, surfactant adsorption occurs in two stages: (i) diffusion of surfactant from the bulk solution to the region near the interface and (ii) transfer of the surfactant molecules from this region to the interface. Thus, depending on the relative kinetics of the two stages, one can observe diffusion-controlled adsorption, where the surfactant

Fig. 7 Qualitative adsorption curve of a surfactant onto a hydrophilic surface as a function of the bulk concentration

Log surfactant concentration
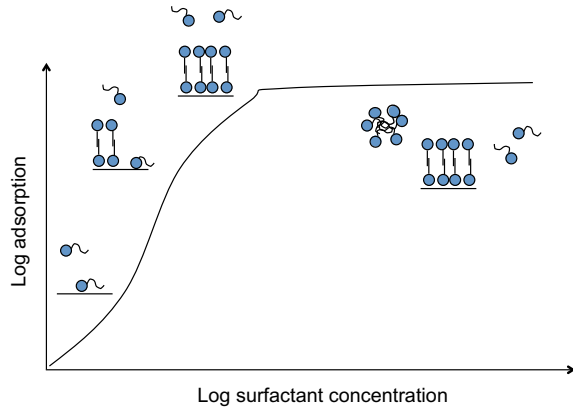
diffusion is much slower than the second stage, and hence determines the rate of adsorption, and barrier-controlled adsorption, where the second stage is much slower than diffusion due to the presence of some kinetic barrier, which slows down the transfer of the surfactant molecules from the region near the interface to the adsorption monolayer. The adsorption kinetics may also be affected by electrostatic interactions in case of ionic surfactants and, if surfactant aggregates are present in the bulk, by reactions of aggregate formation and decay.

When the surface or interface is nearly at maximum coverage, molecules begin to aggregate in the bulk phase to minimize further free energy. This occurs at a well-defined concentration, specific to each surfactant-fluid system, known as the critical micellar concentration (CMC). Above the CMC, the system then consists of an adsorbed monomolecular layer at the interface, and of free monomers and surfactant aggregates (micelles) in the bulk, with all these three states in equilibrium (see the sketch in Fig. 7).

Typically, micelles are clusters of ∼50–∼200 surfactant molecules, whose size and shape are governed by geometric and energetic considerations (Israelachvili 2011). These self-assembled aggregates are structured in such a way so as to expose the lyophilic (hydrophilic) part to the solvent, and to conceal the lyophobic (hydrophobic) part inside, and therefore their shape is usually spherical or rod like, as shown in Fig. 8a. If micelles are highly packed, they may rearrange into ordered structures, generating hexagonal or lamellar phases (Fig. 8b).

The phase behaviour of a given surfactant system can be usefully portrayed in binary or ternary phase diagrams, such as the example shown in Fig. 9a, which displays the occurrence of different phases as a function of temperature and of the surfactant concentration, for a well-known surfactant system, sodium dodecyl sulphate–water (Kékicheff et al. 1989). Since surfactant phases can be strongly anisotropic, such as in the case of hexagonal or lamellar phases, they may affect significantly the behaviour of surfactant systems in shear flow; in particular, the transition from an isotropic phase (e.g. a dispersion of spherical micelles) to a lamellar phase (or vice versa) can change the apparent shear viscosity of the system of orders
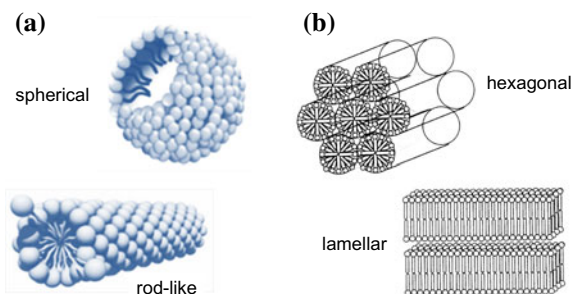
Fig. 8 Examples of surfactant aggregates or micelles (**a**), and examples of surfactant phases (**b**)
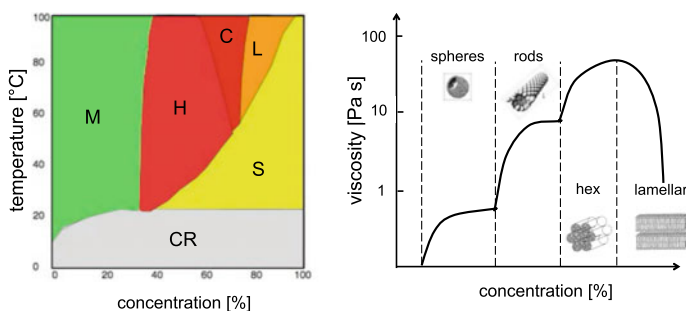
Fig. 9 Binary phase diagram of the sodium dodecyl sulphate–water system (Kékicheff et al. 1989) displaying: micelles, M; hexagonal phase, H; cubic phase, C; lamellar phase, L; phase separation, S; crystal phase, CR (**a**). Qualitative plot of shear viscosity as a function of surfactant concentration (**b**)

of magnitude, as shown in the example given in Fig. 9b, where viscosity drops in the transition from hexagonal packing to lamellar phase because in the latter the surfactant bilayers can shear on each other with the solvent acting as a lubricant.

The transition from isotropic to non-isotropic phases in surfactant systems may occur even without changing the structure of surfactant aggregates; sometimes, it is sufficient a change in the micelle conformation under shear flow. Shear-induced phase transitions are very common in liquid crystals and worm-like micellar solutions (Fischer and Callaghan 2001; Cates and Fielding 2006). For example, a surfactant system containing rod-like micelles with large aspect ratio will appear isotropic at zero or low shear rates; however, at high shear rates, micelles will align parallel to the flow direction, inducing a transition to a nematic phase.

Interfacial behaviour of surfactant solutions Interfaces between two immiscible fluids represent a boundary across which there is a more or less abrupt change of the fluid structure, and, in particular, of the intermolecular forces characteristic of the two phases. To compensate this difference, an interfacial tension arises in the interfacial region; in the case of interfaces between a liquid and a gas, where intermolecular interactions are negligible, this is called the *surface tension*. Although fluid interfaces
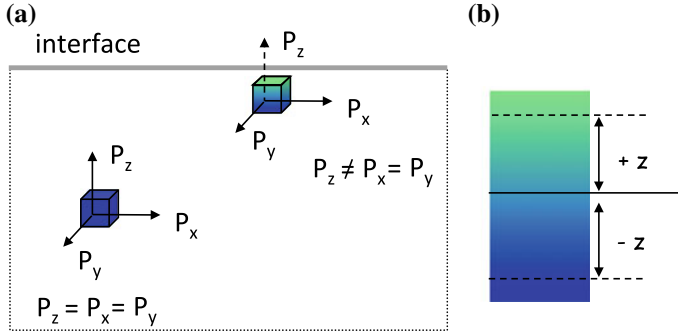
Fig. 10 Schematic description of pressure anisotropy on a fluid element near the surface as opposed to one in the bulk fluid (**a**), and normal cross section of a real fluid interface displaying the mutual diffusion layer (**b**)

are usually represented as mathematical surfaces with no thickness, in reality, they can be identified with a layer of small but finite thickness where the two fluids mix due to Brownian diffusion.

From the point of view of classical mechanics, surface tension is understood as a pressure anisotropy. With reference to Fig. 10a, pressure is isotropic in the bulk fluid, i.e. $p_x = p_y = p_z$; however, the presence of the surface creates a local anisotropy, and therefore near the surface $p_x = p_y \neq p_z$. Integrating the difference between the tangential and normal pressure components over the interface thickness, $2z$ (i.e. the thickness of the mutual diffusion layer, see Fig. 10b), yields the surface tension:

$$\gamma = \int_{-z}^{+z} |p_n - p_t| \, d\xi \qquad (28)$$

where $p_t = p_x = p_y$ and $p_n = p_z$. Equation (28) shows its dimensions are force per unit length.

From the point of view of thermodynamics, surface tension represents a Gibbs excess property of the interface, namely, the energy per unit area of the interface. Since energy is an extensive quantity, the surface energy is proportional to the surface area; the larger the area, the larger the number of molecules that must be extracted from the bulk to create the new surface, which requires more work against the intermolecular forces. If increasing the surface requires work, then in the plane tangent to the surface there is a force opposing the expansion and perpendicular to the surface boundary, as shown schematically in Fig. 11a. For a homogeneous surface, the force per unit length is constant, and if a boundary of length L moves over a distance dx in the direction of the force, the work required to increase the surface area is

$$dW = \gamma L dx = \gamma dA \qquad (29)$$

The Gibbs free energy of the surface then writes (Gibbs 1961):
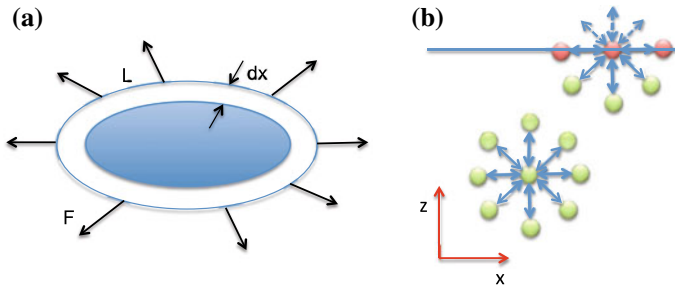
Fig. 11 Work of forces acting on the boundary of a fluid interface (**a**), and schematic description of molecular interactions in the bulk fluid and at the interface (**b**)

$$dG = -SdT + pdV + \gamma dA \tag{30}$$

and for a transformation at constant pressure and temperature, surface tension can be defined as

$$\gamma = \left(\frac{dG}{dA}\right)_{T,P} \tag{31}$$

Similarly, the surface tension can be defined in terms of the Helmholtz free energy for a process at constant temperature and volume. A remarkable feature of the thermodynamic approach is that the Gibbs interface is a mathematical surface with no thickness, whereas real surfaces extend over the mutual diffusion layer.

Finally, from the point of view of statistical mechanics surface tension arises from the imbalance of intermolecular forces at an interface, which is represented schematically in Fig. 11b. Thus, surface tension can be computed directly, in principle at least, by adding up all the mutual interactions between molecule pairs, by assuming, for example, a Lennard-Jones interparticle potential. In any case, all statistical mechanics approaches to calculate surface tension take as starting point either Eq. (28), i.e. the classical mechanics definition (Kirkwood and Buff 1949), or Eq. (31), i.e. the thermodynamic definition (Triezenberg and Zwanzig 1972), and express pressure and free energy, respectively, as a function of the intermolecular potential and of the interfacial density profile and the direct correlation function (Hansen and Mc Donald 2013).

The surface tension of liquids decreases monotonically with increasing temperature, because intermolecular forces decrease with an increase of molecular thermal activity. Theoretically, the value of surface tension should become zero at the critical temperature, T_C, since at this temperature, the interface between a liquid and its vapour disappears, although for some liquids the interface disappears a few degrees below the critical temperature. According to the Eötvös correlation, the surface tension decreases with temperature as (Eötvös 1886)

$$\gamma = \frac{k}{V^{\frac{2}{3}}} (T_C - T) \tag{32}$$

where $k = 2.1 \times 10^{-7}$ J/(K·mol$^{2/3}$) is the Eötvös constant and the molar volume, V, is given by the ratio between the molar mass and density.

A direct consequence of interfacial tension is the existence of a pressure difference across any curved interface between two fluids, also known as Laplace pressure (Young 1805; Laplace 1805), which is proportional to the surface curvature according to the Young–Laplace equation:

$$\Delta p = \gamma = \left(\frac{1}{R_1} + \frac{1}{R_2} \right) = -\gamma \nabla \cdot \mathbf{n} \tag{33}$$

where R_1 and R_2 are the principal radii of curvature at a given point of the interface and $\mathbf{n}$ is the unit normal pointing out on the convex side of the interface in the same point. The Laplace pressure is responsible, for example, of the capillary rise of liquids in tubes of small diameter, and of the onset of nucleate boiling at temperatures higher than the saturation temperature of a liquid.

Interfacial tension also determines the orientation of interfaces in the vicinity of a three-phase contact line, which is of exceptional importance in the understanding of wetting phenomena. The balance of interfacial tensions at a solid–liquid–gas contact line yields the contact angle of a liquid drop deposited on a solid surface, θ, defined as the angle between the solid surface and the liquid-air interface on the side of the liquid phase (Young 1805):

$$\gamma_{SG} = \gamma_{SL} + \gamma_{LV} \cos \theta \tag{34}$$

where γ_{SG}, γ_{SL} and γ_{LV} are, respectively, the solid–gas, solid–liquid and liquid–gas interfacial tensions. Although Eq. (34) was originally understood as the balance of three surface tensions, it can be derived more rigorously by interpreting γ_{SG}, γ_{SL} and γ_{LV} as interfacial energies per unit area, and minimizing the total free energy of the system (Gibbs 1961).

When surfactants are adsorbed at fluid interfaces, they lower the value of the surface (or interfacial) tension, according to the Gibbs adsorption equation (Gibbs 1961; Ono and Kondo 1960; Adamson 1976):

$$d\gamma = -k_B T \sum_i C_i^S d \ln C_i \tag{35}$$

where k_B is the Boltzmann constant, T is temperature, C_i and C_i^S are, respectively, the bulk concentration and the surface concentration (adsorption) of the i-th component in the solution; the summation in Eq. (35) is carried out over all components. Integrating Eq. (35), and recalling Eq. (27), yields the Frumkin equation (Frumkin 1925), which relates the interfacial tension of a surfactant solution to the surfactant adsorption:

$$\gamma = \gamma_0 + k_B T \ln \left(1 - \frac{C^S}{C_\infty^S} \right) \tag{36}$$
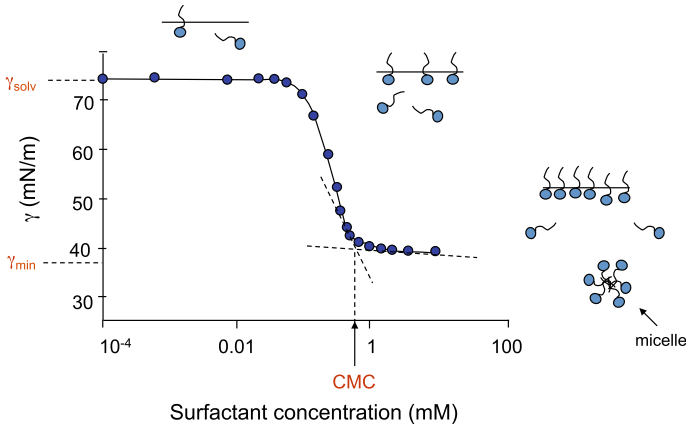
Fig. 12 Surface tension isotherm as a function of surfactant concentration

where γ_0 is the surface tension of the solvent.

Figure 12 displays a typical surface tension isotherm for an aqueous surfactant solution as a function of the bulk surfactant concentration. Adsorption of surfactant molecules at the surface causes an abrupt decrease of surface tension until the bulk concentration reaches the critical micellar value. Above the CMC, surface tension remains practically constant, and one can observe the formation of micellar aggregates in the bulk fluid.

The interface adsorption kinetics of surfactants depends on several factors, including diffusion, adsorption energy barriers, electrostatic interactions, as mentioned in Sect. 2.2. In the case of small surfactants with high mobility and low adsorption energy barrier, the time to migrate to the interface can be as short and 10^{-6} s, whereas for large surfactants, such as polymers and proteins, the migration time may range between 1 second and several days. As an example, one can consider the aqueous solution of a high molecular weight flexible polymer, polyethylene oxide (Glass 1968): at a bulk concentration of 0.001% (w/w), the surface tension is 68 mN/m for a surface age of 30 s; however, one must wait for more than 13 h to reach the equilibrium surface tension of 63.5 mN/m.

Increasing the bulk concentration of surfactant reduces the migration time, because there are more surfactant molecules placed at a shorter distance from the surface. Thus, the time to reach equilibrium varies considerably from system to system, and can be very long in some cases. Figure 13 displays typical surface tension isotherms plotted as a function of time, for different bulk concentrations, as well as a schematic description of the migration process. The time dependence of surface tension at timescales shorter than the time to reach equilibrium implies that besides the concept of equilibrium surface tension, which is an equilibrium thermodynamic property and is time-independent, one must introduce the concept of *dynamic surface tension*, which should not be interpreted in terms of equilibrium thermodynamics.

Fig. 13 Surface tension isotherms plotted as a function of time (top), and sketch of surfactant adsorption process (bottom)
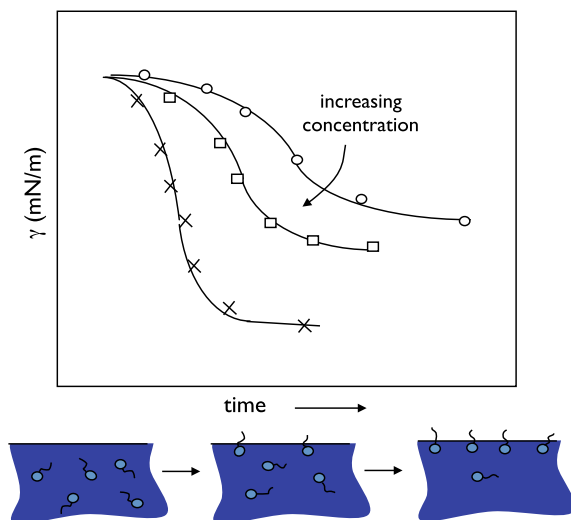
The dynamic surface tension of polymer and surfactant solutions is relevant to those situations where surfaces or interfaces are created at a rate much faster than that of the adsorption kinetics. In these cases, the dynamic surface tension corresponding to a surface age equal to the timescale of the process should be used instead of the equilibrium value. A typical example is the impact of surfactant-laden droplets on solid surfaces, where the free surface of drops expands rapidly during the inertial spreading stage, with a timescale of ∼5 ms (Mourougou-Candoni et al. 1997; Zhang and Basaran 1997).

Dynamic surface tension effects should also be considered when measuring the surface tension of polymer, surfactant or colloidal particle solutions. In fact, depending on the measurement technique used and on the adsorption kinetics, the measured surface tension may not correspond to the equilibrium value, as discussed in Sect. 2 of chapter "Experimental Methods to Characterize Complex Fluids" about surface tension measurement techniques.

2.3   Colloids

Colloids are small particles with size in the range between 1 nm and 1 μm; when colloidal particles are suspended in a continuous medium, such as a fluid, they form a colloidal system. The word colloid comes from the Greek κολλα, which means glue, and reflects the tendency of colloidal particles to irreversibly aggregate because of attractive van der Waals interactions. Due to their intermediate (mesoscopic) size between the atomic scale and the macroscopic scale, colloidal particles are large enough to look at the solvent molecules as a continuum, but small enough to experi-

ence Brownian fluctuations and to consider gravity negligible compared to interparticle and particle–solvent interactions (Einstein 1905). By tuning the interparticles and particle–solvent interactions, colloidal systems can be used to reproduce phenomena occurring at atomic or molecular scale; an example is the identity between the barometric distribution in an ideal gas and the sedimentation profile of a colloidal suspension (Perrin 1910).

Van der Waals forces originate from the interactions between the fluctuating electron distributions of atoms and molecules and are therefore present for any object, including electrically neutral objects. For atomic systems, the van der Waals force scales as $\sim r^6$, where r is the distance between the two atoms; for spherical colloids, similar expression can be derived by integrating over all atomic pair contributions, which yields the following van der Waals potential:

$$U_{vdW}(r) = -\frac{A}{12}\left[\frac{4R^2}{r^2 - 4R^2} + \frac{4R^2}{r^2} + 2ln\left(1 - \frac{4R^2}{r^2}\right)\right] \qquad (37)$$

where r is the distance between the centres of the two particles, R is their radius and A is the Hamaker constant (Israelachvili 2011). In the limit of large distances between colloids, one finds

$$\lim_{r\to\infty} U_{vdW}(r) = -\frac{16}{9}A\left(\frac{R}{r}\right)^6 \qquad (38)$$

while in the limit of very close particles, the interaction potential becomes

$$\lim_{r\to 0} U_{vdW}(r) = -\frac{A}{12}\left(\frac{R}{r - 2R}\right) \qquad (39)$$

Thus, if the particles come close together their attraction becomes rapidly larger than the thermal energy, $k_B T$, which leads to irreversible aggregation. To prevent particles from coming too close to one another, one must envelop each particle with a repulsive shield, which can have either electrostatic nature (*charge stabilization*) or mechanical nature (*steric stabilization*).

Charge stabilization is possible when colloidal particles have ionisable groups on their surface, which dissociate when the particles are suspended in polar solvents. The dissociated ions partially diffuse away in solution due to Brownian motion, but tend to remain near the particle due to Coulomb attraction. Thus, the charged particle is surrounded by a cloud of the dissociated ions and of any other electrolyte present in solution, which forms a *double layer* of ions as shown schematically in Fig. 14a. The charge distribution in the double layer results from the balance between the ions diffusion and the attractive Coulomb force, and generates a potential described by the Debye–Hückel equation:

$$U_C(r) = \frac{(Qe)^2}{4\pi\epsilon\epsilon_0 r}\frac{exp\left[-(r - 2R)/\lambda_{DH}\right]}{(1 + R/\lambda_{DH})^2} \qquad (40)$$

Fig. 14 Schematic of charge stabilization (**a**) and steric stabilization (**b**)
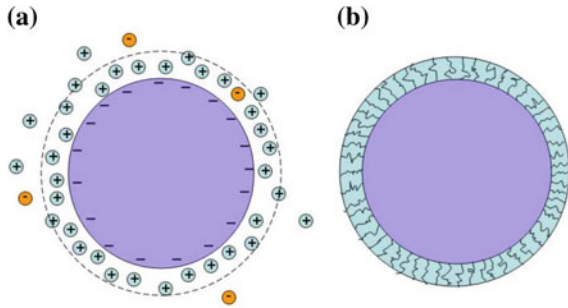
where Q is the number charge per particle, e is the electron charge, ϵ and ϵ_0 are, respectively, the vacuum permittivity and the solvent dielectric constant and λ_{DH} is the Debye–Hückel length, defined as

$$\lambda_{DH} = \sqrt{\frac{\epsilon\epsilon_0 k_B T}{e^2 \sum_i z_i^2 n_i}} \tag{41}$$

where k_B is Boltzmann's constant, T is temperature, z_i is the valence of the i-th ion species and n_i is the corresponding number density; the sum is carried out over all the ion species in solution (Israelachvili 2011). The Debye–Hückel length represents the distance over which the electrostatic repulsion decays, and hence it defines the double layer thickness.

Steric stabilization is obtained by coating the particle surface with a layer of chemically grafted polymer molecules that stretch out into the solvent, as shown schematically in Fig. 14b. This is possible if the polymer is in a good solvent, at a temperature above the theta point (Strobl 1997). When two particles approach each other, the two polymer layers begin to overlap, which reduces the number of possible conformations of the single polymer chains due to Brownian motion, and therefore reduces the entropy of the system increasing the free energy; this generates a repulsive potential U_{HS}. If the thickness of the polymer layer is larger then the range of van der Waals attraction, particles are fully stabilized. However, if temperature falls below the theta point, polymer chains assume a random coil conformation and the stabilizing action is lost.

The full interaction potential between colloidal particles in suspension, known as Derjaguin–Landau–Verwey–Overbeek (DLVO) potential (Derjaguin and Landau 1993), is obtained by adding up all the contributions introduced above:

$$U_{DLVO}(r) = U_{vdW}(r) + U_C(r) + U_{HS}(r) \tag{42}$$

Although the DLVO potential describes well many colloidal systems, its validity is not universal (Ninham 1999).

The simplest model colloidal system consists of a suspension of identical, infinitely rigid spherical particles which have only elastic interactions; their rigidity prevents any overlap or deformation, and therefore the interaction potential is a Dirac delta function of the distance between the particle centres. As a consequence, the phase behaviour of the system is determined only by the particles packing in a given volume, expressed by the volume fraction, Φ. The phase diagram of ideal hard spheres was calculated by numerical simulations (Wood and Jacobson 1957; Hoover and Ree 1968), and can be summarized as follows:

- Below a volume fraction $\Phi_F = 0.494$, the stable phase is a fluid suspension of colloidal particles; there is no long-range order, and the particles are free to explore the full available space by Brownian random motion.
- For $0.494 < \Phi_F < 0.545$, the equilibrium state is a coexistence of a fluid phase and a crystalline phase. The ratio of the two phases is related to the volume fraction by the lever rule.
- For $0.545 < \Phi_F < 0.58$, all the suspensions are crystalline.
- For $0.58 < \Phi_F < 0.64$, particles fail to crystallize, and remaining blocked in a non-equilibrium phase known as the colloidal glass (Pusey and van Megen 1986). As the volume fraction of the system increases, particles are more and more caged by their neighbours, and structural rearrangements which relax the system towards the equilibrium structure become so slow that particles are permanently caged by their neighbours and the structure of the suspension is frozen. The maximum packing fraction of a disordered arrangement of identical hard spheres is $\Phi_{RCP} \approx 0.64$ (Bernal 1959; Bernal and Mason 1960). In the glassy state, particles are arranged in a structure analogous to the one of a dense liquid, and therefore no long-range order is present in the system.
- For $0.64 < \Phi_F < 0.74$, the system is crystalline up to the maximum crystalline close packing fraction, $\Phi_{CP} = 0.74$.

The hard-sphere phase diagram can be modified if the interactions between the particles deviate from the ideal case. In particular, the presence of charges shifts the liquid–solid phase boundary and the value of Φ_G towards lower values. In fact, the presence of a charged double layer increases the effective size of particles, because a particle will start to feel the presence of another particle at a distance much larger than its diameter due to the long-range Coulombic repulsion. By screening the charge, the size of the double layer can be reduced to the point that the effective size is very close to the actual particle size and the hard-sphere behaviour is almost fully recovered.

Polydispersity, defined as the ratio between the standard deviation and the mean of the size distribution, also affects the phase behaviour of hard-sphere suspensions (Evans et al. 1999). In particular, crystallization is suppressed for polydispersities larger than a critical value of $\Phi = 0.12$, since the size distribution distorts the crystalline lattice. For polydispersities $\Phi < 0.06$, the behaviour is similar to monodisperse systems, while for intermediate ranges, the dynamics of crystallization is considerably slower.
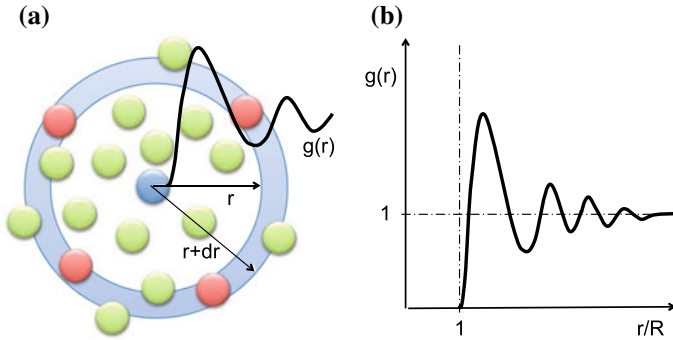
Fig. 15 Schematic description of the radial distribution function concept (**a**) and qualitative plot of $g(r)$ as a function of the dimensionless distance from a particle (**b**)

The packing structure of spheres is often characterized using the radial distribution function or pair correlation function, $g(r)$, which describes how the local, time-averaged density $\rho(r)$ varies as a function of the distance from a reference particle:

$$\rho(r) = \frac{N}{V} g(r) \tag{43}$$

where N and V are the total number of particles in the system and the system volume, respectively. In a homogeneous and isotropic system, it represents the probability of finding a particle in a shell of thickness dr at a distance r from a given reference particle, as shown schematically in Fig. 15a.

If the positions of the particles are completely uncorrelated, such as in an ideal gas, the probability is independent of the distance; if the system is arranged into a crystalline lattice, then the probability will be peaked at the lattice spacings. For liquids or amorphous systems like glasses, there is no long-range order, and therefore $g(r)$ decays to the ideal gas profile at long distances, but the presence of short-range order produces peaks at short distances (a qualitative example plot is displayed in Fig. 15b). Typically, the structure of a suspension is lost after 3–4 particle diameters from the initial particles.

The dynamics of a colloidal particle in a dilute solution is determined by diffusion. The characteristic timescale is the Brownian or diffusion time, $\tau_B = R^2/6D_0$, defined as the time that a particle takes to diffuse over a distance equal to its radius, where $D_0 = k_B T/6\pi\eta R$ is the Stokes–Einstein diffusion coefficient of a single particle of radius R in a solvent of viscosity η at temperature T. For systems with large τ_B, the role played by Brownian motion in events happening on shorter time scales becomes less important. For example, in the simple case of a uniformly sheared colloidal suspensions, two timescales are present in the problem: the diffusion time and the timescale set by the flow equal to the inverse of the applied shear rate, $\dot{\gamma}$. The Péclet number, $Pe = \tau_B \dot{\gamma}$, is defined as the ratio of the two timescales, and gives an indication of the relative importance of each mechanism. For $Pe \ll 1$,

Brownian motion dominates the dynamics of the suspension, while for $Pe \gg 1$, the system behaves analogously to an a-thermal system, and therefore the dynamics is determined only by the flow.

References

Adamson AW (1976) Physical chemistry of surfaces. Wiley

Banerjee S, Chan AMC (1980) Separated flow models—I. Analysis of the averaged and local instantaneous formulations. Int J Multiph Flow 6(1):1–24

Bernal JD (1959) A geometrical approach to the structure of liquids. Nature 183:141–147

Bernal JD, Mason J (1960) Packing of spheres: co-ordination of randomly packed spheres. Nature 188:910–911

Bertola V, Cafaro E (2007) On the speed of heat. Phys Lett Sect A Gen At Solid State Phys 372(1):1–4

Bertola V, Cafaro E (2010) Diffusion phenomena and thermodynamics. Phys Lett Sect A Gen At Solid State Phys 374(34):3373–3375

Bird RB, Stewart WE, Lightfoot EN (2007) Transport phenomena, 2nd edn. Wiley

Borwankar RP, Wasan DT (1988) Equilibrium and dynamics of adsorption of surfactants at fluid-fluid interfaces. Chem Eng Sci 43(6):1323–1337

Brandrup J, Immergut EH, Grulke EA, Abe A, Bloch DR (2005). Wiley

Cates ME, Fielding SM (2006) Rheology of giant micelles. Adv Phys 55(7–8):799–879

Davies JT (1957) A quantitative kinetic theory of emulsion type, I. physical chemistry of the emulsifying agent, gas/liquid and liquid/liquid interface. In: Proceedings of the International Congress of Surface Activity, vol 1, pp 426–438

de Gennes PG (1979) Scaling concepts in polymer physics. Cornell University Press

Delhaye J-M, Achard JL (1977) On the use of averaging operators in two-phase flow modelling. Light Water React 1:289–332

Derjaguin B, Landau L (1993) Theory of the stability of strongly charged lyophobic sols and of the adhesion of strongly charged particles in solutions of electrolytes. Prog Surf Sci 43(1):30–59

Einstein A (1905) Über die von der molekularkinetischen Theorie der Wärme geforderte Bewegung von in ruhenden Flüssigkeiten suspendierten Teilchen. Annalen der Physik 17:549–560

Eötvös R (1886) Ueber den zusammenhang der oberflächenspannung der flüssigkeiten mit ihrem molecularvolumen. Annalen der Physik 263(3):448–459

Evans RML, Fairhurst DJ, Poon WCK (1999) Phase equilibria of polydisperse colloids. In Težak D, Martinis M (eds). Trends in Colloid and Interface Science XIII. Springer, Berlin Heidelberg, pp 172–176

Fainerman VB, Miller R (1995) Hydrodynamic effects in measurements with the drop volume technique at small drop times. 2. Drop time and drop volume bifurcations. Coll Surf A: Physicochem Eng Asp, 97(3):255–262

Fischer E, Callaghan PT (2001) Shear banding and the isotropic-to-nematic transition in wormlike micelles. Phys Rev E 64:011501

Flory PJ (1953) Principles of polymer chemistry. Cornell University Press

Frumkin A (1925) Electrocapillary curve of higher aliphatic acids and the state equation of the surface layer. Zeitschrift für Physikalische Chemie 116:466–470

Gibbs JW (1961) The scientific papers of J.W. Gibbs, vol.1. Dover

Glass JE (1968) Adsorption characteristics of water-soluble polymers. II. Poly(ethylene oxide) at the aqueous-air interface. J Phys Chem 72(13):4459–4467

Griffin WC (1949) Classification of surface-active agents by HLB. J Soc Cosmet Chem 1(5):311–326

Griffin WC (1954) Calculation of HLB values of non-ionic surfactants. J Soc Cosmet Chem 5(4):249–256

Hansen J-P, Mc Donald IR(2013) Theory of simple liquids with applications to soft matter. Academic Press

Hoover WG, Ree FH (1968) Melting transition and communal entropy for hard spheres. J Chem Phys 49(8):3609–3617

Israelachvili JN (2011) Intramolecular and surface forces, 3rd edn. Academic Press

Jho C, Burke R (1983) Drop weight technique for the measurement of dynamic surface tension. J Colloid Interface Sci 95(1):61–71

Kékicheff P, Grabielle-Madelmont C, Ollivon M (1989) Phase diagram of sodium dodecyl sulfate-water system: 1. A calorimetric study. J Colloid Interface Sci 131(1):112–132

Kirkwood JG, Buff FP (1949) The statistical mechanical theory of surface tension. J Chem Phys 17(3):338–343

Kittel C, Kroemer H (1980) Therm Phys, 2nd edn. Freeman, W.H

Langmuir I (1918) The adsorption of gases on plane surface of glass, mica and platinum. Res Lab Gen Electr Co 40:1361–1402

Laplace PS (1805) Sur l'action capillaire. Livre X. Courcier, In Traité de mécanique celeste, Tome IV

Leal LG (2007) Advanced transport phenomena: fluid mechanics and convective transport processes. Cambridge University Press

Mourougou-Candoni N, Prunet-Foch B, Legay F, Vignes-Adler M, Wong K (1997) Influence of dynamic surface tension on the spreading of surfactant solution droplets impacting onto a low-surface-energy solid substrate. J Colloid Interface Sci 192(1):129–141

Ninham BW (1999) On progress in forces since the DLVO theory. Adv Colloid Interface Sci 83(1):1–17

Ono S, Kondo S (1960) Molecular theory of surface tension in liquids. In: Flugge S (ed) Handbuch der Physik, vol 10. Springer, Berlin Heidelberg

Perrin J (1910) Mouvement brownien et molécules. J Phys Theor Appl 9:5–39

Pusey PN, van Megen W (1986) Phase behaviour of concentrated suspensions of nearly hard colloidal spheres. Nature 320:340–342

Rosen MJ (1978) Surfactants and interfacial phenomena. Wiley

Strobl G (1997) The physics of polymers. Springer

Teraoka I (2002) Polymer solutions. An introduction to physical properties. Wiley-Interscience.

Triezenberg DG, Zwanzig R (1972) Fluctuation theory of surface tension. Phys Rev Lett 28(18):1183–1185

van Hunsel J, Bleys G, Joos P (1986) Adsorption kinetics at the oil/water interface. J Colloid Interface Sci 114(2):432–441

Wood WW, Jacobson JD (1957) Preliminary results from a recalculation of the Monte Carlo equation of state of hard spheres. J Chem Phys 27(5):1207–1208

Yadigaroglu G, Lahey RT (1976) On the various forms of the conservation equations in two-phase flow. Int J Multiph Flow 2(5):477–494

Young T (1805) An essay on the cohesion of fluids. Philos Trans R Soc Lond 95:65–87

Zhang X, Basaran OA (1997) Dynamic surface tension effects in impact of a drop with a solid surface. J Colloid Interface Sci 187(1):166–178

Constitutive Models of Complex Fluids

Volfango Bertola

Abstract This chapter provides an overview of the most common constitutive models used to describe the behaviour of non-Newtonian flows. For practical purposes, models are sorted into generalised Newtonian models, viscoelastic flow models and models for viscoplastic flows.

1 Introduction

Constitutive models, or constitutive equations, express in general a relationship between the force applied to a material and the consequent deformation; in the case of a fluid, which does not have a reference shape, the relationship is between the applied force and the rate of deformation. Since the applied force is always distributed over the fluid, usually constitutive models relate, more conveniently, the applied stress to the rate of deformation, or velocity gradient, which is expressed in tensorial form as

$$\boldsymbol{\Sigma} = f(\boldsymbol{\Gamma}) \tag{1}$$

where $\boldsymbol{\Sigma}$ is the symmetric stress tensor, with six independent components:

$$\boldsymbol{\Sigma} = \begin{pmatrix} \sigma_{xx} & \sigma_{xy} & \sigma_{xz} \\ \sigma_{yx} & \sigma_{yy} & \sigma_{yz} \\ \sigma_{zx} & \sigma_{zy} & \sigma_{zz} \end{pmatrix} \tag{2}$$

with $\sigma_{xy} = \sigma_{yx}$, $\sigma_{xz} = \sigma_{zx}$ and $\sigma_{yz} = \sigma_{zy}$, and $\boldsymbol{\Gamma}$ is the deformation rate tensor, also symmetric:

V. Bertola (✉)
School of Engineering, University of Liverpool, Liverpool, UK
e-mail: Volfango.Bertola@liverpool.ac.uk

$$\mathbf{\Gamma} = \frac{1}{2} \begin{pmatrix} 2\frac{\partial u}{\partial x} & \frac{\partial u}{\partial y} + \frac{\partial v}{\partial x} & \frac{\partial u}{\partial z} + \frac{\partial w}{\partial x} \\ \frac{\partial u}{\partial y} + \frac{\partial v}{\partial x} & 2\frac{\partial v}{\partial y} & \frac{\partial v}{\partial z} + \frac{\partial w}{\partial y} \\ \frac{\partial u}{\partial z} + \frac{\partial w}{\partial x} & \frac{\partial v}{\partial z} + \frac{\partial w}{\partial y} & 2\frac{\partial w}{\partial z} \end{pmatrix} = \frac{1}{2} \left(\nabla \mathbf{v} + \nabla \mathbf{v}^T \right) \qquad (3)$$

where u, v and w are the velocity components in the three Cartesian directions x, y, z, and $\nabla \mathbf{v}$ is the velocity gradient tensor.

Such constitutive equations can be obtained directly from first principles using a statistical mechanics approach, such as in the case of the steady flow of a hard sphere gas (Zwanzig 1979), from empirical measurements, or, more frequently, from purely mathematical models that are able to reproduce certain behaviours observed either at macroscopic or at molecular level.

In order to formulate mathematical models that are physically significant, it is necessary to introduce at least two assumptions: (i) the system is local and causal, i.e. the stress at a material point depends only on the history of that material point and its neighbours, and cannot depend on future events; (ii) constitutive models should not depend on the translation, rotation or acceleration of the reference frame (e.g. Cartesian), i.e. the stress at a material point does not change if calculated before and after any transformation of the reference frame. Of course, these assumptions are necessary but not sufficient, which explains why mathematical models can only approximate the behaviour of a physical system within a limited range of the system parameters. The assumption of material frame indifference has important consequences on the mathematical formulation of constitutive models of viscoelastic flows, which will be discussed in Sect. 3.

The simplest constitutive equation describes the so-called Newtonian flows, where the stress tensor is a linear function of the deformation rate:

$$\mathbf{\Sigma} = -p\mathbf{I} + 2\eta\mathbf{\Gamma} \qquad (4)$$

where p is pressure, $\mathbf{I}$ is the identity matrix, and η is the Newtonian viscosity. The Newtonian constitutive model given by Eq. (4) is commonly used to describe the flow of simple fluids, such as water and air. Constitutive models that cannot be reduced to Eq. (4) describe non-Newtonian flows. Since Eq. (4) expresses a relationship between flow variables, the attributes "Newtonian" and "non-Newtonian" always refer to a flowing fluid, therefore they are by no means attributes of the fluid itself. For example, fluids that usually exhibit Newtonian behaviour may become shear-thinning at high shear rates (Pipe et al. 2008).

Non-Newtonian constitutive models can be sorted into two main families: time-independent fluids, if the response of the material to an applied stress is instantaneous and fully reversible, and time-dependent, if the material response depends on its previous history. It is important to remark that, depending on the flow parameters, the behaviour of the same fluid can be described either by a time-independent or by a time-dependent model.

A comprehensive analysis of constitutive models can be found in a number of excellent reference books (Larson 1999; Bird et al. 1987; Joseph 1990; Phan-Thien 2002). In the following sections, the most common constitutive models to describe the flow of complex fluids are sorted into generalised Newtonian models, viscoelastic flow models and models for viscoplastic flows.

2   Constitutive Models for Generalised Newtonian Flows

In generalised Newtonian constitutive models, viscosity is a function of the second invariant (or quadratic invariant) of the strain rate tensor, defined as

$$
\begin{aligned}
I_2 &= \frac{1}{2}\left[(tr\,\mathbf{\Gamma})^2 - tr\,(\mathbf{\Gamma})^2\right] = \\
&= \frac{1}{4}\left[\left(\frac{\partial u}{\partial y} + \frac{\partial v}{\partial x}\right)^2 + \left(\frac{\partial v}{\partial z} + \frac{\partial w}{\partial y}\right)^2 + \left(\frac{\partial w}{\partial x} + \frac{\partial u}{\partial z}\right)^2\right] + \\
&\quad - \left(\frac{\partial u}{\partial x}\frac{\partial v}{\partial y} + \frac{\partial u}{\partial x}\frac{\partial w}{\partial z} + \frac{\partial v}{\partial y}\frac{\partial w}{\partial z}\right)
\end{aligned}
\tag{5}
$$

Similar to Newtonian flows, in generalised Newtonian flows the stress depends only on the instantaneous flow and not on the flow history. In simple shear flow, Eq. (5) reduces to

$$
I_2 = \frac{1}{4}\left(\frac{\partial u}{\partial y}\right)^2 = \frac{1}{4}\dot{\gamma}^2
\tag{6}
$$

where $\dot{\gamma} = \partial u/\partial y$ is the shear rate.

The simplest type of generalised Newtonian flow behaviour occurs when the viscosity coefficient is a monomial function of the shear velocity gradient (power law, or Ostwald–De Waele model):

$$
\eta = K\dot{\gamma}^{n-1}
\tag{7}
$$

where the consistency coefficient, K, and the power-law index, n, are empirical constants. The power-law index is indicative of the shear-thinning ($n < 1$) or shear-thickening ($n > 1$) behaviour of the fluid, whereas for $n = 1$ the Newtonian behaviour is retrieved. The consistency coefficient describes the fluid viscosity at low shear rates, and coincides with the Newtonian viscosity for $n = 1$. The shear-thinning, shear-thickening and Newtonian behaviours of the shear stress and of the viscosity as described by the power-law constitutive model are shown, respectively, in Fig. 1a, b.

In the limit $n \to 0$, the shear stress has a constant value, irrespective of the imposed shear rate. Although this picture may seem unphysical, stress plateaus can be observed experimentally over limited shear rate intervals, for example in the flow

(a)

(b)
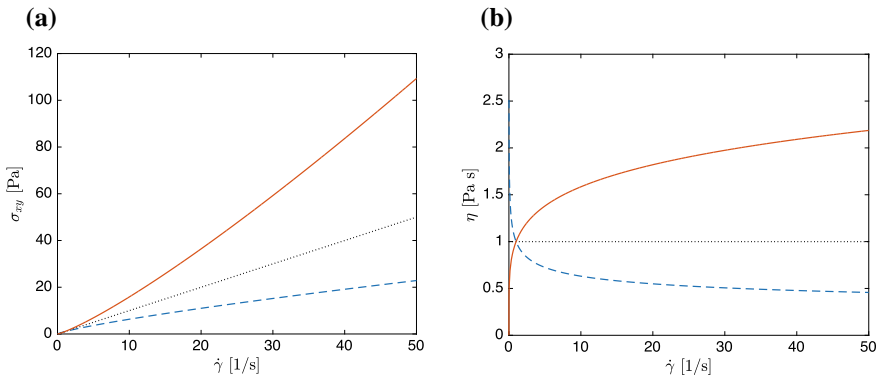
Fig. 1 Shear stress (**a**) and viscosity (**b**) obtained with the power-law model (Eq. 7) with $K = 1$ and: $n > 1$ (shear-thickening, solid line); $n = 1$ (Newtonian, dotted line); $n < 1$ (shear-thinning, dashed line)

of monodispersed polymer melts and solutions (Yang et al. 1998). For $n < 0$, the shear stress decreases monotonically upon increasing the shear rate, which means the flow is unstable.

Power-law fluids are time-independent, i.e. the shear stress does not depend on the previous deformation history. Physically, shear-thinning is usually explained by the breakdown of structure formed by interacting particles within the fluid, while shear-thickening is often due to flow-induced jamming (Frith et al. 1996).

The Ostwald–De Waele equation implies that viscosity will change indefinitely for any values of the shear rate. In other words, in the case of shear-thinning fluid ($n < 1$) viscosity tends to grow unlimited for $\dot{\gamma} \to 0$, and to vanish for $\dot{\gamma} \to \infty$; in these limits, the power-law model fails to describe the behaviour of real fluids accurately. To account for a more realistic behaviour, where viscosity varies between a minimum and a maximum value, respectively, at very low and very high shear rates, a number of constitutive equations have been proposed, such as the Cross model (Cross 1965):

$$\frac{\eta - \eta_\infty}{\eta_0 - \eta_\infty} = \frac{1}{1 + (C\dot{\gamma})^{1-n}} \tag{8}$$

and the Bird–Carreau–Yasuda model (Bird and Carreau 1968; Carreau 1972; Yasuda and Cohen 1981), which was initially developed to describe shear-thinning observed in many viscoelastic (i.e. time-dependent) flows:

$$\frac{\eta - \eta_\infty}{\eta_0 - \eta_\infty} = \frac{1}{[1 + (C\dot{\gamma})^a]^{(1-n)/a}} \tag{9}$$

where η_0 and η_∞ are the viscosities at zero shear and infinite shear, respectively, a is a parameter with a default value of 2, and C is the Cross time constant. This parameter is the reciprocal of the strain rate at which the zero-strain rate component and the power-law component of the flow curve intersect.

Fig. 2 Comparison between the power-law model (dashed line) with parameters $K = 2.5$, $n = 0.14$ and the Cross model (solid line) with parameters $C = 3$, $n = 0.05$; for $\dot{\gamma} \to 0$ and $\dot{\gamma} \to \infty$ the Cross model tends to the asymptotic values $\eta_0 = 10$ Pa s and $\eta_\infty = 0.01$ Pa s, respectively, whereas the power-law model continues to grow or decrease indefinitely
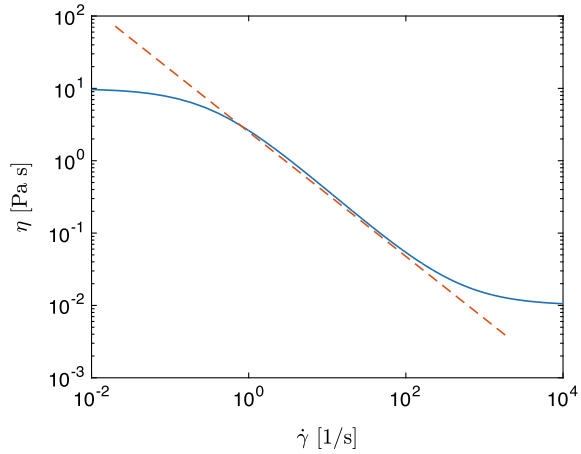
Figure 2 shows a comparison between the viscosities calculated with the power-law model (Eq. 7) and the Cross model (Eq. 8). Although the model parameters can be adjusted so that the two constitutive equations coincide within a certain range of shear rates, there is a significant deviation at low and at large shear rates.

Finally, the Ellis model is obtained by setting $\eta_\infty = 0$ in the Cross model:

$$\frac{\eta}{\eta_0} = \frac{1}{1 + \left(\frac{\sigma_{xy}}{\sigma_{1/2}}\right)^{n-1}} \tag{10}$$

where σ_{xy} is the applied shear stress, and $\sigma_{1/2}$ is the shear stress at which viscosity is exactly half of the zero-shear viscosity value, η_0.

3 Constitutive Models for Viscoelastic Flows

In viscoelastic fluids, such as polymer melts or solutions, a part of the deformation energy is stored as elastic energy, and released with a certain delay depending on the relaxation time of the fluid. The basic feature that essentially all viscoelastic fluids share is the occurrence of elastic stress effects: when the shear rate is sufficiently strong, the forces along the normals of a little cubical fluid element are different in different directions, unlike what happens for a Newtonian fluid where the pressure is isotropic. From the microscopic point of view, this behaviour is usually related to conformational rearrangements of the macromolecules which compose the fluid under the action of hydrodynamic forces. The entropic tendency of polymers that are stretched by the flow to recover their equilibrium chain conformation generates an elastic stress, the macroscopic manifestation of which is a difference in stress between the flow direction and the direction normal to it. Viscoelasticity manifests itself in

a variety of phenomena, including creep (the time-dependent strain resulting from a constant applied stress), stress relaxation resulting from a steady deformation, the Weissenberg rod-climbing effect due to nonzero normal stress difference, and many others, as discussed in Chapters Introduction to Transport Phenomena in Complex Fluids and Transport Phenomena in Viscoelastic Fluids.

The non-isotropic principal components of the stress tensor allow one to characterise the elasticity of polymer solutions and melts through normal stress differences: the first normal stress difference, $N_1 = \sigma_{xx} - \sigma_{yy}$, and the secondary normal stress difference, $N_2 = \sigma_{zz} - \sigma_{yy}$. In most cases, the magnitude of N_2 is around 10% of N_1 or less. The ratio N_1/σ is often taken to be a measure of the severity of viscoelastic behaviour, and can be used to classify a fluid as inelastic ($N_1 \ll \sigma$) or as viscoelastic ($N_1 \gg \sigma$).

The dissipation of energy associated to the process of stretching and relaxation of macromolecules is described by introducing the concept of elongational (or extensional) viscosity, the ratio of the first normal stress difference to the rate of elongation of the fluid:

$$\eta_E = \frac{\sigma_{xx} - \sigma_{yy}}{\epsilon_{xx}} \tag{11}$$

where $\epsilon_{xx} = \Gamma_{1,1}$ is the rate of deformation in the direction of stretching. For a Newtonian incompressible fluid, one can easily verify that the elongational viscosity is three times the shear viscosity (Trouton 1906). For a polymer solution the ratio η_E/η, also known as the Trouton ratio, can be of the order of 10^3–10^4.

If the relaxation time is small compared to the characteristic time of the flow ($\tau = L/v$, where L is a characteristic length scale and v a characteristic velocity), the material structure rearranges almost instantaneously in response to any imposed deformation, and consequently the stress decays abruptly once the material has been deformed; this response is characteristic of simple liquids which exhibit Newtonian

Fig. 3 Schematic of Newtonian, elastic, linear, and non-linear viscoelastic regimes as a function of deformation and relaxation time during deformation of polymeric materials (Phan-Thien 2002). (1) Newtonian regime; (2) linear viscoelasticity; (3) elastic regime; (4) non-linear viscoelasticity; (5) non-linear elasticity/viscoplastic regime
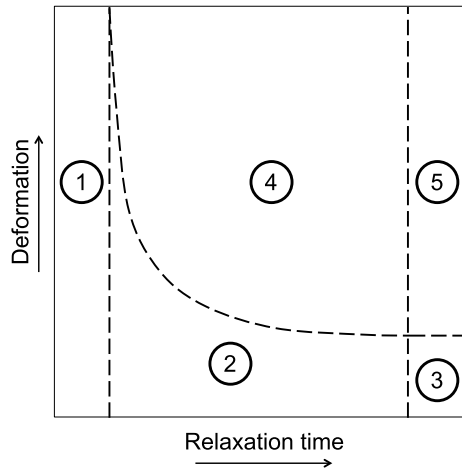
behaviour (Fig. 3). When the relaxation time increases, and becomes of the same order of the characteristic time of the flow, the material structure takes time to re-arrange, therefore it is necessary to apply a stress in order to keep the material deformed; as the material structure rearranges, the stress decays exponentially. This behaviour is typical of viscoelastic materials, and one can distinguish a linear viscoelastic behaviour in case of small deformations, and a non-linear viscoelastic behaviour in case of large deformations. When the relaxation time becomes very large compared to the characteristic time of the flow, the material structure takes such a long time to rearrange that in practice it never rearranges; thus, in order to keep the material deformed one must continuously apply a stress, which does not decay in time. If the stress is removed, the material returns to its initial shape (i.e. the shape of the material before the deformation). This behaviour is characteristic of elastic materials; again, one can distinguish a linear elastic regime in case of small deformations, and a non-linear elastic regime in case of large deformations; sometimes, large deformations cause a permanent change of the material structure, resulting into plasticity.

3.1 Linear Viscoelasticity

In linear viscoelasticity, the elastic component of the material behaves like an ideal Hookean spring, i.e. the elastic force is proportional to the spring extension through the spring constant. Linear viscoelasticity applies only to materials undergoing small deformations; non-linearities arise as soon as the deformation is large enough to alter significantly the conformation of the polymer chains or more in general the material microstructure. In the following sections, linear viscoelastic constitutive models are discussed with reference to single shear stress and shear deformation components, however, their extension to their tensorial equivalent is straightforward.

Lumped parameters models The earliest constitutive model to describe linear viscoelastic fluids, which combined elastic and viscous effects, was introduced by Maxwell (1867), and can be represented graphically by an instantaneous extension of a spring and a time-dependent reaction of a dash-pot in series, as illustrated in Fig. 4a. In this system, mechanical equilibrium is satisfied if the stress, σ_{xy}, is the same in the elastic and in the viscous element, while the total rate of deformation, $\dot{\gamma}_{xy}$, is the sum of the deformation rates in the two elements:

$$\dot{\gamma}_{xy} = \frac{d}{dt}\left(\frac{\sigma_{xy}}{G}\right) + \frac{\sigma_{xy}}{\eta} \tag{12}$$

where G is the elastic modulus, and η the fluid viscosity. This equation can be rearranged as

$$\lambda\frac{d\sigma_{xy}}{dt} + \sigma_{xy} = \eta\dot{\gamma}_{xy} \tag{13}$$

where $\lambda = \eta/G$ is the relaxation time.
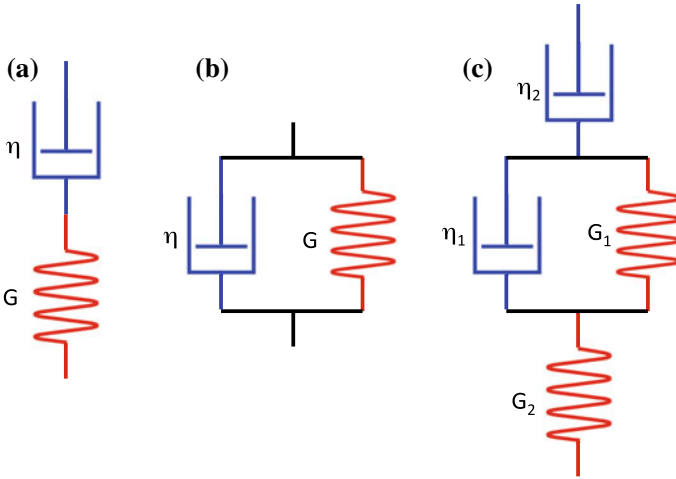
Fig. 4 Lumped parameter schematic of simple linear viscoelastic constitutive models: **a** Maxwell model; **b** Kelvin–Voigt model; **c** Burgers model

In a similar fashion to Maxwell's approach, one can derive a constitutive model where the elastic and the viscous element are connected in parallel (Voigt 1890), which is known as the Kelvin–Voigt model (Fig. 4b). In this case, the two components experience the same deformation, but their reacting forces have different magnitude:

$$\sigma_{xy} = G\gamma_{xy} + \eta\dot{\gamma}_{xy} \tag{14}$$

Linear viscoelastic models of increasing complexity can be built by combining together an arbitrary number of elastic and viscous elements. For example, one can connect in series one Maxwell element and one Kelvin–Voigt element as illustrated in Fig. 4c (Burgers 1935). The resulting constitutive equation is

$$\sigma_{xy} + \left(\frac{\eta_1 + \eta_2}{G_1} + \frac{\eta_2}{G_2}\right)\frac{d\sigma_{xy}}{dt} + \frac{\eta_1\eta_2}{G_1G_2}\frac{d^2\sigma_{xy}}{dt^2} = \eta_2\dot{\gamma}_{xy} + \frac{\eta_1\eta_2}{G_1}\frac{d\dot{\gamma}_{xy}}{dt} \tag{15}$$

Another example is the generalised Maxwell model, where an arbitrary number of Maxwell elements are combined in parallel, i.e. they are all subjected to the same deformation. Since each element has a different viscosity and a different elastic modulus, increasing the number of elements generates models featuring a spectrum of relaxation times, which provide a more accurate description of real materials.

Response to Heaviside forcing The simplest way to analyse the dynamic response of linear viscoelastic models to an external forcing is to apply a Heaviside stress step, $\sigma(t) = \sigma_0 H(t)$, or a Heaviside deformation step, $\gamma(t) = \gamma_0 H(t)$, where the Heaviside step function is defined as

$$H(t) = \begin{cases} 0 & t < 0 \\ 1 & t \geq 0 \end{cases} \tag{16}$$

When a constant stress, σ_0, is applied to the Maxwell model (Eq. 13), the response is

$$\gamma_{xy} = \frac{\sigma_0}{\eta}t + \frac{\sigma_0\lambda}{\eta} \tag{17}$$

One can observe an instantaneous elastic deformation in the spring, followed by a constant rate of deformation in the viscous element, $\dot{\gamma}_{xy} = \sigma_0/\eta$, as shown schematically in Fig. 5a. If after a certain time the stress is removed, the elastic deformation is entirely recovered, while the viscous deformation is permanent. When the Maxwell model is forced by imposing a fixed deformation, γ_0, solution of Eq. (13) yields

$$\sigma_{xy} = \frac{\eta}{\lambda}\gamma_0 e^{-t/\lambda} \tag{18}$$

As the deformation is applied, there is an instantaneous buildup of stress due to the spring loading; however, when the viscous element starts to move the spring elongation reduces, which means the stress decays exponentially with time, a phenomenon commonly referred to as stress relaxation. This behaviour is illustrated qualitatively in Fig. 5b.

If a constant stress, σ_0, is applied to the Kelvin–Voigt model at $t = 0$, the solution of Eq. (14) is:

$$\gamma_{xy} = \frac{\sigma_0}{G}\left(1 - e^{-t/\lambda}\right) \tag{19}$$

Initially, the spring cannot stretch, because it is held back by the viscous element, which cannot react instantaneously and therefore takes up all the stress, while the spring is unloaded. After some strain starts to take place, the stress starts to decrease in the viscous element and increase in the spring, i.e. the stress is transferred from the viscous element to the elastic element. In the limit $t \to \infty$, the viscous element is unloaded and the spring carries all the stress; thus, the maximum strain is $\gamma_{\max} = \sigma_0/G$. If after a certain time $t = \tau$ the applied stress is removed, the spring will not be able to contract instantaneously due to the resistance of the viscous element, but eventually pulls the viscous element back to its initial position. The Kelving–Voigt response to a constant applied stress is depicted qualitatively in Fig. 5c. Unlike in the case of the Maxwell model, it is not possible to apply a fixed deformation to a Kelvin–Voigt element instantaneously.

Response to harmonic forcing The dynamic response of linear viscoelastic models to a harmonic forcing, either $\sigma(t) = \sigma_0 \sin(\omega t)$ or $\gamma(t) = \gamma_0 \sin(\omega t)$, is another canonical case in the theory of linear dynamical systems (Casti 1987). In particular, for a sinusoidal forcing the response is another sinusoid with the same frequency,

(a)

(b)

(c)
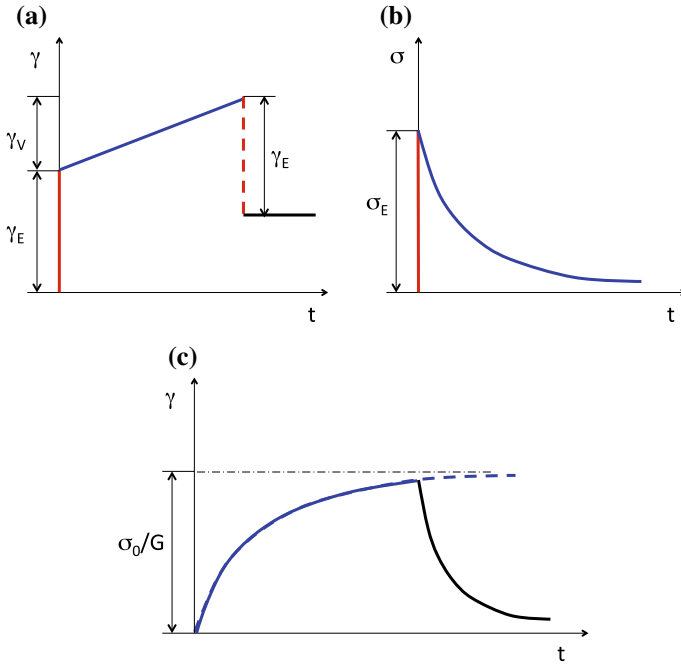
Fig. 5 Qualitative response of the Maxwell model (Eq. 13) to a constant applied stress, where γ_E and γ_V are the elastic and viscous deformations, respectively (**a**), and to a constant deformation, where σ_E is the elastic stress buildup (**b**). Qualitative response of the Kelvin–Voigt model (Eq. 19) to a constant applied stress, σ_0 (**c**)

but with a different amplitude and a phase shift; thus, the response to a sinusoidal stress is

$$\gamma_{xy}(t) = \gamma_0 \sin(\omega t + \phi) \tag{20}$$

and the response to a sinusoidal deformation is

$$\sigma_{xy}(t) = \sigma_0 \sin(\omega t + \phi) \tag{21}$$

In the limit of a Hookean solid (purely elastic limit), the stress is related linearly to strain, and the response to a shear deformation which varies sinusoidally with time, $\gamma(t) = \gamma_0 \sin(\omega t)$, is

$$\sigma_{xy}(t) = G\gamma_0 \sin(\omega t) \tag{22}$$

Thus, in elastic solids there is no phase shift between the shear stress and shear strain. In the Newtonian fluid limit, the response to the same type of forcing is

$$\sigma_{xy}(t) = \eta\dot{\gamma} = \eta\gamma_0 \cos(\omega t) = \eta\gamma_0 \sin(\omega t + \frac{\pi}{2}) \tag{23}$$

In this case, the resulting shear stress is out of phase from the applied strain by $\pi/2$. In a viscoelastic material, the phase angle can vary continuously between zero (purely elastic response) and $\pi/2$ (purely viscous response), therefore, it provides a quantitative indicator of the level of viscoelasticity. In particular, small values of the phase angle represent predominantly elastic behaviour whereas large values of the phase angle correspond to viscous behaviour.

In the general viscoelastic case, the elastic and viscous parts of the response can be made explicit by expanding the harmonic terms in Eqs. (20) and (21):

$$\gamma_{xy}(t) = \gamma_0 \cos\phi \sin(\omega t) + \gamma_0 \sin\phi \cos(\omega t) \tag{24}$$

$$\sigma_{xy}(t) = \sigma_0 \cos\phi \sin(\omega t) + \sigma_0 \sin\phi \cos(\omega t) \tag{25}$$

For a harmonic imposed deformation, the amplitude of the component of the response in phase with the forcing is expressed by introducing the *storage modulus*, $G' = \sigma_0 \cos\phi/\gamma_0$, which reflects the elastic energy stored in the fluid, and the the component out of phase by $\pi/2$ is expressed by the *loss modulus*, $G'' = \sigma_0 \sin\phi/\gamma_0$, which reflects the energy loss by viscous dissipation. For a harmonic imposed stress, the amplitude of the component in phase with the forcing is expressed by the *storage compliance*, $J' = \gamma_0 \cos\phi/\sigma_0$, and the component out of phase is expressed by the *loss compliance*, $J'' = \gamma_0 \sin\phi/\sigma_0$. Using these quantities Eqs. (24) and (25) become, respectively,

$$\gamma_{xy}(t) = \sigma_0 \left[J' \sin(\omega t) + J'' \cos(\omega t) \right] \tag{26}$$

and

$$\sigma_{xy}(t) = \gamma_0 \left[G' \sin(\omega t) + G'' \cos(\omega t) \right] \tag{27}$$

The problem of harmonic forcing is often formulated in terms of complex numbers using Euler's formula:

$$e^{\pm i\theta} = \cos\theta \pm i \sin\theta \tag{28}$$

For a harmonic stress input $\sigma(t) = \sigma_0 e^{i\omega t}$ the response is:

$$\begin{aligned} \gamma_{xy}(t) = \gamma_0 e^{i\omega t + \phi} = \gamma_0 e^{\phi} e^{i\omega t} = \gamma_0 \left(\cos\phi + i \sin\phi\right) e^{i\omega t} = \\ = \sigma_0 \left(J' + i J'' \right) e^{i\omega t} \end{aligned} \tag{29}$$

while for a harmonic deformation $\gamma(t) = \gamma_0 e^{i\omega t}$ the response is

$$\begin{aligned} \sigma_{xy}(t) = \sigma_0 e^{i\omega t + \phi} = \sigma_0 e^{\phi} e^{i\omega t} = \sigma_0 \left(\cos\phi + i \sin\phi\right) e^{i\omega t} = \\ = \gamma_0 \left(G' + i G'' \right) e^{i\omega t} \end{aligned} \tag{30}$$

(a)

(b)
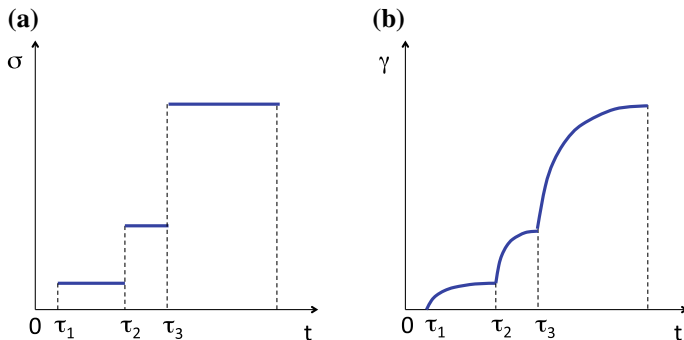
Fig. 6 Example of application of Boltzmann's superposition principle (Eq. 31); for a stepped ramp of the applied stress (**a**), the response of the system is the sum of the responses to individual steps (**b**)

Thus, the phenomenological coefficients related to the elastic and viscous properties of the substance can be expressed through a single complex number, either the *complex modulus*, $G^* = G' + i\,G''$, or the *complex compliance*, $J^* = J' + i\,J''$.

Superposition principle The linearity of Eqs. (12)–(15) implies their solutions can be combined linearly. The Boltzmann superposition principle states that the response of a material to a given load is independent of the response of the material to its previous loading history. For example, in the case of a loading consisting of a sequence of Heaviside steps with different magnitudes of the applied stress, the total strain may be expressed by

$$\gamma_{xy} = \frac{\sigma_1}{G}\,(t - \tau_1) + \frac{\sigma_2 - \sigma_1}{G}\,(t - \tau_2) + \cdots + \frac{\sigma_n - \sigma_{n-1}}{G}\,(t - \tau_n) \qquad (31)$$

A qualitative example of the behaviour described by Eq. (31) is displayed in Fig. 6. In the limit of small stress increments, Eq. (31) becomes

$$\gamma_{xy} = \int_{-\infty}^{t} \frac{1}{G}\,(t - \tau)\,d\sigma(t) = \int_{-\infty}^{t} \frac{1}{G}\,(t - \tau)\,\frac{d\sigma(t)}{dt}\,dt \qquad (32)$$

3.2 The Problem of Time Derivatives

The assumption of material frame indifference has important consequences on the mathematical formulation of constitutive models of viscoelastic flows, which descend from simple vector calculus, and which were addressed systematically in this context by Oldroyd and Wilson (1950). In a generic reference frame, a material point is

characterised by its position vector, r, its velocity, $v = dr/dt$, and its acceleration, $a = dv/dt$. In a second reference frame in relative motion with respect to the initial reference frame, the position vector is given by

$$r' = Q(t)r + c(t) \tag{33}$$

where Q is an orthogonal matrix such that $QQ^T = Q^TQ = I$ and $|Q| = 1$, and c is a vector representing a linear displacement. Since orthogonal matrices preserve isometries, one can easily verify that the distance between two points in the first reference frame, $|r_2 - r_1|$, does not change in the second reference system:

$$|r'_2 - r'_1| = |Q(t)r_2 + c(t) - Q(t)r_1 - c(t)| =$$
$$= |Q(t)(r_2 - r_1)| = |r_2 - r_1| \tag{34}$$

This conclusion does not apply to velocities and accelerations, which in the second reference frame are written, respectively, as

$$v' = \frac{dr'}{dt} = \frac{d}{dt}\left[Q(t)r + c(t)\right] = Q\frac{dr}{dt} + \frac{dQ}{dt}r + \frac{dc}{dt} =$$
$$= Qv + \frac{dQ}{dt}r + \frac{dc}{dt} \tag{35}$$

and

$$a' = \frac{dv'}{dt} = \frac{d}{dt}\left[Qv + \frac{dQ}{dt}r + \frac{dc}{dt}\right] =$$
$$= \frac{dQ}{dt}v + Q\frac{dv}{dt} + \frac{dQ}{dt}\frac{dr}{dt} + \frac{d^2Q}{dt^2}r + \frac{d^2c}{dt^2} =$$
$$= Qa + 2\frac{dQ}{dt}v + \frac{d^2Q}{dt^2}r + \frac{d^2c}{dt^2} \tag{36}$$

Thus, velocities and accelerations are invariant under a coordinate transformation only if the time derivatives on the r.h.s. of Eqs. (35) and (36) are zero, i.e. the two reference frames are not in relative motion. In other terms, velocity and acceleration are not objective and depend on the motion of the observer.

When one considers a tensor representing a physical quantity (e.g. the stress tensor) in a given coordinate system, it must be objective with respect to a change of the coordinate system:

$$\Sigma' = Q\Sigma Q^T \tag{37}$$

However, one can easily verify its time derivative is not objective:

$$\frac{d\Sigma'}{dt} = \frac{d}{dt}\left(Q\Sigma Q^T\right) = \frac{dQ}{dt}\Sigma Q^T + Q\frac{d\Sigma}{dt}Q^T + Q\Sigma\frac{dQ^T}{dt} \tag{38}$$

To preserve the objectivity of a tensor with respect to time derivation, it is necessary to introduce a new definition of derivative operator (Jaumann 1905):

$$\frac{D_\nabla}{Dt}(\cdot) = \frac{d}{dt}(\cdot) - (\nabla \boldsymbol{v})(\cdot) - (\cdot)(\nabla \boldsymbol{v})^T \tag{39}$$

In fact, the velocity gradient tensor transforms in the new coordinate system as

$$(\nabla \boldsymbol{v}') = \boldsymbol{Q}(\nabla \boldsymbol{v})\boldsymbol{Q}^T + \frac{d\boldsymbol{Q}}{dt}\boldsymbol{Q}^T \tag{40}$$

Thus, the *upper convected*[1] derivative defined by Eq. (39) is objective with respect to a transformation of the coordinate system:

$$
\begin{aligned}
\frac{D_\nabla}{Dt}(\boldsymbol{\Sigma}') &= \frac{D_\nabla}{Dt}\left(\boldsymbol{Q}\boldsymbol{\Sigma}\boldsymbol{Q}^T\right) = \\
&= \frac{d}{dt}\left(\boldsymbol{Q}\boldsymbol{\Sigma}\boldsymbol{Q}^T\right) - \boldsymbol{Q}(\nabla \boldsymbol{v})\boldsymbol{Q}^T\left(\boldsymbol{Q}\boldsymbol{\Sigma}\boldsymbol{Q}^T\right) - \frac{d\boldsymbol{Q}}{dt}\boldsymbol{Q}^T\left(\boldsymbol{Q}\boldsymbol{\Sigma}\boldsymbol{Q}^T\right) + \\
&\quad - \left(\boldsymbol{Q}\boldsymbol{\Sigma}\boldsymbol{Q}^T\right)\boldsymbol{Q}(\nabla \boldsymbol{v})^T\boldsymbol{Q}^T - \left(\boldsymbol{Q}\boldsymbol{\Sigma}\boldsymbol{Q}^T\right)\boldsymbol{Q}\frac{d\boldsymbol{Q}^T}{dt} = \\
&= \boldsymbol{Q}\frac{d\boldsymbol{\Sigma}}{dt}\boldsymbol{Q}^T + \frac{d\boldsymbol{Q}}{dt}\boldsymbol{\Sigma}\boldsymbol{Q}^T + \boldsymbol{Q}\boldsymbol{\Sigma}\frac{d\boldsymbol{Q}^T}{dt} - \boldsymbol{Q}(\nabla \boldsymbol{v})\boldsymbol{\Sigma}\boldsymbol{Q}^T + \\
&\quad - \frac{d\boldsymbol{Q}}{dt}\boldsymbol{\Sigma}\boldsymbol{Q}^T - \boldsymbol{Q}\boldsymbol{\Sigma}(\nabla \boldsymbol{v})^T\boldsymbol{Q}^T - \boldsymbol{Q}\boldsymbol{\Sigma}\frac{d\boldsymbol{Q}^T}{dt} = \\
&= \boldsymbol{Q}\frac{d\boldsymbol{\Sigma}}{dt}\boldsymbol{Q}^T - \boldsymbol{Q}(\nabla \boldsymbol{v})\boldsymbol{\Sigma}\boldsymbol{Q}^T - \boldsymbol{Q}\boldsymbol{\Sigma}(\nabla \boldsymbol{v})^T\boldsymbol{Q}^T
\end{aligned}
\tag{41}
$$

Similarly, one can define a *lower convected* derivative as

$$\frac{D_\Delta}{Dt}(\cdot) = \frac{d}{dt}(\cdot) + (\nabla \boldsymbol{v})(\cdot) + (\cdot)(\nabla \boldsymbol{v})^T \tag{42}$$

Finally, the co-rotational derivative for a second-order tensor is formed from the appropriate linear combination of the upper and lower convected derivatives:

$$
\begin{aligned}
\frac{D_\circ}{Dt}(\cdot) &= \frac{d}{dt}(\cdot) + \frac{1}{2}\left[(\nabla \boldsymbol{v})^T - (\nabla \boldsymbol{v})\right](\cdot) + \frac{1}{2}(\cdot)\left[(\nabla \boldsymbol{v}) - (\nabla \boldsymbol{v})^T\right] = \\
&= \frac{d}{dt}(\cdot) - \boldsymbol{W}(\cdot) + (\cdot)\boldsymbol{W}
\end{aligned}
\tag{43}
$$

where $\boldsymbol{W}$ is the spin tensor.

---

[1] The name upper convected arises because the derivative represents the material derivative of the upper (contravariant) components of a vector when convected with the motion.

3.3 Oldroyd-B Model

The most popular constitutive equation for viscoelastic fluids is the Oldroyd-B model, which captures the main features of viscoelastic flows but at the same time is simple enough to allow finding the analytical solution for the flow field in many circumstances. In this model, the total stress tensor, $\boldsymbol{\Sigma}$, is decomposed into the Newtonian solvent component, $2\eta_S\boldsymbol{\Gamma}$, where η_S is the solvent viscosity, and $\boldsymbol{\Gamma}$ is the velocity gradient tensor (Eq. 3), and the viscoelastic polymeric component, $\boldsymbol{\Sigma}_P = \boldsymbol{\Sigma} - 2\eta_S\boldsymbol{\Gamma}$, for which one can write the relation with the velocity gradient as

$$(\boldsymbol{\Sigma} - 2\eta_S\boldsymbol{\Gamma}) + \lambda_1 \frac{D_\nabla}{Dt}(\boldsymbol{\Sigma} - 2\eta_S\boldsymbol{\Gamma}) = 2\eta_P\boldsymbol{\Gamma} \tag{44}$$

where λ_1 is the relaxation time, η_P the polymer viscosity, and D_∇/Dt is the co-deformational (or upper convected) derivative (Oldroyd and Wilson 1950). Rearranging Eq. (44) into a more compact form yields

$$\boldsymbol{\Sigma} + \lambda_1 \frac{D_\nabla \boldsymbol{\Sigma}}{Dt} = 2(\eta_S + \eta_P)\left(\boldsymbol{\Gamma} + \lambda_2 \frac{D_\nabla \boldsymbol{\Gamma}}{Dt}\right) \tag{45}$$

where $\lambda_2 = \lambda_1\eta_S/(\eta_S + \eta_P)$ is the retardation time. When $\lambda_2 = 0$, the Oldroyd-B model reduces to the Upper Convected Maxwell (UCM) model, which has the same structure as Eq. (13) but uses a different derivative operator; when $\lambda_2 = \lambda_1$ the model reduces to viscous Newtonian.

For the Oldroyd-B fluid in steady-state shear flow, the viscosity $\eta = \eta_S + \eta_P$ is constant, the second normal stress difference is zero, and the first normal stress difference is a quadratic function of the shear rate:

$$N_1 = 2\eta(\lambda_2 - \lambda_1)\dot{\gamma}^2 \tag{46}$$

The main limitation of the Oldroyd-B model is due to the fact that the coefficient of the deformation rate in Eqs. (44) and (45) is constant; this means that its contribution to the stress is the same independently of the deformation magnitude or, in other words, a fluid element can be deformed indefinitely keeping its elasticity unchanged. From the microscopic point of view, this means polymer molecules can be stretched to an infinite length behaving like an ideal spring, which is clearly unphysical.

3.4 FENE Model

The Finitely Extensible Non-linear Elastic (FENE) constitutive model was developed to achieve a more realistic description of the long-chained polymers behaviour (Bird et al. 1980). In particular, it accounts for the fact that, unlike ideal elastic springs, polymer molecules can be stretched only up to a maximum length, and the

required stretching force increases more than linearly as the molecule approaches the maximum stretching. In the FENE model, polymers molecules are represented by connecting a sequence of beads with non-linear springs; the elastic force between two consecutive beads is

$$F = \frac{K r}{1 - r^2/r_{\max}^2} \tag{47}$$

where r is the connector vector between the beads, K is the spring constant, r and $r_{\max}$ the instantaneous and maximum lengths of the stretched molecule, respectively. At small extension, the spring is nearly Hookean, when further extended, it becomes strongly non-linear. The connector force grows rapidly so that the spring cannot be stretched beyond some maximal length.

The instantaneous position of a FENE dumbbell as a function of time is described by the following Langevin stochastic differential equation:

$$d r = \left[(\nabla v)^T \cdot r - \frac{2}{\zeta} F \right] + \sqrt{\frac{4 k_B T}{\zeta}} d W(t) \tag{48}$$

where ζ is the friction coefficient of a bead, k_B is Boltzmann's constant, T is the absolute temperature, and $W(t)$ is a Wiener stochastic process (Soong 1973). In this equation, the first term represents the distortion of the beads due to the velocity gradient, the second term represents the effect of the restoring spring force, and the stochastic term models the Brownian motion of the beads. The time evolution of the connector vector of the dumbbell (i.e. the distance between the beads) must be integrated and then averaged over all connectors to describe the macroscopic flow behaviour.

The polymer contribution to the stress is given by

$$\Sigma_P = -N \langle r F \rangle + N k_B T I \tag{49}$$

where N is the total number of connectors, and I the identity matrix. Introducing the expression of the connector force (Eq. 47) yields:

$$\Sigma_P = -N K \left\langle \frac{r r}{1 - r^2/r_{\max}^2} \right\rangle + N k_B T I \tag{50}$$

The ensemble average quantity in Eq. (50) can be calculated using Peterlin's approximation (Peterlin 1966):

$$\left\langle \frac{r r}{1 - r^2/r_{\max}^2} \right\rangle = \frac{\langle r r \rangle}{1 - \langle r^2/r_{\max}^2 \rangle} + r_{\max}^2 I \tag{51}$$

Evaluating the ensemble averages yields the FENE-P constitutive equation for the polymer contribution to the stress:

$$Z\boldsymbol{\Sigma}_P + \lambda\frac{D_\nabla\boldsymbol{\Sigma}_P}{Dt} - \lambda\left[\boldsymbol{\Sigma}_P + \frac{\eta_P}{\lambda}\boldsymbol{I}\right]\frac{d\ln Z}{dt} = 2\eta_P\dot{\boldsymbol{\Gamma}} \qquad (52)$$

where Z is a function of the spring constant and of the maximum stretching:

$$Z = 1 + \frac{3k_BT}{Kr_{\max}^2}\left[1 + \frac{\lambda}{3\eta_P}tr(\boldsymbol{\Sigma})\right] \qquad (53)$$

A modified version of the FENE-P model includes the effect of repulsive charges between the beads in an attempt to incorporate the effect of charge repulsion between ionizable groups on the polymer (Dunlap and Leal 1984). This leads to the same constitutive equation but a different form of Z.

3.5 Other Constitutive Models for Viscoelastic Flows

Whilst the Oldroyd-B and the FENE models provide the most popular constitutive equations used in modelling viscoelastic flows, many other constitutive equations were derived to provide a better match with experimental data for particular fluids and/or flow conditions.

White–Metzner model The White–Metzner model (White and Metzner 1963) was developed for viscoelastic fluids that exhibit also shear-thinning. In summary, it is a modified Maxwell model that allows incorporation of experimental data on viscosity as a function of shear rate. The deviatoric stress is given by

$$\boldsymbol{\Sigma} + \frac{\eta(\dot{\gamma})}{G}\frac{D_\nabla\boldsymbol{\Sigma}}{Dt} = 2\eta(\dot{\gamma})\boldsymbol{\Gamma} \qquad (54)$$

The shear-thinning viscosity, $\eta(\dot{\gamma})$, is often described by a power law. This model can predict correctly the behaviour of nonpolar solutions and polymeric melts and it may work well on polar systems in the range of high deformation rates, i.e. the region of primary industrial interest.

Giesekus model The Giesekus model (Giesekus 1982) includes an additional quadratic term. In this model, the deviatoric stress is divided into a solvent contribution, $\eta_S\boldsymbol{\Gamma}$, and a polymer contribution, which is given by

$$\boldsymbol{\Sigma}_P + \lambda_1\frac{D_\nabla\boldsymbol{\Sigma}_P}{Dt} + \frac{\alpha\lambda_1}{\eta_P}\boldsymbol{\Sigma}_P^2 = 2\eta_P\boldsymbol{\Gamma} \qquad (55)$$

Phan-Thien–Tanner model The Phan-Thien–Tanner constitutive equation (Phan-Thien and Tanner 1977) has a similar structure to the Giesekus model, but has a different non-linear term:

$$\boldsymbol{\Sigma}_P + \lambda_1\frac{D_\nabla\boldsymbol{\Sigma}_P}{Dt} + \left\{\exp\left[\frac{\lambda_1}{\eta_P}Tr(\boldsymbol{\Sigma}_P)\right] - 1\right\}\boldsymbol{\Sigma}_P = 2\eta_P\boldsymbol{\Gamma} \qquad (56)$$

4 Constitutive Models for Viscoplastic Flows

An important type of non-Newtonian fluid is the viscoplastic or yield-stress fluid, which responds like elastic solids for applied stresses lower than a certain threshold value, called the yield stress, and flows only when the yield stress is overcome. Practically, such flow behaviour occurs in many situations, including slurries and suspensions, certain polymer solutions, lavas, muds and clays, heavy oils, avalanches, cosmetic creams, hair gel, liquid chocolate, pasty materials, foams and emulsions.

Research into viscoplastic fluids, their measurement and characterization is extensive and has been summarised in numerous reviews (Barnes 1999; Coussot 2007). One matter still subject of debate is the definition of yield-stress fluid itself, that is, whether fluids can actually exhibit such a physical property as the yield stress. The review by Barnes (1999) examines the evidence for and against its existence, and argues that whereas the concept of a definable yield stress has proven and continues to prove useful in a whole range of applications, if viscosity is plotted as a function of the shear stress, one can clearly identify a Newtonian plateau when the velocity gradient tends to zero (typically less than 10^{-5} s^{-1}), which implies that the material continues to creep although this can be observed only on very long timescales. However, in many practical situations the time frame of observation is much shorter than the time necessary for viscoplastic fluids to exhibit measurable flow characteristics.

Whilst several fluids exhibit an apparent yield stress, Carbopol dispersions are probably the most thoroughly studied model viscoplastic fluid system. Carbopol consists of highly cross-linked polymer particles, with dangling free ends of polymer gel strands that strongly interact with adjacent microgel particles, resulting into to a very high viscosity at low shear stress (Nguyen and Boger 1992; Roberts and Barnes 2001). Carbopol dispersions and gels are found in dozens of everyday products, ranging from toothpastes, through hair and shower gels, to artificial tears.

The simplest constitutive model describing viscoplastic fluids was introduced by Bingham to characterise the behaviour of paints (Bingham 1917), and represents the shear stress component as a linear function of the velocity gradient, with the intercept σ_c corresponding to the threshold yield point:

$$
\begin{aligned}
\dot{\gamma} &= 0 & \sigma_{xy} &\leq \sigma_c \\
\sigma_{xy} &= \sigma_c + \eta\dot{\gamma} & \sigma_{xy} &> \sigma_c
\end{aligned}
\tag{57}
$$

A more refined model is the Herschel–Bulkley equation (Herschel and Bulkley 1926), given by:

$$
\begin{aligned}
\sigma_{xy} &= G\gamma & \sigma_{xy} &\leq \sigma_c \\
\sigma_{xy} &= \sigma_c + K\dot{\gamma}^n & \sigma_{xy} &> \sigma_c
\end{aligned}
\tag{58}
$$

where G is the shear modulus, and γ is the shear deformation. This model is well established and probably the most widely used when analysing yield-stress

behaviour; another popular model, suitable to characterise the behaviour of particle suspensions used in printing inks, was proposed by Casson (1959):

$$\sqrt{\sigma_{xy}} = \sqrt{\sigma_c} + \sqrt{\eta\dot{\gamma}} \qquad \sigma_{xy} > \sigma_c \tag{59}$$

According to Eqs. (57)–(59), the transition from the elastic regime to the fluid regime is abrupt, which means that the shear stress derivative with respect to the shear rate exhibits a first-order discontinuity. This represents a major technical issue when the yield-stress fluid constitutive equation is implemented to find analytical or (especially) numerical solutions of fluid flows. To remove this discontinuity, Papanastasiou proposed a constitutive equation featuring a smooth transition between the two regimes (Papanastasiou 1987), which provides a better description of real materials:

$$\sigma_{xy} = \sigma_c \left[1 - \exp\left(-m\dot{\gamma}\right)\right] + K\dot{\gamma}^n \tag{60}$$

where m is a material-dependent constant with values of the order of 10^2. Figure 7 shows the qualitative flow curves for Bingham fluids (Eq. 57) and Herschel–Bulkley fluids (Eq. 58), as well as the effect of the Papanastasiou regularisation (Eq. 60). A detailed discussion of advanced and time-dependent constitutive models for viscoplastic flows is presented in Chapter Transport Phenomena in Viscoplastic Materials.

Fig. 7 Comparison between the qualitative flow curves of the Bingham model (solid line) and of the Herschel–Bulkley model (dash-dot line); the inset shows the effect of Papanastasiou regularisation (Eq. 60) on the Herschel–Bulkley flow curve
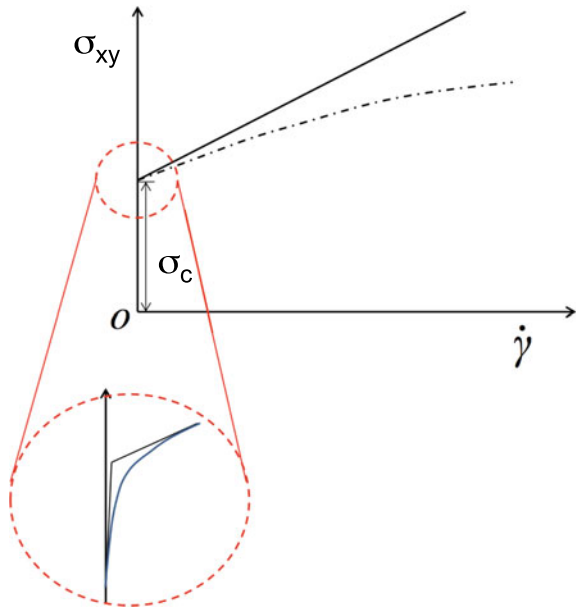
References

Barnes HA (1999) The yield stress-a review or "$\pi\alpha\nu\tau\alpha\ \rho\epsilon\iota$"-everything flows? J Non-Newton Fluid Mech 81(1):133–178

Bingham EC (1917) An investigation of the laws of plastic flow. Bull Bur Stand 13(2):309–353

Bird RB, Carreau PJ (1968) A nonlinear viscoelastic model for polymer solutions and melts-I. Chem Eng Sci 23(5):427–434

Bird RB, Dotson PJ, Johnson NL (1980) Polymer solution rheology based on a finitely extensible bead-spring-chain model. J Non-Newton Fluid Mech 7:213–235

Bird RB, Armstrong RC, Hassager O (1987) Dynamics of polymeric liquids, vols 1 and 2. Wiley

Burgers JM (1935) Mechanical considerations-model systems-phenomenological theories of relaxation and of viscosity. In: Eirich FR (ed) First report on viscosity and plasticity (Verhand. Koninklijke Nederlandse Akademie van Wetenschappen), pp 73–109. N.V. Noord-Hollandsche Uitgevers Maatschappij

Carreau PJ (1972) Rheological equations from molecular network theories. Trans Soc Rheol 16(1):99–127

Casson N (1959) A flow equation for pigment-oil suspensions of the printing ink type. In: Mill CC (ed) Rheology of disperse systems. Pergamon Press, Oxford, pp 84–104

Casti JL (1987) Linear dynamical systems. Academic Press

Coussot P (2007) Rheophysics of pastes: a review of microscopic modelling approaches. Soft Matter 3(5):528–540

Cross MM (1965) Rheology of non-Newtonian fluids: a new flow equation for pseudoplastic systems. J Colloid Sci 20(5):417–437

Dunlap PN, Leal LG (1984) The charged dumbbell model for dilute polyelectrolyte solutions in strong flows. Rheol Acta 23:238–249

Frith WJ, d'Haene P, Buscall R, Mewis J (1996) Shear thickening in model suspensions of sterically stabilized particles. J Rheol 40(4):531–548

Giesekus H (1982) A simple constitutive equation for polymer fluids based on the concept of deformation dependent tensorial mobility. J Non-Newton Fluid Mech 11(1–2):69–109

Herschel W, Bulkley R (1926) Konsistenzmessungen von gummi-benzollösungen. Kolloid Zeitschrift 39(4):291–300

Jaumann G (1905) Grundlagen der Bewegungslehre. Springer

Joseph DD (1990) Fluid dynamics of viscoelastic liquids. Springer

Larson RG (1999) The structure and rheology of complex fluids. Oxford University Press

Maxwell JC (1867) On the dynamical theory of gases. Philos Trans R Soc Lond 157:49–88

Nguyen QD, Boger DV (1992) Measuring the flow properties of yield stress fluids. Annu Rev Fluid Mech 24:47–88

Oldroyd JG, Wilson AH (1950) On the formulation of rheological equations of state. In: Proceedings of the royal society of London. Series A. Mathematical and physical sciences, vol 200(1063), pp 523–541

Papanastasiou TC (1987) Flows of materials with yield. J Rheol 31(5):385–404

Peterlin A (1966) Hydrodynamics of linear macromolecules. Pure Appl Chem 12(1–4):563–586

Phan-Thien N (2002) Understanding viscoelasticity. Springer

Phan-Thien N, Tanner RI (1977) A new constitutive equation derived from network theory. J Non-Newton Fluid Mech 2:353–365

Pipe CJ, Majmudar TS, McKinley GH (2008) High shear rate viscometry. Rheol Acta 47(5):621–642

Roberts GP, Barnes HA (2001) New measurements of the flow-curves for carbopol dispersions without slip artefacts. Rheol Acta 40:499–503

Soong TT (1973) Random differential equations in science and engineering. Academic Press

Trouton FT (1906) On the coefficient of viscous traction and its relation to that of viscosity. In: Proceedings of the royal society of London. Series A. Containing papers of a mathematical and physical character, vol 77(519), pp 426–440

Voigt W (1890) Ueber die innere Reibung der festen Körper, insbesondere der Krystalle. In: Abhandlungen der Königlichen Gesellschaft von Wissenschaften zu Göttingen, Mathem. Kl. Nr. 1, vol 36, pp 3–47

White JL, Metzner A (1963) Development of constitutive equations for polymeric melts and solutions. J Appl Polym Sci 7(5):1867–1889

Yang X, Wang S-Q, Halasa A, Ishida H (1998) Fast flow behavior of highly entangled monodisperse polymers-1. Interfacial stick-slip transition of polybutadiene melts. Rheol Acta 37:415–423

Yasuda RAK, Cohen R (1981) Shear-flow properties of concentrated-solutions of linear and star branched polystyrenes. Rheol Acta 20(2):163–178

Zwanzig R (1979) Nonlinear shear viscosity of a gas. J Chem Phys 71(11):4416–4420

Experimental Methods to Characterize Complex Fluids

Volfango Bertola and Teodor Burghelea

Abstract This chapter presents an overview of measurement techniques to characterize the properties of complex fluids, with focus on the rheological characterization (both shear and extensional rheology), and on the most common surface tension measurement methods.

1 Rheological Characterisation of Complex Fluids

Rheology is one of the very few scientific disciplines whose emergence can be precisely dated: 29 April 1929 (Bingham 1944). The term "*Rheology*" has been coined by Eugene Bingham, professor at the Lafayette College following a suggestion of his colleague Markus Rainer and was inspired by an aphorism of Simplicius (often but incorrectly attributed to Heraclitus) "*panta rhei*"—"*everything flows*". The main scope of rheology is the study of deformation and flow of fluids and soft solids subjected to a varying external stress. The rheology is equally concerned with establishing a correlation between the molecular structure of the materials and their flow properties which is of paramount importance during polymer processing operations.

1.1 Fundamentals of Shear Rheology

In order to relate the stresses and the deformations measured by a rheometer, we refer to the Navier–Stokes equation

V. Bertola (✉)
School of Engineering, University of Liverpool, Liverpool, UK
e-mail: Volfango.Bertola@liverpool.ac.uk

T. Burghelea
Laboratoire de Thermique et Energie de Nantes, University of Nantes, Nantes, France

$$\rho \frac{d\mathbf{v}}{dt} = \nabla \cdot (-p\delta + \boldsymbol{\sigma}) + \rho \mathbf{g} \tag{1}$$

where $\boldsymbol{\sigma}$ is the stress tensor, p is the pressure field, δ is the unitary tensor and the body force $\mathbf{g}$ is just acceleration of the gravity. We note that the inertial term $\mathbf{v}\nabla\mathbf{v}$ has been omitted in the equation of motion (Eq. 1).

For a steady flow, $\frac{d\mathbf{v}}{dt} = 0$ and the momentum equation reduces to

$$\nabla \cdot (-p\delta + \boldsymbol{\sigma}) + \rho \mathbf{g} = 0 \tag{2}$$

If one projects Eq. (2) onto a Cartesian system of coordinates, one obtains

$$
\begin{aligned}
\frac{\partial \sigma_{xx}}{\partial x} + \frac{\partial \sigma_{yx}}{\partial y} + \frac{\partial \sigma_{zx}}{\partial z} &= \frac{\partial p}{\partial x} - \rho g_x \\
\frac{\partial \sigma_{xy}}{\partial x} + \frac{\partial \sigma_{yy}}{\partial y} + \frac{\partial \sigma_{yz}}{\partial z} &= \frac{\partial p}{\partial y} - \rho g_y \\
\frac{\partial \sigma_{xz}}{\partial x} + \frac{\partial \sigma_{yz}}{\partial y} + \frac{\partial \sigma_{zz}}{\partial z} &= \frac{\partial p}{\partial z} - \rho g_z
\end{aligned}
\tag{3}
$$

If one projects Eq. (2) onto a cylindrical system of coordinates, one obtains

$$
\begin{aligned}
\frac{\partial \sigma_{rr}}{\partial r} + \frac{1}{r}\frac{\partial \sigma_{r\phi}}{\partial \phi} + \frac{\partial \sigma_{rz}}{\partial z} + \frac{\sigma_{rr} - \sigma_{\phi\phi}}{r} &= \frac{\partial p}{\partial r} - \rho g_r \\
\frac{\partial \sigma_{r\phi}}{\partial r} + \frac{1}{r}\frac{\partial \sigma_{\phi\phi}}{\partial \phi} + \frac{\partial \sigma_{\phi z}}{\partial z} + \frac{2\sigma_{r\phi}}{r} &= \frac{1}{r}\frac{\partial p}{\partial \theta} - \rho g_\phi \\
\frac{\partial \sigma_{rz}}{\partial r} + \frac{1}{r}\frac{\partial \sigma_{z\phi}}{\partial \phi} + \frac{\partial \sigma_{zz}}{\partial z} + \frac{\sigma_{rz}}{r} &= \frac{\partial p}{\partial z} - \rho g_z
\end{aligned}
\tag{4}
$$

If one projects Eq. (2) onto a spherical system of coordinates, one obtains

$$
\begin{aligned}
\frac{\partial \sigma_{rr}}{\partial r} + \frac{1}{r}\frac{\partial \sigma_{r\theta}}{\partial \theta} + \frac{1}{r \sin\theta}\frac{\partial \sigma_{r\phi}}{\partial \phi} + \\
+ \frac{2\sigma_{rr} - \sigma_{\theta\theta} - \sigma_{\phi\phi} + \sigma_{\theta\theta}cot\theta}{r} &= \frac{\partial p}{\partial r} - \rho g_r \\
\frac{\partial \sigma_{r\phi}}{\partial r} + \frac{1}{r}\frac{\partial \sigma_{\theta\phi}}{\partial \theta} + \frac{1}{r \sin\theta}\frac{\partial \sigma_{\phi\phi}}{\partial \phi} + \\
+ \frac{2\sigma_{r\phi} - \sigma_{\phi r} + (\sigma_{\theta\phi} + \sigma_{\phi\theta})cot\theta}{r} &= \frac{1}{r}\frac{\partial p}{\partial \theta} - \rho g_\phi \\
\frac{\partial \sigma_{r\theta}}{\partial r} + \frac{1}{r}\frac{\partial \sigma_{\theta\theta}}{\partial \theta} + \frac{1}{r \sin\theta}\frac{\partial \sigma_{\theta\phi}}{\partial \phi} + \\
+ \frac{\sigma_{\theta r} + 2\sigma_{r\theta} + (\sigma_{\theta\theta} - \sigma_{\phi\phi})cot\theta}{r} &= \frac{1}{r \sin\theta}\frac{\partial p}{\partial \phi} - \rho g_\theta
\end{aligned}
\tag{5}
$$

Fig. 1 Schematic representation of the capillary rheometer
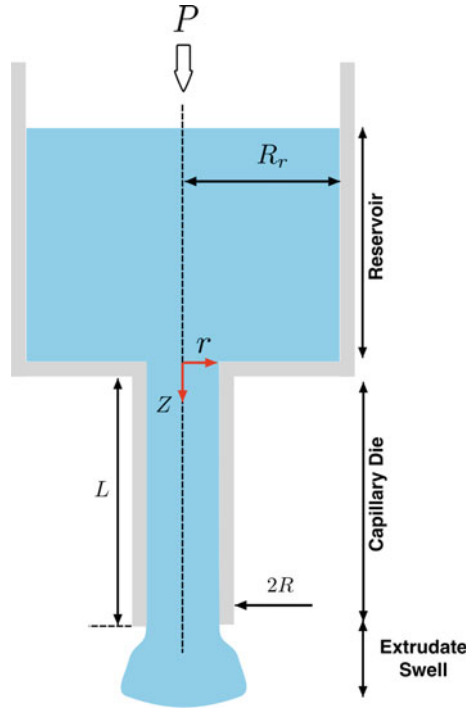
Capillary rheometry During the early days of the rheology, one of the most commonly used rheometric systems was the capillary rheometer, schematically illustrated in Fig. 1. The fluid to be tested initially contained in a reservoir flows through a capillary of radius R and length L in conditions of a controlled applied pressure P that can be supplied either by gravity (in the case of low viscosity fluids) or by the motion of a piston inside the reservoir (in the case of highly viscous fluids, e.g. molten polymers). The viscosity of the fluid may be inferred by simultaneous measurements of the driving pressure P and of the flow rate Q through the capillary if the following conditions are satisfied:

1. The flow is isothermal.
2. The flow is fully developed, linear and laminar.
3. The fluid is incompressible with a viscosity independent on the driving pressure.
4. There exists no slip at the wall, $v_z|_{r=R} = 0$.

The first condition above indicates that, in order to solve such flow problem and assess the viscosity, one needs to refer solely to the momentum conservation equation as there exists no transfer of heat. The linear and laminar nature of the flow translates into the absence of any radial and azimuthal flow component, $v_r = v_\theta = 0$. With these remarks, the Navier–Stokes equation reduces to

$$-\frac{\partial p}{\partial z} + \frac{1}{r}\frac{\partial r\sigma_{rz}}{\partial r} = 0 \qquad (6)$$

Using the assumption that the flow is fully developed, the term $\frac{\partial p}{\partial z}$ is constant along the capillary tube and Eq. (6) may be integrated to

$$\sigma_{rz} = \frac{r}{2}\frac{P_c}{L} \qquad (7)$$

where P_c is the pressure drop along the capillary tube. The stress at the wall of the die is $\sigma_w = \sigma_{rz}|_{r=R} = \frac{R}{2}\frac{P_c}{L}$. To compute the shear viscosity, one needs the rate of shear in the capillary $\dot{\gamma} = \frac{dv_z}{dr}$. This may be obtained from the measured flow rate Q by noting that its relationship with the axial flow speed is

$$Q = 2\pi \int_0^R rv_z(r)dr \qquad (8)$$

By integrating Eq. (8) and using the no slip boundary conditions, one may readily show

$$\frac{Q\sigma_w^3}{\pi R^3} = -\int_0^{\sigma_w} \sigma_{rz}^2 \left(\frac{dv_z}{dr}\right) d\sigma_{rz} \qquad (9)$$

Finally, by differentiating the equation above with respect to σ_w according to the fundamental theorem of calculus and rearranging the terms, one obtains the Weissenberg–Rabinowitsch equation

$$-\frac{dv_z}{dr}|\sigma_w = \dot{\gamma}_w = \frac{1}{4}\dot{\gamma}_{aw}\left[3 + \frac{dlnQ}{dln\sigma_w}\right] \qquad (10)$$

with the apparent shear rate given by $\dot{\gamma}_{aw} = \frac{4Q}{\pi R^3}$.

By measuring the pressure drop P_c and the flow rate and if $n = \frac{dlnQ}{dln\sigma_w}$ can be reliably computed via numerical differentiation of the data, one can compute the viscosity

$$\eta = \frac{\sigma_w}{\dot{\gamma}_w} = \frac{\pi R^4 P_c}{2QL}\left(\frac{n}{3n+1}\right) \qquad (11)$$

We note here that, in the case of a power law fluid, n is simply the power law index. The capillary rheometer has some practical advantages. It is relatively easy to use and provides accurate steady state viscosity measurements. However, entry corrections require a more extensive data analysis procedure (Macosko 1994).

Concentric cylinders rheometry The first operational rotational rheometer was the device built by Maurice Couette (Couette 1880). Couette used a system of concentric cylinders containing within their gap the material to be tested, Fig. 2a. In the original prototype of Couette, the outer cylinder of radius r_o was rotating at a constant angular speed and the inner cylinder of radius r_i was suspended by a torsion wire. The torque
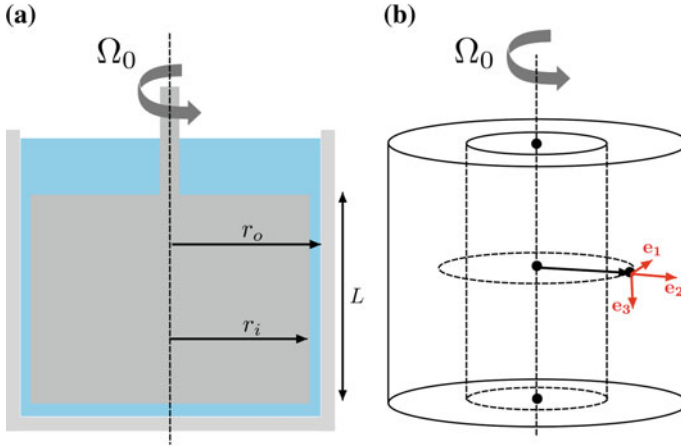
Fig. 2 **a** Schematic representation of the Taylor–Couette setup. **b** Choice of the cylindrical coordinates

acting on the inner cylinder was assessed by measuring the angular deflection using a mirror rigidly attached on the torsional wire. The modern Couette devices use similar operating systems with the difference that, for practical reasons, the inner cylinder is set in rotation by attaching it to the shaft of a rheometer while the outer one is static, Fig. 2a. To describe the flow kinematics in a Couette device, we use the cylindrical coordinates illustrated in Fig. 2b. One can readily show that the shear rate in a Couette device is $\dot{\gamma} = r\frac{d\Omega}{dr}$. Within the narrow gap approximation, $\frac{r_o - r_i}{r} \ll 1$, the following approximation can be made

$$\frac{d\Omega}{dr} \approx \frac{\Delta\Omega}{\Delta r} = \frac{\Omega}{r_o - r_i} \qquad (12)$$

with $\Delta r = r_o - r_i$ and $\Delta\Omega = \Omega(r_o) - \Omega(r_i) = \Omega_0$. With this approximation, the shear rate becomes

$$\dot{\gamma} \approx r\frac{\Omega_0}{\Delta r} \approx \frac{r_i + r_o}{2}\frac{\Omega_0}{\Delta r} = \frac{r_{a}v}{\Delta r}\Omega_0 \qquad (13)$$

with the average radius $r_{av} = \frac{r_i + r_o}{2}$. It can be shown that yet a better approximation for the shear rate is

$$\dot{\gamma}(r) \approx \frac{\Omega_0}{r^2}\frac{r_i^2 r_o^2}{r_{av}\Delta r} \qquad (14)$$

Due to symmetry considerations, a number of terms in the equation of motion will vanish: $\sigma_{\phi z} = \sigma_{z\phi} = \sigma_{rz} = \sigma_{zr} = 0$. Moreover, in the laminar axisymmetric case, all

partial derivatives with respect to the polar angle are zero, $\frac{\partial}{\partial \phi} = 0$. The equations of motion (Eq. 4) reduce to

$$\frac{\partial \sigma_{rr}}{\partial r} - \frac{(\sigma_{\phi\phi} - \sigma_{rr})}{r} = 0 \implies \frac{\partial \sigma_{rr}}{\partial r} - \frac{N_1}{r} = 0 \tag{15}$$

$$\frac{\partial \sigma_{r\phi}}{\partial r} - 2\frac{\sigma_{r\phi}}{r} = 0 \tag{16}$$

$$\frac{\partial \sigma_{zz}}{\partial z} = -\rho g \tag{17}$$

From Eq. (15), one obtains $r\frac{\partial \sigma_{rr}}{\partial r} = N_1$. Within the narrow gap approximation, $\frac{\partial \sigma_{rr}}{\partial r} \approx \frac{\Delta \sigma_{rr}}{\Delta r} = \frac{\sigma_{rr}(r_o) - \sigma_{rr}(r_i)}{r_o - r_i}$. Finally, the first normal stress difference may be approximated by:

$$N_1 \approx \frac{\Delta \sigma_{rr}}{\Delta r} r_{av} \tag{18}$$

By integrating Eq. (16) one obtains $r^2 \sigma_{r\phi} = C = $ constant. The torque acting on the rotating cylinder may be written $T = 2\pi r^2 L \sigma_{r\phi} = 2\pi C L$. An important conclusion is that the torque does not depend on the position in the liquid. The shear viscosity can be readily computed

$$\eta = \frac{\sigma_{r\phi}}{\dot{\gamma}} = \frac{T}{4\pi\Omega_0 L} \frac{r_o^2 - r_i^2}{r_o^2 r_i^2} \tag{19}$$

To conclude, the simultaneous measurements of the angular speed Ω_0 and of the torque T allow one to measure the viscosity (in the narrow gap limit).

Cone and plate rheometry In a cone–plate rheometric setup, the material under investigation is confined within the gap between a cone with a large top angle (typically larger than $170°$) and a flat plate, as shown schematically in Fig. 3a. Consequently, the angle between the cone and the plate is small, $\Delta\Theta \leq 5°$. The top part of the cone is attached to a rotating shaft with the symmetry axis orthogonal to the plate and positioned at its centre. To avoid contact friction, the cone tip is truncated. The shearing surfaces are coaxial conical surfaces with top angles ranging in between π and $\pi - 2\Delta\Theta$. The natural coordinates one may use to describe the kinematics of the motion are the spherical coordinates (Fig. 3b).

The shear rate may be computed (for the details of the calculation, the reader is referred to Macosko (1994), Bird et al. (1977)):

$$\dot{\gamma} = \sin\theta \frac{d\Omega}{d\theta} \approx \frac{\Omega_0}{\Delta\Theta} \tag{20}$$

According to Eq. (20), the shear rate is constant within the entire material under investigation, which makes the cone–plate tool best suited for the measurements
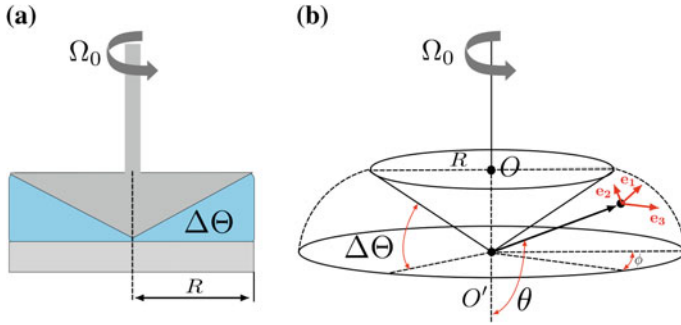
Fig. 3 **a** Schematic representation of the cone–plate setup. **b** Choice of the spherical coordinates

of viscosity and normal stress differences as a function of the applied shear. In the absence of hydrodynamic instabilities, the flow field has a single component, $v_\phi = v_\phi(r)$ and the equations of motion described by Eq. (5) reduce to

$$\frac{\partial \sigma_{rr}}{\partial r} - \frac{N_1 + 2N_2}{r} = -\rho g \cos \theta \tag{21}$$

$$\frac{1}{r}\frac{\partial \sigma_{\theta\theta}}{\partial \theta} - \frac{N_1}{r} \cot \theta = \rho g \sin \theta \tag{22}$$

$$\frac{1}{r}\frac{\partial \sigma_{\theta\phi}}{\partial \theta} + \frac{2\sigma_{\theta\phi}}{r} \cot \theta = \rho g \sin \theta \tag{23}$$

Bearing in mind that $\cot \theta \approx 0$, the integration of Eq. (23) leads to $\sigma_{\theta\phi} = \text{constant} = C$. Consequently, the torque T exerted on the top plate may be computed

$$T = \int_0^{2\pi} \int_0^R r^2 \sigma_{\theta\phi}|_{\pi/2} dr d\phi \tag{24}$$

which leads to $\sigma_{\theta\phi} = \frac{3T}{2\pi R^3}$. The viscosity may be calculated as:

$$\eta = \frac{\sigma_{\theta\phi}}{\dot{\gamma}} = \frac{3T}{2\pi\dot{\gamma}R^3} \approx \frac{3T\Delta\Theta}{2\pi R^3 \Omega_0}. \tag{25}$$

According to the equation above, the viscosity measured with a cone–plate geometry is proportional to the torque acting on the geometry and inversely proportional to its angular speed. Besides the homogeneity of the rate of shear within the entire volume of the sample under investigation, a second notable feature of the cone–plate rheometric setup is that, within the small angle approximation, the result given by Eq. (25) is independent of the constitutive equation of the material.

The normal stress differences $N_1 = \sigma_{\phi\phi} - \sigma_{\theta\theta}$, $N_2 = \sigma_{\theta\theta} - \sigma_{rr}$ can be obtained by measuring the normal force and the pressure distribution along the bottom plate. Because $\cos\theta \approx 0$, Eq. (21) may be approximated[1] by

$$r\frac{\partial\sigma_{rr}}{\partial r} \approx N_1 + N_2 \tag{26}$$

As the shear rate $\dot{\gamma}$ is independent of the radial coordinate r, and N_2 is a steady material function depending only on $\dot{\gamma}$, $\frac{\partial N_2}{\partial r} = \frac{\sigma_{\theta\theta}}{\partial r} - \frac{\sigma_{rr}}{\partial r} = 0$ or $\frac{\sigma_{\theta\theta}}{\partial r} = \frac{\sigma_{rr}}{\partial r}$. With these remarks, Eq. (25) becomes

$$\frac{\partial\sigma_{\theta\theta}}{\partial lnr} \approx N_1 + N_2 \tag{27}$$

The radial distribution of the stress $\sigma_{\theta\theta}$ may be measured using an array of pressure transducers mounted on the bottom plate at various radial positions r. If we can assume that the stress in the radial direction at the rim $\sigma_{\theta\theta}|_{r=R}$ is balanced by the atmospheric pressure p_a (i.e. the surface tension and/or other edge effects may be neglected), then $\sigma_{\theta\theta}(R)$ is just the second normal stress difference

$$N_2 = \sigma_{\theta\theta}(R) - \sigma_{rr}(R) = \sigma_{\theta\theta}(R). \tag{28}$$

From a technical standpoint, it simpler to measure the normal force F_z exerted on the bottom plate of the geometry

$$F_z = -p_a\pi R^2 - \int_0^{2\pi}\int_0^R \sigma_{\theta\theta}(r)drd\phi. \tag{29}$$

The integration of Eq. (29) yields

$$F_z = \frac{1}{2}\pi R^2 N_1 \tag{30}$$

To obtain the relationship above, one has assumed once more that the atmospheric pressure balances the pressure exerted on the free fluid meniscus. To conclude, by combining measurements of the thrust exerted on the bottom plate with measurements of the radial distribution of the pressure, one can measure both normal force differerences.

Parallel plate rheometry Yet another rheometric setup commonly used for the rheological characterisation of fluids is the parallel plate torsional rheometer, displayed in Fig. 4a. The fluid to be investigated is confined in the gap between two parallel plates separated by a finite distance z_0 ranging from hundreds of micrometres to several millimetres. The bottom plate is fixed while the top plate rotates at a constant angular speed Ω_0 around the common symmetry axis of the plates, as shown in Fig. 4.

---

[1]The relationship becomes exact only at the level of the plate, $\theta = \pi/2$.
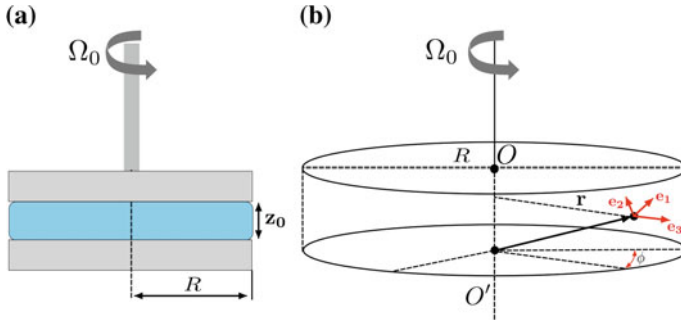
Fig. 4 **a** Schematic representation of the parallel plate setup. **b** Choice of the cylindrical coordinates

In the absence of hydrodynamic instabilities, the trajectories of individual material elements are concentric circles. The natural coordinates one may use to describe the kinematics are the cylindrical coordinates detailed in Fig. 4b. With this choice of coordinates, $v_r = v_\phi = v_z = 0$.

The shear rate may be expressed as

$$\dot{\gamma} = lim_{\Delta z \to 0} \frac{r\Omega(z + \Delta z) - r\Omega(z)}{\Delta z} = r\frac{d\Omega}{dz} \tag{31}$$

Unlike in the case of the cone–plate geometry, the rate of shear is not constant within the gap between the parallel plates. It increases linearly from $\dot{\gamma} = 0$ along the symmetry axis of the device to $\dot{\gamma}(R) = \frac{\Omega_0}{z_0}$ at the rim. This is a significant drawback of the plate–plate system as it can not be used for materials with properties that depend strongly on the shear rate which is the case for a large number of materials that exhibit shear thinning rheological properties.

The equations of motion may be written

$$\frac{\partial \sigma_{rr}}{\partial r} = \frac{N_1 + N_2}{r} \tag{32}$$

$$\frac{\partial \sigma_{\phi z}}{\partial z} = 0 \tag{33}$$

$$\frac{\partial \sigma_{zz}}{\partial z} = \rho g \tag{34}$$

From Eq. (33), it can be shown that

$$v_\theta(r, z) = \frac{r\Omega_0 z}{z_0} \tag{35}$$

$$\dot{\gamma}(r) = r\frac{d\Omega}{dz} = r\frac{\Omega_0}{z_0} \tag{36}$$

The relationship between the shear stress $\sigma_{\theta z}$ and the torque T acting on the top plate is

$$\sigma_{\theta z}(\dot{\gamma}_R) = \frac{T}{2\pi R^3}\left[3 + \frac{dlnT}{dln\dot{\gamma}_R}\right] \tag{37}$$

where the rim shear rate is $\dot{\gamma}_R = R\frac{\Omega_0}{z_0}$. The difference between the first and the second normal stress differences is

$$N_1(\dot{\gamma}_R) - N_2(\dot{\gamma}_R) = \frac{F_z}{\pi R^2}\left(2 + \frac{dlnF_z}{dln\Omega_0}\right) \tag{38}$$

where F_z is the normal force exerted on the bottom plate. Thus, by plotting both the torque and the normal force versus the angular speed on a double logarithmic scale, the dependencies of the slopes $\frac{dlnT}{dln\Omega_0}$ and $\frac{dlnF_z}{dln\Omega_0}$ on the rim shear rate can be determined. This procedure yields $\sigma_{\theta z}$ and $N_1 - N_2$. The apparent (or Newtonian) shear stress obtained with the parallel plate rheometric setup is

$$\sigma_a = \frac{2T}{\pi R^3} \tag{39}$$

1.2 Fundamentals of Extensional Rheology

A significant number of modern polymer processing operations which include (but are not limited to) melt blowing, fibre spinning, compression moulding and extrusion involve flows that combine both shear and extension. As compared to the case of shear flows, the material elements undergo much higher strains during extensional flows which typically leads to a strongly nonlinear dependence of the extensional stresses on the strain. The knowledge of the rheological behaviour in shear does not suffice to describe the behaviour during extension. The rheological response of a complex fluid undergoing shear such as a polymer solution or melt injected into a die or mould, drawn through an extrusion die, blow moulded, calendared, etc. will not correctly predict the processing behaviour during such operations; inferring the extensional flow behaviour from rheological tests performed in shear is usually impossible.

Despite a clear need for extensional measurements of complex fluids, the development of instrumentation evolved slower than the development of shear rheometry. A first daunting task in this context is the generation of a spatially homogeneous extensional flow field. To generate an extensional motion in a fluid, one needs to bring the fluid in contact with a moving solid surface. This generally creates shear in the vicinity of the solid surface which alters the kinematics of the extensional flow. A second difficulty relates to the need of generating high strains during extension.

This requires the development of motion control systems able to operate within a broad range of speeds and achieve significant travel distances.

Unlike in the case of shear rheometry, the design and instrumentation of an extensional rheometric device depend on the range of extensional viscosities to be measured. After providing the reader with a basic description of the kinematics of extensional flows, we will describe several such extensional rheometric devices highlighting both their advantages and practical limitations.

Kinematics of extensional flows A pure extensional flow is an irrotational flow which lacks both vorticity and shear (Bird et al. 1977). As compared to a laminar shear flow where neighbouring fluid elements separate linearly with time, in an extensional flow, the separation is exponential in time. Consequently, such flows are very efficient in elongating and orienting the microscopic structural units of a complex fluid which makes them a valuable tool for probing the microstructure of complex fluids. A simple extensional flow may be described by the following velocity field:

$$
\begin{aligned}
v_x &= -\frac{1}{2}(1+b)\dot{\epsilon}x \\
v_y &= -\frac{1}{2}(1-b)\dot{\epsilon}y \\
v_z &= \dot{\epsilon}z
\end{aligned}
\tag{40}
$$

where b is a constant that affects the way the streamlines change with rotation about the z axis and $\dot{\epsilon}$ is the rate of deformation of fluid elements. Three distinct types of extensional flows may be obtained for different choices of the parameter b and of the sign of the rate of deformation

1. $b = 0, \dot{\epsilon} > 0$: uniaxial extension
2. $b = 0, \dot{\epsilon} < 0$: biaxial stretching
3. $b = 1$: planar elongation

A typical extensional flow field obtained for $b = 0$ is illustrated in Fig. 5.

The deformation of a cubic fluid element of unitary volume by each of the three types of extensional flows is schematically illustrated in Fig. 6.

In practical applications, even in the case when the deformation field is steady, the response of the material is usually unsteady meaning that the material reaches a steady dynamic regime only after a finite period of time. This is because fluids are characterized by a finite response time. In the case of Newtonian fluid, the characteristic timescale of the response is the viscous time whereas for non-Newtonian fluids, it is a relaxation time which describes how fast the microstructure responds to the externally applied deformation field. Bearing this in mind, it appears natural that the material functions characterizing the response to an extensional flow should be sought as time dependent (i.e. "transient") even in the case when the deformation field is steady $\left(\frac{d\dot{\epsilon}}{dt} = 0\right)$. Thus, the transient extensional viscosities may be defined as
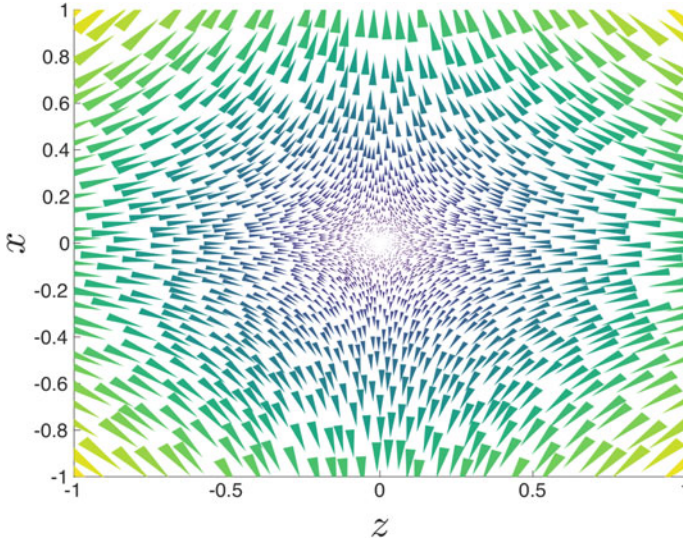
Fig. 5 Steady elongational flow field ($b = 0$)
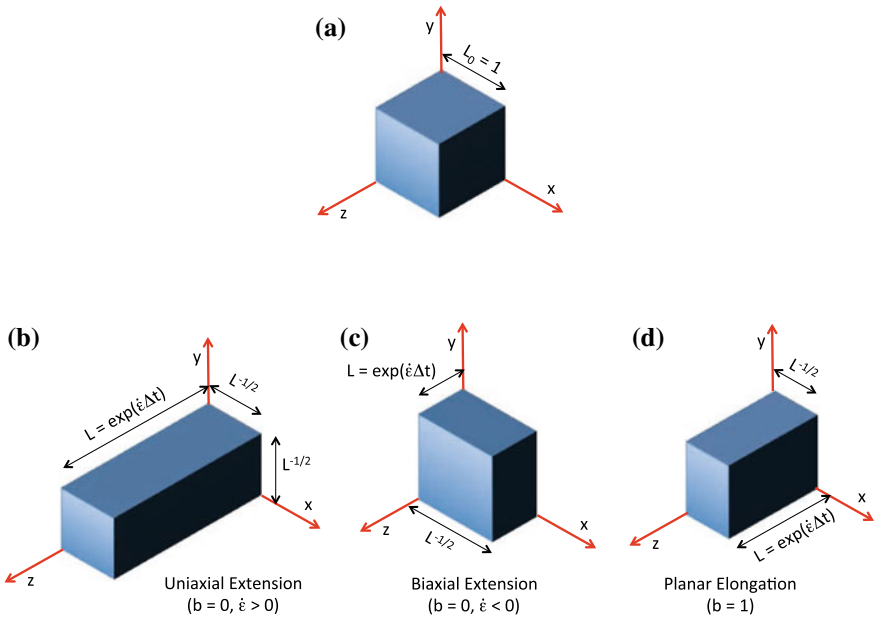
Fig. 6 Deformation of a cube of unitary volume **a** during the time interval Δt by three types of shear free flow: **b** uniaxial extension ($b = 0$, $\dot{\epsilon} > 0$), **c** biaxial extension ($b = 0$, $\dot{\epsilon} < 0$), **d** planar elongation ($b = 1$)

$$\eta_1^+(\dot{\epsilon}, t) = \frac{\sigma_{zz} - \sigma_{xx}}{\dot{\epsilon}}$$

$$\eta_2^+(\dot{\epsilon}, t) = \frac{\sigma_{xx} - \sigma_{yy}}{\dot{\epsilon}}$$

(41)

For the case of the uniaxial extension ($b = 0$) $\sigma_{xx} = \sigma_{yy}$ and the response of the material to deformation is characterized by a single transient extensional viscosity, $\eta^+ = \eta_1^+$.

The total strain accumulated by the material elements during the extensional process may be computed by direct integration of the equations of motion (Eq. 40). In the case of the uniaxial extension ($b = 0$), the position of a material element labelled by [j] varies exponentially in time, $X^j = X_0^j e^{\dot{\epsilon}t}$ and the strain between two neighbouring material elements is the Hencky strain defined logarithmically by

$$\epsilon_H = \dot{\epsilon}t = ln\left[\frac{\Delta X(t)}{\Delta X(0)}\right]$$

(42)

For a linear viscoelastic material characterized by a discrete spectrum of relaxation times $\{\lambda_k\}_{k=1,N}$, the response during uniaxial extension can be solved analytically

$$\eta^+(t) = \sum_{k=1}^{N} 3\eta_k\left[1 - e^{-\frac{t}{\lambda_k}}\right]$$

(43)

In the asymptotic limit of long relaxation times $t \gg \max\{\lambda_k\}$, the response of the material approaches a steady state $\eta_{SS}^+ = lim_{t\to\infty}\eta^+(t) = 3\eta_0$, where η_0 is the zero shear viscosity of the material. This limiting value of the response is called the "*linear viscoelastic envelope*" (LVE). The knowledge of the LVE is crucial for the validation of extensional viscosity measurements because in a linear range of deformation, all transient extensional viscosity curves should asymptotically approach the LVE. The concept of LVE is equally useful in introducing the term of "*strain hardening*" which is observed for a broad class of polymeric systems in the form of a substantial increase (up to several orders of magnitude) of the transient elongational viscosity with respect to the LVE. The magnitude of the strain hardening effect is quantified by the Trouton ratio

$$Tr(\dot{\epsilon}, t) = \frac{\eta^+(t)}{\eta_0}$$

(44)

The strain hardening is a rather complex phenomenon which depends on both the molecular architecture of the polymeric systems (e.g. branched polymeric systems exhibit stronger strain hardening) and the rate of extension, $\dot{\epsilon}$. Thus, the quantification of this effect by measuring the Trouton ratio is a rather sensitive probe of the branched structure of molten polymeric systems.

Capillary breakup rheometry of low viscosity fluids The capillary breakup extensional rheometry is a simple and reliable technique for assessing the extensional rheological properties of low to moderate viscosity fluids. The technique was first
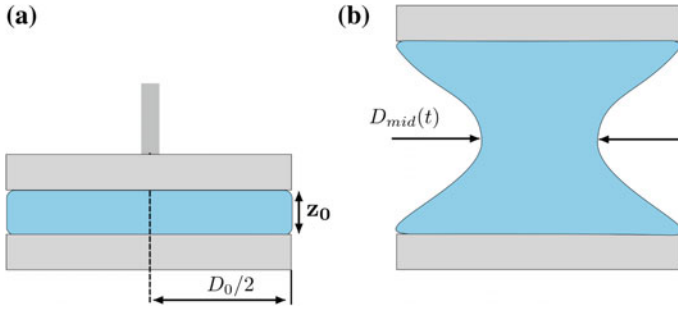
Fig. 7 Schematic representation of the capillary breakup device: **a** initial fluid meniscus. **b** fluid meniscus during the capillary thinning process

described by Bazilevskii et al. (1981) and later revisited in a number of subsequent papers (Bazilevskii et al. 1997, 2001; Bazilevskii and Rozhkov 2015).

In this technique, a drop of liquid is confined between two rigid plates initially set at a distance z_0 apart as schematically illustrated in Fig. 7a. Next, by rapidly moving the top plate to a higher position, an axial step-strain is imposed onto the liquid bridge (Fig. 7b). The shape of the liquid bridge evolves under the combined action of several physical processes; the capillary pressure which here plays the natural role of a "*force transducer*", viscous dissipation that delays the necking of the fluid filament and, in the case of polymeric fluids, the elastic forces that equally oppose the necking process.

Bazilevsky and coworkers were first to propose a theoretical framework to describe the thinning of a Newtonian and an Oldroyd-B fluid filament in terms of measurements of its radius (Bazilevskii et al. 1981, 2001). Their analysis has been extended by Entov and Hinch to account for both the effect of a spectrum of relaxation times and of the finite extensibility of the polymer chains (Entov and Hinch 1997).

For a Newtonian fluid of viscosity η_s and surface tension coefficient γ, a local force balance together with the elimination of the pressure lead to the following equation for the midpoint radius of the filament:

$$3\eta_s \left(-\frac{2}{R_{\mathrm{mid}}(t)} \frac{d R_{\mathrm{mid}}(t)}{dt} \right) = \frac{\gamma}{R_{\mathrm{mid}}(t)} \qquad (45)$$

The derivation of Eq. (45) assumed the total longitudinal stress along the fluid filament to be zero at all times. The term in the brackets may be understood as an extensional deformation rate of a Lagrangian fluid element at the midplane of the fluid column where the radius R_{mid} is measured. By integrating Eq. (45), a linear decay of the midpoint radius of the filament with time is obtained

$$R_{\mathrm{mid}}(t) = \frac{\gamma}{6\eta_s} (t_c - t) \qquad (46)$$
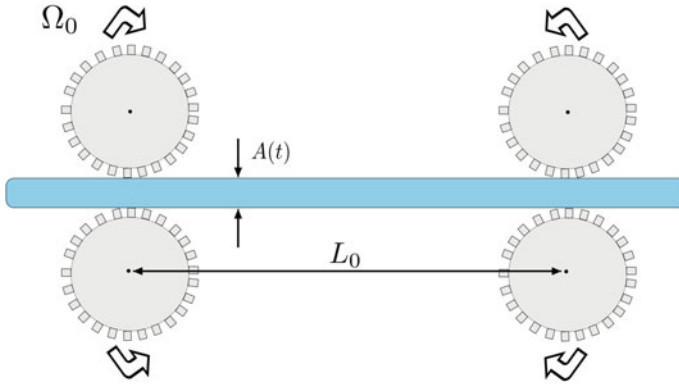
Fig. 8 Schematic representation of the Meissner extensional rheometer

Here $t_c = \frac{6\eta_s R_0}{\sigma}$ is a critical time associated to the filament breakup and R_0 is the initial radius of the filament.

Meissner rheometry of molten polymeric systems Meissner proposed a rotatory clamp extensional rheometer (RME) (Meissner and Hostettler 1994), schematically illustrated in Fig. 8. The basic concept of the device was proposed at the end of 1960s at the Research and Development department of BASF, Ludwigshafen, Germany (Meissner 1969).

The sample is clamped in between four counter-rotatory clamps. The sample is both heated and buoyed by gas injected from below. When the rotatory clamps were set in motion with a constant angular speed, the polymeric sample was experiencing a uniaxial extensional deformation. The samples were carefully prepared by extrusion and their initial length was rather large, $L_0 = 50$ mm. The large initial length of the sample might seem an unimportant detail but is not. One of the particular concerns was related to the geometrical homogeneity of the sample which is of paramount importance in assuring a purely uniaxial deformation. This was specifically stated in page 20 of Meissner and Hostettler (1994): "*When the elongation becomes inhomogeneous (for homogeneous samples the reason often is an inhomogeneous temperature field), any data processing becomes questionable*". An initially long sample together with an extremely careful and elaborated mechanical design of the rotatory clamps insured a geometrical homogeneous deformation of the sample. The RME device could reach Hencky strains $\epsilon_H = 7$ and could operate at strain rates of $\dot{\epsilon}_H = 1$ s^{-1}. The transient tensile force $F(t)$ was measured by a force transducer which was installed on the pairs of rotating clamps.

For a geometrically homogeneous sample, the cross-sectional area decays exponentially with time

$$A(t) = A_0 \left(\frac{\rho_S}{\rho_M} \right)^{2/3} e^{-\epsilon_H} \tag{47}$$

where A_0 is the initial cross-sectional area measured in a solid state (at room temperature) and $\epsilon_H = \dot{\epsilon}_H t$ is the Hencky strain at time t. The prefactor $\left(\frac{\rho_S}{\rho_M} \right)^{\frac{2}{3}}$, where ρ_S is the density of the sample in a solid state while ρ_M is its density in a molten, accounts for the thermal expansion of the sample. The geometric homogeneity of the sample is crucial for the applicability of Eq. (47). In the case of a geometrically inhomogeneous sample, the cross-sectional area also depends on the position along the sample leading to a rate of deformation that is no longer equal to the nominal value $\dot{\epsilon}_H$ and depends on both the time and the position along the sample. As already stated above, Meissner was particularly keen about this aspect (which nowadays, unfortunately, no longer receives the deserved attention) and assessed the homogeneity of the sample during the extension by in situ visualisation of the sample (see Fig. 19 in Meissner and Hostettler (1994)). The transient extensional viscosity may be computed according to

$$\mu^+(t) = \frac{F(t)}{A(t)\dot{\epsilon}_H} \tag{48}$$

Well ahead of its time, the RME device could operate in two distinct modes. The first one as described above is a "*stressing mode*" which corresponds to a constant rate of extension $\dot{\epsilon}_H$. Alternatively, however, the device could operate in "*creep mode*" which corresponds to a constant applied stress. Bearing in mind the limited technology available at the end of the $60's$, this was a remarkable achievement hard to implement even with today's technological advancements as it requires a specially developed controlled feedback system able to maintain the ratio $\frac{F(t)}{A(t)\dot{\epsilon}_H}$ constant during the extension.

Münstedt rheometry of molten polymeric systems Yet an another approach to the extensional rheology of molten polymeric system was proposed by Münstedt (1979). The Münstedt device is schematically illustrated in Fig. 9.

As opposed to the Meissner approach, the device proposed by Münstedt uses an initially short sample (S) with a cylindrical cross section and an initial diameter D_0 attached in a vertical position to the plates P_1, P_2 and immersed in an oil bath OB. The density of the oil is roughly equal to that of the sample thus minimizing gravity and buoyancy effects which can cause inhomogeneous deformations of the specimen. While the bottom plate P_2 is fixed, the top plate P_1 is moved vertically by a ac-servo motor controlled by a personal computer. If L_0 is the initial length of the sample, and $L(t)$ its length at time t, the nominal Hencky strain is defined as

$$\epsilon_H = ln\left(\frac{L(t)}{L_0} \right) \tag{49}$$

The nominal rate of uniaxial deformation is

$$\dot{\epsilon}_H = \frac{L_0}{L(t)} \frac{dL(t)}{dt} \tag{50}$$

Fig. 9 Schematic representation of the Münstedt extensional rheometer according to Münstedt (1979) (not in scale): (S)—sample, (OB)—oil bath, (P_1)—top plate, (P_2)—bottom plate
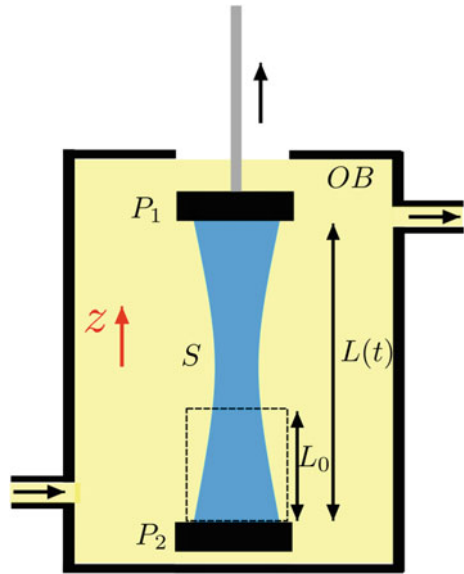
The bottom plate P_2 is equipped with an accurate force transducer which measures the transient tensile force $F(t)$.

As the Meissner device, the Münstedt device may operate in two distinct modes (Münstedt and Laun 1979): "*stressing mode*" (at constant rate of deformation $\dot{\epsilon}$) and "*creep*" (at constant driving stress). In the stressing mode, a feedback loop insures an exponential increase of the distance between plates with time, $L(t) = L_0 e^{\dot{\epsilon}_H t}$ and the transient elongational viscosity is computed as

$$\mu^+(t) = \frac{F(t)}{\dot{\epsilon}_H A(t)} \tag{51}$$

Here $A(t) = \pi D^2(t)/4$ with $D(t)$ being the diameter of the sample at time t is the transient cross-sectional area of the sample.

As in the case of the Meissner device, the homogeneity of the deformation states is crucial in reliably assessing the transient extensional viscosity of the material. It has been demonstrated experimentally that if this condition is not fulfilled, the Hencky strain is not uniform along the sample, and the interpretation of measurements becomes questionable (Burghelea et al. 2009; Starý et al. 2015; Burghelea et al. 2011, 2012). If the homogeneity condition is fulfilled, due to the incompressibility of the polymer melt, it can be readily shown that $D(t) = D_0 e^{-\epsilon_H/2}$ and Eq. (51) becomes

$$\mu^+(t) = \frac{4F(t)}{\pi \dot{\epsilon}_H D_0^2 e^{-\epsilon_H}} \tag{52}$$

In a stressing operating mode, a different feedback loop maintains the ratio $\sigma^+(t) = F/A(t) = FL(t)/(V)$ constant where V is the volume of the sample. Again, these measurements rely on the geometrical homogeneity of the sample and its incompressibility.

Filament stretching rheometry of molten polymeric systems The Filament Stretching Extensional Rheometer (FISER) for viscous fluids was proposed by Tirtaatmadja and Sridhar (1993). The original design of the FISER is schematically illustrated in Fig. 10. Like the Münstedt device, the FISER uses a constant volume sample with a small initial length L_0 clamped in between two plates P_1, P_2 which move in opposite directions with equal speeds $u(t)$.

Variants of the device with the sample oriented vertically were later proposed (Anna et al. 2001; McKinley and Sridhar 2002; Bach et al. 2002). Unlike in the case of the Münstedt device, the sample is not immersed in an oil bath which, at low deformation rates, makes the measurements problematic due to gravity sagging effects, Anna et al. (2001). The theoretical background of the transient elongational viscosity measurements using the FISER device is given by Szabo (1997). Due to the lack of an oil bath, the force balance includes a non-negligible surface tension term and, in a vertical configuration, a gravity term as well. In addition, depending on the operating speeds, an extra inertial term may be involved. Thus, the stress difference computed at the midpoint of the filament is

$$\sigma_{zz}(t) - \sigma_{rr}(t) = \frac{4F(t)}{\pi D_{\text{mid}}(t)^2} - \frac{2\gamma}{D_{\text{mid}}(t)} - \frac{\rho_M g L(t)}{2} - \frac{\rho_M \dot{\epsilon}_H(t)^2 L(t)^2}{8} \quad (53)$$

where γ is the surface tension coefficient of the sample and ρ_M its viscosity. The last term in the right-hand side of Eq. (53), which accounts for inertia, may be neglected if

$$\frac{\rho_M \dot{\epsilon}_H L}{8\mu^+} \ll 1 \quad (54)$$

This inequality is satisfied for highly viscous polymer melts but may break down for materials with smaller viscosities tested at high rates of deformation. The transient extensional viscosity may be calculated as

Fig. 10 Schematic representation of the filament stretching rheometer according to Tirtaatmadja and Sridhar (1993) (not in scale)
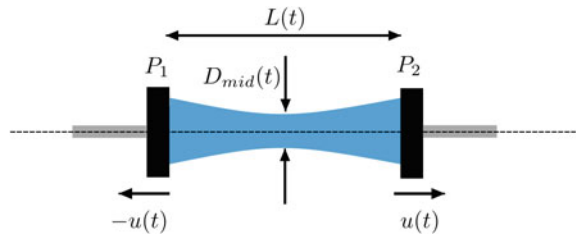
$$\mu^+(t) = \frac{\sigma_{zz}(t) - \sigma_{rr}(d)}{\dot{\epsilon}_H(t)} = \frac{4F(t)}{\pi\dot{\epsilon}_H(t)D_{\mathrm{mid}}(t)^2} - \frac{2\gamma}{\dot{\epsilon}_H(t)D_{\mathrm{mid}}(t)}$$
$$- \frac{\rho_M g L(t)}{2\dot{\epsilon}_H(t)} - \frac{\rho_M \dot{\epsilon}_H(t)L(t)^2}{8} \tag{55}$$

The FISER device may be operated in two distinct ways. The first way is very similar to the operating mode of the Münstedt device. First, the Hencky strain is computed from the instantaneous length of the sample according to Eq. (50). If the deformation of the sample is geometrically homogeneous, the midpoint diameter of the sample may be computed as $D_{\mathrm{mid}}(t) = D_0 e^{-\epsilon_H(t)/2}$. Finally, the transient elongational viscosity is calculated according to Eq. (55).

Alternatively, rather than monitoring the instantaneous length $L(t)$ of the sample in order to compute the Hencky strain, one could measure the instantaneous diameter of the sample $D_{\mathrm{mid}}(t)$ measured at the midpoint of the sample. Such measurements may be performed either using a laser sheet and a photomultiplier or by imaging the sample with a digital camera. The local Hencky strain may be computed as

$$\epsilon_H^{\mathrm{mid}}(t) = 2ln\left(\frac{D_0}{D_{\mathrm{mid}}(t)}\right) \tag{56}$$

Consequently, the rate of deformation at the midpoint of the sample is

$$\dot{\epsilon}_H^{\mathrm{mid}}(t) = -\frac{2}{D(t)}\frac{dD(t)}{dt} \tag{57}$$

If the deformation is geometrically inhomogeneous, the rate of deformation at the midpoint of the sample differs from the nominal value given by Eq. (50) and is not necessarily constant in time. This issue may be addressed by employing a special feedback loop which modifies in real time the separating speed of the plates based on the local measurements of the midpoint diameter of the filament in order to maintain the local rate of deformation given by Eq. (57) constant (Anna et al. 2001; Bach et al. 2002).

The FISER device has been recently become available commercially from *Rheo Filament*.

Sentmanat rheometry of molten polymeric systems An ingenious method of using a commercial rotational rheometer to perform measurements of the transient elongational viscosity was proposed by Sentmanat (2003a, b, 2004).

The idea consisted of designing a fixture that can be mounted on the shaft of a rotational rheometer and "*convert*" the rotation at a constant angular speed Ω_0 in a uniaxial extension flow, as shown in Fig. 11. The Sentmanat extensional fixture consists of two identical drums of radius R separated by a fixed distance L_0 intercoupled by a system of gears (not shown in Fig. 11) such as the rotation of the cylinder connected to the shaft triggers the rotation of the second cylinder at a same angular speed but in an opposite sense. This counter-rotative motion of the cylinders
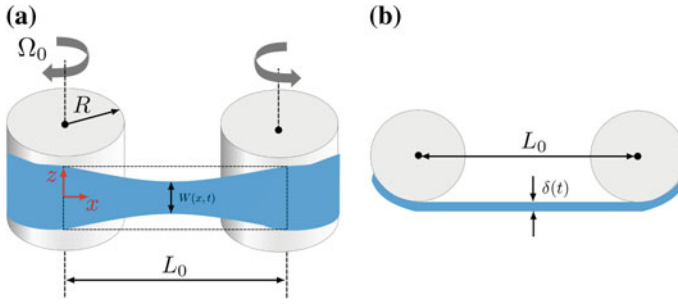
Fig. 11 Schematic representation of the Sentmanat extensional fixture: **a** front view **b** top view

will induce a uniaxial deformation of a rectangular-shaped sample rigidly fixed by a system of clamps onto the frontal surface of the cylinders, as illustrated in Fig. 11a.

For a constant angular speed of the shaft, the Hencky strain associated to the uniaxial extension of the sample increases linearly with time

$$\epsilon_H = \frac{2\Omega_0 R}{L_0} t \tag{58}$$

Accordingly, the Hencky strain rate is given by

$$\dot{\epsilon}_H = \frac{2\Omega_0 R}{L_0} \tag{59}$$

The resistance of the sample to the extensional deformation manifests through a transient tangential force $F(t)$ acting on each cylinder and related to the transient torque $T(t)$ acting on the shaft of the rheometer via

$$F(t) = \frac{T(t)}{2R} \tag{60}$$

If an affine deformation of the specimen is assumed, its cross-sectional area $A(t)$ (see Fig. 11b) will decay exponentially with time according to

$$A(t) = A_0 \left(\frac{\rho_S}{\rho_M}\right)^{\frac{2}{3}} e^{-\dot{\epsilon}_H t} \tag{61}$$

The prefactor $\left(\frac{\rho_S}{\rho_M}\right)^{\frac{2}{3}}$ where ρ_S is the density of the sample in a solid state while ρ_M is its density in a molten accounts for the thermal expansion of the sample.

For a purely uniaxial extension at a constant Hencky strain rate, the transient elongational viscosity can be expressed as

$$\eta^+(t) = \frac{F(t)}{\dot{\epsilon}_h A(t)} \tag{62}$$

As compared to the other techniques of measuring the transient elongational viscosity of polymer melts, the Sentmanat rheometer has a number of advantages as well as some potential disadvantages. A first major advantage of this technique comes from its simplicity; the extensional fixture may be quickly coupled to any commercially available rotational rheometer and the sample can be quickly loaded. This is certainly not the case of the previously discussed methods which all require sophisticated machining, instrumentation and digital control systems as well as a more complicated loading procedure of the sample. Second, as compared to other techniques, the Sentmanat solution is rather affordable.

However, this technique equally has some drawbacks. First, the sample is held in air and, consequently, gravity sagging effects may bias the measurements of the transient elongational viscosity. These effects may become significant in a range of low Hencky strain rates. A second drawback comes from the lack of visual information on the evolution of the sample during extension: when used for molten polymeric systems, the extensional fixture is enclosed in an oven which makes the visualization of the sample impossible. Thus, if some undesired effects such as gravity sagging or slippage of the sample at the contact points with the cylinders come into play, the operator will only see spurious data after the end of the experiment. A third and perhaps the most important drawback of this technique relates to the impossibility of assuring a geometrical uniform deformation of the sample at all times. In terms of flow kinematics, this means that the frontal shape of the sample must remain rectangular at all times during the extension (as hinted by the dotted lines in Fig. 11a). Any deviation from this would translate a rate of deformation that differs from the nominal value given by Eq. (59) and is a function of the horizontal coordinate x. Equation (62), used to compute the transient extensional viscosity using the torque measurements performed by the rotational rheometer, is applicable if and only if the deformation is a purely uniaxial one which, of course, is no longer the case if the shape of the sample deviates from a rectangular one.

This aspect is generally neglected while performing measurements with the Sentmanat fixture. On the other hand, according to the Considère rule, an inhomogeneous deformation will regularly appear at a finite Hencky strain, Considére (1885). This inhomogeneous deformation is triggered by the presence of the rigid boundary conditions at the clamping points of the sample and appears in the form of a primary necking.

2 Surface Tension Measurement Techniques

The interfacial tension between immiscible fluids can be measured using several different techniques, many of which are commercially available (Rusanov and Prokhorov 1996; Drelich et al. 2002). Such measurement techniques can be broadly classified according to the physical process used to determine the surface or the interfacial tension magnitude: direct measurement of the force required to create new surface; measurement of the pressure difference across a curved interface (Laplace pressure); deformation of an interface due to an external force (e.g. gravity).

2.1 Direct Force Measurement

When a fluid interface at equilibrium is deformed mechanically, it tends to recover the initial shape to minimize the surface energy, which is proportional to the interfacial area. Thus, interfacial tensions can be measured directly by deforming the interface with a simple probe (such as a wire, a rod or a plate), and measuring the restoring force of the interface on the probe itself by means of a microbalance or a force sensor. Dividing the measured force by the wetted length of the probe, one obtains the value of the interfacial tension.

Du Noüy ring The du Noüy ring (du Noüy 1925) is one of the most common methods to measure the interfacial tension between two fluids. The probe consists of a wire ring, with a radius R of a few cm and usually made up of a platinum–iridium alloy, which is placed exactly on the interface and then gently pulled in the direction perpendicular to the interface. The wire radius, r, usually ranges between $R/60$ and $R/30$ (Vold and Vold 1983). As the ring moves, it lifts a cylindrical liquid film increasing the interfacial area, as shown schematically in the cross-sectional view of the ring probe displayed in Fig. 12a. This creates a restoring force along the three-phase line on the ring, F, which can be measured by a microbalance or a force sensor and used to calculate the interfacial tension as

$$\gamma = \frac{F}{4\pi R \cos\theta} C \tag{63}$$

where θ is the contact angle of the fluid interface with respect to the ring surface, and C is a correction factor to account for the weight of the liquid lifted by the ring, initially introduced by Harkins and Jordan (1930), which depends on the ring geometry and on the fluid densities, and can be calculated using the following expression (Zuidema and Waters 1941):

$$C = 0.725 + \sqrt{\frac{0.00363 F}{(\pi R)^2 (\rho_{max} - \rho_{min})} + 0.04534 - 1.679\frac{r}{R}} \tag{64}$$
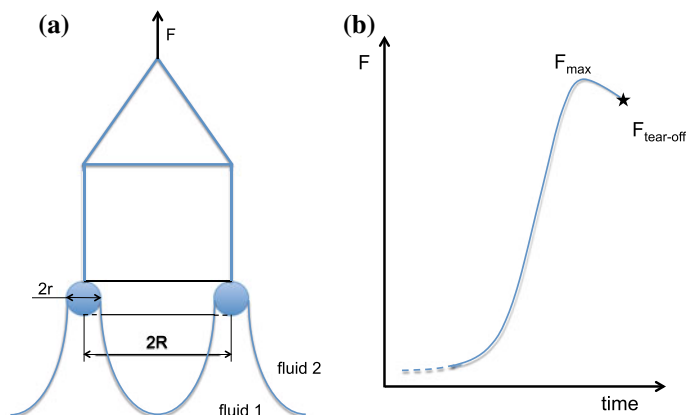
Fig. 12 Schematic of the du Noüy ring (**a**) and qualitative behaviour of the measured force (**b**)

The value of the force F in Eqs. (63) and (64) corresponds to the maximum pull, which is measured just before the film rupture, as shown schematically in Fig. 12b. This value can be measured accurately by an automated instrument; however, manual microbalances will measure the slightly smaller tear-off force instead.

The main sources of error of this method are accidental deformations of the ring probe during handling or cleaning, poor alignment (the ring must be perfectly parallel to the interface, and poor cleaning, which may change significantly the ring wettability. For this reason, the ring probe must be cleaned from organic contaminants by an organic solvent and then flamed to remove any organic molecules before each test.

Wilhelmy plate In this method (Wilhelmy 1863), the probe used to deform the interface is a thin vertical plate, made of platinum or platinum–iridium alloy. Unlike in the du Noüy method, the plate is kept at a fixed position level with the interface, and the liquid wets the plate as shown schematically in Fig. 13.

$$\gamma = \frac{F \cos \theta}{2(L + t)} \approx \frac{F}{2L} \tag{65}$$

where L and t are, respectively, the width and the thickness of the plate, and θ is the contact angle, which in case of complete wetting is negligibly small ($\cos \theta \approx 1$). In Eq. (65), no correction for liquid weight or buoyancy is necessary.

The Wilhelmy plate method is generally more accurate than the du Noüy ring method, and does not require knowledge of the fluid densities. Adsorption of organic molecules from the laboratory environment or test solutions can be a major source of experimental error when measuring surface tensions using the Wilhelmy plate method, therefore they must be removed by flaming the probe before tests.

Fig. 13 Schematic of the
Wilhelmy plate method
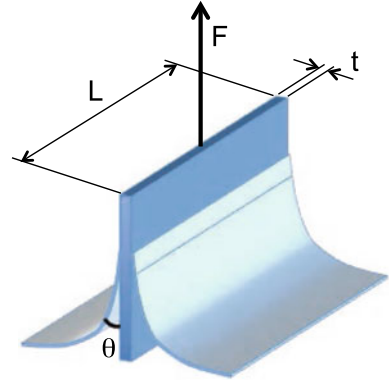
2.2 Measurement of Laplace Pressure

One of the effects of interfacial tension is to generate a pressure difference between
fluids on either side of a curved interface (Laplace pressure), with the higher pressure
on the concave side of the interface. This pressure difference is responsible for phe-
nomena such as capillary rise, bubble and drop formation, etc., and can be calculated
using the Young–Laplace equation

$$\Delta P = \gamma \left(\frac{1}{r_1} + \frac{1}{r_2} \right) \tag{66}$$

where r_1 and r_2 are the principal radii of curvature of the interface at a given point.
Thus, Eq. (66) can be used to find the interfacial tension when the pressure difference
and the system geometry are known.

Maximum bubble pressure This method yields the surface tension as a function
of the maximum pressure (p^*) to force a gas bubble out of a calibrated capillary
tube of radius r^* (Simon 1851; Sugden 1922, 1924), and is illustrated
schematically in Fig. 14. The measured pressure in the growing bubble is the sum of
the capillary (Laplace) pressure, $\Delta P_L(r)$ caused by the interfacial tension and the
hydrostatic pressure caused by the liquid column above the orifice of the capillary:

$$p = \Delta P_L(r) + \rho_L g h \tag{67}$$

where r is the bubble radius and h the depth of the orifice immersed into the liquid.

When the bubble starts to grow at the tip of the capillary, its radius, r, is larger
than the radius of the capillary, r^* (Fig. 14a); as the bubble grows, its radius becomes
increasingly smaller until it becomes equal to the radius of the capillary hence the
Laplace pressure in Eq. (67) increases monotonically (Fig. 14b). If the bubble con-
tinues to grow beyond this point, its radius also grows therefore the Laplace pressure
in Eq. (67) decreases monotonically; as a consequence, the measured pressure in the
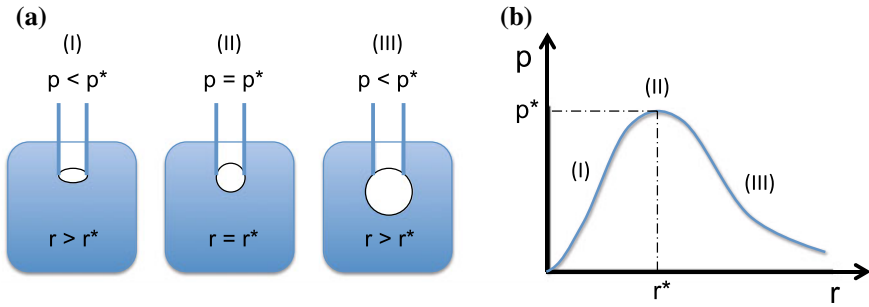
Fig. 14 Maximum bubble pressure method

bubble goes through a maximum ($p = p^*$) which corresponds to a hemispherical bubble with radius $r = r^*$. In these conditions, the bubble is hemispherical, and the surface tension force on the orifice is parallel to the tube axis, so that

$$\gamma = \frac{1}{2}(p^* - \rho_L gh)r^* \tag{68}$$

To account for gravity effects, various corrections to Eq. (68) are discussed in the literature (Sugden 1924; Fainerman and Miller 1998; Sonntag 1982; Drelich et al. 2002). Usually multiplicative correction factors for Eq. (68) are expressed as polynomials such as

$$C = \sum_{i=0}^{5} a_i \left(\frac{r^*}{a}\right)^i \tag{69}$$

where $a = \sqrt{2\gamma/(\rho_L - \rho_G)g}$ is the capillary length, $a_0 = 0.99951$, $a_1 = 0.01359$, $a_2 = -0.69498$, $a_3 = -0.11133$, $a_4 = 0.56447$, $a_5 = -0.20156$.

Since the bubble growth rate is an independent parameter of the process, the maximum bubble pressure method is particularly suitable to measure the dynamic surface tension. Figure 15 shows the typical pressure oscillations observed during the formation and detachment of two consecutive bubbles; the time interval between two bubbles, t_B, is the sum of the surface age (or surface lifetime), t_L, where pressure grows between a minimum and a maximum, and a dead time, t_D, where pressure decreases from a maximum to a minimum. By adjusting the time interval between two bubbles, or the bubble frequency, one can change the surface age hence the rate at which new surface is created. The characteristic bubble times, and in particular, the surface age can be determined more accurately from the analysis of oscillations of air flow fed into the system.

The surface tension values obtained at small lifetimes of the bubble are influenced by hydrodynamic effects. These effects depend on the viscosity of the liquid and the diameter of the capillary, and decrease with increasing lifetimes (Fainerman et al. 1993).

Fig. 15 Pressure variation during bubble growth and detachment; the time interval between two bubbles, t_B, is the sum of the surface age, t_L, and a dead time, t_D
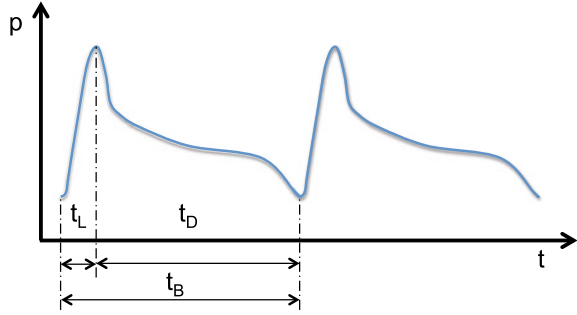
Fig. 16 Schematic of the micropipette method
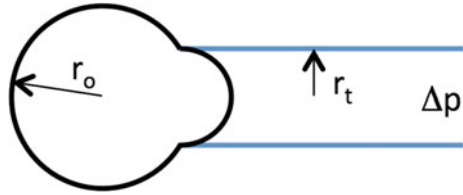
Micropipette method In the micropipette method (Yeung et al. 1998; Moran et al. 1999), a liquid droplet placed on the tip of a micropipette is gently drawn into the micropipette tube until a hemispherical protrusion is formed, as shown in Fig. 16. The pressure difference required to create the hemispherical protrusion is given by

$$\Delta p = 2\gamma \left(\frac{1}{r_t} - \frac{1}{r_o} \right) \tag{70}$$

where r_t and r_o are the radii of the micropipette tube and of the external spherical cap of liquid, respectively.

2.3 Capillary–Gravity Balance

Capillary rise tensiometer When a vertical capillary tube makes contact with the free surface of a liquid that wets the tube material (i.e. the contact angle is less than 90°), the liquid is drawn into the tube by surface tension until the weight of the liquid column inside the tube equals the surface tension force. Assuming the contact angle is small ($\cos \theta \approx 1$), the force balance writes

$$(\rho_L - \rho_G)gh = \gamma \left(\frac{1}{r_1} + \frac{1}{r_2} \right) \tag{71}$$

where ρ_L and ρ_G are the densities of the liquid and of the surrounding medium (air), respectively, g is gravity, h is the height of the liquid column, r_1 and r_2 are

the principal radii of curvature at the centre of the interface. For capillaries of small diameter, $r_1 = r_2 = r$ and the surface tension can be calculated as

$$\gamma = \frac{1}{2}(\rho_L - \rho_G)ghr \tag{72}$$

The capillary rise method offers a very good accuracy at low cost, and is used primarily to measure the surface tension of pure liquids. Commercial capillary tubes for surface tension measurements are generally made of glass and diameter $d < 1$ mm. It is important the diameter is uniform along the capillary tube, which depends on the manufacturing process; in particular, tubes manufactured by extrusion are of higher quality than those produced by centrifugation. To achieve a higher accuracy, or in case of capillary tubes of larger diameter, it is necessary to correct the radius of curvature of the meniscus for the gravitational deformation (Strutt 1916)

$$\gamma = \frac{1}{2}(\rho_L - \rho_G)ghr \left(1 + \frac{r}{3h} - 0.1288\frac{r^2}{h^2} + 0.1312\frac{r^3}{h^3}\right) \tag{73}$$

Drop weight In the drop weight method, or stalagmometric method, a drop is generated at the tip of a vertical capillary nozzle, such as a blunt hypodermic needle. The drop starts to detach from the nozzle when its weight equals the surface force at the nozzle tip (Tate 1864)

$$V(\rho_L - \rho_G)g = 2\pi r\gamma \tag{74}$$

where V is the drop volume, and r the radius of the wetted nozzle tip; it is important to observe that since the wall of the capillary tube has a finite thickness, r is equal to the inner radius if the drop liquid does not wet the nozzle tip, and to the outer radius if the drop liquid wets the nozzle tip.

In practice, the weight of the falling drop is lower than the weight expressed in Eq. (74), because some liquid remains attached to the tip of the capillary (experiments show that up to 40% of the drop volume may be left on the stalagmometer tip). Thus, one must introduce a correction factor for the drop weight to obtain the surface tension from Eq. (74)

$$\gamma = \frac{V(\rho_L - \rho_G)g}{2\pi r f\left(\frac{r}{V^{1/3}}\right)} \tag{75}$$

where the correction factor is given by (Drelich et al. 2002)

$$f\left(\frac{r}{V^{1/3}}\right) = 0.167 + 0.193\left(\frac{r}{V^{1/3}}\right) - 0.0489\left(\frac{r}{V^{1/3}}\right)^2 - 0.0496\left(\frac{r}{V^{1/3}}\right)^3 \tag{76}$$

To increase the measurement accuracy, it is a common practice to measure the weight of several drops and calculate an average drop weight. Drop detachment should be very slow (ideally quasi-static) to avoid inertial effects. The method is

extremely sensitive to vibrations, which may cause early detachment of drop. While the method is good for pure fluids, it may not be suitable to multicomponent solutions if there is adsorption of one or more chemical species on the stalagmometer tip, which changes the wettability hence the adhesion of the liquid to the tip.

2.4 Gravity-Induced Deformation

In the absence of external forces, drops have a spherical shape to minimize the excess interface energy; however, when an external force (e.g. gravity) is applied, the equilibrium drop shape results from the combination of gravity and capillary forces. Thus, the drop shape geometry can be used to find the surface tension magnitude.

The shape of an axisymmetric liquid drop deposited on a horizontal solid surface (sessile drop) can be related to the surface tension by including gravity in the Laplace equation (Bashforth and Adams 1883)

$$\gamma \left(\frac{1}{r_1} + \frac{1}{r_2} \right) = (\rho_L - \rho_G)gz + C \tag{77}$$

where C is a constant. With reference to Fig. 17a, which displays a cross section of the interface including the axis of revolution, r_1 is the radius of curvature in the cross-sectional plane at any point P of the interface. If ϕ is the angle between the normal to the surface and the axis of revolution, the second radius of curvature at point P is $r_2 = x / \sin \phi$. To find the constant in Eq. (77), one can consider the curvature in the origin (the drop apex), where $r_1 = r_2 = b$, so that $C = 2\gamma/b$. The same equation is applicable to the case of hanging drops, but in that case the vertical coordinate, z, is to be measured upwards from the vertex.
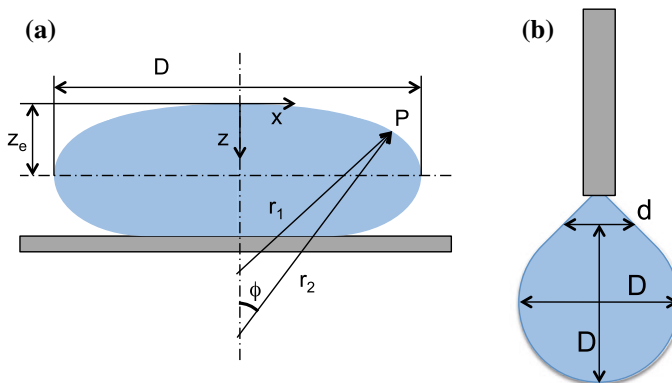
Fig. 17 Schematic of the pendant drop (**a**) and sessile drop (**b**) methods

Table 1 Coefficients of the correction factor F in Eq. (78)

Range of S	A	B_4	B_3	B_2	B_1	B_0
0.401–0.46	2.56651	0.3272	0	0.97553	0.84059	0.18069
0.46–0.59	2.59725	0.31968	0	0.46898	0.50059	0.13261
0.59–0.68	2.62435	0.31522	0	0.11714	0.15756	0.05285
0.68–0.9	2.64267	0.31345	0	0.09155	0.14701	0.05877
0.9–1	2.84636	0.30715	−0.69116	−1.08315	−0.18341	0.20970

Methods based on the drop shape analysis are very popular because they require a simple experimental setup, consisting of a digital camera and a suitable lens to capture a magnified image of the drop. The interface tension can be easily calculated from the geometry of either pendant drops, or sessile drops, or any liquid meniscii.

Pendant drop method In a simplified version of the pendant drop method, the interfacial tension can be obtained from just two geometric parameters: the equatorial diameter, D, and the neck diameter, d, which is measured at a distance from the drop apex equal to the equatorial diameter, as shown schematically in Fig. 17b. The corresponding interfacial tension is calculated as Andreas et al. (1938), Stauffer (1965):

$$\gamma = (\rho_L - \rho_G)g D^2 F \tag{78}$$

The correction factor F is a function of the shape parameter, defined as $S = D/d$, and can be calculated using the following empirical formula (Misak 1968):

$$F = \frac{B_4}{S^A} + B_3 S^3 - B_2 S^2 + B_1 S - B_0 \tag{79}$$

where the numerical values of the coefficients are given in Table 1, for different ranges of the shape parameter. Similar to the drop weight method, the pendant drop method may be affected by adsorption of one or more chemical species on the capillary (few surface-active contaminants can change the drop shape significantly), which must be extremely clean. It is recommended to select capillary tubes with diameter $\leq d/2$.

Sessile drop method A simplified version of the sessile drop method can be used with large drops deposited on a poorly wettable substrate, so that the contact angle is $>90°$. In this case, the interfacial tension can be obtained from one geometric parameters, the distance z_e between the drop apex and the equatorial diameter (see Fig. 17a), according to the following expression (Sonntag 1982):

$$\gamma = \frac{1}{2}(\rho_L - \rho_G)g z_e^2 \tag{80}$$

Other analytical formulae for computation of surface tension directly from the characteristic dimensions are available (Couper 1993), however these methods

require very accurate measurement of the dimensions for good results. For more accurate results, methods that fit the entire shape of the edge of the drop to the Laplace equation are recommended.

The Axisymmetric Drop Shape Analysis (ADSA) method In the Axisymmetric Drop Shape Analysis method (ADSA), a solution of the Laplace equation is fitted to the drop shape by minimizing the error between the theoretical and observed drop boundaries (Rotenberg et al. 1983; Hoorfar and Neumann 2006). The theoretical Laplacian curve, i.e. a curve representing a solution of the Laplace equation of capillarity can be obtained from Eq. (77) expressing the radius of curvature in the cross-sectional plane (see Fig. 17a) in terms of the curvilinear coordinate, s, along the interface

$$\frac{d\phi}{ds} = \frac{2}{b} + \frac{(\rho_L - \rho_G)g}{\gamma}z - \frac{\sin\phi}{x} \tag{81}$$

where $\cos\phi = dx/ds$ and $\sin\phi = dz/ds$.

The objective function which expresses the error between the physically observed and theoretical boundaries is

$$E = \sum_{i=1}^{N} \frac{1}{2}[(x_i - X_i)^2 + (z_i - Z_i)^2] \tag{82}$$

where X_i and Z_i are the coordinates of the observed interface points and x_i and z_i are the Laplace coordinates.

The objective function can be expressed in terms of four parameters, $q_1 = X_0$, $q_2 = Z_0$, $q_3 = b$ and $q_4 = (\rho_L - \rho_G)gb^2/\gamma$. Thus, the set of parameters that minimize the objective function can be used to find the surface tension as

$$\gamma = \frac{(\rho_L - \rho_G)gq_3^2}{q_4} \tag{83}$$

The method of solution is versatile and is not restricted by any particular drop shape or drop size; whether the drop is a sessile drop or a pendant drop, the cases are treated in a unified manner. The amount of physical input data that is required consists of the values of the coordinate points of the discretized interface, the value of the density difference across the interface and the value of the local acceleration of gravity

The first version of ADSA was very inefficient from a computational point of view, however it allowed for the first time the measurement of surface tension from the analysis of pendant drops side views. The first ADSA was followed by several newer versions, each improving some of the drawbacks of the original method (Río and Neumann 1997):

- ADSA-P (the most used one) is probably the fastest implementation of ASDA for pendant drops; however, numerical simplifications introduced uncertainty in the result.

- ADSA-D was the first version designed for contact angle calculation from sessile drops images; in this case, surface tension is a required input parameter.
- ADSA-H and ADSA-HD were developed for simultaneous surface tension and contact angle measurement from sessile drops images.
- LBADSA reduces the computational time required to solve the fitting problem by considering a first-order approximation of the Young–Laplace equation; it calculates both the surface tension for pendant drops and the contact angle for sessile drops (Stalder et al. 2010).

2.5 Forced Deformation

Spinning drop method The spinning drop method (Vonnegut 1942; Princen et al. 1967) is used to measure the interfacial tension between immiscible liquids A and B of different densities, with $\rho_B > \rho_A$. A drop of the lower-density fluid is injected into a horizontal tube filled with the higher-density fluid and spinning around its longitudinal axis. Because of the pressure gradient induced by centrifugal forces, the lower-density drop takes the shape of a coaxial cylinder, as shown in Fig. 18.

The cylindrical drop radius, r, results from the balance between centrifugal forces and interfacial tension, therefore one can calculate the value of the surface tension from the drop geometry and the angular velocity, ω (Slattery and Chen 1978)

$$\gamma = \frac{1}{2} \left(\frac{r}{r*} \right)^3 (\rho_B - \rho_A)\omega^2 \tag{84}$$

where r^* is a characteristic length depending on the aspect ratio of the deformed droplet, r/h. The spinning drop method has a very high sensitivity and can measure surface tension values as low as $\sim 10^{-4}$ mN/m.
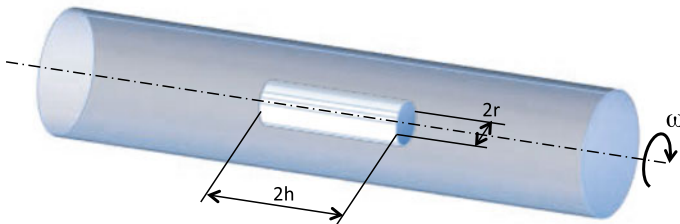
Fig. 18 Schematic of the spinning drop method

References

Andreas JM, Hauser EA, Tucker WB (1938) Boundary tension by pendant drops. J Phys Chem 42(8):1001–1019

Anna SL, McKinley GH, Nguyen DA, Sridhar T, Muller SJ, Huang J, James DF (2001) An inter-laboratory comparison of measurements from filament-stretching rheometers using common test fluids. J Rheol 45(1):83–114

Bach A, Rasmussen HK, Longin PY, Hassager O (2002) Growth of non-axisymmetric disturbances of the free surface in the filament stretching rheometer: experiments and simulation. J Non-Newton Fluid Mech 108(1–3):163–186

Bashforth F, Adams JC (1883) An attempt to test the theory of capillary action. Cambridge University Press

Bazilevskii AB, Rozhkov AN (2015) Dynamics of the capillary breakup of a bridge in an elastic fluid. Fluid Dyn 50(6):800–811

Bazilevskii AV, Voronkov SI, Entov VM, Rozhkov AN (1981) On orientational effects at breakup of jets and threads of dilute polymer solutions. Dokl Akad Nauk SSSR 257(2):336–339

Bazilevskii AV, Entov VM, Lerner MM, Rozhkov AN (1997) Failure of polymer solution filaments. Polym Sci Ser A 39(3):316–324

Bazilevskii AV, Entov VM, Rozhkov AN (2001) Breakup of an Oldroyd liquid bridge as a method for testing the rheological properties of polymer solutions. Polym Sci Ser A 43(7):716–726

Bingham EC (1944) The history of the society of rheology from 1924–1944, executed by directive from the society. In: Original archived in the Niels Bohr Library and Archives. American Institute of Physics, College Park, MD

Bird RB, Hassager O, Armstrong RC, Curtiss CF (1977) Dynamics of polymeric liquids, vol 1. Wiley, New York

Burghelea TI, Starý Z, Münstedt H (2009) Local versus integral measurements of the extensional viscosity of polymer melts. J Rheol 53(6):1363–1377

Burghelea TI, Starý Z, Münstedt H (2011) On the viscosity overshoot during the uniaxial extension of a low density polyethylene. J Non-Newton Fluid Mech 166(19):1198–1209

Burghelea TI, Starý Z, Münstedt H (2012) Response to the reply to: on the viscosity overshoot during the uniaxial extension of a low density polyethylene by rasmussen et al. J Non-Newton Fluid Mech 171–172:107–108

Considére A (1885) Memoire sur l'emploi du fer et de l'acier dans les constructions. Annales des Ponts et Chaussées 6(9):574–775

Couette M (1880) Sur un nouvel appareil pour létude du frottement des fluides. Compt Rend Acad Sci Paris 107:388–390

Couper A (1993) Surface tension and its measurement. In: Rossiter BW, Baetzold RC (eds) Physical methods of chemistry, vol 9A, 2nd edn. Wiley

Drelich J, Fang C, White CL (2002) Measurement of interfacial tension in fluid-fluid systems. In: Hubbard AT (ed) Encyclopedia of surface and colloid science. Marcel Dekker

Entov VM, Hinch EJ (1997) Effect of a spectrum of relaxation times on the capillary thinning of a filament of elastic liquid. J Non-Newton Fluid Mech 72(1):31–53

Fainerman VB, Miller R (1998) The maximum bubble pressure tensiometry. In: Mbius D, Miller R (eds) Drops and bubbles in interfacial research, vol 6. Studies in interface science Elsevier, pp 279–326

Fainerman VB, Makievski AV, Miller R (1993) The measurement of dynamic surface tensions of highly viscous liquids by the maximum bubble pressure method. Colloids Surf A Physicochem Eng Asp 75:229–235

Harkins WD, Jordan HF (1930) A method for determination of surface and interfacial tension from the maximum pull on a ring. J Am Chem Soc 52(5):1751–1772

Hoorfar M, Neumann AW (2006) Recent progress in axisymmetric drop shape analysis (ADSA). Adv Colloid Interface Sci 121(1):25–49

Lecomte du Noüy P (1925) An interfacial tensiometer for universal use. J Gen Physiol 7(5):625–631

Macosko CW (1994) Rheology: principles, measurements, and applications. Wiley, New York

McKinley Gareth H, Tamarapu Sridhar (2002) Filament-stretching rheometry of complex fluids. Annu Rev Fluid Mech 34(1):375–415

Meissner J (1969) Rheometer zur untersuchung der deformations-mechanischen eigenschaften yon kunststoff- schmelzen unter definierter zugbeanspruchung. Rheol Acta 8:78–88

Meissner J, Hostettler J (1994) A new elongational rheometer for polymer melts and other highly viscous liquids. Rheol Acta 33:1–21

Misak MD (1968) Equations for determining 1/h versus s values in computer calculations of interfacial tension by the pendent drop method. J Colloid Interface Sci 27(1):141–142

Moran K, Yeung A, Masliyah J (1999) Measuring interfacial tensions of micrometer-sized droplets: a novel micromechanical technique. Langmuir 15(24):8497–8504

Münstedt H (1979) New universal extensional rheometer for polymer melts. Measurements on a polystyrene sample. J Rheol 23(4):421–436

Münstedt H, Laun HM (1979) Elongational behaviour of a low density polyethylene melt. Rheol Acta 18(4):492–504

Princen HM, Zia IYZ, Mason SG (1967) Measurement of interfacial tension from the shape of a rotating drop. J Colloid Interface Sci 23(1):99–107

Río OI, Neumann AW (1997) Axisymmetric drop shape analysis: computational methods for the measurement of interfacial properties from the shape and dimensions of pendant and sessile drops. J Colloid Interface Sci 196(2):136–147

Rotenberg Y, Boruvka L, Neumann AW (1983) Determination of surface tension and contact angle from the shapes of axisymmetric fluid interfaces. J Colloid Interface Sci 93(1):169–183

Rusanov AI, Prokhorov VA (1996) Interfacial tensiometry. Elsevier

Sentmanat ML (2003a) A novel device for characterizing polymer flows in uniaxial extension. Soc Plastics Engineers, Tech Papers, CD-ROM, 49

Sentmanat ML (2003b) Dual wind up extensional rheometer. US Patent No. 6578413

Sentmanat ML (2004) Miniature universal testing platform: from extensional melt rheology to solid-state deformation behavior. Rheol Acta 43(6):657–669

Simon M (1851) Recherches sur la capillarité. Ann Chim Phys 32(3):5–41

Slattery JC, Chen J (1978) Alternative solution for spinning drop interfacial tensiometer. J Colloid Interface Sci 64(2):371–373

Sonntag H (1982) Koloidy. PWN

Stalder AF, Melchior T, Müller M, Sage D, Blu T, Unser M (2010) Low-bond axisymmetric drop shape analysis for surface tension and contact angle measurements of sessile drops. Colloids Surf A Physicochem Eng Asp 364(1–3):72–81

Starý Z, Papp M, Burghelea T (2015) Deformation regimes, failure and rupture of a low density polyethylene (LDPE) melt undergoing uniaxial extension. J Non-Newton Fluid Mech 219:35–49

Stauffer CE (1965) The measurement of surface tension by the pendant drop technique. J Phys Chem 69(6):1933–1938

Strutt JW (1916) On the theory of the capillary tube. Proc R Soc Lond Ser A 92(637):184–195

Sugden S (1922) The determination of surface tension from the maximum pressure in bubbles. J Chem Soc Trans 121:858–866

Sugden S (1924) The determination of surface tension from the maximum pressure in bubbles. Part II. J Chem Soc Trans 125:27–31

Szabo P (1997) Transient filament stretching rheometer part I: force balance analysis. Rheol Acta 36:277–284

Tate T (1864) On the magnitude of a drop of liquid formed under different circumstances. Lond Edinb Dublin Philos Mag J Sci 27(181):176–180

Tirtaatmadja V, Sridhar T (1993) A filament stretching device for measurement of extensional viscosity. J Rheol 37(6):1081–1102

Vold RD, Vold MJ (1983) Colloid and interface chemistry. Addison-Wesley Publishing Co.

Vonnegut B (1942) Rotating bubble method for the determination of surface and interfacial tensions. Rev Sci Instrum 13:6–9

Wilhelmy L (1863) Ueber die abhängigkeit der capillaritäts-constanten des alkohols von substanz und gestalt des benetzten fasten körpers. J Phys Chem 195(6):177–217

Yeung A, Dabros T, Masliyah J (1998) Does equilibrium interfacial tension depend on method of measurement? J Colloid Interface Sci 208(1):241–247

Zuidema H, Waters G (1941) Ring method for the determination of interfacial tension. Ind Eng Chem Anal Ed 13(5):312–313

Transport Phenomena in Viscoelastic Fluids

Teodor Burghelea

Abstract After a discussion of the molecular scale picture of viscoelasticity given in Sect. 1, several macroscopic flow phenomena triggered by viscoelasticity are described in Sect. 2. The hydrodynamic stability of flows of viscoelastic fluids is discussed in Sect. 3. The rest of the chapter is dedicated to the phenomenon of *Elastic Turbulence* in dilute polymer solutions. The main features of *Elastic Turbulence* observed in a macroscopic von Karman swirling flow are detailed in Sect. 4. A systematic description of the *Elastic Turbulence* in a micro-channel is presented in Sect. 5. The transport of mass (mixing) and heat by *Elastic Turbulence* are described in Sects. 6, 7, respectively. The theory of *Elastic Turbulence* and its agreement with the experimental observations are discussed in Sect. 8.

1   Molecular Origins of Viscoelasticity in Dilute Polymer Solutions

A distinct class of complex fluids is represented by dilute solutions of high molecular weight linear polymers. The *dilute* limit refers to the situation when polymer–polymer interaction can be neglected. A typical linear polymer strand consists of a large number of sequentially bonded monomer units of molecular weights typically of the order of 10^2 Da with a total molecular weight M of the order $10^6 \div 10^7$ Da.

The simplest picture of a high molecular weight linear polymer molecule immersed in a low molecular weight (Newtonian) solvent is that of an elastic spring with two beads connected at its ends (elastic dumb-bell model). In the absence of flow and external forces acting on the chain, the most probable state of the molecule is the coiled state (Fig. 1a). In the presence of flow, each bead interacts hydrodynamically with the solvent via Stokes like frictional forces (the Reynolds number based on the size of the polymer molecule is negligibly small). If the magnitude of the largest eigenvalue of the velocity gradient tensor becomes of the order of the inverse

T. Burghelea (✉)

Laboratoire Thermique et Energie, University of Nantes, Nantes, France
e-mail: Teodor.Burghelea@univ-nantes.fr
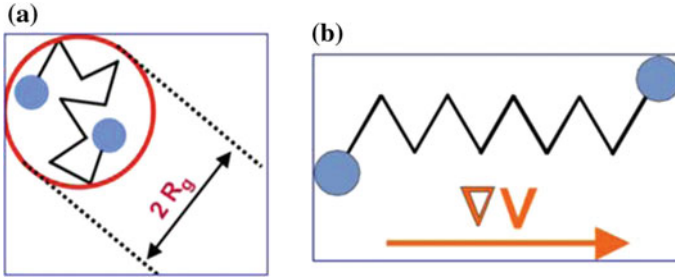
Fig. 1 Possible configurations of a linear polymer molecule in a flow: **a** coiled state and **b** stretched state

characteristic relaxation time of the polymer molecule, the coil-stretch transition occurs (Fig. 1b).

The coil-stretch transition was first predicted by P.-G. de Gennes in his seminal 1974 paper (de Gennes 1974). As the microscopic coil-stretch transition is naturally associated to the emergence of a polymer component in the stress tensor, its dynamics will consequently impact the macroscopic flow features discussed through this chapter. For this reason, a brief discussion of the main elements and predictions of the de Gennes's theory is in order. A first subtle element of the theory was to realise that the dynamics of the coil-stretch transition depends on the kinematics of the flow. Thus, two cases are considered: shear flows and shear free (extensional) flows. A two-dimensional flow field (V_x, V_y) is characterised by the vorticity $\omega = \frac{1}{2} \left(\frac{\partial V_x}{\partial y} - \frac{\partial V_y}{\partial x} \right)$ and the extensional part $A = \frac{1}{2} \left(\frac{\partial V_x}{\partial y} + \frac{\partial V_y}{\partial x} \right)$. The sketch presented in Fig. 2a exemplifies the coil-stretch transition for the case when the vorticity ω is gradually decreased while A is maintained constant (but large). The transition is a second-order (imperfect) bifurcation and the width of the transitional region is approximately Z^{-1} where Z is the number of monomers in the chain (de Gennes 1974).

The nature of the bifurcation from a coiled to a stretched state changes when a shear free flow is considered: $V_x = \dot{\epsilon}x$, $V_y = -\dot{\epsilon}y$.

In this case, the dependence of the fractional extension of the polymer molecules folds back and in a certain range of rates of extension $\dot{\epsilon}$ and a bistable equilibrium is observed. There is one critical value of $\dot{\epsilon} = \dot{\epsilon}^*$ at which the system (if it is operated very slowly) will switch from a coiled state to a stretched one. A first-order phase transition takes place at $\dot{\epsilon} = \dot{\epsilon}^*$.

A first experimental confirmation of the de Gennes theory has been reported by Schroeder and coworkers for the case of a planar extensional flow of a dilute solution of highly flexible Escherichia coli DNA molecules (Schroeder et al. 2003). By tracking a statistically relevant number of individual polymer molecules stained with a fluorescent compound for various Deborah numbers $De = \lambda\dot{\epsilon}$ they confirm the first-order bifurcation conjectured by de Gennes in 1974 for the case of a steady
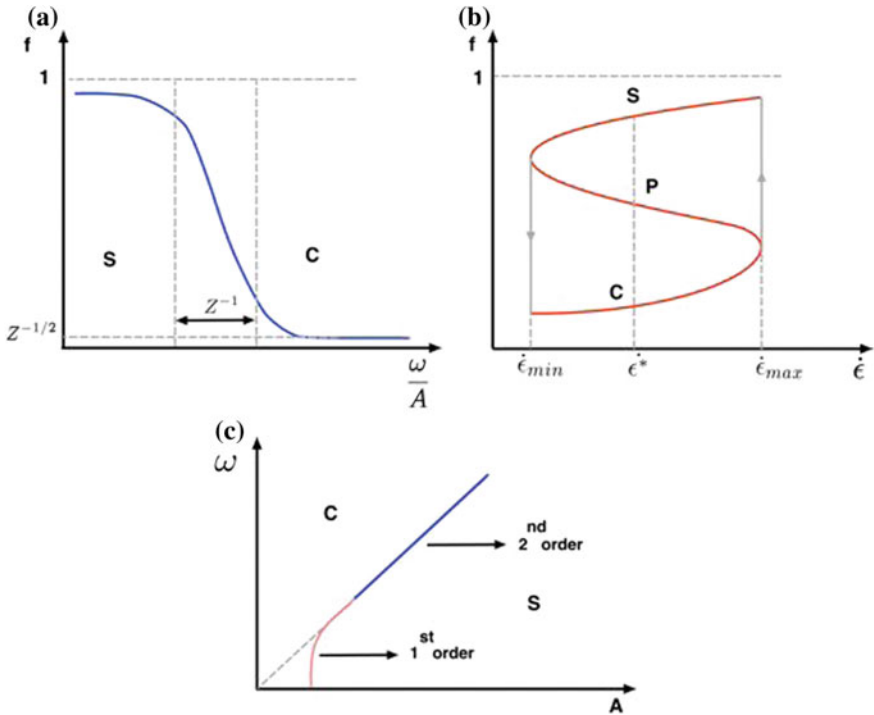
Fig. 2 **a** Sketch of a second-order coil-stretch transition in a two-dimensional flow when the vorticity ω increases while A is large but constant. The width of the transition zone is Z^{-1} (where Z is the number of monomers on one chain). **b** Sketch of a first-order coil-stretch transition in an extensional flow. **c** Phase diagram corresponding to the coil-stretch transition: blue line—second order; red line—first order. The sketches in each panel are reproductions of the sketches presented in de Gennes (1974)

extensional flow. To our best knowledge, the prediction of a second-order bifurcation for the case of a steady shear flow (see the sketch in Fig. 2a) still awaits an experimental validation.

2 Macroscopic Flow Phenomena Triggered by the Microscopic Coil-Stretch Transition

2.1 The Rod-Climbing Effect

The generation of a macroscopic elastic stress component associated to the microscopic coil-stretch transition is responsible for a number of somewhat counterintuitive flow phenomena. The best known such effect is, probably, the *rod-climbing* or the Weissenberg effect (Weissenberg 1947).
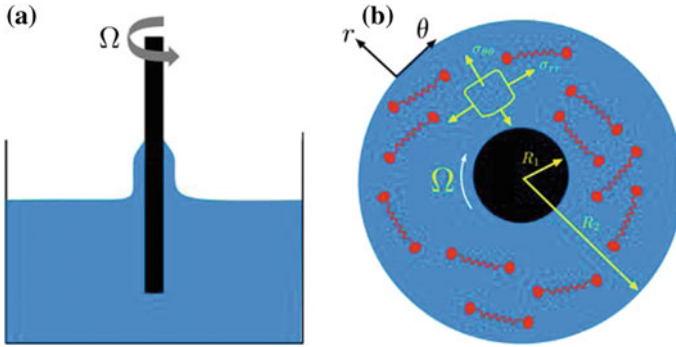
Fig. 3 **a** Schematic illustration of the Weissenberg effect. **b** Cross-sectional view illustrating the physical mechanism of the Weissenberg effect

As schematically illustrated in Fig. 3a, a polymeric fluid possessing 'enough' elasticity climbs on a rod rotating at a constant angular speed Ω in the fluid rather being repelled by the centrifugal force (which is obviously what would happen if the fluid was Newtonian).

A simple phenomenological explanation of this effect may be formulated as follows. The individual polymer molecules get stretched along the streamlines which are closed circles which generates an extra tension along these lines which generates an inwards fluid motion which makes the polymeric fluid climb the rod. This is schematically illustrated in Fig. 3b.

More rigorously, it can be shown that actually the first normal stress difference $N_1 = \sigma_{\theta\theta} - \sigma_{rr}$ which is proportional to the square of the rate of shear and the largest relaxation time of the polymer relaxation time and generally negative generates a body force $F = \frac{N_1}{r}$ called *hoop stress* oriented inwards (Bird et al. 1977). In the case of a Newtonian $N_1 = 0$, the only acting force is the centrifugal one and the liquid is pushed outwards. For dilute polymer solutions $N_1 > 0$ and, subsequently, the polymeric fluid climbs the rod.

2.2 Extrudate Swell Effect

If a Newtonian fluid exits a capillary of diameter D at low Reynolds number it forms a jet of a smaller diameter $D_N < D$ as schematically illustrated in Fig. 4a. Typically D_N is up to ten percents smaller than the diameter of the capillary. This phenomenon is called '*vena contracta*' and was first described by Torricelli (1644).

The overall picture is dramatically different if the same experiment is performed with a polymeric fluid, Fig. 4b. The diameter of the exiting fluid jet D_P may be up to three times larger than the diameter of the capillary. This phenomenon is called the '*extrudate swell*'. A simplified phenomenological interpretation of this effect may

Fig. 4 **a** Newtonian fluid exiting a capillary tube, $D_N < D$. **b** Polymeric fluid exiting a capillary tube, $D_P > D$
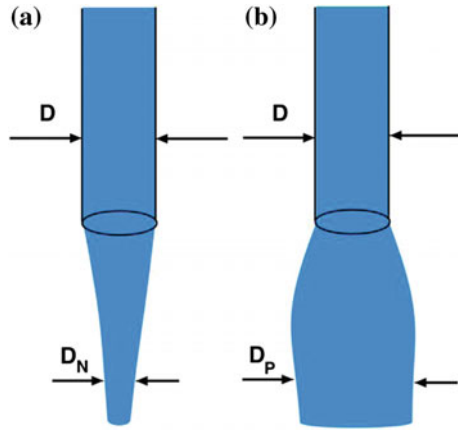
be given if one resorts once again to the original idea of Weissenberg of tension generation along the streamlines in flows of polymeric fluids. When the fluid exits the capillary this extra tension cannot be accommodated and, as a result, the fluid will contract axially and expand radially.

A more rigorous and quantitative result which relates the swelling ratio $\frac{D_P}{D}$ to the ratio between the first normal stress difference N_1 shear stress measured near the wall at the capillary exit was given by Tanner (1970):

$$\frac{D_P}{D} = 0.1 + \left[1 + \frac{1}{2} \left(1 + \left(\frac{N_1}{\sigma_{xy}} \right)^2_w \right) \right]^{1/6} \tag{1}$$

2.3 Drag Reduction

In 1949 Toms discovered that a small addition of a flexible linear polymer (roughly 10 ppm of polymethylacrylate) to an inertially turbulent leads to a substantial reduction of the turbulent drag (defined by the pressure drop ΔP needed to maintain a given flow rate) that may reach 40% (Toms 1949). This phenomenon has been coined the *drag reduction* phenomenon. The reduction of the drag may be intuitively associated to a decrease of the strength of the secondary flow as schematically illustrated in Fig. 5.

The early studies of drag reduction in dilute polymer solutions revealed two types of drag reduction in dilute polymer solutions (Hershey and Zalkin 1967). In dilute polymer solutions, the drag reduction emerges in a fully developed turbulence regime beyond a critical Reynolds number where the friction factor decreases below that for an ordinary Newtonian turbulent flow. For Reynolds numbers smaller than the onset value, no drag reduction is observed. In more concentrated polymer solutions, the

(a) Re>Rec, no polymer

(b) Re>Rec, polymer added
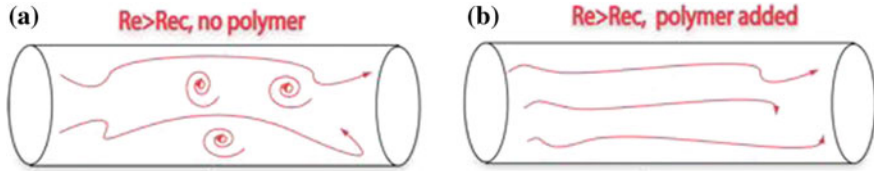
Fig. 5 **a** Sketch of a turbulent pipe flow with no polymer added. **b** Sketch of a turbulent pipe flow after a small amount of polymer has been added

drag reduction is observed near the upper bond of the laminar region. In this case, the onset conditions are reached at low Reynolds numbers, that is, the laminar–turbulent transition is not observed. The main difference between these two kinds of drag reduction is the region where drag reduction occurs. The former begins in the fully developed turbulent region. The latter is observed in the extended laminar region. They were later labelled type A and type B drag reduction (Virk and Wagger 1990). Despite a large number of theoretical, numerical and experimental studies (Lumley 1969; Yarin 1997) that span almost eight decades, the mechanism by which the polymer addition inhibits the momentum transfer to the channel walls and the drag reduction occurs it is still not fully understood.

3 Hydrodynamic Stability of Dilute Polymer Solutions

Stretching of individual polymer molecules in the flow leads to generation of additional elastic stresses that relax with a macroscopic characteristic time λ, are flow history-dependent and grow in a strongly nonlinear fashion with the external forcing. Thus, the stress tensor, σ, can be decomposed in two parts, $\sigma = \sigma_s + \sigma_p$. The polymer part of the stress tensor depends in a strongly nonlinear fashion on the field of velocity gradients which is a consequence of the strong nonlinearity of the coil-stretch transition particularly in flows with an extensional component (Fig. 2). The balance between the nonlinear elastic terms and the linear dissipative terms is quantified by a second dimensionless quantity usually referred as the Weissenberg number, $Wi = \lambda \cdot \frac{v}{L}$. The mechanical properties of a dilute polymer solution become increasingly nonlinear as Wi is increased.

In the context of two potential sources of nonlinearity in the hydrodynamic equations of a dilute polymer solution, inertial and elastic, a natural question arises: how is the hydrodynamic stability affected by each nonlinear contribution. This question can be only partially answered. Figure 6 shows a sketch of a stability diagram in the parameter space ($Wi - Re$).

If both Re and Wi are smaller than unity, the flow is steady and laminar. In the limit of negligible Wi, the flow loses its stability only if the inertial nonlinearity is large comparative to the viscous dissipation. Thus when Reynolds number exceeds a threshold value, $Re > Re_c$, the flow evolves to turbulent states (the region labelled
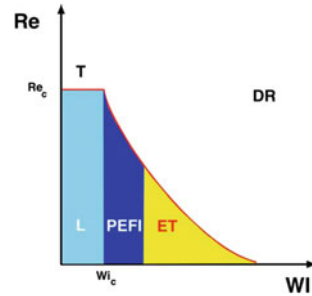
IT in Fig. 6). This is, of course, an oversimplified picture. In most of the realistic situations, the transition to fully developed turbulence does not occur directly but via secondary instabilities. When Re is small but the values of Wi slightly exceed unity, flows with curvilinear streamlines can undergo a purely elastic instabilities (Muller et al. 1989; Larson 1992). As a result of these instabilities, secondary flows have been observed experimentally (Muller et al. 1989) together with a sharp increase in flow resistance (Magda and Larson 1988).

The onset of the purely elastic instability in flows of polymer solutions with curvilinear streamlines is related to both the mean curvature of streamlines $\kappa = R^{-1}$ (here R stands for the radius of the curvature) and the rheological properties (polymer relaxation time, zero shear viscosity) via the Pakdel–McKinley criterion (McKinley et al. 1996):

$$\left[\lambda v \kappa \frac{\sigma_{11}}{\eta_0 \dot{\gamma}}\right]^{1/2} \geq M_{cr} \qquad (2)$$

The first term $\lambda v \kappa$ (where v is a scale for the flow velocity) represents the contribution of the curvilinear geometry to the stretching of the polymer molecules. A second term involved in the left-hand side of the Pakdel–McKinley criterion is the ratio between the extensional stress component σ_{11} and the shear stress $\eta_0 \dot{\gamma}$. The value of the non-dimensional onset number M_{cr} depends on the rheological properties of the solution and the topology of the base flow and can be computed via linear stability analysis. For a Taylor–Couette geometry and a polymer solution described by the upper convected Maxwell model, it was found $M_{cr} = 8.37 \pm 0.03$ (Larson 1992). For other flow configurations (parallel plate, cone-plate), M_{cr} remains of order of unity.

When both Re and Wi numbers are large, the drag reduction effect is observed. The region of the space diagram corresponding to a negligibly small Re but Wi significantly larger than the onset of the primary elastic instabilities has particularly interested both theoreticians and experimentalists during the past two decades. Within this regime, a fully developed chaotic flow solely driven by nonlinear elastic stresses coined as '*Elastic Turbulence*' has been observed. The rest of this chapter is dedicated to this phenomenon.

4   Elastic Turbulence in Dilute Polymer Solutions: Turbulence Without Inertia

The first experimental observation of a chaotic flow state solely driven by the strongly nonlinear elastic stresses coined as '*Elastic Turbulence*' dates back to mid-1960s (Vinogradov and Manin 1965). This discovery by the group of late Prof. Vinogradov in the former Soviet Union remained, however, unnoticed by the scientific community and, it is fair to say the Elastic Turbulence has been practically rediscovered by Groisman and Steinberg (2000).

The observations by Groisman and Steinberg have been performed in a von Karman swirling flow, schematically illustrated in Fig. 7. The experimental setup consists of an acrylic made cup **FC** mounted on the bottom plate of a commercial rheometer. The flow was visualised from below through a flat mirror **M**. The flow was driven by a rotating disc **D** connected to the shaft of the rheometer. By combined measurements of the dependence of the torque needed to drive the top disc at a constant angular speed, point-wise velocity measurements performed via laser Doppler velocimetry (LDV) and visualisation of a drop of ink in the flow, they highlighted several important features of the Elastic Turbulence: sharp growth of flow resistance as the Weissenberg number is increased past the onset of the primary elastic instability, a power-law decay of the spectra of fluctuations of the point-wise velocity. The chaotic

Fig. 7 Schematic view of the experimental setup: **FC**—fluid container, **R**—rheometer shaft, **D**—rotating disc, **CCD**—digital camera, **M**—flat mirror, **L**—laser, **COB**—cylindrical optics block and **LS**—laser sheet
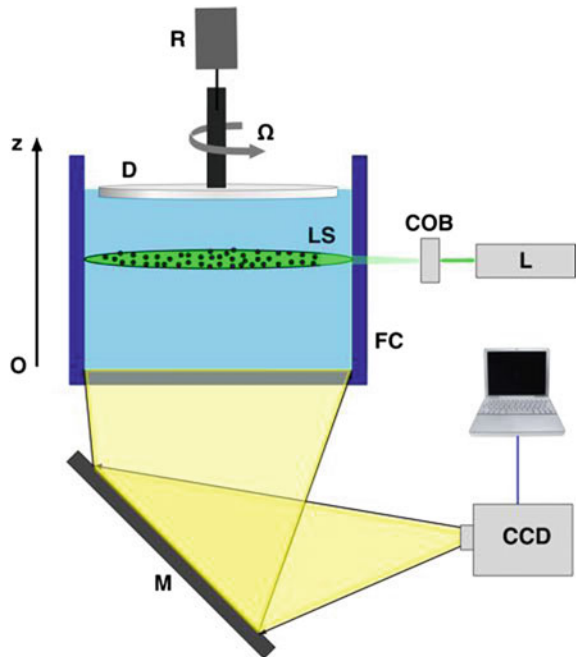
nature of the flow has been qualitatively shown by monitoring the mixing of a drop of ink initially located at the centre of flow system.

Following the (re)discovery of the Elastic Turbulence, a number of experimental studies have revealed several of its key features in various flow macroscopic configurations (Burghelea et al. 2004c, 2005, 2006, 2007).

Below we detail several of the main features of the elastic turbulence observed in a von Karman swirling flow similar to the one studied by Groisman and Steinberg. In order to check the sensitivity of the results with respect to the geometrical aspect ratio and to explore a broad range of Weissenberg numbers, two versions of the von Karman swirling flow system are used: first one had $R_c = 2.2$ cm, $R_d = 2$ cm and the distance between plates $d = 1$ cm and the second had $R_c = 4.9$ cm, $R_d = 4.7$ cm and $d = 1$ cm. The two setups will be further referred as setup 1 and 2. The rheometer can be driven either in constant (within 0.5%) angular speed mode either in constant (within 0.5%) torque mode. The two forcing modes will be further referred as Ω-forcing and T-forcing. The momentum of inertia of the shaft of the rheometer is $I_s \approx 14 \, \mu \text{Nms}^2$ and the momentum of inertia of the upper plate, I_d, was about $61 \, \mu \text{Nms}^2$ for setup 1, and about $84 \, \mu \text{Nms}^2$ for setup 2. The accuracy of the angular speed measurements in constant torque mode is about 2% and the accuracy of the torque measurements in the constant speed mode is about 1%. One has to point out here that smallness of the fluctuations rate of the angular velocity is not a sufficient criterion to have a constant speed forcing. Corresponding to the Ω-mode, $(I_r + I_d)\frac{\partial \Omega}{\partial t}$ should be also much smaller than the typical values of torque, T.

The system was illuminated laterally by a thin(30 μm in the centre of the setup and about 120 μm at the edges of the setup) laser sheet at the middle distance between plates. The laser sheet was generated by passing a laser beam delivered by a 300 mW argon-ion laser, **L**, through a block of two crossed cylindrical lenses, **CO**, mounted in a telescopic arrangement. Flow images are acquired with a digital camera (PixelFly from PCO with 12 bit quantisation and 640×512 pixels resolution) from below, through a 45° flat mirror, **M**.

For a swirling flow between parallel plates, the Reynolds number can be defined as $Re = \frac{\Omega \cdot R_c \cdot d \cdot \rho}{\eta}$. For all the experiments we discuss in the following the inertial contribution was always low, $Re < 16$. The relevant control parameter is the Weissenberg number, $Wi = \lambda(\dot{\gamma}) \cdot \dot{\gamma}$ where the shear rate, $\dot{\gamma}$, can be estimated[1] as $\dot{\gamma} = \frac{\Omega \cdot R_c}{d}$. The polymer used was polyacrylamide, PAAm (from Polysciences Inc.) with the molecular weight $M_w = 1.8 \times 10^7$ Da which was the same polymer used by Groisman and Steinberg (2001). The polymer was dissolved at a concentration of 80 ppm in a Newtonian solvent. The Newtonian solvent was about 65% saccharose in water.

The rheological properties of the solvent and the polymer solution were measured with two different rheometers: AR-1000 (TA Instruments) and Vilastic 3 (Vilastic Scientific). The viscosity of the solvent was $\eta_s = 114$ mPas at 22 °C, and the viscosity of the solution was $\eta = 138$ mPas at a shear rate of $2 \, \text{s}^{-1}$. The polymer relaxation time, λ, was measured in oscillatory tests at different shear rates, $\dot{\gamma}$, ranging from $0.4 \, \text{s}^{-1}$

---

[1]Due to the strong non-homogeneity of the shear rates in a swirling flow, even in laminar regime, this choice is somewhat arbitrary.

Fig. 8 Polymer relaxation obtained from oscillation measurements in a Mooney–Ewart geometry mounted on the AR-1000 rheometer. The full line is a fit $\dot{\gamma}^{-0.29}$
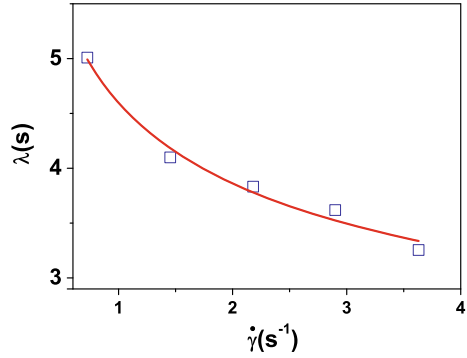
to $3.6\,\mathrm{s}^{-1}$. The real and imaginary part of the complex viscosity (or the components in-phase and out-of-phase with the applied shear), η' and η'', respectively, were measured in long series at different angular frequencies ranging from 0.1 to 1 Hz. Corresponding to each frequency, the results were averaged over six different runs. The same procedure was applied with the solvent ant its viscosity components, η'_s and η''_s were measured as well. The values for the polymer in-phase and out-of-phase viscosity were calculated as $\eta'_p = \eta' - \eta'_s$ and $\eta''_p = \eta'' - \eta''_p$. The polymer relaxation time was finally calculated $\lambda = \lim_{\omega \to 0}[\frac{1}{\omega}(\frac{\eta''_p(\omega)}{\eta'_p(\omega)})]$.

The dependence of the polymer relaxation time on the shear rate is presented in Fig. 8.

4.1 Flow Resistance

One of the main features of the transition to Elastic Turbulence is the substantial growth of flow resistance above the onset of the instability (Groisman and Steinberg 2000; Burghelea et al. 2004a, 2007). In the case of a von Karman swirling flow, a measure of the flow resistance is either the power needed to spin the upper plate a constant angular speed, P_Ω, either the power needed to spin the upper plate in a regime of constant torque, T, on the shaft of the rheometer, P_T (Fig. 9).

The dependence of the time-averaged power measured in the Ω mode on the control parameter Wi is presented in Fig. 10a. The data are normalised by the time-averaged power measured prior to the onset of the primary elastic instability, P_{lam}. The transition to Elastic Turbulence is marked by a sharp increase of the flow resistance. Within a fully developed elastic turbulent regime, the flow resistance scales as $P/P_{lam}. \propto Wi^{0.49}$. A slight hysteresis upon increasing/decreasing Wi is observed Fig. 9a. As shown by Traore et al. (2015), this is not the signature of a first-order bifurcation but merely related to the finite averaging time of the injected power.
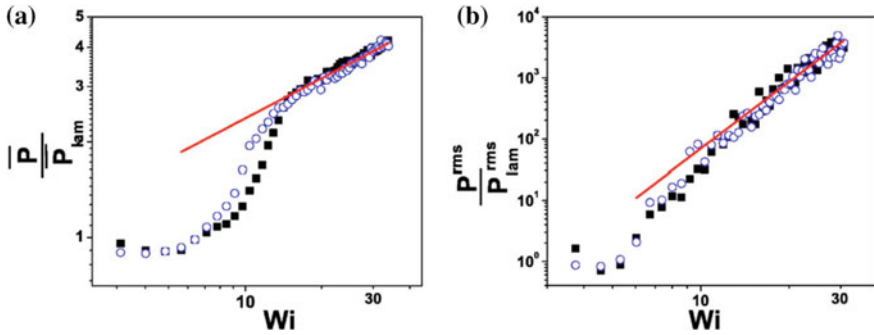
Fig. 9 a Dependence of the scaled time-averaged power P/P_{lam} on the control parameter Wi. The full line is guide for the eye $Wi^{0.49}$. **b** Dependence of the scaled rms of the power fluctuations P_{rms}/P_{lam}^{rms} on Wi. The full line is guide for the eye $Wi^{3.2}$. In both panels, the symbols are: squares—increasing Wi; circles—decreasing Wi. Data were collected in setup 2 in the Ω mode. The data were replotted from Burghelea (2005)

The transition to Elastic Turbulence is equally accompanied by a sharp increase of the root mean square (rms) fluctuations of the injected power (Fig. 9b). In a regime of Elastic Turbulence, the reduced rms of fluctuations scales as $P_{rms}/P_{lam}^{rms} \propto Wi^{3.2}$.

Time series of the injected power measured in the Ω forcing mode at several Weissenberg numbers are shown in Fig. 10a. The corresponding probability distributions (pdfs) of the power fluctuations are shown in Fig. 10b. For values of the Weissenberg number below the onset of the primary elastic instability $Wi_c \approx 8.37$, the power fluctuations are solely related to the instrumental noise of the measurements and the corresponding pdfs have a Gaussian shape. Strongly fluctuating power signals are measured past the onset of elastic instability (curves (4, 5) in Fig. 10a) and the corresponding pdf's deviate strongly from a Gaussian shape: strong intermittent events are visible in the form of a right skewness—the diamonds and the circles in Fig. 10b.

4.2 Flow Structure in a Regime of Elastic Turbulence

In the case of inertial turbulence, the emergence of the flow resistance is typically associated to a major reorganisation of the flow. The qualitative measurements of Groisman and Steinberg performed by monitoring the time evolution of a drop of ink injected into the flow indicated that this is equally the case for the Elastic Turbulence (Groisman and Steinberg 2000). More systematic investigations of the flow structure in a regime of Elastic Turbulence combining several experimental techniques (LDV, PIV, laser-induced fluorescence) have been reported in several subsequent papers (Burghelea et al. 2004c, 2005, 2006, 2007).

Examples of instantaneous and time-averaged flow fields measured at mid-distance between the plates of setup 1 at three distinct Wi are presented in Fig. 11.

(a)

(b)
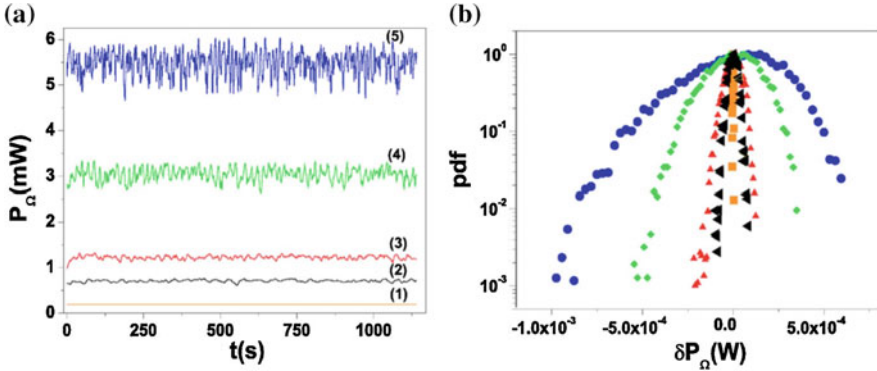
Fig. 10 a Time series of the injected power measured in the Ω forcing mode at different Wi. The labels are: (1)—$Wi = 5$, (2)—$Wi = 19$, (3)—$Wi = 24$, (4)—$Wi = 31.5$, and (5)—$Wi = 40$. **b** Probability density distributions of the power fluctuations measured in the Ω forcing mode at different Wi: squares—$Wi = 5$, left triangles—$Wi = 19$, up triangles—$Wi = 24$, diamonds— $Wi = 31.5$ and circles—$Wi = 40$. Data were collected in setup 2 in the Ω mode. The data were replotted from Burghelea (2005)

The upper row of Fig. 11 presents instantaneous flow fields while the bottom row presents time-averaged flow fields. Above the onset of the elastic instability $Wi_c \approx 6.95$, one can clearly identify the core of a toroidal vortex and a spiral vortex that additionally occurs in a regime of fully developed Elastic Turbulence.

Magnified flow fields (the size of the field of view is 1 cm × 1 cm) separated in time by 50 s are presented in Fig. 12a and b).

Figures 11 and 12 reveal an important features of the flow fields in a regime of Elastic Turbulence: spatial smoothness manifested through the lack of small-scale features. The sole dominant space scale of the flow is comparable in magnitude to the size of the fluid container. For the case of inertial turbulence, the picture is very different. Inertially turbulent flows are spatially smooth only beyond the Batchelor scale. Another distinct feature of the flow fields in a regime of Elastic Turbulence relates to their chaotic temporal evolution: the core of the vortex illustrated in Figs. 11 and 12 moves randomly in time which corroborates with the chaotic behaviour of the time series of the power injected into the flow (Fig. 10a).

Yet another method of visualising the flow structure is via the laser-induced fluorescence (LIF) technique. For this purpose, a drop of fluorescent die is injected near the centre of the setup, illuminated with a thin horizontal laser sheet traversing the fluid container at mid-distance between the plates and visualised from below. The temporal evolution of the drop of die is illustrated in Fig. 13.

As advected by the randomly fluctuating vortex discussed above the blob of die gets stretched and folded (panels **b, c** in Fig. 13) and, in about a minute, it becomes perfectly mixed with the surrounding polymer solution. The topology of the vortex is clearly visible in Fig. 13d. The change in the flow structure with Wi may be equally observed by plotting the time-averaged in-plane velocity components $\bar{V}_\theta$, $\bar{V}_r$.
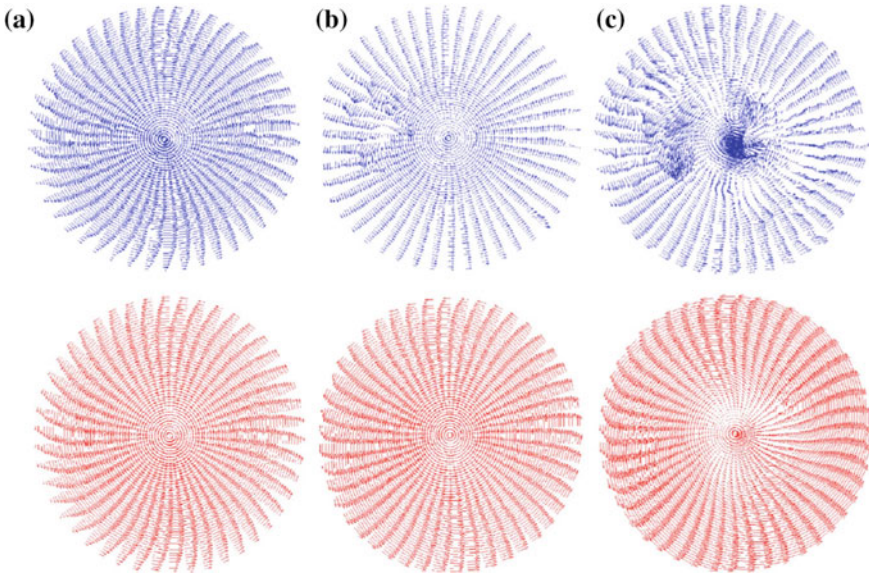
Fig. 11 Instantaneous (upper row) and time-averaged (lower row) velocity fields measured for several values of Wi: **a**—$Wi = 2.48$, **b**—$Wi = 9.88$ and **c**—$Wi = 18.9$. Data were collected in setup 1 ($Wi_c = 6.95$) at middle distance between plates and replotted from Burghelea (2005)

Below the onset of elastic instability (curves (1, 2) in Fig. 14), there exists no radial flow component. The azimuthal flow component depends linearly on the radial coordinate in the vicinity of the centre of the flow system which is consistent with a rigid body rotation, see the inset in Fig. 14a.

Above the onset of the primary elastic instability, a major reorganisation of the flow manifested through the emergence of a strong radial velocity component may be observed, (curves (3, 5) in Fig. 14b). The presence of a non-zero radial component is related to the formation of the vortical structure illustrated in Figs. 11, 12 and 13.

The flow reorganisation above the onset of the primary elastic instability is accompanied by a sharp increase of the level of velocity fluctuations. This point is well supported by measurements of time series of the azimuthal velocity component V_θ at $Wi = 36.1$ at several radial positions at mid-distance between the plates of setup 2 (Fig. 15a). In the central ($r/R_c = 0$) and peripheral region of the flow ($r/R_c = 15/16$) the velocity signal displays no significant intermittency whereas at $r/R_c = 2$ it is strongly intermittent. The radial dependence of the level of intermittency reflects the presence of the randomly fluctuating spiral vortex and the position $r = R_C/2$ most probably corresponds to the arm of the spiral.

This behaviour is also reflected in the shape of the probability distribution functions of the normalised azimuthal velocity presented in Fig. 15b: near the centre and the vertical wall of the cell, the distributions are symmetric and single peaked whereas around $r = R_c/2$ they become strongly skewed and doubly peaked.
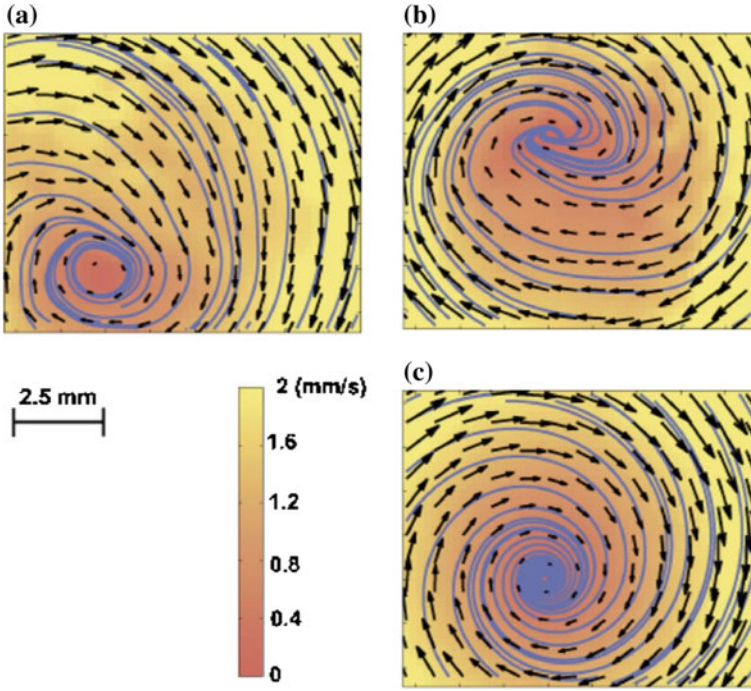
Fig. 12 **a–b** Instantaneous velocity fields separated in time by 50 s. **c** Time-averaged (over 120 s) velocity field. The false colour map indicates the magnitude of the velocity and the full lines are streamlines. The data have been acquired in setup 2 at $Wi = 17.35$ at the mid-distance between plates and replotted from Burghelea (2005)

Next, we monitor the evolution of the turbulence intensity defined by $I_t = \frac{V_\theta^{rms}}{\bar{V}_\theta}$ with Wi at several radial positions in setup 2 (Fig. 16a). Regardless the radial position, a sharp increase of the turbulence intensity is observed past the onset of the primary elastic instability. In a fully developed elastic turbulent regime, the turbulence intensity scales as $I_t \propto Wi^{0.5}$. This scaling is an indicator of an imperfect bifurcation.

The dependence of the turbulence intensity on the reduced radial coordinate r/R_c measured for several Wi is presented in Fig. 16b. Within a fully developed elastic turbulent regime, the turbulence intensity is the largest in the core of the main vortex.

4.3 Space-Time Correlations and Spectra in a Regime of Elastic Turbulence

In Sect. 4.2 it has been shown that, in a regime of Elastic Turbulence, the flow fields bear two key features. First, they are spatially smooth meaning that their characteristic space scale is comparable to the size of the fluid container. Second, they have a chaotic
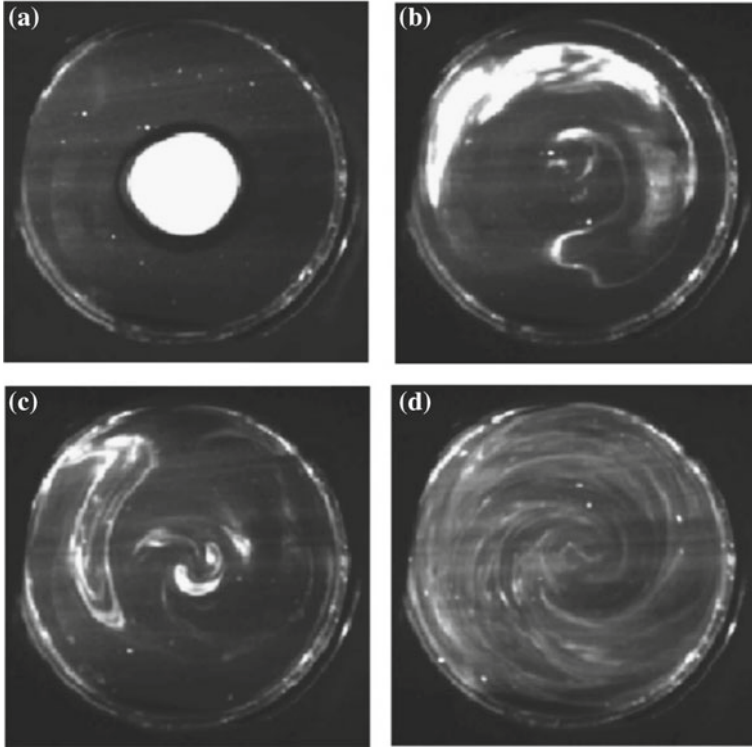
Fig. 13 Representative laser-induced fluorescence snapshots acquired at mid-distance between the plates at several time instants: **a** $t = 0$ s, **b** $t = 16.8$ s, **c** $t = 26.52$ s and **d** $t = 55.92$ s. The data have been acquired in setup 2 ($Wi_c \approx 8.37$) at $Wi = 17.35$ at the mid-distance between plates and replotted from Burghelea (2005)
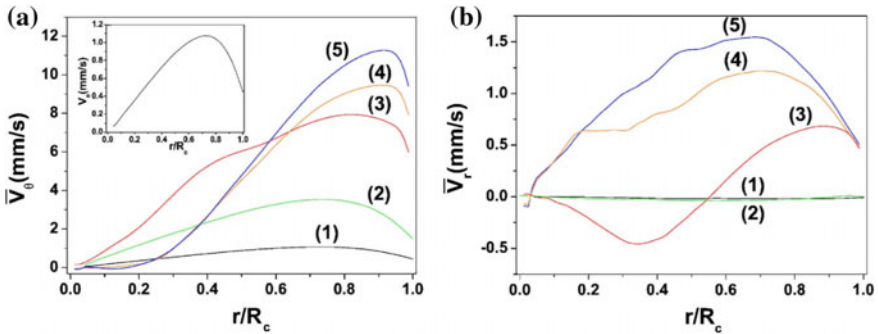
Fig. 14 **a** Radial profiles of the time-averaged azimuthal velocity component $\bar{V}_\theta$, **b** measured for several Wi. For reference, the inset shows a typical laminar velocity profile. **b** Radial profiles of the time-averaged radial velocity component $\bar{V}_r$ measured for several Wi. In both panels, the labels are: (1)—$Wi = 2.48$, (2)—$Wi = 4.4$, (3)—$Wi = 11.1$, (4)—$Wi = 15$ and (5)—$Wi = 18$. The data have been acquired in setup 1 ($Wi_c \approx 6.95$) at $Wi = 17.35$ at the mid-distance between plates and replotted from Burghelea (2005)
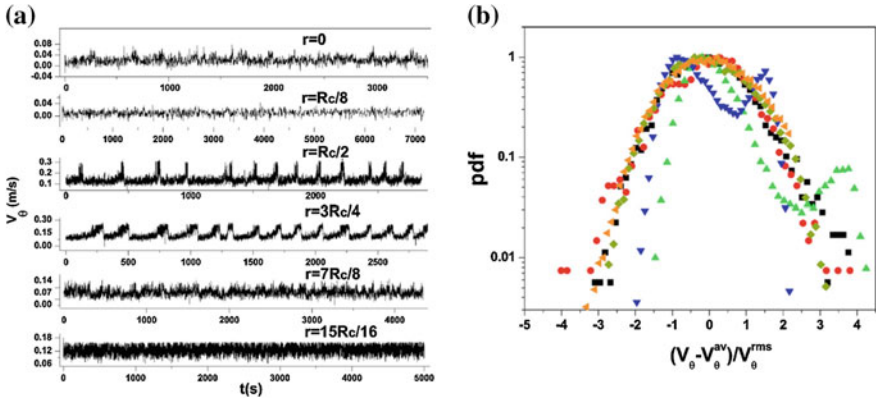
Fig. 15 a Time series of the azimuthal velocity component measured for $Wi = 36.1$ at several radial positions indicated in the inserts. **b** Probability distribution functions of the normalised azimuthal velocity measured at $Wi = 36.1$ and several radial positions: squares—$r = 0$, circles—$r = R_c/8$, up triangles—$r = R_c/2$, down triangles—$r = 3R_c/4$, diamonds—$r = 7R_c/8$ and left triangles—$r = 15R_c/16$. The data were collected at mid-distance between the plates setup 2 ($Wi_c \approx 8.37$) and replotted from Burghelea (2005)
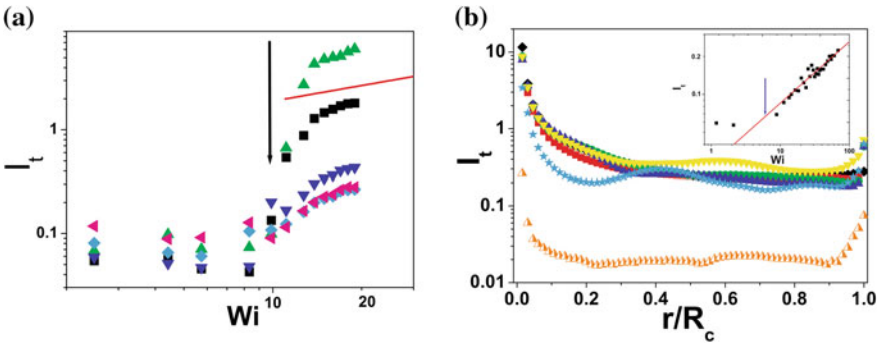
Fig. 16 a Dependence of the turbulence intensity I_t on the Weissenberg number measured at different radial positions: squares—$r = 1$ cm, up triangles—$r = 0.7$ cm, down triangles—$r = 1.5$ cm, diamonds—$r = 1.74$ cm and left triangles— $r = 1.89$ cm. The full line is a guide for the eye, $I_t \propto Wi^{0.5}$. **b** Dependence of the turbulent intensity I_t on the reduced radial coordinate r/R_c measured for several Weissenberg numbers: diamonds—$Wi = 31.56$, squares,—$Wi = 27.73$, circles—$Wi = 23.67$, up triangles—$Wi = 19.29$, down triangles—$Wi = 15.48$, stars—$Wi = 17.54$ and half filled triangles—$Wi = 2.82$. The inset shows the dependence of I_t on Wi measured at $r/R_c = 0.85$ and the full line is a power-law fit $I_t \propto Wi^{0.49\pm0.06}$, the arrow marks the onset of the primary elastic instability. The data were collected in setup 2 ($Wi_c \approx 8.37$) and replotted from Burghelea (2005)

appearance meaning their temporal evolution is predictable solely during finite times. The adequate mathematical tools for characterising such flows are the statistical tools. In this section, we focus on the description of several important physical quantities

in a regime of Elastic Turbulence: spectra of velocity fluctuations, time correlations, space correlations.

Groisman and Steinberg have first shown that the spectrum of the velocity fluctuations decays algebraically with the frequency $P(f) \propto f^{\alpha_1}$ with $\alpha_1 \approx -3.3$ (Groisman and Steinberg 2000). They performed the spectral measurements by measuring via the LDV technique long time series of the azimuthal velocity component in a single point of the flow. To obtain the spatial frequency spectra of the velocity fluctuations one needs to resort to the Taylor's frozen flow hypothesis (Taylor 1938). As shown in Burghelea et al. (2005) and latter discussed through this chapter, for the case of Elastic Turbulence in a von Karman swirling flow this has to be done with caution. On the other hand, the measurements of time series of full velocity fields exemplified in Sect. 4.2 allow a direct computation of the space spectra without using the Taylor hypothesis.

Figure 17 displays space spectra of the velocity fluctuations for different values of the control parameter within a regime of Elastic Turbulence. Prior to reaching a plateau related to the level of instrumental noise of the PIV measurements, the spectra decay algebraically, the full line in Fig. 17. In contrast to the inertial turbulence, the spectrum of the velocity fluctuations is not related to an energy cascade (Fouxon and Lebedev 2003). A phenomenological explanation for the shape of the velocity power spectra displayed in Fig. 17 may be formulated as follows.

In a regime of Elastic Turbulence, the flow is dominated by a large-scale randomly fluctuating velocity field. The passive advection of the stress field by the large-scale velocity fields leads to generation of smaller scales stress fields, which are permanently decaying to polymer relaxation. The situation is similar to the decay of a passively advected tracer in the Batchelor regime of mixing. The small-scale velocity fluctuations are a result of the small-scale fluctuations of the stress field.

A spatial typical scale at which elastic stresses are pumped can be estimated using the power spectra shown in Fig. 17,

$$L = 2\pi \frac{\int P(k)dk}{\int k \cdot P(k)dk} \tag{3}$$

Corresponding to fully developed chaotic flow states($Wi > Wi_{et}$), one obtains $L = 2.4$ cm for setup 1 and $L = 5.9$ cm for setup 2, suggesting that the main energy dissipation takes place at large scale and the physics behind the spectra is similar to the linearly decaying passive scalar problem. Thus, as already hinted by the topology of the flow fields illustrated in Figs. 11, 12, 13 and 14 the statistically dominant space scale of the elastic turbulent flow is comparable in magnitude to the size of the fluid container.

Unlike in the case of high Re turbulence, here there exists no analogue of the Kolmogorov scale (the apparent flattening of the spectra for large wave numbers is only due to the finite spatial resolution of the PIV measurements) and the spectra should terminate at wave numbers $k_{diff} \approx 1/\sqrt{D \cdot \lambda}$ defined by the diffusivity D of the polymer molecules and their relaxation time, λ. The simultaneous passive

Fig. 17 Power spectra of the fluctuations of tangential velocity component at different Wi: circles—$Wi = 4.41$, up triangles—$Wi = 5.72$, down triangles—$Wi = 8.32$, left triangles— $Wi = 11.1$, right triangles—$Wi = 12.7$, hexagons—$Wi = 13.8$, diamonds—$Wi = 16$, half filled squares—$Wi = 18$ and empty circles—$Wi = 19$. Data were collected in setup 1 and replotted from Burghelea (2005)
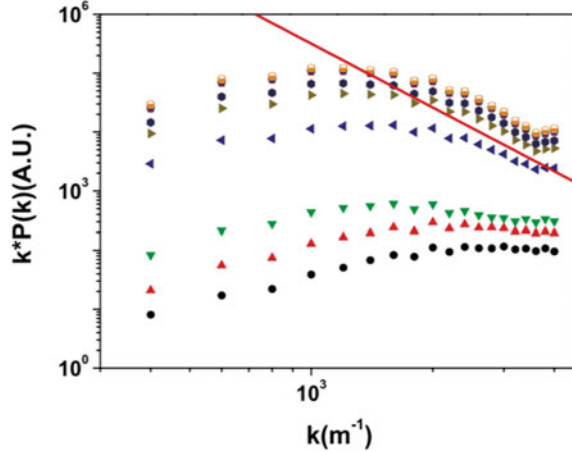
advection and relaxation of the elastic stresses results in a fast decay of the stress fluctuations at small scales, which should produce $P(k) \sim k^{-\alpha}$ velocity spectra with $\alpha > 3$. The data presented in Fig. 17 displays a decay region $k^{-3.6}$ which agrees rather well with the theoretical prediction (Fouxon and Lebedev 2003), and with previous experimental results[2] (Groisman and Steinberg 2000).

Unfortunately, an experimental technique that allows measurements of the stresses embedded in a fluid flow is not currently available. It was suggested that the stress generation in the flow of a dilute polymer solution is directly related to the local Lyapunov exponents of the flow (defined by the average logarithmic rate of separation of two initially close Lagrangian trajectories) or, equivalently, to the rms of fluctuations of the velocity gradients (Balkovsky and Fouxon 1999; Balkovsky et al. 2001). A systematic Lagrangian frame description of the Elastic Turbulence in a macroscopic von Karman swirling flow will be presented in Sect. 4.6.

An important quantity characterising a chaotic flow field is its Eulerian correlation time. The Eulerian correlation time can be defined as

$$\tau_c = \int t\, C(t)dt \Big/ \int C(t)dt \qquad (4)$$

---

[2]In Groisman and Steinberg (2000) the spatial spectra of the velocity fluctuations have been derived from point velocity measurements by using the Taylor hypothesis. For random flows of a dilute polymer solution in a regime of Elastic Turbulence, this hypothesis generally fails (see Sect. 1.6). The remarkable agreement between the spectra measured in Groisman and Steinberg (2000) and the directly measured spectra deserves a brief discussion. Following Lumley (1965), the relation between the spatial spectra, $P(k)$ and the frequency domain spectra, $P_1(f)$ can be written: $P(k) = V \cdot P_1(f) - \frac{I_t^2}{2} \cdot \frac{d^2(k^2 \cdot P(k))}{dk^2} + O(I_t^4)$. If $P(k) \propto k^{\alpha_2}$ and $P(f) \propto f^{\alpha_1}$, the equation above leads to: $\alpha_2 - \alpha_1 \propto \frac{log[1+\frac{I_t^2}{2} \cdot \alpha_2 \cdot (\alpha_2+2)]}{log(k)}$. If one plugs in the last equation $\alpha_2 \approx -3.6$, the difference between the exponents is (for $k \approx 1000m^{-1}$) as small as $\alpha_2 - \alpha_1 \approx 0.2$.

Fig. 18 Eulerian correlation times of the tangential velocity component measured at $r = R_c/2$ as function of Wi: squares—setup 1; circles—setup 2. The data were replotted from Burghelea (2005)
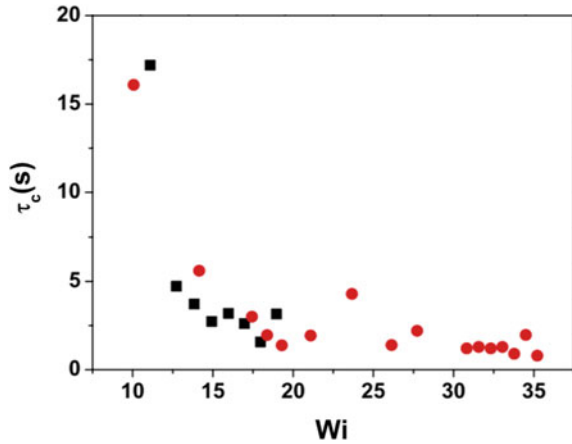
Fig. 19 Schematic view of the flow geometry: (M)—mean flow line, (L)—measured Lagrangian trajectory and (C)—circular arc
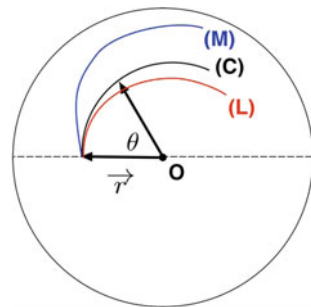
where $C(t)$ is the Eulerian correlation function of the velocity in a regime of Elastic Turbulence.

Measurements of the Eulerian correlation time performed at $r = R_c/2$ at mid-distance between the plates are presented in Fig. 18. The transition to Elastic Turbulence is accompanied by a significant decrease of the correlation times, τ_c, from values of order of 15 s in the intermediate flow regime to values of about 1 s (Fig. 18). An apparent saturation of the correlation time in the Elastic Turbulence regime was observed in both setups, suggesting that some sort of dynamical equilibrium is reached. The saturation level is of the order of the polymer relaxation time λ (Fig. 8).

Yet another important physical quantity needed to describe a chaotic flow is its spatial correlation length. Its measurement is a non-trivial task as it requires monitoring the degree of correlation of the velocity of a fluid element as it is advected by the flow. As a relevant advection path, we have several choices (Fig. 19): the mean flow line (which inherently accounts for the topology of the flow field), a circular trajectory or a Lagrangian path.

Figure 20 displays velocity time series at three different locations along the mean flow line (M). As one can see from panels (a) and (b), for sufficiently small separa-

Fig. 20 Simultaneous tangential velocity time series (partially shown) at $Wi = 57.6$ for three values of the displacement along the mean flow line (M): **a** $s = 0$ cm, **b** $s = 1.5$ cm and **c** $s = 3.2$ cm. The data were collected at mid-distance between the plates setup 2 ($Wi_c \approx 8.37$) and replotted from Burghelea (2005)
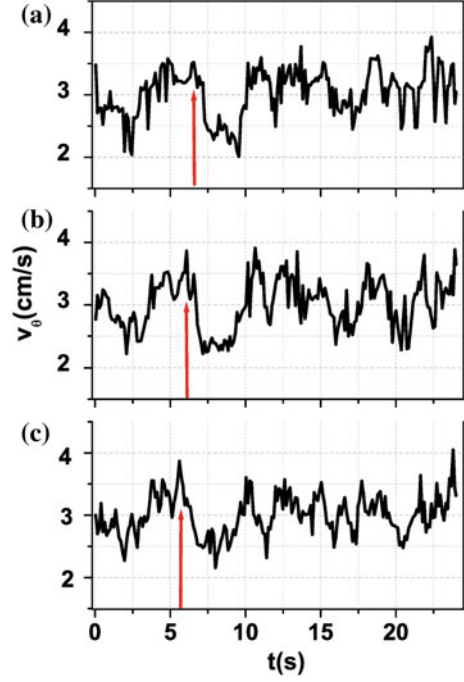
tions, s, the two velocity time series are almost identical, up to a shift in time. For larger separations (panel (c)), the velocity fluctuations are less correlated, and the two time series display clear differences.

In order to check whether the velocity fluctuations are transported without evolving dynamically (the flow is frozen) and directly assess the degree of applicability of the Taylor's hypothesis, we measure the cross-correlation of the velocity fluctuations between neighbouring points separated by the distance s, $C_{ij}(\tau, \overrightarrow{\Delta r}, \overrightarrow{r})$ defined by:

$$C_{ij}(\tau, \overrightarrow{\Delta r}, \overrightarrow{r}) = \frac{\langle v_i(\overrightarrow{r}, t) \cdot v_j(\overrightarrow{r} + \overrightarrow{\Delta r}, t - \tau)\rangle_t}{v_{i1}^{rms} \cdot v_{j2}^{rms}} \tag{5}$$

where $v_{1,2}^{rms}$ is the rms of velocity at the points $\overrightarrow{r}$, $\overrightarrow{r} + \overrightarrow{\Delta r}$ and $i, j = r, \theta$ are the polar coordinates (Fig. 19). It is worth noting that, since the mean flow is curvilinear, C_{ij} depends not only on the magnitude of the displacement between neighbouring points, $|\overrightarrow{\Delta r}|$, but also on the path along which the displacement is considered and its length s. Thus, in order to check the sensitivity of our results on the choice of the displacement path, we have alternatively considered displacements along circular arcs (around the centre of the setup), time average flow lines, and Lagrangian trajectories.

The spatial smoothness demonstrated in Figs. 11, 12, 13 and 14 mathematically translates into neglecting the high-order spatial derivatives of the fluctuating part of the velocity components, $\frac{\partial^k \vec{v}(\vec{r},t)}{\partial \vec{r}^k} \approx 0, k \geq 3$.

Within the approximation of vanishing high-order spatial derivatives and for small displacements, s, and delay times, τ, one can easily decouple the space and time dependencies in the definition of the cross-correlation function (Eq. 5):

$$C_{ij}(\tau, s, \vec{r}) \simeq \frac{\langle v_i(\vec{r}, t) \cdot v_j(\vec{r}, t)\rangle_t}{v_{i1}^{rms} \cdot v_{j2}^{rms}} + s \cdot \frac{\langle v_i(\vec{r}, t) \cdot \frac{\partial v_j(\vec{r},t)}{\partial r}\rangle_t}{v_{i1}^{rms} \cdot v_{j2}^{rms}} -$$

$$\tau \cdot \frac{\langle v_i(\vec{r}, t) \cdot \frac{\partial v_j(\vec{r},t)}{\partial t}\rangle_t}{v_{i1}^{rms} \cdot v_{j2}^{rms}} - s \cdot \tau \cdot \frac{\langle v_i(\vec{r}, t) \cdot \frac{\partial^2 v_j(\vec{r},t)}{\partial r \partial t}\rangle_t}{v_{i1}^{rms} \cdot v_{j2}^{rms}} +$$

$$\frac{\tau^2}{2!} \cdot \frac{\langle v_i(\vec{r}, t) \cdot \frac{\partial^2 v_j(\vec{r},t)}{\partial t^2}\rangle_t}{v_{i1}^{rms} \cdot v_{j2}^{rms}} + \frac{s^2}{2!} \cdot \frac{\langle v_i(\vec{r}, t) \cdot \frac{\partial^2 v_j(\vec{r},t)}{\partial r^2}\rangle_t}{v_{i1}^{rms} \cdot v_{j2}^{rms}} \qquad (6)$$

A typical space-time cross-correlation surface computed according to Eq. (6) using as a principal direction of advection the mean flow line is shown in Fig. 21.

For sufficiently small time delays τ and displacements s along the mean flow line, the correlation function surface can be well fitted by a paraboloidal surface. Unfortunately, the limited time resolution of the PIV measurements did not allow a full comparison of the coefficients of the expression above with those resulted from the fit. However, the parabolic dependence of $C_{ij}(\tau, \vec{r}, \vec{s})$ on the delay time τ at a given spatial displacement s or at a given delay time τ has been verified experimentally. In Fig. 22 we display several cross-correlation functions collapsed onto a single curve being rescaled by the their maxima, C_{rr}^{max}.

Fig. 21 Space-time correlation surface. The data were collected at mid-distance between the plates setup 2 ($Wi_c \approx 8.37$) and replotted from Burghelea (2005)
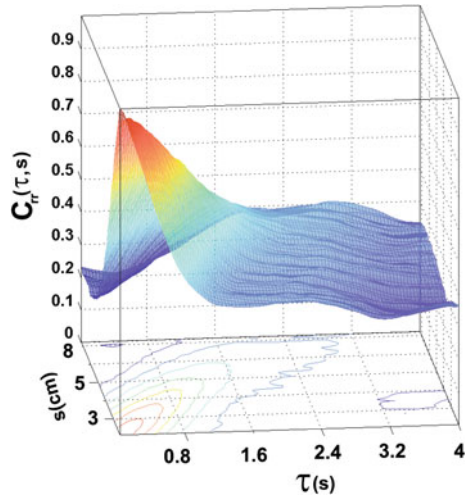
Fig. 22 Scaled
cross-correlation functions
for displacements s along the
mean flow line ranging from
7 mm–4 cm. The dotted line
is a parabolic fit. The data
were replotted from
Burghelea (2005)
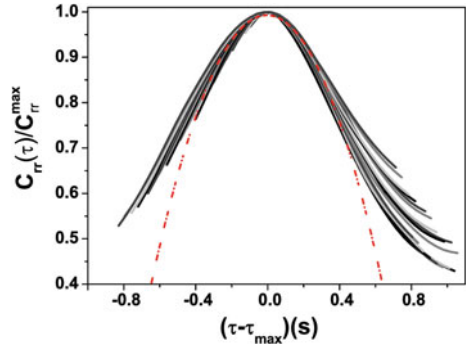
Fig. 23 Space dependence
of cross-correlation
functions at fixed time
delays: squares—$\tau = 0$;
circles—$\tau = \tau_{max}$. The full
lines are parabolic fits. The
data were replotted from
Burghelea (2005)
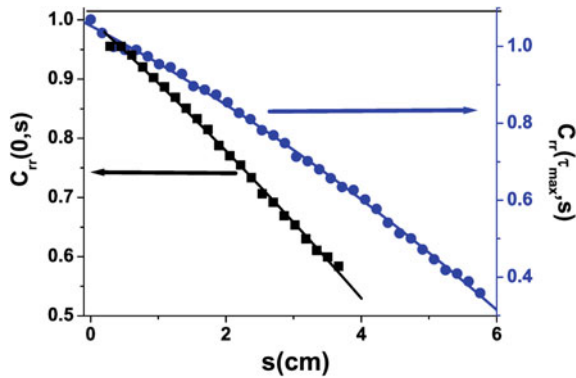
Second, as resulted from the fit, the second-order spatial derivative is about one
order of magnitude smaller than the first-order one, which is a direct confirmation
of the flow smoothness hypothesis. One can notice that for small enough delay
times and space displacements the cross-correlations are well fitted by a parabola as
suggested by Eq. (6). Second, the weakly parabolic dependence of $C_{ij}(0, \overrightarrow{r}, \overrightarrow{s})$ on
the displacement s has also been verified experimentally (Fig. 23).

Figure 24 shows $C_{rr}(\tau, s, \overrightarrow{r})$ for few separations s along the mean flow line and
corresponding to $\overrightarrow{r} = (\frac{2 \cdot R_c}{3}, 0)$.

As one can see in Fig. 24, for a given value of the displacement in space, s, the
temporal part of the cross-correlation displays a well-defined maxima at $\tau_{max}(s, \overrightarrow{r})$,
defined by $\frac{\partial C_{rr}(\tau_{max}, s, \overrightarrow{r})}{\partial \tau}|_{s=const.} = 0$. If Taylor's frozen flow hypothesis is valid and
the information on velocity fluctuations is not altered during the passage between
two points separated by s in the flow, then the peaks of the temporal part of the
cross-correlations are sharp and $C_{rr}^{max}(\tau_{max})$ close to unity. Moreover, the values of
the delay time τ that maximise the correlations should scale linearly with the space
displacements, that is $\tau_{max} = \frac{s}{V}$. Here, as discussed above, in order to correctly
account for the flow non-homogeneity, one should consider the spatial dependence
of the velocity field, $V = V(\overrightarrow{r})$.

Fig. 24 The cross-correlation of velocity fluctuations, $C_{rr}(\tau, s)$ versus the delay time τ for different values of the displacement s along the mean flow line. The data were replotted from Burghelea (2005)
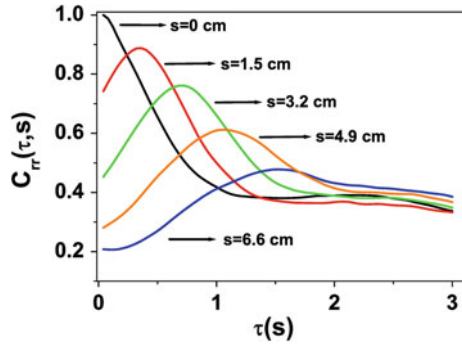
Validity of the Taylor hypothesis One way of quantifying the validity of the Taylor hypothesis is to measure the deviation of the slope p_1 of the dependence $\tau_{max} = \tau_{max}(\frac{s}{V})$ from unity (Belmonte et al. 2000).

A typical dependence of the maximum delay time τ_{max} on the spatial displacement s is shown in Fig. 25. For this case, we have obtained from a linear fit $p_1 \simeq 0.73 \pm 0.006$.

As one can see from Fig. 26, in the central region of the flow the deviations from the frozen flow assumption are significant.

The Taylor hypothesis is best verified towards the boundaries of the system. However, p_1 never exceeds 0.83.
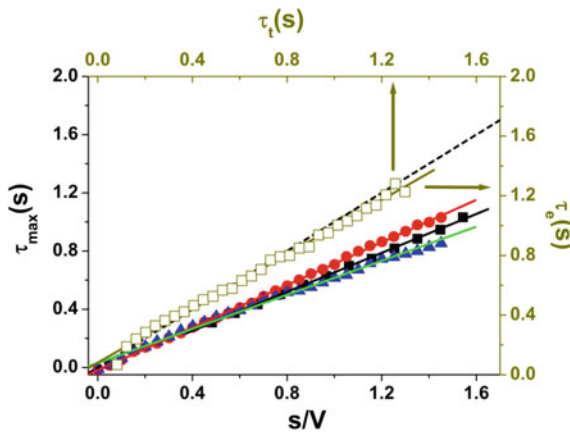
Fig. 25 Bottom-left axis: the delay time τ_{max} that maximises the cross-correlation functions versus the length of the displacement along three different paths: squares—circular arcs, circles—mean flow line and triangles–Lagrangian trajectory. The horizontal axis is normalised by the mean velocity at s = 0. The full lines are linear fits with slopes 0.6, 0.7 and 0.73, respectively. The dotted line has slope 1. Top-right axis: the delay time τ_e (see text) versus the transit time τ_t. The full line is a linear fit with slope 0.96. The initial position was $\vec{r} = (\frac{2R_c}{3}, 0)$. The data were replotted from Burghelea (2005)

Fig. 26 Validity of the
Taylor hypothesis (see text
for discussion) versus the
radial coordinate. The data
were replotted from
Burghelea (2005)
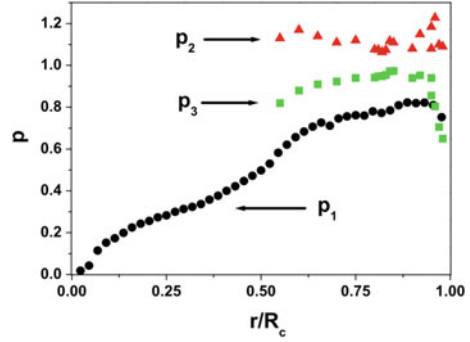
Whereas the breakdown of the Taylor hypothesis in the central flow region can be easily understood in the context of large (relatively to the mean flow) velocity fluctuations and practically zero mean flow, the applicability of the frozen flow assumption in the off central flow region deserves a separate discussion. Although chaotic in time, the flow is structurally different from high *Re* turbulent flows. As we have already pointed out, the main difference is the absence of any analogue of the Kolmogorov length scale, absence of eddies of different sizes in the scaling range swept by larger eddies, and the flow is smooth at all spatial scales. The main consequence of the flow smoothness is the high space coherence of the velocity fluctuations (the cross-correlations do not decay to 0 even over distances comparable to the size of the container, as shown in Figs. 23 and 24).

This fact explains why three physically different choices of the path of particle displacement (circular arcs, mean flow line, Lagrangian trajectories) (Fig. 19), lead to similar values of the maximal delay times τ_{max} (Fig. 25).

Second, it is worth noting that the validity coefficient p_1 is always smaller than unity (Figs. 25 and 26) for each of the three displacement choices we have considered and the deviation from unity (which accounts at best for 20%) is clearly outside the error bar of the linear fit. This suggests that the breakdown of the Taylor hypothesis in the off-central flow region is not necessarily due to the level of fluctuations (which is the case in the central region) but rather to an underestimation of the advection velocity. Similar results have been previously reported in experimental studies of coherent structures in turbulent jets and turbulent boundary layers (Fisher and Davies 1964; Zaman and Hussain 1981; Koeltzsch 1998; Krogstad et al. 1998). The central conclusion of these studies was that the velocity transporting the fluctuation information at scales comparable to the size of the coherent structure is substantially different from the local mean flow velocity. This seems to be indeed the case of the data presented in Fig. 25: if one rescales the displacements s with a velocity about 20% larger than the mean flow velocity V, the data would overlap with the unitary slope line. Consistently with a different choice of the advection velocity (Fisher and Davies 1964; Koeltzsch 1998), one can focus on the dependence of $\tau_e(s, \overrightarrow{r})$ defined implicitly by $\frac{\partial C_{rr}(\tau_e, s, \overrightarrow{r})}{\partial s}|_{\tau=const.} = 0$ on the transit time τ_t between two points sepa-

rated by s. If the Taylor hypothesis applies, this dependence is linear and has unitary slope.

Thus, a second way to quantify the validity of the frozen flow assumption is to measure the deviation of the slope p_2 of the dependence $\tau_e = \tau_e(\tau_t)$ from unity.

Following a suggestion made by Koeltzsch (1998) one can define an additional validity coefficient $p_3 = \sqrt{p_1 \cdot p_2}$. As shown in Fig. 26, these corrections seem to work rather well for regions away from the vortex core.

As an alternative method, the applicability of the Taylor hypothesis can be verified by comparing directly measured spatial structure functions and spatial power spectra of velocity fluctuations with the ones derived using the frozen flow assumption. We focus in the following on the second-order structure function

$$S_2(s) = \langle |v_\theta(\overrightarrow{r}, t) - v_\theta(\overrightarrow{r} + \overrightarrow{\Delta r}, t)|^2 \rangle \tag{7}$$

and compare its values obtained from direct spatial measurements with those obtained using the Taylor hypothesis, $s = V \cdot t$.

As shown in Fig. 27, corresponding to the characteristic scale L the structure functions saturate at values roughly equal to $2 \cdot v_{rms}^2$. Near the core of the main vortex, the two structure functions are significantly different (Fig. 27a), indicating once more a clear breakdown of the Taylor hypothesis whereas closer to the boundary

Fig. 27 Second-order velocity structure functions: squares—resulted from direct measurements, circles derived by using the Taylor hypothesis. Here we have considered displacements along the mean flow line and the initial position was: **a** $\overrightarrow{r} = (R_c/3, 0)$; **b** $\overrightarrow{r} = (2 \cdot R_c/3, 0)$. The data were replotted from Burghelea (2005)
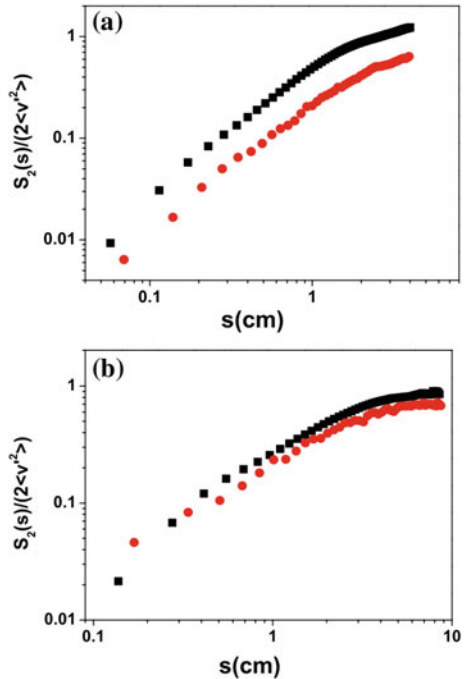
(Fig. 27b) the difference diminished to about 20% of their saturation value that is rather consistent with the result shown in Fig. 26.

4.4 Statistics of Velocity Gradients in a Regime of **Elastic Turbulence**

As discussed in Sect. 1, the elastic stresses are generated in flows of viscoelastic fluids by extension of individual polymer molecules past the onset of the coil-stretch transition and, the extension of individual polymer molecules is a result of the velocity gradients existing in the base flow. Thus, it appears natural to focus on the spatio-temporal properties of the velocity gradients. As we are going to discuss in Sect. 8, understanding the behaviour of the velocity gradients and their level of fluctuations is a cornerstone for the theoretical understanding of the Elastic Turbulence.

One of the main advantages of the DPIV technique is that it provides a direct access to this physical quantity whereas point-wise measurements (LDV, hot wire anemometry require the use of the Taylor frozen flow hypothesis).

Time-averaged measurements of the radial gradients of the tangential velocity component performed in setup 1 at mid-distance between plates are presented in Fig. 28. The averaging time was significantly larger than the characteristic relaxation time of the polymer solution in order for the ensemble average to be statistically relevant.

Below the onset of the primary elastic instability, the velocity gradients are located near the circular boundary of the setup, panel (a) in Fig. 28. Around the onset of the primary elastic instability, two concentric rings of local maxima of the velocity gradients are formed around the centre of the setup, panels (b–c). In a regime of Elastic Turbulence, the two rings merge into a single ring which grow in width as the Weissenberg number is further increased, panels (d–g). The evolution of spatial distribution of the time-averaged velocity gradients with the Wi suggests a scenario for the emergence of the Elastic Turbulence. Initially, the velocity gradients are concentrated near the boundaries of the system indicating that the elastic stresses originate from a boundary layer. As the system undergoes a purely elastic instability, the velocity gradients extend towards the entire setup and, consequently, the elastic stresses get homogeneously distributed in the system.

Radial profiles of the time-averaged gradient of the tangential velocity component in the radial direction displayed in Fig. 29a reveal a rather uniform distribution of the gradients in the bulk of the flow and a sharp increase near the boundary. The typical dependencies of the gradients measured at different radial positions on the control parameter are displayed in Fig. 29b.

The behaviour of the root mean square (rms) of the velocity gradients is illustrated in Fig. 30. Below the onset of the primary elastic, the rms values are small and solely related to the instrumental error of the measurements, Fig. 30a. Within the elastic
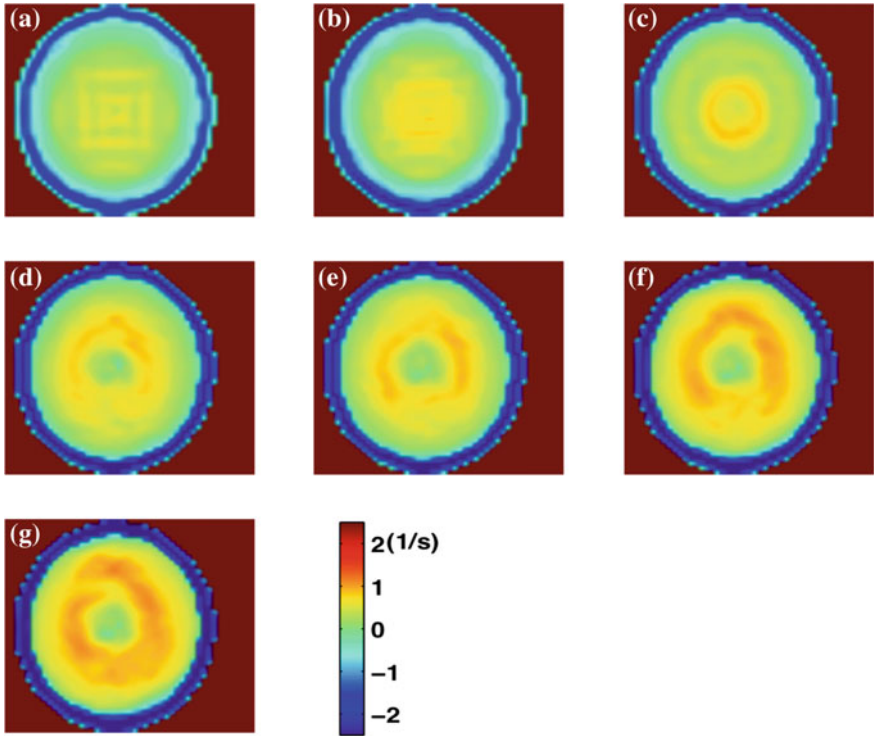
Fig. 28 Average gradient of the tangential velocity component in the radial direction, $\frac{\partial v_\theta}{\partial r}$, at different Wi: **a** $Wi = 8.32$, **b** $Wi = 9.88$, **c** $Wi = 11.1$, **d** $Wi = 12.72$, **e** $Wi = 13.83$, **f** $Wi = 17$ and **g** $Wi = 19$. Data were collected in setup 1 at middle distance between plates. The squared pattern slightly visible in panel (**a**) is a result of combined peak locking effect and numerical differentiation and should be disregarded. The data are replotted from Burghelea (2005)

turbulence, the rms values are the largest around the centre of the setup which is due to spiral topology of the time-averaged flow field (Fig. 12).

The dependence of the rms of the velocity gradients measured at several radial positions is illustrated in Fig. 30b. Regardless the radial position, the rms of the gradients increase significantly past the onset of the primary elastic instability. In a regime of fully developed Elastic Turbulence, closer the observation point is to the centre of the setup (the core of the vortex), larger the rms values are.

The *rms* of the fluctuations of the vorticity increases monotonically with the radial position reaching a maximum value near the boundary of the fluid container, Fig. 31a. This is another indication that the elastic stresses are mainly produced near the boundary and chaotically advected through the bulk of the flow. The dependence of the scaled *rms* of the fluctuations of vorticity $\lambda\omega_{rms}$ on Wi presented in Fig. 31b reveals an increase of the level of fluctuations close to the boundary of the fluid container (the diamonds) and a saturation in the bulk of the flow.
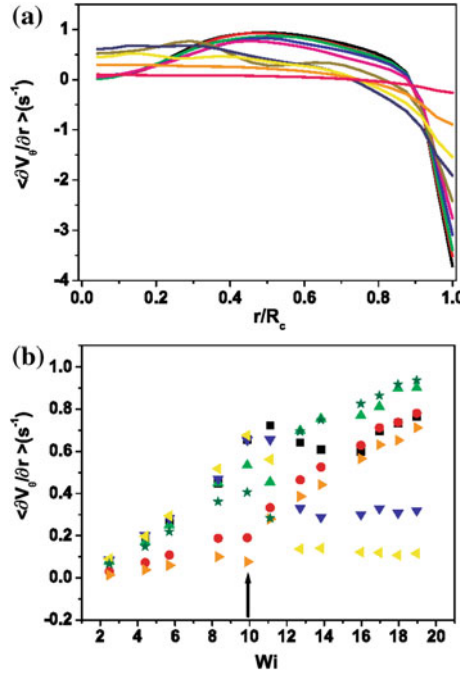
Fig. 29 a Profiles of the average radial gradient of the tangential velocity at different Wi: black—$Wi = 19$, red—$Wi = 18$, green—$Wi = 11$, blue—$Wi = 16$, magenta—$Wi = 13.83$, olive—$Wi = 11.1$, dark blue—$Wi = 9.88$, yellow—$Wi = 8.32$, orange—$Wi = 5.73$ and pink—$Wi = 2.48$. **b** Dependence of the average radial gradient of the tangential velocity on Wi at different radial positions: squares—$r/R_c=0.3$, circles—$r/R_c = 0.66$, up triangles—$r/R_c = 0.4$, down triangles—$r/R_c = 0.2$, left triangles—$r/R_c = 0.1$, right triangles—$r/R_c = 0.7$ and stars—$r/R_c = 0.5$. The arrow indicates the onset of the elastic instability. Data were collected in setup 1 at middle distance between plates and replotted from Burghelea (2005)

4.5 Boundary Layer in a Regime of Elastic Turbulence

The analysis of the velocity gradients and the rms of their fluctuations presented in Sect. 4.4 indicate that the dynamics observed in the bulk of the flow is strongly different from that observed near the boundary of the flow. This prompts us to perform a systematic analysis of the boundary regions of the flow.

We distinguish three distinct relevant boundary regions (Fig. 32): *vbl*—a vertical boundary region located in the vicinity of the lateral wall of the fluid container, *bbl*—a bottom boundary region located near the bottom plate of the fluid container and *tbl*—a top boundary region located near the top rotating disc.

To study the *tbl* and *bbl*, we use Laser Doppler Velocimetry (*LDV*) to measure the time-averaged azimuthal component of the velocity $\bar{V}_\theta$ at a fixed radial position $r = 3R_c/4$ and several vertical positions z.
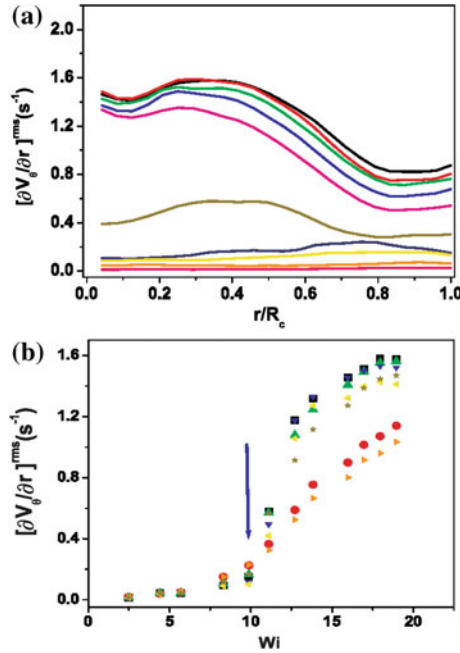
Fig. 30 a Profiles of the rms of fluctuations of the radial gradient of the tangential velocity at different Wi: black—$Wi = 19$, red—$Wi = 18$, green—$Wi = 11$, blue—$Wi = 16$, magenta—$Wi = 13.83$, olive—$Wi = 11.1$, dark blue—$Wi = 9.88$, yellow—$Wi = 8.32$, orange—$Wi = 5.73$ and pink—$Wi = 2.48$. **b** Dependence of the rms of fluctuations of the radial gradient of the tangential velocity on Wi at different radial positions: squares—r/R_c=0.3, circles—$r/R_c = 0.66$, up triangles—$r/R_c = 0.4$, down triangles—$r/R_c = 0.2$, left triangles—$r/R_c = 0.1$, right triangles—$r/R_c = 0.7$ and stars—$r/R_c = 0.5$. The arrow indicates the onset of the elastic instability. Data were collected in setup 1 at middle distance between plates and replotted from Burghelea (2005)

The dependence of the normalised (by the speed of the top disc at $r = 3R_c/4$) azimuthal velocity $\tilde{V}_\theta = \frac{\tilde{V}_\theta}{V_\theta^{max}}$ on the reduced vertical coordinate z/H measured in a regime of Elastic Turbulence at various Wi is presented in Fig. 33.

Several important points can be made based on the data presented in Fig. 33. First, regardless the value of the Weissenberg number, in a regime of Elastic Turbulence all normalised profiles collapse onto a single master curve.

Second, within regions of width $\Delta z/H \approx 0.1$ in the vicinity of top and bottom plates the normalised profiles are linear (whereas in the bulk of the flow they are flat). This indicates two velocity boundary layers, *tbl*, *bbl* of equal width are formed. As all data collapse onto a single master curve, their width does not depend on Wi. By repeating the same type of measurements with several different polymer solutions we observed a power lax dependence of the width of *tbl* and *bbl* with the viscosity $w \propto \eta^{0.26\pm0.05}$ (the inset in Fig. 33).
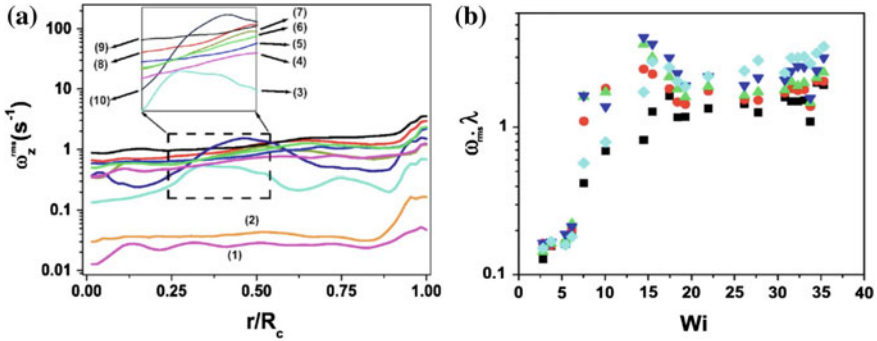
Fig. 31 **a** Radial profiles of the *rms* of fluctuations of the vorticity measured at several *Wi* at $z = H/2$. The labels are: (1)—$Wi = 2.8$, (2)—$Wi = 5.4$, (3)—$Wi = 10$, (4)—$Wi = 15$, (5)—$Wi = 17.4$, (6)—$Wi = 19.3$, (7)—$Wi = 26$, (8)—$Wi = 25$, (9)—$Wi = 27.7$ and (10)—$Wi = 32.3$. **b** Dependence of the scaled *rms* of the vorticity ω^{rms} on *Wi* at different radial positions r/R_c: full squares—0.2, open squares—0.33, full circles—0.4, open circles—0.5, and diamonds—0.66. Data were collected in setup 2 at middle distance between plates and replotted from Burghelea ([2005](#))

Fig. 32 Cartoon illustrating the topology of the relevant flow regions. The highlighted regions are the velocity boundary layers: *vbl*—vertical boundary layer of width w_θ, *bbl*—bottom boundary layer located near the bottom of the fluid container and *tbl*—the top boundary layer located near the top rotating disc. The figure is reproduced from Burghelea ([2005](#))
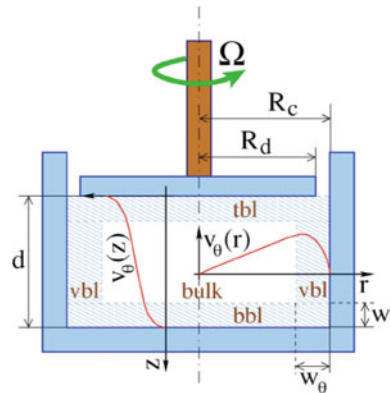
Third, one may note that velocity profiles are not symmetric with respect to the midplane $z = H/2$ of the fluid container. This fact deserves a brief discussion. Due to the principle of frame invariance, the polymer elasticity cannot break the symmetry alone. This can be achieved only if some other sources of asymmetry are present in the problem. We identify two possible sources of asymmetry in the problem: inertial effects and the vertical distribution of hydrostatic pressure. In order to understand which contribution is dominant in the flow, one has to calculate the Froude number $Fr = \frac{\Omega R_c}{\sqrt{gH}}$. For $\Omega = 5$ rad/s (which corresponds to the largest Re and Wi investigated) one obtains (for setup 2) $Fr = 0.74$. This numerical estimate suggests that, during our experiments, the gravity contribution due to the vertical gradient of hydrostatic pressure dominates the inertial contribution. We therefore conclude that the gravity effects are responsible for the symmetry breaking in the vertical velocity profiles. To conclude this section, the fully developed elastic turbulent flow is characterised by a
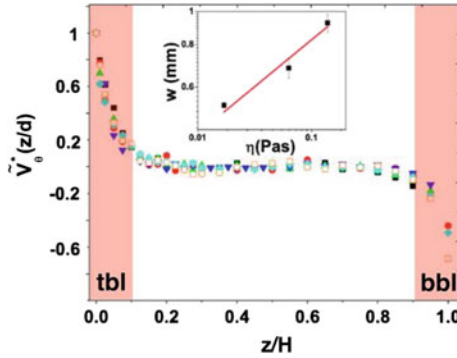
Fig. 33 Dependence of the reduced time-averaged azimuthal component of the velocity measured at $r = 3R_c/4$ and various Wi (all in a regime of fully developed Elastic Turbulence) on the reduced vertical coordinate z/H. The symbols refer to the value of the Weissenberg number: full squares—$Wi = 39$, circles-, up triangles—$Wi = 27$, down triangles—$Wi = 24$, diamonds—$Wi = 20$ and open squares—$Wi = 17$. The top boundary layer (*tbl*) and the bottom boundary layer (*vbl*) are highlighted. The inset presents the dependence of the width of the *tbl* on the viscosity of the polymer solution

second (as previously shown in this chapter, the first characteristic length scale is the size of the fluid container) length scale defined by the width of the top and bottom boundary layer.

We now focus on the flow behaviour in the *vbl* region (Fig. 32). For this purpose, we focus on the near-wall behaviour of the time-averaged azimuthal and radial velocity components measured at $z = H/2$ by means of $DPIV$ (Fig. 34).

As shown in Fig. 34a, the near-wall azimuthal velocity $\bar{V}_\theta$ depends linearly on the radial coordinate. This agrees with the requirements of incompressibility, boundary condition for the velocity and smoothness of the velocity field. In a regime of fully developed Elastic Turbulence, the slopes of the linear fit functions increase monotonically with Wi, the inset in Fig. 34a. The spatial extent of the linear part of the near-wall azimuthal profiles defines the width of the *vbl* region, w_θ.

As shown in Fig. 35, the width of the *vbl* decreases abruptly as Wi is increased past the onset of the primary elastic instability and saturates in a fully developed Elastic Turbulence. Unfortunately, the limited accuracy of the measurements of the radial velocity component near the wall presented in Fig. 34b did not allow us to assess beyond doubt the functional behaviour of the radial profiles there (note that the radial velocities are about an order of magnitude smaller than the azimuthal ones).

In order to improve the spatial resolution of the velocity field measurements near the wall, and particularly to resolve the horizontal boundary layer by looking at the rms of the radial gradient of the azimuthal velocity $\left(\frac{\partial V_\theta}{\partial r}\right)^{rms}$ the field of view of the $DPIV$ measurements has been reduced down to 10 mm in the radial direction.

The near-wall radial profiles of normalised *rms* of the near-wall velocity gradients $\left(\frac{\partial V_\theta}{\partial r}\right)^{rms}_{norm}$ measured at several Wi are presented in Fig. 36. The normalisation was performed by fitting linearly the dependence of $\left(\frac{\partial V_\theta}{\partial r}\right)^{rms}$ on the radial coordinate near
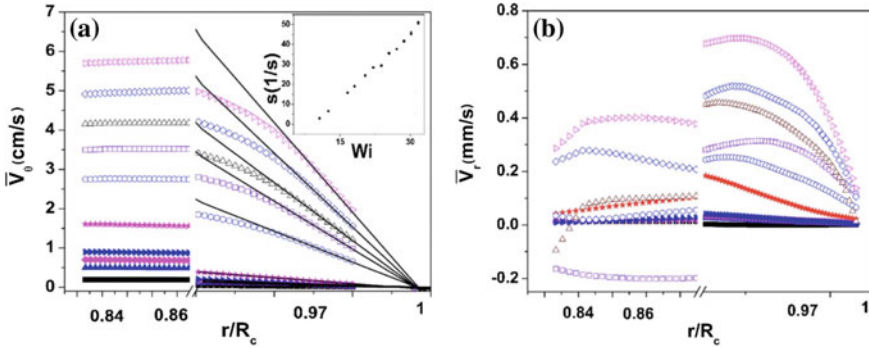
Fig. 34 a Near-wall radial profiles of the time-averaged azimuthal velocity $\bar{V}_\theta$ measured at $z = H/2$ in setup 2 at different Wi. The full lines are linear fit functions and the inset presents the dependence of their slope s on Wi. **b** Near-wall radial profiles of the time-averaged radial velocity $\bar{V}_r$ measured at $z = H/2$ in setup 2 at different Wi. In both panels, the symbols are: full squares—$Wi = 2.4$, full up triangles—$Wi = 4$, full diamonds—$Wi = 5.9$, full right triangles—$Wi = 7$, full stars— $Wi = 10.6$, empty circles—$Wi = 16.6$, empty squares—$Wi = 20.3$, empty up triangles—$Wi = 23.8$, empty diamonds—$Wi = 23.8$ and empty right triangles—$Wi = 30.2$. For a better visibility of the behaviour near the wall region, a discontinuity at $r/R_C \approx 0.87$. The data are replotted from Burghelea (2005)

Fig. 35 Dependence of the width of the vbl on Wi measured at $z = H/2$ in setup 2. The data are replotted from Burghelea (2005)
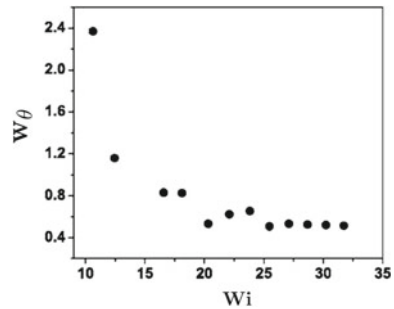
the wall and subtraction of the linear part. Well-defined local maxima positioned independently on Wi can be easily identified within the velocity boundary layer vbl which indicates that the elastic stresses are produced within the boundary layer and dissipated within the entire volume of the fluid.

The dependence of the maximal rms of the velocity gradient measured in the vbl on Wi is presented in Fig. 37. In a regime of fully developed Elastic Turbulence a linear increase of the $\lambda \left(\frac{\partial V_\theta}{\partial r}\right)^{rms}$ measured at the edge of the vbl is observed in contrast to the saturation observed in the bulk (Fig. 31).
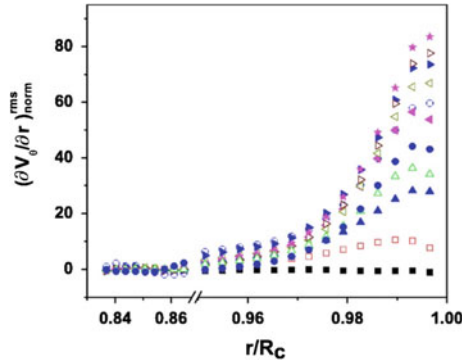
Fig. 36 Dependence of the $\left(\frac{\partial V_\theta}{\partial r}\right)^{rms}_{norm}$ on the radial coordinate measured at $z = H/2$ in setup 2. The symbols are: full squares—$Wi = 10.6$, empty squares—$Wi = 12.4$, full up triangles—$Wi = 16.5$, empty up triangles—$Wi = 18$, full circles—$Wi = 20.3$, full left triangles—$Wi = 22$, empty circles—$Wi = 23.8$, empty left triangles—$Wi = 25.4$, full right triangles—$Wi = 27$, empty right triangles—$Wi = 28.6$ and stars—$Wi = 30.2$. The data are replotted from Burghelea (2005)

Fig. 37 Dependence of the maximum of the *rms* of velocity gradients (see Fig. 36) scaled by the relaxation time of the polymer λ on Wi. The data are replotted from Burghelea (2005)
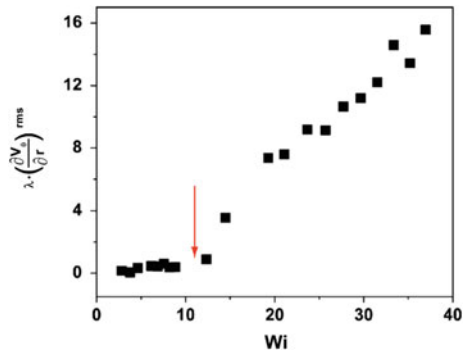
4.6 Lagrangian Frame Dynamics in a Regime of Elastic Turbulence

The discovery of a deterministic chaos has substantially changed the classical viewpoint on the origin of randomness in a fluid flow and provided a considerable number of powerful tools in understanding bifurcation phenomena in hydrodynamic systems (Brandstäter et al. 1983). One of the quantitative measures of the degree of randomness of a fluid flow is the largest Lyapunov exponent (*LLE*), which defines the average rate of an exponential separation of two neighbouring trajectories:

$$LLE = \lim_{t \to \infty} \lim_{\delta(0) \to 0} \frac{1}{t} \log\left(\frac{\delta(t)}{\delta(0)}\right) \qquad (8)$$

where $\delta(t) = \|x_2(t) - x_1(t)\|$ is the Euclidian distance between two trajectories at time t. The *LLE* is the main flow characteristics that determine both the local dynamics and conformations of the polymer molecules (Balkovsky and Fouxon 1999; Balkovsky et al. 2001; Gerashchenko et al. 2005). Thus, the knowledge of the *LLE* together with the knowledge of the single molecule polymer relaxation time τ_r defines the criterion for the coil-stretch transition (Balkovsky and Fouxon 1999; Balkovsky et al. 2001; Gerashchenko et al. 2005): $\lambda \cdot \tau_r = 1$. In most of the previous experimental works, the *LLE* was measured by reconstruction of the phase portrait from measurements of a single point observable. Although from technical point of view this approach might look less demanding than a direct measurement of the particle pair separations, there are few rather sensitive issues that should be carefully addressed: a proper choice of the time delays and the embedding dimension, length and noise level of the data sets. We are aware of only one experimental work that deals with direct measurements of the Lagrangian trajectories and the statistics of pair separations (Boffetta et al. 1999). The main purpose of this Lagrangian frame investigation is to understand the relation between *LLE*s and the relevant Eulerian timescales of the flow: velocity correlation time, inverse velocity gradients and the magnitude of their fluctuations. In experimental and numerical simulations the infinite time limit required by Eq. (8) is unattainable. Besides, due to the finite size of experimental setups, the dispersion of initially closely located particles cannot reach a truly asymptotic regime due to interaction with boundaries. A way to overcome these difficulties is to use the finite time Lyapunov exponents approach (*FTLE*) (Boffetta et al. 2002; Lacorata et al. 2001; Artale et al. 1997; Boffetta et al. 2003), that is to look on the average rate of separation of initially close particles during finite times. This approach is particularly suitable in the case when the characteristic scale of the velocity field, l_u, is comparable with the system size, L, and it has been recently employed in experiments and numerical simulations (Gerashchenko et al. 2005; Boffetta et al. 2002; Artale et al. 1997). The *FTLE* is defined by

$$\gamma(t) = \frac{1}{t} \langle \log \frac{\delta(t)}{\delta(0)} \rangle_e \tag{9}$$

where the ensemble average is taken over all particle pairs initially contained in clusters of radius $\delta(0) \ll l_u$. For sufficiently small initial particle separation, $\delta(0)$, the *FTLE* becomes a rather good estimate of the LLE (Boffetta et al. 2002; Artale et al. 1997).

We conducted our measurements above the elastic instability threshold at ($Wi > 6$) and higher (Groisman and Steinberg 2000; Larson 1992), where the chaotic flow results from the elastic stresses only since inertial contribution is low ($Re < 16$). The velocity field measurements presented in the previous section show that above the onset of the elastic instability, the swirling flow is dominated by a randomly fluctuating large-scale vortex. In contrast to the case of inertial turbulence, where the flow can be considered smooth only below the Kolmogorov scale, the elastic turbulent flow is smooth at all scales, and no analogue of the dissipation scale exists. The large scale of the velocity field, on which energy pumping takes place, is defined by the
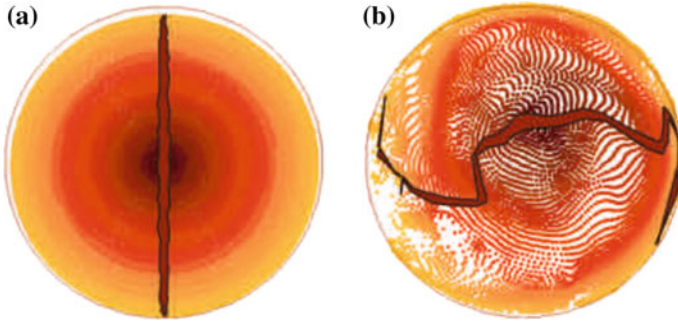
Fig. 38 Numerical tracers at $t = 0$ (**a**) and $t = 1$ s (**b**) for $Wi = 33$. The false colour maps the radial coordinate

elastic instability and is about the system size, i.e. $l_u \approx R_d$. Thus, the flow smoothness over a broad range of scales fully justifies the use of the *FTLE* approach. Numerical Lagrangian trajectories were obtained by integrating in time $\frac{d\overrightarrow{x}}{dt} = \overrightarrow{v}(\overrightarrow{x}, t)$ with a fifth-order adaptive step Runge–Kutta integrator (Shampine and Watts program based on Fehlberg's Runge–Kutta pair of order 4 and 5). Instantaneous velocity at a tracer position was obtained by a trilinear space-time interpolation of the velocity field measured by PIV at regularly gridded space-time points. The time step of the interpolation was 40 ms. Figure 38 shows the initial distribution of the numerical tracers (Fig. 38a) and after 1 s (Fig. 38b).

Statistics of particle pair separations The statistics of particle pair separations was carried out for all the particle pairs initially distributed (uniformly) inside clusters of radius $R = 0.1R_c$ during 0.4 s (this total integration time was smaller than a half turnover time in the whole range of angular velocities). In order to collect statistically sufficient separation data, this procedure was repeated 200 times until the whole velocity field time series has been used. However, a major concern was whether the average length of the numerical trajectories is consistent with that of real particle trajectories. Thus, in order to check the correctness and consistency of our approach, we have alternatively used particle tracking velocimetry (*PTV*) technique to measure the statistics of real particle pair separations. Direct measurements of particle trajectories have shown that the average persistence time of real particles in the observation plane was consistent with the average length of the numerical trajectories. This additional check is fully justified in our case because above the onset of the primary elastic instability, the flow is three-dimensional, and tracking numerical tracers for too long times would be physically meaningless.

As shown in the previous section, the Eulerian correlation time is $\tau_c \approx 1$ s (Fig. 18), which is about 2.5 times larger than the integration time of the numerical trajectories and about 240 times smaller than the total data acquisition time. For each angular velocity investigated, we have defined FTLE by the position of the peak of the probability distribution function (PDF), $P(\gamma, t)$ of the separation rates. In Fig. 39 we show the Cramer rate functions defined by

Fig. 39 Cramer functions of
particle pair separation rates
for 25 different separation
times (ranging from 0.16 to
2.08 s) at $Wi = 34$. The full
line is the parabolic fit
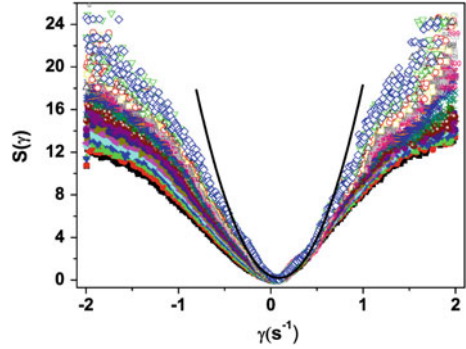
$$S(\gamma) = -\frac{1}{t} \cdot \log(\frac{P(\gamma, t)}{P_{max}}) \tag{10}$$

where P_{max} is the maximum of the PDFs.

The *FTLE*s as function of Wi are shown in Fig. 40. Although the scale dependence
of the mean separation rates plotted in the inset of Fig. 40 does not show the expected
decay corresponding to the mean turnover time (Boffetta et al. 1999), its flatness in
the range of separation times considered is rather encouraging and suggesting that
FTLE approach works rather robustly for our random flow. The *FTLE* dependence
on Wi exhibits a sudden jump corresponding to the first flow reorganisation in the
intermediate regime, followed by a slower increase in the fully developed elastic
turbulent states.

Comparing the values of *FTLE* (Fig. 40) with the Eulerian correlation times
(Fig. 18) one notices that in fully developed random flow the following relation
holds: $\gamma_{av} \cdot \tau_c \approx 0.1$. This discrepancy with the suggestion made in Balkovsky and
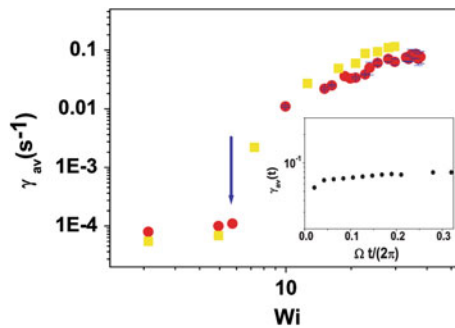
Fig. 40 Finite time Lyapunov exponents defined by the location of the minima of the Cramer rate
functions of the particle pairs separations versus Wi: squares, from PTV approach, circles from PIV-
based approach. The arrow indicates the onset of the primary elastic instability. The inset shows
the dependence of FTLE on the separation time; the horizontal axis is normalised by the period of
rotation of the disc

Fouxon (1999) is probably due to the long-range correlations[3] existing in the flow and to insufficient time statistics (which is one of the limitations of image-based flow investigation techniques, such as PIV and PTV).

Comparison of *FTLE*s with rms of the velocity gradients led to the conclusion that

$$\left(\frac{\partial v_\theta}{\partial r}\right)^{rms} \approx 7 \cdot \gamma_{av} \tag{11}$$

Lagrangian frame flow intermittency The *FTLE*s are the first moments of PDF, and they give no information about the degree of intermittency. Equation (8) defines the average rate of a separation of nearby trajectories but does not provide any information about the fluctuations around this average. In order to characterise the Lagrangian flow intermittency, one has to reconstruct PDF of the particle pair separations by calculating the generalised Lyapunov exponents (*GLE*), which are related to the high-order moments of the statistics of the particle pair separations (Paladin and Vulpiani 1987). The *GLE* of order q is defined by

$$L(q) = \lim_{t \to \infty} \lim_{\delta(0) \to 0} \frac{1}{t} \log(|\frac{\delta(t)}{\delta(0)}|^q) \tag{12}$$

In the infinite time limit, when the Central Limit Theorem is expected to work, it has been shown (Paladin and Vulpiani 1987) that for small values of q:

$$L(q) = \lambda \cdot q + \frac{\mu}{2} \cdot q^2 \tag{13}$$

where the second cumulant is defined as

$$\mu = \lim_{t \to \infty} \lim_{\delta(0) \to 0} \frac{1}{t} [\langle \log |\frac{\delta(t)}{\delta(0)}|^2 \rangle_e - (\lambda \cdot t)^2] \tag{14}$$

In Fig. 41 we show as a *GLE* as a function of the order q of the moments.

According to Paladin and Vulpiani (1987) the onset of intermittent behaviour corresponds to $\frac{\mu}{\gamma_{av}} \approx 1$ that is well above of the value obtained in the experiment. Although the parabolic dependence of the generalised Lyapunov exponents agrees well with theory (Paladin and Vulpiani 1987), the second cumulants obtained from the fit (Fig. 41) display a rather big scatter being plotted versus the angular velocity of the upper plate. This is probably related to the power-law propagation of the instrumental errors in the calculation of $L(q)$. Alternatively, one can characterise the intermittency by measuring the deviation of PDFs from a Gaussian shape (as illustrated in Fig. 39, around γ_{av} the Cramer function shows a parabolic behaviour). Recalling the scaling of the even order moments of the Gaussian PDF with the variance, one should look at the normalised moments:

---

[3]The measurements of the time space cross-correlation function presented in the next section support this point.

Fig. 41 Generalised
Lyapunov exponents as a
function of the order q of the
moments at different Wi:
squares—$Wi = 33$;
triangles—$Wi = 2.82$. The
full line is the parabolic fit,
which gives
$\mu = 0.0167 \pm 0.00005$
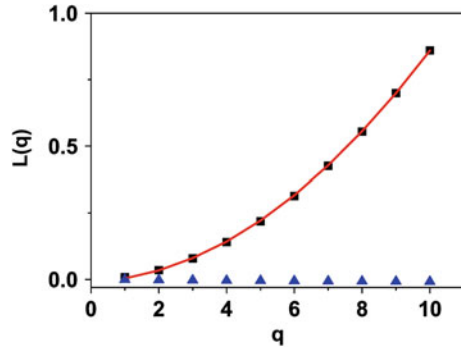
Fig. 42 Normalised (see
text) high-order moments at
different Wi:
squares—$Wi = 1.9$, up
triangles—$Wi = 4.8$,
diamonds—$Wi = 29$,
circles—$Wi = 33.3$,
crosses—$Wi = 38$, right
triangles—$Wi = 56$ and left
triangles—$Wi = 58$. The
inset shows an estimate of
the degree of the flow
intermittency versus Wi
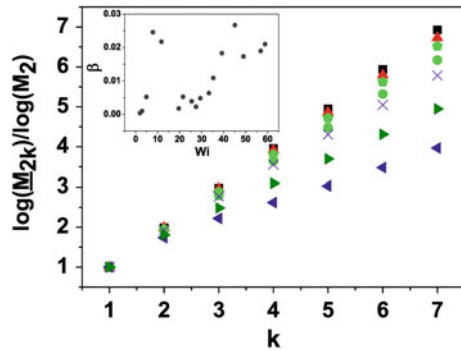
$$\overline{M_{2k}} = M_{2k} \cdot \frac{2^k \cdot k!}{(2k)!} \tag{15}$$

The deviation from the Gaussian shape can be quantified by the parameter defined
as

$$\frac{\log(\overline{M_{2k}})}{\log(M_2)} = k - \beta \cdot k^2 \tag{16}$$

The dependence of the right-hand side of Eq. (16) on the order of the moment is
shown in Fig. 42.

As the angular velocity of the upper plate increases, the flow intermittency exhibits
a sudden jump corresponding to the primary elastic instability followed by a second
discontinuity corresponding to the second flow reorganisation (see inset in Fig. 42).
As one can see from the plot in Fig. 42 at sufficiently large angular velocities the
deviation from a Gaussian linear dependence is rather significant indicating a flow
intermittency.

5 Characterisation of *Elastic Turbulence* in Microscopic Curvilinear Flows

During the past two decades, the microfluidics has emerged as a powerful technique which interests various distinct scientific fields: physics, chemistry and biology. The use of microfluidic devices has few key practical advantages such as the dramatic reduction of the amount of reagents required for fine chemistry and biochemistry (Hansen et al. 2002) applications, well-controlled manipulation and sophisticated experiments on single cells (Li Jeon et al. 2002; Takayama et al. 2001; Mao et al. 2003) and macromolecules (Chou et al. 1999).

From a fluid dynamic standpoint, microscopic flows are generally linear, laminar and steady because for flow channels with sizes of the order of micro-metres the Reynolds number is small. Increasing *Re* sufficiently in order to trigger inertial instabilities typically requires large driving pressure drops which, for most microfluidic devices, are not sustainable. The laminar nature of microscopic flows might be a drawback for a number of practical applications including (but not limited to) efficient mixing, efficient transport of heat and efficient chemical reactions. From this perspective of efficient transport phenomena, the usefulness of microscopic flows of Newtonian fluids is somewhat limited.

Few techniques have been suggested to generate stirring by a three-dimensional flow in order to increase the mixing efficiency in micro-channel flows. They include application of time-dependent external force fields (Oddy et al. 2001; Tsai and Lin 2002) and increasing *Re* to moderately high values in curvilinear three-dimensional channels (Therriault et al. 2003; Vijayendran et al. 2003). An ingenious solution to generate chaotic advection in a microscopic flow was suggested by Stroock et al. (2002). It involves a special 'herringbone' patterning of a micro-channel wall which enhances a secondary flow normal to the mean flow direction. The continuous stretching and folding of the fluid elements (as they advance downstream) results in exponential separation of initially close fluid particles and efficient mixing. However, the flow was stationary in laboratory frame.

On the other hand, as demonstrated in Sect. 4, elastic instabilities and Elastic Turbulence may be observed in flows of dilute polymer solutions at arbitrarily small *Re* provided that *Wi* is sufficiently large. This indicates that Elastic Turbulence could be observed in micro-channels and consequently, several practical applications related to efficient transport of mass (mixing), momentum and heat could be envisaged in microscopic flows of dilute polymer solutions. However, we point out that a direct analogy with the behaviour observed in macroscopic channels previously discussed in this chapter is not obvious. If the size of the flow channel is reduced to a microscopic scale, the extension of polymer molecules in the flow may become comparable to the size of the setup. Therefore, the question whether a microscopic flow of a dilute polymer solution can undergo a purely elastic instability and evolve towards random flow states (in a regime of Elastic Turbulence) cannot be answered by a simple analogy with the macroscopic case and needed to be addressed experimentally.
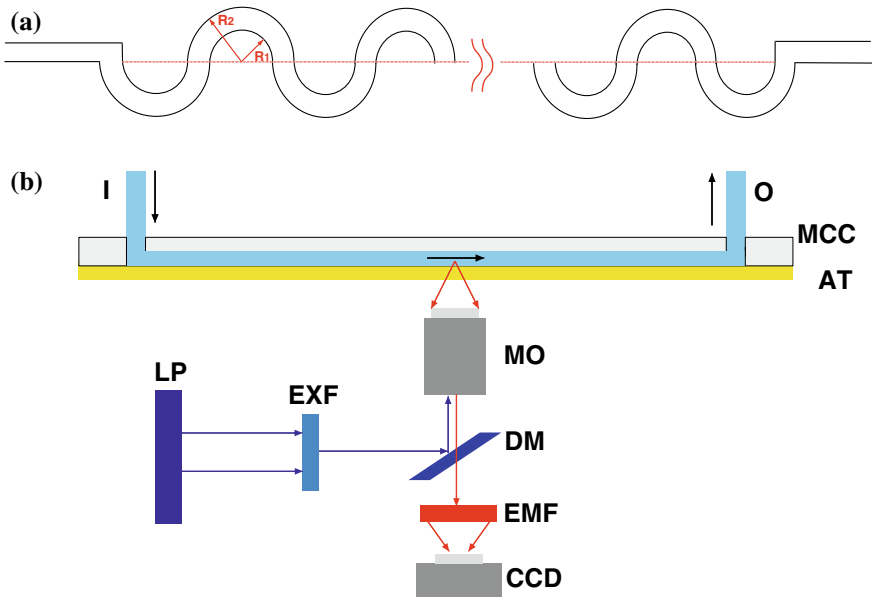
Fig. 43 **a** Schematic view of the serpentine micro-channel. **b** Schematic view of the experimental setup (not in scale): MCC—micro-channel chip, I—micro-channel inlet, O—micro-channel outlet, AT—adhesive tape, MO—microscope objective, DM—dichroic mirror, LP—led, EXF—excitation filter, EMF—emission filter and CCD—digital camera

We dedicate this section to a systematic description of Elastic Turbulence in curvilinear micro-channels.

The experiments have been performed with a serpentine micro-channel schematically illustrated in Fig. 43a. It consists of $N = 200$ smoothly interconnected half circular rings with the inner radius $R_1 = 50 \, \mu m$ and the outer radius $R_2 = 250 \, \mu m$. The width of the micro-channel is $W = R_2 - R_1 = 200 \, \mu m$ and its depth is $H = 200 \, \mu m$. The geometric aspect ratio relevant to the onset of the primary elastic instability (McKinley et al. 1996; Zilz et al. 2012) is $\alpha = R_1 / W = 0.25$.

The spatial and temporal features of the flow fields have been investigated by means of a digital particle image velocimetry technique implemented in house. Particularly important here were both the spatial resolution of the velocity fields ($1.5 \, \mu m$) and the total data acquisition time, $T_{total} = 1200$ s. This value is roughly 300 times larger than the largest relaxation time of the polymer molecules, $\lambda \approx 4$ s.

5.1   Onset and Development of Elastic Turbulence in Micro-channel, Flow Structure

A visual assessment of the hydrodynamic stability of the flow is illustrated in Fig. 44 by means of the streak imaging technique. Whereas a laminar flow is observed for low values of the driving pressure $\Delta p = 63$ Pa (Fig. 44a), a strongly irregular fluid motion is observed corresponding to $\Delta p = 2.3$ kPa (Fig. 44b). At this driving pressure, a major reorganisation of the flow is apparent in the form of a large-scale non-stationary spiral vortex in agreement with the observation performed by means of laser scanning confocal microscopy reported in Burghelea (2005).

Measurements of the dependence of the time-averaged tangential velocity component measured at the centre line of the channel ($\xi = 0$) on the driving pressure (global Weissenberg numbers) are presented in Fig. 45. The average was performed over 1200 s (a time roughly 320 times longer than the average relaxation time of the polymer $\bar{\lambda}$) which guarantees that the flow field information is statistically sufficient.

The dependence of time-averaged tangential flow component $\langle U_\theta \rangle_t$ on the Weissenberg number remains roughly linear up to a critical value $Wi_c \approx 4$. Beyond this value, the dependence becomes sub-linear indicating a significant reorganisation of the flow associated to an elastic flow instability. This is a signature of flow resistance phenomenologically similar to that observed in a von Karman swirling flow. It is noteworthy that the transition to Elastic Turbulence is smooth and, within the instrumental accuracy of the measurements, reversible upon increasing/decreasing pressure drops (the full/empty symbols in Fig. 45). The value of the critical Weissenberg number is comparable to the values reported in the literature (Burghelea 2005; Burghelea et al. 2004a, b). However, a significantly larger discrepancy is found with the onset value given in a recent paper (Jun and Steinberg 2011), $Wi_c \approx 200$. This difference cannot be explained by the different aspect ratios of the channel ($R_1/W = 1$) using the Pakdel–McKinley scaling (McKinley et al. 1996; Zilz et al. 2012). As they have used a similar polymer solution, the reasons for this discrepancy remain elusive.
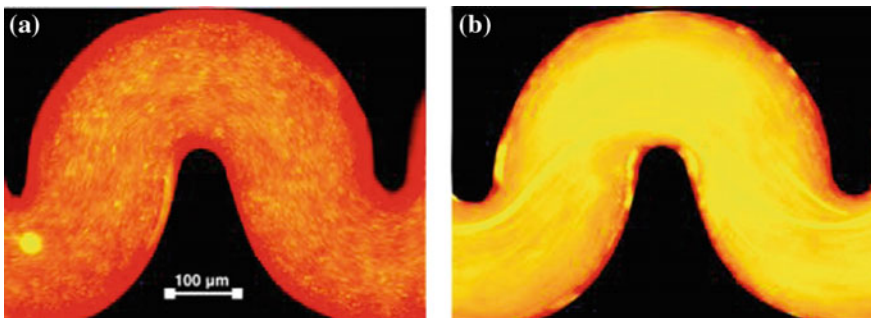
Fig. 44 Epifluorescent flow micrographs acquired at **a** $\Delta p = 63$ Pa ($Wi = 0.36$—laminar regime); **b** $\Delta p = 2.3$ kPa ($Wi = 18$—elastic turbulent regime). A $X10$ magnification objective was used

Fig. 45 Dependence of the
time-averaged tangential
velocity component on the
driving pressure (bottom
horizontal axis) and on the
integral Weissenberg number
(top horizontal axis). The
full/empty symbols refer to
the increasing/decreasing
branches of the pressure
ramp. The shaded regions
highlight the level of
fluctuations. The full line is a
linear fit
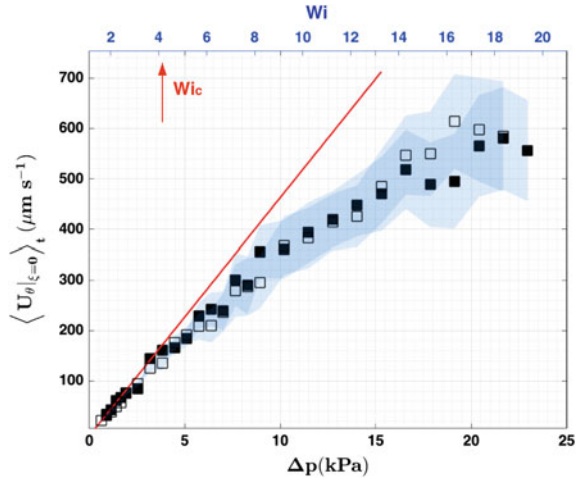
To get further insights into the evolution of the flow structure as the global Weissenberg number is increased we focus on the time-averaged transversal profiles of each velocity component (Fig. 46).

At low driving pressures corresponding to the laminar flow regime, the profile of the tangential velocity component $\langle U_\theta \rangle_t$ is non-symmetric (the circles in Fig. 46a). Due to the curvilinear geometry of the micro-channel, a non-zero time-averaged radial component $\langle U_r \rangle_t$ is measured even in a laminar state (Fig. 46b). An increase of the Weissenberg number past the onset of the primary elastic instability Wi_c results in a significant reorganisation of the flow: the transversal profiles of the tangential
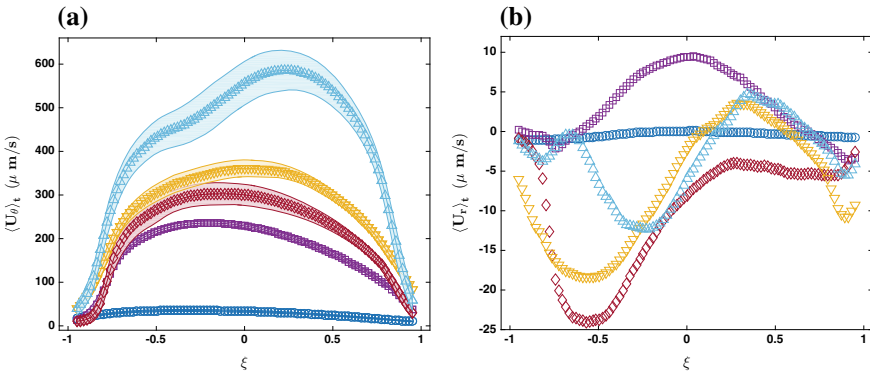
Fig. 46 Time-averaged transversal profiles of the tangential velocity component (**a**) and of the radial velocity component (**b**). The symbols in panel refer to the driving pressures (global Weissenberg number): ○—$\Delta p = 0.9$ kPa ($Wi = 1.1$), □—$\Delta p = 5.7$ kPa ($Wi = 7.4$), ◇—$\Delta p = 7.6$ kPa ($Wi = 9.5$), ▽—$\Delta p = 10.2$ kPa ($Wi = 11.3$) and △—$\Delta p = 23$ kPa ($Wi = 18.3$). The shaded regions in panel b indicate the level of fluctuations of the velocity around its mean
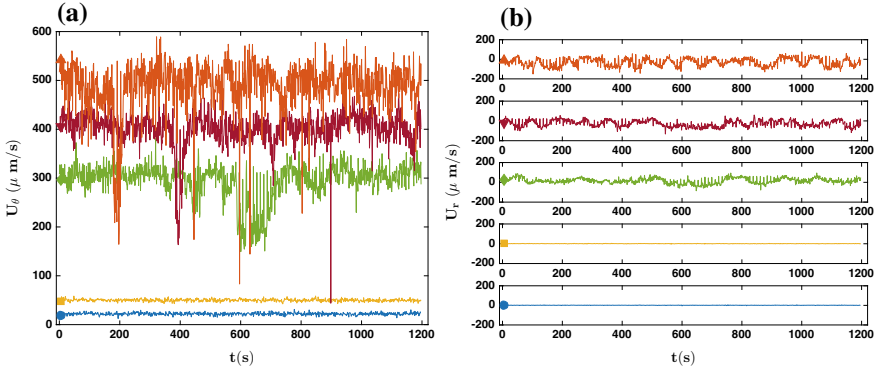
Fig. 47 Time series of the tangential (**a**) and the radial velocity component (**b**) measured at the midpoint of the channel ($\xi = 0$) at half depth. The symbols in panel refer to the driving pressure (Weissenberg number): ●—$\Delta p = 0.9$ kPa ($Wi = 1.1$), ■—$\Delta p = 5.7$ kPa ($Wi = 7.36$), ♦—$\Delta p = 7.6$ kPa ($Wi = 9.5$), ▼—$\Delta p = 10.2$ kPa ($Wi = 11.3$) and ▲—$\Delta p = 23$ kPa ($Wi = 18.3$) (Colour figure online)

velocity component become more symmetric and a strong inward radial motion is observed. The flow structure illustrated in Fig. 46 is qualitatively consistent with that observed by the particle tracking velocimetry measurements presented in Burghelea (2005). The time series of both the tangential and the radial components of the flow velocity measured at the centre line of the curvilinear micro-channel ($\xi = 0$) are presented in Fig. 47. Within a laminar regime (the time series labelled by a circle and square, respectively), the fluctuations visible in the time series of each velocity component are solely related to the instrumental error of the micro-DPIV technique. As the Weissenberg number is increased, the velocity time series exhibit a chaotic like behaviour which reproduces the early measurements reported in Burghelea et al. (2004a) and Burghelea (2005). As the measurements illustrated in Fig. 47a and b are performed over a total time 12 times larger than the acquisition time in Burghelea et al. (2004a) and Burghelea (2005) we are now able to observe a new dynamical flow feature in the form of rare '*crash*' events manifested by a significant slowing down of the flow (see the series labelled by a diamond and a down triangle in Fig. 47a). These rare events emerge right above the onset of the primary elastic instability and the frequency of their appearance increases with increasing control parameter.

A closer look into the emergence of rare events near the onset of the Elastic Turbulence is presented in Fig. 48 by monitoring instantaneous flow fields (the bottom line) before, during and after the emergence of a rare event. One can note that a rare event is associated to a dramatic reorganisation of the flow which persists for times significantly larger than the average polymer relaxation time, $\Delta T \approx 250$ s. The emergence of rare events has been previously observed during experiments performed on a macroscopic von Karman swirling flow between two discs of a dilute polymer solution (Burghelea et al. 2007). In contrast to the observation illustrated in Fig. 48, in a von Karman flow the rare events are manifested through a local flow acceleration
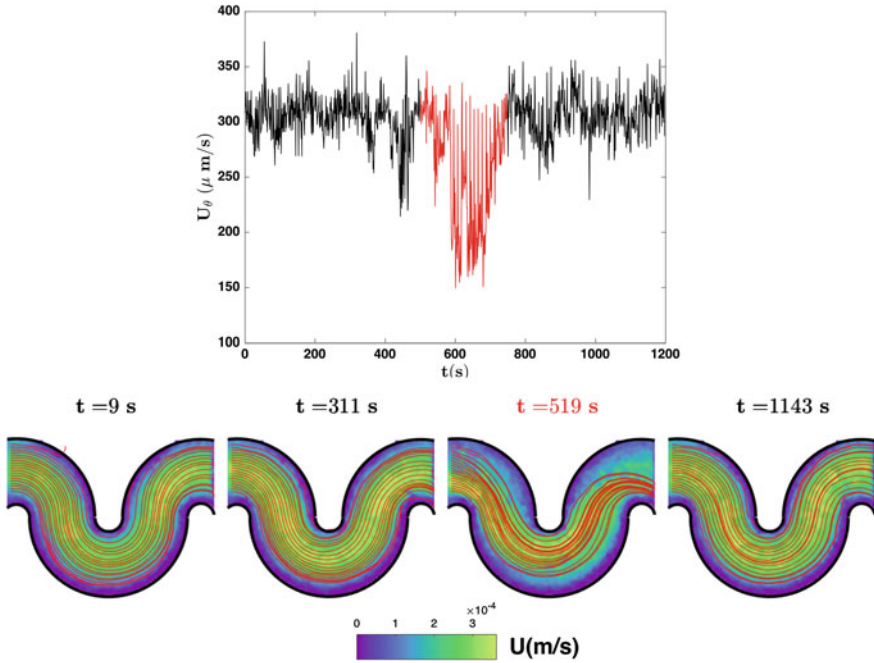
Fig. 48 Top: Time series of the tangential velocity component acquired at $Wi = 9.5$. The bottom plots illustrate maps of the velocity modulus at several time instants indicated on the top. The full lines in each bottom panel are streamlines

rather than a deceleration, see Figs. 20a and 21a in Burghelea et al. (2007). The difference may originate in the different topologies of the mean flow.

5.2 On the Nature of the Bifurcation Towards Elastic Turbulence

A next important point relates to the nature of the bifurcation towards elastic turbulent states. To address this point, we focus on the dependence of the rms of fluctuations of each velocity component measured at the centre line of the micro-channel on the Weissenberg number (Fig. 49). A strong increase of the level of fluctuations of both the tangential velocity component (Fig. 49a) and the radial velocity component (Fig. 49b) accounting for up to 35% of the mean flow speed is observed.

As already noted for the Weissenberg dependence of the time-averaged tangential velocity component presented in Fig. 45, the transition is smooth and, within the level of scatter of the data, reversible upon increasing/decreasing Wi. Moreover, the data
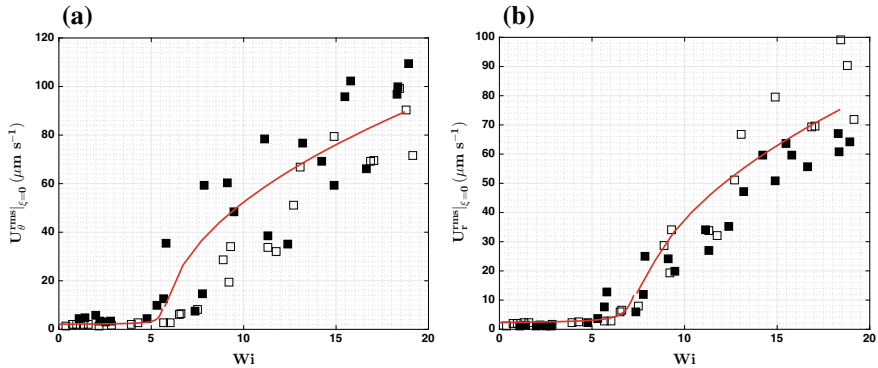
Fig. 49 Dependence of the rms of fluctuations of the tangential velocity component (**a**) and of the radial velocity component (**b**) measured at the midpoint of the channel ($\xi = 0$) on the global Weissenberg number Wi. The full/empty symbols refer to the increasing/decreasing driving pressures. The full line in each panel is a fit by the stationary Ginzburg–Landau equation (see text for description)

can be fitted by the stationary Landau–Ginzburg equation with a field (the full lines in Fig. 49a and b):

$$\epsilon U_i^{rms} - a \left(U_i^{rms} \right)^3 + h = 0 \quad i = r, \theta \tag{17}$$

where $\epsilon = Wi/Wi_c - 1$ is the reduced control parameter and a and h are fitting parameters. One can conclude that the transition to Elastic Turbulence in a curvilinear micro-flow occurs via a supercritical bifurcation. This result is interesting in itself, somewhat unexpected and it deserves being discussed. In a Taylor–Couette geometry, the elastic instability is experimentally found to emerge via a subcritical bifurcation (Groisman and Steinberg 1998) in agreement with the theoretical prediction (Sureshkumar et al. 1994). A systematic and pedagogical description of the subcritical elastic instability in parallel shear flows of viscoelastic fluids is presented in Morozov and van Saarloos (2007). The early investigation of the transition to Elastic Turbulence in a von Karman swirling flow between discs suggested a similar subcritical bifurcation in the form of a hysteresis of the time-averaged injected power, calculated as the product between the angular speed of the top disc and the torque that drives it (Burghelea et al. 2006, 2007; Burghelea 2005). However, more recent measurements of the injected power into a von Karman swirling flow averaged over significantly longer times reported by Traore et al. (2015) revealed a smooth and reversible transition consistent with a supercritical bifurcation, see Fig. 4 therein. To conclude this part, the nature of the transition to Elastic Turbulence remains elusive and future theoretical and numerical studies are needed to clarify this point.

5.3 Statistics and Spatial Distribution of the Velocity Gradients; Analysis of Boundary Layers

As pointed out in Sect. 8, the key physical quantities that need to be measured in order to verify the predictions of the theory of Elastic Turbulence are the time-averaged fields of the velocity gradients and their level of fluctuation. Particularly, the production of the elastic stresses that destabilise the flow is directly related to the magnitude of the velocity gradients and the level of their fluctuations and one of the key ingredients of the theory of Elastic Turbulence relates to the saturation of the rms of fluctuations of the velocity gradients due to a strong back reaction of the polymers to the flow. This motivates us to take advantage of the excellent temporal and spatial resolution of the DPIV method to provide a full description of the spatial distribution of the velocity gradients and the long time statistics of their fluctuations.

The spatial distributions of the time-averaged second invariant of the rate of strain $\left\langle \underline{\underline{\dot{\gamma}}} \right\rangle_t$ measured for three distinct Weissenberg numbers are presented in Fig. 50. One can note that the spatial distribution of the second invariant of the rate of strain is strongly in-homogenous and exhibits pronounced local maxima of unequal magnitude (except for the highest Wi illustrated in panel (d)) distributed at a constant distance from the inner and outer boundaries of the channel (Fig. 50a). As the extension of the linear polymer chains is controlled by the local velocity gradients, we attribute the observation of the local maxima of the velocity gradients to the formation of inner and outer boundary layers of the elastic stresses.

The primary elastic instability is accompanied by a sharp increase of the velocity gradients particularly in the vicinity of the inner boundary of the channel (Fig. 50b). The lack of symmetry of the spatial distribution of the velocity gradients with respect to the centre line of the micro-channel indicates a strongly inhomogeneous distribution of elastic stresses along the transversal flow direction. Within a fully developed elastic turbulent regime, the symmetry of the distribution of the elastic stresses with respect to the centre line of the channel is restored. A more systematic investigation of the transversal distribution of the time-averaged velocity gradients and of their fluctuations as a function of the global Weissenberg number is presented in Fig. 51.

The emergence of a boundary layer of the elastic stresses when the global Weissenberg number is increased is clearly visible in Fig. 51a. As already noted in Fig. 50, as one advances within the regime of fully developed Elastic Turbulence, the two local maxima of the profiles of the time-averaged gradients tend to be become equal in magnitude. Corresponding to the edge of the boundary layers, local maxima are also observed in the transversal distributions of the rms of fluctuations of the second invariant of the rate of deformation tensor (Fig. 51b).

The evolution of the width of the inner and outer boundary layers determined by the location of the peaks of the spatial distribution of the time-averaged second invariant of the rate of strain tensor (Fig. 51a) with the global Weissenberg number is presented in Fig. 52. The width of the inner boundary layer (the squares) is systematically larger than the width of the outer boundary layer (the circles) up to a Weissenberg number
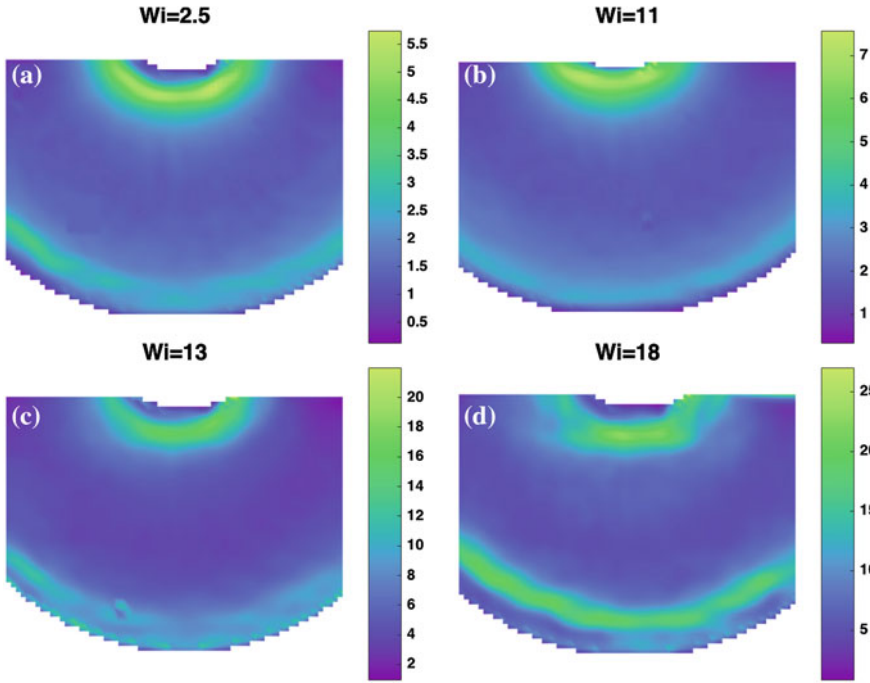
Fig. 50 Spatial distribution of the time-averaged second invariant of the rate of strain measured at different Weissenberg numbers indicated in the top inserts. The units of the colour bars are s^{-1}
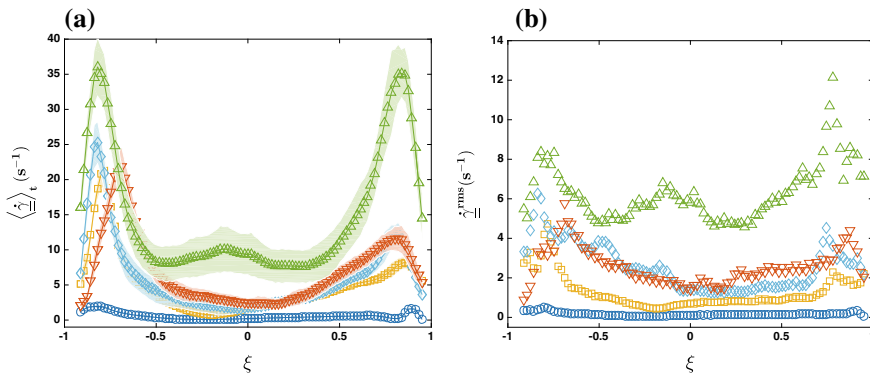
Fig. 51 Transversal profile of the time-averaged second invariant of the rate of deformation (**a**) and of the rms of fluctuations of the second invariant (**b**) measured at various driving pressures (global Weissenberg numbers): ○—$\Delta p = 0.9$ kPa ($Wi = 1.1$), □—$\Delta p = 5.7$ kPa ($Wi = 7.3$),◇—$\Delta p = 7.6$ kPa ($Wi = 9.5$), ▽—$\Delta p = 10.2$ kPa ($Wi = 11.3$) and △—$\Delta p = 23$ kPa ($Wi = 18.3$). The shaded regions in panel a indicate the level of fluctuations around the mean value (Colour figure online)

Fig. 52 Dependence of the reduced width of the inner boundary layer ($\square$, $\blacksquare$) and of the outer boundary layer ($\bullet$, $\circ$) on the global Weissenberg number. The full/empty symbols refer to increasing/decreasing global Weissenberg numbers, respectively (Colour figure online)
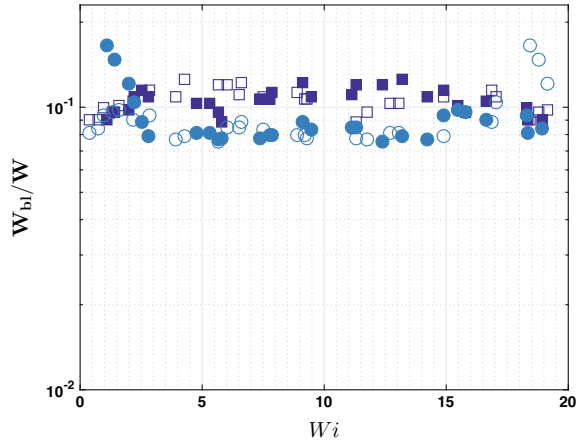
$Wi \approx 15$ corresponding to the fully developed elastic turbulent regime when the two boundary layers become practically identical.

We note that within a regime of Elastic Turbulence, the width of the inner and outer boundary layers is $W_{bl}/W \approx 0.1$ and independent on the global Weissenberg number. This result is consistent with the measurements presented by Jun and Steinberg (2011) and with earlier measurements performed in a macroscopic von Karman swirling flow (Burghelea et al. 2007; Burghelea 2005).

The evolution of the time-averaged velocity gradients and of the local Weissenberg number defined as $Wi_{loc} = \bar{\lambda}\dot{\bar{\gamma}}^{rms}$ measured at the edge of the inner/outer boundary layers (corresponding to the local maxima in Fig. 51a and b) and in the bulk of the flow (averaged around the centre line of the micro-channel) with the global Weissenberg number is presented in Fig. 53.

The primary elastic instability is accompanied by a sharp increase of both the time-averaged velocity gradients (panel Fig. 53a) and of the local Weissenberg number (panel Fig. 53b). For $Wi \leq 17$ the time-averaged velocity gradients measured at the edge of the inner boundary layer are systematically larger than those measured at the edge of the outer boundary layer (Fig. 53a). The local Weissenberg number measured at the edge of the inner boundary layer is systematically larger than the one measured at the centre line of the flow (Fig. 53b). Within a fully developed elastic turbulent regime, the local Weissenberg number measured at the edge of the boundary layers increases linearly with the global Weissenberg number $Wi_{loc}^{bl} = -25.58 + 3.54Wi$ (the dashed line in Fig. 53b). On the other hand, a linear fit of the local Weissenberg number measured in the bulk of the flow gives $Wi_{loc}^{bulk} = 15.21 + 0.12Wi$ (the full line in Fig. 53b). Thus, one can conclude that in a fully developed Elastic Turbulence regime Wi_{loc} saturates in the bulk of the flow but keeps increasing at the edge of the boundary layers. The result is in a qualitative agreement with the theoretical prediction for the Elastic Turbulence (Fouxon and Lebedev 2003; Balkovsky et al. 2001). Corresponding to the bulk measurements one
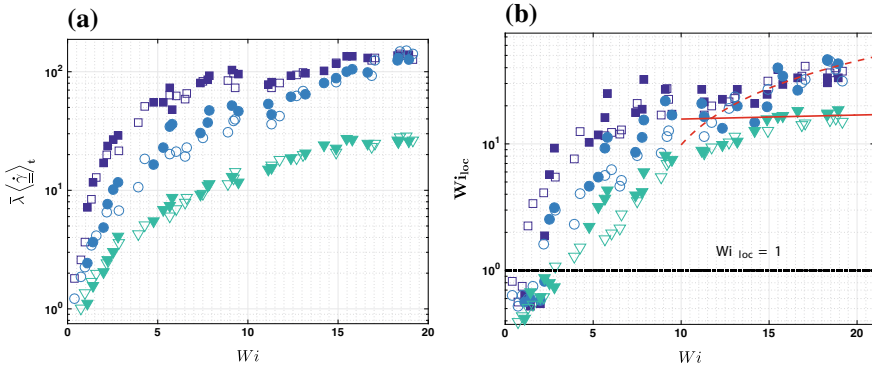
Fig. 53 **a** Dependence of the time-averaged second invariant of rate of deformation on the global Weissenberg number. **b** Dependence of the local Weissenberg number Wi_{loc} on the global Weissenberg number. The full and dashed lines are linear fit functions (see text for description). In both panels, the symbols refer to different radial locations ξ of the measurements: ($\square$, $\blacksquare$)—the edge of the inner boundary layer, ($\bullet$, $\circ$)—the edge of the outer boundary layer, ($\blacktriangledown$ *and* $\triangledown$)—average in the bulk of the flow within the range $\xi \in [-0.4, 0.4]$. In both panels, the full/empty symbols refer to increasing/decreasing global Weissenberg numbers, respectively (Colour figure online)

obtains $Wi_{loc}^{bulk} \approx 15.5$ which is significantly larger than the unitary value predicted theoretically indicating that no quantitative agreement with the theory is found. A similar conclusion has been reached for the case of an elastic turbulent flow in a macroscopic von Karman swirling flow configuration (Burghelea et al. 2006, 2007; Burghelea 2005). The local Weissenberg number was defined in these references as $Wi_{loc} = \omega^{rms} \lambda$ (here ω stands for the vorticity) saturates at the value $Wi_{loc} \approx 2$ (Fig. 19b in Burghelea et al. 2007, and inset of Fig. 2 in Burghelea et al. 2006) which is twice larger than the value predicted by the theory. We conclude that the main assumption of the theory of Elastic Turbulence concerning with the saturation of the velocity gradients is verified only qualitatively. Quantitatively, the experiments revealed a systematic discrepancy which is more pronounced in a microscopic flow than a macroscopic one. This aspect may originate in the strong spatial confinement of the microscopic flow and needs to be addressed by further theoretical development.

The result on the saturation of the local Weissenberg number in the bulk of the flow is at odds with recent measurements (Jun and Steinberg 2011), which indicate a linear increase of Wi_{loc} with Wi rather than a saturation.

Finally, we note that the measurements of the time-averaged velocity gradients and of the rms of their fluctuations are reproducible upon increasing/decreasing Wi proving once more the reversibility of the bifurcation towards Elastic Turbulence (the full/empty symbols in Fig. 53) in a curvilinear micro-channel flow in full agreement with the behaviour observed in Figs. 45 and 49.

6 Efficient Microscopic Mixing by *Elastic Turbulence*

A main consequence of the laminar character of microscopic flows is the inefficient mass transfer across the main flow direction which occurs mainly due to molecular diffusion. Mixing of viscous fluids by diffusion is slow comparative to the mixing that occurs in a random flow. Even for a moderate size protein, such as bovine serum albumin (with a diffusion coefficient $D \approx 3 \times 10^{-7} \, \text{cm}^2/\text{s}$ in water), the diffusion time d^2/D across a micro-channel with a width of $100 \, \mu\text{m}$ is of the order of 100 s.

Groisman and Steinberg have that a macroscopic curvilinear flow (in serpentine channel with the width of 3 mm) of a viscoelastic fluid (a polyacrylamide–sucrose mixture similar to the one used in Sect. 5) can lead to very efficient mixing in a regime of Elastic Turbulence (Groisman and Steinberg 2001). In Sect. 5 we have shown that Elastic Turbulence can be triggered in a serpentine micro-channel similar in shape to the macroscopic channel used by Groisman and Steinberg (2001).

We study in the following the mixing of two viscoelastic in a curvilinear micro-channel geometrically similar with the one used in Sect. 5 (Fig. 54).

The mixing experiments have been conducted by evenly injecting two streams of dilute polymer solution one of which contained also a small amount of fluorescent dye (Fig. 57a). The mixing efficiency is studied at different locations downstream (or versus time, if one assumes that Taylor hypothesis is valid for this flow[4]) by monitoring the brightness of the passive scalar field. A critical requirement during the experiments was to visualise the mixing patterns in a narrow horizontal plane, in order to avoid space averaging which could lead to wrong conclusions on the mixing efficiency.

This is achieved by imaging the passive scalar fields through a Confocal Scanning System (Fluoview FV500 by Olympus), an example of which is displayed in Fig. 55. It was equipped with a $40X$, $NA = 0.85$ infinity-corrected objective and a 12-bit photomultiplier. The scanning was done at a rate of 56 lines per second and 512 pixels per line corresponding to a step of $0.18 \, \mu\text{m}$ per pixel.

Prior to discussing the decay regime of mixing in a random microscopic flow, we illustrate the chaotic flow structure as revealed by confocal scanning microscopy (Fig. 56).

As already discussed in detail in Sect. 5, the flow is dominated by a large-scale vortex evolving randomly in time.

6.1 Decay Regime of Mixing in a Random Micro-Flow

Mixing of a low diffusivity passive tracer by a turbulent flow particularly in a region of small scales, attracted recently significant attention from both theory (Shraiman

---

[4]A detailed discussion of the validity of the Taylor Hypothesis in a similar flow was presented in Sect. 1.5.
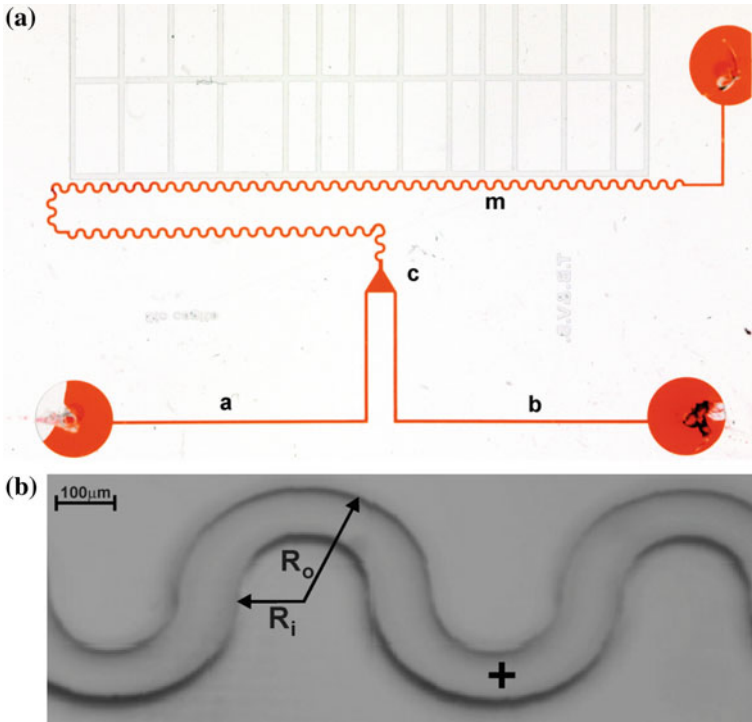
Fig. 54 **a** Photograph of the microfluidic device. The micro-channel was filled with ink for better contrast. **b** Photograph of a section of the functional curvilinear element. The point where instantaneous flow velocity measurements (averaged over a $20 \times 20\,\mu$m square region) were made is marked by a cross. The figure is reproduced from Burghelea (2005)

and Siggia 1994; Chertkov et al. 1995; Shraiman and Siggia 2000; Falkovich et al. 2001; Son 1999) and experiment (Jullien et al. 2000; Groisman and Steinberg 2001).

This so-called Batchelor regime of mixing exists in a viscous-convective range of wave numbers, $k_K < k < k_B$, where the random-in-time velocity field can be treated as smooth. Here $k_K = (\epsilon/\nu^3)^{1/4}$ is the Kolmogorov dissipation scale, $k_B = (\epsilon/\nu D^2)^{1/4}$ is the Batchelor wave number, ν and D are the kinematic viscosity and the diffusion constant, respectively, and ϵ is the rate of energy dissipation (Batchelor 1959). The inverse injection scale should be used here instead of k_K, if the former is larger than k_K. The range of the Batchelor regime is defined by the value of the Schmidt number $Sc = \nu/D$, which can be rather large for a viscous fluid with a low diffusivity tracer. The smoothness of the velocity field for developed turbulence below the Kolmogorov scale is explained by an exponential decay of the velocity spectrum there. The Batchelor–Kraichnan approach (Batchelor 1959; Kraichnan 1968) can be extended to an algebraic type velocity spectrum $\propto k^{-\delta}$ with $\delta > 3$. Then fluctuation spectrum of the velocity gradients scale as $k^{-\delta+2}$, so that the flow becomes increasingly homogeneous on small scales, and the mixing occurs mainly
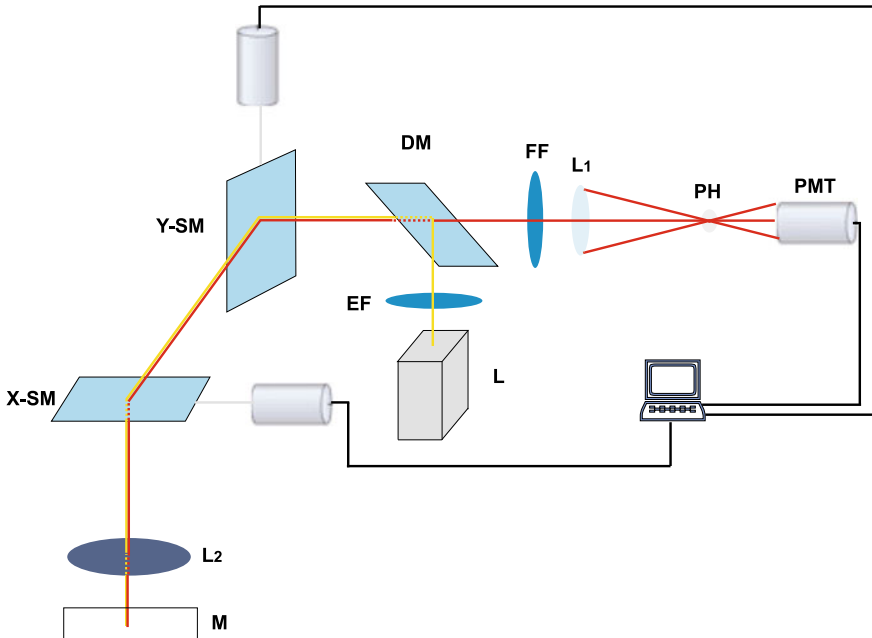
Fig. 55 Confocal scanning system: **PMT**—photomultiplier, **PH**—pin hole, **L1**—focusing lens, **FF**—fluorescence filter, **DM**—dichroic mirror, **EF**—excitation light selection filter, **L**—laser, **Y-SM**—Y direction scanning mirror, **X-SM**—X direction scanning mirror, **L2**—objective lens and **M**—micro-channel. The figure is reproduced from Burghelea (2005)
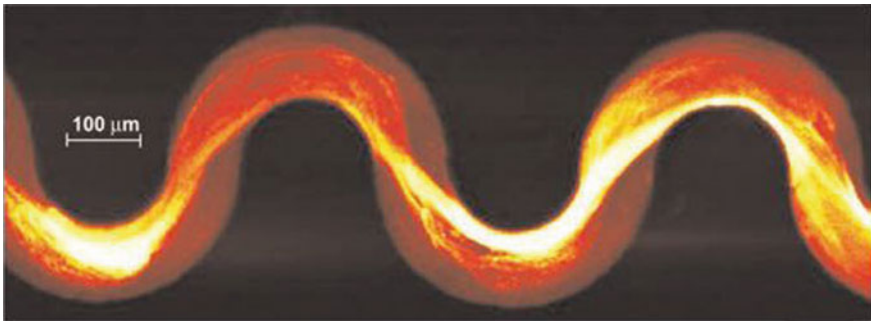
Fig. 56 Middle plane horizontal confocal snapshot. The flow is seeded with $0.2\,\mu m$ fluorescent spheres. The driving pressure is 120 Pa per channel segment. The data are replotted from Burghelea (2005)

due to eddies corresponding to the border of the velocity smoothness. Batchelor and Kraichnan (Batchelor 1959; Kraichnan 1968) considered a stationary regime of turbulent mixing with a tracer continuously injected into a turbulent flow on a large scale. Then the mixing is produced by stretching and folding of a tracer blob by

the random velocity field creating components of higher and higher wave numbers up to k_B. A more recent theory of the passive scalar decay in the Batchelor regime of mixing, which is more relevant to a real experiment, makes predictions about the statistics of the passive scalar (Son 1999).

Various theoretical predictions for the stationary and decay cases of the Batchelor regime of mixing were verified recently in macro-systems (Jullien et al. 2000; Groisman and Steinberg 2001). However, the theories mentioned (Batchelor 1959; Chertkov et al. 1995; Son 1999) consider an unbounded case only. As shown by Chertkov and Lebedev (2003), a non-uniform velocity distribution particularly close to a wall can alter significantly the efficiency of mixing in the decay regime due to turbulent advection. Indeed, due to a reduced velocity near the wall, the boundary layer becomes a sink for the passive tracer. This excess of the tracer is intermittently injected from the boundary layer into the bulk. Thus, the tracer decay, e.g. along a channel, is controlled by the rate of tracer injection from the boundary layer that caused a significant slow down of the decay compared with an unbounded case. As a result, the scaling of the mixing length with the Péclet number, $Pe = V_{av}d/D$, changes from logarithmic one to an algebraic, $L_{mix} \propto Pe^{1/4}$. Here Pe defines the relative rate of advection versus diffusive transport in a flow, V_{av} is the average longitudinal velocity, and d is the channel width. Besides, the boundary layer width for mixing in the decay regime in scales as $W \propto Pe^{-1/4}$.

As demonstrated in Sect. 5, above the onset of the elastic instability the micro-flow is spatially smooth and dominated by a large-scale randomly fluctuating spiral vortex (Fig. 56). The small-scale homogeneity of the micro-flow suggests that the mixing of a passive tracer injected at large scale in the micro-flow should occur mainly due to the large-scale eddies in a Batchelor regime.

6.2 Scaling of the Mixing Length with Pe

The small-scale homogeneity of the micro-flow emphasised in the previous subsection suggests that the mixing of a passive scalar injected at large scales in the flow should occur mainly due to the large-scale eddies in a so-called Batchelor regime of mixing.

Although the Batchelor regime in unbounded systems has been intensively studied theoretically, it has been shown only recently (Chertkov and Lebedev 2003) that the mixing efficiency is significantly altered in bounded systems where the boundary layer becomes a sink for the passive tracers. In order to check the theoretical predictions made in Chertkov and Lebedev (2003), we have varied Pe about 37 times by using fluorescent tracers with different diffusion coefficients and by varying the mean flow velocity. The mixing experiments have been carried out by injecting two streams of polymer solution, one with and one without a fluorescent tracer. The two streams of polymer solution have been injected at equal flow rates by a careful adjustment of the driving pressures (Fig. 57a).

Fig. 57 **a** Epifluorescent microphotograph of the entrance area of a micro-channel. Wide triangular region in front of a curvilinear channel allows to adjust equal flow rates for polymer solutions with (from the top) and without FITCD. **b** Confocal micrograph of the flow in the micro-channel (at N = 30) without polymers added. Left wall of the channel is shown by a dotted line. Confocal images of mixing in a random micro-flow of a dilute polymer solution at different locations downstream: **c** N = 5, **d** N = 11 and **e** N = 17. The data are replotted from Burghelea (2005)
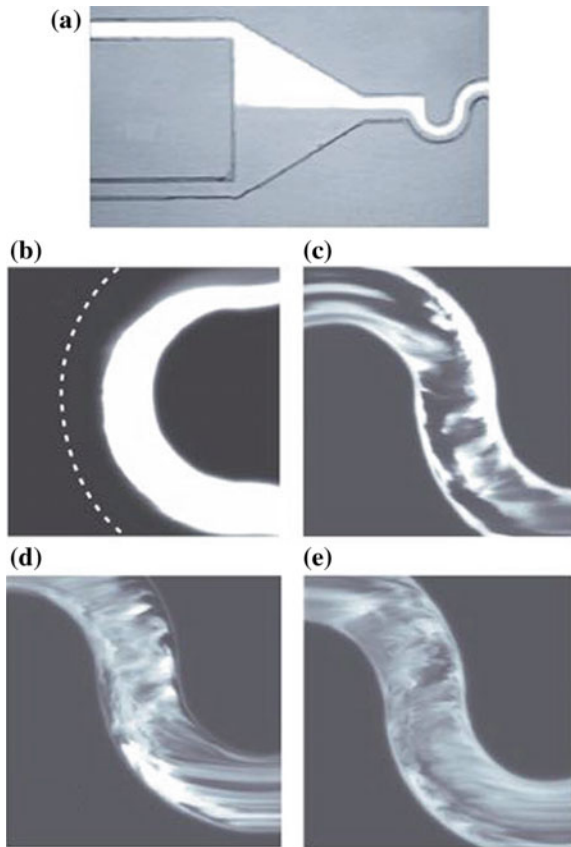
As a passive tracer, we have used dextran molecules labelled with fluorescein isothiocyanate (*FITCD*). The molecular weights of the passive tracers used in different experiments were 10, 70, 500 kDa and 2 MDa. These different choices of tracers together with variations of the mean flow velocity allowed us to modify *Pe* about 37 times in the range $1.6 \times 10^4 \div 4.14 \times 10^5$. As a result, the Batchelor scale, $\eta_B = d \cdot Pe^{-\frac{1}{2}}$, changed from 1×10^{-4} down to 0.15×10^{-4} cm.

First, the setup was tested by running experiments with the plain solvents without PAAm added. The flow appeared laminar and steady in the full range of driving pressures, Δp_s, and the interface between the streams with and without FITCD remained smooth and sharp along the whole channel with only a minor smearing by diffusion (Fig. 57b).

The situation was similar when polymer solutions have been injected in the linear regime corresponding to low values of the driving pressures, Δp_s. However, when the driving pressure was raised above the nonlinear transition threshold, $\Delta p_s^\star = 50$ Pa (which corresponds to $Wi_c \simeq 6.5$), the randomly fluctuating flow velocity produced significant stirring, complex and chaotically changing tracer fields. In Fig. 57c–e,
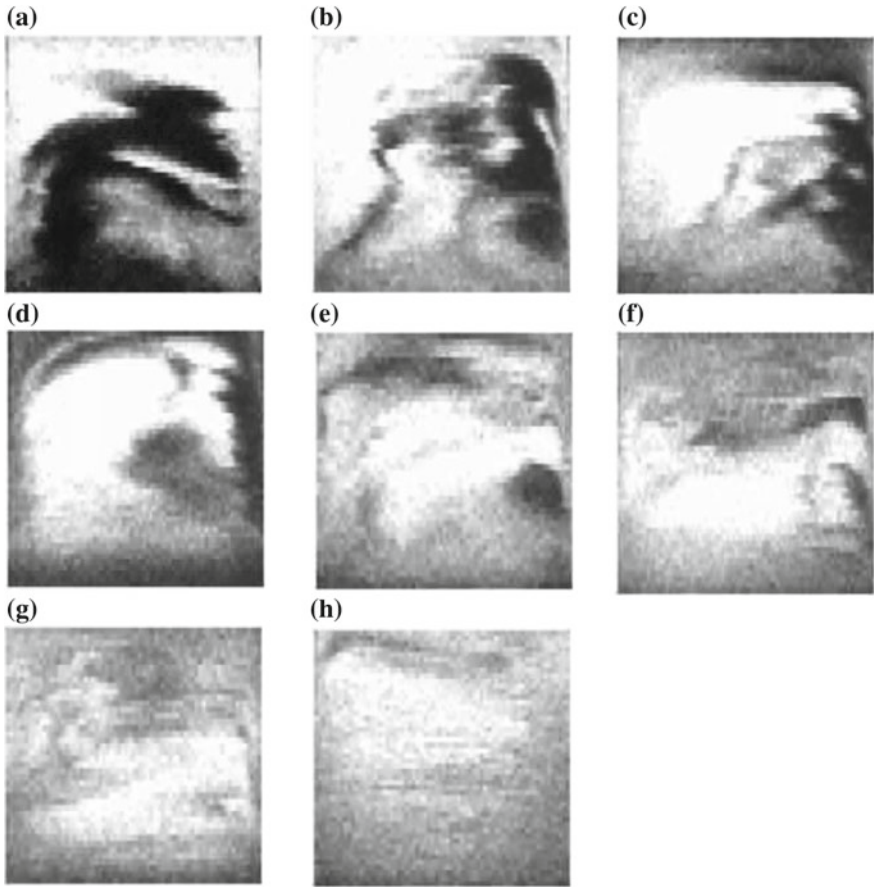
Fig. 58 Distribution of tracer concentration in the vertical cross section of the micro-channel at different locations downstream: **a** N = 5, **b** N = 7, **c** N = 9, **d** N = 11, **e** N = 13, **f** N = 15, **g** N = 17 and **h** N = 25. The data are replotted from Burghelea (2005)

typical scalar fields at different locations downstream are displayed. One can easily see that, as one advances downstream, the scalar field has an increasingly random appearance.

Figure 58 shows the distribution of tracer concentration in the vertical cross section of the micro-channel at different locations downstream. Close to the entrance of the channel (Fig. 58a–c), the mixing is mainly carried out at large scale by a randomly fluctuating vortex. As one advances downstream, the random stretching and folding of fluid elements results in an increasingly efficient mixing at small scales. The confocal scans in a horizontal plane (Fig. 57b–e) were made at a scanning rate of 56 lines per second, contained 750 individual lines and took about 13 s to complete. The vertical scan in Fig. 57b–e was performed with a scanning rate of 24 lines per second, contained 45 lines and took about 1.8 s to complete. The characteristic time of

Fig. 59 Time average of FITCD concentration, $\bar{c}$, as a function of the normalised coordinate across the micro-channel at different locations downstream: red—$N = 7$, green—$N = 11$ and blue—N $= 41$. The data are replotted from Burghelea (2005)
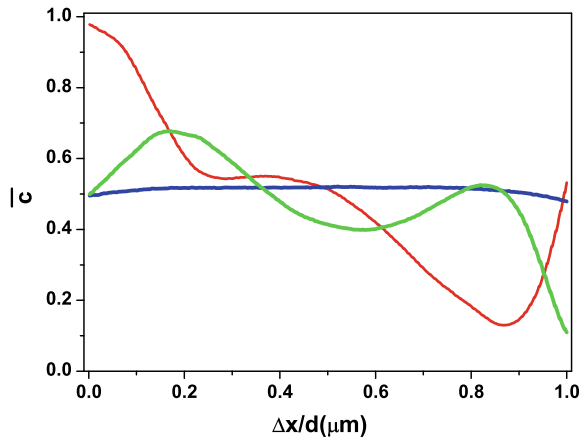
concentration variation was about 2.5 s. Therefore, although individual horizontal lines in Fig. 57b–e and vertical lines in Fig. 58 represent virtually instantaneous passive tracer distributions, the 2D concentration diagrams in Figs. 57b–e and 58 should not be considered as snapshots and are shown only for purpose of illustration. However, none of these diagrams was used for any quantitative measurements.

Corresponding to each value of *Pe* tested, mixing efficiency has been investigated by focusing on the long-time statistics of the concentration distribution across the micro-channel at different positions,*N*, downstream. Typical time-averaged concentration distributions across the micro-channel, $\bar{c}$, are displayed in Fig. 59. One can see that the concentration distribution close to the inlet, at $N = 7$, is strongly influenced by the asymmetric conditions at the channel entrance. As one can learn from the curve corresponding to $N = 11$, however, the imprint of the initial conditions is clearly fading out as the liquid is advancing downstream and the stirring becomes increasingly efficient. Further downstream, at $N = 41$, asymmetry in the tracer distribution introduced by the initial conditions disappears completely.

Fading of the initial condition influence with time and restoration of symmetry in flow in the statistical sense are both distinct features of chaotic and turbulent flows. Therefore, the curves displayed in Fig. 59 provide further evidence for truly chaotic nature of the microscopic flow. Variation of tracer concentration profiles with time at different distances from the inlet is illustrated by the space-time plots displayed in Fig. 60. One can see that the tracer concentration appears to fluctuate quite randomly in time. Next, as one can see in Fig. 60a, which refers to $N = 5$, that the left side of the channel, where the tracer was initially injected, looks much brighter and has a higher average concentration of the tracer. Although also noticeable in Fig. 60b taken further downstream at $N = 18$, this feature is clearly weaker here.

A quantitative measure of the mixing efficiency is given by the *i*th-order moments, M_i, of a probability distribution function (PDF) of FITCD concentration, c, defined by $M_i = \frac{\langle |c - \bar{c}|^i \rangle}{\bar{c}^i}$. Statistics of concentration has been carried out over about 6×10^6 points, that is over 10^4 individual concentration profiles across the micro-channel

Fig. 60 Space-time plots of FITCD distribution across the channel at different locations downstream: **a** N = 5, **b** N = 13, **c** N = 21 and **d** N = 35. Confocal scanning was done along the same line across the channel in the midplane at equal distances from the half-ring interconnections, with even time intervals of 0.0177 s. The data are replotted from Burghelea (2005)
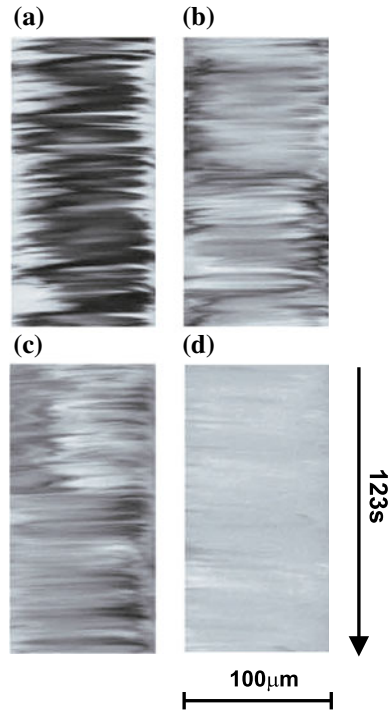
(Fig. 60). In Fig. 61 are presented the dependencies of M_1 and M_2 on the position along channel, N, corresponding to the largest value of Pe we investigated. As shown in Fig. 61, both moments exhibit exponential decay up to $N \simeq 40$ as predicted by theory (Son 1999; Chertkov and Lebedev 2003).
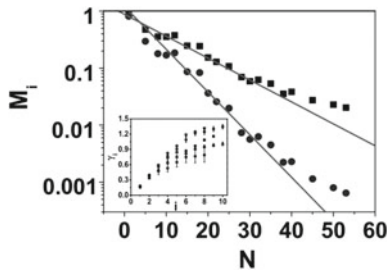
Fig. 61 The first- (squares) and second-order (circles) moments decay versus position, N, at $Pe = 4.15 \times 10^5$; solid lines are the fit. Inset: the decay exponents of the moments, γ_i, as a function of the moment order, i, at different Pe: diamonds, $Pe = 1.6 \times 10^4$; up triangles, $Pe = 3.3 \times 10^4$; squares, $Pe = 9.09 \times 10^4$; circles, $Pe = 1.74 \times 10^5$; down triangles, $Pe = 4.15 \times 10^5$. The data are replotted from Burghelea (2005)

Fig. 62 The mixing length, measured in the number of turns, N_{mix}, versus Pe: squares are the data, the solid line is the fit, and the dotted line shows the logarithmic dependence. The data are replotted from Burghelea (2005)
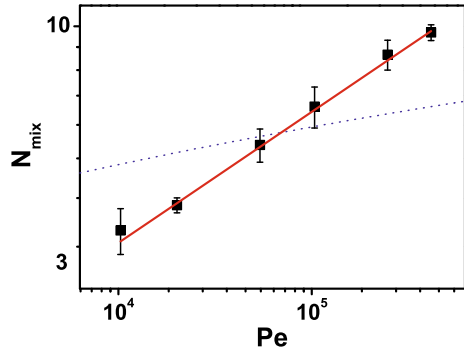
Second, the rate of decay of M_2 is twice as high as that of M_1. And third, M_1 is reduced more than 30 times and reaches the noise level at $N > 40$, as well as M_2. In the inset of Fig. 61 are shown the decay exponents of the higher order moments, γ_i, as a function of their order, i, for each value of Pe. One can notice that the saturation occurs for all curves at about the same value of $i = 6$, but the saturated value of the decay exponents depends on Pe.

The mixing length, measured in the number of units, N_{mix}, and obtained from the exponential rate of decay of M_2, is presented in Fig. 62 as a function of Pe. The data are well fitted by $N_{mix} \propto Pe^{0.26\pm0.01}$, which is in good agreement with theory (Chertkov and Lebedev 2003).

The latter results indicates that the efficiency of the chaotic mixing is reduced due to finite size effects, which increase the mixing length in an bounded system compared to that in an unbounded one.

6.3 Analysis of the Mixing Boundary Layer

In order to establish the source of the algebraic dependence of the mixing length instead of logarithmic, as predicted for an unbounded system, we have studied the Pe dependence of the mixing boundary layer width, W. The latter was identified from the spatial distribution across the micro-channel of the first- and second-order moments of the probability distribution function of FITCD concentration fluctuations (Fig. 63).

We have associated well-defined peaks in a spatial dependence of the moments with the boundary layer edge (note in Fig. 63 the asymmetry in the left and the right peak locations due to the flow asymmetry). The average value of the right peak location for the first moment (averaged along the micro-channel) as a function of Pe is presented in the inset of Fig. 63 together with the fit: $W \propto Pe^{-0.28\pm0.06}$. This result is once more in fair agreement with the theoretical prediction $W \propto Pe^{-\frac{1}{4}}$ (Chertkov and Lebedev 2003).

Fig. 63 Spatial dependence of the first- (blue line) and second-order (black line) moments of FITCD concentration fluctuations across micro-channel. Inset: width of the boundary layer, W, versus Pe. The solid line is the fit. The data are replotted from Burghelea (2005) (Colour figure online)
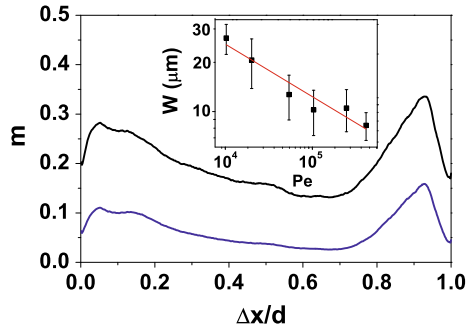
6.4 Spatial and Temporal Correlations of the Passive Scalar Fluctuations

The spatial correlation across the micro-channel and temporal correlation functions of passive scalar concentration fluctuations in the bulk and in the boundary layer were studied at different Pe. The spatial correlation functions decay logarithmically at distances above the diffusion length (which was varied from 1 to 4 µm) and are almost independent on Pe (Fig. 64a). The relatively narrow spatial range of the correlation function decay does not allow one to reliably distinguish between the logarithmic and power-law behaviour, if the exponent is small, as predicted by theory (Chertkov and Lebedev 2003) (the exponent $\sim Pe^{-\frac{1}{4}}$). This logarithmic like decay can be explained by the fact that the mixing in the bulk occurs rather efficiently. The mixing boundary layer permanently supplies the passive scalar into the bulk which mimics the Batchelor stationary regime of mixing (Batchelor 1959) and leads to logarithmic decay.

The temporal correlation functions in the bulk and in the boundary layer (Fig. 64b and c) show similar behaviour with about twice as large correlation time in the boundary layer as in the bulk ($t_{\frac{1}{2}} \approx 13$ s instead of 6 s in the bulk).

7 Macroscopic Heat Transport by *Elastic Turbulence*

The efficient transport of mass and heat within fluids is of paramount importance in many industrial settings such as the development of efficient heat exchangers, cooling the magnetic coils of particle accelerators and the central processing units (CPUs) of personal computers. The natural mechanisms by which the mass and the heat are transported within a fluid are the molecular diffusion and the thermal conduction, respectively. These mechanisms, however, are the least efficient ones in the sense that the characteristic times over which they take place are significantly large. As for the case of mixing discussed in Sect. 6, an increase in the efficiency of the heat transport can be obtained by generating flows with divergent Lagrangian trajectories which are
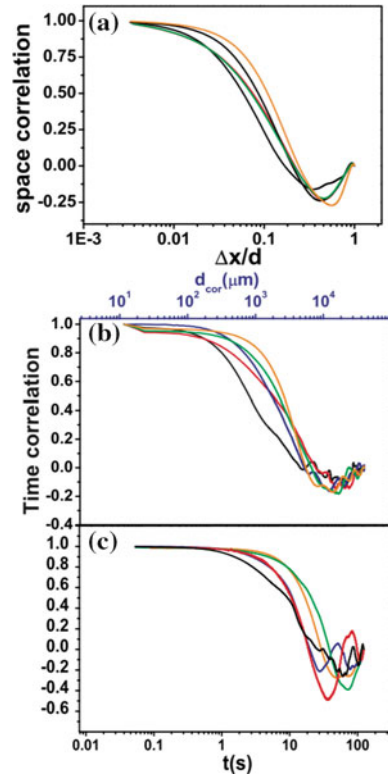
able to efficiently stretch, fold and break up the fluid elements down to sufficiently
small spatial scales when the molecular diffusion and the thermal conduction can
effectively homogenise the mass/temperatures distributions. One way of generating
random fluid motion and enhance the heat transport is to trigger inertial turbulent flow
states by ensuring sufficiently large values of the Reynolds number $Re = \rho UL/\eta$.
Here ρ stands for the density of the fluid, L for the characteristic size of the flow
container, U for the scale of the fluid velocity and η for the viscosity of the fluid.

It has been demonstrated that inertial turbulent flows transport efficiently both
mass and heat (Gollub et al. 1991; Lane et al. 1993; Warhaft 2000; Shraiman and
Siggia 2000; Lee and Hyun 1999; Kim and Hyun 1997). As already pointed out
for the case of mixing, there exist various practical situations when increasing the
Reynolds number is a difficult task, particularly when the characteristic size of the
fluid container L is small, e.g. in a microchannel. In such situations, it is desirable
to replace the inertial nonlinearity in the momentum equation with other types of
nonlinearities. Exponentially divergent Lagrangian fluid trajectories can be gener-
ated by the laminar chaotic advection (Aref 1990; Ottino 1989) and, consequently,
such flows are able to efficiently transport both mass and heat (Toussaint et al. 1995,
2000; Hobbs and Muzzio 1997; El Omari and Le Guer 2010; Narasimha et al. 1992;

Mota et al. 2007). Triggering the laminar chaotic advection at moderate Re requires, however, a special design of the flow channel and/or a particular flow control, e.g. controlled pulsations. This can also become quite challenging in the case of microscopic flows due to technical limitations/difficulties in manufacturing elaborated three-dimensional microstructures.

As we have shown that the Elastic Turbulence can enhance the mass transport (Sect. 6) it seems reasonable to expect an increase in the efficiency of the heat transport by the Elastic Turbulence. The rest of this section is dedicated to this point.

The experimental setup is similar to the one used in Sect. 4 and schematically illustrated in Fig. 65. The only difference is the addition of temperature sensors in order to measure the spatio-temporal features of the temperature distribution in the fluid. The flow is driven by a rotating top disc **D** with a radius $R_d = 39$ mm mounted on the shaft of a commercial rheometer, Mars III (from Thermofischer). The use of the commercial rheometer in driving the flow is justified by the accurate control of both the rotation speed Ω and the driving torque M.

The temperature of the bottom of the fluid container is controlled via a circulating fluid bath **CFB** fed with de-ionised water by a thermally stabilised fluid circulator (Lauda, model Proline RP 855). To avoid triggering the thermal convection (which does not make the object of this study), the temperature within the circulating fluid bath **CFB** is set to $T_b = 13\,°C$ which is smaller than the room temperature $T_0 = 23\,°C$. To ensure a good repeatability and reproducibility of the experiments, the room temperature has been regulated (with an accuracy of $\pm 0.5\,°C$) at all times and for each of the experiments reported herein by an air conditioning system installed in the experimental room.

The distribution of the temperature into the flow is point-wise monitored by an array of six thermocouples T_{1-6} (Chromel–Alumel, $100\,\mu m$ in size) disposed equidistantly along the vertical direction z and positioned at the radial position $r = R_c/2$ (Fig. 65). The thermocouples are mounted through thin metal tubes which allows one to scan the temperature distribution along the radial direction. The signals of the thermocouples are passed to the digitising block $\mathbf{A_2D}$ via the reference box **RB**. The subtraction of the reference temperature by the reference box **RB** diminishes the instrumental error of the temperature readings down to roughly 0.5% of the measured value.

Together with the point-wise measurements of the temperature, the flow has been investigated by local measurements of the flow fields by the digital particle image velocimetry (*DPIV*) technique. Time series of the velocity fields were obtained by a iterative multi-grid DPIV algorithm implemented in house under Matlab (Raffel et al. 2007; Scarano and Rhiethmuller 2001) and the flow states have been identified by a statistical analysis of the flow fields.

The polymer solution was identical to that used in Sects. 4, 5 and 6. Its density was measured at room temperature by accurately weighting fixed volumes of fluid, $\rho = 1200\,kg m^{-3}$.

The thermal properties of the polymer solution have been investigated using a hot-disc thermal conductivity analyser. The *transient plane source* (TPS), or the *Hot-Disc* method is a commonly used experimental technique for measuring thermal
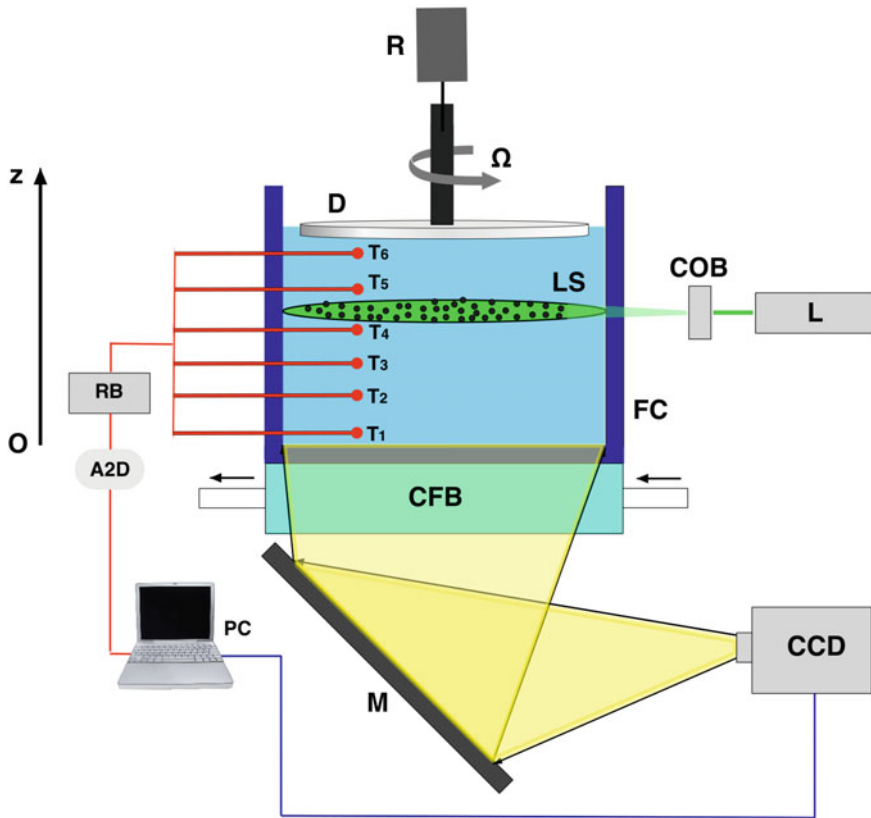
Fig. 65 Schematic view of the experimental setup: **R**—the shaft of the rheometer, **D**—rotating disc, **FC**—fluid container, **CFB**—circulating fluid bath, **T₁₋₆**—thermocouples, **RB**—reference box, **A₂D**—analogue to digital converter, **L**—solid-state laser, **LS**—laser sheet, **COB**—cylindrical optics block, **M**—planar mirror, **CCD**—video camera and **PC**—personal computer

properties of materials in either a solid or fluid state proposed by Gustaffson in early 1990s (Gustafsson 1991; Gustavsson et al. 1994).

The thermal diffusivity of the pure solvent was measured $\kappa_s = 2.21 \cdot 10^{-7} \mathrm{m}^2 \, \mathrm{s}^{-1}$. The thermal diffusivity coefficient of the polymer solution was measured $\kappa = 1.31 \cdot 10^{-7} \mathrm{m}^2 \, \mathrm{s}^{-1}$ and the characteristic time associated to the thermal diffusion may be estimated as $t_d = H^2/\kappa \approx 25714$ s. We also note that within the temperature range explored through our experiments no significant temperature dependence of the thermal diffusivity coefficient was observed.

The temperature-dependent rheological properties of the solvent and of the polymer solution were measured with the same Mars III rheometer around which the complete experimental setup was built. The shear viscosity of the solution was measured with a cone and plate geometry ($D = 60$ mm, 2° truncation) via a controlled rate flow ramp at three temperatures which are relevant during the heat transfer pro-
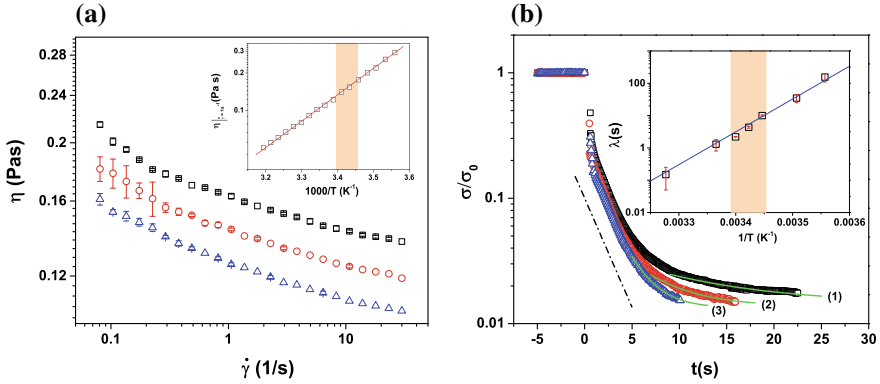
Fig. 66 a Flow curves measured during controlled rate flow ramps. The insert presents the temperature dependence of the viscosity measured at $\dot{\gamma} = 1s^{-1}$ and the full line is an Arrhenius fit. **b** Stress relaxation data. The full lines are exponentially decaying functions characterising the slow relaxation mode. The dashed-dotted line is a guide for the eye, $\sigma/\sigma_0 \propto e^{-t/2.6(\pm0.2)}$, highlighting the fast decay mode. The temperature dependence of the longest relaxation time is presented in the insert. The error bars are defined via the nonlinear fitting error. In each panel, the symbols refer to different operating temperatures: squares ($\square$)—$T = 17\,°C$, circles ($\circ$)—$T = 19\,°C$, triangles ($\triangle$)—$T = 21\,°C$ (Colour figure online)

cess, $T = 17\,°C$, $19\,°C$, $21\,°C$. Corresponding to each value of the imposed shear rate the stress was allowed to equilibrate during 50 s and the averaging was performed during the last 10 s. The choice of this temperature range was based on the value of the room temperature and of the thermal equilibrium temperature achieved during our experiments, $T_e \approx 16.9\,°C$. The temperature was controlled during the rheological measurements by a Peltier system. The geometry has been enclosed by a Teflon made solvent trap in order to minimise the sample evaporation and insure the reliability of the measurements. For each temperature, the viscosity measurement has been repeated three times with a freshly loaded sample in order to check the reliability and specify an error bar. The results of the shear viscosity measurements performed in a range of shear rates and temperatures relevant to the heat transport experiments are presented in Fig. 66a. The viscosity follows an Arrhenius time dependence on the temperature (see the full line in the insert of Fig. 66a), $\eta \propto e^{\frac{E_a^\eta}{R\,T}}$, where R is the ideal gas constant. The viscosity activation energy is found $E_a^\eta \approx 40.625(\pm1.2)\text{kJ/(mol K)}$. The largest polymer relaxation time has been assessed using the stress relaxation method (Liu et al. 2007, 2009). For this purpose, a constant rate of shear $\dot{\gamma} = 1s^{-1}$ has been maintained for 50 s. At the time instant $t_0 = 0$ the rate of shear has been set to 0 and the time decay of the stress has been monitored. As compared to the small amplitude oscillatory measurements, the relaxation time assessed via this technique is independent on the value of the initial shear (if the initial shear rate is sufficiently small so the inertial effects associated to both the shaft of the rheometer and the measuring geometry do not play a significant role) (Liu et al. 2007). In addition to that, the largest relaxation time obtained via this method is directly comparable to

the relaxation time measured via the relaxation of single molecules observed via fluorescent microscopy (Liu et al. 2007). Relaxation measurements performed at the same temperatures as the shear measurements are illustrated in Fig. 66b. At each temperature, a two-mode exponential decay is observed. The fast mode highlighted by the dashed-dotted line has a characteristic time $\lambda_1 = 2.6$ s(± 0.2 s) which is independent on the operating temperature. The largest relaxation time λ associated to the slow mode (see the full lines in Fig. 66b) depends on the temperature according to an Arrhenius type law $\lambda \propto e^{\frac{E_a^\lambda}{R\,T}}$, the insert in Fig. 66b. Although it is commonly believed that the viscosity activation energy should be close to the relaxation time activation energy, we obtain a significantly larger value, $E_a^\lambda \approx 193.5(\pm 4)$kJ/(mol K). A possible explanation for this rather unexpected result is that the changes of the relaxation time with the temperature for this polymer solution are triggered not only by the changes of the solvent viscosity but some other changes in the molecular properties of the polymer chains. By taking into account the shear-thinning of the viscosity illustrated in Fig. 66a, the Reynolds number was calculated according to $Re = \frac{\Omega R_c^2 \rho}{\eta(\dot{\gamma})}$ where Ω is the angular speed of the top driving disc **D**. Corresponding to the largest value of Wi we have explored and considering an average value of the shear viscosity within the relevant temperature range, we have found $Re \approx 26$. The main conclusion of the thermorheological analysis presented above is that in spite of a rather limited temperature range non-negligible changes in both the shear viscosity and the largest polymer relaxation time are observed. Thus, even in the absence of a buoyancy term in the momentum equation (in which case the temperature acts as an *active* scalar field), one cannot a priori establish a similarity between the dynamics of a *passive* scalar in a random smooth flow and the transport of heat by elastic turbulence. This further reinforces the motivation of our study. The Prandtl number $Pr = \frac{\eta(\dot{\gamma})}{\rho \kappa}$ which quantifies the balance between the viscous momentum diffusion and the thermal diffusion varied during our experiments (because of the shear-thinning behaviour of the viscosity and its T dependence) in the range $Pr \in [744; 1336]$. The balance between natural and forced convection is quantified by the Richardson number which may be defined as $Ri = \frac{g\beta\Delta T}{R_c \Omega^2} h^3$ where g is the acceleration of gravity, $\beta \approx 2 \cdot 10^{-4}$K^{-1} is the thermal expansion coefficient, $\Delta T = T_0 - T_b$ and $h = H/R_c$ is the geometric aspect ratio of the flow cell. By varying the angular speed of the top disc, the Richardson number was varied during our experiments in the range $Ri \in [4.7; 48.8]$.

7.1 Observation and Characterisation of Elastic Turbulent Flow States

We focus in the following on a brief characterisation of the transition to elastic turbulence and its main flow features in isothermal conditions at the room temperature T_0. One of the main issues to address here is to what extent is the elastic turbulent flow modified by the presence of the thermocouples (Fig. 65).
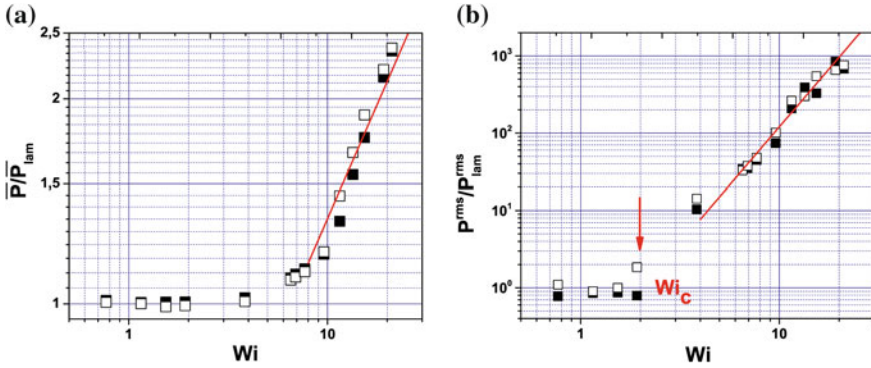
Fig. 67 **a** Dependence of the normalised time-averaged injected power $\bar{P}/\bar{P}_{lam}$ on the Weissenberg number Wi. The full line is a guide for the eye, $\bar{P}/\bar{P}_{lam} \propto Wi^{0.67}$. **b** Dependence of the reduced rms of the power fluctuations P^{rms}/P^{rms}_{lam} on the Weissenberg number Wi. The full line is a guide for the eye, $P^{rms}/P^{rms}_{lam} \propto Wi^3$. The full/empty symbols refer to increasing/decreasing Wi. The vertical arrow indicates the onset of the primary elastic instability Wi_c

At an integral scale, the transition to elastic turbulence via a primary elastic instability can be monitored by measurements of the statistics power P injected into the flow as a function of the Weissenberg number (a more systematic discussion of this was provided in Sect. 4). The injected power is calculated for the case of a swirling flow as $P = M \cdot \Omega$ where M is the torque acting on the shaft of the rheometer.

The statistics of the power fluctuations measured with the polymer solution as a function of the Weissenberg number is illustrated in Fig. 67. The Weissenberg number was calculated as $Wi = \dot{\gamma} \cdot \lambda$. Based on the measurements presented in Fig. 66b, we have chosen $\lambda = 5.5$ s which is the average value within the temperature interval considered. Corresponding to a critical value of the Weissenberg number $Wi_c \approx 2$, an increase of the flow resistance is observed in the form of an increase of the averaged injected power beyond its laminar value $\bar{P}_{lam}$, Fig. 67a. This corresponds to a primary elastic instability that occurs in the flow. Simultaneously with this, an increase of the rms of the power fluctuations is observed, Fig. 67b. The experimentally determined scaling laws of both the flow resistance $\bar{P}/\bar{P}_{lam} \propto Wi^{0.67}$ and of the reduced rms of the fluctuations, $P^{rms}/P^{rms}_{lam} \propto Wi^3$, are consistent with previous measurements (Burghelea et al. 2007; Burghelea 2005).

The evolution of the flow structure with the Weissenberg number is illustrated in Fig. 68. The DPIV measurements are performed in an horizontal plane located in the vicinity of the thermocouple T_4 at $z \approx H/2$ (Fig. 65). The top row of Fig. 68 presents the flow fields averaged over times typically 10 times larger than the polymer relaxation time λ and the bottom row presents the time-averaged in-plane vorticity $\langle \omega_z \rangle_t$.

The flow field measured below the onset of the primary elastic instability at $Wi = 0.8$ is dominated by a stationary and off-centred Ekman vortex (Ekman 1905). This flow structure is different from that of the laminar flow observed in Burghelea et al.
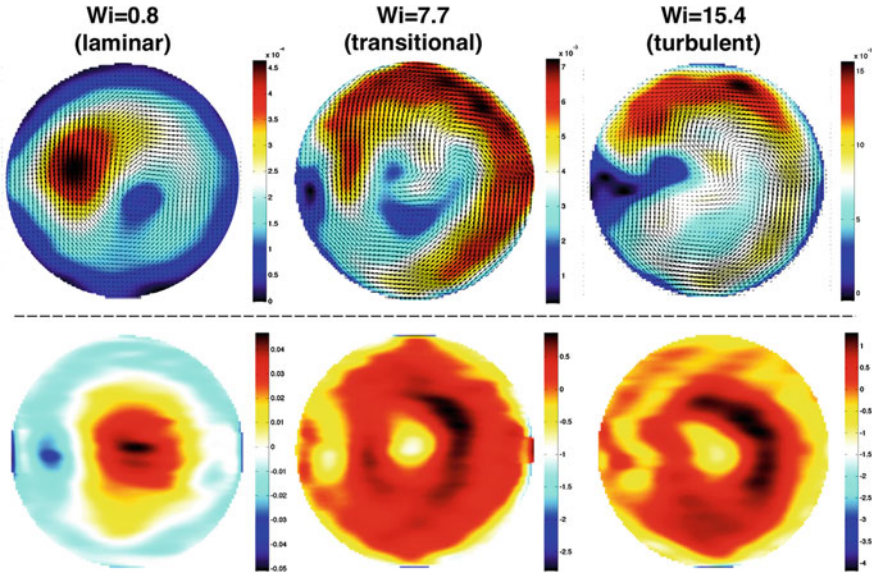
Fig. 68 Top row: time-averaged flow patterns for various Weissenberg numbers indicated in the top inserts. The colour map refers to the modulus of the in-plane velocity. For the clarity of the presentation, the overlapped vector fields were down-sampled by a factor of 2 along each direction. Bottom row: time-averaged vorticity, $\langle \omega_z \rangle_t$. The measurements were performed in isothermal conditions at the room temperature T_0

(2007) (see Fig. 10a therein), which was consistent with a rigid body rotation around the symmetry axis of the fluid container **FC** and had no vertical velocity component. This difference can be explained by the presence of the array of thermocouples which perturb the base flow, see Fig. 65. The off-centred flow topology observed in the laminar regime is consistent with the presence of a steady vertical flow component which may slightly enhance the heat transfer (as compared to the purely conductive state) even below the onset of the elastic instability. The effect of the thermocouples on the laminar flow can also be noticed in the map of the time-averaged vorticity presented on the second row of Fig. 68. The topology of the mean flow and vorticity field changes as one moves towards the transitional ($Wi = 7.7$) and fully developed elastic turbulent ($Wi = 15.4$) flow regimes. Within the transitional regime, the flow is dominated by an unsteady toroidal vortex. Within the elastic turbulent regime, the flow topology changes to a randomly fluctuating spiral vortex, in agreement with the previous results on the elastic turbulence in von Karman flows, Burghelea et al. (2007), Burghelea (2005). Within the elastic turbulent regime, the flow is spatially smooth, strongly correlated over space and its characteristic correlation length is comparable to the radius R_c of the fluid container **FC** (Burghelea et al. 2004c, 2005). The main flow illustrated above are consistent with previous experimental results (Burghelea et al. 2007; Burghelea 2005) and recommend the elastic turbulence as a potential candidate to efficiently transport the heat within the von Karman flow.

7.2 Heat Transport by Elastic Turbulence

Prior to investigating the heat transfer process in a regime of elastic turbulence, we focus on the heat transfer within the flow of the sucrose solvent at $Re \approx 125$ which is significantly larger than the largest Re number investigated during the experiments with the polymer solution. Transient measurements of the reduced temperature $\theta = \frac{T_0 - T}{T_0 - T_b}$ performed at various vertical positions z and $r = R_c/2$ are presented in Fig. 69a. Each transient data set may be formally[5] fitted by $\theta = A \cdot erfc\left(\frac{B}{\sqrt{t}}\right)^C$ (the full lines in Fig. 69a) where *erfc* is the complementary error function, the parameter A describes the equilibrium temperature and $B = \frac{z}{(4\kappa)^{1/2}}$ describes the local intensity of the heat transfer process. By fitting linearly the values obtained for the coefficient B against the positions z of the thermocouples (see the insert in Fig. 69a) one obtains for the thermal diffusivity of the solvent $\kappa_s \approx 2.6 \cdot 10^{-7}$ m^{2}s^{-1} $(\pm 2.3 \cdot 10^{-8}$ m^{2}s$^{-1})$ which is fairly close to the measured value. The equilibrium reduced temperatures reached by each thermocouple are strongly dependent on the vertical coordinate z indicating that no efficient mixing occurs in the flow which is consistent with the laminar and linear flow behaviour of the solvent alone. In addition to that, no fluctuations of the reduced temperature can be noted in Fig. 69a which is once more consistent with a laminar flow behaviour. To conclude, the tests performed with the Newtonian sucrose solvent alone at the largest Reynolds number explored through the experiments with the polymer solution revealed a conductive like heat transport mechanism characterised by a strong spatial dependence of the equilibrium temperatures and a lack of temperature fluctuations. We now turn our attention to the case when the polymer solution is used and the *Elastic Turbulence* is triggered.

Measurements of the time series of the reduced temperature θ performed within each flow regime are presented in Fig. 69b. The horizontal axis is normalised by the characteristic diffusion time t_d. Due to the presence of the secondary flow, one can no longer resort to the complementary error function nonlinear fit used in the case of the pure solvent illustrated in Fig. 69a. On the other hand it can be noted that, regardless the value of the Weissenberg number and the measuring position, each reduced temperature time series exhibits a logarithmic scaling part (note that the data is plotted in lin–log coordinates) $\theta \propto a + b \cdot ln(t/t_d)$ before reaching a steady state plateau corresponding to $t/t_d \approx 1$.

The six data sets acquired within the laminar regime at $Wi = 0.8$ never collapse indicating that a temperature gradient along the vertical direction z exists at all times, top panel in Fig. 69b. Second, the local slope b of the log scaling part of the reduced temperature series decreases monotonically from the bottom plate (the data set marked by a circle) to the top plate of the fluid container. This indicates that the intensity of the heat transfer is strongly inhomogeneous along the vertical

---

[5]This functional dependence with $C = 1$ is an exact solution for the $1 - D$ transient heat transfer problem only in the case of a semi-infinite planar domain with a constant temperature boundary condition. Deviations from the analytically exact result related to finite size effects may be accounted for by letting C vary as an extra fit parameter.
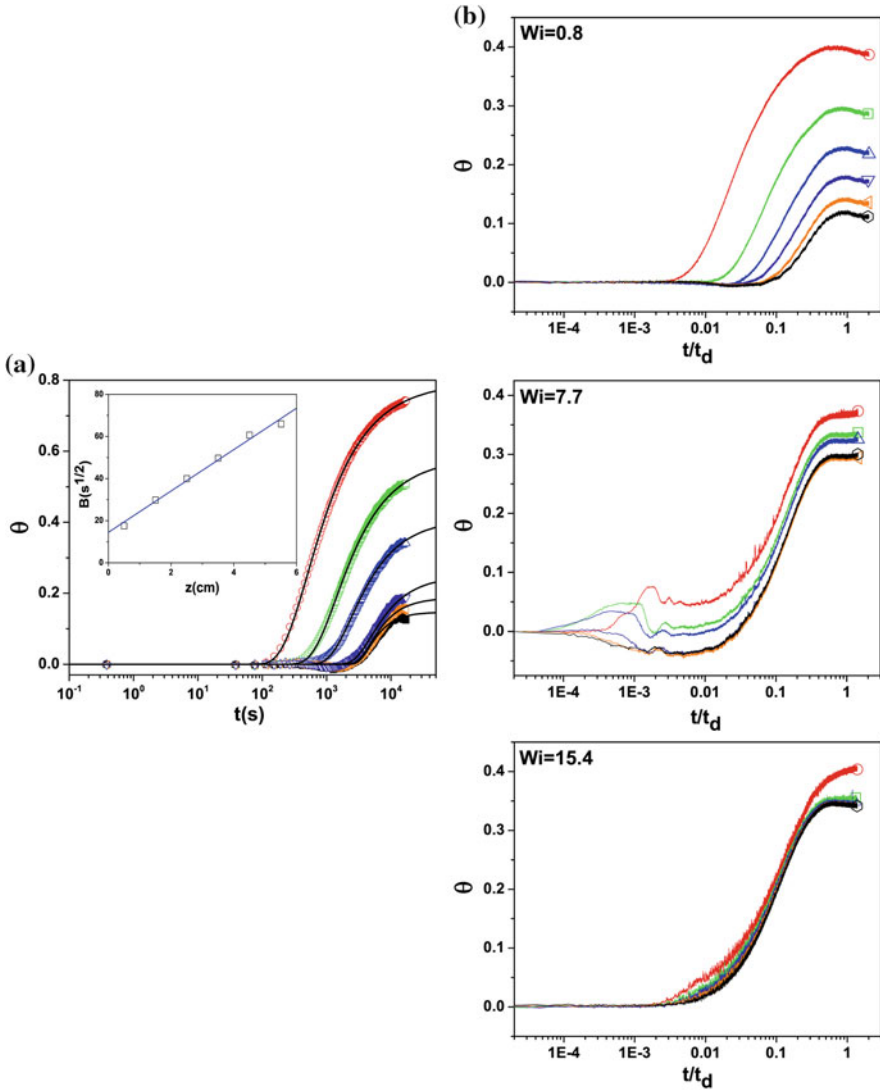
Fig. 69 **a** Time series of the reduced temperature measured with the sucrose solvent at $Re \approx 125$: circle (∘)—T_1, square (□)—T_2, up triangle (△)—T_3, down triangle (▽)—T_4, left triangle (◁)—T_5, hexagon (◯)—T_6. All measurements were performed at a distance $r = R_c/2$ from the symmetry axis of the flow container. The full lines are nonlinear fitting functions (see explanation in the text). The dependence of the fit parameter B (see text for explanation) on the vertical coordinate is presented in the insert. **b** Time series of the reduced temperature measured at three Weissenberg numbers indicated in the inserts of each panel. The symbols in each panel refer to the vertical position of the thermocouple (see Fig. 65): circle (∘)—T_1, square (□)—T_2, up triangle (△)—T_3, down triangle (▽)—T_4, left triangle (◁)—T_5, hexagon (◯)—T_6. All measurements were performed at a distance $r = R_c/2$ from the symmetry axis of the flow container (Colour figure online)

direction and it is the highest near the heat sink (the bottom plate) which is what one would expect in the case of a conduction dominated heat transfer regime. Prior to entering the logarithmic scaling regime, the time series of the reduced temperature pass through a local minimum $\theta^{min} < 0$. The magnitude of this minimum decreases as one moves from the top part of the fluid container to its cooled bottom and it practically disappears at the level of the thermocouple T_1. We interpret this effect in terms of local viscous heating of the polymer solution.

The reduced temperature time series acquired within the transitional regime ($Wi = 7.7$) are presented in middle panel in Fig. 69b. As compared to the laminar case, several differences may be noted. First, within the logarithmic scaling range, the separation between the measurements performed at the six vertical positions is much smaller and so are the differences in the plateaus observed around $t \approx t_d$. This is an indication that the unsteady vortical flow observed within the transitional regime (see Fig. 68) homogenises the vertical distribution of the temperature more efficiently than the steady laminar vortex. Second, one can clearly observe in the middle panel of Fig. 69b a fluctuating component of the temperature signal which is most pronounced near the bottom plate of the flow container (the data set labelled by a circle). Third, the local minimum of the temperature series acquired near the top plate is more pronounced than in the laminar case and occurs earlier which corroborates with our interpretation in terms of local viscous heating.

The six temperature time series acquired within the fully developed elastic turbulent regime at $Wi = 15.4$ nearly collapse onto a single master curve which indicates a perfectly homogeneous distribution of the temperature within the system, bottom panel of Fig. 69b. Together with this, an increased level of fluctuations is observed within the logarithmic scaling range. No local minimum related to viscous heating is observed which can be explained by an efficient transport of the heat from the top of the flow cell (note the viscous heating is more effective near the top driving disc **D** due to the inhomogeneous shear in a von Karman flow configuration) to the colder bottom via the randomly fluctuating spiral vortex. For a quantitative assessment of the local intensity of the heat transfer at various Weissenberg numbers, we resort to the logarithmic slope b introduced above. The dependence of the intensity factor b obtained from the data acquired at various vertical positions on the Weissenberg number Wi is presented in Fig. 70.

Because the base flow does have a non-zero vertical component, an increase of the local intensity of the heat transfer related to the increase of the in-plane vorticity is observed even below the onset of the primary elastic instability, $Wi = Wi_c$.

As compared to the purely conductive case, the transition to the elastic turbulence is accompanied by a roughly $3.5-4$ fold increase of the local intensity of the heat transfer at the position of the thermocouples T_4-T_6. At large Wi, the intensity reaches a plateau which is related to the plateau of the mean flow vorticity.

We also note that an increase of the local intensity of the heat transfer is observed in the vicinity of the top driving disc slightly below the onset of the primary elastic instability. This is due to the presence of the laminar Ekman vortex induced by the intrusive presence of the thermocouples and pictured in Fig. 68 (first column, top

Fig. 70 Dependence of the
efficiency factor b obtained
at various vertical positions
indicated in the insert on the
Weissenberg number. The
symbols refer to the position
along the vertical axis z (see
Fig. 65): (□)—T_1, (○)—T_2,
(△)—T_3, (▽)—T_4, (◇)—T_5,
(◁)—T_6. The vertical dashed
line indicates the onset of the
primary elastic instability
Wi_c (Colour figure online)
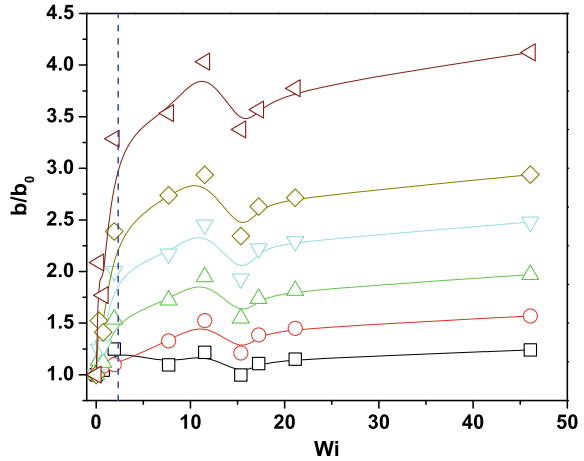
row). Unfortunately, this effect can be neither removed nor decoupled from the elastic
turbulence contribution and this is a clear drawback of our experimental technique.

It is interesting to compare the increase in the intensity of the heat transport
by elastic turbulence with similar experiments performed with Newtonian fluids at
large Re in a regime of inertial turbulence. Gollub et al. (1991) assess the efficiency
of the heat transfer via the effective thermal diffusivity $D^* = K^*/\rho c_p$ where the
global heat transport coefficient K^* is obtained from the ratio of the total measured
heat flux and the local temperature gradient, ρ is the density of the fluid, and c_p
is its the heat capacity. As illustrated in Fig. 2 of their paper, an increase of the
efficiency of up to a factor of ten is observed at $Re = 6000$. The local increase in the
heat transport intensity of roughly $3.5-4$ times we have measured within a regime
elastic turbulence at $Wi = 15.4$ corresponds to the increase observed by Gollub et al.
(1991) at $Re \approx 1600$. It is equally interesting to compare our results with numerical
simulations performed for the case of a von Karman flow of a Newtonian fluid. Prior
to discussing this, we note however that a rigorous and systematic comparison of
the increase of the heat transfer efficiency by elastic turbulence with the Newtonian
counterpart in a swirling flow is not possible for several reasons. First, unlike in
numerical simulations, we are unable to measure the Nusselt number and we have
provided only a local measure of the intensity of the transfer by the coefficient b.
Second, during our experiments, when the Weissenberg number is increased, both the
Richardson and the Prandtl numbers are varied and their range does not necessarily
match that studied in numerical simulations (both numbers are larger in our case). Last
but not least, the flow structure within a regime of elastic turbulence and its evolution
with the Weissenberg number depart significantly from the Newtonian case. For these
reasons, only a qualitative (and most probably incomplete) comparison with the case
of a Newtonian swirling flow will be attempted below. Corresponding to $Pr = 1$ and
$Re = 2000$ the numerical simulations presented by Iwatsu (2004) for the von Karman
swirling flow of a Newtonian fluid predict a maximal increase of the heat transport

efficiency (quantified by the space-averaged Nusselt number) of roughly 9 times corresponding to $Ri = 0.01$. As they increase the Richardson number, however, the increase in the transport efficiency at $Re = 2000$ decreases down to roughly 1.5 times corresponding to $Ri = 1$, see Fig. 15 in Iwatsu (2004). Similar numerical results are found by Kim and Hyun (1997) for $Pr = 0.7$, $Re = 2000$ and Ri ranging from 0.01 to 10.

The central conclusion of this part is that the efficiency of the heat transport by elastic turbulence is comparable in magnitude to that of the Newtonian counterpart studied by others although during our experiments both Ri and Pr were larger. In addition to that, based on the data presented in Fig. 70 the intensity of the heat transport by elastic turbulence is practically insensitive to these non-dimensional numbers if Wi is sufficiently large. This is a significant difference (and perhaps an advantage) with respect to the swirling flow of a Newtonian fluid where an increase of both Pr and Ri translates into a decrease of the transport efficiency. As the elastic turbulent flow field has a single relevant spatial scale set by the dimensions of the fluid container **FC** and there exists no physical equivalent of the cascade towards smaller scales observed in the inertial turbulence, a natural question to be answered in the following is how does the intensity of the heat transfer depend on the position z in the flow. To address this point, we plot in Fig. 71 the local intensity factor b versus the vertical position z for various Weissenberg numbers spanning the relevant flow regimes. In the absence of a flow ($Wi = 0$) when the heat is transported solely by thermal conduction, a strong spatial dependence of the intensity factor is observed (the diamonds in Fig. 71). As expected for a purely conductive case, the intensity of the heat transport decreases monotonically as one moves away from the heat sink located at $z = 0$ cm. A slight increase of the local intensity factor is observed within the laminar and steady flow regime ($Wi = 0.8$), particularly in the proximity of the top driving disc **D** (the squares). This slight increase in the intensity of the heat transfer process may be explained by the presence of the steady Ekman vortex induced by the array of the thermocouples (Fig. 68). A notable increase of the heat

Fig. 71 Dependence of the intensity factor b on the vertical coordinate. The symbols refer to the Weissenberg number: diamonds ($\diamond$)—$Wi = 0$, squares ($\square$)—$Wi = 0.8$, triangles ($\triangle$)—$Wi = 7.7$ and circle ($\circ$)—$Wi = 15.4$ (Colour figure online)
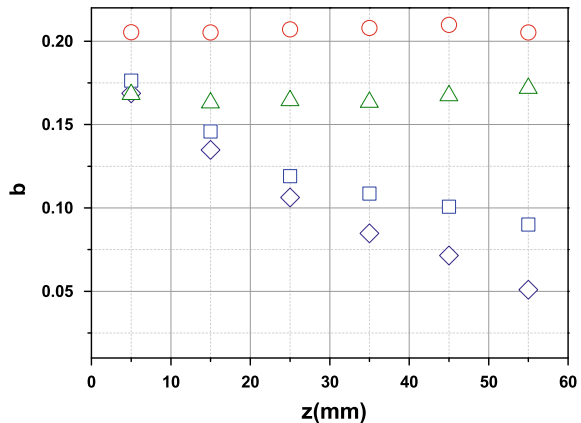
transport intensity is observed at any measuring position within the transitional and the fully developed elastic turbulent regimes (the triangles and the circles). We point out that within these flow regimes the intensity is independent on the flow coordinate consistently with a full homogenisation of the temperature field. The largest increase in the local intensity is observed near the top disc **D** and accounts for nearly four times the intensity measured in a purely conductive state (Fig. 71).

7.3 *Statistical and Scaling Properties of the Temperature Fluctuations:* **Passive** *or* **Active** *Scalar?*

In a random flow, the scalar temperature field may act either as a passive scalar when it does not react back on the flow field or, if it does, as an active scalar. A classical example where the temperature acts as an active scalar is that of a fluid heated from below: the density gradient may induce a thermo-convective instability and thus the temperature reacts back on the flow field. In the passive case, the homogenisation of the temperature field by a random and spatially smooth flow field in a regime of *Elastic Turbulence* is similar to the mixing problem (Burghelea et al. 2004a, b; Burghelea 2005) and several fundamental features have been highlighted:

1. The probability distributions of the passive scalar fluctuations have exponential tails and the second-order moment of these distributions decays exponentially in time.
2. The temporal correlations of the passive scalar fluctuations decay over times of the same order of magnitude with the correlation times of the flow field and the largest relaxation time of the polymer molecules.
3. The spectra of the passive scalar fluctuations decay algebraically, $P \propto k^{\delta}$, with $\delta \approx -1$.

For all the experiments we reported above, the fluid has been cooled from below. Thus, thermo-convective instabilities are ruled out and, at least at a first glance, one would be tempted to believe that the temperature field acts as a passive scalar meaning that the heat transport process is physically equivalent to the mixing problem. At a more careful inspection, this is actually not granted. As illustrated in Fig. 66, the rheological properties (shear viscosity and relaxation time) are strongly dependent on the temperature. Thus, the temperature field is directly coupled to the stress tensor which may in turn act on the flow field. Thus, whether the temperature acts as a passive or an active scalar remains to be investigated experimentally which sets the main scope of this section.

To get a first insight into the statistics of the temperature fluctuations at various Weissenberg numbers, we extract the fluctuating part of each time series of the reduced temperature presented in Fig. 69b by subtracting from the original signal its pedestal $\mathcal{P}$ obtained via a fifth-degree polynomial fit, $\theta_r (t/t_d) = \theta (t/t_d) - \mathcal{P} (t/t_d)$.

As by in situ measurements of the apparent viscosity η_a of the polymer solution during the heat transfer process we have observed that at high Weissenberg numbers
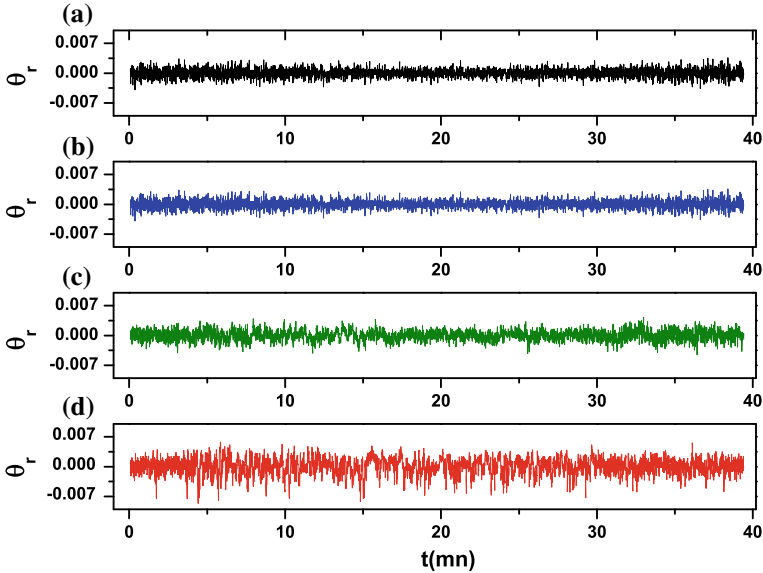
Fig. 72 Time series of the fluctuating part of the reduced temperature θ_r obtained from the measurements of the thermocouple T_4 (see Fig. 65) at various Weissenberg numbers: **a** $Wi = 0$, **b** $Wi = 0.8$, **c** $Wi = 7.7$ and **d** $Wi = 15.4$

the mechanical degradation occurs (manifested through a significant decrease of η_a) at very late stages of the process ($t/t_d > 0.5$), the whole statistical analysis we present below was restricted to time windows within the logarithmic scaling range, $0.1 < t/t_d < 0.3$ and no conclusions were drawn from the temperature data acquired beyond this range. In the absence of a flow ($Wi = 0$) the pedestal of the signal characterises the purely conductive heat transport and in a laminar regime ($0 < Wi < Wi_c$) it describes the summed contributions of the conduction and the laminar convective transport carried on by the stable vortex illustrated in Fig. 68. Several time series of the fluctuating part of the reduced temperature θ_r obtained according to the procedure described above from the raw data acquired by the thermocouple T_4 positioned at $r = R_c/2$ (see Fig. 65) at various Weissenberg numbers increasing from the top to the bottom are presented in Fig. 72.

In the absence of a flow ($Wi = 0$) and below the onset of the primary elastic instability ($Wi = 0.8$), these fluctuations are of a purely instrumental nature. Upon an increase of the Weissenberg number within the fully developed elastic turbulent regime a significant increase of the level of fluctuations beyond the instrumental level is observed (Fig. 72c and d). At $Wi = 15.4$ the randomly fluctuating temperature time series also exhibits some intermittency.

The spatial distribution of the root mean squared of the fluctuations of the reduced temperature within each flow regime is illustrated in Fig. 73.

Fig. 73 Space distribution of the rms of the fluctuations of the reduced temperature, θ_r^{rms} measured at various Weissenberg numbers: diamonds (◇)—$Wi = 0$, squares (□)—$Wi = 0.8$, triangles (△)—$Wi = 7.7$ and circle (○)—$Wi = 15.4$ (Colour figure online)
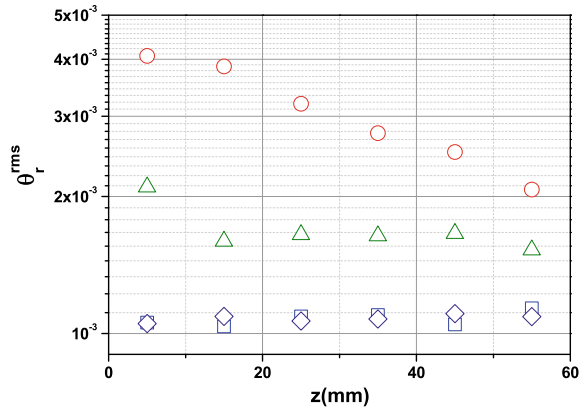
In the absence of a flow and within the laminar regime, no dependence of the level of the fluctuations on the vertical coordinate z can be observed (which was expected, as the six thermocouples are identical, i.e. the instrumental error of their measurements is the same). Within the transitional regime and the fully developed elastic turbulent regime a clear spatial dependence of the temperature fluctuations can be observed (the triangles and the squares in Fig. 73). Due to the particular topology of the randomly fluctuating spiral vortex illustrated in Fig. 68 at $Wi = 15.4$, the fluctuations are the largest in the vicinity of the bottom plate of the flow container **FC** and decrease monotonically as one approaches the level of the top driving disc **D**. Near the bottom plate, the temperature fluctuations due to the advection of the temperature field by the random flow field are about 3.5 times larger than the instrumental fluctuations observed in the laminar regime. We point out that in spite of the clear anisotropy of the temperature fluctuations within the fully developed elastic turbulent regime, the intensity of the heat transport quantified by the parameter b introduced above is practically independent on the spatial coordinate (the circles in Fig. 71).

The dependence of the level of fluctuations measured in the fully developed elastic turbulent regime near the bottom plate of the fluid container on the vertical coordinate indicates the possible existence of a boundary layer for the heat transfer with its edge roughly located around $z = 15$ mm (Fig. 71). As the spatial resolution of our measuring technique along the vertical direction is limited and the construction of the experimental apparatus does not allow one to move the thermocouples along this direction, a systematic investigation of this fact similar to that performed for the velocity boundary layer (Burghelea et al. 2007) or the passive scalar boundary layer (Burghelea et al. 2004b) was not possible and should to be addressed by future experimental studies.

The probability density functions (pdfs) of the fluctuations of the reduced temperature measured by the thermocouple T_4 are presented in Fig. 74a. In the absence of a flow (the diamonds) and within a laminar flow regime (the squares) the pdfs can be fitted by a Gaussian function (the full line).
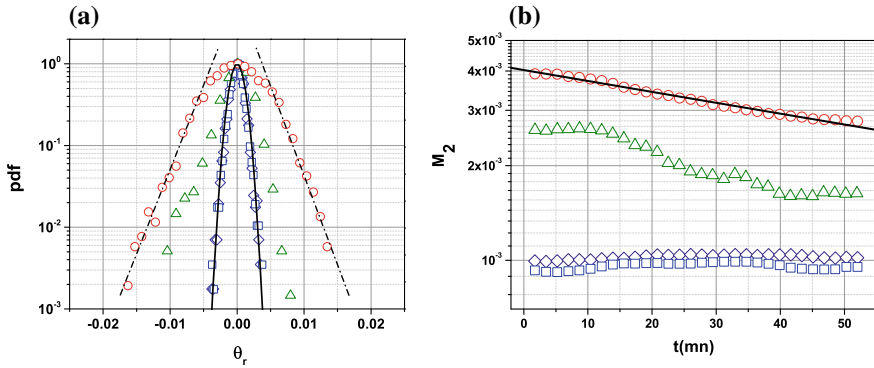
Fig. 74 **a** Probability density functions (pdfs) of the fluctuations of the reduced temperature, T_r^{rms}, obtained from the measurements of the thermocouple T_4. The full line is a Gaussian fit, the dashed-dotted lines are guides for eye highlighting the exponential tails of the pdfs. **b** Time dependence of the second-order moment M_2 of the distribution of the temperature fluctuations obtained from the measurements of the thermocouple T_4. The full line is an exponential decay fit, $M_2 \propto e^{-t/7523}$. In both panels, the symbols refer to different Wi: diamonds ($\diamond$)—$Wi = 0$, squares ($\square$)—$Wi = 0.8$, triangles ($\triangle$)—$Wi = 7.7$ and circles ($\circ$)—$Wi = 15.4$ (Colour figure online)

Upon an increase of the Weissenberg number beyond the onset of the primary elastic instability (the triangles and the circles) the distributions become significantly broader and exhibit exponential tails (see the dashed-dotted lines).

A certain degree of asymmetry of the pdfs which may be associated to the intermittency of the temperature fluctuations visible in Fig. 72c–d can be equally observed.

The decay of the second-order moments M_2 of the probability density functions is illustrated in Fig. 74b. Within the elastic turbulent regime (the circles), an exponential decay of the second-order moment is observed, $M_2 \propto e^{-t/t_{mix}}$. Here t_{mix} is a characteristic timescale for the decay of the temperature fluctuations and is equivalent to the mixing time in the passive scalar problem. By an exponential fit of the data presented in Fig. 74b one obtains $t_{mix} \approx 7523$ s which is about 3.4 times smaller than the characteristic time diffusion time t_d. This result corroborates with the 3.5 times increase in the efficiency of the heat transfer quantified by the slope b and illustrated in Figs. 70 and 71.

The pdfs of the fluctuations of the reduced temperature measured at each vertical position for various Wi are presented in Fig. 75. In the absence of a flow and within the laminar regime the pdfs acquired at each of the six vertical positions collapse onto a single master curve which can be well fitted by a Gaussian distribution (panels (a–b)).

Within the transitional regime ($Wi = 7.7$) a strongly intermittent distribution is observed particularly in the vicinity of the bottom plate (the squares and the circles in Fig. 75c). The degree of intermittency decreases as one approaches the top disc but does not vanish.
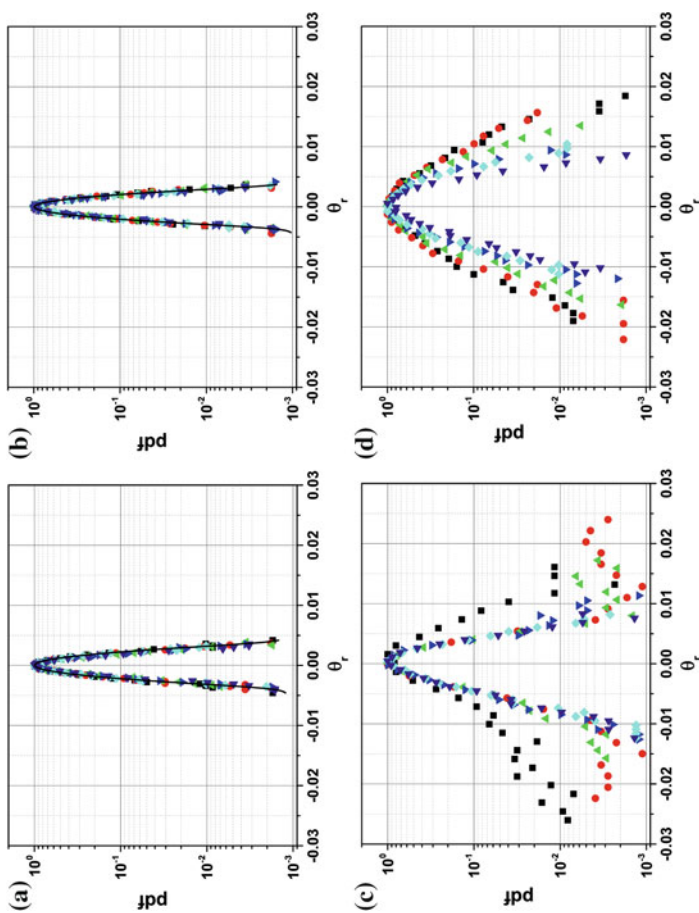
Fig. 75 Pdfs of the fluctuations of the reduced temperature measured at various vertical positions and several *Wi*: **a** *Wi* = 0, **b** *Wi* = 0.8, **c** *Wi* = 7.7 and **d** *Wi* = 15.4. In each panel the symbols refer to different thermocouples (see Fig. 65): squares (■)—T_1, circles (●)—T_2, up triangles (▲)—T_3, down triangles (▼)—T_4, diamonds (◇)—T_5, left triangles (◀)—T_6. The full lines in panels (a, b) are Gaussian fitting functions (Colour figure online)
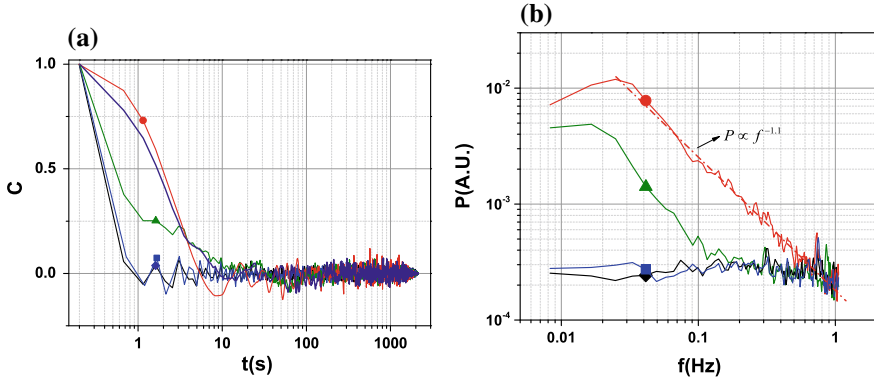
Fig. 76 **a** Temporal autocorrelation functions C of the fluctuations of the reduced temperature. **b** Spectra of the fluctuations of the reduced temperature. The data were measured by the thermocouple T_4 (see Fig. 65). The symbols in both panels refer to various Weissenberg numbers: diamond ($\diamond$)—$Wi = 0$, square ($\blacksquare$)—$Wi = 0.8$, triangle ($\blacktriangle$)—$Wi = 7.7$ and circle ($\bullet$)—$Wi = 15.4$. The dashed-dotted line is a guide for the eye, $P \propto f^{-1.1}$ (Colour figure online)

In the fully developed elastic turbulent regime, the pdfs exhibit an intermittent behaviour and exponential tails regardless the vertical position (Fig. 75d).

These results on the statistics of the fluctuations of the reduced temperature presented above are in a good agreement with the theoretical prediction for the decay of a passive scalar in a random smooth flow (Chertkov et al. 1995; Balkovsky and Fouxon 1999), and with the experiments on the mixing of a passive scalar in a macroscopic curvilinear channel (Groisman and Steinberg 2001), and in a microchannel (Burghelea et al. 2004a, b).

The temporal autocorrelation functions of the fluctuations of the reduced temperature measured within each relevant flow regime are presented in Fig. 76a.

In the absence of a flow and within the laminar regime the fluctuations of the reduced temperature are solely related to the instrumental noise of the temperature measurements and, consequently, the signals are short correlated (the curves labelled by a diamond and a square in Fig. 76a). Within the transitional and the fully developed elastic turbulent regimes the reduced temperature de-correlates over characteristic times τ_c comparable to the relaxation time of the polymer λ. This behaviour is quite similar to the behaviour of the time autocorrelation functions of the azimuthal velocity component, see Fig. 24 in Burghelea et al. (2007) which is probably due to the coupling between the flow field and the temperature field.

8 Hydrodynamic Theory of *Elastic Turbulence*

The existing theory of Elastic Turbulence of a dilute solution of polymers with linear elasticity and the feedback reaction on the flow only deals with an unbounded flow

system (Balkovsky et al. 2001; Fouxon and Lebedev 2003). As already pointed out in the introduction of this chapter, the distinctive property of solutions of high molar mass linear polymers is the dependence of the stresses on the flow history (Bird et al. 1977). Thus, once the flow forcing is removed, the stress decays with a macroscopic relaxation time λ (quite often as large as tens of seconds) rather than instantly vanishing.

For clarity reasons, we briefly recall the Oldroyd-B model already discussed in chapter "Constitutive Models of Complex Fluids". By noting that for a dilute solution the total stress tensor can be decomposed into a solvent and a polymer contribution $\sigma = \sigma_s + \sigma_p$, the equation of motion takes the form:

$$\frac{\partial \vec{V}}{\partial t} + \left(\vec{V} \nabla \right) \vec{V} = -\frac{\nabla p}{\rho} + \frac{\eta_s}{\rho} \Delta \vec{V} + \frac{\nabla \sigma}{\rho} \tag{18}$$

The mathematically simplest model accounting for the evolution of the stress tensor in a flow is a single mode Maxwell type constitutive relation:

$$\sigma_{\mathbf{p}} + \lambda \frac{D \sigma_{\mathbf{p}}}{Dt} = \eta_p \left[\nabla \vec{V} + \left(\nabla \vec{V} \right)^{\dagger} \right] \tag{19}$$

Here $D\sigma_{\mathbf{p}}/Dt$ stands for the material time derivative and $\eta_p = \eta - \eta_s$ is the polymer contribution to the solution viscosity. A commonly used definition of the material time derivative is the upper convective time derivative:

$$\frac{D\sigma_{\mathbf{p}}}{Dt} = \frac{d\sigma_{\mathbf{p}}}{dt} + \left(\vec{V} \nabla \right) \cdot \sigma_{\mathbf{p}} - \left(\vec{V} \nabla \right)^{\dagger} \cdot \sigma_{\mathbf{p}} - \sigma_{\mathbf{p}} \cdot \left(\vec{V} \nabla \right) \tag{20}$$

The nonlinear terms in the right-hand side of Eq. 20 account for the translation, rotation and stretching of fluid elements and are all of the order of $\lambda \frac{V}{L} \sigma_p$.

Equations (19) and (20) are referred to as the Oldroyd-B rheological model for polymer solutions (Bird et al. 1977).

A key ingredient of the theory of the Elastic Turbulence is to relate the dynamics of the elastic stress tensor $\sigma_{\mathbf{p}}$ to the dynamics of a vector field with a linear damping (Fouxon and Lebedev 2003; Ogilvie and Proctor 2003; Chertkov 1998; Balkovsky et al. 2001). This can be done by noting that if one neglects the thermal fluctuations the elastic stress tensor is uniaxial, $\sigma_p^{i,j} = B_i B_j$ which allows one to derive an equation similar to the equation for the magnetic field in magnetohydrodynamics (MHD):

$$\frac{\partial \vec{B}}{\partial t} + \left(\vec{V} \nabla \right) \vec{B} = \left(\vec{B} \nabla \right) \vec{V} - \frac{\vec{B}}{\lambda}, \nabla \cdot \vec{B} = 0 \tag{21}$$

The stretching of the magnetic field lines is similar to the stretching of polymer molecules in the flow and the sole difference with respect to the MHD case comes from the linear relaxation term $\frac{\mathbf{B}}{\lambda}$ which replaces the diffusion term. In the absence of inertial contributions, $Re << 1$, the momentum conservation equation can be

written:

$$\nabla P = \rho \left(\vec{B} \nabla \right) \vec{B} + \eta_s \Delta \vec{V}, \nabla \cdot \vec{V} = 0 \tag{22}$$

In the absence of significant inertial contributions ($Re \ll 1$) which is the case for the Elastic Turbulence, the kinetic energy of the polymer solution can be neglected in comparison with the elastic one. The dissipation of the elastic energy is, however, due to both viscous dissipation due to the solvent viscosity and polymer relaxation:

$$\frac{d}{dt} \int d\vec{r} \frac{B^2}{2} = -\frac{1}{\lambda} \int d\vec{r} \frac{B^2}{2} - \frac{\eta_s}{\rho} \int d\vec{r} \left(\nabla_j V_i \right)^2 \tag{23}$$

With the appropriate boundary conditions, Eqs. (21) and (22) exhibit an elastic instability at $Wi = Wi_c$ where $Wi = \lambda \dot{\gamma}$ and the instability results in a chaotic and statistically stationary dynamics. Here $\dot{\gamma}$ is the second invariant of the rate of strain tensor.

The theory of Elastic Turbulence in an unbounded flow of a polymer solution is upon two central assumptions:

1. The local feedback of the stretched polymer molecules on the flow field leads to a statistically stationary state characterised by a saturation of both the polymer contribution to the stress tensor τ_p and the rms of the fluctuations of the velocity gradients $\left(\frac{\partial V_i}{\partial x_j} \right)^{rms}$. Consequently, corresponding to a fully developed elastic turbulent regime the local Weissenberg number defined as $Wi_{loc} = \lambda \left(\frac{\partial V_i}{\partial x_j} \right)^{rms}$ saturates and, in the bulk of the flow, its saturation value is $Wi_{loc} \approx 1$.

2. Both dissipative terms due to viscosity and polymer relaxation that appear in the equation for the dissipation of elastic energy are of the same order of magnitude $\frac{\sigma_p}{\lambda} \approx \frac{\eta}{\rho} \left(\nabla \vec{V} \right)^2$ or, equivalently, $\frac{\sigma_p \lambda}{\eta} \approx Wi_{loc}^2$.

According to Balkovsky et al. (2001), the first assumption may be phenomenologically understood in the context of a strong back reaction of the extended polymer molecules to the flow as follows. If the instantaneous velocity gradients exceed the reciprocal relaxation time $1/\lambda$ the polymer coils are stretched which results in an increase of the elastic stresses that damps the velocity gradients. Conversely, if the velocity gradients are much smaller than $1/\lambda$, the polymer molecules retract and produce no feedback to the flow. Thus, the velocity gradients tend to increase to the characteristic value corresponding to the pure solvent which is significantly larger than $1/\lambda$ above the onset of the transition. The second assumption is consistent with a saturation of the elastic stresses far above the onset of the primary elastic instability.

Next, if one denotes by $\vec{V}'$ and $\vec{B}'$ the small-scale fluctuating parts of the fields $\vec{V}$ and $\vec{B}$ it can be shown that the Fourier components satisfy the linear relationship $\vec{V}' = \frac{i\rho \left(\vec{k} \cdot \vec{B} \right)}{\eta k^2} \vec{B}'$ which allows one to derive for the spherically normalised spectra of fluctuations of $\vec{V}'$ and $\vec{B}$ the following relationships (Fouxon and Lebedev 2003):

$$E(k) \propto \eta^2 L(kL)^{-\delta} \tag{24}$$

$$F(k) \propto B^2 L(kL)^{2-\delta} \tag{25}$$

With the assumptions $\nabla V' \ll \nabla V$ and $B' \ll B$ it can be shown that $\delta > 3$ (Fouxon and Lebedev 2003).

The algebraic decay of the velocity spectrum has been first observed by means of *LDV* measurements (and using the Taylor's frozen flow hypothesis was switch from the frequency domain to the wave number domain) in a macroscopic von Karman flow and, subsequently, in a macroscopic serpentine channel by Groisman and Steinberg (2000, 2001). Direct measurements of the spectra in the space domain by means of *DPIV* revealed a decay exponent $\delta \approx 3.5$. Contrary to the case of the inertial turbulence, the algebraic scalings of the kinetic and elastic energy are not related to any cascade of energy (or other conserved physical quantity). Because the velocity spectrum decays faster than k^{-3}, the dominant space scale is set by the size of the fluid container L and the velocity fluctuations are strongly correlated over distances comparable to L. The spatial smoothness of the flow has been probed by measurements of the flow fields in both o macroscopic von Karman swirling flow and in a microscopic flow in a serpentine micro-channel. The characteristic timescale associated to the fluctuations of the flow fields in a regime of *Elastic Turbulence* which is the Eulerian correlation time is found to be comparable in magnitude to the largest relaxation time of the polymer molecules.

A k^{-1} like decay of the spectrum of the fluctuations is characteristic for the decay of a passive scalar in a smooth random flow field in the so-called Batchelor regime of mixing (Batchelor 1959). Such algebraic decay has been observed for the mixing of a fluorescent tracer by an elastic turbulent flow in both microscopic (Burghelea 2005; Burghelea et al. 2004a, b) and macroscopic channel flows (Jun and Steinberg 2010). More recently and somehow unexpectedly a similar spectral decay has been observed for the fluctuations of the temperature in an elastic turbulent von Karman swirling flow cooled from below (Traore et al. 2015). This indicates that, in spite of the strong temperature dependence of the rheological properties (notably the relaxation time and the shear viscosity) the temperature field behaves like a passive scalar. Thus, if the decay exponent of velocity spectrum is $\delta \approx 3$ (Eq. 25) suggests that the stress is passively advected by the large-scale chaotic smooth flow in a regime of Elastic Turbulence.

Although many fundamental features of elastic turbulent flows (such as flow smoothness, the algebraic decay of spectra of fluctuations, the decay of the flow correlation) have been investigated experimentally in various macroscopic flows (Couette flow between rotating cylinders, von Karman swirling flow, curvilinear channel flow), the main assumption of the theory concerning with the saturation of velocity gradients has been demonstrated only recently. The experimental results presented in this chapter revealed the emergence of a boundary layer for the elastic stresses in both the macroscopic and microscopic setups. The present theory of *Elastic Turbulence* solely refers to an unbounded system. Thus, the scaling properties in the boundary layer still await for future theoretical developments.

References

Aref H (1990) Chaotic advection of fluid particles. Philos Trans R Soc Lond Ser A Phys Eng Sci 333(1631):273–288

Artale V, Boffetta G, Celani A, Cencini M, Vulpiani A (1997) Dispersion of passive tracers in closed basins: Beyond the diffusion coefficient. Phys Fluids 9(11):3162–3171

Balkovsky E, Fouxon A (1999) Universal long-time properties of lagrangian statistics in the batchelor regime and their application to the passive scalar problem. Phys Rev E 60:4164–4174

Balkovsky E, Fouxon A, Lebedev V (2001) Turbulence of polymer solutions. Phys Rev E 64:056301

Batchelor GK (1959) Small-scale variation of convected quantities like temperature in turbulent fluid Part 1. General discussion and the case of small conductivity. J Fluid Mech 5(1):113–133

Belmonte A, Martin B, Goldburg WI (2000) Experimental study of taylor's hypothesis in a turbulent soap film. Phys Fluids 12(4):835–845

Bird RB, Hassager O, Armstrong RC, Curtiss CF (1977) Dynamics of polymeric liquids, vol 1. Wiley, New York

Boffetta G, Cencini M, Espa S, Querzoli G (1999) Experimental evidence of chaotic advection in a convective flow. Europhys Lett 48(6):629–633

Boffetta G, Cencini M, Falcioni M, Vulpiani A (2002) Predictability: a way to characterize complexity. Phys Rep 356(6):367–474

Boffetta G, Celani A, Musacchio S (2003) Two-dimensional turbulence of dilute polymer solutions. Phys Rev Lett 91:034501

Brandstäter A, Swift J, Swinney HL, Wolf A, Farmer JD, Jen E, Crutchfield PJ (1983) Low-dimensional chaos in a hydrodynamic system. Phys Rev Lett 51:1442–1445

Burghelea T (2005) Elastic turbulence and mixing in a dilute polymer solution. PhD thesis, Feinberg Graduate School of the Weizmann Institute of Science

Burghelea T, Segre E, Bar-Joseph I, Groisman A, Steinberg V (2004a) Chaotic flow and efficient mixing in a microchannel with a polymer solution. Phys Rev E 69(6):066305

Burghelea T, Segre E, Steinberg V (2004b) Mixing by polymers: experimental test of decay regime of mixing. Phys Rev Lett 92(16):164501

Burghelea T, Segre E, Steinberg V (2004c) Statistics of particle pair separations in the elastic turbulent flow of a dilute polymer solution. Europhys Lett 68(4):529–535

Burghelea T, Segre E, Steinberg V (2005) Validity of the Taylor hypothesis in a random spatially smooth flow. Phys Fluids 17(10):103101

Burghelea T, Segre E, Steinberg V (2006) Role of elastic stress in statistical and scaling properties of elastic turbulence. Phys Rev Lett 96(21):214502

Burghelea T, Segre E, Steinberg V (2007) Elastic turbulence in von Karman swirling flow between two disks. Phys Fluids 19(5):1–26

Chertkov M (1998) On how a joint interaction of two innocent partners (smooth advection and linear damping) produces a strong intermittency. Phys Fluids 10(11):3017–3019

Chertkov M, Lebedev V (2003) Decay of scalar turbulence revisited. Phys Rev Lett 90:034501

Chertkov M, Falkovich G, Kolokolov I, Lebedev V (1995) Statistics of a passive scalar advected by a large-scale two-dimensional velocity field: analytic solution. Phys Rev E 51:5609–5627

Chou H-P, Spence C, Scherer A, Quake S (1999) A microfabricated device for sizing and sorting DNA molecules. Proc Natl Acad Sci 96(1):11–13

de Gennes P-G (1974) Coil-stretch transition of dilute flexible polymers under ultrahigh velocity gradients. J Chem Phys 60(12):5030–5042

Ekman VW (1905) On the influence of the earth's rotation on ocean currents. Ark Mat Astron Fys 2(11):1–53

El Omari K, Le Guer Y (2010) Thermal chaotic mixing of power-law fluids in a mixer with alternately rotating walls. J Non Newton Fluid Mech 165(11–12):641–651

Falkovich G, Gawędzki K, Vergassola M (2001) Particles and fields in fluid turbulence. Rev Mod Phys 73:913–975

Fisher MJ, Davies POAL (1964) Correlation measurements in a non-frozen pattern of turbulence. J Fluid Mech 18(1):97–116

Fouxon A, Lebedev V (2003) Spectra of turbulence in dilute polymer solutions. Phys Fluids 15(7):2060–2072

Gerashchenko S, Chevallard C, Steinberg V (2005) Single-polymer dynamics: coil-stretch transition in a random flow. Europhys Lett 71(2):221–227

Gollub JP, Clarke J, Gharib M, Lane B, Mesquita ON (1991) Fluctuations and transport in a stirred fluid with a mean gradient. Phys Rev Lett 67:3507–3510

Groisman A, Steinberg V (1998) Mechanism of elastic instability in couette flow of polymer solutions: experiment. Phys Fluids 10(10):2451–2463

Groisman A, Steinberg V (2000) Elastic turbulence in a polymer solution flow. Nature 405(6782):53–55

Groisman A, Steinberg V (2001) Efficient mixing at low reynolds numbers using polymer additives. Nature 410(6831):905–908

Gustafsson SE (1991) Transient plane source techniques for thermal conductivity and thermal diffusivity measurements of solid materials. Rev Sci Instrum 62(3):797–804

Gustavsson M, Karawacki E, Gustafsson SE (1994) Thermal conductivity, thermal diffusivity, and specific heat of thin samples from transient measurements with hot disk sensors. Rev Sci Instrum 65(12):3856–3859

Hansen CL, Skordalakes E, Berger JM, Quake SR (2002) A robust and scalable microfluidic metering method that allows protein crystal growth by free interface diffusion. Proc Natl Acad Sci 99(26):16531–16536

Hershey HC, Zalkin ZL (1967) Existence of two types of drag reduction in pipe flow of dilute polymer solutions. Number 3.

Hobbs DM, Muzzio FJ (1997) The kenics static mixer: a three-dimensional chaotic flow. Chem Eng J 67(3):153–166

Iwatsu R (2004) Flow pattern and heat transfer of swirling flows in cylindrical container with rotating top and stable temperature gradient. Int J Heat Mass Trans 47(12–13):2755–2767

Jullien M-C, Castiglione P, Tabeling P (2000) Experimental observation of batchelor dispersion of passive tracers. Phys Rev Lett 85:3636–3639

Jun Y, Steinberg V (2010) Mixing of passive tracers in the decay batchelor regime of a channel flow. Phys Fluids 22(12):123101

Jun Y, Steinberg V (2011) Elastic turbulence in a curvilinear channel flow. Phys Rev E 84:056325

Kim WN, Hyun JM (1997) Convective heat transfer in a cylinder with a rotating lid under stable stratification. Int J Heat Fluid Flow 18(4):384–388

Koeltzsch K (1998) On the relationship between the Lagrangian and Eulerian time scale. Atmos Environ 33(1):117–128

Kraichnan RH (1968) Small-scale structure of a scalar field convected by turbulence. Phys Fluids 11(5):945–953

Krogstad P-A, Kaspersen JH, Rimestad S (1998) Convection velocities in a turbulent boundary layer. Phys Fluids 10(4):949–957

Lacorata G, Aurell E, Vulpiani A (2001) Drifter dispersion in the adriatic sea: lagrangian data and chaotic model. Ann Geophys 19(1):121–129

Lane BR, Mesquita ON, Meyers SR, Gollub JP (1993) Probability distributions and thermal transport in a turbulent grid flow. Phys Fluids A Fluid Dyn 5(9):2255–2263

Larson RG (1992) Instabilities in viscoelastic flows. Rheol Acta 31(3):213–263

Lee CH, Hyun JM (1999) Flow of a stratified fluid in a cylinder with a rotating lid. Int J Heat Fluid Flow 20(1):26–33

Li Jeon N, Baskaran H, Dertinger SKW, Whitesides GM, Van De Water L, Toner M (2002) Neutrophil chemotaxis in linear and complex gradients of interleukin-8 formed in a microfabricated device. Nat Biotechnol 20:826–830

Liu Y, Jun Y, Steinberg V (2007) Longest relaxation times of double-stranded and single-stranded dna. Macromolecules 40(6):2172–2176

Liu Y, Jun Y, Steinberg V (2009) Concentration dependence of the longest relaxation times of dilute and semi-dilute polymer solutions. J Rheol (1978-present), 53(5):1069–1085

Lumley JL (1965) Interpretation of time spectra measured in high-intensity shear flows. Phys Fluids 8(6):1056–1062

Lumley JL (1969) Drag reduction by additives. Annu Rev Fluid Mech 1(1):367–384

Magda JJ, Larson RG (1988) A transition occurring in ideal elastic liquids during shear flow. J Non Newton Fluid Mech 30(1):1–19

Mao H, Cremer PS, Manson MD (2003) A sensitive, versatile microfluidic assay for bacterial chemotaxis. Proc Natl Acad Sci 100(9):5449–5454

McKinley GH, Pakdel P, Öztekin A (1996) Rheological and geometric scaling of purely elastic flow instabilities. J Non Newton Fluid Mech 67:19–47

Morozov AN, van Saarloos W (2007) An introductory essay on subcritical instabilities and the transition to turbulence in visco-elastic parallel shear flows. Phys Rep 447(3–6):112–143

Mota JPB, Rodrigo AJS, Saatdjian E (2007) Optimization of heat-transfer rate into time-periodic two-dimensional stokes flows. Int J Numer Methods Fluids 53(6):915–931

Muller SJ, Larson RG, Shaqfeh ESG (1989) A purely elastic transition in Taylor-Couette flow. Rheol Acta 28(6):499–503

Narasimha A, Mihir S, Chang H-C (1992) Heat transfer enhancement in coiled tubes by chaotic mixing. Int J Heat Mass Trans 35(10):2475–2489

Oddy MH, Santiago JG, Mikkelsen JC (2001) Electrokinetic instability micromixing. Anal Chem 73(24):5822–5832

Ogilvie GI, Proctor MRE (2003) On the relation between viscoelastic and magnetohydrodynamic flows and their instabilities. J Fluid Mech 476:389–409

Ottino JM (1989) The kinematics of mixing: stretching, chaos, and transport. Cambridge University Press

Paladin G, Vulpiani A (1987) Anomalous scaling laws in multifractal objects. Phys Rep 156(4):147–225

Raffel M, Willert CE, Wereley ST, Kompenhans J (2007) Particle image velocimetry: a practical guide (Experimental Fluid Mechanics), 2nd edn. Springer

Scarano F, Rhiethmuller ML (2001) Advances in iterative multigrid PIV image processing. Exp Fluids 29:S051–S060

Schroeder CM, Babcock HP, Shaqfeh ESG, Chu S (2003) Observation of polymer conformation hysteresis in extensional flow. Science 301(5639):1515–1519

Shraiman BI, Siggia ED (1994) Lagrangian path integrals and fluctuations in random flow. Phys Rev E 49:2912–2927

Shraiman BI, Siggia ED (2000) Scalar turbulence. Nature 405(6787):639–646

Son DT (1999) Turbulent decay of a passive scalar in the batchelor limit: Exact results from a quantum-mechanical approach. Phys Rev E 59:R3811–R3814

Stroock AD, Dertinger SKW, Ajdari A, Mezić I, Stone HA, Whitesides GM (2002) Chaotic mixer for microchannels. Science 295(5555):647–651

Sureshkumar R, Beris AN, Avgousti M (1994) Non-axisymmetric subcritical bifurcations in viscoelastic taylor-couette flow. Proc R Soc Lond A Math Phys Eng Sci 447(1929):135–153

Takayama S, Ostuni E, LeDuc P, Naruse K, Ingber DE, Whitesides GM (2001) Subcellular positioning of small molecules. Nature 411:1016

Tanner RI (1970) A theory of die-swell. J Polym Sci Part A-2 Polym Phys 8(12):2067–2078

Taylor GI (1938) The spectrum of turbulence. Proc R Soc Lond A Math Phys Eng Sci 164(919):476–490

Therriault D, White SR, Lewis JA (2003) Chaotic mixing in three-dimensional microvascular networks fabricated by direct-write assembly. Nat Mater 2:265–271

Toms BA (1949) Proceedings of the international conference on rheology. North Holland, Amsterdam, pp II.135–II.141

Torricelli E (1644) Opera geometrica

Toussaint V, Carriere P, Raynal F (1995) A numerical Eulerian approach to mixing by chaotic advaection. Phys Fluids 7(11):2587–2600

Toussaint V, Carriere P, Scott J, Gence JN (2000) Spectral decay of a passive scalar in chaotic mixing. Phys Fluids 12(11):2834–2844

Traore B, Castelain C, Burghelea T (2015) Efficient heat transfer in a regime of elastic turbulence. J Non Newton Fluid Mech 223:62–76

Tsai J-H, Lin L (2002) Active microfluidic mixer and gas bubble filter driven by thermal bubble micropump. Sens Actuators A Phys 97-98:665–671. Selected papers from Eurosenors XV

Vijayendran RA, Motsegood KM, Beebe DJ, Leckband DE (2003) Evaluation of a three-dimensional micromixer in a surface-based biosensor. Langmuir 19(5):1824–1828

Vinogradov GV, Manin VN (1965) An experimental study of elastic turbulence. Kolloid-Zeitschrift und Zeitschrift für Polymere 201(2):93–98

Virk PS, Wagger DL (1990) Aspects of mechanisms in type B drag reduction. In: Gyr A (ed) Structure of turbulence and drag reduction. Springer, Berlin, pp 201–213

Warhaft Z (2000) Passive scalars in turbulent flows. Ann Rev Fluid Mech 32(1):203–240

Weissenberg K (1947) A continuum theory of rheological phenomena. Nature 159(4035):310–311

Yarin AL (1997) On the mechanism of turbulent drag reduction in dilute polymer solutions: dynamics of vortex filaments. J Non Newton Fluid Mech 69(2):137–153

Zaman KBMQ, Hussain AKMF (1981) Taylor hypothesis and large-scale coherent structures. J Fluid Mech 112:379–396

Zilz J, Poo RJ, Alves MA, Bartolo D, Levaché B, Lindner A (2012) Geometric scaling of a purely elastic flow instability in serpentine channels. J Fluid Mech 712:203–218

Transport Phenomena in Viscoplastic Materials

Teodor Burghelea

Abstract This chapter focuses on various transport phenomena in yield stress materials. After a brief introduction, an overview of the phenomenology of the solid–fluid transition is given in Sect. 2. Section 3 introduces a microscopic theory able to describe the solid–fluid transition in both thixotropic and non-thixotropic yield stress materials. A discussion of the hydrodynamic stability of yield stress materials is presented in Sect. 4. Some non-isothermal transport phenomena are discussed in Sect. 5.

1 Introduction

A broad class of materials exhibits a dual response when subjected to an external stress. For low applied stresses, they behave as solids (loosely speaking they may deform but they do not flow) but, if the stress exceeds a critical threshold generally referred to as the "*yield stress*", they behave as fluids (typically non-Newtonian) and a macroscopic flow is observed. This distinct class of materials has been termed as "*yield stress materials*" and, during the past several decades, it attracted a constantly increasing level of interest from both theoreticians and experimentalists. The motivation behind this issue is twofold. From a practical standpoint, such materials have found a significant number of applications in several industries (which include food, cosmetical, pharmaceutical, oil field engineering, etc.) and they are encountered in daily life in various forms such as food pastes, hair gels and emulsions, cement, mud, etc. More recently, hydrogels which exhibit a yield stress have found a number of future promising applications including targeted drug delivery (Jeong et al. 1997; Qiu and Park 2001), contact lenses, noninvasive intervertebral disc repair (Hou et al. 2004) and tissue engineering (Beck et al. 2007).

From a fundamental standpoint, yield stress materials continue triggering intensive debates and posing difficult challenges to both theoreticians and experimentalists

T. Burghelea (✉)

Laboratoire Thermique et Energie, University of Nantes, Nantes, France
e-mail: Teodor.Burghelea@univ-nantes.fr

from various communities: soft matter physics, rheology, physical chemistry and applied mathematics. The progress in understanding the flow behaviour of yield stress materials made the object of several review papers (Nguyen and Boger 1992; Coussot 2014; Balmforth et al. 2014; Bonn et al. 2017). The best known debate concerning the yield stress materials is undoubtedly that related to the very existence of a "true" yield stress behaviour (Barnes 1999; Barnes and Walters 1985). During the past two decades, however, a number of technical improvements of the rheometric equipment made possible measurements of torques as small as 0.1 n Nm and of rates of deformation as small as $10^{-7} \, s^{-1}$). Such accurate rheological measurements proved unequivocally the existence of a true yielding behaviour (Putz and Burghelea 2009; Bonn and Denn 2009; Denn and Bonn 2011). The physics of the yielding process itself on the other hand remains elusive. The macroscopic response of yield stress fluids subjected to an external stress, σ, has been classically described by the Herschel–Bulkley model (Herschel and Bulkley 1926a, b):

$$\sigma = \sigma_y + K\dot{\gamma}^N. \tag{1}$$

Here, σ_y is the yield stress, $\dot{\gamma}$ is the rate of shear, i.e. the rate at which the material is being deformed, σ is the macroscopically applied stress (the external forcing parameter), K is a so-called consistency parameter that sets the viscosity scale in the flowing state and N is the power law index which characterises the degree of shear thinning of the viscosity beyond the yield point.

In spite of its wide use by rheologists, fluid dynamicists and engineers, the Herschel–Bulkley model (and its regularised variants, e.g. Papanastasiou 1987) is in fact applicable only for a limited number of yield stress materials, sufficiently far from the solid–fluid transition, i.e. when $\sigma > \sigma_y$, and in the conditions of a steady-state forcing, i.e. when a constant external stress σ is applied over a long period of time. The behaviour of a large number of the yield stress materials encountered in daily life applications cannot be accurately described by the simple Herschel–Bulkley model. This fact has initiated the "*quest*" for a "*model*" yield stress fluid.

A "*model*" yield stress material should fulfil a number of quite restrictive conditions:

1. As the externally applied stresses are gradually increased, a solid–fluid transition occurs at a well-defined value of the applied stress, $\sigma = \sigma_y$.
2. Past the yield point the relationship between the applied stress σ and the macroscopic rate of shear $\dot{\gamma}$ follows faithfully the Herschel–Bulkley model described by Eq. (1).
3. The solid–fluid transition is reversible upon increasing/decreasing forcing, that is, no thixotropic effects are present.

For nearly two decades, aqueous solution of Carbopol® has been chosen as the best candidates as "*model*" yield stress materials (Curran et al. 2002; Ovarlez et al. 2013). Carbopol® is the generic trade name of an entire family of cross-linked polyacrylic acids with the generic chemical structure $H - A$. Upon dissolution in water, the polyacrylic acid dissociates as $H - A \Longleftrightarrow H^+ + A^-$, resulting in a mixture

with $pH \approx 3$. Upon neutralisation with an appropriate basic solution (e.g. a sodium hydroxide solution, NaOH) the micro-gel particles swell up to 2000 times and a physical gel is obtained. The Carbopol gels are optically transparent, chemically stable over long periods of time which makes them ideal candidates for experimental studies.

To illustrate the limitations of the classical Herschel–Bulkley picture in accurately describing the solid–fluid transition even in the case of a Carbopol® gel, we discuss below several experimental observations performed in kinematically "*simple*" flows of aqueous solutions of Carbopol® that are at odds with the picture of a "*model*" yield stress fluid.

1.1 Sedimentation of a Spherical Object in an Elasto-Viscoplastic Material (Carbopol® 940)

The first experimental observation relates to the flow patterns around a spherical object freely falling in an aqueous solution of Carbopol® 940 discussed in detail by Putz et al. (2008).

The experiment consisted of measuring time series of the velocity fields around a sphere freely falling in a container filled with a Carbopol® solution via digital particle image velocimetry (DPIV). To test the reliability of the method, flow fields were first measured in a Newtonian fluid (an aqueous solution of Glycerol), as shown in Fig. 1a. As the Reynolds numbers (calculated using the size and the terminal speed of the spherical object) did not exceed unity, a perfect fore-aft symmetry of the flow pattern is observed and a quantitative agreement with the analytical solution (Landau and Lifschitz 1987) is found, which fully confirms the reliability of both the experimental procedure and data analysis technique.

For several cases involving different Carbopol® solutions and different sizes of the spherical object, however, the flow patterns are strikingly different though the Reynolds number was kept in the same range, as shown in Fig. 1b. As compared to Newtonian flow patterns, two distinct features may be observed:

1. For each of the cases illustrated in Fig. 1b, the fore-aft symmetry of the flow patterns is broken in spite of the laminar character of the flow.
2. For each of the cases illustrated in Fig. 1b, a negative wake manifested through a reversal of the flow direction is clearly visible.

None of these distinctive features can be understood in the classical Bingham/ Herschel–Bulkley frameworks. Numerical simulations using either the Bingham or the Herschel–Bulkley constitutive equations predict fore-aft symmetry of the flow pattern (Beris et al. 1985; Fraggedakis et al. 2016). The second feature is even more intriguing as the negative wake phenomenon has been observed in strongly elastic shear-thinning solutions with no yield stress (Arigo and McKinley 1998).

We have proposed the following phenomenological explanations (Putz et al. 2008). Bearing in mind that the material in the fore region of the object is

Fig. 1 Experimentally measured flow field around a sphere freely falling in a Newtonian fluid (glycerol) at $Re < 1$ (1a). Experimentally measured flow fields around a sphere freely falling in Carbopol® solutions at $Re < 1$ (1b). The radii of the spheres and the yield stresses of the solutions in each panel are (1)—$R = 3.2$ mm, $\sigma_y = 0.5$ Pa, (2)—$R = 1.95$ mm, $\sigma_y = 0.5$ Pa, (3)—$R = 3.2$ mm, $\sigma_y = 1.4$ Pa, (4)—$R = 1.95$ mm, $\sigma_y = 1.4$ Pa. The colour maps in all panels refer to the modulus of velocity and the full lines are streamlines. The acceleration of gravity is oriented from right to left
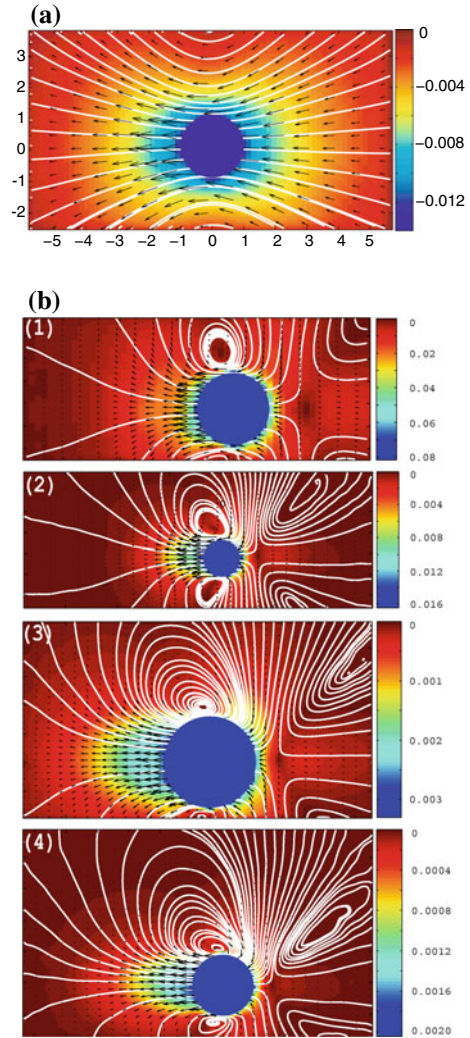
subjected to a forcing that gradually increases past the solid–fluid transition and the aft region is subjected to a forcing that gradually decreases past the fluid–solid transition, we have conjectured that the solid–fluid transition is not reversible upon increasing/decreasing stresses. As the emergence of the negative wake is concerned, we have conjectured that, around the solid–fluid transition, the elastic effects are dominant which, in conjunction with the curvature of the streamlines, leads to the emergence of a first normal stress difference that ultimately causes a "*flow reversal*" or negative wake. Although quite debated for nearly a decade by part of the viscoplastic community, these phenomenological explanations have been confirmed by the recent numerical simulations (Fraggedakis et al. 2016).

1.2 The Landau–Levich Experiment with an Elasto-Viscoplastic Material (Carbopol® 980)

A second and equally simple experiment one can perform is to withdraw a vertical plate at a constant speed U from a bath filled with a Carbopol® gel. This is referred to in the literature as the "Landau–Levich" problem (Landau and Levich 1972). An instantaneous flow field measured using DPIV is exemplified in Fig. 2. Similar to the case of the sedimentation experiment previously illustrated, a negative wake is clearly visible behind the moving plate. As in the previous case, the material located in the wake region of the flow is subjected to a decreasing stress and gradually transits from a fluid state to a solid one. The emergence of a negative wake is once again associated to the presence of elasticity.

1.3 The Solid–Fluid Transition in a Carbopol® Gel Revisited

The "*simple flows*" examples presented above bear two common features:

1. The material is subjected to an external forcing (stress) around the solid–fluid transition.
2. The material is forced in an unsteady manner. By this, we mean that the stress locally applied changes with a characteristic time t_0 set by the characteristic scale of the speed U and a characteristic space scale L by $t_0 = L/U$. In the case of the

Fig. 2 The Landau–Levich flow problem: instantaneous flow field around a rigid plate being withdrawn at constant speed from a bath filled with a Carbopol® gel
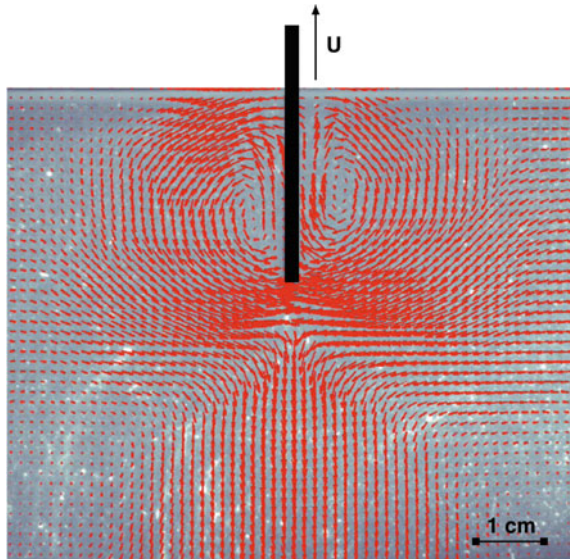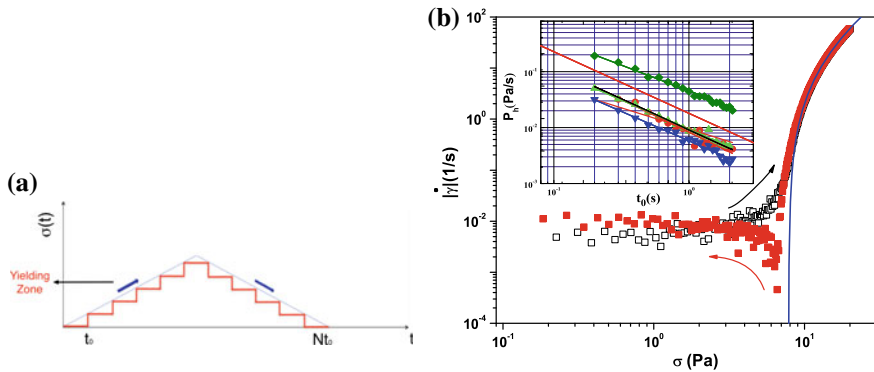
Fig. 3 **a** Schematic illustration of the controlled stress flow ramp. **b** Rheological flow curve measured via the controlled stress ramp illustrated in (**a**) for a 0.1% (wt) solution of Carbopol® 940. The full line is a nonlinear fitting functions according to the Herschel–Bulkley model. The full/empty symbols refer to the increasing/decreasing branches of the stress ramp schematically illustrated in (**a**). The inset presents the dependence of the hysteresis area on the characteristic forcing time t_0. The full line in the inset is a guide for the eye $P_h \propto t_0^{-1}$

sedimentation problem, L is just the size of the spherical object $L = R$ and U is its terminal speed which, for the experiments illustrated in Fig. 1b, give $t_0 < 1s$.

The points above prompted us to revisit the macroscopic solid–fluid transition. The solid–fluid transition may be investigated during macroscopic rheological experiments by subjecting the material to a controlled stress ramp and monitoring its response (the rate of shear $\dot{\gamma}$). Prior to yielding negligibly, small shear rates are measured whereas above the yield point non-zero values are recorded which allows one to "*guess*" the yield point. We have implemented a rheological protocol that "*mimics*" an unsteady forcing rather than following the rheological "*golden rule*" of imposing a steady-state forcing ($t_0 \to \infty$).

In Fig. 3b, we illustrate such measurements performed on a controlled stress rheometer (Mars III from Thermo Fischer Scientific) equipped with a serrated plate–plate geometry with a 0.1% (wt) solution of Carbopol® 940 by using the forcing scheme illustrated in Fig. 3a with $t_0 = 0.5$ s. As opposed to previous measurements by others that seemed to indicate that the Carbopol® gels are "*model*" or "*ideal*" yield stress fluids—i.e. free of thixotropic effects and with a rheological behaviour well described by the Herschel–Bulkley constitutive law—the data presented in Fig. 3b reveals the following features of the solid–fluid transition:

1. The solid–fluid transition is not direct (does not occur at a well-defined value of the applied stress $\sigma = \sigma_y$) but gradual and spanning a finite interval of the applied stresses.
2. The Herschel–Bulkley law describes well the rheometric response only in a range of large applied stresses, the full line in Fig. 3b.

3. The data corresponding to the increasing/decreasing branches of the controlled stress ramps overlap *only* far above the solid–fluid transition. Additionally, a cusp visible on the decreasing stress branch is visible. At this point, the rate of shear $\dot{\gamma}$ changes sign which indicates an elastic recoil effect typically observed with viscoelastic fluids. This feature has not been reported before and may phenomenologically explain the emergence of a negative wake in Figs. 2, 1b.

4. The degree of the irreversibility of the deformation states upon increasing/decreasing forcing quantitatively described by the area of the hysteresis visible in Fig. 3b scales as a power law with the degree of steadiness of the controlled stress ramp t_0—see the inset in Fig. 3b.

A natural question arises at this point: *How universal is the irreversible flow behaviour observed with a* Carbopol® *gel?* To answer this question, we present in Fig. 4 controlled rheological stress ramps performed with three microstructurally distinct yield stress materials: a commercially available mayonnaise, a commercially
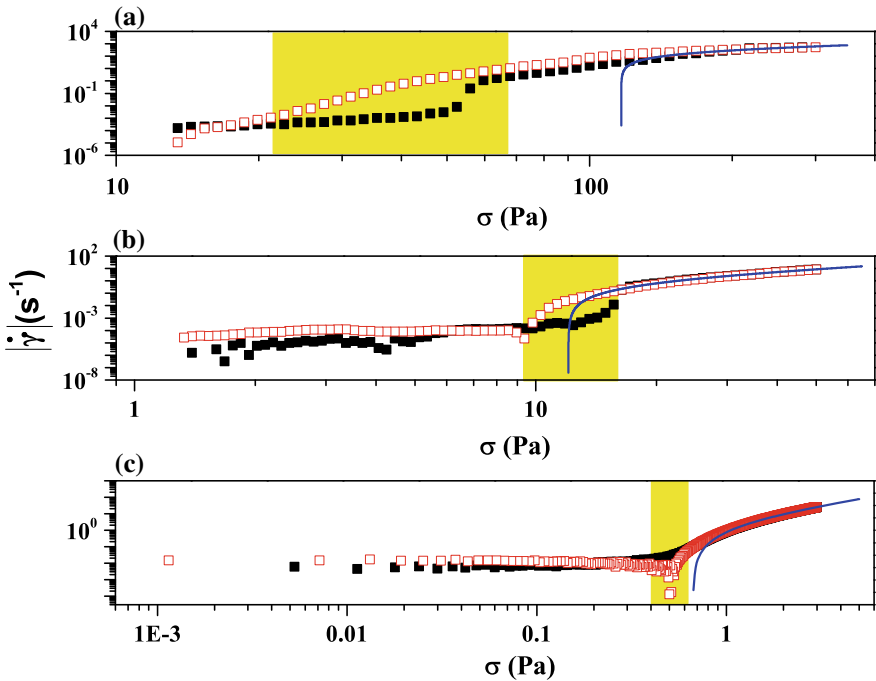
Fig. 4 Rheological flow curves measured via controlled stress ramps for various materials: **a** mayonnaise (Carrefour, France) **b** mustard (Carrefour, France) **c** 0.08% (wt) aqueous solution of Carbopol® 980. For each stress value, the response of the material was averaged during $t_0 = 10$ s. The range of applied stresses corresponding to the yielding transition is highlighted in each subplot. The full lines are nonlinear fitting functions according to the Herschel–Bulkley model. The full/empty symbols in each panel refer to the increasing/decreasing branches of the stress ramp schematically illustrated in Fig. 3a

available mustard and a different type of Carbopol® gel (Carbopol® 980). Each of
these rheological tests reveals a gradual solid–fluid transition characterised by a more
or less pronounced hysteresis that departs from the Herschel–Bulkley constitutive
relation. This indicates that, irrespective to the chemical identity of the material, the
solid–fluid transition follows a rather universal scenario. It is equally interesting to
monitor how the magnitude of the hysteresis depends on the degree of steadiness of
the external forcing—the time t_0 the stress is maintained constant during the stress
ramp (see Fig. 3a).

We present in Fig. 5 the dependence of the magnitude of the rheological hysteresis
on the characteristic time t_0 for each of the materials characterised in Fig. 4.

For the case of mayonnaise and mustard (the circles and the squares in Fig. 5), a
non-monotonic dependence of the magnitude of the hysteresis on the characteristic
forcing time t_0 is observed. Corresponding to low values of t_0 (fast forcing), the hys-
teresis area first increases and then, for large values of t_0 (slow forcing), decreases
following a power law. This non-monotone behaviour agrees well with the mea-
surements of Divoux and his coworkers performed for several yield stress materials:
mayonnaise, Laponite gel and carbon black gel (Divoux et al. 2013). As pointed
out by Divoux et al. (2013), these non-monotone dependencies may be fitted by a
log-normal function (the dashed lines in Fig. 5). The presence of a local maximum
of these curves has been attributed to the existence of a critical timescale $t_0^\star$ specific
to each material which describes the restructuration dynamics of the solid material
units.

It has been shown recently that a clear departure from the Herschel–Bulkley
behaviour can be observed even for "*simple*" yield stress fluids such as the Carbopol®
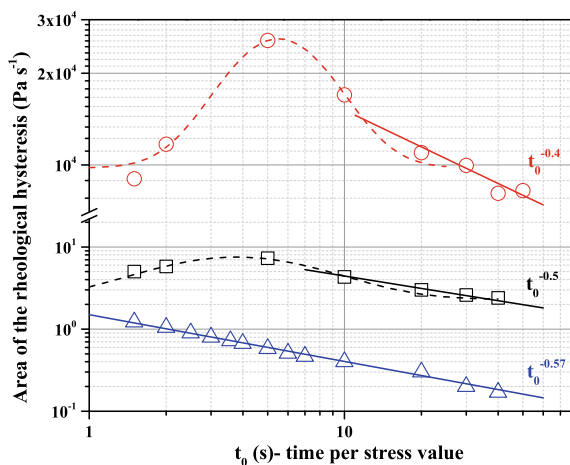
Fig. 5 Dependence of the hysteresis area on the characteristic forcing time t_0 (see text for descrip-
tion) measured with several yield stress materials via controlled stress flow ramps: circle (○)—
mayonnaise (Carrefour, France), square (□)—mustard (Carrefour, France), up triangle (△)—0.08%
(wt) aqueous solution of Carbopol® 980. The dashed lines are log-normal fitting functions (see text
for the discussion); the full lines are power law fitting functions indicated in the inserts

gels particularly during unsteady flows taking place around the yield point (Putz and Burghelea 2009; Weber et al. 2012; Divoux et al. 2013; Poumaere et al. 2014). The yielding behaviour of a Carbopol® gel is illustrated here in Fig. 3b and in panel (c) of Fig. 4. As compared to the mayonnaise and the mustard, no local maximum was observed in the dependence of the hysteresis area on the characteristic forcing time but a negative power law scaling which indicates that in the limit of very slow forcing (large t_0) the Carbopol® gels behave as non-thixotropic yield stress fluids.

2 Phenomenological Modelling of the Solid–Fluid Transition in an Elasto-Viscoplastic Material

As argued in the previous section, the simple Herschel–Bulkley picture cannot accurately describe the solid–fluid transition even in the case when the time-dependent effect (thixotropy) are not very pronounced, e.g. for the case of a Carbopol® gel. This prompted the development of more sophisticated phenomenological models. It is widely believed that the macroscopic yield stress behaviour originates from the presence of a microstructure which can sustain a finite local stress prior to breaking apart and allowing for a macroscopic flow to set in. To illustrate this, we present in Fig. 6 micrographs (acquired in a quiescent state) of several materials that exhibit a yield stress behaviour. In spite of clear differences in the chemical nature (and, consequently, physico-chemical properties) of these materials, heterogeneous and soft-solid-like aggregates are visible in each of the micrographs presented in Fig. 6. A microscopic experimental study of the yielding would require monitoring in real time both the motion of such aggregates and the dynamics of their break-up (and, possibly, reforming) during flow. This experimental approach is difficult to implement, and we are aware of very few previous works that describe the evolution of the microstructure during yielding (Dimitriou and McKinley 2014). Although the structural heterogeneity and the characteristic space scales of a Carbopol® gel are quite clearly probed by diffusion experiments (Oppong et al. 2006; Oppong and de Bruyn 2007), a detailed experimental description of the Carbopol® microstructure is still missing. This is mainly due to practical difficulties in visualising the microstructure without altering it Piau (2007). We present in the following a minimalistic model that uses no explicit microstructural assumption but is yet able to describe both shear and oscillation rheological experiments. As previously suggested by several authors (Möller et al. 2006; Dullaert and Mewis 2006), the fluidisation process of a physical gel sample under shear can be interpreted in terms of a "*dissociation*" reaction, $\mathbf{S} \rightleftharpoons \mathbf{S} + \mathbf{F}$ which can be modelled by the following kinetic equation:

$$\frac{d\bar{a}(t)}{dt} = R_d\left[\bar{a}(t), t, \Gamma\right] + R_r\left[\bar{a}(t), t, \Gamma\right] + \delta, \tag{2}$$

where S, F denote the solid and fluid phases, respectively, $\bar{a}(t) = [S]$ is the concentration of the solid phase, $\Gamma = \frac{\sigma}{\sigma_y}$ is the non-dimensional forcing parameter, R_d is
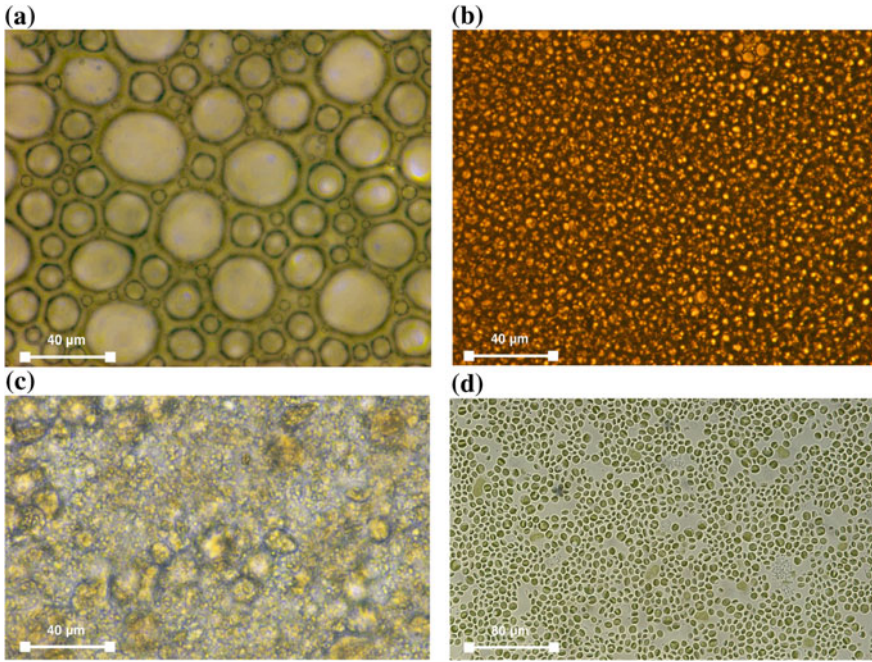
Fig. 6 Micrographs of several yield stress materials: **a** commercial shaving gel (Gillette Series) **b** mayonnaise (Carrefour, France) **c** 5% bentonite in water **d** suspension of Chlorella Vulgaris unicellular microalga (reproduced from Souliès et al. 2013)

the rate of destruction of solid units, R_r is the rate of fluid recombination of fluid elements into a gelled structure and δ is a small thermal noise term.

The exact form of the terms R_r and R_d is usually chosen on an intuitive basis: the destruction of solid structural units increases monotonically with increasing applied forcing, whereas the recombination probability may be even constant or monotonically decreasing with increasing forcing.

One of the simplest choices of a microstructural equation was introduced by Coussot and coworkers (Coussot et al. 2002a).

It considers an evolution equation for a microstructural parameter λ in the following form:

$$\frac{d\bar{a}}{dt} = \frac{1}{\tau} - \alpha\dot{\gamma}\bar{a}, \tag{3}$$

where τ is a characteristic timescale of the aggregation of microstructural units and α is a positive constant related to role of the external shear in destroying the solid structural units. Furthermore, the model considers a viscosity function that depends on the microstructure in the following form:

$$\eta = \eta_0 \left(1 + \bar{a}^n \right), \tag{4}$$

where η_0 is a constant asymptotic viscosity when the microstructure is entirely destroyed, $\eta_0 = \lim_{\bar{a} \to 0} \eta(\bar{a})$.

The parameter $\bar{a}$ can be loosely defined as the degree of flocculation for clays, a measure of the free energy landscape for glasses or as the fraction of particles in potential wells for colloidal suspensions (Coussot et al. 2002a). An obvious difficulty of this microstructural approach relates to the fact that the parameter $\bar{a}$ is not easily accessible experimentally and, consequently, a direct comparison with rheometric measurements remains elusive (Coussot 2007).

Due to its simplicity and formal elegance, this model is quite appealing to both physicists and rheologists.

In a recent publication, it has been claimed that this simple microstructural model is able to accurately fit rheological flow curves measured during a controlled stress ramp (Dinkgreve et al. 2018)—see Fig. 7 therein. This result is highly questionable. Even if one neglects the emergence of a hysteresis of the deformation states illustrated in Fig. 3, far above the yield point Carbopol® gels are shear-thinning fluids. On the other hand, in a fluid state ($\bar{a} \to 0$) the above-mentioned model predicts a constant viscosity η_0 according to Eq. (4). This is at odds with any rheological tests performed with Carbopol® gels we are aware of. As a cautionary note to the reader, we point out that in spite of their appeal, phenomenological models that are too simple may be deceptive when compared to experimental results.

We present in the following a minimalistic phenomenological model able to describe the main features of the solid–fluid transition of a Carbopol® gel subjected to stress (Putz and Burghelea 2009; Moyers-Gonzalez et al. 2011b).

We make the following assumptions concerning the terms R_r and R_d involved in the microstructural equation Eq. (2):

1. $R_d(\bar{a}(t), t, \dot{\gamma})$ is proportional to the relative speed of neighbouring solid units and the existing amount of solid, i.e. $R_d(\bar{a}(t), t, \dot{\gamma}) = -g(\Gamma)\bar{a}(t)$ and $g(\Gamma) = K_1|\Gamma|$ is a linear amplitude of shear-induced destruction.
2. Unlike in solutions of micelles or suspensions, where the external shear may induce aggregation (Goveas and Olmsted 2001; Heymann and Aksel 2007), in the case of a physical gel the rate of fluid recombination decreases with the relative speed of neighbouring fluid elements being practically zero in a fast enough flow. Therefore, we consider $R_r(\bar{a}(t), t, \Gamma) = f(\Gamma)\bar{a}(t)(1 - \bar{a}(t))$, where $f(\Gamma) = K_r \left[1 - \tanh\left(\frac{\Gamma - 1}{w} \right) \right]$ is a smooth decaying function of the applied forcing. Here, we have considered that recombination of the gel network takes place via binding of single polymer molecules to already existing solid blobs. Although we are not aware of any theoretical prediction in this sense, different recombination schemes (**S + S→ S, L + L→ S, S + S + L→ S**, etc.) are in principle possible and we note here that they actually lead to a qualitatively similar behaviour of the phase parameter $\bar{a}(t)$.

With the assumptions above, the kinetic Eq. 2 may be written as

$$\frac{d\bar{a}}{dt} = -K_d \Gamma \bar{a} + K_r \left[1 - \tanh\left(\frac{\Gamma - 1}{w}\right) \right] \bar{a}(1 - \bar{a}) + \delta. \tag{5}$$

We would like to point out that a constant recombination term as previously employed by several authors (Möller et al. 2006; Roussel et al. 2004) seems to us somewhat unphysical in this context. Precisely, if one solves the phase equation (Eq. 5) with a constant recombination term and a forcing parameter linearly increasing with time, $\Gamma \propto t$, one obtains a non-monotone dependence $\bar{a} = \bar{a}(t)$ which we consider to be unrealistic for a Carbopol® gel as it will further imply a non-monotone stress rate of strain dependence.

The phase equation admits two steady-state solutions:

$$\bar{a}_{SS1} = \begin{cases} 1 - \frac{g}{f} & , g < f \\ 0 & \text{otherwise} \end{cases} , \text{ stable} \tag{6}$$

and

$$\bar{a}_{SS2} = \begin{cases} 1 - \frac{g}{f} & , g \geq f \\ 0 & \text{otherwise} \end{cases} , \text{ unstable.} \tag{7}$$

It can be easily noted that the first steady state $\bar{a}_{SS1}$ is stable, whereas $\bar{a}_{SS2}$ is unstable and their separation is insured by the small parameter δ.

As a constitutive equation, we use a thixoelastic Maxwell (**TEM**)-type model (Quemada 1998a, b, 1999):

$$\frac{\eta(\dot{\gamma})}{G} \bar{a} \frac{d\sigma}{dt} + \sigma = \eta(\dot{\gamma})\dot{\gamma}, \tag{8}$$

where the viscosity is given by a regularised Herschel–Bulkley model, $\eta = K (\epsilon + |\dot{\gamma}|)^{N-1} + \frac{\sigma_y}{\epsilon + |\dot{\gamma}|}$. Here, G is the static elastic modulus, K is the consistency, N is the power law index and ϵ is the regularisation parameter (typically of order of 10^{-12}). A detailed discussion of several regularisation techniques is presented by Frigaard and Nouar (2005).

The choice of this constitutive equation is motivated by the presence of elastic effects in the intermediate deformation regime (see the cusp in decreasing stress branch in Figs. 3b and 4c, and the corresponding discussion). It is easy to note that in the limit $\bar{a} \to 1$, Eq. (8) reduces to Hooke's law, $G = \sigma\gamma$, and in the limit $\bar{a} \to 0$ it reduces to a regularised Herschel–Bulkley model.

A nonlinear fit of the controlled stress ramp presented in Fig. 3b is presented in Fig. 7a (the full line). Quite remarkably, without any other adjustment of the fit parameters, the model is able to fit controlled stress oscillatory tests performed with the same material (Fig. 7b) and the corresponding Lissajoux figure (Fig. 7c).

A central conclusion of this part is that the usage of an evolution equation that describes a smooth change of a microstructural parameter $\bar{a}$ coupled to a constitutive equation that contains information on both the viscous and the elastic behaviours suffices to describe rheological measurements.
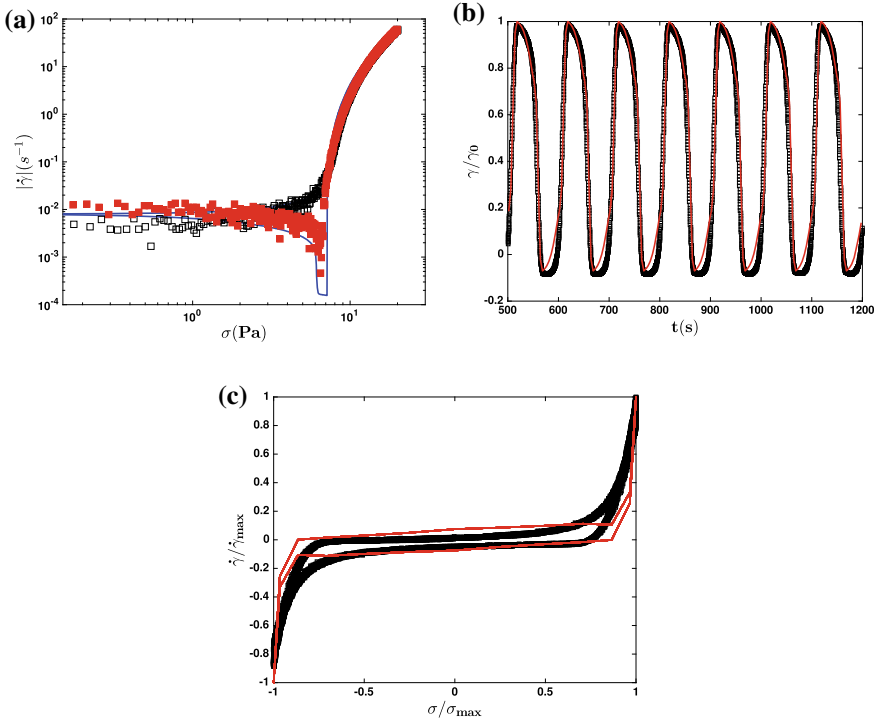
Fig. 7 **a** Rheological flow curve measured via the controlled stress ramp illustrated in Fig. 3a for a 0.1% (wt) solution of Carbopol 940. The full/empty symbols refer to the increasing/decreasing branches of the stress ramp schematically illustrated in Fig. 3a. **b**. Normalised strain measured during a controlled stress oscillatory sweep. **c** Lissajoux figure corresponding to the controlled stress oscillatory sweep. The full line in each panel is the prediction of the model

Though able to model sufficiently complex rheological data (ranging from controlled stress/strain unsteady flow ramps, creep tests and oscillatory tests in a wide range of frequencies and amplitudes), the phenomenological model has a number of limitations:

1. As the functional dependence of the microstructural parameter Eq. (5) is generally chosen on an intuitive basis rather derived from first principles, the model by Putz and Burghelea (2009) can teach little about the microscopic-scale physics of the yielding process.
2. The model involves a rather large number of parameters some of which are not directly and easily measurable and can be obtained only by fitting the experimental data, e.g. K_r, K_d, w.
3. The model is not inherently validated from a thermodynamical standpoint as the choice of R_d, R_r is not made based on first principles. The second law of thermodynamics is not necessarily satisfied and such a validation is not always

straightforward as it requires the derivation of a thermodynamic potential (Picard et al. 2002; Bautista et al. 2009; Hong et al. 2008).

To circumvent these limitations, we present in the next section a different and more fundamental approach for the yielding of a soft material subjected to a varying external stress based on principles of Statistical Physics and Critical Phenomena.

3   Microscopic Modelling for the Yielding of a Physical Gel as a Critical Phenomenon

For a detailed account of these theoretical developments, the reader is referred to two recent publications (Sainudiin et al. 2015b; Burghelea et al. 2017).

We propose in the following a microscopic model for the yielding or gelation, corresponding to $\overline{a}$ approaching 0 or 1, respectively, of a physical gel using an essentially bi-parametric family of a correlated site percolation that is inspired by the two-dimensional Ising model for the $+1$ or -1 magnetization of a ferromagnet (Ising 1925; Stanley 1987). Our model builds on the analogy between the local agglomerative interactions in terms of assembly/disassembly of neighbouring gel particles in a microscopic gel network (see Slomkowski et al. 2011, (2.5, 2.6, 5.9, 5.9.1, 5.9.1.1, 8.1.4) and Jones (2009) for standardised nomenclature subjected to an external stress and the local ferromagnetic interactions in terms of spin up $(+1)$/spin down (-1) of neighbouring particles in a microscopic ferromagnetic network subjected to an external magnetic field).

By the analogy with the Ising model for the ferromagnetism, we are placing the problem of yielding of a soft solid under stress in the more general context of "*Phase Transitions and Critical Phenomena*" and fully benefit from a number of theoretical tools developed during the past five decades for gaining physical insights into the solid–fluid transition.

This thermodynamically consistent microscopic model with only two parameters that reflect the chemical nature of the gel and only two energy-determining configuration statistics the number of gelled particles and the number of gelled pairs of neighbouring particles is able to capture the macroscopic behaviours of yielding and gelation for any stress regime given as a function of time, including hysteretic effects, if any. This approach is fundamentally probabilistic and formalises Gibbs fields as time-homogeneous and time-inhomogeneous Markov chains over the state space of all microscopic configurations. It not only provides simulation algorithms to gain insights but also allows one to derive an approximating nonlinear ordinary differential equation for $\overline{a}(t)$, the expected volume fraction of the unyielded material at a rescaled time t, which we show to be a robust qualitative determinant of the probabilistic dynamics of the system.

3.1 A Microscopic Gibbs Field Model for the Macroscopic Yielding of a Yield Stress Material

Let us model an idealised yield stress material or viscoplastic fluid as a network of microscopic constituents in an appropriate solvent that are capable of assembling by "forming bonds" or disassembling by "breaking bonds" with their neighbours. Without making any assumption about either the nature of the bonds or the physical nature of the interactions among neighbouring microscopic constituents, we investigate the model when the network of particles is the regular graph given by the toroidal two-dimensional square lattice as illustrated in Fig. 8 and the bonds/interactions are accounted for in a generic manner as detailed in the following.

Let the set of nodes or sites be

$$\mathbb{S}_n = \{1, 2, \ldots, n\}^2 = \{(1, 1), (1, 2), \ldots, \ldots, (n, n)\} .$$

Let $N_s = \{r : \|\overline{(r - s)}_n\| = 1\}$ denote the set of four nearest neighbouring sites of a given site $s \in \mathbb{S}_n$, where $\overline{(r - s)}_n$ denotes coordinate-wise subtraction modulo n and $\|\cdot\|$ denotes the Euclidean distance. Then the set of edges between pairs of sites is

$$\mathbb{E}_n = \bigcup_{s \in \mathbb{S}_n} \{\langle s, r \rangle : r \in N_s\} \subset \mathbb{S}_n^2 .$$

Let $|A|$ denote the size of the set A. Note that $|\mathbb{S}_n| = n^2$ and $|\mathbb{E}_n| = 2n^2$. Each site $s \in \mathbb{S}_n$ can be thought to represent a microscopic *clump* of particles in a particular region of the material and each edge $\langle s, r \rangle \in \mathbb{E}_n$ represents a potential *connection* between neighbouring clumps at sites s and r. At the finest resolution of the model, each site can be a monomer molecule in the material and each edge can represent a potential bond between neighbouring molecules. Let $x_s \in \Lambda = \{0, 1\}$ denote the
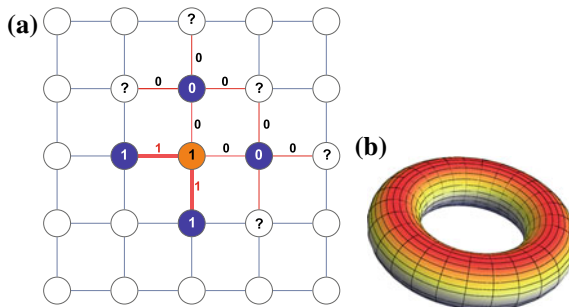
Fig. 8 **a** The regular graph represented for $n = 5$. The vertices labelled with $1/0$ represent micro-gel particles in a *unyielded/yielded* state, respectively. The labels $1/0$ of the edges indicate whether two sites are *connected/unconnected*. **b** $2D$ toroidal lattice suggesting the periodic boundary conditions used through the simulations

phase at site s. Phase 0 corresponds to being *yielded* or *un-gelled* and phase 1 corresponds to being *unyielded* or *gelled*. The phase at a site directly affects its *connectability* with its neighbouring sites. We assume that only two gelled sites can be connected with one another. Thus, the connectivity between sites s and r is given by

$$
y_{\langle s,r \rangle} = \begin{cases} 1 & \text{if } r \in N_s \text{ and } x_r x_s = 1 \\ 0 & \text{otherwise.} \end{cases} \tag{9}
$$

In other words, we say that sites s and r are *connected*, i.e. $y_{\langle s,r \rangle} = 1$, if and only if $x_s = x_r = 1$ and s and r are neighbours. Otherwise, we say s and r are *unconnected*, i.e. $y_{\langle s,r \rangle} = 0$. These definitions are schematically illustrated in Fig. 8a. Since the phase of sites determines their connectedness, we refer to sites in phase 1 as *connectable* and those in phase 0 as *un-connectable*. Thus, every site configuration $x \in \mathbb{X}_n := \Lambda^{\mathbb{S}_n}$ has an associated *edge configuration* $y \in \mathbb{Y}_n := \Lambda^{\mathbb{E}_n}$ which characterises the connectivity information between all pairs of neighbouring sites. We use X to denote a *random site configuration* and $Y = Y(X)$ to denote the associated *random edge configuration*. Two extreme site configurations are $\mathbf{1} := \{x_s = 1 : s \in \mathbb{S}_n\} \in \mathbb{X}_n$, with all sites gelled, and $\mathbf{0} := \{x_s = 0 : s \in \mathbb{S}_n\} \in \mathbb{X}_n$, with all sites un-gelled. Their corresponding extreme edge configurations are $\mathbf{1} := \{y_{\langle s,r \rangle} = 1 : \langle s, r \rangle \in \mathbb{E}_n\} \in \mathbb{Y}_n$, with all neighbouring pairs of sites connected, thus making the material to be in a fully solid state, and $\mathbf{0} := \{y_{\langle s,r \rangle} = 0 : \langle s, r \rangle \in \mathbb{E}_n\} \in \mathbb{Y}_n$, with all neighbouring pairs of sites unconnected, thus making the material to be in a fully fluid state, respectively. Note that $Y(x) : \mathbb{X}_n \to \mathbb{Y}_n$ is neither injective nor surjective.

Let $\mathcal{E}(x)$ be the energy of a site configuration x, k be the Boltzmann constant and T be the temperature. Then the probability distribution of interest on the site configuration space $\mathbb{X}_n$ is

$$
\pi(x) = \frac{1}{Z_{kT}} \exp\left(-\frac{1}{kT}\mathcal{E}(x) \right) ,
$$

where Z_{kT} is the normalising constant or partition function

$$
Z_{kT} = \sum_{x \in \mathbb{X}_n} \exp\left(-\frac{1}{kT}\mathcal{E}(x) \right) .
$$

By $X \sim \pi$, we mean that the random site configuration X has probability distribution π, i.e.

$$
\Pr(X = x) = \begin{cases} \pi(x) & \text{if } x \in \mathbb{X}_n \\ 0 & \text{otherwise .} \end{cases}
$$

Next we show that π is a Gibbs distribution by expressing the energy in terms of a potential function describing local interactions. Due to $\{N_s : s \in \mathbb{S}_n\}$, the neighbour-

hood system, we have only singleton and doubleton cliques. Therefore, the Gibbs potentials over the two types of cliques are

$$V_{\{s\}}(x) = (\sigma - \alpha)x_s = \begin{cases} 0 & \text{if } x_s = 0 \\ \sigma - \alpha & \text{if } x_s = 1 \end{cases},$$

and

$$V_{\langle s,r \rangle}(x) = -\beta x_s x_r = \begin{cases} 0 & \text{if } (x_s, x_r) = (0, 0) \\ 0 & \text{if } (x_s, x_r) = (1, 0) \\ 0 & \text{if } (x_s, x_r) = (0, 1) \\ -\beta & \text{if } (x_s, x_r) = (1, 1) \end{cases},$$

where $\{s\}$ is the singleton clique, $\langle s, r \rangle$ is the doubleton clique with $r \in N_s$, $\sigma \geq 0$ is the external stress applied, $\alpha \geq 0$ is the site-specific threshold, and $\beta \in (-\infty, \infty)$ is the *interaction constant* between neighbouring sites. The parameters α and β can be thought to reflect fundamental rheological properties of the material under study.

The energy function corresponding to this potential is therefore

$$\begin{aligned} \mathcal{E}(x) &= \sum_C V_C(x) \\ &= \sum_{s \in \mathbb{S}_n} V_{\{s\}}(x) + \sum_{\langle s,r \rangle \in \mathbb{E}_n} V_{\langle s,r \rangle}(x) \\ &= \left(-\beta \sum_{\langle s,r \rangle \in \mathbb{E}_n} x_s x_r + (\sigma - \alpha) \sum_{s \in \mathbb{S}_n} x_s \right). \end{aligned}$$

Since $\mathcal{E}(x)$, the energy of a configuration x, only depends on β and the difference $(\sigma - \alpha)$, we can define this difference as the parameter $\tilde{\sigma} := \sigma - \alpha \geq -\alpha$ in order to reparametrize

$$\mathcal{E}(x) = \left(-\beta \sum_{\langle s,r \rangle \in \mathbb{E}_n} x_s x_r + \tilde{\sigma} \sum_{s \in \mathbb{S}_n} x_s \right),$$

through $(\tilde{\sigma}, \beta) \in [-\alpha, \infty) \times (-\infty, \infty)$.

Let the expectation of a function $g : \mathbb{X}_n \to \mathbb{R}$, with respect to π, be

$$\mathbf{E}_\pi(g) := \sum_{x \in \mathbb{X}_n} g(x)\pi(x)$$

then the *internal energy* of the system is

$$\mathcal{U} = \mathbf{E}_\pi(\mathcal{E}) = \sum_{x \in \mathbb{X}_n} \mathcal{E}(x)\pi(x),$$

and the *free energy* of the system is

$$\mathcal{F} = -kT \ln(Z_{kT}) \ .$$

Our model satisfies the standard thermodynamic equality:

$$- T^2 \frac{\partial}{\partial T} \left(\frac{\mathcal{F}}{T} \right) = -T^2 \frac{\partial}{\partial T} \left(\frac{-kT \ln(Z_{kT})}{T} \right) = kT^2 \frac{\partial}{\partial T} (\ln(Z_{kT}))$$

$$= kT^2 \frac{1}{Z_{kT}} \frac{\partial}{\partial T} (Z_{kT}) = kT^2 \frac{1}{Z_{kT}} \frac{\partial}{\partial T} \left(\sum_{x \in \mathbb{X}_n} \exp \left(-\frac{1}{kT} \mathcal{E}(x) \right) \right)$$

$$= kT^2 \frac{1}{Z_{kT}} \left(\sum_{x \in \mathbb{X}_n} \exp \left(-\frac{1}{kT} \mathcal{E}(x) \right) \frac{\mathcal{E}(x)}{kT^2} \right) = \sum_{x \in \mathbb{X}_n} \mathcal{E}(x) \pi(x)$$

$$= \mathcal{U} \ .$$

We sometimes emphasise the dependence of the energy and the corresponding distribution upon α, β and σ by subscripting as follows:

$$\mathcal{E}(x) = \mathcal{E}_{\alpha,\beta,\sigma}(x) \quad \text{and} \quad \pi(x) = \pi_{\alpha,\beta,\sigma}(x) \ .$$

Let the number of neighbours of site s that are in phase 1 be $x_{N_s} := \sum_{r \in N_s} x_r$. Then, $\mathcal{E}_s(x)$, the *local energy* at site s of configuration x, is obtained by summing the Gibbs potential $V_C(x)$ over all $C \ni s$, i.e. over cliques C containing site s, as follows:

$$\mathcal{E}_s(x) = \sum_{C \ni s} V_C(x) = V_{\{s\}}(x) + \sum_{r \in N_s} V_{\langle s,r \rangle}(x)$$

$$= (\sigma - \alpha)x_s - \beta \sum_{r \in N_s} x_s x_r$$

$$= x_s \left((\sigma - \alpha) - \beta \sum_{r \in N_s} x_r \right)$$

$$= x_s \left((\sigma - \alpha) - \beta x_{N_s} \right) \ .$$

Let $(\lambda, x(\mathbb{S} \setminus s))$ denote the configuration that is in phase λ at s and identical to x everywhere else. Then the *local specification* is

$$\pi_s(x) = \frac{\exp(-\frac{1}{kT} \mathcal{E}_s(x))}{\sum_{\lambda \in \Lambda} \exp(-\frac{1}{kT} \mathcal{E}_s(\lambda, x(\mathbb{S} \setminus s)))}$$

$$= \begin{cases} \frac{\theta}{1+\theta} & \text{if } x_s = 0 \\ \frac{1}{1+\theta} & \text{if } x_s = 1 \end{cases} , \tag{10}$$

where

$$\theta = \theta(s, \alpha, \beta, \sigma) = \exp\left(-\frac{1}{kT}\left(\beta x_{N_s} - (\sigma - \alpha)\right)\right) . \tag{11}$$

We focus on the effect of varying external stress σ at a constant ambient temperature, and therefore without loss of generality, one may set $kT = 1$ and work with $\pi(x) = Z_1^{-1} \exp(-\mathcal{E}(x))$.

We can think of this model as an $\mathbb{X}_n$-valued Markov chain $\{X(m)\}_{m=0}^\infty$, where $X(m) = (X_s(m), s \in \mathbb{S}_n)$ and $X_s(m) \in \Lambda$, in discrete time $m \in \mathbb{Z}_+ := \{0, 1, 2, \ldots\}$. Let the initial condition, $X(0) = x(0)$, be given by the initial distribution $\delta_{x(0)}$ over $\mathbb{X}_n$ that is entirely concentrated at state $x(0)$. Then the conditional probability of the Markov chain at time step m, given that it starts at time 0 in state $x(0)$, is

$$\Pr\{X(m) \mid X(0) = x(0)\} = \delta_{x(0)}\left(P_{\alpha,\beta,\sigma}\right)^m , \tag{12}$$

where the $|\mathbb{X}_n| \times |\mathbb{X}_n|$ transition probability matrix $P_{\alpha,\beta,\sigma}$ over any pair of configurations $(x, x') \in \mathbb{X}_n \times \mathbb{X}_n$ is

$$P_{\alpha,\beta,\sigma}(x, x') = \begin{cases} \frac{1}{n^2}\frac{1}{1+\theta} & \text{if } ||x - x'|| = 1, 0 = x_s \neq x'_s = 1 \\ \frac{1}{n^2}\frac{\theta}{1+\theta} & \text{if } ||x - x'|| = 1, 1 = x_s \neq x'_s = 0 \\ \frac{1}{n^2}\frac{1}{1+\theta} & \text{if } ||x - x'|| = 0, 1 = x_s = x'_s = 1 \\ \frac{1}{n^2}\frac{\theta}{1+\theta} & \text{if } ||x - x'|| = 0, 0 = x_s = x'_s = 0 \\ 0 & \text{otherwise .} \end{cases} \tag{13}$$

$\theta = \theta(s, \alpha, \beta, \sigma)$ is indeed a function of the site s and the three parameters: α, β and σ. By $||x - x'|| = 1$, we mean that the configurations x and x' differ at exactly site s, i.e. $x_s \neq x'_s$. Similarly, by $||x - x'|| = 0$ we mean that the two configurations are identical, i.e. $x = x'$ or $x_s = x'_s$ at every site $s \in \mathbb{S}_n$. We can think of our Markov chain evolving according to the following probabilistic rules based on Eqs. (10) and (11):

- Given the current configuration x, we first choose one of the n^2 sites in $\mathbb{S}_n$ uniformly at random with probability n^{-2};
- Denote this chosen site by s and let the number of bondable neighbours of s be $i = N_s(x) \in \{0, 1, 2, 3, 4\}$; and
- Finally, change the phase at s to 1, i.e. set $x_s = 1$ with probability

$$p_i := (1 + \theta)^{-1} = (1 + \theta(s, \alpha, \beta, \sigma))^{-1} = 1/(1 + e^{(\sigma - \alpha - i\beta)}) \tag{14}$$

and set $x_s = 0$ with probability $1 - p_i$.

We emphasise the dependence of p_i on the parameters α, β and σ by $p_i(\alpha, \beta, \sigma)$. This is illustrated in Fig. 9 for different parameter values. Just as in the Ising model, our model can be classified into three behavioural regimes depending on the sign of the interaction parameter β. When the interaction parameter $\beta > 0$ the model is said
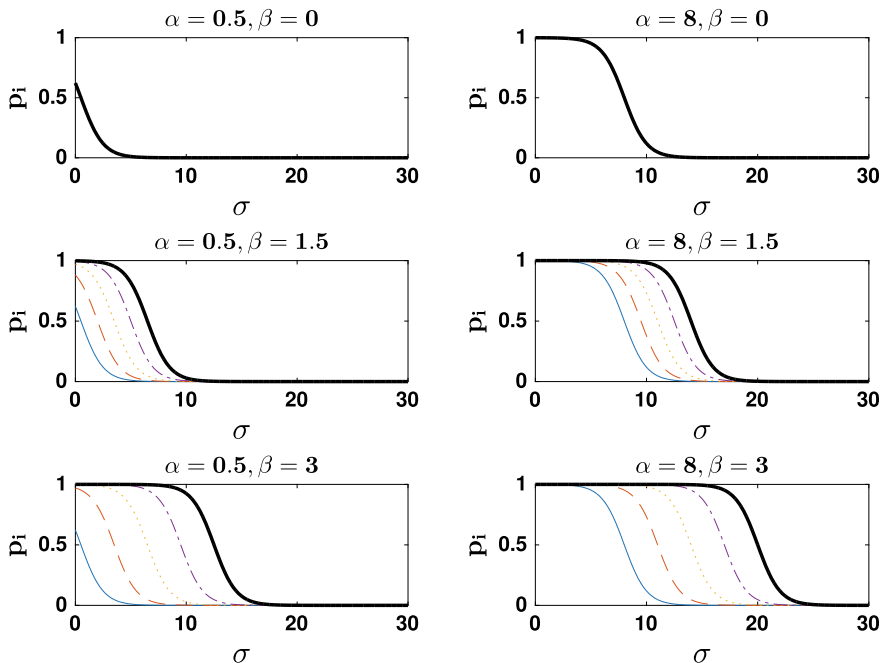
Fig. 9 Plots of p_i, the probability that site s with $i = x_{N_s}$ neighbours in phase 1, is also in phase 1, as a function of external stress σ for different values of α, β. From the plots it is clear that α is a location parameter while β controls the scale of the relative difference between p_i's

to have "*agglomerative interactions*" analogous to the *ferromagnetic* interactions of the Ising model whereby the probability of a site being in phase 1 increases with the number of its neighbouring sites also being in phase 1, i.e. if $\beta > 0$, then $0 < p_0 < p_1 < p_2 < p_3 < p_4 < 1$. When $\beta = 0$, the model is said to be "*non-interactive*" since the probability of a site being in phase 1 is independent of the phase of the neighbouring sites and identically p at each site, i.e. $0 < p = p_0 = p_1 = p_2 = p_3 = p_4 = 1/(1 + e^{\sigma - \alpha}) < 1$. When $\beta < 0$, our model captures the "*anti-agglomerative*" interactions that are analogous to the "*anti-ferromagnetic*" interactions of the Ising model since the probability of a site being in phase 1 decreases with the number of its neighbouring sites also being in phase 1, i.e. if $\beta < 0$ then $1 > p_0 > p_1 > p_2 > p_3 > p_4 > 0$.

Note that our transition probabilities allow *self-transitions*, i.e. there is a positive probability that we will go from a configuration x to itself. Although we think of $\{X(m)\}_{m=0}^{\infty}$ on the state space of all configurations $\mathbb{X}_n$ as a discrete-time Markov chain, with transition probability matrix $P_{\alpha, \beta, \sigma}$ in Eq. (13), we can easily add exponentially distributed holding times with rate 1 at each configuration and use Eq. (13)

to choose a possibly new configuration and thereby obtain a continuous-time Markov chain $\{X(t)\}_{t \geq 0}$ in the usual way from $\{X(m)\}_{m=0}^{\infty}$. This Markov chain over $\mathbb{X}_n$ is nothing but our Gibbs field (or Markov random field) model (Brémaud 1999 see, e.g. Chap. 7).

If the external stress varies as a function of discrete-time blocks of length $\underline{h} = \lfloor hn^2 \rfloor$ and given by the function $\sigma(m)$ for each time block $m = 0, 1, \ldots, M$, then we have the time-inhomogeneous Markov chain $\{X(k)\}_{k=0}^{M\underline{h}}$ with the transition probability matrix at time k given by

$$P(k) = P_{\alpha, \beta, \sigma(\lfloor k/\underline{h} \rfloor)} \ , \tag{15}$$

and the k-step configuration probability, with $k < M\underline{h}$ under initial distribution $\delta_{x(0)}$, given by

$$\Pr \left\{ X(k) = x(k) \mid X(0) = x(0) \right\}$$

$$= \delta_{x(0)} \left(\prod_{m=0}^{\lfloor k/\underline{h} \rfloor} \left(P_{\alpha, \beta, \sigma(m)} \right)^{\underline{h}} \right) \left(P_{\alpha, \beta, \sigma(\lfloor k/\underline{h} \rfloor + 1)} \right)^{\overline{(k)}_{\underline{h}}} \ . \tag{16}$$

As before, $\overline{(k)}_{\underline{h}}$ is k modulo $\underline{h}$.

We can use the local specification to obtain the Gibbs sampler, a Monte Carlo Markov chain (MCMC), to simulate from $\{X(m)\}$. Let h denote the average number of hits per site. Thus, $\lfloor h |\mathbb{S}_n| \rfloor = \lfloor hn^2 \rfloor$ gives the number of hits on all n^2 sites in $\mathbb{S}_n$ chosen uniformly at random. Given h and the parameters determining the local specification, i.e. α, β and σ, $\texttt{GibbsSample}(x(0), \alpha, \beta, \sigma, h)$ produces a sample path of configurations from the Markov chain $\{X(k)\}_{k=0}^{m}$ given by Eqs. (12) and (13) and initialized at $x(0)$ as it undergoes $m = \lfloor hn^2 \rfloor$ transitions in $\mathbb{X}_n$.

If we are interested in simulating configurations with stationary distribution $\pi_{\alpha, \beta, \sigma}$, then for large $m = \lfloor hn^2 \rfloor$, the m-step probabilities, $\Pr \{ X(m) \mid X(0) = x(0) \}$, by construction will approximate samples from $\pi_{\alpha, \beta, \sigma}$ Brémaud (1999, see, e.g. Chap. 7, Sect. 6), i.e.

$$\lim_{m \to \infty} d_{TV} \left(\Pr \{ X(m) \mid X(0) = x(0) \}, \pi_{\alpha, \beta, \sigma} \right) = 0 \ .$$

Here, $d_{TV}(\varpi, \pi) = 2^{-1} \sum_{x \in \mathbb{X}_n} |\varpi(x) - \pi(x)|$ is the total variation distance between two distributions ϖ and π over $\mathbb{X}_n$.

Two informative singleton clique statistics of a configuration $x(m)$ at time m are the number and fraction of gelled sites given, respectively, by

$$a(x) := \sum_{s \in \mathbb{S}_n} x_s \quad \text{and} \quad \overline{a}(x) := |\mathbb{S}_n|^{-1} a(x) = \frac{a(x)}{n^2} \ .$$

Similarly, two informative doubleton clique statistics of a configuration x are the number and fraction of connected pairs of neighbouring sites given, respectively, by

$$b(x) := \sum_{\langle s,t \rangle \in \mathbb{E}_n} y_{\langle s,r \rangle} = \sum_{\langle s,r \rangle \in \mathbb{E}_n} x_r x_s \quad \text{and}$$

$$\overline{b}(x) := |\mathbb{E}_n|^{-1} b(x) = \frac{b(x)}{2n^2} \ .$$

When the configuration is a function of time m and given by $x(m)$, then the corresponding configuration statistics are also functions of time and are given by $a(m) = a(x(m))$, $\overline{a}(m) = \overline{a}(x(m))$, $b(m) = b(x(m))$ and $\overline{b}(m) = \overline{b}(x(m))$. The energy of a configuration x can be succinctly expressed in terms of $\overline{a}(x)$ and $\overline{b}(x)$ as

$$\mathcal{E}(x) = -\beta b(x) + (\sigma - \alpha)a(x) = -\beta 2n^2 \overline{b}(x) + (\sigma - \alpha)n^2 \overline{a}(x) \ ,$$

and therefore

$$\mathcal{E}(x) \propto -2\beta\overline{b}(x) + (\sigma - \alpha)\overline{a}(x) = -2\beta\overline{b}(x) + \tilde{\sigma}\overline{a}(x) \ , \tag{17}$$

where $\beta \in (-\infty, \infty)$ and $\tilde{\sigma} = \sigma - \alpha \geq -\alpha$ for a given $\alpha \geq 0$. Since the energy of a configuration x, given n, only depends on its $\overline{a}(x)$ and $\overline{b}(x)$, we can easily visualise any sample path $(x(0), \ldots, x(m)) \in \mathbb{X}_n^{m+1}$ in configuration space as the following sequence of $(m + 1)$ ordered pairs in the unit square:

$$\left(\left(\overline{a}(x(0)), \overline{b}(x(0))\right), \ldots, \left(\overline{a}(x(m)), \overline{b}(x(m))\right) \right) \in \left([0, 1]^2\right)^{m+1} \ .$$

Finally, we reserve upper case letters for random variables. Thus, $A(X)$, $\overline{A}(X)$, $B(X)$ and $\overline{B}(X)$ are the statistics of the random configuration X. And the notation naturally extends to $A(m)$, $\overline{A}(m)$, $B(m)$ and $\overline{B}(m)$ when $X(m)$ is a random configuration at time m.

The macroscopic behaviour of a configuration x can be described by other statistics of x. We can obtain the connectivity information in the site configuration x through y, its edge configuration, according to (9). By representing the connectivity in y and/or x as the adjacency matrix of the graph whose vertices are $\mathbb{S}_n$, we can obtain various alternative graph statistics:

1. $C_x = \left\{ C_x^{(1)}, C_x^{(2)}, \ldots, C_x^{(n_y)} \right\}$, a partition of $\mathbb{S}_n$ that gives the set of connected components of x;
2. $C_x^{(*)} = argmax_{C_x^{(i)} \in C_x} |C_x^{(i)}|$, the first largest connected component;
3. $|C_x^{(*)}|/n^2$, the size of the first largest connected component per site; and
4. $F_x^{(*)}$, the fraction of the rows of $\mathbb{S}_n$ that are permeated (from top to bottom) by $C_x^{(*)}$.

3.1.1 Equilibrium Behaviour Under Constant Stress

We are interested in the effect of applying constant external stress σ for a long period of time to an yield stress material with rheological properties specified by parameters α and β.

The subplot (a) of Fig. 10 approximates the time asymptotic behaviour of $\overline{a}$ when the Monte Carlo simulation of Gibbs field was initialized from **1** ($h = 100$ hits per site were performed) and subplot (b) presents the same information when the Gibbs field was initialized from **0**. For both simulations, we have used $n = 100$ and $(\tilde{\sigma}, \beta)$ taken from a grid of linearly spaced points in $[-10, 15] \times [0, 4]$. In both panels (a–b) of Fig. 10, one can note that if the interaction parameter is smaller than a critical value of the interaction parameter $\beta < \beta_c$ ($\beta_c \approx 1.5$), both the solid–fluid and fluid–solid transitions are smooth. When the interaction parameter β is gradually increased past this critical value both transitions become increasingly sharp.

To assess the reversibility of the deformation states in the time asymptotic limit, we focus at the difference between the subplots (a) and (b) which is presented in Fig. 10c. In the range $\beta < \beta_c$, the steady-state transition from solid to fluid evolves through the same intermediate states as the steady-state transition from fluid to solid and no hysteresis effect can be observed. When the interaction parameter β exceeds the critical value β_c, a triangular hysteresis region may be observed in Fig. 10c.

This is an interesting result as it tells us that in the presence of strong interactions a "*genuine*" hysteresis of the deformation states would be observed even in conditions of a steady-state forcing. At a given applied stress $\tilde{\sigma}$, the size of the hysteresis region increases when the strength of the interactions is increased.
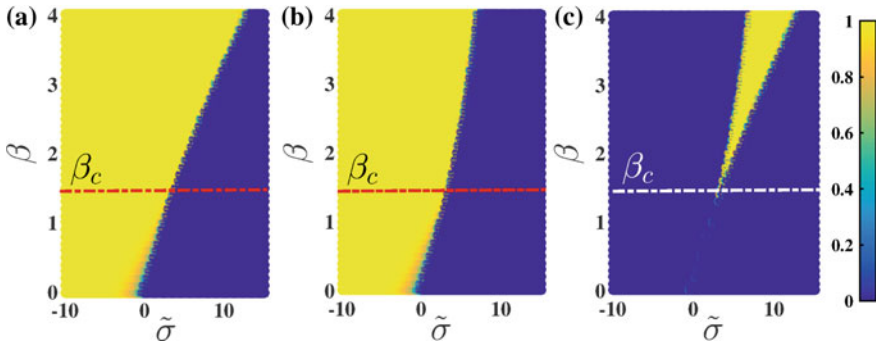
Fig. 10 The value of $\overline{a}$ at rescaled time $t = 100$ from Monte Carlo simulations of the Gibbs field for fixed parameters $(\tilde{\sigma}, \beta)$ when initialized from **1** (panel (a)) and from **0** (panel (b)). The difference in $\overline{a}$ between the subplots (a) and (b) is shown in panel (c). The horizontal dashed lines indicate the critical value of the interacting parameter β_c (see the discussion in the text)

3.1.2 Configurations at the Solid–Fluid Interface

Let us now focus on the nature of the configuration x for a given β at the solid–fluid interface, i.e. when $\overline{a} = 1/2$, as $\tilde{\sigma}$ reaches a specific value. Site configurations at the solid–fluid interface provide the random environment for restricted diffusion of small tracer particles near gel transition. This phenomenon is of experimental and theoretical interest (Oppong et al. 2006; Oppong and de Bruyn 2007; Putz and Burghelea 2009) and has been recently studied for the case of $\beta = 0$ (de Bruyn 2013). We are interested here in gaining insights on the nature of the site configurations at the solid–fluid interface for values of β below, above and equal to zero.

Figure 11 shows two random site configurations at the solid–fluid interface when $\overline{a} \approx 1/2$ for three different values of β. Without loss of generality, we fixed $\alpha = 8$ and focus on the properties of the material that is capable of forming a gel in the absence of external stress. Clearly, the site configurations are dependent on the magnitude and sign of the interaction parameter β. Recall that $\overline{a}$, the fraction of gelled sites, and $\overline{b}$, the fraction of pairs of neighbouring gelled sites, are the sufficient statistic of the configuration, i.e. the energy of the configuration only depends on its $(\overline{a}, \overline{b})$.

Three distinct cases can be distinguished. If $\beta = 0$, the non-interactive case of the classical site percolation model studied in de Bruyn (2013), and $\tilde{\sigma}$ is chosen so that $\overline{a} = 1/2$, then due to the site-filling probability being independently and identically distributed across all n^2 sites $\overline{b} = \overline{a}^2 = 1/4$. Two typical configurations when $\beta = 0$, $n = 100$ and $t = 100$ at the solid–fluid interface are shown by the subplots in the second row of Fig. 11. More configurations were visually explored, and their distinguishing site configuration feature is characterised by the independence of the site-filling probability over sites and is apparent by the concentration of their sufficient statistics $(\overline{a}, \overline{b})$ about $(\overline{a}, \overline{a}^2) = (1/2, 1/4)$ at the solid–fluid interface. This is the only case considered by de Bruyn (2013) when obtaining the random environment for restricted diffusion of small tracer particles near gel transition.

When β is increased from 0 to 2, we have a very different distribution over site configurations at the solid–fluid interface as shown by two samples in the first (top) row of Fig. 11. It is easy to understand this "*patchy*" pattern in site configurations with large positive β by realising that new gelled sites can occur with a higher probability at sites neighbouring existing gelled sites that have a larger $i = x_{N_s}$, number of neighbours in phase 1, than at sites surrounded by un-gelled sites with a smaller $i = x_{N_s}$. As β gets larger, the probability of forming gelled sites around existing gelled sites is much larger than that of forming gelled sites around un-gelled sites, and this concentrates $(\overline{a}, \overline{b})$ about $(\overline{a}, \overline{a}) = (1/2, 1/2)$ at the solid–fluid interface.

Finally, when β is decreased from 0 to -2, we have a "*checkered*" pattern of site configurations at the solid–fluid interface as shown by two samples in the third (bottom) row of Fig. 11. As β gets negative, the probability of forming gelled sites around existing gelled sites gets much smaller (see top row of Fig. 9). In the extreme asymptotic case, as $\beta \to -\infty$, we obtain configurations with increasingly checkered patters with $(\overline{a}, \overline{b}) \to (1/2, 0)$, the sufficient statistics of the extreme "chessboard" configuration (such patterns occur already for $\beta = -8$ with $n = 100$ but are not shown here).
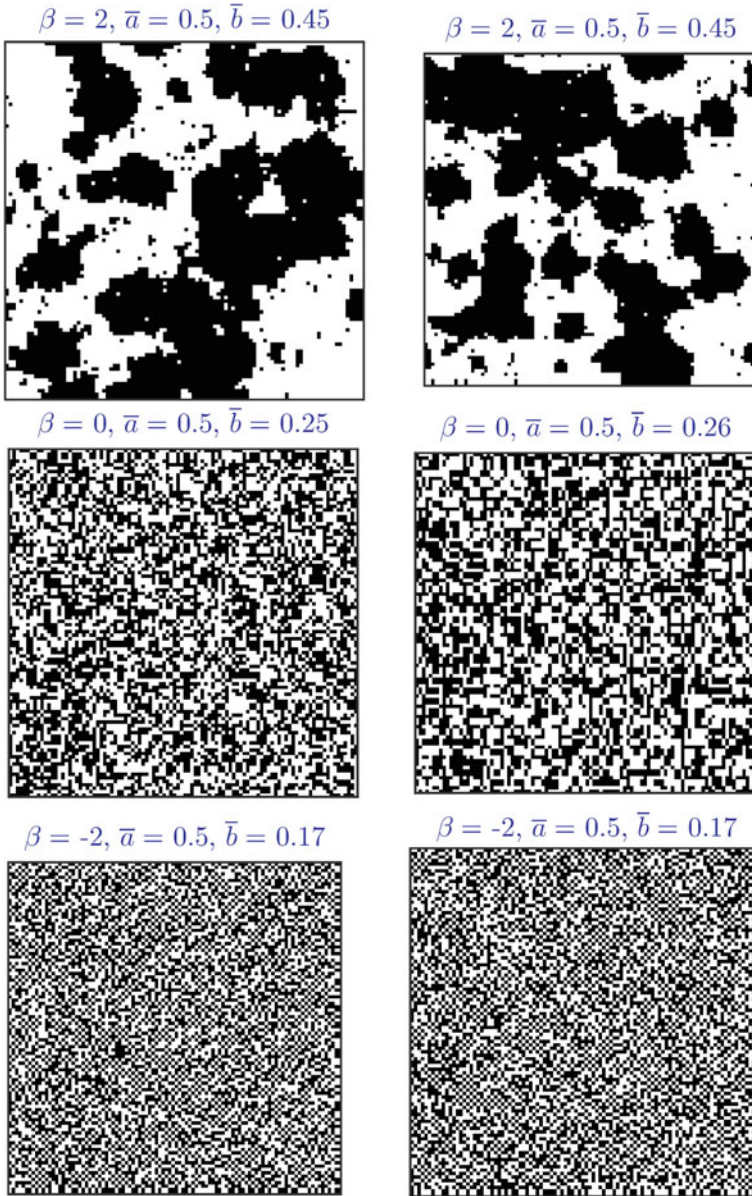
Fig. 11 Effect of β on preferred energy minimising configurations. Two sample configurations are shown for each $\beta \in \{-2, 0, +2\}$ over a toroidal square lattice of 100×100 sites. Sites in phase 0 and 1 are shown in black and white, respectively, at the solid–fluid interface when $\bar{a} \approx 1/2$

Thus, from the β-dependent site configurations at the solid–fluid interface depicted in Fig. 11, it is clear that the trajectories of tracer particles (see Fig. 1 of Putz and Burghelea 2009 from Oppong et al. 2006) that can only diffuse through the un-gelled (black) contiguous regions are heavily dependent on whether there is interaction between adjacent gelled sites. This interaction is captured in our correlated site percolation model by the interaction parameter β.

3.1.3 Behaviour Under Varying Stress

The energy of $X(t)$, the random site configuration at time t, depends on two of its highly correlated statistics: $\overline{A}(t)$, the random fraction of gelled sites at time t, and $\overline{B}(t)$, the random fraction of connected sites at time t. One of our primary interests is to study $\overline{A}(t)$ and $\overline{B}(t)$ as $X(t)$ is under the influence of time-varying externally applied stress $\sigma(t)$. This test will be the closest equivalent of a controlled stress ramp typically used in experiments (see Fig. 3a in Sect. 1.3).

Using Monte Carlo simulations of the time-inhomogeneous Markov chain $\{X(m)\}_{m=0}^{Mh}$ given by Eqs. (15) and (16), under an initially increasing and subsequently decreasing time-dependent stress $\sigma(m)$ given in the bottom panel of Fig. 12, we obtained multiple independent trajectories of $\overline{A}(\sigma)$, the fraction of gelled sites as a function of the external stress σ. Five such simulated trajectories are shown in the first four panels of Fig. 12. In order to mimic an asymptotic steady state of deformation (which is typically what a rheologist would be interested in characterising during a rheological measurement), the holding time per stress value has been chosen large, $h = 1000$ hits per site. We note that regardless the value of the interaction parameter β the results of the five individual simulations overlap nearly perfectly which indicates that the grid size of the simulation is sufficiently large and the simulated trajectories are robust.

For low values of the interaction parameter ($\beta \in \{0, 1\}$, top row of Fig. 12), the dependence $\overline{a}(\sigma)$ corresponding to the decreasing branch of the stress ramp overlaps with that corresponding to the increasing branch and no hysteresis is observed. This indicates that in the presence of weak interactions and provided that an asymptotically steady state is reached the deformation states are fully reversible upon increasing/decreasing the external forces. In this case, a smooth solid–fluid transition is observed.

As the value of the interaction parameter is increased ($\beta \in \{2, 4\}$, middle row of Fig. 12), a significantly different yielding behaviour is observed. First, the deformation states are no longer reproducible upon increasing/decreasing stresses and a clear hysteresis is observed. Second, the larger the value of the interaction parameter is, the steeper the solid–fluid transition becomes.

To conclude this part, the realisations of the time-inhomogeneous Markov chain under time-dependent stress $\sigma(m)$ corresponding to an asymptotically steady forcing reveal a smooth and reversible solid–fluid transition if the interactions are either absent or weak and a steep and irreversible transition in the presence of strong interactions. This result is consistent with the result presented in Fig. 10 where we have
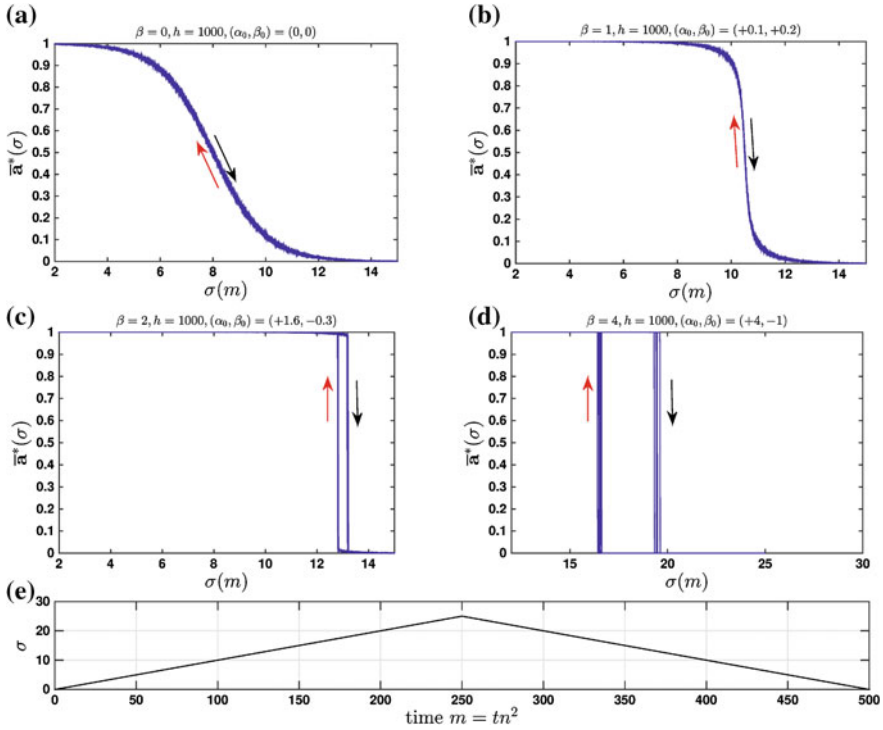
Fig. 12 Results of five distinct Gibbs field simulations corresponding to an increasing/decreasing stress ramp (illustrated in the bottom panel) with $\alpha = 8$ and $\beta \in \{0, 1, 2, 4\}$ indicated on the top of each panel). The stress was increased from 0 to 25 in units of 0.01 and decreased back to 0 with a holding time of $h = 1000$ (nearly asymptotic state for each value of the applied stress) as the site configuration varied from **1** to **0** and then back to **1**. The arrows indicate the increasing/decreasing branches of the stress ramp

seen that for $\beta > \beta_c$ a genuine irreversibility of the deformation state is observed during the steady yielding process. An experimental validation of these conclusions has been recently presented in Souliès et al. (2013). The rheological flow curves measured for a suspension of spherical and electrically charged non-motile microalgae (*Chlorella Vulgaris*) reveal an abrupt solid–fluid transition and exhibit a strong hysteresis even in the limit of very slow forcing, see Fig. 11 in Souliès et al. (2013). In the case of a Carbopol gel where the microscopic interactions are presumably weaker than the interactions between electrically charged Chlorella cells, a much smoother solid–fluid transition is observed and, in the asymptotic limit of steady forcing, the hysteresis effects become negligibly small, Putz and Burghelea (2009). This is perhaps the main reason why Carbopol gels have been considered for decades "*model*", "*simple*" or "*ideal*" yield stress fluids.

3.1.4 Effect of Holding Time (Steadiness of the External Forcing) on the Hysteresis

A large number of flows of yield stress fluids are unsteady in the sense that the applied stress is maintained for a finite time t_0. For the case of a rheometric configuration, we have illustrated the unsteady response of the material in Figs. 3b and 4. An important feature of the deformation curves presented in these figures is the irreversibility of the deformation states upon increasing/decreasing applied stresses. The magnitude of this effect is found to depend systematically on the degree of steadiness of the forcing, the time t_0 the applied stress is maintained constant (Fig. 5).

The question we address in the following is to what extent is the Gibbs field model able to describe the unsteady yielding behaviour observed in macroscopic experiments, see the discussion in Sects. 1 and 2. To answer this question, we calculate trajectories $\bar{a}$ similar to those presented in Fig. 12 which are realised during an increasing/decreasing stress ramp (bottom panel).

To place ourselves in the conditions of an unsteady forcing, we chose during the simulations finite values of the holding time (or average number of hits per site). We note that the average holding time per site in our simulations is the closest equivalent we could find for the characteristic forcing time t_0 imposed during macroscopic rheological measurements (Figs. 3b and 4 and the discussion in Sect. 1). To quantify the degree of reversibility of the deformation states, we calculate after each run the area of the hysteresis encompassed by the increasing/decreasing branches of the dependence $\bar{a} = \bar{a}(\sigma)$.

The dependencies of the hysteresis area on the holding time obtained from such simulations performed for a fixed value of the site threshold α and several values of the interaction parameter β are presented in Fig. 13.

Fig. 13 Effect of increasing β on the relative hysteresis area for $\bar{a}$ for different holding times t_0 per stress level in a stress ramp from 0 to 25 in increments of 1 (with $\alpha = 8$). The dash line is a log-normal fit and the full lines are the fitted power laws indicated in the inserts. The symbols refer to the value of the interaction parameter β: circles (○)—$\beta = 0$, up triangles (△)—$\beta = 1.5$, down triangles (▽)—$\beta = 3$, hexagons (⬡)—$\beta = 3.5$
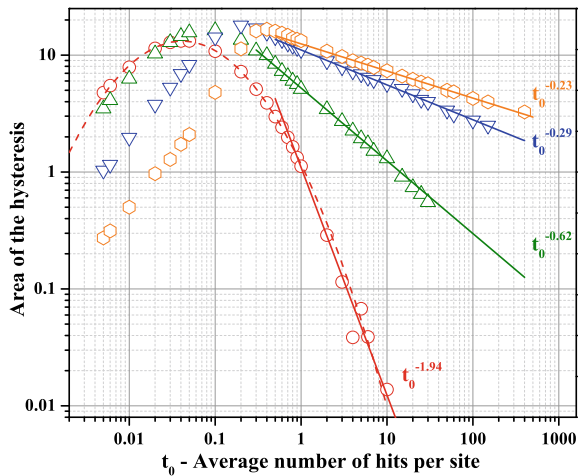
Regardless of the strength β of the interaction, a non-monotone dependence of the hysteresis area on the holding time is obtained. By carefully inspecting the individual dependencies $\bar{a} = \bar{a}(\sigma)$, we have noticed that prior to the local maximum the lattice yields only partially ($\bar{a}$ never reaches 0) corresponding to the largest value of the applied stress σ. Corresponding to the local maxima $t_0^\star$ of the dependencies presented in Fig. 13, the lattice yields completely (the terminal value of $\bar{a}$ is 0) and the area of the hysteresis starts decaying with the holding time t_0. This behaviour of the degree of irreversibility of deformation states as a function of the steadiness of the forcing is qualitatively similar to the experimental results illustrated in Fig. 5. In the absence of interactions ($\beta = 0$), the hysteresis area follows a log-normal correlation with the holding time (see the circles and the dashed line in Fig. 13), which once more comes into a qualitative agreement with the experimental results. For non-zero values of β, we could not accurately fit the data by a log-normal function. Corresponding to the largest values of the average number of hits per site we have tested, we have found a power law decay of the hysteresis area, the full lines in Fig. 13), which is once again similar to the behaviour illustrated in Figs. 3b and 4 and consistent with experimental results obtained with Carbopol gels (Putz and Burghelea 2009; Poumaere et al. 2014).

It is equally interesting to note that the stronger the interaction is (larger the parameter β is), the weaker the decay of the hysteresis area with the characteristic forcing time t_0 is. This indicates that in the presence of strong interactions a full reversibility of the deformation states cannot be achieved regardless of the degree of steadiness of the external forcing. This is indeed the case of several highly thixotropic materials such as bentonite gels, Laponite gels where steady-state rheological measurements cannot be truly achieved even during very slow controlled stress flow ramps. Among the data we illustrate in Figs. 4 and 5, the mayonnaise seems to behave as such as well.

3.2 A Nonlinear Dynamical System Approach for the Yielding Behaviour of a Viscoplastic Material

Though able to capture most of the relevant features of the solid–fluid transition in a thermodynamically consistent manner and making use of solely two internal parameters, the microscopic Gibbs field model presented in the previous section is rather difficult to implement and requires a number of skills in both statistics and programming. As practical applications regarding the dynamics of the solid–fluid transition in a pasty materials are concerned, one would often prefer dealing with a continuum microstructural equation with a general form given by Eq. (2) which, unlike the simple phenomenological model described in the second part of Sect. 2, is derived from first principles.

Here, based on the microscopic Gibbs field model, we derive a nonlinear first-order differential equation to asymptotically approximate $\mathbf{E}(\overline{A}(t))$, the expected fraction of sites in the solid phase, in continuous time t that is measured in units of n^2 discrete time steps as the number of sites $n^2 \to \infty$, under a fixed externally applied stress σ and fixed rheological parameters α and β.

First, consider the discrete-time Markov chain $\{X(m)\}_{m=0}^{\infty}$ of Eqs. (12) and (13) and recall that $X(m)$ is the random site configuration of the chain at discrete time m and $A(m) = \sum_s X_s(m)$ is the number of sites that are in phase 1. We will derive the approximation first for the case when $\beta = 0$ in Eq. (13) and then for the general setting of $\beta \neq 0$.

3.2.1 Non-interactive Case with $\beta = 0$

If $\beta = 0$ then the probability of the phase in site s at the next time step is independent of the current configuration, i.e.

$$\Pr\Big\{X_s(m+1) = x_s(m+1) \mid X(m) = x(m)\Big\}$$

$$= \Pr\Big\{X_s(m+1) = x_s(m+1)\Big\}$$

$$= \begin{cases} p = \left(1 + e^{\sigma-\alpha}\right)^{-1} & \text{if } x_s(m+1) = 1 \\ 1 - p = 1 - \left(1 + e^{\sigma-\alpha}\right)^{-1} & \text{if } x_s(m+1) = 0 \\ 0 & \text{if } x_s(m+1) \notin \{0, 1\} \ . \end{cases}$$

Therefore, the probability that the total number of sites in phase 1 increases by 1 in one time step is obtained by adding the probability of a transition from phase 0 to phase 1 over every uniformly chosen site s as follows:

$$\Pr\{A(m+1) = a(m) + 1 \mid A(m) = a(m)\}$$

$$= \sum_{s \in \mathbb{S}_n} \Pr\{X_s(m+1) = 1, X_s(m) = 0, S = s \mid A(m) = a(m)\}$$

$$= \sum_{s \in \mathbb{S}_n} \underbrace{\Pr\{X_s(m+1) = 1 \mid X_s(m) = 0, S = s, A(m) = a(m)\}}_{p}$$

$$\times \underbrace{\Pr\{X_s(m) = 0 \mid S = s, A(m) = a(m)\}}_{(n^2 - a(m))/n^2}$$

$$\times \underbrace{\Pr\{S = s \mid A(m) = a(m)\}}_{1/n^2}$$

$$= \sum_{s \in \mathbb{S}_n} p\left(1 - \frac{a(m)}{n^2}\right)\frac{1}{n^2} = p\left(1 - \overline{a}(m)\right) \ .$$

Dividing both sides of the equality that defines the above event by n^2, we get

$$\Pr\left\{A(m+1)/n^2 = a(m)/n^2 + 1/n^2 \mid A(m)/n^2 = a(m)/n^2\right\}$$
$$= \Pr\left\{\overline{A}(m+1) = \overline{a}(m) + 1/n^2 \mid \overline{A}(m) = \overline{a}(m)\right\} = p\,(1 - \overline{a}(m)) \ .$$

By an analogous argument, we can obtain the probabilities for the remaining two possibilities

$$\Pr\left\{\overline{A}(m+1) = \overline{a}(m) - 1/n^2 \mid \overline{A}(m) = \overline{a}(m)\right\} = (1 - p)\overline{a}(m) \ ,$$
$$\Pr\left\{\overline{A}(m+1) = \overline{a}(m) \mid \overline{A}(m) = \overline{a}(m)\right\} = p\overline{a}(m) + (1 - p)(1 - \overline{a}(m)) \ .$$

Now we can define a continuous-time Markov chain $\{\overline{A}(t)\}_{t\geq 0}$ on the unit interval $[0, 1]$ by a rescaling of the discrete-time Markov chain $\{\overline{A}(m)\}_{m=0}^{\infty}$ and letting the number of sites $n^2 \to \infty$. These two Markov chains are notationally distinguished only by their time indices. The rescaled time t is m in units of n^2, i.e. $m = \lfloor tn^2 \rfloor$ and $m + 1 = \lfloor (t + 1/n^2)n^2 \rfloor$. Then by taking $\Delta_t = O(1/n^2)$ and letting

$$\Delta_A = \overline{A}(t + \Delta_t) - \overline{a}(t) = \overline{A}(\lfloor (t + \Delta_t)n^2 \rfloor) - \overline{a}(\lfloor tn^2 \rfloor) \ ,$$

we get

$$\Pr\left\{\frac{\Delta_A}{\Delta_t} = \frac{\Delta_a}{\Delta_t} \,\middle|\, \overline{A}(t) = \overline{a}(t)\right\}$$
$$= \begin{cases} p\,(1 - \overline{a}(t)) + O(\Delta_t) & \text{if } \frac{\Delta_a}{\Delta_t} = 1 \\ (1 - p)\overline{a}(t) + O(\Delta_t) & \text{if } \frac{\Delta_a}{\Delta_t} = -1 \\ p\overline{a}(t) + (1 - p)(1 - \overline{a}(t)) + O(\Delta_t) & \text{if } \frac{\Delta_a}{\Delta_t} = 0 \\ O(\Delta_t) & \text{otherwise} \ . \end{cases} \tag{18}$$

Finally, by considering the instantaneous rate of change of the expected fraction of sites in phase 1

$$\frac{d}{dt}\overline{\mathbf{a}}(t) := \lim_{\Delta_t \to 0} \mathbf{E}\left(\frac{\overline{A}(t + \Delta_t) - \overline{A}(t)}{\Delta_t} \,\middle|\, \overline{A}(t)\right),$$

we get the limiting differential equation approximation as

$$n^2 \to \infty, \quad \Delta_t \to 0, \quad \Delta_a \to 0 \ ,$$

such that

$$\Pr\{\Delta_a/\Delta_t \in \{0, -1, +1\}\} \to 1$$

based on Eq. (18) as follows:

$$\dot{\mathbf{a}} = \frac{d}{dt}\overline{\mathbf{a}}(t) = p(1 - \overline{\mathbf{a}}(t)) - (1 - p)\overline{\mathbf{a}}(t) = p - \overline{\mathbf{a}}(t) \ ,$$

or simply by

$$\dot{\mathbf{a}} = p - \overline{\mathbf{a}} = (1 + e^{\sigma - \alpha})^{-1} - \overline{\mathbf{a}} \ . \tag{19}$$

The simple relationship above is mathematically very similar to the so-called "lambda-model" introduced by Coussot et al. (2002a, b) with the remark that we consider the stress σ as a forcing parameter rather than the rate of deformation. Given the initial condition $\overline{\mathbf{a}}(0) = \overline{\mathbf{a}}_0$, the analytic solution is

$$\overline{\mathbf{a}}(t) = p + (\overline{\mathbf{a}}_0 - p)e^{-t} = (1 + e^{\sigma - \alpha})^{-1} + (\overline{\mathbf{a}}_0 - (1 + e^{\sigma - \alpha})^{-1})e^{-t}$$

with only one asymptotically stable fixed point

$$\overline{\mathbf{a}}^* = p = (1 + e^{\sigma - \alpha})^{-1} \ . \tag{20}$$

Thus, $\overline{\mathbf{a}}(t)$ in the above differential equation is the expected fraction of sites in phase 1 at time t in the limit of an infinite toroidal square lattice with $|\mathbb{S}_n| = n^2 \to \infty$ and a realisation of the continuous-time Markov chain $\{\overline{A}(t)\}_{t \geq 0}$ is $\overline{a}(t)$. Since $\beta = 0$, the probability of a site being in a given phase is independent of the phases of its neighbouring sites. Thus, we can obtain $\overline{\mathbf{b}}(t)$, the expected fraction of bonds, by simply multiplying $\overline{\mathbf{a}}(t)$, the probability of finding a randomly chosen site in phase 1, by itself, i.e.

$$\overline{\mathbf{b}}(t) = \overline{\mathbf{a}}(t)^2 \text{ and } \overline{\mathbf{b}}^* = \left(\overline{\mathbf{a}}^*\right)^2 \ . \tag{21}$$

3.2.2 Interactive Case with $\beta \neq 0$

If $\beta \neq 0$, then the probability of site s being in phase 1 at time $m + 1$ depends on the configuration of the neighbouring sites of s at time m through $X_{N_s}(m) = \sum_{r \in N_s} X_r(m)$, the number of neighbouring sites of s in phase 1 at time m.

$$\Pr\left\{X_s(m+1) = x_s(m+1) \mid X(m) = x(m)\right\}$$
$$= \Pr\left\{X_s(m+1) = x_s(m+1) \mid X_{N_s}(m) = i\right\}$$
$$= \begin{cases} p_i = \left(1 + e^{\sigma - \alpha - i\beta}\right)^{-1} & \text{if } x_s(m+1) = 1 \\ 1 - p_i = 1 - \left(1 + e^{\sigma - \alpha - i\beta}\right)^{-1} & \text{if } x_s(m+1) = 0 \\ 0 & \text{if } x_s(m+1) \notin \{0, 1\} \ . \end{cases}$$

Thus the probability that the phase changes from 0 to 1 in one time step at site s given that $a(m)$ is the total number of sites in phase 1 at time m is

$$\Pr\left\{X_s(m+1) = 1, X_s(m) = 0 \mid S = s, A(m) = a(m)\right\}$$

$$= \sum_{i=0}^{4} \Pr\left\{X_s(m+1) = 1, X_{N_s}(m) = i, X_s(m) = 0\right.$$

$$\left. \mid S = s, A(m) = a(m)\right\}$$

$$= \sum_{i=0}^{4} \Pr\left\{X_s(m+1) = 1 \mid X_{N_s}(m) = i,\right.$$

$$\underbrace{X_s(m) = 0, S = s, A(m) = a(m)\}}_{p_i}$$

$$\times \Pr\left\{X_{N_s}(m) = i \mid X_s(m) = 0, S = s, A(m) = a(m)\right\}$$

$$\times \underbrace{\Pr\{X_s(m) = 0 \mid S = s, A(m) = a(m)\}}_{(n^2 - a(m))/n^2 = 1 - \bar{a}(m)}.$$

Since there are $4!/((4-i)!i!)$ distinct neighbourhood configurations with i of the four nearest neighbours of site s in phase 1, one can make the following approximation for $\Pr\left\{X_{N_s}(m) = i \mid X_s(m) = 0, S = s, A(m) = a(m)\right\}$ in the above expression and obtain

$$\Pr\left\{X_s(m+1) = 1, X_s(m) = 0 \mid S = s, A(m) = a(m)\right\}$$

$$= \sum_{i=0}^{4} p_i(1 - \bar{a}(m))$$

$$\times \Pr\left\{X_{N_s}(m) = i \mid X_s(m) = 0, S = s, A(m) = a(m)\right\}$$

$$\approx \sum_{i=0}^{4} p_i\left(1 - \bar{a}(m)\right) \binom{4}{i} (\bar{a}(m))^i (1 - \bar{a}(m))^{4-i} .$$

Therefore, the probability that the total number of sites in phase 1 increases by 1 in one time step is obtained by adding the probability of a transition from phase 0 to phase 1 over every uniformly chosen site s as follows:

$$\Pr\left\{A(m+1) = a(m) + 1 \,|\, A(m) = a(m)\right\}$$

$$= \sum_{s \in \mathbb{S}_n} \Pr\left\{X_s(m+1) = 1,\, X_s(m) = 0,\, S = s \,|\, A(m) = a(m)\right\}$$

$$= \sum_{s \in \mathbb{S}_n} \Pr\left\{X_s(m+1) = 1,\, X_s(m) = 0 \,|\, S = s,\, A(m) = a(m)\right\}$$

$$\times \underbrace{\Pr\left\{S = s \,|\, A(m) = a(m)\right\}}_{1/n^2}$$

$$\approx \sum_{s \in \mathbb{S}_n} \left(\sum_{i=0}^{4} p_i\big(1 - \overline{a}(m)\big) \binom{4}{i} (\overline{a}(m))^i \, (1 - \overline{a}(m))^{4-i} \right) \frac{1}{n^2}$$

$$= \big(1 - \overline{a}(m)\big) \sum_{i=0}^{4} p_i \binom{4}{i} (\overline{a}(m))^i \, (1 - \overline{a}(m))^{4-i} \ .$$

Dividing both sides of the equality that defines the above event by n^2, we get

$$\Pr\left\{\overline{A}(m+1) = \overline{a}(m) + 1/n^2 \,|\, \overline{A}(m) = \overline{a}(m)\right\}$$

$$\approx (1 - \overline{a}(m)) \sum_{i=0}^{4} p_i \binom{4}{i} (\overline{a}(m))^i \, (1 - \overline{a}(m))^{4-i} \ .$$

By an analogous argument, we can obtain the probability that $\overline{A}(m+1)$ decreases by $1/n^2$ as

$$\Pr\left\{\overline{A}(m+1) = \overline{a}(m) - 1/n^2 \,|\, \overline{A}(m) = \overline{a}(m)\right\}$$

$$\approx \overline{a}(m) \sum_{i=0}^{4} (1 - p_i) \binom{4}{i} (\overline{a}(m))^i \, (1 - \overline{a}(m))^{4-i} \ .$$

Using the same limiting approximation in the previous section, we can obtain the following differential equation approximation for $\mathbf{a} = \mathbf{a}(t)$ one obtains:

$$\begin{aligned}
\dot{\mathbf{a}} &= \frac{d}{dt}\overline{\mathbf{a}}(t) \\
&= (1 - \overline{\mathbf{a}}) \big(p_0 \,(1 - \overline{\mathbf{a}})^4 + p_1 \, 4\overline{\mathbf{a}}(1 - \overline{\mathbf{a}})^3 \\
&\quad + p_2 \, 6\overline{\mathbf{a}}^2(1 - \overline{\mathbf{a}})^2 + p_3 \, 4\overline{\mathbf{a}}^3(1 - \overline{\mathbf{a}}) + p_4 \, \overline{\mathbf{a}}^4 \big) \\
&\quad - \overline{\mathbf{a}} \big((1 - p_0) \,(1 - \overline{\mathbf{a}})^4 + (1 - p_1) \, 4\overline{\mathbf{a}}(1 - \overline{\mathbf{a}})^3 \\
&\quad + (1 - p_2) \, 6\overline{\mathbf{a}}^2(1 - \overline{\mathbf{a}})^2 + (1 - p_3) \, 4\overline{\mathbf{a}}^3(1 - \overline{\mathbf{a}}) \\
&\quad + (1 - p_4) \, \overline{\mathbf{a}}^4 \big) \ .
\end{aligned}$$

This simplifies after factoring and extracting coefficients of $\overline{\mathbf{a}}$ as follows:

$$
\begin{aligned}
\dot{\overline{\mathbf{a}}}(t) = \quad & p_0 - (4\,p_0 - 4\,p_1 + 1)\overline{\mathbf{a}} + 6\,(p_0 - 2\,p_1 + p_2)\overline{\mathbf{a}}^2 \\
& - 4\,(p_0 - 3\,p_1 + 3\,p_2 - p_3)\overline{\mathbf{a}}^3 \\
& + (p_0 - 4\,p_1 + 6\,p_2 - 4\,p_3 + p_4)\overline{\mathbf{a}}^4 \; .
\end{aligned}
\tag{22}
$$

We can understand Eq. (22) directly as a quartic polynomial in $\overline{\mathbf{a}}$ whose coefficients are given by an alternating binomial series corresponding to the increase and decrease in $\overline{\mathbf{a}}$ based on a combinatorial averaging over the transition diagram of site configurations at the four nearest neighbours of a given site.

We now focus on the stability of the fixed points of the evolution equation for the volume of fraction of solid $\bar{a}$ (Eq. 22). In the left panel of Fig. 14, we present three different stability scenarios for the fixed points of Eq. (22) in the $(\tilde{\sigma}, \beta)$ plane: (i) In the blue-shaded region, the right-hand side of Eq. (22) has four real roots and only one of them is in [0, 1]; this fixed point is stable. (ii) In the yellow region, starting at point (2.589145, 1.2945725), we have four distinct real roots with three of them in [0, 1]. Only one of the three distinct real roots is an unstable fixed point, while the other two roots are stable fixed points. This naturally corresponds to a family of pitchfork bifurcations and the associated hysteresis depending on where the system is initialised from. (iii) The unshaded region in the left panel of Fig. 14 corresponds to the parameter space where the quartic discriminant Δ_4 is negative and thus implying the existence of two real roots (with one of them in [0, 1], stable fixed point) and two complex conjugate roots.

The real roots and their derivatives over each $(\tilde{\sigma}, \beta)$ in a grid of parameter values from $[-8, 12] \times [-4, 4]$ were obtained through interval analytic methods (Hofschuster and Krämer 2003).

Figure 15 shows the set of fixed points $\overline{\mathbf{a}}^*$ of the dynamical system as a function of $(\tilde{\sigma}, \beta)$. The parameter space corresponding to the central shaded region of Fig. 14 containing the line $\beta = \tilde{\sigma}/2$ is evident in Fig. 15 with three fixed points in [0, 1]. The pitchfork bifurcations along the plane $\tilde{\sigma} = 2\beta$ or $\beta = \tilde{\sigma}/2$ determined by the non-negative sign of the cubic discriminant along the black line in Fig. 14 is displayed to highlight the dynamics with one unstable fixed point at $1/2$ and two other stable fixed points that are equidistant on either side of $1/2$.

We are interested in varying the externally applied stress σ for a given material characterised by fixed rheological parameters α and β. This amounts to varying $\tilde{\sigma}$ for a fixed β since the fixed α is absorbed into $\tilde{\sigma} = \sigma - \alpha$. The asymptotic dynamics when we apply a constant external stress for a long period of time are given by the fixed points $\overline{\mathbf{a}}^*$ in Fig. 15. Note that the ODE model for $\beta \neq 0$ is only in qualitative agreement with $\overline{\mathbf{a}}(t)$, the expected volume fraction of the unyielded material at time t. This is because we are ignoring the dependent statistic $\overline{\mathbf{b}}(t)$, the expected fraction of bonds or pairs of neighbouring unyielded material at time t. Despite this simplification, as we will see through this section, there is qualitative agreement between the ODE and the Gibbs simulations presented in Sect. 3.1. Furthermore, an admittedly *ad hoc* correction of the ODE through a translation of the vector field by
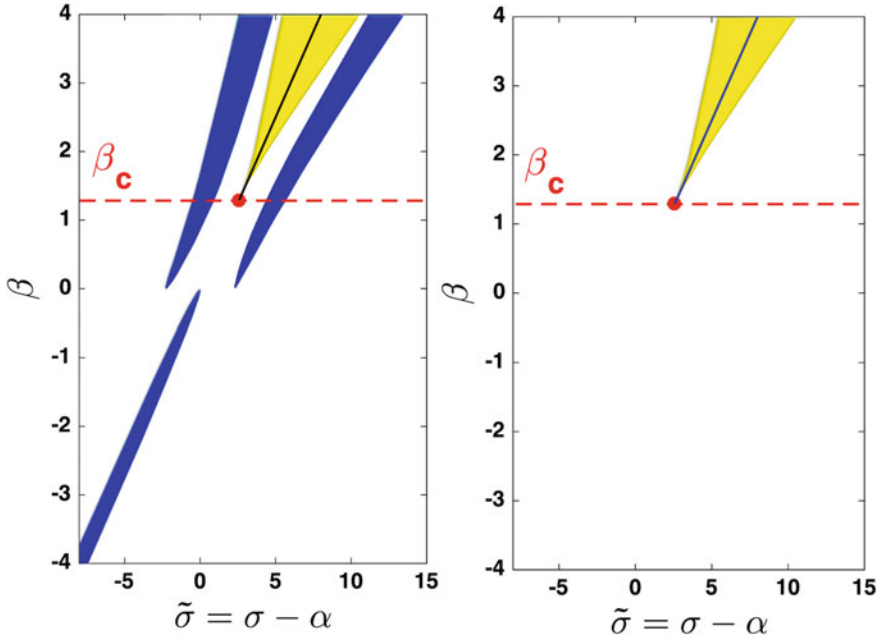
Fig. 14 Four real roots of the quartic occur in the shaded regions (blue and yellow) over $\tilde{\sigma} = \sigma - \alpha$ and β is shown in the left panel. The black line is $\beta = \tilde{\sigma}/2$ started at (2.589145, 1.2945725). The parameter space with only three distinct real roots in [0, 1] is shown in the right panel

(α_0, β_0) even improves the quantitative approximation. We postpone a formal quantitative approximation of the ODE using perturbation theoretic methods to the future and focus here on obtaining insights from the Gibbs sampler that is in qualitative agreement with the ODE approximation.

3.2.3 Comparison Between Microscopic Gibbs Field Model Described in Sect. 3.1 and ODE Approximation Under Varying Stress

The energy of $X(t)$, the random site configuration at time t, depends on two of its highly correlated statistics: $\overline{A}(t)$, the random fraction of gelled sites at time t, and $\overline{B}(t)$, the random fraction of connected sites at time t. One of our primary interests is to study $\overline{A}(t)$ and $\overline{B}(t)$ as $X(t)$ is under the influence of time-varying externally applied stress $\sigma(t)$. Using Monte Carlo simulations from Algorithm 2 in Sainudiin et al. (2015a) of the time-inhomogeneous Markov chain $\{X(m)\}_{m=0}^{Mh}$, under a time-dependent stress σ ramp, we can obtain multiple independent trajectories of $\overline{A}(\sigma)$, the fraction of gelled sites as a function of the external stress σ. This is to emulate conditions of an unsteady forcing during macroscopic rheological measurements. In the following, h is the average hits per site in the Gibbs sam-
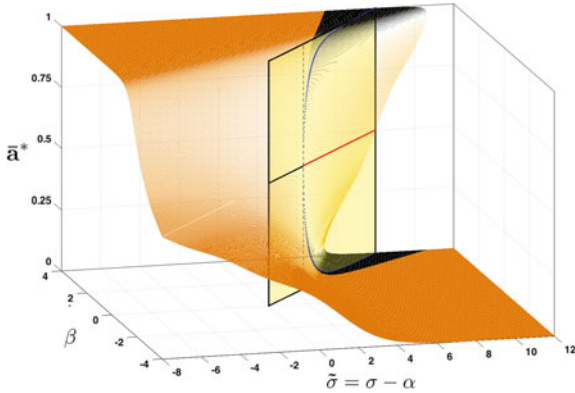
Fig. 15 The fixed points $\bar{\mathbf{a}}^*$ as a set-valued function of the parameters $\tilde{\sigma} = \sigma - \alpha$ and β. The blue, black and azure points are the stable fixed points, while the red and green points are the unstable fixed points of the system. There is a pitchfork bifurcation along $\tilde{\sigma} = 2\beta$ that starts at (2.589145, 1.2945725) where the fixed point at 0.5 becomes unstable with two stable fixed points on either side

pler algorithm and we define it also as the characteristic forcing time t_0 for the stress ramp in our ODE simulations. We set $h = 1000$ in order to reach steady state for each value of σ. In Fig. 16, the trajectories are shown as thin lines and the curves for the ODE approximation have the $\square$ symbol on them. Note the reversibility of the response of the material when $\beta \in \{0, 1\}$ (top row of Fig. 16) upon increasing/decreasing applied stresses. The microscopic model and the ODE approximation quantitatively agree quite well when $\beta < \beta_c$ ($\beta_c \approx 1.3$), the threshold for three fixed points in [0, 1] for the ODE model. As we increase β beyond the aforementioned threshold β_c, we see that irreversible behaviour in the material appears and the comparison between the two models (discrete and continuous) is only qualitative in nature. This is due to the fact that our ODE approximation only models $\bar{\mathbf{a}}$, instead of modelling the dependent pair $(\bar{\mathbf{a}}, \bar{\mathbf{b}})$ that is sufficient for the energy, see Sect. 3.1. This effect can also be seen if we compare the right panel of Fig. 14 with Fig. 10c. Clearly, the light region of Fig. 10c corresponds to the yellow region where the hysteresis is always present. The main discrepancy is the value of β_c. In the ODE approximation, the calculated value is $\beta_c \approx 1.3$, whereas from the Gibbs sampler simulations one obtains $\beta_c^{GS} \approx 1.5$. As mentioned above this difference is due to the fact that in the ODE approximation all bond interactions between neighbours have been disregarded. Further details on improving the agreement between the predictions of the approximating nonlinear dynamical system model with those of the Gibbs field model are given in Sect. 4.4 and in Fig. 9 of Sainudiin et al. (2014).

As a qualitative remark, one can note that even in the presence of strong interactions $\beta > \beta_c$, both models predict an increase of the steepness of the solid–fluid transition (defined as the slope of the dependence $\bar{a}(t)$ on σ around the point where $\bar{a} \approx 1/2$).
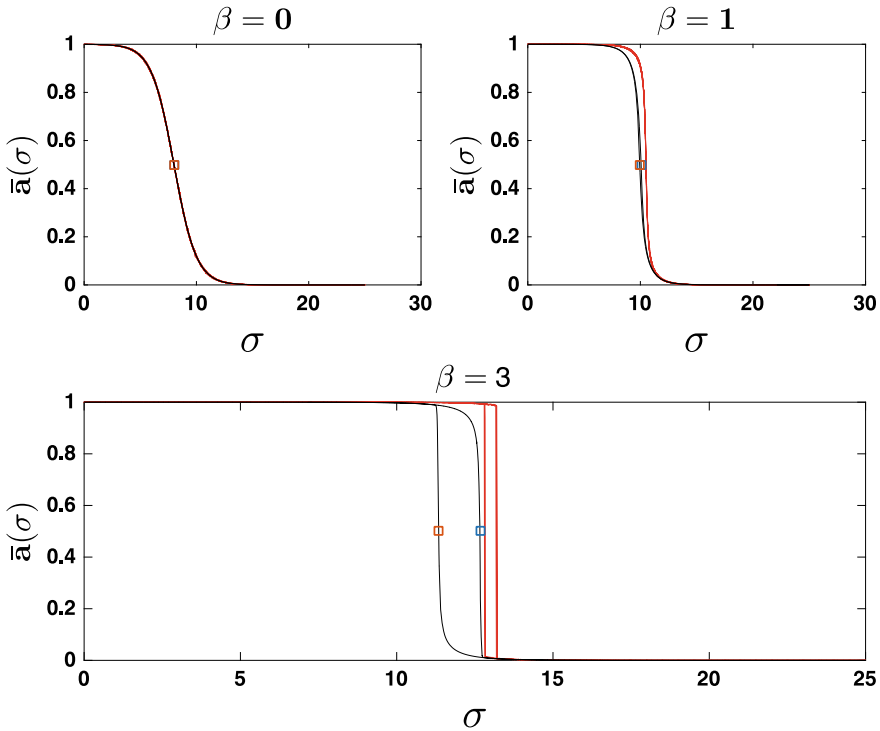
Fig. 16 Gibbs field and ODE approximation simulations with $\alpha = 8$ and $\beta \in \{0, 1, 3\}$. The stress was increased from 0 to 25 in units of 0.01 and decreased back to 0 with a holding time of $t_0 = 1000$ (nearly asymptotic state for each distinct stress) as the site configuration varied from **1** to **0** and then back to **1**. The curves with the symbol ($\square$) are the ODE simulations

3.2.4 Comparison Between Model by Putz and Burghelea Putz and Burghelea (2009) and ODE Approximation

In this section, we will consider the model developed by Putz and coworkers (Putz and Burghelea 2009; Moyers-Gonzalez et al. 2011b). As already highlighted in Sect. 2, this model is phenomenological in the sense that, unlike the Gibbs field model presented in Sect. 3.1 it is not derived from first principles. In this type of modelling, one mimics the behaviour of the microstructure through the definition of a macroscopic structural variable with range in [0, 1], where 0 means completely unstructured or fluid and 1 means completely structured or solid. As explained in Sect. 2, the structural variable a_p satisfies a kinematic equation and usually depends explicitly on the stress and/or rate of strain. In the case of the model by Putz and Burghelea (2009), we have
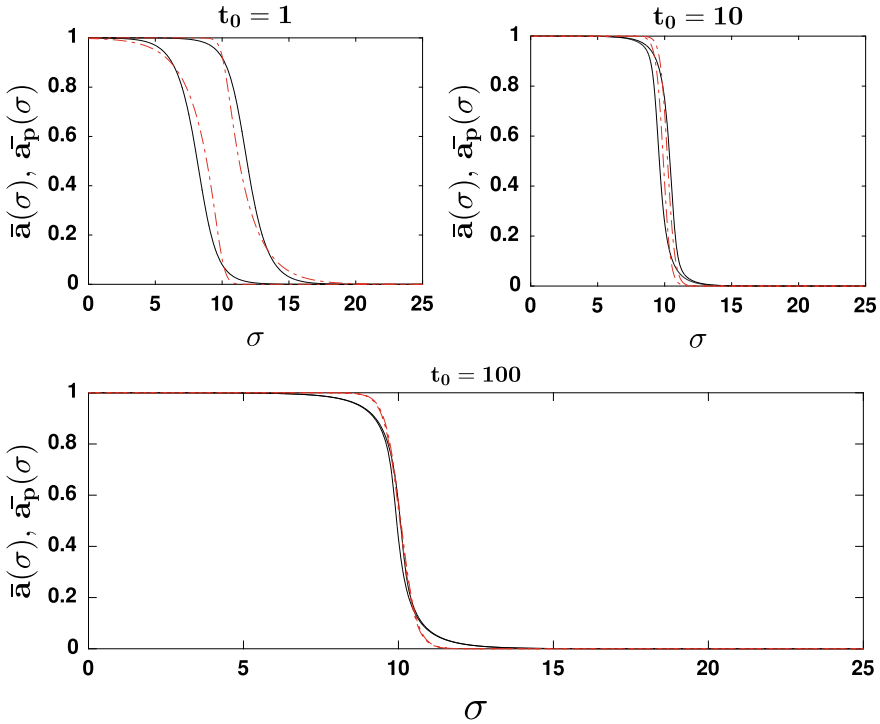
Fig. 17 Comparison between ODE approximation and the model by Putz and Burghelea (2009) detailed in Sect. 2 for different holding times t_0. ODE model with $\alpha = 8$ and $\beta = 1$, the model by Putz and Burghelea (2009) with $k_d = k_r = 0.3$, $w = 0.5$ and $\sigma_y = 10$. Full lines are the ODE approximation and broken lines the model by Putz and Burghelea (2009)

$$\frac{d}{dt} a_p(t) = k_r \left[1 - \tanh \left(\frac{\sigma - \sigma_y}{w} \right) \right] (1 - a_p(t))$$
$$- k_d \left[1 + \tanh \left(\frac{\sigma - \sigma_y}{w} \right) \right] a_p(t), \tag{23}$$

where k_r is the rate of recombination of microstructural units, k_d is the rate of destruction of the solid phase, σ_y is the yield stress and w is a constant that controls how steep the change in the microstructure from solid to fluid and fluid to solid is.

In Fig. 17, we present the simulations of Eqs. (22) and (23) for three characteristic forcing times t_0. As expected we have very good agreement between the models. This could be considered as a qualitative "*proof*" that the phenomenological models can actually approximate the behaviour of the microscopic models derived from first principles.

3.2.5 Determination of the Yield Point in the Limit of a Steady-State Forcing

A reliable estimation of the yield point is important to many practical applications involving yield stress materials. This is typically done by fitting *steady-state* rheological measurements with models with various degrees of complexity ranging from the mathematically simple and classical Herschel–Bulkley correlation up to structural models. Thus, it appears natural to attempt in the following to obtain an estimate of the yield point for the case of a steady-state forcing from the nonlinear dynamical system model presented herein.

To get an approximation for the yield point σ_y during a steady-state forcing process, we will make the assumption (well supported by the results presented in Figs. 12 and 17) that, corresponding to the yield point, the absolute value of the slope of the dependence $\bar{a}^*(\sigma)$ passes through a maximum:

$$\left| \frac{d\bar{a}^*}{d\sigma} \right| \stackrel{\sigma \approx \sigma_y}{\longmapsto} Max. \tag{24}$$

For simplicity, let us focus first on the non-interacting case, $\beta = 0$. From Eq. (20), one can readily show that the condition given in Eq. (24) reduces to $\sigma_y = \alpha$. Thus, in the non-interactive case, the yield point obtained during a steady-state stressing practically coincides with the site-specific threshold α of the Gibbs field model.

We now consider the interactive case $\beta \neq 0$. To a leading order in $\bar{a}^*$ and assuming that around the yield point $\bar{a}^* \approx 1/2$, it can be shown using Eq. (22):

$$\frac{d\bar{a}^*}{d\tilde{\sigma}} \Bigg|_{\sigma \approx \sigma_y} \approx e^{\tilde{\sigma}} \left[\frac{1}{\left(1 + e^{\tilde{\sigma}}\right)^2} - 2 \frac{e^{-\beta}}{\left(1 + e^{\tilde{\sigma}} e^{-\beta}\right)^2} \right]. \tag{25}$$

Fig. 18 Dependence of the approximate yield stress shifted by the site-specific threshold $\tilde{\sigma}_y = \sigma_y - \alpha$ on the interaction parameter β. The dashed line is $\tilde{\sigma}_y = \beta$, and the dash-dotted line is $\tilde{\sigma}_y = 2\beta$. The circles mark the critical point corresponding to $\beta_c \approx 1.3$
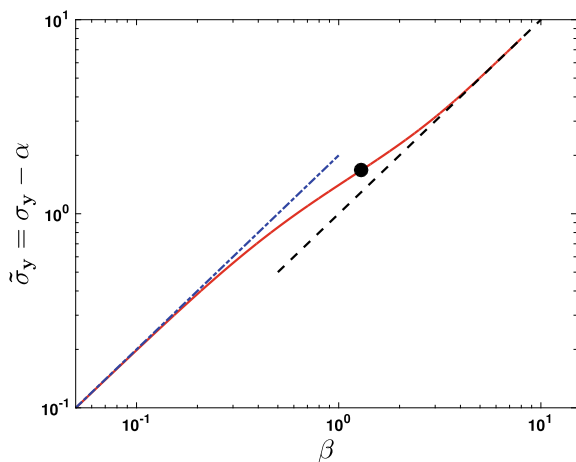
The implicit dependence of the approximate yield stress $\tilde{\sigma}_y$ on the interaction parameter β may be obtained by solving numerically $\left|\frac{d\bar{a}^*}{d\tilde{\sigma}}\right| = 0$. The result is presented in Fig. 18. For interactions weaker than the critical threshold β_c, the apparent yield stress scales as $\tilde{\sigma}_y = \sigma - \alpha = \beta$ (the dash-dotted line in Fig. 18). Beyond this threshold, the scaling becomes steeper, $\tilde{\sigma}_y = \sigma - \alpha = 2\beta$ (the dashed line in Fig. 18). To conclude this part, the yield stress assessed via steady-state controlled stress ramps is (according to our model) expected to depend linearly on both the site-specific threshold α which may be intuitively understood as a measure of the strength of the microscopic constituents of the fluid and the strength β of their interaction and the slope of this behaviour switches when the strength of the interaction passes through the threshold $\beta = \beta_c$.

In Fig. 19, we investigate the dependence of right-hand side of Eq. (25) with respect to $\tilde{\sigma}$ (left panel) and with respect to β (the right panel).

Regardless of the value of the interaction parameter, the stress dependence of the slope passes through a local maximum marked by a full symbol in Fig. 19a. As previously explained, this may be considered as an indicator of the yield point. While β increases, the location of this maximum shifts towards larger stress values as already illustrated in Fig. 18. The value of this maximum slope increases monotonically with β, as shown by the dashed line in Fig. 19a. As we approach β_c, the slope diverges Fig. 19b. This is consistent with the fact that our steady solution becomes discontinuous as a function of $\tilde{\sigma}$. Recall that we have a pitchfork bifurcation with stable fixed points $\{0, 1\}$; hence, the value of σ_y is not unique and depends on the initial condition.
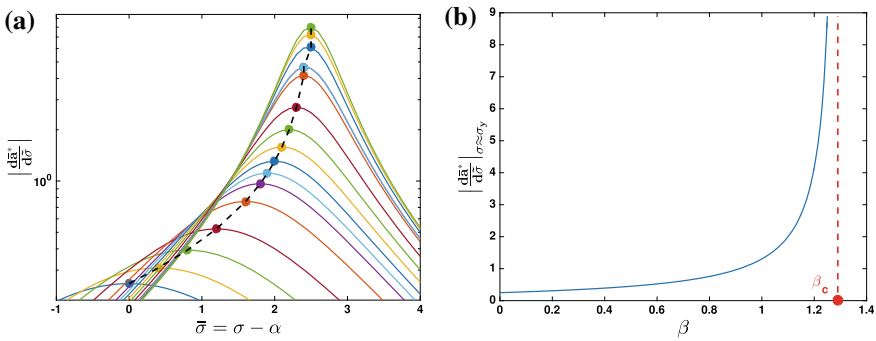
Fig. 19 **a** Dependance of the slope of $\bar{a}^*$ on the applied stress on the yield stress for various values of β ranging from 0 to 2 (β increases from bottom to top). **b** Dependance of the maximum value of the slope $\frac{d\bar{a}^*}{d\tilde{\sigma}}\Big|_{\sigma \approx \sigma_y}$ given by Eq. 24 calculated around the yield point on the interaction parameter β

3.2.6 Description of Linear Controlled Stress Flow Ramps

To demonstrate the practical usefulness of our approach, we focus in the following on the description of an experimentally measured data set acquired during a linear controlled stress flow ramp with a 0.2% (wt) aqueous solution of Carbopol 980, the symbols in Fig. 20. The characteristic forcing time for the rheological test was $t_0 = 2$ s, and the empty/full symbols refer to the increasing/decreasing branch of the stress ramp. As already pointed out, the control parameter of our model is an energy supplied to the lattice rather than a true stress. Yet, in order to describe a one-dimensional data set, one can interpret the stress as the energy supplied per unit volume of material and attempt to couple the evolution equation for the number of sites in a gelled state to a constitutive relation.

To describe the experimentally measured flow ramp, Eq. (22) describing the evolution of the microstructural parameter $\bar{a}(t)$ is complemented by a Maxwell-type thixoelastic constitutive equation (as in the case of the model by Putz and Burghelea (2009) discussed in Sect. 2):

$$\frac{\eta(\dot{\gamma})}{G}\bar{a}\frac{d\sigma}{dt} + \sigma = \eta(\dot{\gamma})\dot{\gamma}, \tag{26}$$

where G is the elastic modulus, $\dot{\gamma}$ is the rate of shear and $\eta(\dot{\gamma}) = K\dot{\gamma}^{N-1} + \sigma_y\frac{1-e^{-m|\dot{\gamma}|}}{|\dot{\gamma}|}$ is a Papanastasiou regularised Herschel–Bulkley viscosity function.

The best fits using both the model by Putz and Burghelea (2009) and the current approach are presented in Fig. 20 as full and dashed lines, respectively.

The fit parameters for the model (the full line in Fig. 20) are $\sigma_y^u = 66.2$ Pa, $\sigma_y^d = 63.45$ Pa, $k_d^u = k_d^d = 0.1\text{s}^{-1}$, $k_r^u = 0.263$ s^{-1}, $k_r^d = 0.95$ s^{-1}, $w_u = 0.93$ Pa, $w_d = 0.143$ Pa, $N_u = N_d = 0.31$, $K_u = 24.33$ Pas^N, $K_d = 27.12$ Pas^N, $G_u = 2036$ Pa and $G_d = 457$ Pa.

Fig. 20 Flow curve measured for increasing (empty symbols) and decreasing (full symbols) values of the applied stress. The full line is a fit by the model by Putz and Burghelea (2009), and the dashed line is the prediction of the nonlinear dynamical system model
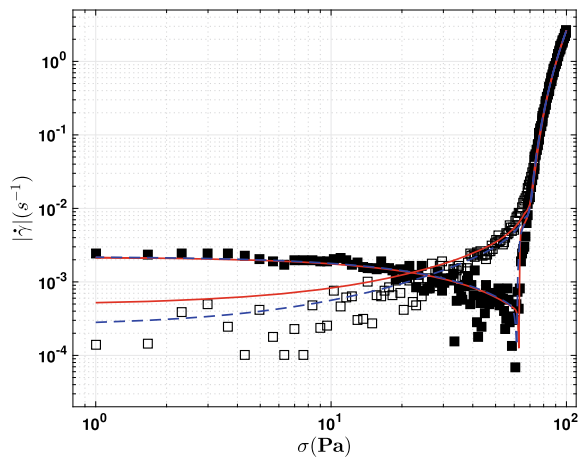
The fit parameters for the nonlinear dynamical system approach (the dashed line in Fig. 20) are $\sigma_y^u = 64.38$ Pa, $\sigma_y^d = 63.48$ Pa, $\alpha_u = 64.72$, $\alpha_d = 62$, $\beta_u = 0.73$, $\beta_d = 0.98$, $N_u = 0.31$, $N_d = 0.3$, $K_u = 26.21$ Pas^N, $K_d = 27$ Pas^N, $G_u = 3929$ Pa and $G_d = 451$ Pa.

The goodness of the fit by the current model is comparable to that by the model (the PMM, see Sect. 2) which demonstrates the practical usefulness of this approach. It is equally worth noting that, for the Carbopol gel used in the rheological test illustrated in Fig. 20, the interactive parameter β obtained for each branch of the stress ramp is smaller than the critical value $\beta_c \approx 1.3$ that defines the cross-over from a reversible to irreversible yielding scenario. This indicates that the Carbopol gels fall into the class of weakly interactive viscoplastic materials that show no thixotropic effects in the limit of a steady-state forcing.

To conclude this section, a fundamental understanding of the yielding of a viscoplastic material may be obtained via a probabilistic approach developed using the main tools of the Statistical Physics similar to the Ising model of magnetisation. Unlike the phenomenological approaches that typically involve a rather large number of parameters some of which have an unclear physical meaning (and, consequently, are difficult to assess experimentally), this approach involves only two internal parameters: a site-specific threshold and the strength of interaction of neighbouring building blocks of the viscoplastic material. These two parameters are responsible for a number of experimentally observed features of the solid–fluid transition: its onset (the yield stress), its reversibility upon increasing/decreasing stresses and its steepness.

4 Viscoplasticity and Hydrodynamic Stability

The flows discussed so far through this chapter were hydrodynamically stable and the only source of nonlinearity in the momentum equation was related to the constitutive relation describing the viscoplastic material. The aim of this section is to introduce the reader into the hydrodynamic stability of yield stress materials. We discuss two distinct types of instabilities involving viscoplastic materials. In Sects. 4.1, 4.2, we discuss the inertial instability of flows of a viscoplastic material in a pipe flow and in a plane channel flow, respectively. In Sect. 4.3, we discuss a low Reynolds number hydrodynamic instability triggered by a fast chemical reaction occurring at the interface between two fluids which locally creates a yield stress material or, in other words, a strong stratification of stresses.

4.1 Transition to Hydrodynamic Turbulence in a Shear-Thinning Physical Gel

In this section, we summarise some key results of an experimental study of the laminar, transitional and turbulent flows of a viscoplastic fluid in a cylindrical pipe

(Hagen–Poiseuille flow). For a more comprehensive account of the main results, the reader is referred to Güzel et al. (2009). As compared to the laminar flows previously studied through this chapter, such flows are expected to be significantly more complex as two sources of nonlinearity are present in the Navier–Stokes equation: *inertial* (related to large *Reynolds* numbers) and *rheological* (related to the dependence of the stresses on the rate of strain).

The motivation of studying the hydrodynamic stability of yield stress fluids is threefold:

1. Fluids of shear-thinning type with a yield stress abound in industrial settings, as well as some natural ones. The particular motivation here comes from both the petroleum industry and the pulp and paper industry, where design/control of the inherent processes often requires knowledge of the flow state at different velocities. Similar fluid types and ranges of flows occur in food processing, polymer flows, and in the transport of homogeneous mined slurries. Although many of these industrial fluids exhibit more complex behaviour (e.g. thixotropy, viscoelasticity, etc.), as noted by Bird et al. (1977), the shear-dependent rheology is often the dominant feature.

2. In line with the above, there is a demand from industrial application to predict the Reynolds number ($Re = UD/\nu$, where U is the average velocity, D is the diameter of the pipe and ν is the kinematic viscosity), or other bulk flow parameter, at which transition occurs, for a range of fluid types, so that different frictional pressure closures may be applied to hydraulics calculations above/below this limit. One of the such earliest attempts, and probably still the most popular, was that of Metzner and Reed (1955). Perhaps, the most obvious weakness with such phenomenological formulae is that turbulent transition occurs over a wide range of Reynolds numbers and not at a single number. For example, in careful experiments, Hof et al. (2003) report retaining laminar flows in Newtonian fluids up to $Re = 24000$, whereas the common observation of transition initiating in pipe flows is at $Re \approx 2000$. Thus, there is a difficulty with interpreting the predictions of phenomenological formulae, many of which we note were either formulated before a detailed understanding of transitional phenomena has developed.

3. A third and most important motivation of such study is of a scientific nature. Since Reynolds' famous experiment (Reynolds 1883), transition in pipe flows has been an enduring unsolved problem in Newtonian fluid mechanics. It is thus natural that there have been far fewer studies of non-Newtonian fluids in this regime, either experimental or numerical/theoretical. The intellectual challenge is related to dealing with two sources of strong nonlinearity in the momentum equation discussed in the *Introduction*: inertial and rheological—coming from nonlinearity of the stress rate of strain relationship. The existing studies that have been conducted for shear-thinning viscoplastic fluids leave a large number of intriguing questions unanswered. In the first place, experimental studies by Escudier and Presti (1996) using Laponite suspensions and by Peixinho et al. (2005b) using Carbopol® solutions have revealed interesting flow asymmetries in the mean axial velocity profile during transition, which have been largely unexplained. These have been summarised by Escudier et al. (2005).

4.1.1   Experimental Setup and Procedures

All the results we report herein are from tests performed in a $L = 10$-m-long flow loop with an inner diameter of $2R = 50.8$ mm. The setup is illustrated schematically in Fig. 21. The flow is generated by a variable-frequency-driven screw pump fed to a carbon steel inlet reservoir $\mathbf{R_1}$ of approximately 120 L capacity to an outlet reservoir $\mathbf{R_2}$ of the same capacity. The pump can provide a maximum flow rate of ≈ 22 l/s, which is equivalent to a maximal mean flow velocity of ≈ 10 m/s. Two honeycomb sections are placed inside the reservoir $\mathbf{R_1}$ before the tube inlet in order to suppress any swirl or other fluid entry effects. We used a Borda style entry condition in which the pipe extended backwards approximately 50 cm into the tank. Two honeycomb elements were inserted into this section. The fluid reservoir $\mathbf{R_2}$ is pressurised to damp mechanical vibrations induced by the pump motor and a flexible hose is used between the pump and reservoir in order to diminish flow pulsations.

The flow structure has been investigated using the laser Doppler velocimetry (LDV) technique. A detailed description of the LDV optical arrangement is given in Güzel et al. (2009). Two pressure transducers ($\mathbf{PT_{1,2}}$) are located near the inlet and outlet of the flow channel (Model 210, Series C from www.gp50.com). These are bonded strain gauge transducers with internal signal conditioning to provide a Vdc output signal in direct proportion to the input pressure. The accuracy of each transducer is 0.02% of the full scale, and they were calibrated with an externally mounted pressure gauge. Pressure drop readings Δp were averaged over 150 s and used to estimate the radius of the plug according to
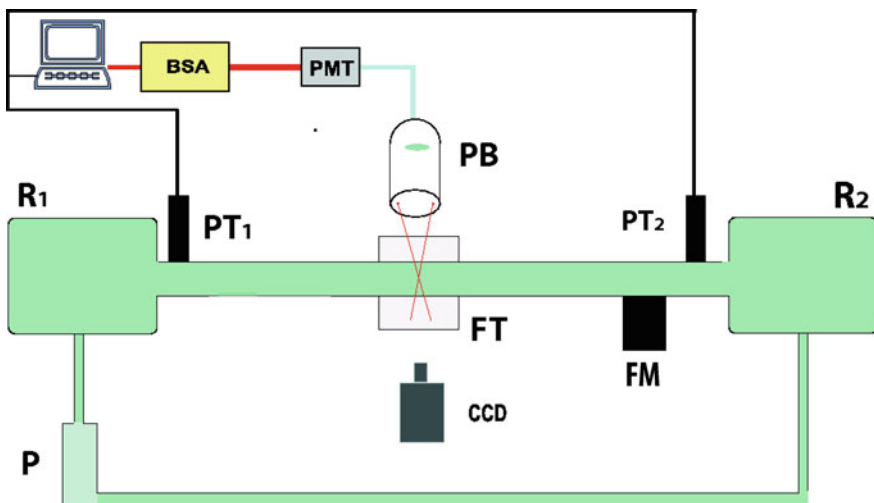
Fig. 21 Schematic view of the experimental setup: $\mathbf{R_{1,2}}$—fluid reservoirs, **P**—pump, **FM**—flowmeter, $\mathbf{PT_{1,2}}$—pressure transducers, **FT**—fish tank, **CCD**—digital camera, **PB**—laser Doppler velocimetry probe, **PMT**—photomultiplier, **BSA**—burst spectrum analyzer

$$r_p = 2L \frac{\sigma_y}{R \Delta p}. \tag{27}$$

Flow rates were estimated using two methods: (i) using an electromagnetic flowmeter (**FM**) installed near the outlet reservoir, as shown in Fig. 21; (ii) by numerically integrating the measured axial velocity profiles. The latter estimate is used to calculate the relevant flow parameters reported through this section. The transversal profiles of the axial velocity have been measured at a position $L_m = 108D$ downstream where the flow is fully developed (corresponding to a Reynolds number $Re \approx 3000$ the entry length was estimated $L_e \approx 100D$).

The Reynolds number can be defined in a number of ways for a non-Newtonian fluid. Here, we define a generalised number that accounts for the shear thinning of the solution across the pipe by

$$Re_G = \frac{4\rho}{R} \int_0^R \frac{\bar{u}(r)}{\eta [\dot{\gamma}(r)]} r dr, \tag{28}$$

where ρ and η are the density and the effective viscosity of the fluid. The latter depends on the strain rate of the base flow $\dot{\gamma}(r)$ which is calculated locally from the transversal profile of the time-averaged axial velocity $\bar{u}(r)$. As a yield stress material, we have used several aqueous solutions of Carbopol® 940. As a first approximation, we consider here for simplicity a Herschel–Bulkley constitutive relationship, $\eta = \sigma_y \dot{\gamma}^{-1} + K \dot{\gamma}^{N-1}$. As already discussed in Sects. 1 and 2, the Herschel–Bulkley constitutive relationship does not accurately describe the yielding of a Carbopol® gel. In our context, the main problem arises from the term $\eta(\dot{\gamma})$ which around the solid–fluid transition diverges. The experimental measurements presented in Sect. 1 indicate that prior to yielding the viscosity is very large but finite. The Herschel–Bulkley correlation, however, remains useful to get an estimate for the yield stress.

4.1.2 Transition to Turbulence in the Pipe Flow of a Shear-Thinning Yield Stress Fluid: Phenomenological Observations

Before proceeding to the main findings, it is instructive to first examine representative transversal profiles of the time-averaged velocity. To this end, we plot transversal profiles of the time-averaged velocity $\bar{u}$ as a function of Re_G, see Fig. 22 measured with a 0.1% Carbopol® solution at various Re_G. At each radial position, over one-hundred thousand instantaneous velocity measurements were used in the ensemble average and the confidence interval for each point is very small. It should be noted that the results have been made dimensionless by scaling the ensemble average with the centreline velocity u_c. Under laminar conditions, that is, with $Re_G < 1700$, the fully developed laminar profiles are included in these graphs as the solid lines. This was performed in order to ascertain the validity of our results. For the higher flow rates, we present cases for both transitional and turbulent flows. Dashed lines are drawn to highlight an apparent asymmetry in the measurements. The dashed lines
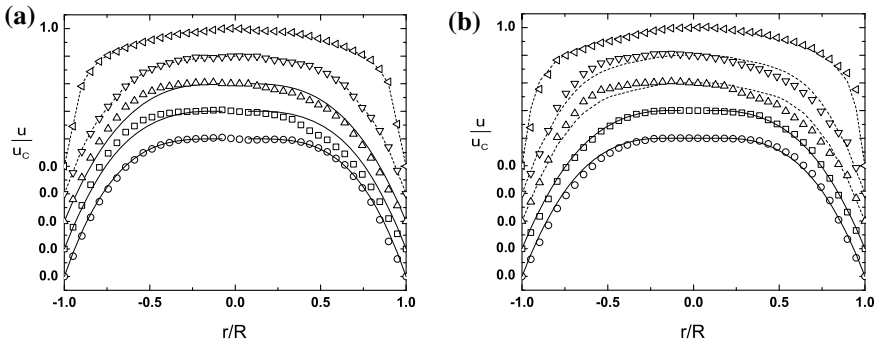
Fig. 22 The transversal profiles of the time-averaged velocity $\bar{u}$ for 0.1% (wt) Carbopol: **a** Re_G=378 ($\bigcirc$), 937 ($\square$), 1160 ($\triangle$), 1735 ($\triangledown$) and 2920 ($\triangleleft$) **b** Re_G=397 ($\bigcirc$), 914 ($\square$), 2001 ($\triangle$), 2238 ($\triangledown$) and 2612 ($\triangleleft$). These data are from replicate tests obtained from similar experimental conditions

were constructed by averaging the data at equivalent radial positions on either side of the central axis. The asymmetry is apparent and disappears once a fully turbulent flow regime is achieved. It is worth noting that the asymmetry is systematic, i.e. these data were taken from time-averaged data and the asymmetry is consistently in the same part of the pipe for the same fluid. This persistent flow asymmetry runs contrary to the intuitive notion that transitional flow structures, when ensemble averaged over a suitably long time, should occur with no azimuthal bias. A similar asymmetry has been reported by other groups in their experiments (Escudier and Presti 1996; Peixinho et al. 2005b; Escudier and Presti 1996). The initial reaction to this rather unexpected flow asymmetry was to look for and eliminate any directional bias in the apparatus or in the flow visualisation technique. However, even after extensive precautions the asymmetry still persists and is fully reproducible in subsequent tests and for several concentrations of Carbopol®(a more comprehensive discussion and additional data are presented in Güzel et al. 2009).

To characterise the transition to turbulence in a Carbopol® gel, the turbulence intensity is monitored at various radial positions r/R. The turbulence intensity is defined as $I = \frac{u_{rms}}{\bar{u}}$ where u_{rms} stands for the root mean square of the fluctuations of the point-wise velocity.

After a rapid increase through transition, the turbulent intensity relaxes as we enter the fully developed turbulent regime, as shown in Fig. 23. An important experimental observation is that transition does not involve a simultaneous and sharp increase in turbulent intensity across the pipe radius. Instead, one may notice in Fig. 23 that the turbulent intensity begins to increase at $r/R = \pm 0.75$ at markedly lower generalised Reynolds numbers than at the centreline. This observation was systematically reproduced for several other Carbopol® solutions indicating that this transition scenario is rather universal.

To get additional insights into the evolution of the flow structure around the onset of the laminar–turbulent transition, we resort to a qualitative imaging of the flows. For this purpose, the flow was seeded with a minute amount of Kalliroscope reflective

Fig. 23 Turbulence intensity measured at $r/R = 0$ (circles), $r/R = -0.75$ (up triangles) and $r/R = 0.75$ (down triangles) for a 0.1% (wt) solution of Carbopol® 940
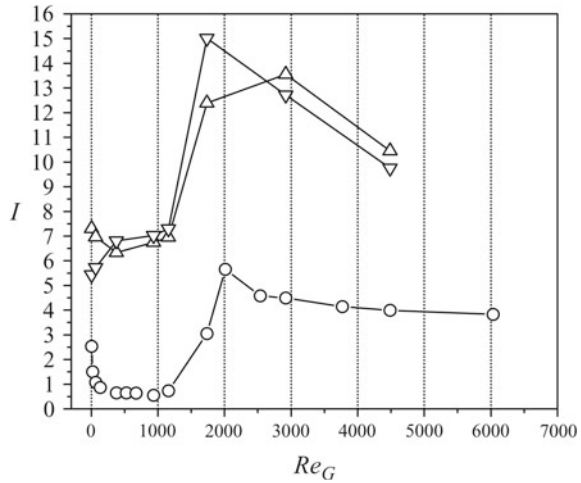
flakes. Thus, turbulent "puffs" passing the point of observation cause mixing of the tracer particles which result in "grainy" flow image due to local changes in mean orientation (i.e. reflectance) of the seeding particles. Instant puff images obtained for a 0.075% (wt) solution of Carbopol® at a Re_G close to the onset of the instability are illustrated in Fig. 24. With these images, we attempted to characterise the size and velocity of the leading and trailing edges of the puff by an object tracking method. We have also produced spatiotemporal plots of the images. Here, the images are filtered and the variation of greyscale intensity at one axial position is reported as a function of time, see Fig. 25. What is clear in this sequence of images is that an asymmetry is once more evident. As compared to the Newtonian case (data not shown here but shown in Fig. 10 of Güzel et al. 2009), the leading edge of the puff is elongated and is located in the vicinity of the wall. Moreover, the puffs observed with the Carbopol® solution will spread axially at a significantly slower rate than those typically observed with Newtonian fluids. Another observation for the case of a Carbopol® solution is that the elongation of the leading edge gets smaller with decreasing concentrations of Carbopol®, i.e. the tip observed in Fig. 25 is both reduced in size and located closer to the centre line of the pipe.

To summarise our observations, we measured the axial velocity as a function of radial position using the LDV for several aqueous solutions of Carbopol® solutions undergoing Hagen–Poiseuille flow within a wide range of Reynolds numbers. We find that for all the fluids tested there exists a persistent asymmetry in the velocity profiles present during transition. Symmetrical flows were found for both laminar and fully turbulent cases. These observations were confirmed using high-speed imaging. No physical explanation is given at this point. We do, however, attempt to quantify the transition more precisely by presenting a more in-depth statistical analysis of these results. To this is dedicated the next section.
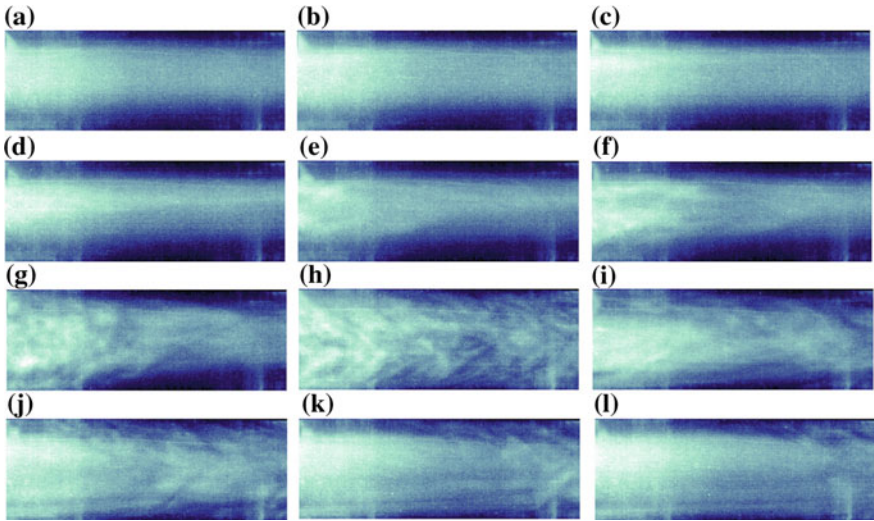
Fig. 24 Instant puff images taken for 0.075% solution of Carbopol® 940 at $Re_G = 1850$ at different time instants: **a** $t = 130$ ms, **b** $t = 225.5$ ms, **c** $t = 255.5$ ms, **d** $t = 320$ ms, **e** $t = 422.5$ ms, **f** $t = 447.5$ ms, **g** $t = 497.5$ ms, **h** $t = 600$ ms, **i** $t = 755$ ms, **j** $t = 1117.5$ ms, **k** $t = 1155$ ms and **l** $t = 1187.5$ ms
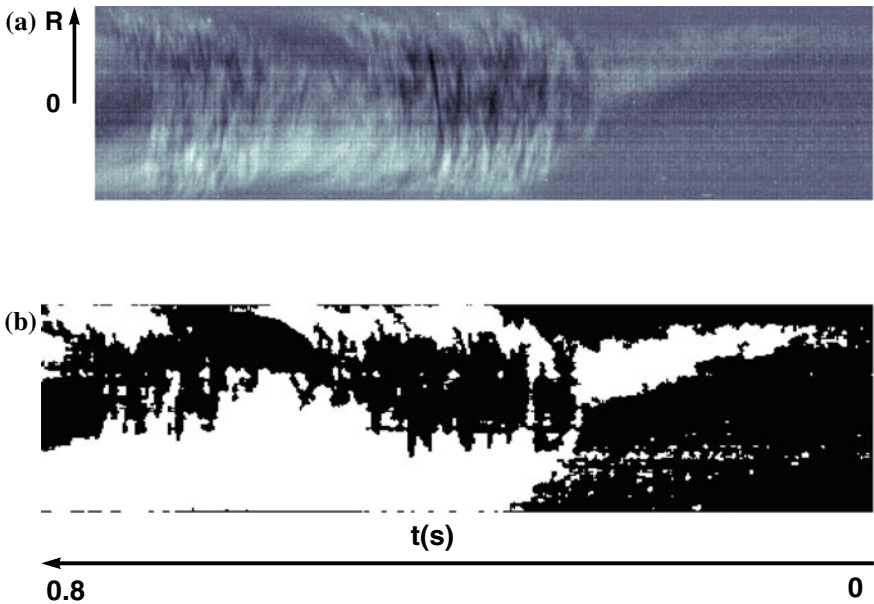
Fig. 25 Space-time plot measured with a 0.075%(wt) Carbopol® at $Re_G = 1850$ **a** obtained from raw images **b** obtained from filtered, background subtracted and binarised images. The puff length is ≈1.69 m. The images sequence consisted of 320 frames

4.1.3   Statistics of Weak Turbulence

Landau and Lifschitz indicate that inertially turbulent flows are traditionally charac-
terised by random fluid motion in a broad range of spatial and temporal scales (Landau
and Lifschitz 1987). We have attempted to characterise these relevant scales using
several statistical measures as indicated by Frisch (1995).

A first statistical measure is the Eulerian autocorrelation of the velocity defined by

$$C(t) = \frac{\langle u(t)u(t + \tau)\rangle_\tau}{u_{rms}^2} \tag{29}$$

and determined using the LDV data. This quantity is a measure of the time over
which the instantaneous velocity $u(t)$ is correlated with itself. In other words, $C(t)$
is bounded by unity as t approaches zero and by zero as $t \to \infty$, because a process
becomes un-correlated with itself after a long time.

We report measurements of the temporal autocorrelation function as a function of
both Re_G and the radial position in the pipe, Fig. 26. Before we proceed to interpret
these figures, we must spend some time explaining how the data is represented. Each
figure is given as three panels, i.e. at three different radial positions. Within each
panel, four data sets are presented representing four different Reynolds numbers. The
data series labelled (**1**) and (**2**) represent laminar flow while (**3**) is in the transitional
regime and (**4**) in a turbulent regime. With regards to (**1**), which corresponds to
the lowest Re_G, in each of the panels the velocity signal is probably dominated by
high-frequency noise which results in a fast decay of $C(t)$ with a characteristic decay
time which we find to be of the order of the inverse data rate of the LDV signal.
Proceeding through (**4**), we find the fully turbulent state characterised by rapid decay
of the autocorrelation to the noise level.

A striking difference is found in curve (**2**) in comparison to the other curves. We
observe that there are plateaus in these curves, for some radial positions for each of the
fluids, e.g. at $C(\tau) \sim 0.4$ for both $r/R = \pm 0.75$. Although this data was obtained in
a region which we define as laminar, it is clear that there are some weakly correlated
structures at this radial position in the pipe. For the Newtonian fluid, the plateau in the
autocorrelation is at a lower value than for the non-Newtonian fluids and is visible
also at the centreline (data are not shown here but detailed in Güzel et al. 2009).
For the case of the Carbopol® solution illustrated in Fig. 26, the plateau is strongly
attenuated at the centreline but evident at the radial positions $r/R = \pm 0.75$. Using
Taylor's frozen flow hypothesis (Taylor 1938), we may estimate the axial length scale
of these structures to be $\sim 10^{-1}$ m, being longer for the Newtonian fluids than for the
non-Newtonian fluids (again, for a full account of this issue the reader is referred
to Güzel et al. 2009). This is significantly lower than the size of the puffs and slugs
estimated via the high-speed imaging technique. We comment also that consistently
with the flow asymmetry of the velocity profiles illustrated in Fig. 22 an asymmetry
is observed in many of the autocorrelations curves as well.
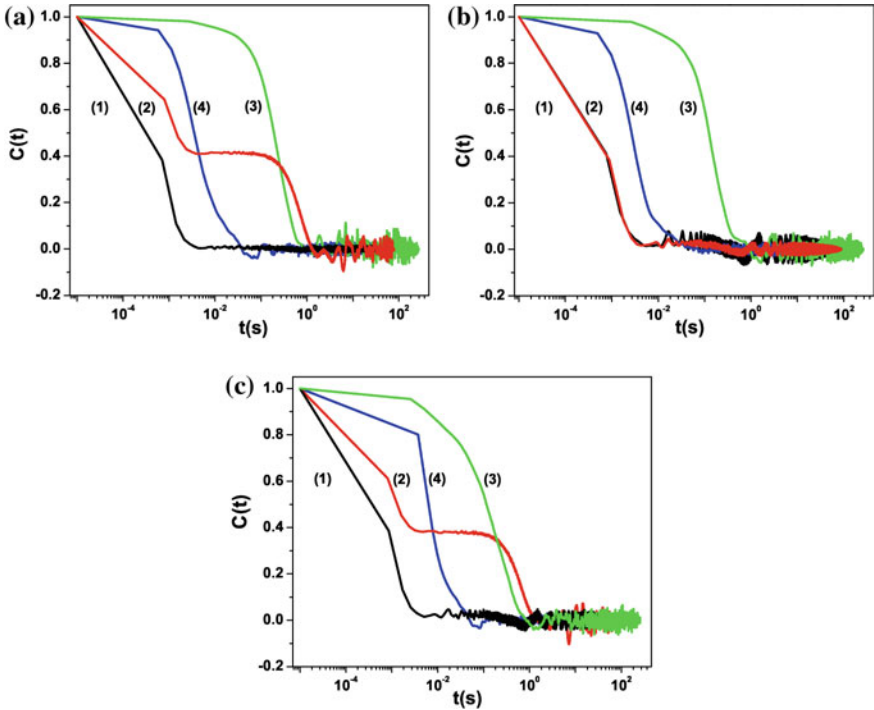
Fig. 26 Correlation functions measured for a 0.1% solution Carbopol® at three different radial positions: **a** $r/R = -0.75$ **b** $r/R = 0$ **c** $r/R = 0.75$. The data sets in each panel are (**1**) $Re_G = 397$, (**2**) $Re_G = 914$, (**3**) $Re_G = 2238$, (**4**) $Re_G = 3309$

4.1.4 Evolution of the Plug Region During Transition

For yield stress fluids, the role of the plug region in retarding transition is largely unknown. If one interprets the yield stress fluid to be fully rigid below the yield stress, then the laminar flow is analogous to that with the plug replaced by a solid cylinder moving at the appropriate speed. Presumably, since the effective viscosity becomes infinite at the yield surface, the flow should be locally stabilised. Two different scenarios may be postulated at transition:

1. Transition may occur in the yielded annulus around the plug, leaving intact the plug region;
2. Transition is retarded until the plug region thins to such an extent that the Reynolds stresses (in the annular region) can exceed the yield stress.

In the first scenario (Peixinho 2004; Peixinho et al. 2005a), during the first stage of transition the turbulence intensity level on the centreline is reported as being similar to laminar levels. This is also the scenario assumed explicitly in some phenomenological theories of transition (Slatter 1999) treats the plug as a rigid body in developing his

Fig. 27 Axial Reynolds stresses normalised by yield stress for four different concentration levels of Carbopol®. The filled symbols indicate points where the flow becomes transitional, with puffs/slugs first observed
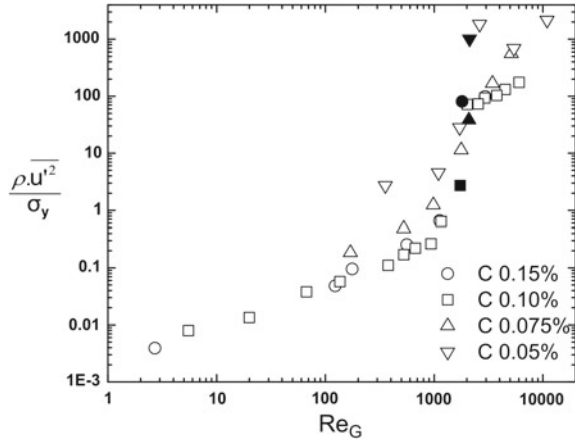
formula for transition. In Fig. 27, we present the ratio of averaged Reynolds stress at the centreline (where the level of velocity fluctuations is minimum) to the yield stress, as a function of the generalised Reynolds number Re_G for the four different Carbopol concentrations that we have used. The filled symbols in Fig. 18 mark the lowest value of Re_G for which puffs or slugs were detected in the experiments, for each of the different concentrations of Carbopol.

One can observe that the mean Reynolds stress exceeds the yield stress in each case. This remains true even if we subtract the laminar flow fluctuations from the Reynolds stresses, interpreting them as instrumental noise. This suggests that the second explanation given above is the more plausible, i.e. the viscoplastic plug has broken when transition starts. This is further reinforced by the results of the previous section on the structure functions, i.e. at these transitional/weak turbulent Reynolds numbers we have observed very similar intermittency characteristics with Carbopol, right across the pipe radius, as with Xanthan, where there is no yield stress. We should also comment that for the concentrations of Carbopol that we have used, if we calculate the (laminar) unyielded plug diameters using Eq. (27), for the largest flow rates for which puffs or slugs are not detected (see Fig. 28) these plug diameters are at most of the order 2 mm. Thus, we do not anyway have a strong plug close to transition.

There is no contradiction with the data from other works (Peixinho 2004; Peixinho et al. 2005a), simply with its interpretation. Even with this thinning and break-up of the plug, in the Reynolds number range preceding transition flow instabilities are not sustained. Peixinho et al. (2005a) report measuring low-frequency oscillations away from the central region. Such low-frequency forcing, presumably with slow axial variation, could easily be responsible for slow extensional straining that yields the true plug of the base flow into a pseudo-plug. This type of psuedo-plug also occurs, for example, in thin-film flows (Balmforth and Craster 1999), and in channels of

Fig. 28 Plug radius normalised by pipe radius for four different concentration levels of Carbopol® indicated in the insert
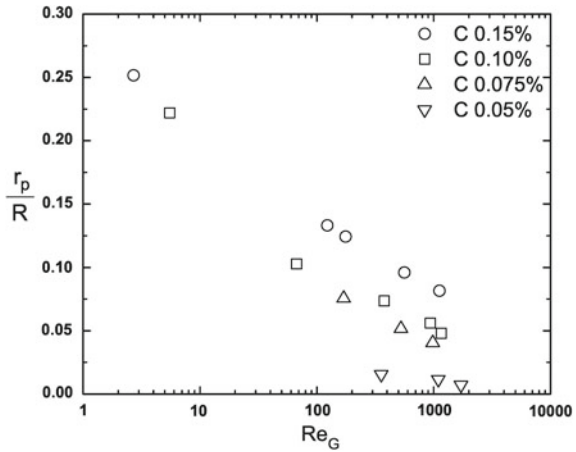
slowly varying width (Frigaard and Ryan 2004). In such flows the velocity remains asymptotically close to the base flow solutions, while shear and extensional stresses combine to maintain the pseudo-plug at just above the yield stress. Such flows are laminar but yielded and the psuedo-plug is characterised by large effective viscosity, which would presumably give similar characteristics to the base laminar flow in controlling fluctuation level, Peixinho (2004), Peixinho et al. (2005a). From our measurements of the velocity profiles, the mean velocity remains very plug-like in the centre of the pipe in this upper range of laminar Reynolds numbers and it is simply not possible to discern whether what is observed is a true plug or not. Evidently, the ideal situation would be to visualise transition within a plug region of significant size in comparison to the pipe. Interestingly, this was the intention of our experiments. Our study was started after discussions with C. Nouar about ongoing experiments (Peixinho 2004; Peixinho et al. 2005a). These were conducted in a 30 mm pipe at lower speeds, and for the flow rates at which transition occurred the plug region had radius of the order of 1 mm: too small to detect if broken or not. This prompted our interest in the role of the plug during transition, and we therefore designed our experiments at a larger scale so that we could potentially achieve transition with higher yield stress fluids, in larger diameter pipes and at higher speeds, hopefully also with a larger plug radius at transition. This objective could not be attained, as the small values of r_p/R in Fig. 28 indicate. Together with these experiments (Peixinho 2004; Peixinho et al. 2005a), the results described above contribute to the evidence that the plug region must thin to such an extent that the Reynolds stresses can break it, before transition commences.

4.2 Hydrodynamic Stability of a Plane Poiseuille Flow of a Carbopol® Solution Within the P M M Framework

We have argued in Sect. 1 of this chapter that the yielding scenario of a Carbopol® gel is somewhat more complex that one would have expected and it cannot be accurately described by the classical Herschel–Bulkley framework. To circumvent these difficulties, we have proposed in Sect. 2 a phenomenological model able to both account for a gradual solid–fluid transition and describe the elastic effects observed in both rheological (controlled stress ramps) and tabletop (e.g. the sedimentation problem discussed in Sect. 1 and illustrated in Fig. 1b).

The fundamental question we address in this section is: *To what extent the novel yielding scenario proposed in* Sect. 2 *could influence our understanding of hydrodynamic stability?*.

At a first glance, this question might appear groundless: the yielding transition occurs at very low Re (typically $Re \ll 1$), whereas the loss of hydrodynamic stability due to the inertial term in the momentum equation occurs at significantly larger Re (typically $Re > 1000$); therefore, what is the physical connection between the two phenomena? Given a second thought, the relevance of the yielding scenario to the hydrodynamic problem may be defended as follows. The base flows usually considered in the linear analysis of the hydrodynamic stability of channel flows of yield stress fluids are characterised by a significant stratification of the velocity gradients: large values near the channel boundaries which are consistent with a yielded flow region and vanishing values near the centre line, which are consistent with a plug region. The experimental investigation of the laminar–turbulent transition in the pipe flow of a yield stress fluids we have briefly presented in Sect. 4.1 (Güzel et al. 2009) demonstrates that the transition to turbulence occurs when the Reynolds stresses balance the yield stress of the fluid, that is, when the plug is broken. These findings corroborate well with the idea that, contrary to our initial intuition, the nature of the solid–fluid transition and the yielding scenario may actually play a role in the hydrodynamic stability problem.

To test this, we briefly discuss in the following the linear stability of a plane channel flow of an elasto-viscoplastic material described by the phenomenological presented in Sect. 2 and compare our results with the results obtained from a Casson regularised constitutive relationship. For the details of this analysis, the reader is referred to Moyers-Gonzalez et al. (2011a).

The plane channel flow of the elasto-viscoplastic fluid is described by the following set of equations depending on the variables $(p, \mathbf{u}, \boldsymbol{\sigma}, \bar{a})$:

$$\rho \left(\frac{\partial \mathbf{u}}{\partial t} + (\mathbf{u} \cdot \nabla) \mathbf{u} \right) = -\nabla p + \eta_s \nabla \cdot \dot{\gamma} + \nabla \cdot \boldsymbol{\sigma} \qquad (30)$$

$$\nabla \cdot \mathbf{u} = 0, \qquad (31)$$

where η_s is the solvent viscosity and $\dot{\gamma}$ is the rate of strain tensor. The constitutive relation is the one we have proposed in Sect. 2 in the framework of the phenomenological yielding model but adapted to a tensorial form in order to be coupled to the Navier–Stokes (Eq. 30):

$$\boldsymbol{\sigma} + \lambda\left(\dot{\gamma}, \bar{a}\right) \underset{\nabla}{\nabla} \boldsymbol{\sigma} = \eta\left[\dot{\gamma}(\mathbf{u})\right] \dot{\gamma}, \tag{32}$$

where $\underset{\nabla}{\nabla} \cdot = \frac{D \cdot}{Dt} - \nabla \mathbf{u} \cdot - \cdot \nabla \mathbf{u}^T$ is the upper convected derivative ($\frac{D \cdot}{Dt}$ is the classical material derivative), $\lambda\left(\dot{\gamma}, \bar{a}\right) = \frac{\eta\left[\dot{\gamma}(\mathbf{u})\right]}{G}\bar{a}$ is the relaxation time and G is the elastic modulus. The concentration of the unyielded material $\bar{a}$ satisfies the kinematic equation below:

$$\frac{\partial \bar{a}}{\partial t} + (\mathbf{u} \cdot \nabla)\,\bar{a} = R_d\left[\bar{a}, \sigma(\mathbf{u})\right] + R_r\left[\bar{a}, \sigma(\mathbf{u})\right]. \tag{33}$$

As detailed in Sect. 2, R_d, R_r are the rates of destruction and re-formation of solid structural units, respectively. The hydrodynamic stability problem is governed by the Reynolds (Re), the Weissenberg (Wi) and the Bingham (Bi) number defined as

$$Re = \frac{\rho L U_{max}}{\eta} \tag{34}$$

$$Wi = \frac{\lambda_H U_{max}}{L} \tag{35}$$

$$Bi = \frac{\sigma_y L}{\eta U_{max}} \tag{36}$$

The relaxation time λ_H is defined here as $\lambda_H = \frac{\eta_\infty}{G}$ with η_∞ being the infinite shear viscosity and G the elastic modulus. The plasticity number, $Pl = Re\,Bi = \frac{\sigma_y \rho L}{\eta^2}$, is defined as the product between the Reynolds number and the Bingham number. Note that Pl depends solely on the rheological properties of the fluid and the geometry of the problem, thus as we increase Re in our analysis Pl will remain fixed. For this reason, we chose Pl as control parameter through our analysis.

As is common in linear stability analysis, we consider an infinitesimal perturbation ($\epsilon u'$, $\epsilon p'$) superimposed upon the base flow and linearise the momentum Eq. (30) around the base flow solution. We do not show here the full development of the linear stability analysis (for these mathematical details, the reader is referred to Moyers-Gonzalez et al. 2011a) but solely focus on the main results. Unlike pipe flows of Newtonian fluids which are linearly stable at all Re, the plane Poiseuille flow becomes linearly unstable at $Re_{Newt} = 5772$.

We have studied the onset of instability for two cases: the case of an yield stress fluid described by the classical Herschel–Bulkley constitutive relation and the case of a fluid described by the model by Putz and Burghelea (2009). The dependence

Fig. 29 Normalised critical
Re for increasing *Pl*
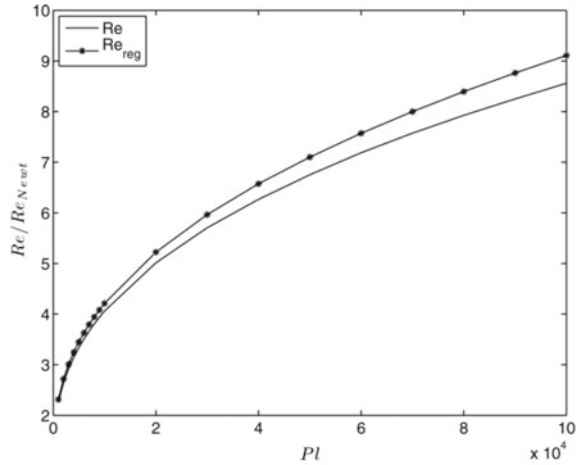
of the normalised onset of the instability on the plasticity number for each case is
illustrated in Fig. 29.

   As with the regularised Herschel–Bulkley model, the existence of a pseudo-plug
region (spatially stratified viscosity) is sufficient to greatly enhance the stability of
the flow. The critical Reynolds number appears to be a monotone increasing function
of plasticity number *Pl*, just as with the regularised viscoplastic model. We should
also note that the inclusion of a highly viscous viscoelastic fluid as a plug destabilises
the flow when comparing it with the regularised model (shown as the lower curve
in Fig. 29). In relative terms, when $Pl = 1000$ the critical Reynolds number for the
elasto-viscoplastic model is 2.66% smaller than the critical Reynolds number for
regularised model. For $Pl = 10^5$, this percentage increases to around 6%; this is due
to the fact that the pseudo-plug and solid–fluid regions increase and are closer to
the wall. Thus, the central conclusion of this study is that the presence of a solid–
fluid coexistence transitional regime marked by the presence of elastic effects which
is properly accounted for by the model by Putz and Burghelea (2009) proposed in
Sect. 2 has a destabilising role.

4.3 Unstable Flows Triggered by a Fast Chemical Reaction

Generating high Reynolds number flows as illustrated in Sect. 4.1 may sometimes
prove to be un-practical, e.g. in the case of highly viscous fluids flowing in spatially
confined environments. An alternative way of breaking the hydrodynamic stability
in the absence of any significant inertial contribution ($Re \ll 1$) is to "*switch on*"
another source of nonlinearity in the Navier–Stokes equation. This can be done by
inducing a strong spatial heterogeneity of the viscosity (and/or yield stress) in the
flow. Although the hydrodynamic stability of miscible shear flows with a strong

Fig. 30 Schematic overview of the reactive flow configurations: **a** displacement configuration **b** Hele–Shaw parallel flow configuration. The colours in each panel refer to the pH of the fluid—see text for description
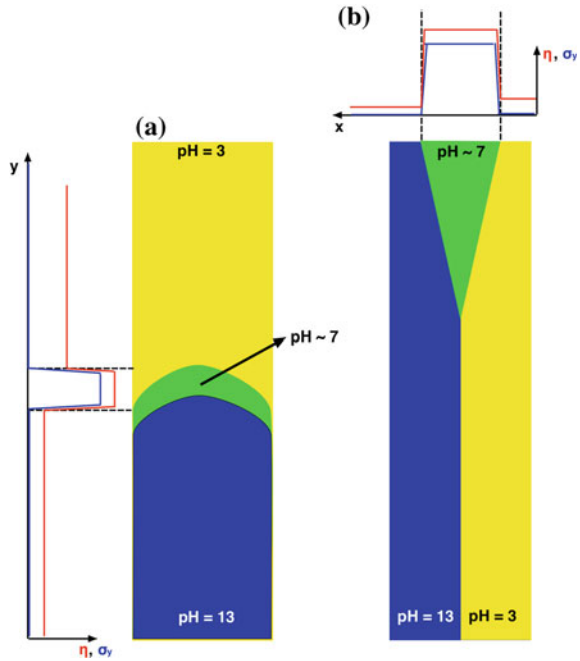
monotonic variation in viscosity has been analysed theoretically (Ern et al. 2003), we have found no clear experimental demonstration of these instabilities. With flows of simple Newtonian fluids, it is difficult to vary the viscosity locally to induce an instability. With complex or "*structured*" fluids, however, the situation is significantly different: the rheology is strongly coupled to the molecular-scale organisation of the fluid. This opens a new possibility of locally controlling the viscosity by inducing local changes in the molecular structure via a chemical reaction taking place at the interface between two complex fluids as schematically illustrated in Fig. 30. The advantage of such a method is that a chemical reaction may be controlled by either mass transfer or by local heating or cooling.

Here, we demonstrate experimentally that a fast (acid–base) chemical reaction taking place at the interface between two miscible fluids and resulting in the local formation of a gel may indeed destabilise the flow in the absence of any relevant inertial contribution. The chemical reaction takes place at the interface between a Newtonian fluid (an aqueous of sucrose) at $pH \approx 13$ and an un-neutralised aqueous solution of Carbopol® 980 at $pH \approx 3.5$. The neutralised Carbopol® located around the interface of the reacting fluids exhibits an yield stress behaviour and thus a large viscosity contrast is generated in the flow. The pH-dependent rheology is illustrated in Fig. 31.

In a neutral state, the viscosity of the Carbopol® solution is two orders of magnitude larger than in the initial acid state ($pH \approx 3$), panel (b) in Fig. 31 and the Carbopol® solution exhibits yield stress, panel (c) in Fig. 31.
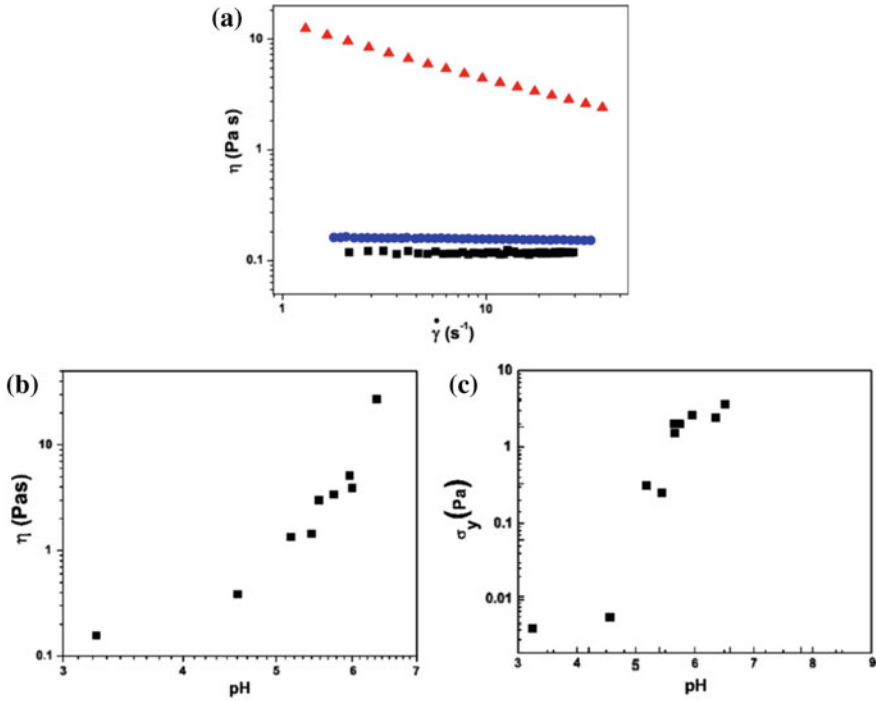
Fig. 31 **a** Strain rate dependence of the effective viscosity of the two reacting fluids: circle—displaced Carbopol solution at $pH = 3$, squares—displacing sucrose solution at $pH = 13$, triangles—neutralised Carbopol® solution($pH = 7$). **b** pH dependence of the viscosity of the Carbopol® solution measured at $\dot{\gamma} = 1s^{-1}$. **c** pH dependence of the yield stress of the Carbopol® solution

We show through this section that this spatially inhomogeneous fluid rheology triggered by the acid–base reaction that locally neutralises the Carbopol® structural units leads to an inertia free hydrodynamic instability. We have focused on two distinct flow configurations:

1. a displacement flow configuration where the less viscous Newtonian fluid displaces the more viscous Carbopol® solution, as shown in Fig. 30a.
2. a parallel flow configuration where the two reacting fluids are injected side by side, displayed in Fig. 30b.

Besides the fundamental interest in understanding how a stratification of the viscosity influences the hydrodynamic stability of the flow, each of the aforementioned flow configurations had a clearly defined practical motivation. The motivation for the displacement flow configuration illustrated in Fig. 30a came from the construction of oil and gas wells. Since the early 1990s, there have been an increasing number of wells that are constructed with long horizontal sections. The worlds longest extended reach wells have horizontal sections in the 10–15 km range, but these are exceptional.

More routinely, wells are built with horizontal extensions of up to 7 km. One of the key barriers in constructing longer wells comes from simple hydraulic friction. In a vertical well, both the pore pressure of reservoir fluids and the fracture pressure of the reservoir rock increase with depth, approximately linearly. Judicious choice of fluid density and circulating flow rates keeps the well-bore pressure inside the so-called "pore-frac envelope", i.e. the region where the porous rock does not fracture. In a horizontal well section, the pore-frac envelope is unchanged with length along the well, but the frictional pressure increases with length, leading to eventual breaching of the envelope.

To avoid large pressure drops but yet achieve an efficient displacement, our original idea was to locally increase the viscosity of the fluid *only* in the vicinity of the interface (see the sketch in Fig. 30a rather than using a high viscosity displacing fluid over the entire length of the pipe. A brief discussion of the main experimental findings for this flow configuration is given in Sect. 4.3.1. For a detailed account, these findings the reader is referred to Burghelea et al. (2007).

The second flow configuration illustrated in Fig. 30b might find some useful applications in efficiently mixing viscous fluids in the absence of significant inertial contributions, e.g. in micro-channels. A brief discussion of the main experimental findings for this flow configuration is given in Sect. 4.3.2. For a detailed account of these findings, the reader is referred to Burghelea and Frigaard (2011).

4.3.1 Unstable Displacement Flows in the Present of a Fast Chemical Reaction

A typical stable displacement experiment performed with two Newtonian fluids at low *Re* is illustrated in Fig. 32. A small amount of fluorescein has been added to the displacing fluid in order to visualise the interface between the two fluids. The fluid displacement process laminar, steady and dominated by a long finger of the displacing fluid penetrating into the displaced fluid.
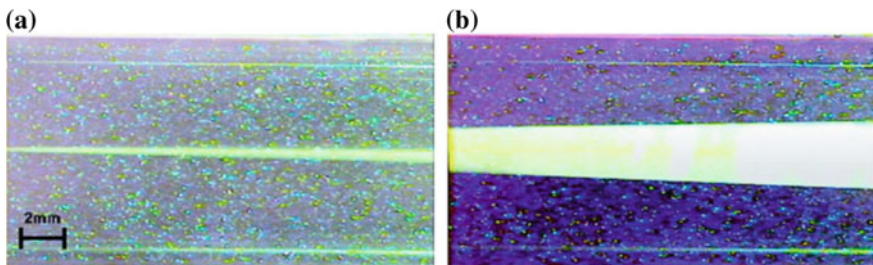
Fig. 32 Example fluorescent images of the interface in an experiment from control sequence: displacing fluid 65% saccharose solution, displaced fluid −66% saccharose solution. The flow rate $\hat{Q} = 0.145$ ml/s. The two images are separated in time by 5 s
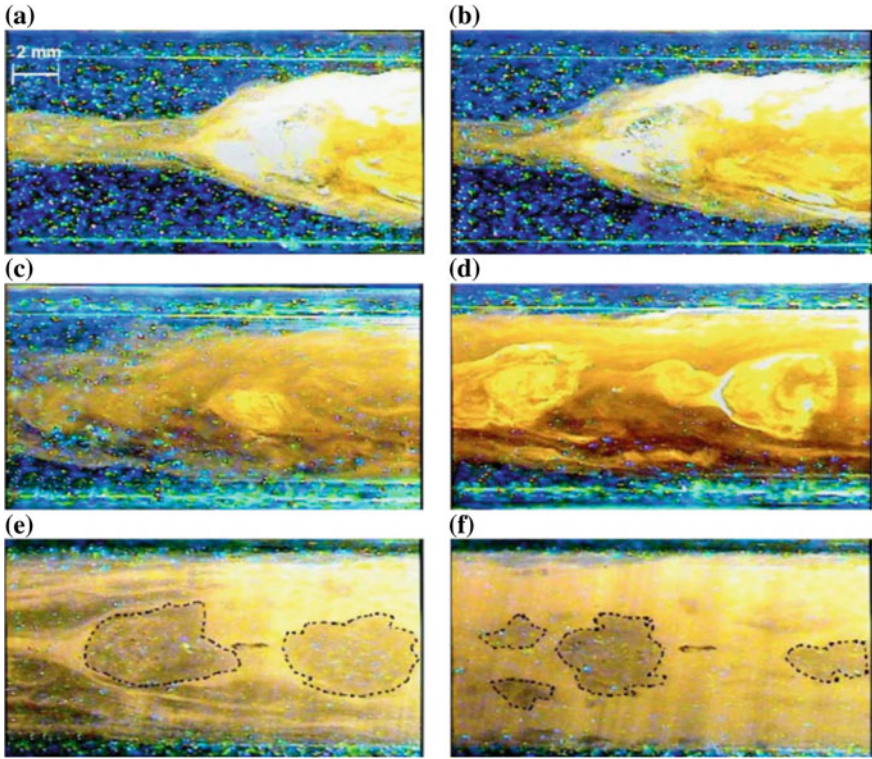
Fig. 33 a–f Fluorescent images of the interface in a reactive displacement: displacing fluid—-65% saccharose solution, displaced fluid—0.1% Carbopol® in 66% saccharose solution. **e–f** Fluorescent flow images long after the entrance of the unstable interface in the field of view; the images are separated in time by approximately 5 s. The dotted lines highlight gelled structures tumbling downstream. The direction of the flow in each panel is from right to left

The flow behaviour was significantly different from the control experiments in the reactive case, when the Carbopol® solution at $pH = 3$ was displaced by a saccharose solution at $pH = 11$, at different flow rates. The initial interface penetrates in a sharp spike as before, but this is destabilised and the finger rapidly widens to nearly fill the pipe. A complex secondary flow develops at the interface between fluids. The flow seems to be dominated by large vortices advected by the flow, with a typical size of the order of the pipe radius. Typical images are shown in Fig. 33. As the front of the finger passes, the secondary flow instabilities persist along the sides of the finger. The secondary flow provides a feedback mechanism for the instability by bringing into contact new unreacted fluid elements and taking away reacted highly viscous fluid. The initial pass of the finger front does not remove all the fluid 2 from the walls. However, the secondary flows result in a fairly rapid erosion of the residual layers. After the initial instability, small parcels of fluid 2 pulled into the fluid 1 stream react to form gelled solid regions that are advected along with the fluid. Close observation
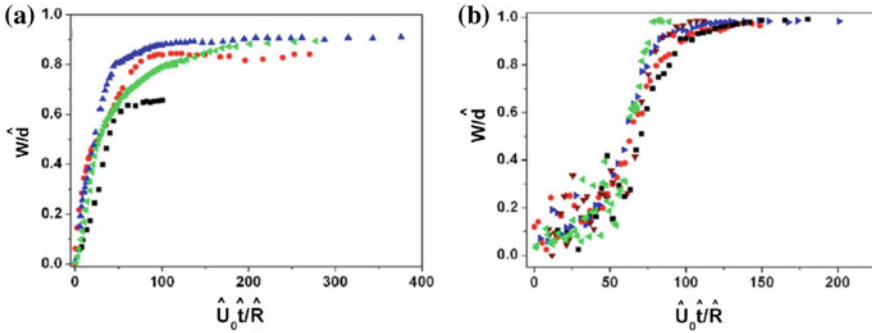
Fig. 34 **a** Normalised width of the tip versus the normalised displacement distance, $\hat{U}_0\hat{t}/\hat{R}$, for several values of the flow rate: $\hat{Q} = 0.063$ ml/s, $\hat{Q} = 0.145$ ml/s, $\hat{Q} = 0.19$ ml/s, $\hat{Q} = 0.3$ ml/s. The experiments with the Newtonian fluids pair that undergoes a stable displacement flow. **b** Normalised width of the tip versus the normalised displacement distance, $\hat{U}_0\hat{t}/\hat{R}$, for several values of the flow rate: $\hat{Q} = 0.13$ ml/s, $\hat{Q} = 0.18$ ml/s, $\hat{Q} = 0.2$ ml/s, $\hat{Q} = 0.31$ ml/s, $\hat{Q} = 0.47$ ml/s. The experiments belong to the reactive sequence

of video images reveals that some of these parcels appear to be in rigid motion as shown in Fig. 33e and f.

To quantitatively assess the impact of the instability on the efficiency of the fluid displacement, we monitor the dependence of the normalised width of the finger $\frac{W}{2\hat{R}}$ (here $\hat{R}$ stands for the radius of the pipe) versus the strain $\gamma = \frac{\hat{U}_0\hat{t}}{\hat{R}}$. Here U_0 stands for the mean flow velocity and $\hat{t}$ for the time.

When a Newtonian fluid pair is used, the displacement efficiency depends strongly on the flow rate and, at the higher rate, does not exceed 0.9, as shown in Fig. 34. This is what one would expect for a laminar flow and a displacing fluid less viscous than the displaced one. The picture is quite different when a reactive fluid pair is used. Due to the flow instability, efficient mixing occurs near the interface (Fig. 33). As compared to the Newtonian case, two major differences are observed. First, the temporal evolution of the displacement efficiency is little sensitive to the flow rates: the points measured for various flow rates collapse onto a single master curve. Second, the displacing efficiency reaches now 0.98 indicating that the instability leads to a nearly complete displacement which the desirable case for the oil well engineering context we described in the beginning of this section.

4.3.2 Unstable Parallel Flows in the Present of a Fast Chemical Reaction

We now focus on reactive flows in a parallel flow configuration (Fig. 30b) where the reacting fluids are injected side by side. As in the case of the displacement flow configuration discussed in Sect. 4.3.1, in the absence of a chemical reaction, the flow
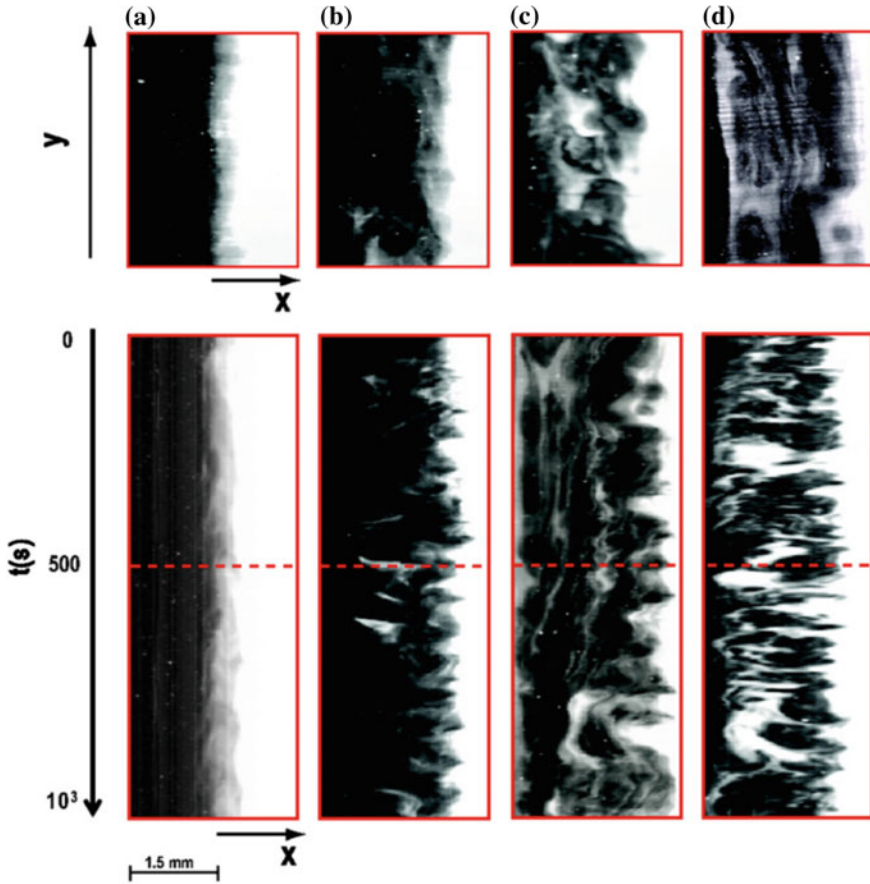
Fig. 35 Space-time diagrams measured at a fixed driving pressure drop $\Delta p = 500$ Pa at several locations downstream: **a** $y = 3.2$ cm, **b** $y = 14$ cm, **c** $y = 17$ cm, and **d** $y = 35$ cm. The flow patterns have been visualised using the laser-induced fluorescence (LIF) technique. LIF flow images acquired in the horizontal plane corresponding to each space-time diagram are presented on the top row. The dotted lines in the bottom row indicate the time instant when the LIF flow images have been acquired. The concentration of Carbopol® in the *acid* fluid was 0.1%

is linear, laminar and steady. Thus, the mixing of the fluids is poor as it is carried on by molecular diffusion alone.

The spatial development of the flow downstream in the channel for the reactive fluid pair is presented in Fig. 35, at an intermediate pressure drop $\Delta p = 500$ Pa. Four positions downstream are selected. The top row presents a snapshot of the spatial structure at each position, while the bottom row presents space-time diagrams for a time period of 500 s including the snapshot. The space-time diagrams are obtained by monitoring a single brightness profile acquired at a fixed location across successive laser-induced fluorescence (LIF) images evenly spaced in time.

The interface between the two fluids is unstable from the very entry of the channel $y = 3.2$ cm (Fig. 35a). As one advances downstream, the interface between the two fluids becomes increasingly unstable and the degree of mixing increases, panels (b)–(d) in Fig. 35. The diffuse layer visible near the interface in Fig. 35a is suggestive of a spreading reaction–diffusion front. We can observe unevenness of the diffuse layer thickness at small spatial scales (which could correspond to a reactive–diffusive instability), but we also see larger wavy variations in the interface itself which are likely to have a hydrodynamic origin. This larger scale waviness is evident in the spatiotemporal plot and appears to evolve spatially along the channel, while the diffuse interfacial layer is lost. On the scale of the channel, the characteristic diffusion timescale is much larger than the advection timescale. This implies that the apparently random mixing patterns illustrated in panels (b)–(d) are not related to molecular diffusion but rather to a (chaotic) advection phenomenon. The degree of mixing increases, extending across the entire channel (Fig. 35c and d), but it is remains intermittent with significant regimes of black and white showing in the LIF images. This suggests that the mixing mechanism is interfacially controlled, rather than by bulk fluid motion. Presumably, those interfacial regions that react quickly on mixing will form highly viscous (or unyielded) layers. These layers may either separate regions of pure fluid or may even encapsulate such regions through advective instability. Fluid which is bounded by highly viscous (or unyielded) layers will respond much less to local stress gradients. At the same time, unstable motions will continue to bring new unreacted fluids into contact. This probably explains the preservation of some larger scale structures together with seemingly diffuse well-mixed regions, as the flow progresses. In Fig. 35d, we see a more longitudinal spatial structure developing. A plausible mechanism for this is that the regions of unreacted fluid will move relatively fast along the channel and help to orient near rigid regions with the flow. These regions may agglomerate, but in doing so will move slower and hence have an increased possibility of further growth via agglomeration.

5 Non-isothermal Problems Involving Yield Stress Materials

5.1 Thermo-Rheological Behaviour of a Shear-Thinning Yield Stress Material

Whereas a clear progress towards understanding the isothermal deformation of viscoplastic materials has been made, there exist a limited number of studies dealing with temperature-dependent viscometric and non-viscometric flows of Carbopol® solutions. An experimental study of the heat transfer in the transitional pipe flow of a Carbopol® solution is presented in Peixinho et al. (2008). The authors of this study consider a Herschel–Bulkley-type yielding scenario and analyse their rheological measurements accordingly. The hydrodynamic stability of the flow and the heat

transfer problem are discussed in terms of the rheological properties of the material and their temperature dependence.

The previous studies regarding the thermo-rheology of Carbopol® gels may be divided into two classes. A first class of previous rheological studies found a "normal" temperature correlation of the rheological properties that can be modelled by the Arrhenius law (Islam et al. 2004; Peixinho et al. 2008; Alain and Bardet 1982; Fresno Contreras et al. 2001). Islam et al. (2004) found an Arrhenius scaling of the viscosity of the Carbopol® gel with temperature which gave rather low values of the activation energy, ΔE_a consistent with a low-temperature sensitivity. The gels studied in this work were prepared in a glycerol solvent which behaves as a rheologically simple fluid and has a rather large flow activation energy (Magazu et al. 2007) which could potentially "*mask*" a significantly weaker anomalous behaviour related to the swollen gel network. Peixinho et al. (2008) found no temperature dependence of the power law index and yield stress and an Arrhenius-type decay of the consistency. They used a neutralised 0.2% (wt) aqueous solution of Carbopol® 940 and a controlled stress rheometer (AR2000 from TA Instruments) equipped with a steel 0.5 deg cone/40 mm plate and truncation of 15 μm. It is worth noting that the maximum temperature investigated in this work is as large as 85 °C (and therefore the fluid evaporation could have played a significant role during the measurements) and that the scatter of their yield stress measurements accounts for nearly 30% of the measured values which makes the observation of a particular trend difficult. There exists a second class of previous rheological studies which observe an anomalous temperature–viscosity correlation, i.e. an increase of the viscosity with the temperature (Owen et al. 2003; Park and Jr. 1997; Park and Irvine 1997; Todica et al. 2010).

Barry and Meyer (1979a, b) were among the first to provide a very complete description of the rheological properties of Carbopol® at various temperatures by combined shear measurements, creep measurements and small amplitude oscillatory measurements. Although the general conclusion is that the rheological properties of Carbopol® gels are practically insensitive to temperature variations (their flow activation energy is small), the authors did observe an anomalous temperature dependence of the viscosity (see the discussion in page 8 of Barry and Meyer 1979a) but they discard the observation by noting "*As an increase in apparent viscosity is inconsistent with an activation energy for viscous flow these data were not used to derive such values*". By using a Brookfield Model DV-III Digital Rheometer (Brookfield Engineering Laboratories Inc., Stoughton, MA, USA) and a cone and plate configuration, Owen et al. (2003) observed an anomalous temperature viscosity correlation for two neutralised polyacrylic acid derivatives used in contraception under the trade names "Advantage-S" and "KY-Plus". In the same study, however, for two other contraceptive gel formulations, "Ginol II" and "Conceptrol" and by using the same rheological procedure, a "normal" (Arrhenius-like) temperature correlation of the viscosity is observed. This indicates that the correlation between the temperature and the rheological behaviour is intrinsically related to the physico-chemical properties of the gel mixture.

By using a falling needle viscometer, Park and Jr. (1997); Park and Irvine (1997), an anomalous temperature dependence of the viscosity of Carbopol® 934 is at three

distinct concentrations (which they express in parts per million): $c = 5000\,\text{ppm}$, $c = 7500\,\text{ppm}$ and $c = 10000\,\text{pm}$. They did not elaborate any further on this rather unexpected result but they did note, however, that "*Perhaps this phenomenon originates from a structural change of the polymer molecules with concentration and temperature*". The most recent observation of an anomalous behaviour we are aware of is due to Todica et al. (2010). They performed their measurements on a Brookfield DV II Pro viscometer, using cylindrical spindle. A detailed explanation for this anomalous behaviour is not given in this paper either.

Both classes of previous works briefly discussed above have, most probably, a limited number of things in common which makes a pertinent comparison quite difficult. Although they use a variety of rheometric equipment (note that these studies span the last four decades during which the rheometric devices have significantly evolved), it is, in our opinion, unlikely that the differences in the observed temperature correlations are due to this. This idea corroborates with the fact that sometimes, within the same study (thus using the same device and rheological method) both "*normal*" and "*anomalous*" behaviours are found, depending on grade of Carbopol® used (Owen et al. 2003).

At a second analysis of the bibliography given above, one can find, however, other significant differences between these studies: the physico-chemical properties of the gels. Thus, various studies used various grades of Carbopol (934, 940, Ultrez 10, etc.) or even custom gel formulations (Owen et al. 2003). Additionally, many of these studies do not discuss in detail the chemical nature of the cross-linking agent, the ionic content and the interaction of the polyacrylic acid molecules with various types of solvent used (water, water/ethanol mixtures, water ethylene/glycol mixtures and glycerol).

To conclude this part, a pertinent comparison and analysis of the existing body of literature on the thermo-rheological properties of Carbopol® is difficult to make based on the published results. This is due in our opinion to an incomplete understanding and control of the physico-chemical interactions that govern the cross-linking, ionisation, swelling and jamming dynamics of the individual molecules. Each of these molecular-scale physico-chemical processes is temperature-dependent (and they are characterised by their own chemical activation energies which are largely unknown) and the overall temperature dependence observed in a macroscopic rheological experiment is the result of a highly non-trivial "average" of these microscopic dependencies. We discuss in the following the thermo-rheological properties of a Carbopol® gel under shear. For a more comprehensive account of the main results, the reader is referred to Weber et al. (2012).

5.1.1   Experimental Setup and Methods

To prevent the wall slip, a parallel plate geometry with cleated surfaces has been used, Fig. 36a. The radius of the parallel plates is $R = 40\,\text{mm}$, and the gap measured by the rheometer is $d = 1\,\text{mm}$. The cleats have an equal height $H = 600\,\mu\text{m}$ and are disposed in a rectangular grid over each plate. Several advantages of cleated
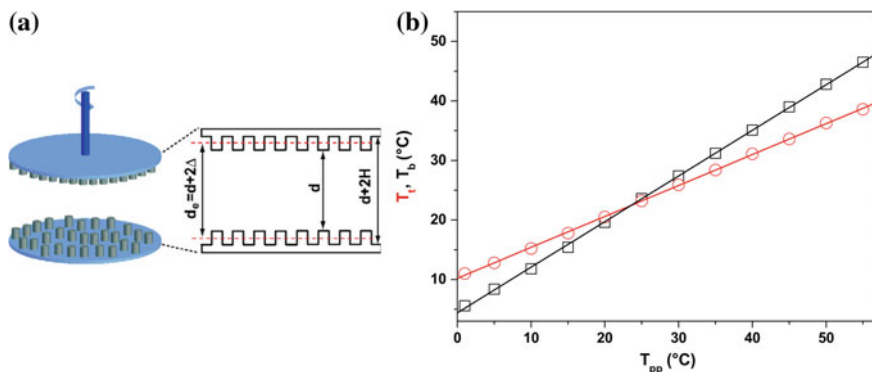
Fig. 36 **a** Schematic illustration of the cleated parallel plate geometry. **b** Temperature calibration measurements. The symbols are circles—the top plate, squares—the bottom plate. A thermo-rheologically simple silicon oil with a known activation energy has been used

geometries over other methods of preventing the wall slip effect (such as using a sandblasted geometry or a vane tool) have been recently demonstrated experimentally (Nickerson and Kornfield 2005). Among these advantages, the cleated geometry allows suppression of the wall slip effect even in the absence of significant normal forces and creates a well-defined shear.

The flow between neighbouring cleats is restricted and stops over a finite distance Δ (the flow penetration length) along the vertical axis (see Fig. 36a) and thus, two parallel no-slip surfaces are formed at an effective distance $d_e = d + 2\Delta$. Consequently, the stress measurements should be corrected according to $\sigma = \sigma_a \frac{d_e}{d}$ where σ_a is the apparent stress value recorded by the rheometer. A second concern was related to the possible artefacts introduced by fluid evaporation during long experimental runs. In order to prevent this, a solvent trap has been placed around the free fluid meniscus. The sealing of the solvent trap on the base plate of the rheometer has been insured by a thin layer of vacuum grease. After each experimental run, it has been carefully checked (by visual inspection) that no significant changes in the shape of the meniscus occurred. Additionally, we have checked at the end of each run that one can reproduce the viscosity measured during the pre-shear step which indicated us that the evaporation effects were either minimal or absent. A third concern is related to the temperature gradient which develops within the space between the parallel plates of the measuring geometry. To monitor and account for this effect, two temperature probes have been embedded in each of the parallel plates of the geometry. The temperature of each plate (T_t, T_b) has been measured as a function of the temperature set to the Peltier plate of the rheometer T_{pp} in the range 5–55 °C. Beyond this range of temperatures, we have found that the measurements are not reproducible (a scatter of nearly 75% over several subsequent runs with fresh samples was observed) and, consequently, unreliable. During these measurements, a Carbopol® sample was loaded but the top plate of the rheometer was held static. The transient temperature signals have been monitored using a digital oscilloscope
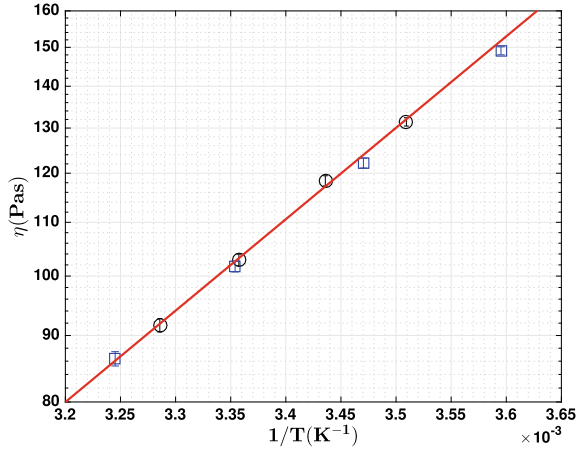
and each temperature reading has been made only after the temperature of each plate
has reached a steady state. Calibration measurements of the temperature at the top
and bottom plate of the rheometer as a function of the temperature set to the Peltier
plate are presented in Fig. 36b.

As the temperature set to the Peltier plate, T_{pp}, departs the room temperature,
a linear increase of temperature difference between the top and the bottom plates
is observed. By measuring the temperature difference between the plates at a fixed
temperature of the Peltier plate for various values of the distance d between the plates,
it was checked that the temperature varies linearly within the gap. This allowed
us to define an effective temperature of the sample as an arithmetic mean of the
temperatures of the top and the bottom plates of the rheometer, $T = (T_t + T_b)/2$.
The reliability of the stress and temperature corrections described above was assessed
by comparative thermo-rheological measurements performed on a calibrated silicon
using both the cleated geometry described above (together with the stress and the
temperature corrections) and a standard cone and plate geometry. The result of this
comparison is presented in Fig. 37.

The viscosity measurements performed on the two geometries come into a per-
fect agreement which indicates that both the stress correction related to the cleated
geometry and the temperature correction related to the temperature gradient between
the parallel plates are reliable and can be safely employed in the thermo-rheological
measurements concerning the Carbopol® gel.

5.1.2 Thermo-Rheological Properties of a Carbopol® Gel

Each of the thermo-rheological measurements performed with Carbopol® gels fol-
lowed the procedure in Sect. 1. More specifically, corresponding to each average
temperature T the material has been subjected to a controlled stress stepped ramp

similar to the one schematically illustrated in Fig. 3a, and flow curves qualitatively similar to those illustrated in Figs. 3b, 4c and 7a were recorded. The characteristic forcing time (see Sect. 1 for a detailed discussion) has been kept constant, $t_0 = 0.66$ s. For each ascending/descending controlled stress ramp, 1000 linearly spaced stress values have been explored ranging between 0.1 and 20 Pa.

The advantage of this rheological protocol is twofold. First, it allows the simultaneous assessment of both elastic and viscous rheological parameters. Second, it allows a more accurate measurement of the yield stress within the phenomenological framework briefly introduced in Sect. 2 (and detailed in Putz and Burghelea 2009), thus avoiding the inherent inaccuracies related to the classical Herschel–Bulkley nonlinear fitting procedure.

At low values of the applied stress corresponding to the solid deformation regime ($\bar{a} \rightarrow 1$) the elasto-viscoplastic constitutive relation defined by Eq. 8 reduces to the Hooke's law, $\sigma = G\gamma$. Bearing in mind that the controlled stress ramp is linearly spaced in time, this provides us with a quick way of estimating the elastic modulus by monitoring the plateau observed in the solid range on each branch of the
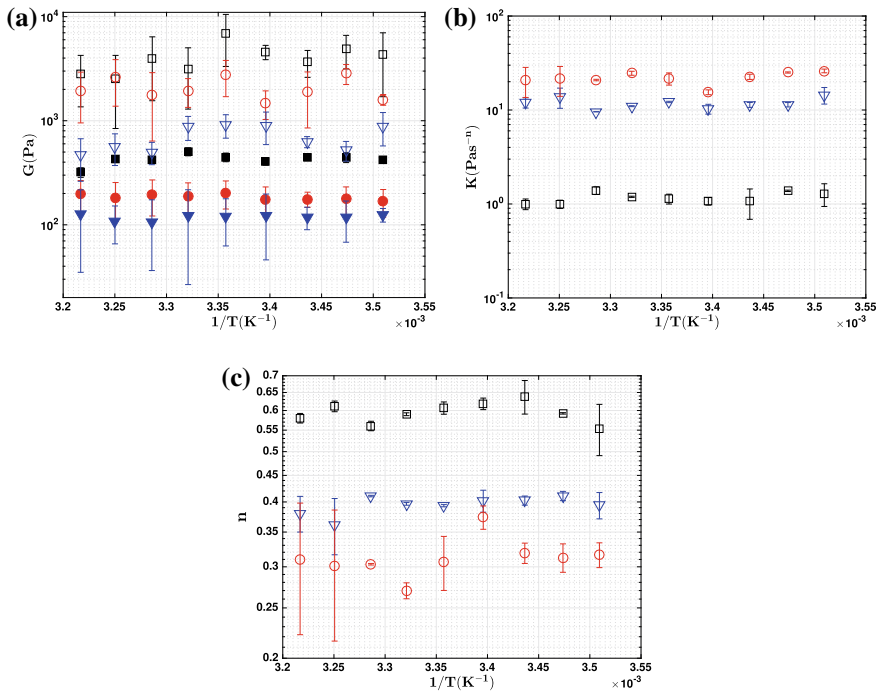
Fig. 38 **a** Temperature dependence of the elastic moduli, measured from the increasing (the empty symbols) and decreasing (the full symbols) branches of the controlled stress ramp. **b** Temperature dependence of the consistency. **c** Temperature dependence of the power law index. The symbols in each panel refer to different Carbopol® weight concentrations: squares—$c = 0.1\%$; triangles—$c = 0.15\%$; circles—$c = 0.2\%$

stress ramp (increasing/decreasing stresses). The measured dependence of the elastic moduli G_u, G_d measured on the increasing/decreasing branches of the flow ramp (full/empty symbols) performed with Carbopol® is presented in Fig. 38a. The error bars have been calculated to be repeating each test four times with a fresh sample. Within the accuracy of the measurements, no sensitive temperature dependence of the elastic moduli is observed (but only an obvious dependence on the concentration of Carbopol®). Thus, the solid-like deformation observed in a range of low applied stresses is inconsistent with a rubber-like behaviour, which typically manifests through a proportional increase of the elastic modulus with the temperature (Larson 1999).

By fitting controlled stress ramps measured at various temperatures with the phenomenological model presented in Sect. 2, one obtains the temperatures dependencies of the consistency K, power law index n and the yield stress, σ_y. Similarly, neither the consistency presented in Fig. 38b nor the power law index presented in Fig. 38c depends on the temperature but solely on the polymer concentration. The invariance of the consistency with the temperature is at odds with the observations by Peixinho et al. (2008), which indicate an Arrhenius-type exponential decay of the consistency with the temperature.

A strikingly different behaviour is observed for the temperature dependence of the yield stress, σ_y (Fig. 39). Corresponding to a critical temperature T_c, a local minimum of the dependence is observed. This unexpected behaviour has been observed for each value of the Carbopol® concentration, and the non-monotone trend of the curves clearly highlighted by the dashed line in Fig. 39 falls beyond the error bars of the measurements. The critical temperature T_c marks the transition from a Arrhenius-like behaviour described by $\sigma_y = \sigma_y^0 e^{\frac{\Delta E_a}{RT}}$ (the full lines in Fig. 39) to a anomalous non-Arrhenius one and decreases with increasing Carbopol® concentration. Here, ΔE_a and R stand for the activation energy and the universal gas constant, respectively.

Fig. 39 Temperature dependence of the yield stress measured for three distinct values of the Carbopol® concentration: squares—$c = 0.1\%$; triangles—$c = 0.15\%$; circles—$c = 0.2\%$. The dashed line marks the transition from an Arrhenius temperature dependence to a non-Arrhenius one
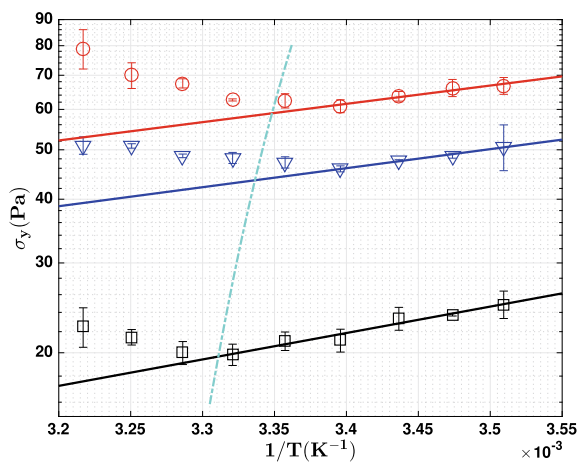
As the observation of an anomalous temperature dependence of the yield stress
(and implicitly of the viscosity measured at a given applied stress, because the consis-
tency and the power law index are temperature invariant, as shown in Fig. 38b and c)
was quite unexpected and intriguing (particularly the increase of σ_y for $T > T_c$), the
calibration measurements presented in Fig. 39 have been repeated several times and
subsequently reproduce this result. As the same stress calibration and temperature
correction have been employed for all the measurements performed on the various
Carbopol® gels as in the case of the calibration measurements illustrated in Fig. 37,
we may safely rule out the possibility that the anomalous temperature dependence
observed in Fig. 39 is the result of an experimental artefact.

Attempting to qualitatively understand the temperature dependence of the yield
stress above the critical temperature within the classical framework of the Arrhenius
law would quickly lead to an unphysical conclusion: the activation energy is negative
which apparently violates the second law of thermodynamics. This prompts one to
seek an explanation for the experimentally observed anomalous behaviour beyond the
"*classical*" Arrhenius framework. To this discussion, we dedicate the next subsection.

5.1.3 A Possible Qualitative Explanation for the Anomalous Temperature Dependence of the Yield Stress

The Arrhenius viscosity–temperature correlation emerges as a particular case from
the more general theory developed by Henry Eyring which described the fluid flow
as an activation process (Eyring 1936; Ree and Eyring 1955). At its turn, the Eyring
theory of flow as an activated process emerged as a particular case of the *Theory
of Rate Processes* which has significantly reshaped the modern chemical physics
(Glasstone et al. 1941). We briefly present in the following the main results of the
Eyring theory.

For a detailed discussion, we refer the reader to the classical textbook by Bird
et al. (2002). Similarly to the excitation of atoms from their ground state to various
energetic levels, Eyring has interpreted the motion of a "*flow unit*" (we use the term
originally employed in Eyring 1936) along a given direction x as a tunnelling process
of an energy barrier. Although the Eyring flow activation theory has been employed by
several authors to explain the yielding in extension of amorphous polymers (Richeton
et al. 2005; Bauwens-Crowet et al. 1972), we are not aware of any similar work for
viscoplastic materials under shear.

In the absence of a shear force, the energy barrier associated to the displacement
of the neighbouring material layers along the x-direction is symmetric and, conse-
quently, the probabilities of hopping (or hopping rates) along and opposite to the
x-direction are equal, $\nu_+ = \nu_- = \nu_0 e^{\frac{\Delta E_a}{RT}}$. Here, ν_0 is the equilibrium hopping fre-
quency, ΔE_a is the activation energy per mol of material and R is the universal gas
constant.

When an external shear force f_+ is applied onto the material layers along the direction x, the symmetry of the activation energy barrier is broken, $\Delta E_{-,+} = \Delta E_a \pm f_+ D N_A$) where N_A stands for the Avogadro's number and D is a characteristic space scale (measured along the shearing direction, "+") associated to the gel network. Consequently, the hopping rates along and opposite to the direction of the shearing force ν_+, ν_- are no longer equal and an effective hopping rate along the direction of the imposed shear can be calculated by the difference:

$$\nu = \nu_+ - \nu_- = 2\nu_0 e^{-\frac{\Delta E_a}{RT}} sinh \left[\frac{f_+ D}{2 k_B T} \right]. \tag{37}$$

Denoting by A the characteristic shearing area between two neighbouring gel elements and interpreting the effective hopping rate as a microscopic rate of shear $\nu = \dot{\gamma}$, one can invert Eq. (37) and obtain the viscosity[1]:

$$\eta(\dot{\gamma}, T) = \frac{2 k_B T}{V^* \dot{\gamma}} sinh^{-1} \left[\frac{\dot{\gamma}}{2\nu_0} e^{\frac{\Delta E_a}{RT}} \right], \tag{38}$$

where $V^* = AD$ stands for a characteristic volume of the gel network. In the case of a Carbopol® gel, we expect V^* to be a non-trivial function of the molar mass of the polyacrylic acid, the polymer concentration and the pH which controls the degree of swelling of individual molecules (Gutowski et al. 2012).

For simple fluids, it is often assumed that

$$\frac{f_+ D}{2 k_B T} \ll 1, \tag{39}$$

and Eq. (38) reduces to the well-known Arrhenius law[2]:

$$\eta(\dot{\gamma}, T) = \frac{k_B T}{V^* \dot{\gamma}} e^{\frac{\Delta E_a}{RT}}. \tag{40}$$

To test the applicability of the simplifying condition given by the inequality Eq. (39) for the case of a Carbopol® gel, one can consider as a typical space scale related to the gel network $D \approx 1\,\mu m$, $A \approx 1\,\mu m^2$, which are of the same order of magnitude with the values assessed via diffusion measurements (Oppong et al. 2006; Oppong and de Bruyn 2007), and $\sigma = 1\,Pa$ which leads to $\frac{f_+ D}{2 k_B T} \approx 240$.

These simple numerical estimates indicate that, in the case of a percolated Carbopol® gel structure, one should not expect the simplified Arrhenius law to apply in the whole range of temperatures and one should consider instead the full Eyring dependence given by Eq. (38).

---

[1]The derivation of Eq. (37) has been related to the shearing force via $\eta(\dot{\gamma}) = \frac{f_+}{A\dot{\gamma}}$.

[2]This can be easily seen if one retains from the series expansion of the right-hand side of Eq. (37) only the first-order term.

If one assumes that V^* is temperature invariant,[3] it can readily be shown that there exists a critical temperature T_c corresponding to which the viscosity given by Eq. (38) passes through a local minimum. By solving numerically the equation $\frac{\partial \eta(\dot{\gamma},T)}{\partial T} = 0$, it can be readily shown that the critical temperature T_c which marks the transition from a thermo-rheologically simple (Arrhenius-like) behaviour to a anomalous one is a decreasing function of $\frac{\dot{\gamma}}{\nu_0}$ at a fixed value of the activation energy ΔE_a.

We emphasise once more that the Eyring model does not directly refer to the temperature dependence of the yield stress but to that of the viscosity. However, within a Herschel–Bulkley framework and due to the temperature invariance of both the consistency and the power law index (see the data presented in Fig. 38b and c), the yield stress σ_y at a given temperature T is a linear function of the viscosity measured at the same temperature and a fixed rate of shear, $\sigma_y = \eta(\dot{\gamma}, T)\dot{\gamma} - K\dot{\gamma}^n$. Thus, one can conclude that the Eyring theory may qualitatively describe the anomalous temperature dependence of the yield stress illustrated in Fig. 39.

We propose in the following a simplistic phenomenological interpretation for the existence of a critical temperature T_c beyond which an anomalous temperature correlation is observed. The microstructure of a polyacrylic micro-gel system statistically described by the characteristic volume V^* is the result of two competing effects: swelling of individual micro-gel particles and osmotic de-swelling.

Following Cloitre et al. (2003) and Borrega et al. (1999), the swelling behaviour of a polyelectrolyte gel is governed by three contributions: the mixing entropy of the polymer molecules, the balance of osmotic pressure exerted by the counterions trapped within the micro-gel particles and the pressure of the ions present in the solution and the elasticity of the gel network. At a neutral pH, the degree of ionisation of individual polyacrylic acid molecules is high and, consequently, the mixing entropy can be neglected in the swelling equation:

$$\Pi_{in} + \Pi_e = \Pi_{out}. \tag{41}$$

Here, Π_e stands for the elastic pressure exerted upon the micro-gel particles and Π_{in}, Π_{out} stand for the osmotic pressures due to the mobile ions inside and outside the micro-gel particles. The osmotic pressures are related to the concentrations of ions C_{in}, C_{out} via $\Pi_{in,out} = RTC_{in,out}$. Assuming that all ions are contained within the micro-gel particles (which is reasonable provided that no salt is added to the system), Eq. (41) reduces to $\Pi_{in} = \Pi_e$. The concentration of ions trapped into the micro-gel particles may be written as $C_{in} = \alpha C_0 z Q^{-1}$ where C_0 is the average concentration of polyacrylic acid inside the micro-gel particles, α is the degree of ionisation, z is the molar fraction of acidic groups and $Q = V^*/V_0$ is the swelling ratio (V_0 is the characteristic volume of the un-swollen micro-gel particles).

---

[3]This is for now only a plausible assumption and a direct experimental investigation by fluorescent visualisation of the gel network as recently performed by Gutowski et al. (2012) would be highly needed to test it.

Because the macroscopic elastic modulus reflects the microscopic-scale elasticity of the micro-gel structure, the temperature invariance illustrated in Fig. 38a indicates that the elastic pressure of the gel network Π_e is temperature invariant. With these considerations, a simple algebraic manipulation of Eq. (41) would lead to the conclusion that the swelling ratio is proportional to the temperature or, equivalently $V^* \propto T$. Thus, within this regime, the pre-factor in Eq. (38) is practically temperature independent which explains why the temperature dependence of yield stress (viscosity) can be fairly well described by an Arrhenius-type correlation, see the full lines in Fig. 39. The osmotic de-swelling occurs when counter-ions may escape from the core of micro-gel particles into the solution by penetrating the outer shell of the particles where the local electro-neutrality condition is not fulfilled. The fraction Γ of these counter-ions is proportional to the Debye length, $\Gamma \propto \lambda_D$, (Cloitre et al. 2003; Israelachvili 2010). Bearing in mind that the Debye length scales as $T^{1/2}$ one can conclude that an increase of the temperature translates into an increase of the number of counter-ions that leave the micro-gel particles which promotes the de-swelling process. According to Cloitre et al. (2003), if one accounts for the competing effects of the swelling and osmotic de-swelling and if one denotes the volume fraction of micro-gel particles by Φ, the concentrations $C_{in,out}$ may be rewritten as

$$C_{in} = \frac{\alpha\,(1-\Gamma)\,zC_0}{Q} \tag{42}$$

$$C_{out} = \frac{\alpha\Gamma zC_0}{Q}\frac{\Phi}{1-\Phi}. \tag{43}$$

A dynamical equilibrium between the swelling and the osmotic de-swelling may be achieved when the concentration of ions trapped within the micro-gel particles becomes comparable to that of the counter-ions that leave the micro-gel particles, $C_{in} \approx C_{out}$. This, together with Eq. (42) and with the square root temperature scaling of Γ, indicates the existence of a critical temperature T_c and a critical characteristic volume defied implicitly via $\Gamma_c = 1 - \Phi_c$. Beyond this critical temperature T_c, the osmotic de-swelling wins over the swelling and a further increase of the characteristic volume V^* with the temperature is no longer possible. Consequently, the pre-factor in Eq. (38) is proportional to the temperature which translates into the anomalous behaviour observed in Fig. 39. For high polymer concentration, the range of temperatures within which individual molecules can freely swell upon an increase of the temperature becomes narrower and the critical condition will be fulfilled at a lower temperature T_c. As a consequence, within this phenomenological picture, one should expect a decrease of the critical temperature T_c with increasing Carbopol®️ concentration. This trend is apparent in Fig. 39. A quantitative description of the data presented in Fig. 39 by the Eyring model could not be obtained. The reason behind this might be that Eq. (38) considered a single (plastic) "flow unit" characterised by a single specific volume V^* related to the average size of the percolated gel network. A more realistic model should account for the presence of the Newtonian solvent (in our case the water trapped into the swollen polymer network) and a realistic statistical

distribution of V^*. Such a statistical distribution is difficult to predict theoretically from first principles and, most probably should be tackled experimentally by direct visualisation of the polymer network, as very recently performed (Gutowski et al. 2012).

5.2 *Rayleigh–Bénard Convection in a Shear-Thinning Yield Stress Material*

The Rayleigh–Bénard convection in a fluid heated from below is a paradigm of pattern-forming systems (Cross and Hohenberg 1993).

Imposing a vertical temperature gradient within a Newtonian fluid by heating it from below translates into a vertical gradient of the fluid density or buoyancy which, beyond a critical value of the temperature gradient ΔT_c, may overcome the viscous dissipation and trigger an upward motion of the fluid elements. Within a finite-size system and in the virtue of the mass conservation, this instability results in a regular and steady fluid motion in the form of rolls or hexagons which is classically referred to as the Rayleigh–Bénard thermal convection.

The transition to laminar Rayleigh–Bénard convection in Newtonian fluids has been intensively studied during the past five decades both theoretically and experimentally. Among a large amount of published work on the topic, we can refer the reader to textbook of Koschmieder (1993) and the review article by Bodenschatz et al. (2000).

A Newtonian fluid heated from below loses its hydrodynamic stability when the stresses associated to the buoyancy forces exceed those associated to the viscous dissipative forces.

The balance between the buoyancy and the viscous forces is quantified by the Rayleigh number:

$$Ra = \frac{\beta \Delta T g H^3}{k \cdot \nu}, \tag{44}$$

where β is the coefficient of thermal expansion, g is the gravitational constant, k is the thermal diffusivity, ν is the kinematic viscosity, ΔT is the temperature difference measured between the plates and H is the distance between plates. It has been shown both theoretically and experimentally that the onset of the convection corresponds to $Ra_c \approx 1708$.

Within the Boussinesq approximation, it has been demonstrated theoretically that the Rayleigh–Bénard convection emerges via a backward bifurcation (which may become an imperfect bifurcation in a finite system) and its onset can be described via a linear theory (Joseph 1970; Sani 1964). Moreover, it is demonstrated that a finite-amplitude bifurcation is not possible in this case.

If Q is the amount of heat transported between plates via the thermal convection, the balance between the convective and conductive heat transfer is quantified by the Nusselt number:

$$Nu = \frac{QH}{\alpha \Delta T}, \tag{45}$$

where α is the thermal conductivity of the fluid.

Whereas there exist an overwhelming number of fundamentally important studies of the Rayleigh–Bénard convection in Newtonian fluids, much less progress has been achieved in understanding the thermal convection in non-Newtonian fluids. The reason for this most probably originates in the highly non-trivial coupling between the hydrodynamic problem, the rheological properties of the fluids and their thermal dependence.

A systematic theoretical analysis of the Rayleigh–Bénard convection in shear-thinning fluids is presented by Albaalbaki and Khayat (2011). Using the Carreau–Bird rheological model, they show that although the onset of the thermal convection is the same as in the Newtonian case, the non-Newtonian fluids can convect in the form of rolls, squares or hexagons, depending on the degree of shear thinning. They also predict that in the case of a strong enough degree of shear thinning the bifurcation may turn sub-critical.

The experimental investigation presented by Lamsaadi and his coworkers for a power law fluid revealed an increase of the Nusselt number with the shear-thinning index (Lamsaadi et al. 2005). There exist several systematic studies of the Rayleigh–Bénard convection in viscoelastic fluids focusing on the role of elasticity (quantified by the Weissenberg number) on the onset of convection and on the main features of the transition (Park and Ryu 2001; Park and Park 2004). The experimental investigation presented by Martinez-Mardones and his coworkers for a viscoelastic fluid has captured the influence of the rheological parameters on the critical conditions (Martinez-Mardones et al. 2000). The experiments performed on viscoelastic shear-thinning fluids by Liang and Acrivos (1970) indicate that the transition to convective states emerges as a supercritical bifurcation. They also conclude that the experimentally observed convective patterns are similar to the Newtonian ones. The main effect of the non-Newtonian rheological behaviour on the Rayleigh–Bénard convection is an increase of the Nusselt number as compared to a Newtonian fluid with the same viscosity.

The practical interest in understanding thermo-convective instabilities in viscoplastic originates from the fact that such materials are relevant to various geophysical flows such as magma flows within the Earth's mantle (Griggs 1939; Meinesz 1947; Orowan 1965; Le Bars and Davaille 2004).

Systematic studies of the hydrodynamic stability of yield stress fluids have been performed only recently (Frigaard et al. 1994; Landry et al. 2006; Metivier et al. 2005). In this context, there exist several fundamental mathematical and physical problems yet to be understood. One of these problems concerns with the occurrence of the Rayleigh–Bénard instability in yield stress materials.

The very first theoretical study of the Rayleigh–Bénard convection in a yield stress fluid was performed by Zhang et al. (2006). Using a linear stability approach formulated within the framework of the Bingham rheological model, they show that base state is stable to infinitesimally small perturbations regardless the finite value

of the yield stress. This is due to the fact that, corresponding to the stable base flow state, the Bingham model predicts an infinite viscosity which cannot be destabilised by infinitesimally small perturbations.

The weakly nonlinear stability analysis performed by Balmforth and Rust (2009) carried out within the framework of the Bingham rheological model indicates that a sufficiently large finite-amplitude perturbation of the base state of a viscoplastic fluid may trigger Rayleigh–Bénard convection.

The experiments that complement their theoretical investigation confirm that the presence of the yield stress generally suppresses the convection in the sense that the fluids will not spontaneously convect unless a perturbation of a finite amplitude is applied. The magnitude of the perturbation needed to initiate the convection increases with the yield number Y which characterises the competition between the buoyancy-induced stresses and the yield stress of the fluid.

A numerical simulation study of the Rayleigh–Bénard convection of a Bingham fluid in a square enclosure is presented by Turan et al. (2012). By a systematic scaling analysis Turan and his coworkers assess the scaling of the relevant non-dimensional numbers corresponding to the onset of the instability and relate the results to the strength of the gel.

An experimental study of the development of thermal plumes within a Carbopol® gel due to local heating was recently presented by Davaille et al. (2013). Depending on the yield number Y, they have observed three distinct dynamic regimes: stable, small-scale convective (the convection is localised around the heater) and thermal plumes. A systematic description of the morphology of the thermal plumes is provided as a function of the yield number. The study by Davaille et al. (2013) reinforces the main conclusion of the study by Balmorth and Rust that finite-amplitude perturbations may indeed destabilise the base flow of fluids with a finite yield stress.

Darbouli et al. (2013) have studied experimentally the Rayleigh–Bénard convection within various Carbopol® gels confined in a cylindrical cavity and heated from below. Although they did not intentionally applied a finite-amplitude perturbation, they did observe convective states various values of the yield stress that cover a limited range (0.0047–0.104 Pa) (according to their Table 1). Bearing in mind that the accuracy of the determination of the yield stress via classical rheometry is somewhat limited and the uncertainties becomes increasingly larger when the yield stress is diminished, it is not fully clear whether their materials truly possessed a yield stress or they were merely shear-thinning fluids (which is the case when the concentration of Carbopol® is smaller than the overlap concentration even at neutral pH).

In the case of a viscoplastic fluid, the onset of the Rayleigh–Bénard convection coincides with the onset of the solid–fluid transition (yielding) and thus, the viscous stresses are infinite at the onset. This suggests that, in the case of a viscoplastic fluid, the onset condition should be reconsidered. For this purpose, the force balance criterion can be modified by considering that the thermal convection is triggered when the stresses associated to the buoyancy overcome the yield stress τ_y of the gel and by replacing the viscous timescale with a characteristic timescale associated to the microstructure of the gel:

$$Ra = \frac{\rho\beta\Delta T g H}{\tau_y}\frac{t_d}{t_g} \geq Ra_c \tag{46}$$

Here, $t_d = \frac{H^2}{\kappa}$ is the characteristic timescale associated to the thermal diffusion and t_g is a characteristic timescale associated to the gel microstructure near the onset of the convection (i.e. near the yield point) which will be discussed in detail through our paper in connection to the rheological properties of the Carbopol® gels. As the yield stress has been considered as a scale for the stresses, the definition above is valid only around the onset of the instability which coincides with the onset of the solid–fluid transition (yielding). Far beyond the onset, the Rayleigh number should be rewritten in terms of a shear-thinning viscosity.

From a phenomenological point of view and following the basic ideas of the (energy) *balance theorem* initially introduced by Chandrasekhar (1961), one can alternatively consider that the thermal convection in a yield stress fluid is initiated when the energy dissipated per unit volume of material by the buoyancy forces becomes comparable in magnitude to the maximal elastic energy that the gel network can locally store per unit volume prior to yielding: $W_b \geq W_e$. Here, $W_e = \rho g\beta\Delta T$ is the energy dissipated per unit volume by the buoyancy forces and $W_e = \tau_y$ is the elastic energy per unit volume. With these considerations, the energy criterion for the convective instability in a yield stress fluid can be formulated in terms of the yield number Y:

$$Y = \frac{\tau_y}{\rho\beta g H \Delta T} \leq Y_c \tag{47}$$

To the best of our knowledge, there exists no experimental assessment of the validity of the force and energy balance criteria for the transition to thermal convective states in a Carbopol® gel given by Eqs. (46) and (47).

The present study concerns with an experimental investigation of the Rayleigh–Bénard convection in Carbopol® gels with various concentrations (yield stresses). Among the primary goals of the study, we mention the accurate detection of the onset of the instability in relation with the rheological properties of the gel (yield stress), the characterisation of the convective flow patterns as a function of the control parameter. Of particular interest is the assessment of the nature of the bifurcation towards convective states which is little documented by the existing body of experimental work. In addition to these goals, we are interested in the scaling of the physical parameters characterising the onset of the convective instability with the rheological properties of the solutions which will allow one to probe the applicability of the force and energy balance stability criteria discussed above.

5.2.1 Experimental Setup and Methods

The Rayleigh–Bénard convection cell is schematically illustrated in Fig. 40. It consists of a rectangular cavity with acrylic-made flat transparent walls. The length of the
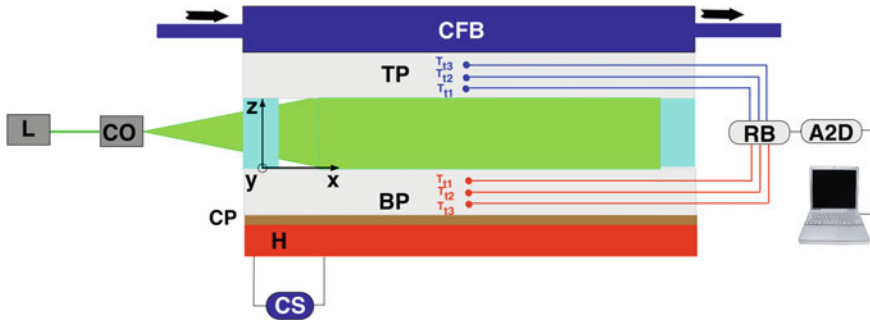
Fig. 40 Schematic view of the experimental setup **L**—solid-state laser, **CO**—cylindrical optics block, **CP**—copper plate, **TP**—top plate, **BP**—bottom plate, **CFB**—cooling fluid bath, **A₂D**—analogical to digital signal conditioning block, **RB**—reference box

fluid cavity is $L = 386$ mm, the width is $W = 186$ mm and its height is $H = 20$ mm. The length-to-height aspect ratio of the cavity is $L/W = 19.3$. The bottom and the top enclosures of the cavity are 3-cm-thick polycarbonate plates. The smooth surfaces of the plates have not been treated neither chemically nor mechanically, and thus the wall slip phenomenon was present during the experiments with Carbopol® gels. The significant width of these two plates and their small thermal conductivity coefficient have been purposely chosen in order to obtain a uniform temperature distribution along the entire fluid cavity. The bottom plate was heated electrically by a resistive circuit fed by a constant current I supplied by the stabilised current supply **CS**. The heating power was calculated as $P = RI^2$ where $R = 25.5 \, \Omega$ is the resistance of the electrical heater. To avoid the thermal damage of the bottom polycarbonate plate, a copper plate **CP** is interposed in between the polycarbonate plate and the resistive heater.

The top plate was uniformly cooled by means of a circulating fluid bath **CFB**. The circulating fluid is a mixture of glycerin and anti-freeze, and its temperature is maintained constant through our experiments, $T_{wb} = -10\,°C$.

The transition to the Rayleigh–Bénard convection was simultaneously investigated by both integral measurements of the temperature difference ΔT between plates and local measurements of the amplitude of the convective states.

Prior to characterising the transition to the Rayleigh–Bénard convection within a Carbopol® gel, we have focused on a systematic validation of the experimental system and the measuring techniques with a Newtonian fluid, pure Glycerin. The experimentally measured values of the physical parameters for the Glycerin are $\beta = 5 \cdot 10^{-4} K^{-1}$, $g = 9.8 \, m^2/s$, $\kappa = 1.37 \cdot 10^{-7} \, m^2/s$ and $\nu = 872 \cdot 10^{-6} \, m^2 \, s^{-1}$.

Measurements of the temperature difference ΔT between the plates performed with a Glycerin solution for both increasing and decreasing values of the heating power P are presented in Fig. 41a. A linear increase of the integral temperature difference between the plates ΔT with P which corresponds to a purely conductive heat transfer regime (the slope of this dependence is proportional to the thermal
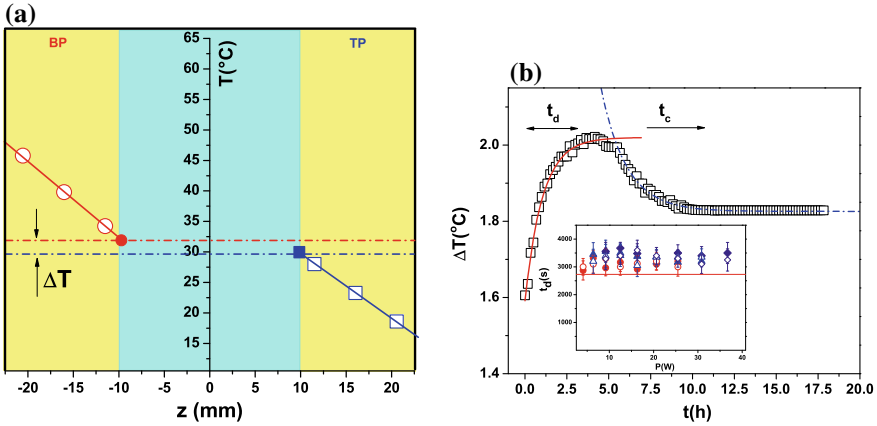
Fig. 41 **a** Temperature measurements within the bottom plate **BP** (the empty circles) and within the top plate **TP** (the empty squares). The full lines are linear fitting functions and the full symbols are the linear extrapolations of the temperature measurement at the contact points with the fluid. **b** Time series of the temperature difference ΔT. t_d stands for the characteristic thermal diffusion time, and t_c stands for the characteristic slowing downtime. The dependence of the thermal diffusion time td on the heating power, P, measured for three Carbopol® solutions with the concentrations $c = 0.06, 0.075, 0.08\%$ for both increasing (full symbols) and decreasing (empty symbols) heating powers is presented in the inset. The full line is the theoretical estimate, $t_d \approx 2730\,\text{s}$ (see text)

conductivity α of fluid) is observed below a critical value of the heating power $P_c \approx 16.32\,\text{W}$. Beyond this onset, the dependence becomes nonlinear consistently with a mixed conductive–convective heat transfer regime. Based on the material parameters enumerated above, the critical Rayleigh number corresponding to the onset of the thermal convection can be estimated $Ra_c \approx 1774$ which is in a very good agreement (within 4%) with the theoretical value $Ra_c^t = 1708$ given in Chandrasekhar (1961).

The dependence of the reduced temperature difference $\Delta T_r = \frac{\Delta T}{\Delta T_{lin}} - 1$ on to the reduced power $P_r = P/P_c - 1$ is presented in the top panel of Fig. 41b. Here ΔT_{lin} represents the linear temperature difference measured within the conductive regime (see the full line in Fig. 41a). It can be observed that the reduced temperature difference ΔT_r increases linearly with the reduced heating power P_r consistent with a supercritical bifurcation towards convective states.

Measurements of the convection amplitude obtained via the **DPIV** technique as a function of the heating power are presented in Fig. 41b.

Around the onset of convection, the velocity amplitude follows the Landau theory of imperfect bifurcations, Landau and Lisfshits (1980):

$$P_r V - a V^3 + h = 0 \tag{48}$$

Here, a is the amplitude coefficient and h is the imperfection coefficient which quantifies the degree of smearing of the bifurcation. This result agrees with both theoreti-

cal predictions (Newell and Whitehead 1969; Segel 1969) and previous experimental findings, Dubois and Bergé (1978).

To conclude this part, the measurements illustrated and discussed above clearly identify the transition to convective states within a Newtonian fluid as an imperfect bifurcation.

After having probed by these measurements the reliability of our experimental setup and measuring methods, we focus in the following section on the transition to the Rayleigh–Bénard convection in various Carbopol® gels.

5.2.2 Experimental Observation of the Thermal Convection in a Carbopol® Gel

To study the thermo-convective stability of a physical gel, we have used various Carbopol® solutions with weight concentrations ranging in between 0.05 and 0.11% as working fluids and the same experimental procedures as for the Newtonian test case discussed in the previous section. The chosen polymer concentrations all lie above the overlap concentration c^* which ensures that our working fluids are indeed yield stress fluids not just weakly shear thinning. A more systematic account of the experimental observations is given in Kebiche et al. (2014).

As for the case of a Newtonian fluid, the transition to convective states within various Carbopol® gels is simultaneously assessed by both local flow speed measurements by the **DPIV** technique and integral measurements of the temperature difference between the top and the bottom plates, ΔT (Fig. 42).
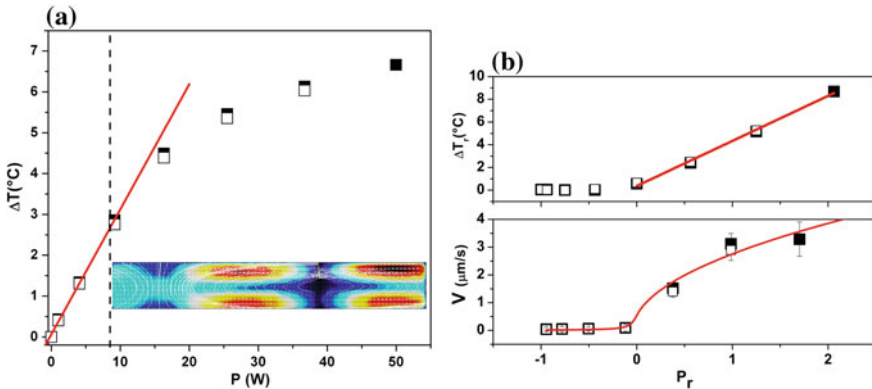
Fig. 42 **a** Dependence of the temperature gradient ΔT within Glycerin on the heat flux P. The full/empty symbols refer to increasing/decreasing heat flux. The vertical dashed line marks the transition between the conductive and convective regimes. A typical **DPIV** measured convection pattern is illustrated in the inset. **b (Top)** Dependence of the reduced temperature ΔT_r on the reduced power. The line is a linear fit. **(Bottom)** Dependence of the pattern amplitude V on the reduced power P_r. The line is a nonlinear fit according to Landau's theory of imperfect bifurcations, Eq. (48)
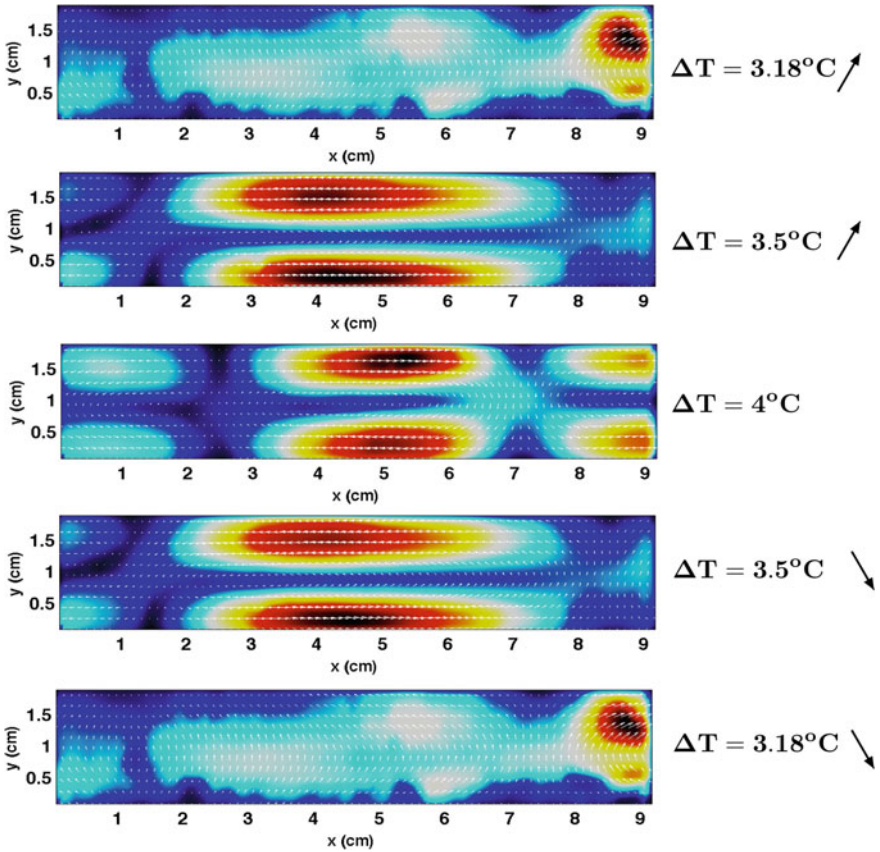
Fig. 43 Evolution of the flow patterns corresponding to several values of the integral temperature difference ΔT indicated in the inserts. The up/down arrows indicate the increasing/decreasing branch of the heating ramp. The false colour map refers to the absolute value of the flow velocity. A 0.08% Carbopol® solution was used and the onset of the Rayleigh–Bénard convection corresponds to $\Delta T_c = 2.58\,°C$

For each value of the concentration of the Carbopol® solution, no measurable flow is observed if the integral temperature difference between plates does not exceed a critical value, $\Delta T < \Delta T_c$. As the temperature difference is increased past this onset, the energy dissipated per unit volume of material by the buoyancy forces overcomes the elastic energy associated with the gel microstructure. Consequently, the gel locally yields and roll flow patterns are observed. The unstable flow patterns are observed in the absence of an external perturbation of a finite amplitude.

The evolution of the flow patterns as the control parameter is varied right above the onset of the convection monitored within a 0.08% Carbopol® solution is illustrated in Fig. 43.

Fig. 44 Dependence of
temperature gradient on the
heat flux for six values of the
Carbopol® concentration:
($\triangle$, $\blacktriangle$)—$c = 0.11\% wt$,
($\circ$, $\bullet$)—$c = 0.1\% wt$,
($\varhexagon$, $\varhexagon$)—$c = 0.08\% wt$,
($\blacklozenge$, $\diamond$)—$c = 0.075\% wt$,
($\star$, $\divideontimes$)—$c = 0.06\% wt$,
($\square$, $\blacksquare$)—$c = 0.05\% wt$. The
full/empty symbols refer to
increasing/decreasing heat
flux. The full line is a linear
fit
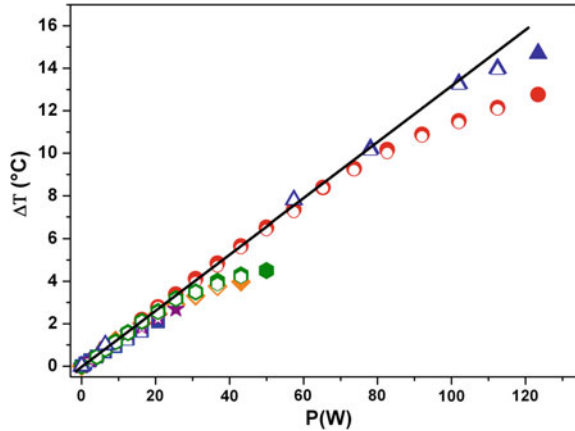
Right above the onset of the convection ($\Delta T = 3.18\,°C$), the flow pattern has a slightly asymmetric appearance. This may be due to the large characteristic times t_c needed for the pattern to reach a steady state or the so-called *critical slowing down* phenomenon which will be discussed in detail through the paper. Upon an increase of the temperature difference between plates, the flow patterns become more regular and the horizontal extent λ of the convection rolls decreases (equivalently with an increase of the horizontal wave number $q_x = \frac{2\pi}{\lambda}$). It is important to note that the flow states are reversible upon a decrease of the heating power (or temperature difference) which is a first indicator that, similarly to the Newtonian case, the transition to the Rayleigh–Bénard convection in the Carbopol® gel is a continuous one and exhibits no hysteresis. This qualitative similarity with the transition to convective states within a Newtonian fluid that deserves being studied in depth.

Integral measurements of the dependence of the temperature difference between plates ΔT performed for six values of the Carbopol® concentration and for both increasing (the full symbols) and decreasing (the empty symbols) values of the heating power P are presented in Fig. 44.

For each value of the Carbopol® concentration, a linear conductive part of the dependence is observed below a critical heating power P_c. The slopes of these linear dependencies are independent on the polymer concentration (see the full line in Fig. 44) indicating that the polymer addition does not significantly alter the thermal conductivity of the aqueous solutions. This result is fully consistent with direct measurements of the thermal conductivity coefficient κ performed for each solution separately (Kebiche et al. 2014). Beyond the onset P_c, the dependence of the temperature difference between plates on the heating power becomes sub-linear and a convective regime is observed.

Regardless of the yield stress of the Carbopol® solution, the transition from a conductive to a convective regime is reversible upon increasing/decreasing values of the heating power and a strong qualitative similarity of these integral measurements to the similar ones performed with a Newtonian fluid previously discussed is observed.
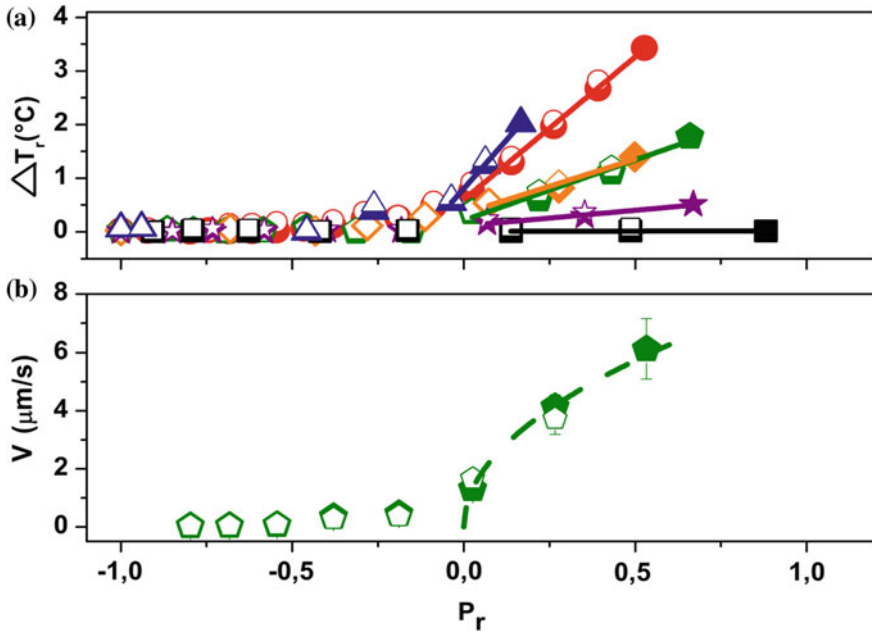
Fig. 45 a Dependence of the reduced temperature ΔT_r on the reduced power P_r for various Carbopol concentrations, see Fig. 44. The full lines are linear fitting functions. **b** Dependence the **DPIV** measured amplitude of the convection pattern V on the reduced power P_r. The line is nonlinear fit function according to the Landau theory of imperfect bifurcation, Eq. 48

To gain a deeper insight into the nature of the bifurcation towards convective states within the Carbopol® solutions, we present the same data in terms of the reduced variables ΔT_r, P_r. The dependence of the reduced temperature ΔT_r on the control parameter P_r for each Carbopol® solution is presented in Fig. 45a.

Above the onset of the bifurcation, the reduced temperature ΔT_r scales linearly with the control parameter and this result is, as in the Newtonian case illustrated in Fig. 42a, typical for a supercritical bifurcation. This fundamentally important conclusion on the nature of the bifurcation towards convective states is reinforced by the local measurements of the convective amplitude V presented in Fig. 45b. Indeed, above the onset of the bifurcation, the amplitude data can be well fitted by the Landau prediction for a supercritical bifurcation. The smearing of the transition data observed near the onset indicates that the bifurcation is an imperfect one. The degree of smearing of the bifurcation is rather small ($h \approx 0.05$), and the bifurcation is rather close to a perfect one.

The dependence of the onset parameters on the yield stress of the Carbopol® solution is illustrated in Fig. 46.

The critical heating power needed to trigger convective states increases exponentially with the yield stress of the Carbopol® solution, Fig. 46a. This indicates that in solutions with a sufficiently large yield stress the thermal convection
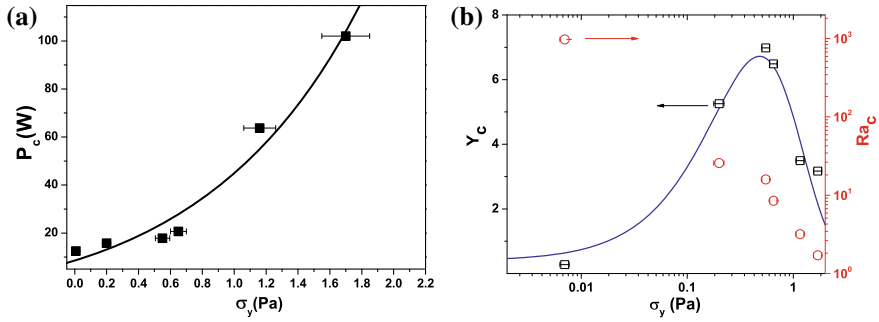
Fig. 46 **a** Dependence of the critical heating power P_c corresponding to the onset of the Rayleigh–Bénard convection on the yield stress σ_y of the Carbopol® solution. The line is an exponential fit. **b** Dependence of the critical yield number Y_c (squares, bottom-left axis) and of the critical Rayleigh number Ra_c (circles, bottom-right axes) on the yield stress σ_y

cannot be experimentally observed as it would require heating powers practically unsustainable.

Another important issue relates to the right control parameter to describe the transition towards convective states. In the case of Newtonian fluids, this is the Rayleigh number (Chandrasekhar 1961). To test if this the case for a Carbopol® gel, we have calculated the critical Rayleigh number corresponding to the onset of convection according to Eq. (46). The result is displayed in Fig. 46b (the circles). Quite remarkably, as the yield stress of the solution varies, the critical Rayleigh number Ra_c spans nearly three orders of magnitude. This clearly indicates that, unlike for the case of Newtonian fluids, Ra is not the right control parameter. On the other hand, the yield number Y calculated at the onset of the instability according to Eq. (47) remains of order of unity over the entire range of yield stresses explored. This indicates that the right control parameter for the thermo-convective instability in a Carbopol® gel is the yield number.

To conclude this section, we have demonstrated that, contrary to the existing theoretical predictions, thermal convection can be triggered in a Carbopol® gel in the absence of any finite-amplitude perturbation and the bifurcation towards convective states is an imperfect one (described by the Landau–Ginzburg formalism). A first physical ingredient that probably needs to be accounted for in the theoretical studies is related to the rather new scenario of the yielding illustrated in Sect. 2 that accounts for a gradual yielding process characterised by both a solid–fluid phase coexistence and elastic effects that are not captured by the classical rheological pictures. Indeed, measurements of the second invariant of the rate of strain (not shown here as shown in Figure 19 of Kebiche et al. 2014) indicate that the onset of convection is practically located within the non-trivial solid–fluid coexistence zone (hysteresis) visible in Figs. 3b and 4. Thus, any theoretical attempt to describe this instability using the Herschel–Bulkley law that is applicable at much larger rates of strain is not expected to accurately predict the transition. A second theoretical ingredient worth to

be accounted for in future theoretical developments is related to the non-trivial (and rather unexpected) thermo-rheological behaviour of the Carbopol® gel presented in Sect. 5.1.

6 Concluding Remarks

During the past decade, the fluid dynamics of viscoplastic materials has emerged as a distinct field of the hydrodynamics of complex fluids rivalling, perhaps, with the well-established field of hydrodynamics of viscoelastic fluids. This intellectually very rich discipline brings together several scientific communities: fluid dynamics, rheology, applied mathematics, thermal science, engineering. The dynamics of yield stress materials poses highly non-trivial problems even in isothermal flow conditions.

The first class of isothermal flows we have studied was that of low Reynolds number flows and the main scope was understanding the physics of the solid–fluid transition in a physical gel subjected to a gradually increasing external stress. The physical complexity of this problem comes from a strong nonlinearity of the stress term in the momentum conservation and a highly non-trivial coupling between the flow field and the microstructure of the material. In this context, the Carbopol® gels have been considered as "*model*" yield stress materials for over two decades and their flows have been traditionally studied within the classical Herschel–Bulkley model. Yet, it has been shown only recently that this classical picture is unable to describe several "*simple*" fluid dynamics problems: the low *Re* sedimentation of a spherical object (Sect. 1), the slow withdraw of a rigid plate at a constant speed (Sect. 1). These rather unexpected experimental facts have prompted us to reconsider the solid–fluid transition by careful and more systematic rheological tests, Sect. 1. Contrary to the common belief that Carbopol® gels behave as "*model*" yield stress fluids accurately described by the Herschel–Bulkley constitutive equation, we have found a gradual and irreversible yielding scenario together with significant elastic effects. Thus, the Herschel–Bulkley constitutive relationship is applicable only far above the transitional region, i.e. at large enough rates of deformation. In an attempt to "*rationalise*" these findings, we have proposed a phenomenological model that we have coined "*The Poor Man Model*", Sect. 2. These results initially published in Putz and Burghelea (2009) have been received with a fair amount of scepticism by the viscoplastic community which prompted us for an additional validation in simple low Reynolds number pipe flow upon an increase/decrease of the driving pressures (Poumaere et al. 2014). This particular experiment has finally dissipated any doubts on the nature of the solid–fluid transition: a hysteresis of the deformation states is equally observed in a pipe flow. Reassured by this result, we have started to develop a scientifically more solid theoretical approach to explain the solid–fluid transition, Sect. 3. This time we have resorted to the tools of *Statistical Physics* and *Critical Phenomena* and derived from first principles a model somewhat similar to the Ising model of the ferromagnetism. The model depends on *solely* two internal parameters and, as it is formulated from first principles, it is inherently validated

from a thermodynamic standpoint. The central conclusion of the approach is that, when the magnitude of the interactions between the microscopic building blocks of a yield stress material exceeds a threshold, an irreversible solid–fluid transition will be observed regardless the manner the material is forced: steadily or unsteadily. This threshold is the exact physical equivalent of the *Curie temperature* in a magnetic system. For weakly interacting systems such as Carbopol® gels, a reversible yielding scenario may be retrieved in the asymptotic limit of a steady-state external forcing.

An extra level of complexity is added to the flow problem of a yield stress material if the Reynolds numbers are sufficiently high. Thus, a fundamental question how does the viscoplasticity couples to the inertial hydrodynamic instability observed at $Re > 1000$, Sect. 4. The complexity of this question comes from two sources of nonlinearity in the momentum equation: inertial and due to the highly nonlinear dependence of the stresses on the rate of strain. An experimental study of the laminar–turbulent transition in a Carbopol® gel is presented in Sect. 4.1. The central conclusion of this study is that the inertial instability sets in when the Reynolds stresses become comparable in magnitude with the yield stress. This suggests that, somewhat peculiarly, the loss of the hydrodynamic stability cannot be fully decoupled from the solid–fluid transition although the onset Reynolds number is large. We have pursued this idea in Sect. 4.2 where we have addressed the question of how the inertial instability of a plane Poiseuille flow is affected by the yielding scenario. The central conclusion of this part was that switching from the classical Herschel–Bulkley yielding scenario to the model by Putz and Burghelea (2009) framework developed in Sect. 2 changes significantly the stability picture: the elasticity present in the model by Putz and Burghelea (2009) has a destabilising role. In Sect. 4.3, we show that if one generates strong spatial gradients of stresses via a chemical reaction that locally produces a Carbopol® gel one obtains a sharp hydrodynamic instability in the absence of any inertial contribution. We have shown that this novel instability may turn useful in both efficiently displacing very viscous fluids from a flow channel and obtaining efficient mixing in situations where increasing Re is un-practical, e.g. micro-fluidics systems.

Yet, a third layer of complexity is added to the flow problem of a viscoplastic material if one considers the non-isothermal case (Sect. 5). What looked at a first glance the most basic and straightforward problem was related to the temperature dependence of the rheological properties of a Carbopol®, Sect. 5.1. Quite surprisingly, the thermo-rheology of a Carpobol® gel departs from the classical Arrhenius picture. We provide a phenomenological explanation in terms of the physico-chemical properties of a swollen system of polyacrylic acid spongy particles in conditions of neutral pH.

In Sect. 5.2, we have shown that, contrary to the existing theoretical predictions, the Rayleigh–Bénard convection can be triggered in a Carbopol® gel in a wide range of *measurable* yield stresses. Although we do not yet have a detailed theoretical explanation for this fact, we believe this discrepancy originates from the non-trivial yielding scenario observed experimentally in Sect. 1 and theoretically described in Sects. 2 and 3.

References

Alain M, Bardet L (1982) Etude energetique de la gelification du carbopol 940. Int J Pharm 12(2):173–183

Albaalbaki B, Khayat RE (2011) Pattern selection in the thermal convection of non-newtonian fluids. J Fluid Mech 668:500–550

Arigo MT, McKinley GH (1998) An experimental investigation of negative wakes behind spheres settling in a shear-thinning viscoelastic fluid. Rheol Acta 37(4):307–327

Balmforth NJ, Craster RV (1999) A consistent thin-layer theory for bingham plastics. J Non-Newton Fluid Mech 84(1):65–81

Balmforth NJ, Rust AC (2009) Weakly nonlinear viscoplastic convection. J Non-Newton Fluid Mech 158(1–3):36–45

Balmforth NJ, Frigaard IA, Ovarlez G (2014) Yielding to stress: recent developments in viscoplastic fluid mechanics. Ann Rev Fluid Mech 46(1):121–146

Barnes HA (1999) The yield stress-a review or '$\pi\alpha\nu\tau\alpha\rho\epsilon\iota$'-everything flows? J Non-Newton Fluid Mech 81(1–2):133–178

Barnes HA, Walters K (1985) The yield stress myth? Rheol Acta 24:323–326

Barry BW, Meyer MC (1979a) The rheological properties of carbopol gels i. Continuous shear and creep properties of carbopol gels. Int J Pharm 2(1):1–25

Barry BW, Meyer MC (1979b) The rheological properties of carbopol gels ii. Oscillatory properties of carbopol gels. Int J Pharm 20(1):27–40

Bautista F, Munoz M, Castillo-Tejas J, Pérez-López JH, Puig JE, Manero O (2009) Critical phenomenon analysis of shear-banding flow in polymer-like micellar solutions. 1. Theoretical approach. J Phys Chem B 113(50):16101–16109

Bauwens-Crowet C, Bauwens C, Homés G (1972) The temperature dependence of yield of poly-carbonate in uniaxial compression and tensile tests. J Mater Sci 7:176–183

Beck J, Madsen B, Britt D, Vernon B, Nguyen KT (2007) Islet encapsulation: strategies to enhance islet cell functions. Tissue Eng 13:589–599

Beris AN, Tsamopoulos JA, Armstrong RC, Brown RA (1985) Creeping motion of a sphere through a Bingham plastic. J Fluid Mech 158:219–244

Bird RB, Hassager O, Armstrong RC, Curtiss CF (1977) Dynamics of polymeric liquids, vol 1. Wiley, New York

Bird RB, Stewart WE, Lightfoot EN (2002) Transport phenomena. Willey, New York

Bodenschatz E, Pesch W, Ahlers G (2000) Recent developments in Rayleigh-Bénard convection. Ann Rev Fluid Mech 32(1):709–778

Bonn D, Denn MM (2009) Yield stress fluids slowly yield to analysis. Science 324(5933):1401–1402

Bonn D, Paredes J, Denn MM, Berthier L, Divoux T, Manneville S (2017) Yield stress materials in soft condensed matter. Rev Mod Phys 89:035005

Borrega R, Cloitre M, Betremieux I, Ernst B, Leibler L (1999) Concentration dependence of the low-shear viscosity of polyelectrolyte micro-networks: from hard spheres to soft microgels. Europhys Lett 47:729–735

Brémaud P (1999) Markov chains: gibbs field, Monte Carlo simulation and queues. Springer, New York

Burghelea T, Wielage-Burchard K, Frigaard I, Martinez DM, Feng JJ (2007) A novel low inertia shear flow instability triggered by a chemical reaction. Phys Fluids 19(8):083102

Burghelea T, Moyers-Gonzalez M, Sainudiin R (2017) A nonlinear dynamical system approach for the yielding behaviour of a viscoplastic material. Soft Matter 13:2024–2039

Burghelea TI, Frigaard IA (2011) Unstable parallel flows triggered by a fast chemical reaction. J Non-Newton Fluid Mech 166(9–10):500–514

Chandrasekhar S (1961) Hydrodynamic and hydromagnetic stability. Clarendon Press, Oxford

Cloitre M, Borrega R, Monti F, Leibler L (2003) Structure and flow of polyelectrolyte microgels. Comptes Rendus Phys 4:221–230

Coussot P (2007) Rheophysics of pastes: a review of microscopic modelling approaches. Soft Matter 3:528–540

Coussot P (2014) Yield stress fluid flows: a review of experimental data. J Non-Newton Fluid Mech 211:31–49

Coussot P, Nguyen QD, Huynh HT, Bonn D (2002a) Avalanche behavior in yield stress fluids. Phys Rev Lett 88:175501

Coussot P, Nguyen QD, Huynh HT, Bonn D (2002b) Viscosity bifurcation in thixotropic, yielding fluids. J Rheol 46(3):573–589

Cross MC, Hohenberg PC (1993) Pattern formation outside of equilibrium. Rev Mod Phys 65:851–1112

Curran SJ, Hayes RE, Afacan A, Williams MC, Tanguy PA (2002) Properties of carbopol solutions as models for yield-stress fluids. J Food Sci 67(1):176–180

Darbouli M, Metivier C, Piau J-M, Magnin A, Abdelali A (2013) Rayleigh-Bénard convection for viscoplastic fluids. Phys Fluids 25(2):023101

Davaille A, Gueslin B, Massmeyer A, Di Giuseppe E (2013) Thermal instabilities in a yield stress fluid: existence and morphology. J Non-Newton Fluid Mechan 193:144–153

de Bruyn JR (2013) Modeling the microrheology of inhomogeneous media. J Non-Newton Fluid Mech 193:21–27

Denn MM, Bonn D (2011) Issues in the flow of yield-stress liquids. Rheol Acta 50:307–315

Dimitriou CJ, McKinley GH (2014) A comprehensive constitutive law for waxy crude oil: a thixotropic yield stress fluid. Soft Matter 10:6619–6644

Dinkgreve M, Fazilati M, Denn MM, Bonn D (2018) Carbopol: from a simple to a thixotropic yield stress fluid. J Rheol 62(3):773–780

Divoux T, Grenard V, Manneville S (2013) Rheological hysteresis in soft glassy materials. Phys Rev Lett 110:018304

Dubois M, Bergé P (1978) Experimental study of the velocity field in Rayleigh-Bénard convection. J Fluid Mech 85(3):641–653

Dullaert K, Mewis J (2006) A structural kinetics model for thixotropy. J Non-Newton Fluid Mech 139:21–30

Ern P, Charru F, Luchini P (2003) Stability analysis of a shear flow with strongly stratified viscosity. J Fluid Mech 496:295–312

Escudier MP, Presti F (1996) Pipe flow of a thixotropic liquid. J Non-Newton Fluid Mech 62(2):291–306

Escudier MP, Poole RJ, Presti F, Dales C, Nouar C, Desaubry C, Graham L, Pullum L (2005) Observations of asymmetrical flow behaviour in transitional pipe flow of yield-stress and other shear-thinning liquids. J Non-Newton Fluid Mech 127 (2-3):143–155

Eyring H (1936) Viscosity, plasticity, and diffusion as examples of absolute reaction rates. J Chem Phys 4(4):283–291

Fraggedakis D, Dimakopoulos Y, Tsamopoulos J (2016) Yielding the yield-stress analysis: a study focused on the effects of elasticity on the settling of a single spherical particle in simple yield-stress fluids. Soft Matter 12:5378–5401

Fresno Contreras MJ, Dieguez Ramirez A, Jimenez Soriano MM (2001) Viscosity and temperature relationship in ethanol/water mixtures gellified with carbopol Ultrez 10. Il Farmaco (5–7):443–445

Frigaard IA, Nouar C (2005) On the usage of viscosity regularisation methods for visco-plastic fluid flow computation. J Non-Newton Fluid Mech 127(1):1–26

Frigaard IA, Ryan DP (2004) Flow of a visco-plastic fluid in a channel of slowly varying width. J Non-Newton Fluid Mech 123(1):67–83

Frigaard IA, Howison SD, Sobey IJ (1994) On the stability of Poiseuille flow of a Bingham fluid. J Fluid Mech 263:133–150

Frisch U (1995) Turbulence: the legacy of A.N. Kolmogorov. Cambridge University Press

Glasstone S, Keith J, Eyring H (1941) The theory of rate processes. McGraw-Hill Book Co, New York

Goveas GL, Olmsted PD (2001) A minimal model for vorticity and gradient banding in complex fluids. Eur Phys J E 6:79–89

Griggs DT (1939) A theory of mountain-building. Am J Sci 237:611–650

Gutowski I, Lee D, de Bruyn J, Frisken B (2012) Scaling and mesostructure of carbopol dispersions. Rheol Acta 1–10

Güzel BT, Burghelea T, Frigaard IA, Martinez DM (2009) Observation of laminar-turbulent transition of a yield stress fluid in Hagen-Poiseuille flow. J Fluid Mech 627:97–128

Herschel WH, Bulkley R (1926a) Konsistenzmessungen von Gummi-Benzollösungen. Kolloid-Zeitschrift 39(4):291–300

Herschel WH, Bulkley T (1926b) Measurement of consistency as applied to rubbery benzene solutions. Am Soc Test Proc 26:621–633

Heymann L, Aksel N (2007) Transition pathways between solid and liquid state in suspensions. Phys Rev E 75(2):021505–9

Hof B, Juel A, Mullin T (2003) Scaling of the turbulence transition threshold in a pipe. Phys Rev Lett 91:244502

Hofschuster W, Krämer W (2003) C-XSC 2.0: A C++ library for extended scientific computing. In: Numerical software with result verification, pp 15–35

Hong W, Zhao X, Zhou J, Suo Z (2008) A theory of coupled diffusion and large deformation in polymeric gels. J Mech Phys Solids 56(5):1779–1793

Hou Q, De Bank PA, Shakesheff KM (2004) Injectable scaffolds for tissue regeneration. J Matter Chem 14:1915

Ising E (1925) Beitrag zur theorie des ferromagnetismus. Z Phys 31:253–258

Islam MT, Rodríguez-Hornedo N, Ciotti S, Ackermann C (2004) Rheological characterization of topical carbomer gels neutralized to different pH. Pharm Res 21(7):1192–1199

Israelachvili JN (2010) Intermolecular and surface forces. Academic Press, 3rd edn, New York

Jeong B, Bae YH, Lee DS, Kim SW (1997) Biodegradable block copolymers as injectable drug-delivery systems. Nature 388:860–862

Jones R (2009) Compendium of polymer terminology and nomenclature IUPAC recommendations, 2008. Royal Society of Chemistry, Cambridge

Joseph DD (1970) Global stability of the conduction-diffusion solution. Arch Ration Mech Anal 36(4):285–292

Kebiche Z, Castelain C, Burghelea T (2014) Experimental investigation of the Rayleigh-Benard convection in a yield stress fluid. J Non-Newton Fluid Mech 203:9–23

Koschmieder EL (1993) Bénard cells and Taylor vortices. Cambridge University Press

Lamsaadi M, Naomi M, Hasnaoui M (2005) Natural convection of non-Newtonian power law fluids in a shallow horizontal rectangular cavity uniformly heated from below. Heat Mass Transf 41: 239–249. ISSN 0947-7411

Landau LD, Levich B (1972) Dragging of a liquid by a moving plate. Acta Physicochim 388(17):42–54

Landau LD, Lifschitz EM (1987) Fluid mechanics. Pergamon Press, Oxford

Landau LD, Lisfshits EM (1980) Statistical physics, part 1: volume 5 (Course of theoretical physics, Volume 5), Third edn. Butterworth-Heinemann

Landry MP, Frigaard IA, Martinez DM (2006) Stability and instability of Taylor-Couette flows of a bingham fluid. J Fluid Mech 560:321–353

Larson RG (1999) The structure and rheology of complex fluids. Oxford University Press

Le Bars M, Davaille A (2004) Whole layer convection in a heterogeneous planetary mantle. J Geophys Res 109:23

Liang SF, Acrivos A (1970) Experiments on buoyancy driven convection in non-Newtonian fluid. Rheol Acta 9(3):447–455

Magazu S, Migliardo F, Malomuzh NP, Blazhnov IV (2007) Theoretical and experimental models on viscosity: I. Glycerol. J Phys Chem B 111(32): 9563–9570

Martinez-Mardones J, Tiemann R, Walgraef D (2000) Thermal convection thresholds in viscoelastic solutions. J Non-Newton Fluid Mech 93(1):1–15

Meinesz FAV (1947) Major tectonic phenomena and the hypothesis of convection currents in the earth. Q J Geol Soc 103(1–4):191–207

Metivier C, Nouar C, Brancher J-P (2005) Linear stability involving the Bingham model when the yield stress approaches zero. Phys Fluids 17(10):104106

Metzner AB, Reed JC (1955) Flow of non-Newtonian fluids: correlation of the laminar, transition, and turbulent-flow regions. AIChE J 1(4):434–440

Möller PCF, Mewis J, Bonn D (2006) Yield stress and thixotropy: on the difficulty of measuring yield stress in practice. Soft Matter 2:274–283

Moyers-Gonzalez M, Burghelea T, Mak J (2011a) Linear stability analysis for plane-Poiseuille flow of an elastoviscoplastic fluid with internal microstructure for large Reynolds numbers. J Non-Newton Fluid Mechan 166(9–10):515–531

Moyers-Gonzalez M, Burghelea T, Mak J (2011b) Linear stability analysis for plane-Poiseuille flow of an elastoviscoplastic fluid with internal microstructure for large Reynolds numbers. J Non-Newton Fluid Mech 166(9–10):515–531

Newell AC, Whitehead JA (1969) Finite bandwidth, finite amplitude convection. J Fluid Mech 38:279–303

Nguyen QD, Boger DV (1992) Measuring the flow properties of yield stress fluids. Ann Rev Fluid Mech 24(1):47–88

Nickerson CS, Kornfield JA (2005) A "cleat" geometry for suppressing wall slip. J Rheol 49(4):865–874

Oppong FK, de Bruyn JR (2007) Diffusion of microscopic tracer particles in a yield-stress fluid. J Non-Newton Fluid Mech 142:104–111

Oppong FK, Rubatat L, Frisken BJ, Bailey AE, de Bruyn JR (2006) Microrheology and structure of a yield-stress polymer gel. Phys Rev E 73:041405

Orowan E (1965) Convection in a non-Newtonian mantle, continental drift, and mountain building. Philos Trans R Soc Lond Ser A Math Phys Sci 258(1088):284–313

Ovarlez G, Cohen-Addad S, Krishan K, Goyon J, Coussot P (2013) On the existence of a simple yield stress fluid behavior. J Non-Newton Fluid Mech 193:68–79. Viscoplastic fluids: from theory to application

Owen DH, Peters JJ, Lavine ML, Katz DF (2003) Effect of temperature and pH on contraceptive gel viscosity. Contraception 67(1):57–64

Papanastasiou TC (1987) Flows of materials with yield. J Rheol (1978-present) 31(5):385–404

Park HM, Park KS (2004) Rayleigh-Bénard convection of viscoelastic fluids in arbitrary finite domains. Int J Heat Mass Transf 47(10–11):2251–2259

Park HM, Ryu DH (2001) Rayleigh-Bénard convection of viscoelastic fluids in finite domains. J Non-Newton Fluid Mech 98(2–3):169–184

Park NA, Irvine TF (1997) Liquid density measurements using the falling needle viscometer. Int Commun Heat Mass Transf 24(3):303–312

Park NA, Irvine TF Jr (1997) Anomalous viscosity-temperature behaviour of aqueous carbopol solutions. J Rheol 41(1):167–173

Peixinho J (2004) Contribution expérimentale a l'étude de la convection thermique en régime laminaire, transitoire et turbulent pour un fluidea seuil en ecoulement dans une conduite. PhD thesis, Université Henri Poincaré, Nancy, France

Peixinho J, Nouar C, Desaubry C, Theron B (2005a) Laminar transitional and turbulent flow of yield stress fluid in a pipe. J Non-Newton Fluid Mech 128:172–184

Peixinho J, Nouar C, Desaubry C, Theron B (2005b) Laminar transitional and turbulent flow of yield stress fluid in a pipe. J Non-Newton Fluid Mech 128(2–3):172–184

Peixinho J, Desaubry C, Lebouche M (2008) Heat transfer of a non-newtonian fluid (Carbopol aqueous solution) in transitional pipe flow. Int J Heat Mass Transf 51(1–2):198–209

Piau JM (2007) Carbopol gels: elastoviscoplastic and slippery glasses made of individual swollen sponges: meso- and macroscopic properties, constitutive equations and scaling laws. J Non-Newton Fluid Mech 144(1):1–29

Picard G, Ajdari A, Bocquet L, Lequeux F (2002) Simple model for heterogeneous flows of yield stress fluids. Phys Rev E 66:051501

Poumaere A, Moyers-Gonzalez M, Castelain C, Burghelea T (2014) Unsteady laminar flows of a carbopol gel in the presence of wall slip. J Non-Newton Fluid Mech 205:28–40

Putz AMV, Burghelea TI (2009) The solid-fluid transition in a yield stress shear thinning physical gel. Rheol Acta 48:673–689

Putz AMV, Burghelea TI, Frigaard IA, Martinez DM (2008) Settling of an isolated spherical particle in a yield stress shear thinning fluid. Phys Fluids (20):033102

Qiu Y, Park K (2001) Environment-sensitive hydrogels for drug delivery. Adv Drug Deliv Rev 53(3):321–339

Quemada D (1998a) Rheological modeling of complex fluids: I: the concept of effective volume fraction revisited. Eur Phys J AP 1:119–127

Quemada D (1998b) Rheological modeling of complex fluids: III: dilatant behaviour of stabilized suspensions. Eur Phys J AP 3:309–320

Quemada D (1999) Rheological modeling of complex fluids: IV: thixotropic and "thixoelastic" behaviour. Start-up and stress relaxation, creep tests and hysteresis cycles. Eur Phys J AP (5):191–207

Ree T, Eyring H (1955) Theory of non-Newtonian flow. i. Solid plastic system. J Appl Phys 26(7):793–800

Reynolds O (1883) An experimental investigation of the circumstances which determine whether the motion of water shall be direct or sinuous, and of the law of resistance in parallel channels. Philos Trans R Soc Lond 174:935–982

Richeton J, Ahzi S, Daridon L, Rémond Y (2005) A formulation of the cooperative model for the yield stress of amorphous polymers for a wide range of strain rates and temperatures. Polymer 46:6035–6043

Roussel N, Le Roy R, Coussot P (2004) Thixotropy modelling at local and macrsocopic scales. J Non-Newton Fluid Mech 117(2–3):85–95

Sainudiin R, Moyers-Gonzalez M, Burghelea T (2014) A microscopic gibbs field model for the macroscopic behavior of a viscoplastic fluid. UCDMS Res Rep 2014(1):1–17

Sainudiin R, Moyers-Gonzalez M, Burghelea T (2015a) A microscopic Gibbs field model for the macroscopic yielding behaviour of a viscoplastic fluid. Soft Matter 11:5531–5545

Sainudiin R, Moyers-Gonzalez M, Burghelea T (2015b) A microscopic Gibbs field model for the macroscopic yielding behaviour of a viscoplastic fluid. Soft Matter 11:5531–5545

Sani R (1964) On the non-existence of subcritical instabilities in fluid layers heated from below. J Fluid Mech 20:315–319, 10

Segel LA (1969) Distant side-walls cause slow amplitude modulation of cellular convection. J Fluid Mech 38:203–224, 7

Slatter PT (1999) The laminar-turbulent transition in large pipes. In: Problems in fluid mechanics and hydrology, Prague, pp 247–256

Slomkowski S, Alemán JV, Gilbert RG, Hess M, Horie K, Jones RG, Kubisa P, Meisel I, Mormann W, Penczek S, Stepto RFT (2011) Terminology of polymers and polymerization processes in dispersed systems (IUPAC recommendations 2011). Pure Appl Chem 83(12):2229–2259

Souliès A, Pruvost J, Legrand J, Castelain C, Burghelea TI (2013) Rheological properties of suspensions of the green microalga chlorella vulgaris at various volume fractions. Rheol Acta 52(6):589–605

Stanley EH (1987) Phase transitions and critical phenomena. Oxford University Press

Taylor GI (1938) The spectrum of turbulence. Proc R Soc Lond Ser A Math Phys Sci 164 (919):476–490

Todica M, Pop CV, Udrescu L, Pop M (2010) Rheological behavior of some aqueous gels of carbopol with pharmaceutical applications. Chin Phys Lett 27(1):018301

Turan O, Chakraborty N, Poole RJ (2012) Laminar Rayleigh-Bénard convection of yield stress
    fluids in a square enclosure. J Non-Newton Fluid Mech 171–172(0):83–96. ISSN 0377-0257
Weber E, Moyers-Gonzalez M, Burghelea TI (2012) Thermorheological properties of a carbopol
    gel under shear. J Non-Newton Fluid Mech 183–184:14–24
Zhang J, Vola D, Frigaard IA (2006) Yield stress effects on Rayleigh-Bénard convection. J Fluid
    Mech 566:389

Transport Phenomena in Particle Suspensions: Sedimentation and Thermophoresis

Roberto Piazza

Abstract This chapter deals with transport phenomena induced in colloidal suspensions and complex fluids either by gravity, which is the well established but nevertheless still stimulating subject of sedimentation, or by thermophoresis, a subtler and very intriguing effect that is still partly understood. Specifically, I shall highlight the wealth of information one can get by investigating the particle concentration profiles generated at equilibrium by sedimentation, or at steady-state by thermophoresis, and discuss some novel optical techniques that have been fruitfully exploited to study them.

1 Introduction

This chapter deals with particle transport driven by external forces, either due to a real external field or induced by a thermal nonequilibrium condition. Specifically, we shall discuss the equilibrium or steady-state particle concentration profiles induced in colloidal suspensions by

(a) *Sedimentation*, arguably the most elementary transport process induced by a simple field like gravity,
(b) *Thermophoresis*, a much subtler and intriguing effect consisting of particle transport along a temperature gradient that generates effective "thermal forces" on disperse particles although no "real" external field is present.

Sedimentation, the progressive deposition of particles settling in a fluid, is widespread in the natural environment. For instance, it begets majestic depositional landforms, provides valuable energy supplies such as vast oil shales (Julien 2010), affects airborne particle pollution (Hind 1999), and controls the distribution of plankton in the oceans (Kiørboe 2008). Besides, forced sedimentation (centrifugation) is extensively

R. Piazza (✉)
Department of Chemistry, Materials Science and Chemical Engineering,
Politecnico di Milano, Milano, Italy
e-mail: roberto.piazza@polimi.it

used as a separation tool in the extractive, chemical, nuclear, and food processing industry (Woon-Fong Leung 1998), or as a preparative and analytic method in biology and medicine (Lebowitz et al. 2002). The investigation of sedimentation processes is, therefore, of primary importance in geophysics and environmental science, and has countless technological applications.

Sedimentation studies in model colloidal systems have also played a seminal role in the development of statistical physics thanks to the landmark experiments performed by Jean–Baptiste Perrin, who by observing and accounting for the equilibrium concentration profiles that the settling process generates in dilute suspensions, turned colloids from a subject of interest for chemists to a benchmark test for Einstein's theory of Brownian motion and, more generally, for the molecular theory of matter (Perrin 1909). As a matter of fact, a lot more can be learnt from the equilibrium sedimentation profiles, which in fact yield the whole phase diagram and the equation of state of a colloidal fluid.

Possibly more interesting and surely much less investigated are the effects of gravity on soft disordered solids like colloidal gels. We shall indeed see that the stresses associated with its own weight may lead to rupture and consistent restructuring of a weak gel. Moreover, by "squeezing" a gel with natural gravity or in a centrifuge one can obtain quite useful information about the compressional rheology of soft solids. In this short review, I shall instead refrain from discussing the *dynamics* of particle settling, which is far from being a closed matter. In fact, due to the presence of hydrodynamic interactions between the settling particles, the kinetics of sedimentation processes is a demanding subject often generating theoretical puzzles even for model suspensions of equal-sized ("monodisperse") particles. For the interested reader, a rather recent discussion of these issues can be found in an extensive review I wrote a few years ago (Piazza 2014).

In the presence of a temperature gradient, particles suspended in a fluid are driven either to the cold or to the hot, fluid mixtures partially demix, colloidal structures rearrange and anneal, thermoelectric fields build up. Besides, airborne particles deposit on cold surfaces, fluids slip along inhomogeneously heated surfaces, selective transport takes place through membranes separating reservoirs at different temperatures. In other words, thermal gradients move matter. If the time evolution and the final outcome of gravity settling processes are anything but trivial, the origin itself of these "thermal forces" is elusive. In what follows, I shall first give a brief account of the historical development of the investigation of thermal forces. Then, guided by the experimental evidence obtained in the past two decades, I shall try and inquire about the physical roots of these phenomena, which arguably play a subtle role in several important processes ranging from membrane exchange in fuel cells to oil transport in reservoirs, focusing in particular on thermophoresis, an exquisite interfacial effect that can be profitably exploited to manipulate matter at the micro and nanoscale.

2   Colloid Sedimentation

Some basic notions of colloid sedimentation can be introduced by considering the landmark experiment by Perrin (1909), whose key result has been proving that, at settling equilibrium, a dilute suspension of monodisperse particles of mass m (in his experiment, carefully selected emulsion droplets) takes on an inhomogeneous density profile along the vertical direction z that mirrors the barometric law for ideal gases,

$$n(z) = n(0)\, e^{-z/\ell_g}, \tag{1}$$

where n is the number of particles per unit volume and ℓ_g, called the gravitational (or sedimentation) length, is given by the ratio of the thermal energy $k_B T$ to the magnitude of net force acting on the particle which is the sum of the particle weight $-mg\hat{\mathbf{z}}$ with the buoyant force $\mathbf{F}_b$ provided by the surrounding fluid. Taking the latter simply given by the weight of a volume of fluid equal to the particle volume V_p, as stated by the Archimedes' Principle[1] and introducing the buoyant mass $m^* = \Delta\rho V_p$, where $\Delta\rho$ is the difference between the particle and solvent densities ρ_p and ρ_0, we have

$$\ell_g = \frac{k_B T}{m^* g}. \tag{2}$$

The gravitational length has a simple physical interpretation once we recall that a colloidal particle, whatever its size, has a kinetic energy of the order of $k_B T$. Hence, ℓ_g is the typical height from the cell bottom at which a particle will rise, obtained by equating the particle kinetic and potential energy. More precisely, the barometric law (Eq. 1) yields the probability distribution of finding a particle at height z, whose expectation is $\langle z \rangle = \ell_g$.

A further very interesting meaning of ℓ_g is obtained by considering the stationary sedimentation velocity v_s (also called the Stokes speed) reached by an isolated colloidal particle, which can be found by equating the net driving force $m^* g$ to the drag $f v_s$, where f is the viscous friction coefficient ($f = 6\pi\eta a$ for a spherical particle of radius a). Indeed, taking into account that the (single) particle Brownian diffusion coefficient D_0 is related to f by the Einstein relation $D_0 = k_B T/f$ (which is the simplest example of a fluctuation–dissipation theorem), we easily get $\ell_g = D/v_s$.

In fact, the physical meaning of the dimensionless ratio of the particle size to the sedimentation length, a/ℓ_g, becomes immediately clear if we compare the relative contribution of advective to diffusive transport, known in hydrodynamics as the Péclet number. The latter can be taken as the ratio of the times $t_b \sim a^2/D_0$ and $t_s \sim a/v_s$ it takes for the particle to diffuse and, respectively, to settle over its own size (the "Stokes time")

$$\text{Pe} = \frac{t_b}{t_s} = \frac{a v_s}{D_0} = \frac{a}{\ell_g}. \tag{3}$$

---

[1]Apparently, this is a rather innocent assumption. However, when the solvent is not a simple fluid, the standard Archimedes' Principle may not hold. See Piazza (2014).

Therefore, when $a \ll \ell_g$ the contribution of gravity settling to the particle motion is just a small perturbation with respect to thermal agitation, hence particles with Pe $\ll 1$ are usually dubbed "Brownian". As mentioned in the introductory section, the theoretical analysis of the settling dynamics of *non*-Brownian particles is extremely complicated because, when Pe $\gg 1$, hydrodynamic interactions substantially perturb the equilibrium structure of the suspension. For spherical particles, the condition Pe $= 1$ corresponds at room temperature to

$$ a = \left(\frac{3k_B T}{4\pi \Delta\rho g} \right)^{1/4} \simeq \left(\frac{0.1}{\Delta\rho} \right)^{1/4} \times 10^{-4} \, \text{cm}. \tag{4} $$

The transition between the two regimes takes, therefore, place for a in the quite narrow range $0.5 \, \mu\text{m} < a < 1.5 \, \mu\text{m}$ even if $\Delta\rho$ is varied between 0.02 and 2 g/cm^3, a density range covering most of the materials common colloidal particles are made of.

Similar considerations apply to forced sedimentation provided the g stands for the centripetal acceleration $\omega^2 r$, where ω is the angular frequency of rotation of the centrifuge. Of course, in this case, the force acting on the particle increases linearly with the distance r from the axis of rotation, so that the "barometric" profile for a dilute suspension is in this case an exponential in r^2. In centrifugation studies, the particle settling velocity is usually rescaled to the acceleration by defining a "sedimentation coefficient" $s = v_0/\omega^2 r$, which has then the dimensions of time and is usually measured in svedbergs (S), where $1 \, \text{S} = 0.1 \, \text{ps}$, a particularly convenient unit for the rotation speed achievable with ultracentrifuges (for $\omega^2 r = 10^6 \, g$, a macromolecule with $s = 1 \, \text{S}$ settles at $v_s = 1 \, \mu\text{m/s}$). By using again Einstein's relation, one easily gets the Svedberg equation $s = m^* D_0/k_B T$.

2.1 Sedimentation Equilibrium and Equation of State

Let us find out what kind of information we can obtain from the vertical concentration profile asymptotically reached in a settling process. While sedimentation proceeds, particles concentrate at the cell bottom and a concentration gradient builds up. This concentration gradient induces an upward osmotic flux $\mathbf{J}_d$ that progressively grows until it equates the downward advective flux $\mathbf{J}_s$ due to gravity. When the total flux $\mathbf{J} = \mathbf{J}_s + \mathbf{J}_d$ vanishes, an equilibrium state (sometimes dubbed "sedimentation–diffusion" equilibrium) is reached. This profile, however, follows the barometric law (Eq. 1) only for very dilute suspensions, namely for suspensions that satisfy the Van't Hoff law $\Pi(z) = k_B T n(z)$, where Π is the suspension osmotic pressure, down to the cell bottom where $n(z)$ attains its maximum.

What about the general case? Vanishing of the total flux means that the hydrostatic equilibrium condition $dP/dz = -\rho g$, where P is the fluid pressure and $\rho = \rho_0 + \Delta\rho\phi$ is the density of the suspension, and $\phi(z) = V_p n(z)$ is the particle volume

fraction at height z. Writing the total pressure as $P(z) = P_0(z) + \Pi(z)$, where $P_0(z)$ is the pressure due to the bare solvent, it is then easy to show that the osmotic pressure profile must satisfy

$$\frac{\mathrm{d}\Pi(z)}{\mathrm{d}z} = -\Delta \rho g \phi(z). \tag{5}$$

Let us integrate this equation from a generic height z to the cell top $z = h$, taking into account that, when the cell is sufficiently high, the top layer will basically contain pure solvent (the supernatant left beyond by the settled particles) so that, since $\phi(h) \simeq 0$, the upper limit of the integral can be safely extended to $+\infty$. We obtain

$$\Pi(z) = \Delta \rho g \int_z^\infty \phi(z')\,\mathrm{d}z' = m^* g \int_z^\infty n(z')\,\mathrm{d}z', \tag{6}$$

which simply means that at equilibrium the osmotic pressure $\Pi(z)$ at a given height z has to match the weight per unit surface of the particles lying above that level.

Suppose, therefore, that we find an experimental technique allowing us to accurately measure the equilibrium concentration profile $\phi(z)$. Then, from a numerical integration of the profile we can also evaluate, using Eq. (6), the local osmotic pressure $\Pi(z)$ at each position z. But then, pairing $\Pi(z)$ and $\phi(z)$ at the same height z, we can extract $\Pi(\phi)$, which is the (osmotic) equation of state of the suspension. A *single* measurement of the equilibrium sedimentation profile provides, therefore, the whole equation of state of a colloidal system up to a maximum volume fraction $\phi(0)$ at the cell bottom.

The latter is surely an exciting possibility, in particular, because direct measurements of the osmotic pressure in colloidal suspensions are usually prohibitive, unless the particles are very small, due to the extremely small values of Π. Yet, as I already mentioned, this requires scanning along the sedimentation profile with a probe that is strictly proportional to the local particle concentration $c(z)$, which is not often the case. For instance, unless the colloid is very diluted the intensity I_s of the light scattered by the sample not only depends on the local particle concentration but also on interparticle interactions, since $I_s(\mathbf{q})$, where $\mathbf{q}$ is the scattering wave-vector, is proportional to the suspension structure factor $S(\mathbf{q})$. For the same reason, the optical absorbance of concentrated dispersions is *not* proportional to $c(z)$ unless the sample turbidity is purely due to optical absorption (namely, not to scattering). Other probing techniques that are in principle immune from particle interaction effects like fluorescence may suffer from practical problems such as bleaching.

Nevertheless, ingenious methods have been exploited to extract from equilibrium sedimentation experiments the equation of state of several model colloidal systems. Some of the most relevant studies are summarized in Table 1 and extensively reviewed in Piazza (2014).

Many of the studies mentioned in the table, however, required to engineer rather peculiar colloidal particles, for instance, embedding a fluorescent dye or with a crystalline core (see Sect. 2.3). For what follows, it might, therefore, be useful to say a

Table 1 Equilibrium sedimentation studies of model colloidal suspensions

Colloidal system	Method	References
Charged colloids	Direct sampling	(Hachisu and Takano 1982)
Hard spheres	Depolarized light scattering	(Piazza et al. 1993)
Hard spheres	X-ray absorption	(Rutgers et al. 1996)
Sticky hard spheres	Depolarized light scattering	(Buzzaccaro et al. 2007)
Active colloids	Confocal microscopy	(Palacci et al. 2010)
Ferrofluids	Absorption in ultracentrifuge	(Luigjes et al. 2012)
Colloidal rods	Confocal microscopy + SAXS	(Kuijk et al. 2012)
Emulsions and foams	Electric conductivity	(Maestro et al. 2013)

few words on a technique that is applicable to a much wider class of colloidal systems, also because, as we shall see, it was actually developed to investigate thermophoresis.

2.2 Useful Mirages: The Beam Deflection Technique (BD)

The working principle of beam deflection is the following. Consider a medium where a refractive index gradient $\nabla n(z)$, originating for instance from a temperature gradient or from the concentration profile generated by sedimentation, is set along a given direction z. Then, a light beam propagating *orthogonally* to z will be bent in the direction of $\nabla n(z)$, simply because the part of the beam facing the region with higher refractive index travels slower than the opposite one (see Fig. 1). One easily gets that the angle of deflection of a beam that travels by an optical path ℓ through such an optically inhomogeneous medium is given to first order by $\vartheta \simeq (\mathrm{d}n/\mathrm{d}z)\ell$. This effect (which is basically the same by which mirages appear in desert regions) is usually rather small, with deflection angles in the milliradian range, but can be easily detected using a position-sensitive detector (PSD), a standard optical device, extensively used in metrology and robotics, that yields the position of a beam spot center with a typical resolution of a few microns. In a simple experimental setup, a laser beam is mildly focused through the sedimentation cell, which can be translated along the vertical direction z by a motorized actuator, and sensed by a PSD placed at a distance L from the cell. When the setup is used to monitor the sedimentation profile of particles that differ in refractive index by Δn with the solvent, the beam position deflection Δz on the sensor is then approximately given by

$$\Delta z \simeq \frac{\mathrm{d}n(z)}{\mathrm{d}z}\ell L = L\ell\Delta n \frac{\mathrm{d}\phi(z)}{\mathrm{d}z}, \tag{7}$$

where $\phi(z)$ is the particle volume fraction profile induced by sedimentation.

$$\vartheta = \ell \frac{dn}{dz}$$

$$\Delta z = L\vartheta$$
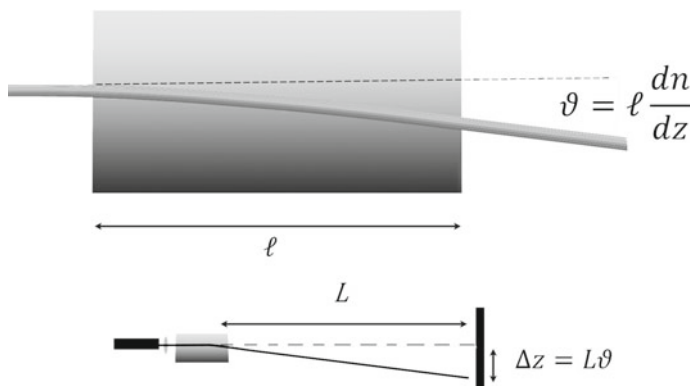
Fig. 1 Sketch of the beam deflection effect (top) and of a simple BD setup (bottom)

Because Eq. (7) is proportional to the *derivative* of the concentration profile, BD data must, however, be integrated twice to obtain the equation of state. While this is not a problem for smooth profiles—on the contrary: the additional integration helps smoothing noisy data—it is a clear disadvantage when dealing with discontinuous jumps. Thus, the exact amount of the concentration jump at the meniscus separating two phases where dn/dz is undefined cannot be extracted, and BD measurements alone cannot yield quantitative phase equilibria. Yet, a crucial advantage of BD compared to most other optical methods is that it works even for quite turbid samples, the sole requirement being that detectable amount of transmitted light reaches the PSD, placed at sufficiently long distance from the cell to limit the collection of light scattered at small angles.

As an example of the power of the BD technique, I discuss the results obtained in our lab on suspensions of monodisperse PMMA (poly(methyl methacrylate) particles with a radius $R = 180$ nm and a density $\rho_p = 1.19$, dispersed in a racemic mixture of *cis*- and *trans*-decalin ($n = 1.474$, density $\rho_s = 0.896$ g/cm^3) at an initial volume fraction ϕ_0 of about 20%. At this concentration, the PMMA suspension shows appreciable multiple scattering, which would have rather seriously affected light scattering measurements. The sample transmittance, however, was still amply sufficient to allow accurate BD measurements to be performed. After about 3 months, approximately corresponding to a Stokes time $t_s = h/v_s$, the lower part of the settled suspensions showed a thin turbid colloidal phase, with a thickness of less than 2 mm, topping a strongly iridescent colloidal crystal phase extending down to the cell bottom.

By numerically integrating the BD data, we have obtained the volume fraction profile shown in the inset of Fig. 2. We can first notice that the upper part of the profile shows indeed the barometric profile (Eq. 1) expected for a dilute suspension, yet with an experimental $l_g \simeq 75\,\mu$m which is about 50% larger than the predicted sedimentation length of the system. This result suggests an increase of the nominal PMMA particle radius by about 13% due to swelling by decalin, a result consistent
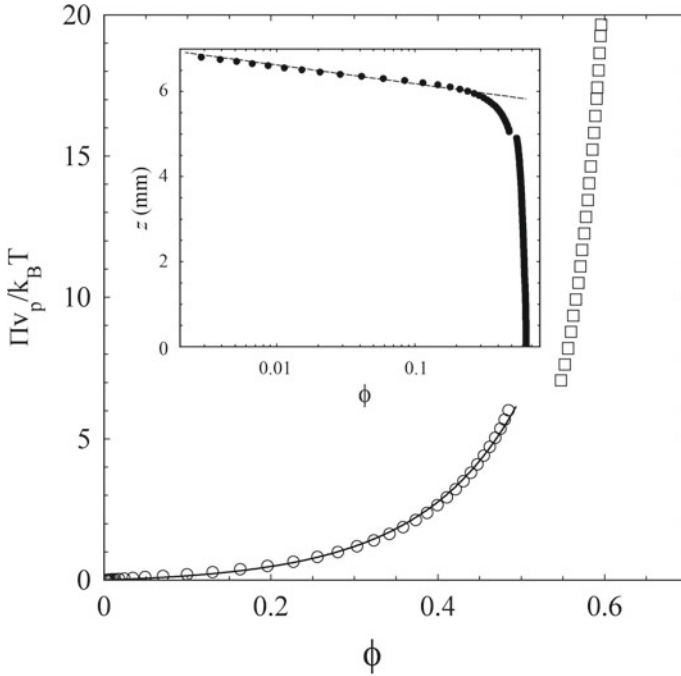
Fig. 2 Inset: Concentration profile, obtained by integrating the BD signal, of a PMMA suspension left settling for about 3 months from an initial uniform state. Body: equation of state of the system, obtained by integrating the profile and setting at $\phi_f = 0.5$ and $\phi_s = 0.55$ the volume fractions of the coexisting fluid and solid phases

with former observations (Phan et al. 1996). Using this experimental value of ℓ_g, one obtains a value $\rho_f \simeq 0.5$ for the particle volume fraction at the interface separating the fluid from the colloidal crystal phase, which is in excellent agreement with the maximum packing fraction of an HS fluid. As already mentioned, however, BD does not allow evaluating concentration jumps at the meniscus separating two coexisting phases, hence we fixed the volume fraction of the colloidal crystal at coexistence with the fluid phase in the inset of Fig. 2 at the value $\phi_c \simeq 0.55$ expected for hard spheres.

A further numerical integration of the profile yields the equation of state shown in the body of Fig. 2. The fluid branch can be rather accurately described by the Carnahan–Starling equation of state for hard spheres:

$$\frac{\Pi}{n k_B T} = \frac{1 + \phi + \phi^2 - \phi^3}{(1 - \phi)^3},\qquad(8)$$

where $n = \phi/v_p$ is again the particle number density, which is drawn in Fig. 2 as a full line. It is useful to stress that, once ℓ_g is experimentally fixed, *no fitting parameter*

is needed. The osmotic pressure in the ordered phase, however, is consistently higher and its dependence on ϕ consistently is steeper than the predictions for a colloidal crystal of hard spheres. As discussed by Piazza et al. (1993) and Phan et al. (1996), this is very presumably due to the fact that the time the sample has been allowed to settle was sufficient to reach equilibrium for the fluid phase, but still too short for a full equilibration of the colloidal crystal.

2.3 Gravity Effects on Colloidal Gels

Colloidal gels are the focus of an intensive research effort for both fundamental and practical reasons. On the one hand, they are model systems to understand the interplay between percolation, phase separation, and dynamical arrest in systems with attractive interactions. On the other hand, colloidal gels are extensively exploited in food, drug, personal care, and cosmetic products, where they are often used as a means to stabilize a complex formulation against macroscopic phase separation.

The simplest and most common route to gelation in colloidal systems is arrested phase separation (Zaccarelli 2007), which consists of the following. The phase diagram of systems of colloidal particles interacting via a short-ranged attractive potential, due, for instance, to depletion forces (Lekkerkerker and Tuinier 2011), displays a coexistence gap that, although metastable with respect to crystallization, is analogous to the gas–liquid transition for a pure fluid (Miller and Frenkel 2004). Hence, when the colloid is quenched inside this gap by increasing the strength of the attractive forces, the system starts to undergo phase separation into a colloid-rich and a colloid-poor phase. Except for very shallow quenches, however, the phase separation process does not reach completion, and the system gets arrested into a disordered gel phase (Buzzaccaro et al. 2007).

Mechanically, colloidal gels are viscoelastic systems with a predominantly solid-like behavior. However, they typically yield under modest stress, often including the gravitational stress exerted by their own weight. It is, therefore, not surprising that many studies have been devoted to the sedimentation behavior of colloidal gels, revealing a wealth of fascinating phenomena. For instance, some colloidal gels show a "delayed collapse", namely they break, but only after an unpredictable delay time, into clusters that rapidly settle until they form a slowly compacting dense phase. Depending on particle concentration and on the strength of the attractive interparticle forces that lead to gelation, other gels may conversely show a much "quieter" settling by compressing very slowly and uniformly (Secchi et al. 2014). Here I shall only focus on the asymptotic concentration profiles observed when the gel has eventually attained mechanical equilibrium to a concentration profile that does not apparently show any further changes.

The specific colloidal system we consider is that of aqueous suspensions of spherical colloidal particles made of a fluorinated copolymer (MFA) that have a refractive index very close to water, which makes them transparent up to very high concen-

tration, and a crystalline core.[2] The latter feature is particularly useful: because of the internal optical anisotropy of the particles the intensity of the light scattered by an MFA suspension contains indeed a strong depolarized component that is strictly proportional to the local particle volume, a peculiar optical property that allows the sedimentation profile to be accurately measured (Degiorgio et al. 1994). A variable amount of nonionic surfactant, Triton X100, is added to the suspensions to induce attractive depletion interactions with a range comparable to the size of the surfactant micelles. A detailed description of the phase behavior of this system can be found in Buzzaccaro et al. (2007). In brief, the phase diagram of the system displays a demixing region, where the suspension state would be the coexistence of two phases at very different particle concentrations. Yet, as discussed above, when the amount of added surfactant is sufficiently large to drive the colloidal suspension into the coexistence region phase separation, which proceeds through a spinodal decomposition process, is hindered and arrested by the formation of a weak network, which however rapidly collapses under the gravitational stress. The "debris" of this collapsed network, which are rather large particle clusters, accumulates at the cell bottom yielding a denser structure that slowly compresses and consolidates until it reaches a stationary profile that does not appreciably change any more.

We first consider the profiles obtained for depletion gels of MFA suspensions prepared either at different initial particle volume fractions ϕ_0, or at different strengths of the depletion interactions, which can be tuned by varying the surfactant concentration c (Buzzaccaro et al. 2012). As one may expect, at constant c the final sediment has a total height that is proportional to ϕ_0. Nevertheless, Fig. 3a shows that the shape of the concentration profiles does *not* depend on ϕ_0, because the profiles can be collapsed onto a master curve by simply shifting them along the z-axis so as to make the top part coincide. This surprising scaling implies that gels prepared at different ϕ_0 compress in the same way and thus must have the same strength. This rather counterintuitive result is probably due to the fact that the debris the original network breaks into to have a similar structure regardless of ϕ_0, so the compacted structures resulting from their accumulation at the bottom of the cell have very similar mechanical properties. But what is the shape that the asymptotic profile takes on? To understand this, we should make a brief detour, and learn something about compressional rheology.

Compressive rheology and the gel yield stress. The distinctive property of all soft materials is that they weakly resist to *shear* stress, while for what concerns *volume* changes, they are basically incompressible like a simple fluid or solid. This does not mean, however, that the *dispersed phase* cannot be squeezed to a smaller volume by expelling part of the solvent. Squeezing can be applied by selective filtration, by using special "vane rheometers" (Liddell and Boger 1996), or more simply by subjecting the dispersed phase and the solvent to different forces, which is what naturally happens in natural gravity or in a centrifuge when the two phases have a different density. Natural or forced sedimentation can, therefore, be exploited to

---

[2]To be more specific, PFA particles can be seen as a collection of polytetrafluoroethylene crystals embedded in a spherical matrix of an amorphous fluorinated comonomer.
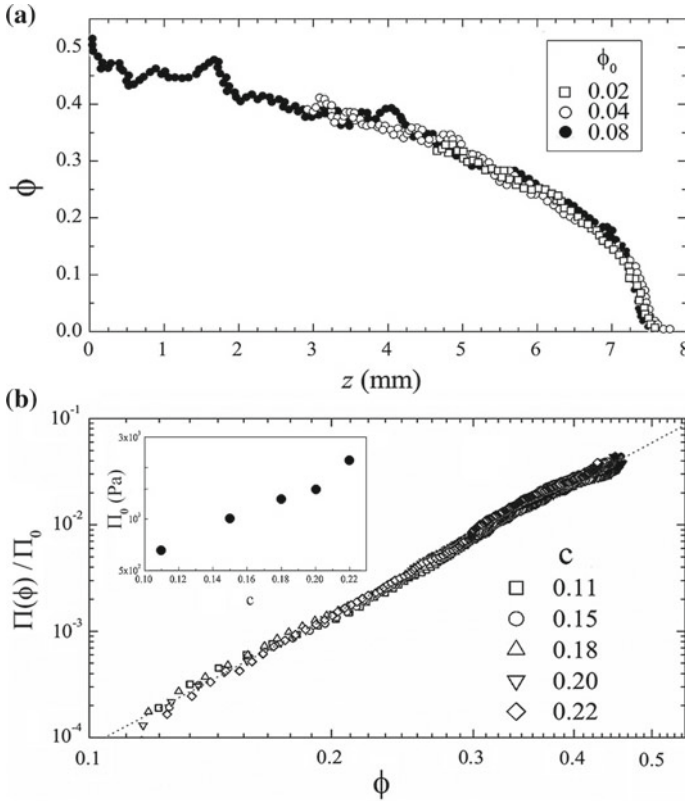
Fig. 3 a Asymptotic volume fraction profile of settled colloidal gels obtained by adding to fluorinated colloidal particles with a radius $R \simeq 90$ nm a fixed concentration $c = 12\%$ of the nonionic surfactant Triton X100, acting as a depletant. The profiles for different initial particle volume fraction ϕ_0 have been superimposed by shifting them along the z-axis, indicating the distance from the cell bottom. **b** Scaled compressive yield stress obtained from Eq. (9) for gels at various surfactant concentrations indicated by the labels. The full line is a power-law fit using Eq. (10). The scaling factors Π_0 are shown in the panel inset

perform *compressive rheology*, a relatively recent term used to generically indicate these "squeezing" techniques, which find applications in several fields (de Kretser et al. 2003).

Very often, when the investigated material is a colloidal gel, the squeezing process is irreversible even for quite small values of the compressive stress, namely, the network undergoes a *plastic* deformation. Modeling the kinetics of the plastic consolidation process of a disordered colloidal solid requires as inputs both the mechanical strength of the network, quantified by compressive yield stress $\Pi(\phi)$, and the rate of escape of the solvent, which is fixed by the permeability of the network (Buscall and White 1987). The latter quantity, which is hard to figure out, is not, however, required to evaluate the final stationary state of the network. Indeed, the strength of

this network is solely quantified by the $\Pi(\phi)$ because a portion of the gel at local solid volume fraction ϕ does not undergo any deformations until the applied stress on the network exceeds $\Pi(\phi)$. When this happens, the structure collapses, structural consolidation occurs, and the local volume fraction increases. This compaction process goes on until, all over the sample, the local volume fraction reaches a value that is large enough so that $\Pi(\phi)$ is barely sufficient to sustain the compressive stress due to the (natural or, in a centrifuge, effective) weight of the material lying above. In the case of natural gravity, balancing the forces on a volume element yields an expression for $\Pi(\phi)$ which is fully analogous to Eq. (6) for the osmotic pressure associated with the equilibrium sedimentation profiles,

$$\Pi(z) = \Delta\rho g \int_z^\infty \phi(z)\,\mathrm{d}z. \tag{9}$$

Concentration dependence of the gel yield stress. Let us then come back to the depletion gels discussed in the previous section. As the depletant concentration increases, the interparticle attractive forces grow and the gels become stronger, leading to smaller compaction under the action of gravity. The change in gel strength is reflected by the fact that the shape of the asymptotic profiles depends on c, thus the simple scaling shown in Fig. 3a does not hold anymore. As shown in Fig. 3b, however, the data for the compressive yield stress $\Pi(z)$ at different values of c obtained by Eq. (9) *do* collapse one on top of the other provided that they are simply scaled by a c-dependent amplitude Π_0. Since the scaled values approximately fall onto a straight line in a log–log plot, this means that the yield stress grows as a power law of the particle volume fraction,

$$\Pi(\phi) = \Pi_0\phi^\alpha, \tag{10}$$

where $\alpha \simeq 4$ and A grow approximately as an exponential of the depletant concentration (see the inset in Fig. 3b).

However, there is something fishy in the previous result. Spheres can pack randomly up to a maximum volume fraction $\phi_{rcp} \simeq 0.64$ (the "random close packing" limit, r.c.p.[3]). In this limit, the systems cannot be further squeezed, so $\Pi(\phi)$ must *diverge*: hence, the power-law growth expressed by Eq. (10) cannot continue indefinitely. Unfortunately, to reach values of ϕ larger than 50% using natural gravity would require extremely tall cells and, more than that, an extremely long waiting time. Recently, however we have performed compression rheology experiments on depletion gels pretty similar to those discussed above using an analytical centrifuge, which allowed us measuring the sedimentation profiles up to relative centrifugal forces (defined as $\text{RCF} = \omega^2 r/g$, where ω is the angular speed of the centrifuge and r the distance from its axis of rotation) larger than 2×10^3.

---

[3]Although it is not easy to define the r.c.p. limit, experimentally it is found to be very close to 64%, which is well below the *ordered* close packing limit of a FCC crystal, $\phi_{ocp} = \sqrt{2}pi/6 \simeq 0.74$.

In forced gravity, Eq. (9) is easily generalized to

$$\Pi(z) = \omega^2 \Delta\rho \int_{R-z}^{R-h} x\phi(x)\, \mathrm{d}x,\tag{11}$$

where h is the final height of the gel, z is the distance from the cell bottom, and R is the distance of the cell bottom from the center of rotation. The log–log plot in Fig. 4, which displays the full dependence of the compressive yield stress $\Pi(\phi)$ on ϕ obtained from the stationary profiles according to Eq. (11), shows that data obtained at different values of ϕ_0 collapse once again onto a single master curve. Note that each curve is obtained by joining without any adjustment the results for the profiles obtained at several values of RCF. For $\phi \lesssim 0.4 - 0.45$, the yield stress is indeed found to grow as a power law with an exponent $\alpha \simeq 4.2$ that is quite close to the value obtained in natural gravity. Provided that the compressive stress is high enough, however, consistently higher values of the sediment volume fraction, approaching the r.c.p. value, can actually be reached with a centrifuge. As evident from Fig. 4, the behavior of $\Pi(\phi)$ drastically deviates for $\phi \gtrsim 0.5$ from the aforementioned power-
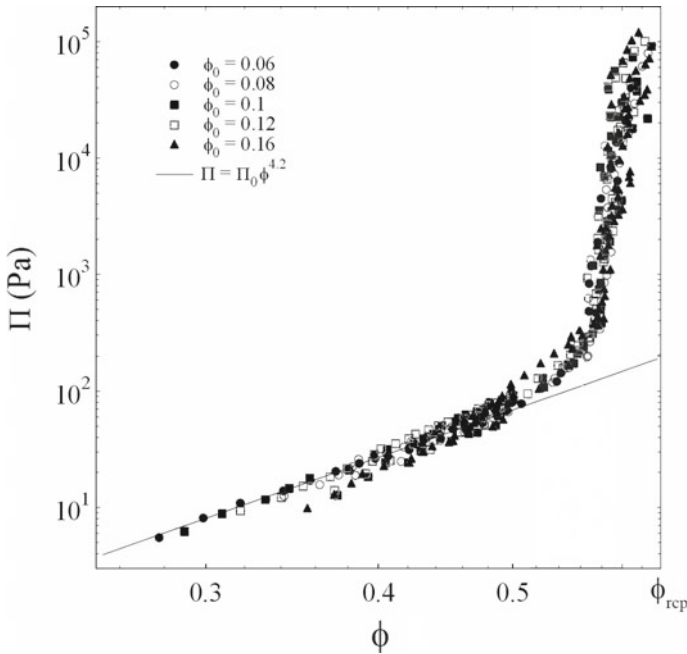
Fig. 4 Analytical centrifuge measurements of the compressive yield stress $\Pi(\phi)$ of depletion gels at a fixed surfactant concentration of about 13% and different values of ϕ_0. Each curve is obtained by joining the results calculated, using Eq. (1), from the profiles obtained at 7 different values of RCF ranging from 6 to 2300. The full line is a power-law fit with an exponent $\alpha = 4.2$ and an amplitude $\Pi_0 = 1265\,\mathrm{Pa}$

law behavior to a much more rapidly increasing trend, which apparently diverges for a volume fraction that is of the order of ϕ_{rcp}. The experiment I have just described opens up the opportunity of using a centrifuge as a "compressional rheometer".

There would be many more things to say about gels, in particular, concerning the relaxation of frozen-in internal stresses that accumulate during the formation of soft solids, which is surely fostered by the presence of gravity. This would unfortunately take too much space, so it is time to turn our attention to the other topic of this chapter, thermal forces.

3   Thermal Forces and Thermophoresis

As stated in the introductory section, thermal gradients move matter. To try and understand why, I shall first briefly retrace a long journey, along which we shall meet scientists like Maxwell, Reynolds, Tyndall, Soret, and Derjaguin. By specifically focusing on thermophoresis, I will then show how recent experiments have allowed us to get some general ideas about the physical roots of thermal forces. Finally, I plan to show how, in spite of our still partial understanding, we can profitably exploit these effects to manipulate matter. For instance, thermal forces can be used to concentrate colloids, anneal colloidal crystals and gels, fractionate proteins, build up traps for DNA replication, thermo-charge nanoparticles, mix fluids in microgravity, and even simulate the collapse of a supernova. Moreover, they arguably play a subtle role in several important processes such as soot formation in combustion, membrane exchange in fuel cells, oil transport in reservoirs.

3.1   Thermal Forces: A Bit of History

The Ludwig–Soret effect. The first evidence of thermal effects on mass transport was collected around the middle of the nineteenth century by Carl Ludwig, the founder of experimental cardiovascular physiology, who observed in 1856 that a sodium sulphate solution placed in a U-shaped tube, whose two ends were maintained in ice and boiling water, tends to concentrate near the cold end (Ludwig 1856). Yet, this mostly qualitative observation by Ludwig went unluckily unnoticed[4] until Charles Soret, a Swiss physicist published those that can be considered the first quantitative studies of thermodiffusion or, as it is correctly called, the Ludwig–Soret effect. In his first seminal work (Soret 1879) Soret writes

---

[4]Another anecdotal fact that went mostly unnoticed is that Ludwig had for many years as a lab assistant Alfred Fick, a scientist whose name is, of course, known to anyone who has studied diffusion processes….

> I propose to investigate if the final equilibrium state is the same when the temperature is varying from one point to another in the liquid. In other words, considering an initially homogeneous solution placed in a container, for example, a vertical cylindrical tube with the upper part maintained at a high temperature and a lower part at a low temperature, the question arises to know if the concentration will remain uniform everywhere, or will increase in some part at the expenses of another part? This question was, to my knowledge, never treated before and a priori the answer cannot be given and could be important for the still obscure theory of diffusive phenomena of solutions.

These words clearly show that he fully appreciated the basic and general interest of the investigation he had performed. He first investigated NaCl and KNO_3 solutions contained in 30 cm long tubes whose extremities were kept at a temperature difference of about 60° for a period extending up to 25 days. Although this time was not sufficient for the solutions to reach a steady-state condition, Soret was nevertheless able to conclude that, in his words:

> …the two salts on which I worked tend to concentrate at the cold side at expenses of the hot side, and this effect rapidly increases with the initial concentration.

Soret than discusses whether his results with the diffusion equation proposed by Fick two decades earlier showing, with appreciable mathematical insight,[5] that this requires to generalize the flux of mass by introducing an additional term that, at first order, can be taken as linear in the temperature gradient. Subsequently, by extending his measurements to longer periods, Soret managed to probe the stationary state that, as we shall shortly discuss, arises from the balance of thermodiffusive with osmotic flow (Soret 1880). Soon it was realized that thermodiffusion takes place not only in solutions, but also in simple liquid mixtures (for a dated but still useful review see review, see Tyrrell 1961).

The Ludwig–Soret effect in a dilute solution at initial homogeneous concentration c can then be quantified by the Soret coefficient

$$S_T = \frac{1}{c} \frac{\nabla c}{\nabla T} = \frac{d(\ln c)}{dT},\tag{12}$$

which physically looks as a susceptibility with the dimensions of the reciprocal of temperature, giving the response to the temperature gradient. Here we already encounter one of the main conceptual problems concerning thermal forces. It is indeed usual to introduce susceptibilities to quantify the response to an external perturbation, like an electric or magnetic field: yet, a thermal gradient is *not* a real external field. How can we then account for it? We shall later see that this question is far from being trivial.

Thermal transpiration and particle thermophoresis in gases. The first evidence that thermal inhomogeneities can affect the motion of airborne particles is due to Tyndall, who observed that a dust-free region of space develops around a heated wire

---

[5]Soret was not only a good experimentalist, but also a skilled theorist: In fact he got a degree in mathematics at the Sorbonne in a 1876, a year when the examinations had been so hard that only a single student besides Soret managed to pass them. And that student was Henri Poincaré….
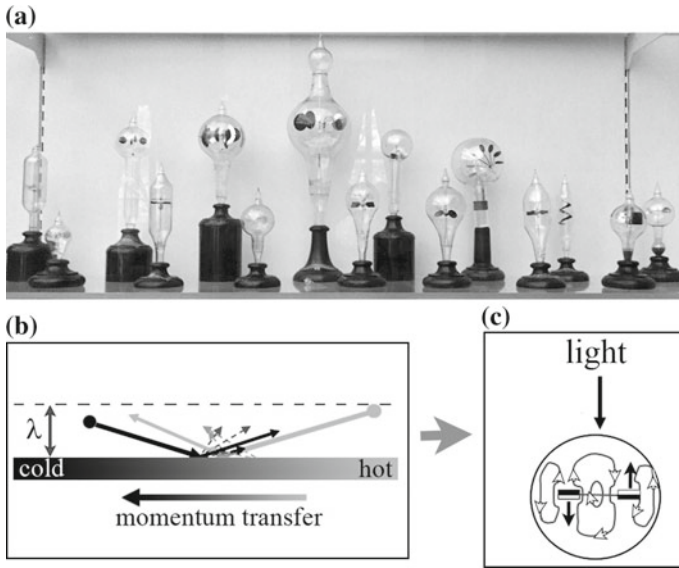
Fig. 5 **a** A series of Crookes' radiometers at the royal society in London. A sketch of Maxwell's working mechanism is shown in (**b**), while the flow in a radiometer is schematized in (**c**)

in an otherwise dusty gas (Tyndall 1870). This evidence, which was little more than an *en passant* observation, was further studied by Lord Rayleigh (Strutt Rayleigh 1882), and extensively investigated by Lodge and Clark, who also discussed the opposite (and technologically much more important) effect of particle *deposition* on cold surfaces (Lodge and Clark 1884). Due to the unavoidable presence of natural convection, however, the effect was too complicated to be given at that time a sound explanation.

Rather curiously, important hints for the understanding of particle transport by thermal gradients, i.e., thermophoresis, came from the investigation of an apparently unrelated subject, namely of "radiometric" forces in rarefied gases. In 1873, William Crookes developed a special tool, consisting of a vertical low-friction rotor with four vanes blackened on one side and silvered on the other, originally meant to detect light pressure(see Fig. 5a). In fact, when illuminated, this "radiometer" turns. Contrary to the Crookes' belief, however, the radiometer does *not* spin because of radiation pressure, which is far too small to account for the effect. Besides, the vanes turn the *wrong* way around, with the black side pushed away by the light.

We, therefore, provided that the gas pressure in the radiometer is sufficiently low, the vanes turn? The argument given in several books (including *Encyclopædia Britannica*) goes as follows: the black side of the vane heats up the surrounding gas molecules, which therefore acquire kinetic energy and "kick" the black side stronger. Unfortunately, this is wrong. To have a stationary gas, we need equalization of *pressure*: therefore, near the black side we have a hotter, but less dense gas, giving

the *same* normal component of momentum transfer to the vane. Even in the presence of convection things do not change: convection patterns around a vertical heated surface do not display transverse pressure gradients, and there is no pressure drop between the thermal boundary layers and the bulk, stationary gas.

It was Maxwell that, in his last paper published in 1879 (Maxwell 1879), unraveled the correct mechanism. By reasoning on the discovery made by Osborne Reynolds of gas "thermal transpiration" through porous membranes, which we discuss more in what follows, Maxwell concluded that the radiometer turns because of *tangential* stresses on the *edges* of the vanes.

Let us try and recast Maxwell's argument in modern terms. Consider a gas bounded by a solid planar surface *S*, with a temperature gradient *along* the plane, and those molecules that lie within a mean free path λ from *S*. The clever intuition by Maxwell, largely stemming from the discussion with the "anonymous" reviewer of his paper (who was Kelvin, as he actually knew), is that molecular impacts with a solid surface are *not* specular reflections and that the momentum distribution after an impact are partly thermalized by the interaction with the surface. Since molecules coming from the hot side carry more momentum than those coming from the cold, this leads to a *longitudinal* transfer of momentum from the gas molecules to the solid surface. The amount of transferred momentum can by gauged by introducing a suitable "accommodation" coefficient that, although hard to evaluate, still plays a key role in kinetic theory (see Fig. 5b).[6]

This mechanism, besides qualitatively accounting for Crookes radiometer motion and explaining gas "thermal creep" in pores, was invoked by Epstein (1929) to give a first explanation of particle thermophoresis in gases, at least in the hydrodynamic near-continuum limit.[7] For an accommodation coefficient close to one (corresponding to full thermalization upon an impact, as usually occurs on metal surfaces) Epstein's expression for the steady-state thermophoretic velocity v_{th} acquired by a particle of thermal conductivity κ_P embedded in a gas with thermal conductivity κ_g and molecular mass *m* can be written as

$$v_T = \frac{3}{2}\sqrt{\frac{k_B T}{2\pi m}}\,\lambda\left(\frac{\kappa_g}{2\kappa_g + \kappa_P}\right)\frac{\nabla T}{T},\tag{13}$$

where the term in brackets accounts for the particle-induced change of the externally imposed gradient ∇T. Since v_T is proportional to λ, thermophoresis is the stronger the lower the gas pressure. Notice also that we can write $v_T \propto (\lambda/\ell_T)v_{th}$, where v_{th} is the thermal velocity of the gas molecules and $\ell_T = \nabla T/T$ is the typical length scale over which temperature varies. Epstein approach was further refined by other researchers

---

[6]It is however important to point out that using an equilibrium Maxwell–Boltzmann distribution $f_0(v)$, this longitudinal momentum transfer *vanishes*. Indeed, one must take into account the first correction to $f_0(v)$, which can be obtained from the Boltzmann equation and explicitly contains ∇T (Kennard 1938).

[7]The mechanism is very different in the extremely dilute, or "Knudsen", regime, where the gas mean free path is large compared to the particle size.

to include higher order terms and extend the solution to the near-continuum regime of higher Knudsen number (Zheng 2002).

For what follows, it is useful to stress some key aspects of Maxwell's mechanism:

- The gas exerts on the surface (or vice versa) of a *tangential* stress. This means that the pressure tensor near the surface, which is anisotropic in the direction of the thermal gradient.
- The inhomogeneous gas region where the velocity distribution differs from the equilibrium value is confined within a surface layer with a thickness of the order of λ. The mean free path acts, therefore, as a *characteristic length scale* controlling the amplitude of the effect.
- Macroscopically, thermophoresis can be seen as an effective *slip* of the particle, namely as a violation of the hydrodynamic stick boundary condition confined within a mean free path from the surface.
- The thermophoretic velocity *does not depend on particle size a* (at least when $a \gg \lambda$). In fact, particle *bulk* properties enter the problem only through the thermal conductivity κ_P that, in relation to κ_g, yields the local distortion of the temperature field.

As we shall see, these points bear strong resemblances with similar features of particle thermophoresis in liquids.

From thermal transpiration in gases to thermo-osmosis in liquids. As we mentioned, Maxwell was driven to conceive his longitudinal momentum transfer mechanism by Reynolds' investigation of "thermodiffusion" (today better known as "thermal transpiration") in gases (Reynolds 1879), which had recently been discovered by Wilhelm Feddersen (Feddersen 1873). Reynolds was actually motivated to study thermal transpiration by his interest in the Crookes radiometer and his clever idea was investigating whether the *opposite* phenomenon takes place, namely the flow of a gas driven by a thermally inhomogeneous surface that is kept still, an effect later known as *thermal creep*.

Reynolds realized that this effect should have depended on the size of the surface compared to the mean free path of the molecules so that, in his words, "by using vanes of comparatively small size the forces should be perceived at comparatively greater pressures of the gas. This however meant that, to obtain any result at moderately high pressure, the vanes would have to be very small indeed, "too small almost to admit an experiment".[8] This is, however, the moment when Reynolds had a real stroke of genius:

> And it was while thinking of some means to obviate this difficulty that I came to perceive that if the vanes were fixed, then instead of the movement of the vanes we should have the gas moving past the vanes – a sort of inverse phenomenon – and then instead of having small vanes, small spaces might be allowed the gas to pass. Whence it was obvious that in porous plugs I should have the means of verifying these conclusions.

---

[8]Remember that, to increase the mean free path of air at room temperature to 1 mm, pressure must be lowered to about 7 Pa.

So, what it did was building what he called a "thermodiffusiometer" connecting two gas chambers kept at different temperatures through porous plugs and measure by means of a differential gauge the pressure difference between the two chambers that builds up while the gas "transpires" through the plug until a stationary state is reached. By performing careful and extensive experiments on several gases (air, hydrogen, carbon dioxide) at various equilibrium pressure using plugs made of different materials (stucco, bisque, meerschaum), Reynolds, in fact, opened up the investigation of thermal stresses in rarefied gas dynamics, which also lead to useful applications like a "thermal transpiration pump" tested by NASA in microgravity (Sone 2000). For a clever student demonstration of thermal creep see Sone (1991).

Fluid flow driven by thermally inhomogeneous surfaces is not limited to gases, but takes place in liquids too, as discovered in 1907 by Lippman, who studied the flow of water through a membrane of gelatin separating two volumes held at different temperatures. A few years later, a more systematic study by Aubert (1912), who gave this effect the name of "thermo-osmosis", showed that, at variance with gases (where the direction of flow is always from the cold to the hot side), some kinds of membranes, made, for instance, of parchment or viscose, drive a water flow from the hotter to the colder reservoir.

The observations by Lippman and Aubert went almost unnoticed, until the investigation of thermo-osmotic phenomena was resumed by Derjaguin (Derjaguin and Sidorenkov 1941; Derjaguin et al. 1987), who performed further experiments and reported remarkable effects for porous plugs of sintered glass in water and other liquids. What is more interesting is that Derjaguin attempted to develop a theoretical model of thermo-osmosis by first considering the reciprocal "mechano–caloric" effect, namely the buildup of thermal gradients due to fluid flow in capillary pores,[9] using then the Onsager reciprocal relations to obtain the slip velocity of the fluid with respect to a horizontal surface, which he found to be

$$v_T = -\frac{2}{\eta} \left(\int_0^\infty z \Delta h(z) \mathrm{d}z \right) \frac{\nabla T}{T}, \tag{14}$$

where η is the viscosity and $\Delta h(z)$ is the local excess enthalpy at a height z above the surface, a quantity that, for short-ranged liquid/surface interactions, is confined within a thin layer close to the surface.

Equation (14) provides a qualitative understanding of the direction of the thermo-osmotic flow: when the liquid/solid interactions are attractive (so that the liquid wets the surface) the excess enthalpy in the internal region is everywhere negative, and the fluid moves to the hot side, whereas the opposite takes place for repulsive fluid/surface interactions. The main problem with this expression, however, is that there is some ambiguity in the microscopic definition of the local excess enthalpy,

---

[9]This ideas may have been suggested by Landau, who regarded the thermomechanical effect to be not solely restricted to superfluid helium (where, however, it is far larger!).

since it is not at all a slow-varying function of *z*. A quantitative assessment of $\Delta h(z)$ (not to say its experimental determination) is then extremely hard.

Extensive work on thermo-osmosis, providing useful results concerning, in particular, the steady-state condition and the temperature dependence of the effect, was later made by the group of F. Gaeta in Italy (Pagliuca et al. 1987). In the recent past, there has been a renewed interest in thermo-osmotic phenomena because of its potential applications to fuel cells, water management, and water recovery. For a recent review, see Barragán and Kjelstrup (2017). For the purposes of this work, the most interesting aspect is the strong relation between thermo-osmosis and particle thermophoresis in liquids, which is the main subject of what follows.

3.2 Thermophoresis in Liquids: Some Useful Definitions

When compared to all the studies of thermal forces we just discussed, the experimental investigation of thermophoresis in liquids began rather late, mostly because the standard techniques to investigate thermal transport of large particles available till the past decades of the past century were extremely time-consuming and often plagued by spurious effects. The first attempts were a natural extension of the investigation of the Soret effect in simple liquid mixtures to macromolecular solutions, and have actually been performed by two giants of polymer science like Peter Debye and Bruno Zimm (Debye and Bueche 1948; Hoffman and Zimm 1955), but were mostly capable of showing that the Soret coefficient is much larger for macromolecules than for small molecules.

Arguably, the first investigation of thermophoresis in a colloidal fluid, specifically for a suspension of 1 μm polystyrene particles, was published in 1972 by McNab and Meisen (McNab and Meisen 1972), who ingeniously used an ultramicroscope to detect changes in the particle sedimentation velocity due to the presence of a thermal gradient. Yet, they tried to interpret their data using various expressions for thermophoresis in gases, obtaining a very poor agreement: as we shall see, the mechanisms causing thermophoresis in liquids and gases are indeed quite different. The experimental situation improved considerably when novel powerful optical methods like the laser beam deflection (Giglio and Vendramini 1977; Zhang et al. 1999) and transient grating (Köhler et al. 1995) techniques became available. These powerful laser techniques originated a real boom in the number and quality of studies of thermophoresis that started at the turn of the century and is still exponentially growing: Just to get a figure, in the past two decades the number of papers concerning particle thermophoresis has increased from about 50 per year to more than 100 per *month*. Before we review the evidence obtained from these studies and the application stemming from them, let me first frame thermophoresis more precisely by providing some useful definitions.

When a colloidal suspension or a macromolecular solution is placed in a temperature gradient, the dispersed particles display, on top of Brownian motion, a steady drift velocity given by

$$\mathbf{v}_T = -D_T \nabla T,$$

where D_T, which is actually a mobility coefficient, is often (and rather improperly) dubbed "thermodiffusion coefficient". Besides the usual diffusion term, the mass flux $\mathbf{J}$ contains, therefore, an additional contribution due to thermophoresis[10]:

$$\mathbf{J} = -D \nabla c - c D_T \nabla T$$

In a closed system, this leads to the buildup of a concentration gradients eventually leading to a stationary concentration profile that, taking ∇T along the z-axis, is given by

$$\frac{\mathrm{d}c}{\mathrm{d}z} = c S_T \frac{\mathrm{d}T}{\mathrm{d}z}, \tag{15}$$

where

$$S_T = \frac{D_T}{D} \tag{16}$$

has exactly the same meaning as the Soret coefficient defined in Eq. (12), but can also be given a 'dynamic' meaning as the ratio between the thermophoretic mobility and the particle diffusion coefficient. We can indeed draw a close analogy between thermophoresis and sedimentation by introducing an intrinsic length scale (a 'thermophoretic length')

$$\ell_T = \frac{D}{v_T} = (S_T \nabla T)^{-1} \tag{17}$$

which plays the same role as the gravitational length in sedimentation. In fact, when the Soret coefficient depends very weakly on concentration *and* temperature, the steady-state profile is simply $c(z) = c(0) \exp(-z/\ell_T)$.

It is, however, worth recalling that, like for thermophoresis in gases, there is a crucial difference between the two situations. Whereas sedimentation is the response to gravity, the thermophoretic mobility D_T is not associated with a real external field, but rather than the nonequilibrium condition of thermal inhomogeneity. This subtle distinction makes grasping the origin of thermophoresis very hard. Nevertheless, recalling that the ℓ_g is the ratio between the thermal energy $k_B T$ and the magnitude of the external force (gravity), this analogy allows us to set out an interesting fact: if we assume that a thermal gradient acts as an effective "thermal force", the magnitude of that force has to be, for consistency, $F_T = k_B T / \ell_T$ or, vectorially,

$$\mathbf{F}_T = -k_B T S_T \nabla T. \tag{18}$$

---

[10]In the following expressions, the concentration c, taken equivalently as a mass or a volume fraction, is assumed to be small.

As we shall see, this expression is easily justified by a microscopic approach to thermophoresis.

3.3 Experimental Methods to Investigate Thermophoresis

Thermogravitational columns. The traditional experimental methods for studying the Soret effect in simple liquid mixtures were based on applying a thermal gradient to a suitable diffusion cell and devising ingenious ways to detect the concentration gradients induced by thermodiffusion. The simplest way to do it is placing the sample between two horizontal plates across which a constant temperature difference ΔT is maintained, and comparing the composition of the solution close to the two plates at steady state. However, the separation of the components is generally small and sampling is not trivial.

Much better results can be obtained by exploiting the concurrent action of thermal diffusion and natural convection in thermogravitational columns, where a horizontal temperature gradient is imposed between two vertical closely spaced plates. Components that, because of thermal diffusion, preferentially drift to the cold (hot) plate becomes enriched at the bottom (top) of the column. Thermogravitational columns, which lead to much larger (and stabler) component separation, have also been used to study thermophoresis in solutions of polymers with moderately large molecular weight (Ecenarro et al. 1994), but they are rather inefficient when dealing with colloidal suspensions of large particles, since the timescale needed to obtain a sufficient separation ratio may be extremely long. The recent design of micro-columns coupled with a optical detection methods may, however, lead to a revival of these techniques (Naumann et al. 2012).

Application of Beam Deflection to thermophoresis. Optical probing of a concentration gradient is a very convenient way to overcome some of the basic limitations of the traditional methods, since it allows one measuring concentration differences that are far smaller than those detectable by common analytic methods. Moreover no sampling is required, thermal gradients can be imposed on small spatial scales using lasers, and absolute values for S_T can often be obtained by direct comparison with optical effects on the pure solvent.

All the previous valuable features are fully exploited by the Beam Deflection method already described in Sect. 2.2, which my group extensively used to obtain results on a wide class of complex fluids ranging from surfactant and protein solutions to polyelectrolytes and colloids (Piazza 2008). In measurements of the Soret effect, the BD effect is obtained by placing the sample between two closely spaced plated metal plates across which a temperature difference is applied, usually by thermoelectric modules. After a fast initial deflection ϑ_{th}, due to the temperature dependence of the refractive index, the beam undergoes further bending due to the progressive buildup of the Soret-induced concentration gradient, leading to an additional steady-state deflection ϑ_s that can be easily singled out since it takes place on
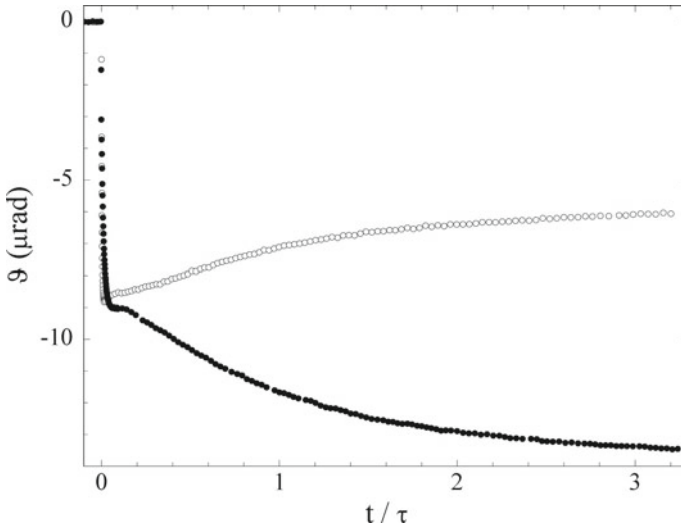
Fig. 6 Typical BD signals when dn/dc and dn/dT have the same (bullets) or the opposite sign (open dots, which is usually the case when $S_T < 0$), plotted as a function of the scaled time t/τ, where $\tau = h^2/(\pi^2 D)$ is the diffusion time over the interplate distance

the much longer time scale of particle diffusion. The Soret coefficient can then be simply evaluated from the ratio $\vartheta_s/\vartheta_{th}$ at steady-state as

$$S_T = -\frac{1}{c}\frac{\partial n/\partial T}{\partial n/\partial c}\frac{\vartheta_s}{\vartheta_{th}}, \tag{19}$$

where $\partial n/\partial T$ and $\partial n/\partial c$ are, respectively, the temperature and concentration dependence of the refractive index of the solution. In addition, the time dependence of the signal $\vartheta_s(t)$, which reaches its steady-state value exponentially with a time constant $\tau = h^2/(\pi^2 D)$, where h is the interplate spacing, allows one to evaluate the particle diffusion coefficient, and therefore the thermophoretic mobility $D_T = S_T D$ (see Fig. 6).

The main limitation of the BD method is that the interplate gap h can hardly be reduced below a minimal value of a few tenths of a millimeter, since the beam cannot be focused within the cell to an arbitrarily small spot size w_0 without consistently reducing the length over which the beam remains reasonably focused, given by the Rayleigh range $z_R = \pi w^2/\lambda$. Hence, the BD technique allows us to extend the size range that can be investigated up to 100–200 nm, but larger particles unavoidably requires the all-optical methods described in the next subsection.

All-optical methods: FRS. A very efficient reduction of the spatial region where particle diffusion is probed, and therefore of the measurement time, can be obtained by inducing localized thermal gradients via laser beams. This can be done either by exploiting a moderate optical absorption of the sample at the frequency of the

incoming beam, or by adding a small quantity of a suitable dye acting as an absorber. At variance with BD, these all-optical methods do not require an ingenious design allowing a uniform thermal gradient to be rapidly imposed and then kept constant for a long time, but on the other hand require careful consideration of spurious convection problems that can seriously limit their performance.

Let me first briefly discuss a rather elaborate all-optical schemes that bears many points in common with similar techniques, commonly dubbed Forced Rayleigh Scattering (FRS), used, for instance, for hydrodynamic flow visualization, particle velocimetry, or colloidal electrophoresis. Basically, they consist of reading, via a probing beam, the transient diffraction grating created in a sample by two mutually coherent excitation (pump) beams propagating through the sample with slightly different incident wave-vectors. If the pump wavelength is partially absorbed by the fluid or, as more commonly made, if a suitable absorbing dye is added to the sample, a diffraction grating due to the temperature dependence of the refractive index builds up on a time scale set by the thermal diffusivity. In the presence of thermal diffusion, the associated sinusoidal temperature field leads to the progressive buildup of a concentration gradient, which in turn modifies the grating diffraction efficiency and the refractive index profile, whose time dependence is read by monitoring the intensity of the Bragg-diffracted probing beam (Köhler and Schäfer 2000).

In FRS, the periodic structure of the temperature field unavoidably entails the occurrence of "inverted" temperature gradients, namely of colder fluid regions standing above warmer ones, which may easily induce natural convection unless the grating wavelength is very small. This can easily be obtained by increasing the crossing angle between the pump beams, which, however, generally leads to a substantial reduction of the diffraction efficiency. FRS is nevertheless a powerful technique, but requires a rather complicated and expensive optical setup. This is not the case for the simple method described in the next subsection, which allowed us to study thermophoresis in suspensions of large particles, and more recently to start investigating the effect of thermal forces on soft solids.

All-optical methods: Thermal Lensing. Thermal lensing (TL) is a self-effect on beam propagation that takes place when a laser beam heats up a partially absorbing medium, generating a locally inhomogeneous refractive index profile. Thermal expansion induces indeed a local density distribution in the sample that, in its turn, produces a refractive index profile acting as a negative lens that increases the divergence of the transmitted beam. Consider then a laser beam of optical power P, incident on a sample of thickness ℓ with absorption coefficient b, thermal conductivity κ, and thermal diffusivity χ. The heat equation yields, close to the optical axis, to a parabolic local refractive index profile, so that the sample acts as a simple diverging lens with inverse focal length

$$\frac{1}{f_{th}} = -\vartheta_{th} \frac{\lambda}{\pi w^2 (1 + \tau_{th}/2t)}, \tag{20}$$

where $\tau_{th} = w^2/4\chi$ is the heat diffusion time over the beam-spot size w, and ϑ_{th} is a dimensionless "thermal lens number".

$$\vartheta_{th} = -\frac{Pb\ell}{\kappa\lambda}\frac{\partial n}{\partial T}, \tag{21}$$

The TL effect can be accurately measured by focusing the incident beam on the sample with a lens and detecting the time-dependence of the light intensity $I(t)$ at the beam center (namely, on the optical axis) with a photodiode. The effect is actually maximal when the cell, assumed to be thin, is displaced from the lens focus (the position of the "beam waist") by $\sqrt{3}z_R$, where z_R is the Rayleigh range. For this position of the cell, $I(t)$ is given by

$$I(t) = \frac{I(0)}{1 + \vartheta_{th}f(t;\tau_{th})}, \tag{22}$$

where the function

$$f(t;\tau) = \frac{\pi}{6}\frac{1}{1+\tau/t}. \tag{23}$$

is evaluated for $\tau = \tau_{th} = w^2/4\chi$, which is the characteristic heat diffusion time over the beam spot size. The time-dependence of the TL signal yields, therefore, a simultaneous measurement of the sample thermal conductivity and diffusivity.

Thermal Lensing can be profitably exploited to investigate thermophoresis. Indeed, the particle thermophoretic drift along the laser-induced temperature profile leads to a progressive buildup of a concentration gradient within the heated region acting as an *additional* lens-like element. This "Soret lens" can be divergent or convergent depending on the preferential direction of motion of the component with the largest index of refraction and, as a result, the spreading of the transmitted beam further increases, or conversely lessens. For instance, in a suspension of particles with a refractive index larger than the solvent, thermophoresis leads to a larger or smaller beam spreading depending on whether S_T is positive or negative.

Equation (22) can be readily extended to the simultaneous presence of thermal and Soret lensing effects as

$$I(t) = \frac{I(0)}{1 + \vartheta_{th}f(t;\tau_{th}) + \vartheta_s f(t;\tau_S)}, \tag{24}$$

where $\tau_S = w^2/4D$ is the mass diffusion time, with diffusion coefficient D, over the beam spot size and we have defined the "Soret lens number"

$$\vartheta_s = -\frac{Pb\ell}{\kappa\lambda}\frac{\partial n}{\partial c}S_T c, \tag{25}$$

where we have again assumed $c \ll 1$. Similarly to what happens in Beam Deflection measurements, the "thermal" and "Soret" lensing effects usually take place on widely

separated time scales due to the different order of magnitudes of thermal diffusivity and mass diffusion. Besides, since

$$\frac{\vartheta_s}{\vartheta_{th}} = -S_T c \, \frac{\partial n/\partial c}{\partial n/\partial T}, \tag{26}$$

an independent determination of the temperature and concentration dependence of the refractive index permits a *differential* measurement of S_T that neither depends on the thermal conductivity and optical absorbance of the medium, nor on the values chosen for P and ℓ.

A seminal investigation of the Soret effect in an aniline/cyclohexane mixture close to the critical point (Giglio and Vendramini [1974]) showed that TL can be regarded as an all-optical technique combining accuracy in generating localized thermal gradients to experimental simplicity. At variance with this strongly absorbing mixture, however, water is highly transparent through the whole visible range. In aqueous solutions, substantial TL effects can nevertheless be obtained in a convenient near-IR spectral region by exploiting a specific vibrational overtone peaked around $\lambda \simeq 970$ nm, where water has an absorption coefficient $b \approx 0.55 \, \text{cm}^{-1}$. This strategy has been originally exploited by our group to successfully measure thermophoresis in several systems (Rusconi et al. [2004]). Recently (Lattuada et al. [2019]), we have also shown that TL can be profitably exploited to investigate thermophoresis in solutions of block copolymers that undergo temperature-induced self-association processes (see Fig. 7). A note of caution should nevertheless be raised for what concerns convective effects. Since a radially symmetric excitation beam generates horizontal temperature gradients, on the long time scales required for thermophoretic studies TL measurements may indeed be influenced by weak natural convection effects that unavoidably set in for *any* value of the incident power. Disturbance of the Soret-induced concentration profile can, however, be made negligible provided that, over the beam-spot length scale, convection is much slower than mass diffusion. A useful trick to ensure this is using a very thin cell and place the optical axis of the setup vertically (see Fig. 7). For a thorough discussion of this delicate issue, see Rusconi ([2007]).

3.4 Particle Thermophoresis in Liquids: The Roots

Which are the physical properties that set out the strength of thermophoretic effects? All experimental results obtained on aqueous colloidal suspensions and complex fluids witness an exquisite sensitivity of thermophoresis to the nature and strength of the interfacial particle/solvent interactions. The crucial role of solvation forces in setting the strength of thermophoresis was originally evidenced in a study of micellar solutions of sodium dodecyl sulfate (SDS), a simple charged (anionic) surfactant, where the Soret coefficient was found to decrease by more than one order of magni-
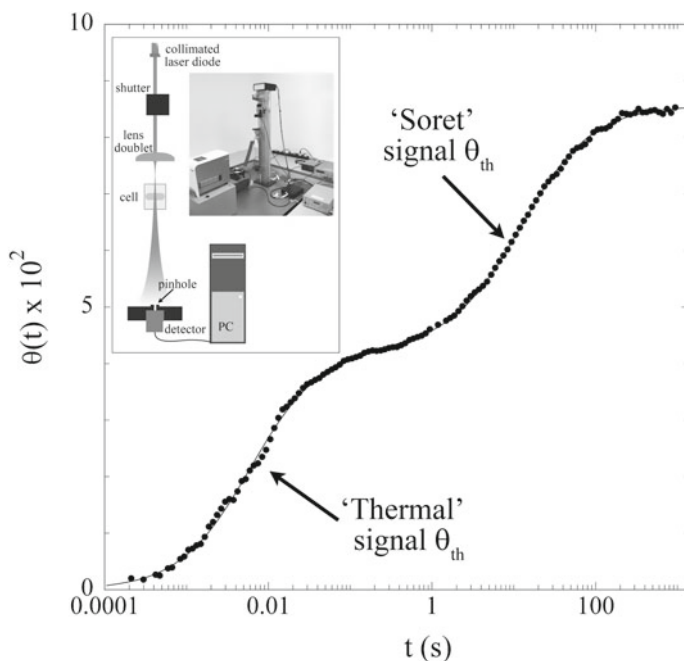
Fig. 7 Thermal Lens number $\vartheta(t) = \vartheta_{th}(t) + \vartheta_s(t)$ from a micellar solution of a poloxamer P407 block copolymer. The log time scale easily allows the "thermal" and "Soret" lens contributions to be set apart. The inset shows the basic optical scheme of a TL apparatus and a picture of the setup built in our lab, vertically mounted to reduce spurious convective effects

tude by increasing the concentration of added salt from 10 to 300 mM (Piazza and Guarino 2002).

The strict relation between thermophoresis and the nature of particle surface has been successively confirmed by many experiments. For instance, while in SDS solutions $S_T > 0$ (namely, SDS micelles are "thermophobic", in solutions of dodecy-maltoside (DM), a surfactant that differs form SDS only in the head group, which is neutral, $S_T < 0$ (i.e., DM micelles are "thermophilic"). Now, if one mixes the two surfactants in different molar ratios, S_T can be continuously varied between the limiting values for the pure compounds (Iacopini et al. 2006).

Similarly, the Soret coefficient of a large colloidal particle is mainly set by the nature of its interface with the solvent. For instance, by adsorbing different moieties (surfactants, polymers) on standard latex particles, the strength and even the *direction* of the thermophoretic motion can be controlled. Interactions with the solvent seem to be less relevant for polymers in organic liquids (as discussed below, D_T seems to depend mostly on the solvent viscosity), but become noticeable when the quality of the solvent changes from good to bad by changing, for instance, temperature.

In any case, particle bulk properties seem to be much less important, if an exception is made for thermal conductivity that of course fixes the temperature field around

the particle (metal particles, for instance, generally display negligible thermophoresis). Recalling that thermophoresis in liquids is strictly related to thermo-osmosis, this evidence fully agrees with Derjaguin's view of the latter and suggests that thermophoresis is basically an interfacial effect. In other words, as originally pointed out by Ruckenstein (1981), thermophoresis stems, therefore, from the inhomogeneity brought in by the thermal gradient in the thin layer that physically constitutes the interface between particle and solvent, whose thickness δ is of the order of the range of particle/solvent interactions (hence typically in the few nanometer range, except for charged particles at very low ionic strength) More specifically, interfacial tension gradients parallel to ∇T lead, very close to the particle surface, to an anisotropic pressure tensor whose net effect is generating in the inhomogeneous layer a slip velocity with respect to the surrounding fluid.

The strong analogy with thermo-osmosis also provides a hint about the dependence of thermophoretic effects on the particle size a, at least when $a \gg \delta$. If the interfacial layer is small compared to the particle size, one easily concludes that, to have a finite thermophoretic velocity (or, correspondingly, a finite thermo-osmotic flow), the thermophoretic mobility D_T should *not* depend on particle size (which is the case of polymers too). Therefore, since the Brownian diffusion coefficient $D \propto a^{-1}$ one expects $S_T \propto a$, as very often (but not always) found in experiments. For a discussion, see Braibanti et al. (2008).

At this point, you may easily see that these general features, which are actually shared by several other kinds of "phoretic" motion (Anderson 1989), strongly resemble those we have pointed out in Sect. 3.1 for particle thermophoresis in gases, provided that we consider δ as the analogous of the mean free path in a gas.

These considerations can be made more quantitative by a hydrodynamic model, whose basic strategy is trying and seek an effective thermal force F_T that leads to an *equilibrium* particle concentration profile that coincides with the *steady-state* profile condition induced by the thermal gradient. *If* F_T is found, then it is easy to show that the Soret coefficient is exactly related to F_T by the expression in Eq. (18) that we guessed from the analogy with sedimentation.

To find F_T is, however, the really hard task, which requires to solve the Navier–Stokes equations, with appropriate boundary conditions, coupled to the Fokker–Planck (or Langevin) equation for the Brownian particle motion. This is analytically feasible only in a limited number of special cases (for instance, charged spherical colloids in the Debye–Hückel approximation), but some general properties of the solution can nevertheless be pointed out. In particular, the Soret coefficient is in general proportional to the temperature derivative of the product between the interfacial tension tension γ between particle and solvent and the width δ of the thin interfacial layer, where due to the effect of the interactions with the particle surface, the solvent is characterized by an anisotropic pressure. A further interesting result is that, provided that both γ and δ depend on T only through the fluid density, S_T turns out to be proportional to the thermal expansivity of the solvent, a feature often suggested by the experimental results.

The hydrodynamic model yields, therefore, some important clues about thermophoresis. In fact, thanks to the huge value of the ratio of the particle size to the

molecular size, allowing for a continuum hydrodynamic description of the solvent, we arguably grasp particle thermophoresis better than the Soret effect in simple liquid mixtures, although several questions are still completely open. For instance, while the temperature dependence of D_T for polymers in non-polar solvents is rather weak, the thermophoretic mobility of many aqueous complex fluids behaves as $D_T(T) = A(T - T^*)$, where T^* is a system-dependent temperature at which the thermophoretic motion switches from thermophilic to thermophobic (Iacopini et al. 2006). So far, the origin of this rather universal behavior is totally unknown.

However, it would be very useful to go beyond a semi-phenomenological model based on hydrodynamics coupled to a stochastic equation for the particle motion, and develop a microscopic description based on correlation functions of well-defined microscopic quantities that may provide a unified view of thermal forces both in gases and in dense fluids. A very interesting attempt in this direction has recently been made by Anzini et al. (2019), who presented a microscopic description of thermo-osmosis based on linear response theory generalized to inhomogeneous and anisotropic environments yielding the thermo-osmotic slip in terms of static and dynamic equilibrium properties of a fluid near a surface. Notably, this approach leads in the appropriate limits to the expressions obtained from kinetic theory for gases and to Derjaguin result (Eq. 14) for liquids, showing however that these two regimes are indeed governed by different physical mechanisms.

3.5 Thermoelectricity in Liquids

Notwithstanding our partial understanding of the microscopic origin of thermal forces, new interesting effects of thermal gradients on complex fluids, which may lead to very interesting applications, have lately been evidenced. Besides, thermal forces are at the roots of several novel strategies useful in microfluidic applications (Geelhoed et al. 2006; Vigolo et al. 2010b) and for particle trapping and manipulation (Cuche et al. 2013; Cong et al. 2018), which are at the core of the new field of thermo-optofluidics (Chen et al. 2019). Finally, thermophoresis has allowed highly selective investigation of biomolecular interactions (Wienken et al. 2010; Seidel et al. 2006), or even to the manipulation of single biomolecules inside a cell. Reichl and Braun (2014), to be developed. In this introduction to thermal forces, there is little room to discuss in detail these exciting advancements, but I really prod my readers into taking a look at the original literature.

To conclude our short survey, I shall just mention one of these developments in which my group has specifically been involved. We began our discussion of thermal forces by mentioning the seminal studies of thermodiffusion in a salt solution by Ludwig and Soret, which originated a large amount of works on the same subject because of its interest in many electrochemical applications. When the investigation was extended to electrolyte mixtures, however, a strange behavior emerged: some electrolytes that, taken alone, concentrated (as usual) at the bottom of a thermogravitational column did exactly the opposite in the presence of additional ionic species.
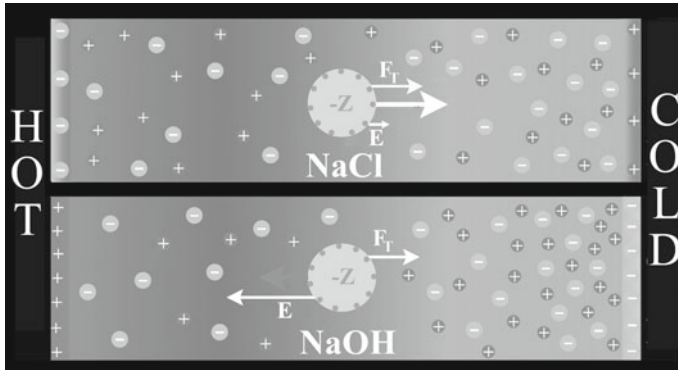
Fig. 8 A little cartoon picturing the investigation of Seebeck effect in liquids made in Vigolo et al. (2010a)

This anomaly was brilliantly explained by Guthrie et al. (1949) who showed that, in mixtures of ions that have a different thermophoretic mobility, a steady-state electric field may build up in a closed cell, which may "compete" with the thermal forces acting on a given ionic species and even drives it along the opposite direction.[11] Similarly to what happens with the Seebeck effect in solids, the sample behaves, therefore, as a thermocell.

A few years ago, Vigolo et al. (2010a) provided clear evidence for the presence of thermoelectric fields in liquids by detecting and quantifying their strong effects on colloid thermophoresis. Specifically, they showed that the presence of highly thermally responsive ions such as OH^- may easily lead to the reversal of particle motion. As a matter of fact, one can see the colloidal particle as a probe that "senses" and allows to measure the thermoelectric field (see Fig. 8). Besides, this methodology allows the particle charge to be obtained without applying any electric field. Thermoelectric measurements may, therefore, support standard electrophoretic techniques under conditions of high ionic strength, where the latter are known to perform rather poorly. Recently, the investigation of thermoelectric effects in liquids has gained interest because of the large Seebeck coefficient in ionic liquids, suggesting that these electrolytes could enable the development of thermoelectric devices to generate electrical energy from low-grade heat (Abraham et al. 2011).

One century and a half after the original observations by Ludwig, Soret, Tyndall, and Reynolds, there is still a lot to be discovered and investigated in thermal forces: the future, of course, is left to the ingenuity of my readers.

---

[11]It is useful to point out the solution remains of course neutral.

References

Abraham TJ, MacFarlane DR, Pringle JM (2011) Seebeck coefficients in ionic liquids-prospects for thermo-electrochemical cells. Chem Commun 47:6260

Anderson JL (1989) Colloid transport by interfacial forces. Ann Rev Fluid Mech 21:61–99

Anzini P, Colombo GM, Filiberti Z, Parola A (2019) Thermal Forces from a Microscopic Perspective. Phys Rev Lett 123:028002

Aubert M (1912) Thermo-osmose. J Phys Chim 26:145–208

Barragán VM, Kjelstrup S (2017) Thermo-osmosis in membrane systems: a review. J Non Equilib Thermodyn 42(3):217–236

Braibanti M, Vigolo D, Piazza R (2008) Does thermophoretic mobility depend on particle size? Phys Rev Lett 100:108303

Buscall R, White LR (1987) The consolidation of concentrated suspensions. Part 1.The theory of sedimentation. J Chem Soc Faraday Trans 83:873–891

Buzzaccaro S, Rusconi R, Piazza R (2007) "Sticky" hard spheres: equation of state, phase diagram, and metastable gels. Phys Rev Lett 99:098301

Buzzaccaro S, Secchi E, Brambilla G, Piazzaand R, Cipelletti L (2012) Equilibrium concentration profiles and sedimentation kinetics of colloidal gels under gravitational stress. J Phys Condens Matter 24:284103

Chen J, Loo JF-C, Wang D, Zhang Y, Kong S-K, Ho H-P (2019) Thermal optofluidics: principles and applications. Adv Optical Mater 1900829

Cong H, Chen J, Ho H-P (2018) Trapping, sorting and transferring of micro-particles and live cells using electric current-induced thermal tweezers. Sens Actuators B 264:224

Cuche A, Canaguier-Durand A, Devaux E, Hutchison JA, Genet C, Ebbesen TW (2013) Sorting nanoparticles with intertwined plasmonic and thermo-hydrodynamical forces. Nano Lett 13:4230–4235

de Kretser RG, Boger DV, Scales PJ (2003) Compressive rheology: an overview. Rheol Rev 125–165:2003

Debye P, Bueche AM (1948) In Robinson HA (ed) High polymer physics. Chemical

Degiorgio V, Piazza R, Bellini T (1994) Static and dynamic light scattering study of fluorinated polymer colloids with a crystalline internal structure. Adv Colloid Interface Sci 48:61–91

Derjaguin BV, Sidorenkov GP (1941) Thermoosmosis at ordinary temperatures and its analogy with the thermomechanical effect in helium II. Dokl Acad Nauk SSSR 32:622

Derjaguin BV, Churaev NV, Muller VM (1987) Surface forces. Consultants Bureau, New York

Ecenarro O, Madariaga JA, Navarro JL, Santamaria CM, Carrion JA, Saviron JM (1994) Thermogravitational thermal diffusion in liquid polymer solutions. Macromolecules 27:4968–4971

Epstein PS (1929) Zur theorie des radiometers. Z Physik 54(7–8):537–563

Feddersen W (1873) V. on thermodiffusion of gases. Lond Edinb Dublin Philos Mag J Sci 46(303):55–62

Geelhoed PF, Lindken RH, Westerweel J (2006) Thermophoretic separation in microfluidics. Chem Eng Res Des 84(5):370–373

Giglio M, Vendramini A (1974) Thermal lens effect in a binary liquid mixture: a new effect. Appl Phys Lett 25:555–557

Giglio M, Vendramini A (1977) Soret-type motion of macromolecules in solution. Phys Rev Lett 38:26

Guthrie G, Wilson JN, Schomaker V (1949) Theory of the thermal diffusion of electrolytes in a clusius column. J Chem Phys 17:310–313

Hachisu S, Takano K (1982) Pressure of disorder to order transition in monodisperse latex. Adv Colloid Interface Sci 16:233–252

Hind WC (1999) Aerosol technology: properties, behavior, and measurement of airborne particles, 2nd edn. Wiley-Blackwell, New York

Hoffman JD, Zimm BH (1955) Rate of thermal diffusion of polymer molecules in solution. J Polym Sci 15:405–411

Iacopini S, Rusconi R, Piazza R (2006) The "macromolecular tourist": universal temperature dependence of thermal diffusion in aqueous colloidal suspensions. Eur Phys J E 19:59–67

Julien PY (2010) Erosion and sedimentation. Cambridge University Press, Cambridge

Kennard EH (1938) Kinetic theory of gases. McGraw-Hill, New York

Kiørboe T (2008) A mechanistic approach to plankton ecology. Princeton University Press, Princeton

Köhler W, Schäfer R (2000) New developments in polymer analytics II. Springer, Heidelberg

Köhler W, Rosenauer C, Rossmanith P (1995) Holographic grating study of mass and thermal diffusion of polystyrene/toluene solutions. Int J Thermophys 16(1):11–21

Kuijk A, Byelov DV, Petukhov AV, van Blaaderen A, Imhof A (2012) Phase behavior of colloidal silica rods. Faraday Discuss 159:181–199

Lattuada E, Buzzaccaro S, Piazza R (2019) Thermophoresis in self-associating systems: probing poloxamer micellization by opto-thermal excitation. Soft Matter 15:2140–2151

Lebowitz J, Lewis MS, Schuck P (2002) Modern analytical ultracentrifugation in protein science: a tutorial review. Protein Sci 11:2067–2079

Lekkerkerker HNW, Tuinier R (2011) Colloids and the depletion interaction. Springer, Netherlands, Amsterdam

Liddell PV, Boger DV (1996) Yield stress measurements with the vane. J Non Newton Fluid Mech 63:235–261

Lodge OJ, Clark JW (1884) On the phenomena exhibited by dusty air in the neighborhood of strongly illuminated bodies. Proc Phys Soc Lond 6:1–29

Ludwig C (1856) Sitzber Kaiserl Akad Wiss Wien Math Natwiss Kl 20:539–540

Luigjes B, Thies-Weesie DME, Erné BH, Philipse AP (2012) Sedimentation equilibria of ferrofluids: II. experimental osmotic equations of state of magnetite colloids. J Phys Condens Matter 24:245104

Maestro A, Drenckhan W, Rio E, Höhler R (2013) Liquid dispersions under gravity: volume fraction profile and osmotic pressure. Soft Matter 9:2531–2540

Maxwell JC (1879) On stresses in rarified gases arising from inequalities of temperature. Phil Trans Roy Soc Lond 170:231–256

McNab GS, Meisen A (1972) Thermophoresis in liquids. J Coll Interface Sci 44:339–346

Miller MA, Frenkel D (2004) Phase diagram of the adhesive hard sphere fluid. J Chem Phys 121:535–545

Naumann P, Martin A, Kriegs H, Larranaga M, Bou-Ali M, Wiegand S (2012) Development of a thermogravitational microcolumn with an interferometric contactless detection system. J Phys Chem B 116(47):13889–13897

Pagliuca N, Bencivenga U, Mita DG, Perna G, Gaeta FS (1987) Isothermal and non-isothermal water transport in porous membranes. II. The steady state J Membr Sci 33(1):1–25

Palacci J, Cottin-Bizonne C, Ybert C, Bocquet L (2010) Sedimentation and effective temperature of active colloidal suspensions. Phys Rev Lett 105:088304

Perrin J (1909) Mouvement brownien et réalité moléculaire. Ann de Chim et de Phys 18:5–114

Phan S-E, Russel WB, Cheng Z, Zhu J, Chaikin PM, Dunsmuir JH, Ottewil RH (1996) Phase transition, equation of state, and limiting shear viscosities of hard sphere dispersions. Phys Rev E 54:6633

Piazza R (2008) Thermophoresis: moving particles with thermal gradients. Soft Matter 4:1740–1744

Piazza R (2014) Settled and unsettled issues in particle settling. Rep Progr Phys 77:056602

Piazza R, Guarino A (2002) Soret effect in interacting micellar solutions. Phys Rev Lett 88:208302

Piazza R, Bellini T, Degiorgio V (1993) Equilibrium sedimentation profiles of screened charged colloids: a test of the hard-sphere equation of state. Phys Rev Lett 71:4267–4270

Reichl MR, Braun D (2014) Thermophoretic manipulation of molecules inside living cells. J Am Chem Soc 136(45):15955–15960

Reynolds O (1879) On certain dimensional properties of matter in the gaseous state. Phil Trans Roy Soc Lond 170:727–845

Ruckenstein E (1981) Can phoretic motions be treated as interfacial tension gradient driven phenomena? J Colloid Interface Sci 83(1):77–81

Rusconi R (2007) Optical investigation of nonequilibrium effects in nanoparticle dispersions. PhD thesis, Politecnico di Milano

Rusconi R, Isa L, Piazza R (2004) Thermal-lensing measurement of particle thermophoresis in aqueous dispersions. J Opt Soc Am B 21(3):605–616

Rutgers MA, Dunsmuir JH, Xue JZ, Russel WB, Chaikin PM (1996) Measurement of the hard-sphere equation of state using screened charged polystyrene colloids. Phys Rev B 53:5043–5046

Secchi E, Buzzaccaro S, Piazza R (2014) Time-evolution scenarios for short-range depletion gels subjected to the gravitational stress. Soft Matter 10:5296–5310

Seidel SAI, Dijkman PM, Lea WA, van den Bogaart G, Jerabek-Willemsen M, Lazic A, Joseph JS, Srinivasan P, Baaske P, Simeonov A, Katritch I, Melo FA, Ladbury JE, Schreiber G, Watts A, Braun D, Duhr S (2006) Microscale thermophoresis quantifies biomolecular interactions under previously challenging conditions. Methods 59:301–315

Sone Y (1991) A simple demonstration of a rarefied gas flow induced over a plane wall with a temperature gradient. Phys Fluids A 3(5):997–998

Sone Y (2000) Flows induced by temperature fields in a rarefied gas and their ghost effect on the behavior of a gas in the continuum limit. Annu Rev Fluid Mech 32:779–811

Soret C (1879) Concentrations differentes d'une dissolution dont deux parties sont à des temperatures differentes. Arch Sci Phys Nat Genève 2:48–61

Soret C (1880) Influence de la température sur la distribution des sels dans leurs solutions. C R Acad Sci Paris 91:289–291

Strutt JW (1882) On the dark plane which is formed over a heated wire in dusty air. Proc Roy Soc Lond 34:414-418 "Rayleigh"

Tyndall J (1870) On Dust and Disease, Weekly evening meeting. Royal Institution of Great Britain, W. Clowes and Sons

Tyrrell JV (1961) Diffusion and heat flow in liquids. Buttherworths, London

Vigolo D, Buzzaccaro S, Piazza R (2010a) Thermophoresis and thermoelectricity in surfactant solutions. Langmuir 26:7792–7801

Vigolo D, Rusconi R, Stone HA, Piazza R (2010b) Thermophoresis: microfluidics characterization and separation. Soft Matter 6:3489–3493

Wienken CJ, Baaske P, Rothbauer U, Braun D, Stefan S (2010) Protein-binding assays in biological liquids using microscale thermophoresis. Nat Comm 1:100

Leung WWF (1998) Industrial centrifugation technology. McGraw-Hill Professional, New York

Zaccarelli E (2007) Colloidal gels. J Phys Condens Matter 19:323101

Zhang KJ, Briggs ME, Gammon RW, Sengers JV (1999) Optical measurement of the soret coefficient and the diffusion coefficient of liquid mixtures. J Chem Phys 104(17):6881–6892

Zheng F (2002) Thermophoresis of spherical and non-spherical particles: a review of theories and experiments. Adv Colloid Interface Sci 97:255–278

Transport Phenomena Across Interfaces of Complex Fluids: Drops and Sprays

Volfango Bertola and Günter Brenn

Abstract This chapter gives an overview of the interfacial dynamics of complex fluids, with focus on non-Newtonian drop impact phenomena and non-Newtonian sprays. After a general introduction about Newtonian drops and sprays, the impact dynamics of viscoelastic and viscoplastic drops on both homothermal and heated surfaces is discussed. Finally, capillary instabilities and the atomisation process of non-Newtonian fluids are described.

1 Introduction

Since the pioneering works of Plateau (1867), Worthington (1876) and Rayleigh (1879), drop impact phenomena and liquid atomisation processes have been the subject of extensive investigations, which had a huge impact on several industrial and everyday applications, from spray cleaning or painting to internal combustion engines, and so on.

The morphology of drop impact on solid surfaces is well known (Rein 1993; Yarin 2006; Josserand and Thoroddsen 2016). Upon impact, the liquid spreads on the surface taking the form of a disc; for low impact velocity, the disc thickness is approximately uniform, while for higher impact velocities, the disc is composed of a thin central part, the so-called *lamella*, surrounded by a toroidal rim. This initial spreading stage is typically very fast and has a duration of about 5 ms. After the drop has reached maximum spreading, two qualitatively different outcomes are possible. If the initial kinetic energy exceeds a threshold value, capillary forces are insufficient to maintain the integrity of the drop, which disintegrates into smaller satellite droplets jetting out of its outermost perimeter; this phenomenon is usually referred to as

V. Bertola (✉)
School of Engineering, University of Liverpool, Liverpool, UK
e-mail: Volfango.Bertola@liverpool.ac.uk

G. Brenn
Institut für Strömungslehre und Wärmeübertragung, Technische Universität Graz,
Graz, Austria

splashing, or less frequently as *drop breakup*. If splashing does not occur, the drop is allowed to retract under the action of capillary forces, which tend to minimise the contact with the surface; in some cases, retraction is so fast that the liquid rises in the middle forming a Worthington jet, which may subsequently result in the complete rebound of the drop.

Impacts onto smooth and chemically homogeneous surfaces, for low or moderate impact kinetic energy, are controlled by three key factors: inertia, viscous dissipation and interfacial energy. During the initial stages of impact with the surface, the vertical inertia of the falling drop is converted into the horizontal motion of the fluid, and as the drop spreads, kinetic energy is partially stored as surface energy. This process is characterised by the Weber number, $We = \rho U^2 D_0/\sigma$, where ρ and σ are the fluid density and surface tension, respectively, D_0 is the equilibrium drop diameter and U is the normal impact velocity. As the fluid spreads across the surface, the kinetic energy of the fluid is partly dissipated by viscous forces in the fluid, which is described using the Reynolds number, $Re = \rho U D_0/\mu$, where μ is the fluid viscosity; this is sometimes used in combination with the Weber number to yield the Ohnesorge number, $Oh = \sqrt{We}/Re$. Finally, the retraction stage is governed by the balance between interfacial energy and viscous dissipation, expressed by the Capillary number, $Ca = \mu U_r/\sigma$, where U_r is the retraction velocity.

Thus, the spreading behaviour of impacting drops is mainly characterised by the Weber and by the Ohnesorge numbers, which portray the driving and the resisting/dissipative forces of the process, respectively. The corresponding asymptotic spreading behaviours are (Schiaffino and Sonin 1997) as follows:

- High We, low Oh (inviscid, impact-driven). The spreading is primarily driven by dynamic pressure. The characteristic time scale of the inertial spreading is very short. Viscous effects are negligible during the initial stage of spreading, however damp the subsequent drop oscillations.
- Low We, low Oh (inviscid, capillarity-driven). The spreading is mainly driven by the capillary forces at the contact line and the impact velocity effects are negligible. Spreading is followed by interfacial oscillations with the timescale of the same order as the spreading.
- Low We, high Oh (highly viscous, capillarity-driven). The spreading is driven by capillary forces and resisted by viscous forces. Impact velocity has negligible effects. The inertial oscillations are overdamped by high viscosity.
- High We, high Oh (highly viscous, impact-driven). The spreading is driven by inertial forces and resisted by viscous forces. Capillarity has negligible effects. Drop oscillations are absent.

There are a number of empirical, semi-empirical and theoretical models to predict the maximum diameter of the drop, D_m, at the end of the inertial spreading stage. These models are based either on scaling considerations (Clanet et al. 2004) or, more frequently, on the energy balance, which can be written as follows:

$$\frac{d}{dt}(E_k + E_g + E_s) + \dot{W} = 0 \tag{1}$$

where E_k denotes the kinetic energy of the drop, E_g is the gravity potential energy, E_s is the surface energy, $\dot{W}$ is the rate of total energy loss during drop impact, including viscous dissipation and the energy transmitted to the substrate due to deformation. However, the energy absorbed by the substrate is often neglected and only the viscous dissipation is considered for the energy loss rate. The viscous dissipation is the most difficult quantity to estimate precisely due to the limited information about the flow field inside the drop. Another difficult quantity to estimate is surface energy, because the precise calculation of the surface energy at the end of spreading strongly depends on the shape of the liquid free surface. In particular, if the drop shape at maximum spreading is approximated as a disc (Ford and Furmidge 1967) its surface energy can be written as follows:

$$E_s = \frac{\pi}{4} D_m^2 \sigma (1 - cos\theta_a) = 0 \qquad (2)$$

where θ_a is the advancing contact angle; if the drop shape is approximated as a spherical cap (Bechtel et al. 1981), the surface energy is

$$E_s = \frac{\pi}{3} D_0^2 \sigma [\xi_m^{-1} + 2\xi_m^2 - (\xi_m^{-1} - \xi_m^2)cos\theta_s] = 0 \qquad (3)$$

where θ_s is the static contact angle and $\xi_m = h_{\min}/D_0$ is the minimum height factor.

Models based on the energy conservation approach were proposed, among others, by Bechtel et al. (1981), Chandra and Avedisian (1991), Pasandideh-Fard et al. (1996), Mao et al. (1997), Attané et al. (2007). However, although these models give reasonably accurate predictions in case of low-viscosity fluids, they almost systematically fail when the importance of the viscous dissipation term is increased (German and Bertola 2009b).

More recently, the analytical self-similar solution which satisfies the full Navier–Stokes equations was obtained for the viscous flow in the spreading drop (Roisman et al. 2009; Roisman 2009). The boundary layer thickness was used for the estimation of the residual film thickness formed by normal drop impact and the maximum spreading diameter. A very similar approach was later used by Eggers et al. (2010) to obtain equivalent results.

Drop splashing occurs as the inertial forces overcome those due to capillarity, expressed by the Laplace pressure:

$$\rho U_0^2 > \frac{\sigma h_L}{D_0^2} \qquad (4)$$

where h_L is the thickness of the lamella. When Eq. (4) is re-formulated in terms of dimensionless numbers, the splashing criterion can be written as $\alpha Oh^\beta We^\gamma > K$ (Stow and Hadfield 1981; Mundo et al. 1995), where α, β, γ and K are constants. A comprehensive review of existing splashing correlations is reported by Moreira et al. (2010), while basic hydrodynamic modelling is discussed by Yarin (2006).

When the target surface is heated, the drop impact phenomenology is characterised by a close interplay of hydrodynamics with different heat transfer modes, under large spatial and temporal gradients of the state variables (Rein 2003). Early studies of these phenomena focused on the heat transfer characteristics (Wachters and Westerling 1966; Gottfried et al. 1966), and less attention was paid to drop impact morphology due to the limitations of stroboscopic imaging (Pedersen 1970). Later on, the development of high-speed imaging allowed researchers to visualise and analyse more quantitatively the various impact regimes, and to get a deeper insight into the physical mechanisms behind different impact outcomes (Fujimoto et al. 2010).

After impact, the drop spreads on the heated surface in a short lapse of time (typically a few milliseconds in case of drops of millimetric size), increasing the area exposed to heat transfer. This induces a heat transfer regime that can be related to the well-known boiling curve, in particular, one can observe: (i) convection heat transfer for surface temperatures below the boiling point of the liquid; (ii) nucleate boiling for surface temperatures just above the boiling point; (iii) film boiling, observed above the critical heat flux (CHF), where the drop is separated from the surface by a vapour layer and (iv) transitional boiling, where the said vapour layer is unstable and the liquid may locally get into contact with the surface. However, the association between heat transfer and impact regimes is not always clear (Wang et al. (2000)).

The classification of impact regimes, reviewed by Moreira et al. (2010), is still somewhat controversial. To rationalise the rich variety of impact morphologies observed for Newtonian drops impinging on heated surfaces, it was proposed to identify *simple* impact regimes, displaying one distinctive feature (deposition, rebound, splashing/breakup) and *mixed* regimes, resulting from the combination of simple regimes with secondary atomisation (Bertola 2015), as shown in Fig. 1. Such unifying classification, on one hand, embraces the different impact morphologies reported in the existing literature, and on the other hand is simple enough to be used for practical purposes; in addition, it allows one to derive simple models for transition boundaries between different impact regimes.

The breakup of a liquid jet into smaller droplet is another process of fundamental importance, because it maximises the free surface of a given volume of liquid, increasing significantly mass, momentum and heat transfer rates, as well as chemical reaction rates, between the fluid and a surrounding medium. Observing the decay of fluid jets travelling through a medium of the same density, Plateau (1867) recognised that perturbations would become unstable if their wavelength λ was greater than a critical value $\lambda_{cr}/R_0 = 2\pi$, where R_0 is the capillary tube radius; however, the wavelength corresponding to the fastest breakup was $\lambda_{cr}/R_0 = 8.76$, significantly higher than the critical value. Upon introducing his method of linear stability, Rayleigh (1879) recognised that the dynamics of the jet had to be taken into account; in particular, he determined that for all unstable wavelengths with $\lambda > \lambda_{cr}$, the one with the fastest growth rate is selected. For inviscid jets, the analysis yields $\lambda_{opt}/R_0 = 9.01$, in close agreement with Plateau.
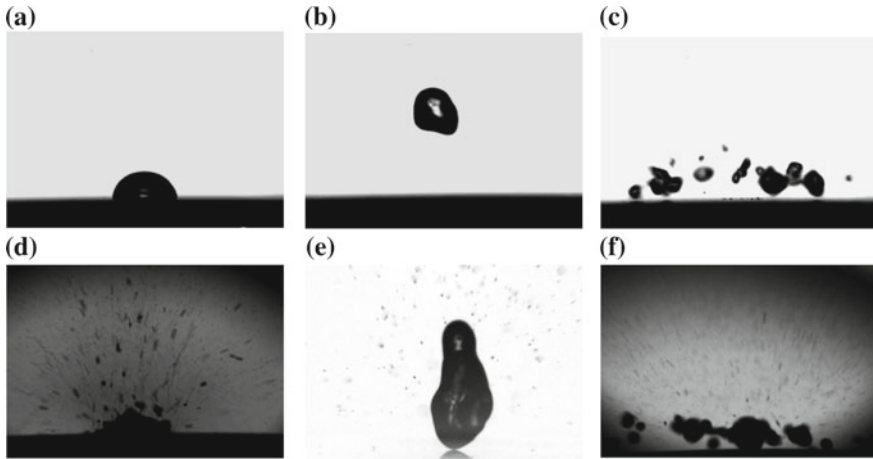
Fig. 1 Newtonian drop impact regimes on heated surfaces: **a–c** simple regimes (deposition, rebound, breakup); **d–f** mixed regimes (secondary atomisation, rebound with secondary atomisation, breakup with secondary atomisation)

According to Rayleigh's approach, an initial disturbance in a jet, α, will exhibit an exponential growth with amplitude of the form $\alpha(t) = \alpha_0 e^{-i\omega t}$, where the inviscid dispersion relation is given by

$$\omega^2 = -\frac{\sigma}{\rho R_0^3}[1 - (kR_0)^2]kR_0 \frac{I_1(kR_0)}{I_0(kR_0)} \tag{5}$$

and $\omega(k)$ is the growth rate. In Eq. 5, σ is the surface tension, k is the longitudinal wave number, ρ is the fluid density and $I_n(kR_0)$ is a modified Bessel function of the first kind. The largest growth rate occurs at $kR_0 = 0.697$, which corresponds to $\lambda_{opt} = 9.01R_0$ ($k = 2\pi/\lambda$); this however does not account for viscous effects.

The effects of viscosity on capillary breakup were first investigated by Plateau (1867) and Weber (1931). Plateau found that as viscous forces become increasingly dominant with respect to inertial forces, the most unstable wavelength increases, corresponding to the greatest reduction in surface area. The growth rate is eventually determined by a balance between surface tension and viscous forces, most simply characterised by the Reynolds number. Chandrasekhar (1961) analysed the problem using the full Navier–Stokes equations, and found an implicit equation that in the limit of both small kR_0 and Re can be written as follows:

$$\omega = \omega_0([\frac{1}{2}x^2(1 - x^2) + \frac{9}{4}Re^{-2}x^4]^{\frac{1}{2}} - \frac{3}{2}Re^{-1}x^2) \tag{6}$$

where $x = kR_0$. The viscous dispersion relation for the fastest growing mode is given by

$$\omega = \frac{1}{6}\omega_\nu(1 - kR_0) \tag{7}$$

where $\omega_\nu = \sigma/R_0\rho\nu$ is the viscous growth rate and ν is the kinematic viscosity.

Close to drop pinch-off, the classical linear stability breaks down and the fluid behaviour enters a regime of self-similar flow, wherein flow lacks a typical scale and the balance of inertial, surface tension and viscous forces become independent of the minimum thickness of the neck filament attaching the falling drop to the capillary (Eggers 1997). In other words, the flow dynamics of viscous fluids in this regime can be characterised by universal scaling functions. In the last stages of detachment, viscous fluid drops can exhibit long and thin threads. After the breakdown of the linear instability, the fluid enters a regime of viscous dominated self-similar Stokes flow (Papageorgiou 1995). Temporal variations in minimum axisymmetric drop neck thickness vary as

$$D_N = \chi\frac{\sigma}{\nu\rho}(t_0 - t) \tag{8}$$

where $\chi = 0.0709$ is the universal scaling parameter determined from $\chi = 1/12(1 + \delta)$ and $\delta = 0.175$ is a positive constant to control the extent of the similarity region.

In practice, the breakup of a liquid jet generated by a plain orifice nozzle is also a function of the fluid velocity at the nozzle outlet, as shown in Fig. 2, which displays the different atomisation regimes along with the *jet stability curve*, which represents the distance from the orifice where jet breakup first occurs (Lin and Reitz 1998; Lefebvre 1988). At very low speed, the jet is essentially affected by gravity, which results in a dripping regime. As the jet speed increases, capillary forces dominate the atomisation process in a regime typically referred to as the Rayleigh breakup regime. For both dripping and Rayleigh regimes, droplet pinching occurs reasonably axisymmetrically at the centreline of the jet, producing drops that are comparable in size to the orifice diameter. At higher velocities, aerodynamic interactions with the ambient gas lead to additional instability of the surface in what is known as *wind-induced* regime. The jet breakup occurs also on the jet surface and periphery and forms drop substantially smaller than the diameter of the orifice. At higher velocities, one finds the atomisation regime, characterised by the appearance of a spray, i.e. a collection of very small drops around a liquid core that vanishes at some distance downstream of the orifice.

Whilst there is a significant volume of literature about single drop impacts and atomisation of simple (Newtonian) fluids, the number of works about fluids with complex microstructure (polymer melts or solutions, gels, pastes, foams, emulsions, etc.) is comparatively very small. However, these fluids are frequently used in common applications, such as painting, food processing and many others. Moreover, with a better understanding of the microscopic structure of complex liquids, working fluids can be tailored specifically to optimise existing industrial processes, by altering their formulation (e.g. by means of chemical additives) in such a way as to change
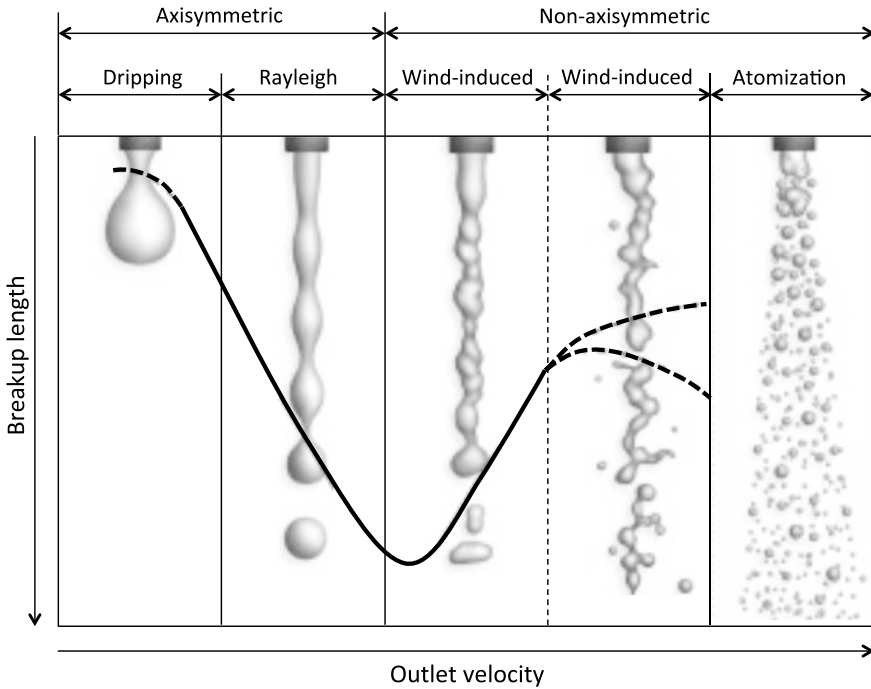
Fig. 2 Atomisation regimes arising from a plain orifice nozzle. Adapted from Bonhoeffer et al. (2017)

one or more physical properties. In the following, the main results about drop impact and atomisation of non-Newtonian fluids are reviewed.

2 Impact of Viscoelastic Drops on Solid Surfaces

2.1 Impact on Homothermal Surfaces

The impact dynamics of viscoelastic drops on solid surfaces did not receive significant attention until about 20 years ago, when high molecular weight flexible polymers were introduced to improve agrochemical formulations (Bergeron et al. 1998, 2003). It was found that very small amounts (of the order of 100 ppm) of high molecular weight flexible polymers, such as polyethylene oxide (PEO), can reduce the tendency of drops to rebound after impacting on low surface energy (hydrophobic) surfaces, which can be exploited to control many spray applications and, in particular, the distribution of agrochemicals (Williams et al. 2008).
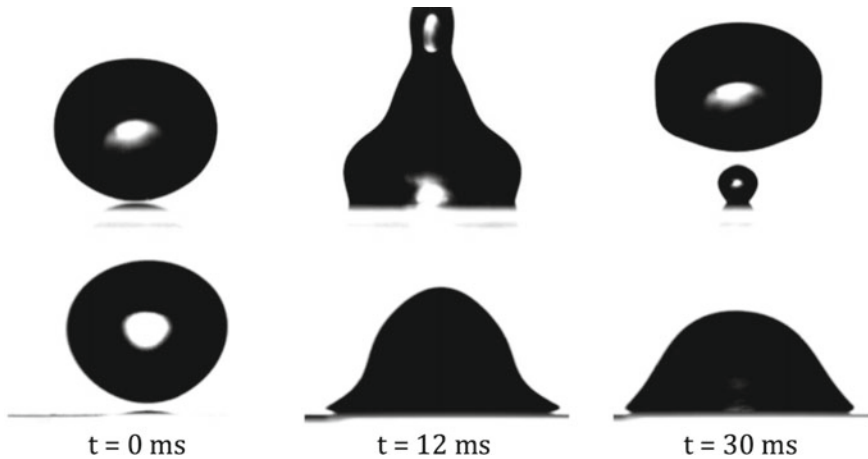
Fig. 3 Impact of water (top) and 200 ppm polymer solution (bottom) drops ($D_0 \approx 3$ mm) impacting on a PTFE surface (release height: 20 mm)

This phenomenon is illustrated in Fig. 3, which compares the impact morphologies of two drops, one of de-ionised water and one of a 200 ppm PEO solution in the same water, impacting with the same velocity on a PTFE surface (equilibrium contact angle with water: $\approx 110°$). After the initial inertial spreading, which is similar for both drops, water drops exhibit fast recoil (≈ 30 ms) under the action of surface forces, which evolves into almost complete dewetting, and rebounds on the impact surface. On the contrary, the recoil of polymer solution drops is very slow and terminates in a sessile equilibrium state only after several seconds. This is somewhat counterintuitive because the shear viscosity and surface tension of such drops are almost identical to those of pure water (Crooks et al. 2001).

Indeed, it took several years to develop a correct understanding of this phenomenon. Initially, the effect of polymer additives on drop rebound was interpreted in terms of the bulk rheology of the fluid, namely, the fluid elongational viscosity, which was thought to provide a large resistance to drop retraction after impact, thereby suppressing droplet rebound (Bergeron et al. 2000; Crooks et al. 2001). However, this interpretation has an obvious weakness, because the large velocity gradients to achieve significant magnitudes of elongational viscosity are observed during the inertial expansion, which has a timescale of ≈ 5 ms, while their effect on drop retraction spans over several seconds. In addition, if energy dissipation occurs during inertial spreading, both the spreading velocity and the maximum spreading diameter of polymer solution drops should be smaller than those of water drops, whereas experimental data suggest there is little or no difference. Later on, it was demonstrated that some of the elongational viscosity data used to support this interpretation of the phenomenon exhibit very poor reproducibility as the same researchers attempted to repeat measurements on the same polymer solutions (Bertola 2013), as shown in Fig. 4.
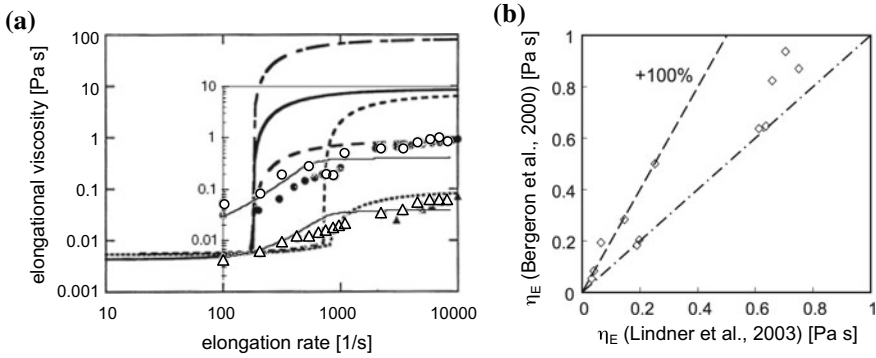
Fig. 4 Elongational viscosity versus elongation rate measurements made with a Rheometrics RFX opposing nozzle for two dilute PEO polymer solutions: 0.25 g/l, molecular weight 4×10^6 (circles); 1.0 g/l, molecular weight 2×10^6 (triangles). **a** Comparison between data by Bergeron et al. (2000), open symbols, and Lindner et al. (2003), filled symbols. **b** A direct comparison in linear scale shows data by Bergeron et al. (2000) are sometimes identical, sometimes up to twice as large as those by Lindner et al. (2003)

More recently, it was suggested that the contact line dynamics is ruled by the competition between the surface tension that drives the retraction and the elastic normal stresses that counter it (Bartolo et al. 2007). In particular, using a generalised lubrication equation accounting for capillarity and normal stresses in addition to shear stresses, it was found that the retraction velocity, v_r, is related to the first normal stress coefficient, Ψ, as $v_r \sim 1/\Psi^{-1/2}$. The main argument against this approach is that dilute polymer solutions do not exhibit appreciable normal stresses in the range of shear rates observed in impacting drops during the retraction stage (Lindner et al. 2003; Bartolo et al. 2007), and therefore the proposed theory cannot explain the slowing down of recoil observed in dilute polymer solution drops. Unfortunately, the theory was naïvely (or perhaps cleverly) validated with experimental data relative to solutions with a content of polymer well above the overlap concentration, i.e. in the semi-dilute regime, and still receives much credit to date, see e.g. Chen et al. (2018) or Wang et al. (2017). Other flaws and mistakes of this work are discussed in detail by Bertola (2013).

Several independent experiments provide evidence that the slowing down of drop retraction is not related to the bulk rheological behaviour of the fluid. A study of drops impacting on small targets, which remove the influence of the substrate, demonstrated that polymer additives do not change the retraction velocity in comparison with water drops (Rozhkov et al. 2003). This suggests that the polymeric additives do not have any effect on the bulk elongational deformations of the drop but instead they influence the interaction of the lamella with the substrate at the retraction stage when the impact happens on a plane, smooth and solid substrate.

Another way to completely remove the influence of the substrate is heating the impact surface to create a thin vapour film between the drop and the substrate, which is known as *dynamic Leidenfrost phenomenon* (Rein 2003; Quéré 2013). Experiments

on Leidenfrost drops of dilute polymer solutions showed that polymer additives cause only a slight reduction of the maximum spreading diameter and of the retraction velocity with respect to water drops (Bertola 2009b, 2014; Black and Bertola 2013), which is by no means comparable with the large reduction of the retraction velocity observed during the impact on solid surfaces. Because in these experiments wetting effects are absent or negligible, one must conclude that the retraction velocity reduction observed in drops containing flexible polymers impacting on solid surfaces is due to the drop–surface interaction rather than to an increased energy dissipation connected to the elongational viscosity of the fluid. In addition, the maximum bouncing height of viscoelastic drops can be significantly higher than that of Newtonian drops; since this quantity represents the fraction of the initial kinetic energy which is not dissipated during impact, these experiments suggest that in some cases polymer additives indeed reduce instead of increasing the overall energy dissipation. A more detailed analysis of viscoelastic Leidenfrost drops is discussed in Sect. 2.2.

These results indicate that the impact dynamics of viscoelastic drops impacting on solid surfaces is mainly driven by wetting rather than by the bulk rheology of the fluid such as the elongational viscosity or the normal stress coefficient. A deeper understanding of the underlying physical mechanism can be obtained through the analysis of four apparently independent aspects (Smith and Bertola 2010b): (i) the velocity field inside the impacting drop; (ii) the apparent dynamic contact angle; (iii) the microscopic contact line morphology and (iv) the polymer conformation near the receding contact line.

Fluid velocity inside impacting droplets The simplest way to quantify the effects of bulk viscous dissipation on fluid flows is to measure velocities and velocity gradients; in the case of impacting droplets, these measurements are not simple because of the small length- and timescales of the process. Recent particle velocimetry measurements inside impacting drops showed that the local velocities measured during expansion and retraction are similar for the drops of polymer solution and for those of pure water (Smith and Bertola 2010a, 2011). Drops were seeded with fluorescent colloids (2 µm diameter), with a concentration of approximately 0.001 wt.%. Movies for particle velocimetry were collected at 2000 fps and, using stroboscopic illumination at a frequency of 8 kHz, each particle was captured four times along its radial trajectory in a single frame. The particles trajectories were then extrapolated to estimate the position of the drop centre and correspondingly the radial distance of each particle, within a negligible error. The velocity at each radial position (i.e. the Eulerian velocity field) was calculated as the distance between two images of the same particle divided by the time interval between two pulses of the stroboscopic illumination.

Figure 5 compares the local, instantaneous velocities measured in a water drop and in a 200 ppm polyethylene oxide solution drop, showing that the velocity fields in the two drops are similar both qualitatively and quantitatively during the inertial expansion as well as during the drop retraction. The velocity gradient in the fluid, obtained from the slope of radial velocity profiles, gives an indication of the rate of deformation of fluid elements within the drop, hence the effects of the elongational
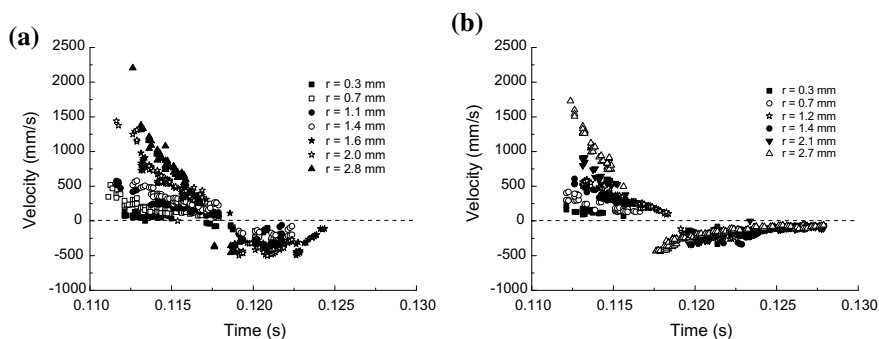
Fig. 5 Fluid velocity measured inside impacting drops at different radial positions during inertial spreading and retraction; **a** water; **b** 200 ppm polyethylene oxide (molecular weight: 4,000 kDa) solution. The impact velocity is about 1.4 m/s, and the plane of focus is set at a distance of about 10 μm above the impact surface

viscosity. Figure 6a shows that the velocity gradients measured in the water and polymer solution drops during the inertial spreading are almost identical; although the magnitude of these velocity gradients is of the order of 10^2 s^{-1}, it is not sufficient to induce polymer molecules' stretching, which require velocity gradients of the order of 10^2 s^{-1} and above (Crooks et al. 2001). During retraction, radial velocity gradients are significantly smaller than those observed during inertial spreading, and fluid elements are in compression rather than extension, which makes the stretching of molecules inside the drop very unlikely (de Gennes 1974).

Whilst velocities and velocity gradients measured inside the droplet are almost identical for water and dilute polymer solutions, a comparison of the fluid velocity in the bulk of the droplet during retraction with the velocity extracted from macroscopic observations of the contact line (i.e. the rate of change of the drop base diameter) shows a dramatic difference between water and PEO drops. Figure 6b shows that the velocity of the contact line for droplets of pure water at the onset of retraction is similar to that of the bulk fluid. By contrast, the motion of the contact line for PEO drops is one order of magnitude slower than that of the corresponding bulk velocity measurements, and further confirms that the difference between the behaviours of the two fluids occurs only at the droplet edge.

Dynamic contact angle The apparent contact angle is perhaps the most significant quantity used to characterise the wetting behaviour of liquids on solid surfaces and the dynamics of drop recoil following inertial spreading. Surprisingly, all of the early attempts to explain the phenomenology of dilute polymer solution drop impact completely ignore dynamic contact angle measurements (Bergeron et al. 2000; Crooks et al. 2001; Bartolo et al. 2007).

A qualitative picture of the contact angle dynamics of water drops and polymer solution drops impacting on the same surface with the same impact Weber number can be obtained from the side views displayed in Fig. 3, which suggest that the polymer additive significantly reduces the dynamic contact angle with respect to pure water;
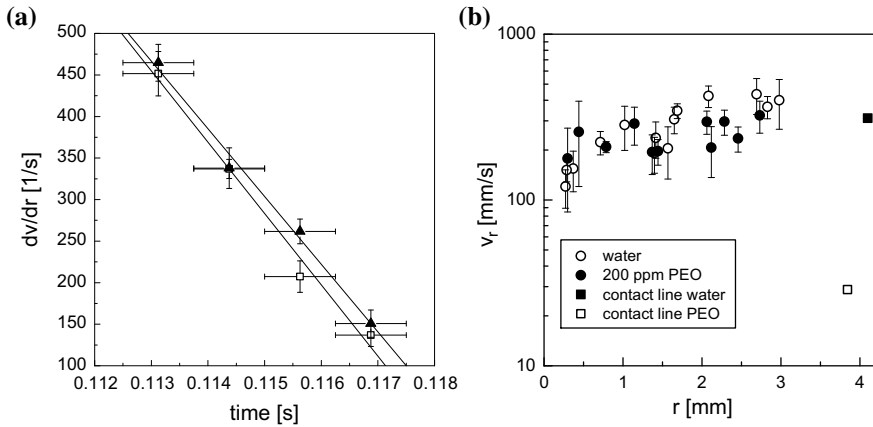
Fig. 6 Velocity gradients measured inside impacting drops during inertial spreading (**a**); comparison between the fluid velocities measured at the largest radial position ($r/R_0 \approx 3.5$) and the contact line velocities of a water drop and a 200 ppm polyethylene oxide (molecular weight: 4,000 kDa) solution drop (**b**). Adapted from Smith and Bertola (2011)

however, the change is localised in the wedge near the contact line, as if the contact line was pinned on the surface, while the bulk fluid seems to flow back towards the drop centre without encountering the same resistance.

Systematic comparative measurements of the apparent dynamic contact angle during drop impact (Bertola 2010; Bertola and Wang 2015) demonstrated that while no differences can be observed between water drops and polymer solution drops during inertial spreading, there are significant differences during the retraction stage. The typical behaviours of the base diameter and of the dynamic contact angle obtained from digital image processing (Biolè and Bertola 2015a, b; Biolè et al. 2016) are displayed in Fig. 7, for two drops impacting on a PTFE surface at low Weber number ($We \approx 15$). The base diameter of water drops (Fig. 7a) grows and decreases approximately at the same rate, and becomes equal to zero at the moment of drop rebound, about 50 ms after impact. After rebound, it reaches the final equilibrium value after a few oscillations, typically in a very short time (20–30 ms). With the exception of a discontinuity in correspondence of the drop rebound, the apparent contact angle has an oscillatory behaviour around the equilibrium value and its magnitude remains bounded between the values of the advancing and receding contact angles.

In polymer solution drops, both the base diameter and the dynamic contact angle are significantly different, as shown in Fig. 7b. The base diameter initially grows at the same rate as in water drops and reaches a maximum approximately of the same magnitude; however, the retraction phase is much slower, and the base diameter takes several seconds to reach the equilibrium value. The retraction phase is characterised by stick-slip dynamics of the drop edge, which corresponds to rapid fluctuations of the base diameter in phase with the dynamic contact angle minima. Unlike in the case of water drops, the dynamic contact angle initially decreases significantly as the drop
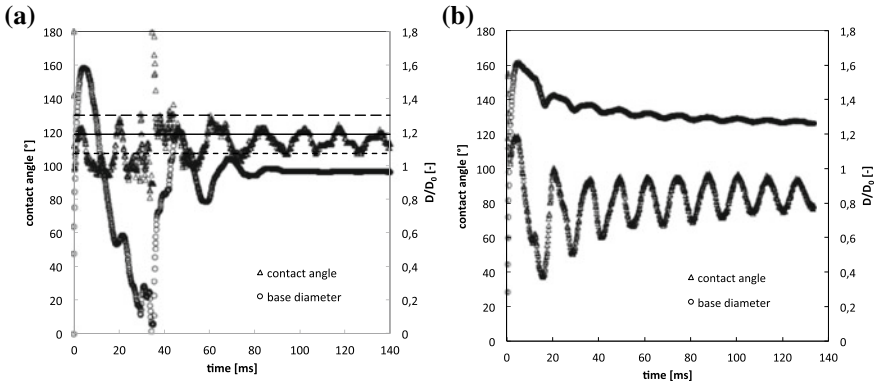
Fig. 7 Base diameter and dynamic contact angle of **a** a water drop and **b** a 200 ppm polyethylene oxide solution drop, impacting on a PTFE surface with $We \approx 15$. The horizontal solid line corresponds to the equilibrium contact angle ($\theta_e = 119°$), while the long- and short-dashed lines correspond to the advancing ($\theta_a = 130°$) and receding ($\theta_r = 107°$) contact angles, respectively
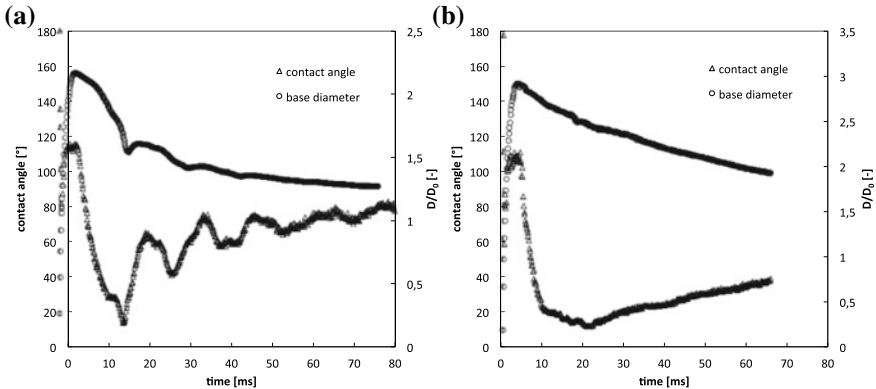
Fig. 8 Base diameter and dynamic contact angle of a 200 ppm polyethylene oxide solution drop impacting on a PTFE surface with **a** $We \approx 55$ and **b** $We \approx 110$

retracts, and then slowly returns to the equilibrium value in an oscillatory fashion. The local minima of these oscillations correspond to the stick-slip fluctuations of the base diameter. During the approach to the equilibrium value, the dynamic contact angle of dilute polymer solution drops remains smaller than the contact angle measured with water drops under the same experimental conditions.

For increasing impact Weber numbers (Fig. 8), the contact line stick-slip is limited to the first contact angle oscillation, and the recoil velocity becomes increasingly smaller. The initial decrease of the dynamic contact angle can attain very small values ($\lesssim 20°$), while the contact angle oscillations gradually die out as the impact Weber number increases.

A simple interpretation of this behaviour can be given in terms of the Young–Laplace force balance: a small contact angle corresponds to a large horizontal component of the liquid–vapour interfacial force that drives the drop retraction. Thus, since the contact angles observed during the retraction of polymer solution drops are significantly smaller than those observed in drops of pure water, one can conclude that the receding movement of the contact line of polymer solution drops requires a larger driving force than in the case of water. It must be remarked that, strictly speaking, the Young–Laplace equation should not be applicable even if the radial velocity is zero because the system is out of equilibrium; however, this approach is still justified because the timescale of the phenomenon is still much longer than molecular timescales ($\sim 10^7 \div 10^9$ s) (Barnes et al. 1995; Borodin and Smith 2000).

Because the advancing contact angle (during drop spreading) is similar for all drops, one can also conclude that polymer solution drops show larger contact angle hysteresis. Contact angle hysteresis around the equilibrium value is generally understood in terms of roughness and/or chemical heterogeneity of the surface (de Gennes 1985). However, more recently, it has been proposed that the contact angle hysteresis may be caused by a liquid film left behind the contact line during retraction (Chibowski 2003, 2007). Since both drops of pure water and those of polymer solution impact on identical surfaces, the difference observed in the contact angle hysteresis cannot be interpreted in terms of surface roughness or chemical heterogeneity. Thus, it can be argued that the polymer additive changes either the chemical structure of the surface, or the properties of the liquid film left behind the contact line during retraction, or both.

The advancing or receding contact line of a liquid drop moving on a solid surface is often described by introducing the concept of line tension (Tadmor 2011):

$$\Pi = \sigma \frac{D}{2}(cos\theta - cos\theta_{eq}) \tag{9}$$

where D is the drop base diameter, and θ_{eq} and θ are the equilibrium and the apparent contact angles, respectively; this approach is equivalent to Furmidge's equation (Dussan 1985). When the radial force per unit length due to polymer stretching, F_P, is taken into account, Eq. (9) becomes

$$\Pi + F_P \frac{D}{2} = \sigma_P \frac{D}{2}(cos\theta_P - cos\theta_{eq,P}) \tag{10}$$

where σ_P is the surface tension of the polymer solution, and $\theta_{eq,P}$ and θ_P are the equilibrium and the apparent contact angles of the polymer solution drop, respectively; since $\sigma_P \approx \sigma$ and $\theta_{eq,P} \approx \theta_{eq}$, one finds

$$F_P/\sigma \approx (cos\theta_P - cos\theta) \tag{11}$$

(a)

(b)

Fig. 9 Microscopic contact line morphology during drop retraction after impact on a hydrophobised glass substrate with Weber number $We \approx 110$: **a** pure water; **b** 200 ppm polyethylene oxide solution. Images are enhanced by background subtraction, histogram equalisation and conversion to binary. Each frame has a size of 700 μm

Using Eq. (11), one can estimate the additional contact line tension arising in dilute polymer solutions from dynamic contact angles of water and polymer solution drops.

Contact line morphology An example of the microscopic contact line morphology during drop retraction on a hydrophobised glass substrate is displayed in Fig. 9, which compares the contact lines of drops of pure water and of a dilute polymer solution in the same experimental conditions. While the contact line of the water drop appears almost perfectly smooth, the contact line of the polymer solution drop exhibits large local deformations, and leaves behind microscopic liquid filaments as it sweeps the surface. Filaments are distributed uniformly around the contact line and their width ranges between approximately 2 μm and 30 μm. The structure and density of these filaments depend on the polymer concentration in the fluid: for $c < 100$ ppm, one can observe linear filaments oriented in the radial direction and their density being increased with the polymer concentration; for $c \gtrsim 100$ ppm, there are less but thicker filaments, displaying numerous dendritic ramifications.

Filaments evolve following a capillary instability mechanism, until they locally break up into secondary microscopic droplets, in a similar fashion to the well-known beads-on-a-string breakup mechanism characteristic of many viscoelastic

(a)

(b)

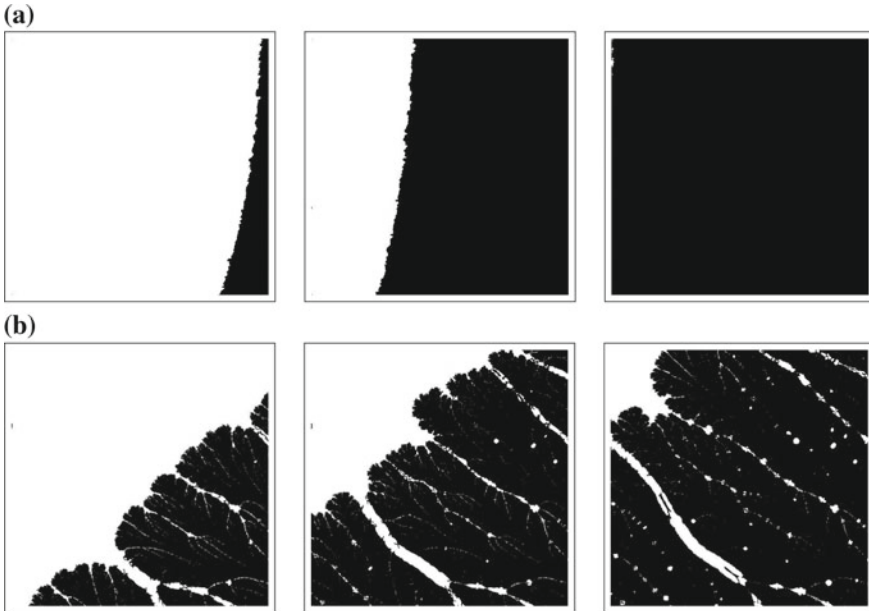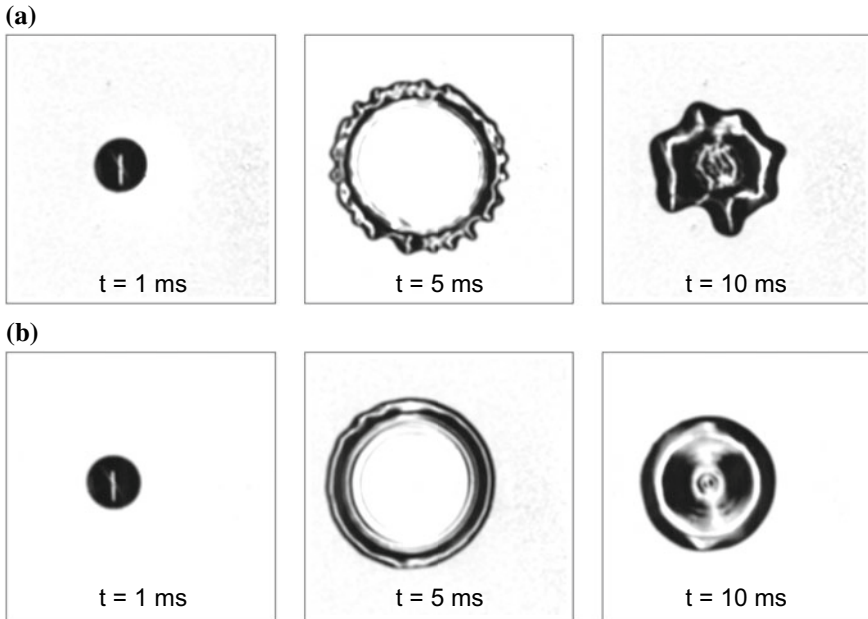**Fig. 10** Contact line morphology during drop impact on a hydrophobised glass substrate with Weber number $We \approx 110$: **a** pure water; **b** 200 ppm polyethylene oxide solution

fluids (Oliveira et al. 2006). At higher polymer concentrations, filaments are more stable, and therefore the breakup mechanism is less noticeable on the timescale of the experiment.

This complex morphology, which can be observed only at the microscale, suggests that even from the macroscopic point of view, the term *contact line* is not appropriate to indicate the drop edge, but one should rather use the expression *apparent contact line*, similar to the convention used for contact angles. Figure 9 also demonstrates the importance of image processing in the identification of the thinner filaments and the smaller beads, which could hardly be observed in raw images.

If the contact line is observed from a macroscopic point of view, the microscopic contact line features peculiar of dilute polymer solution drops are no longer visible. On the contrary, the contact line of polymer solution drops appears smoother than the contact line of water drops, as shown in Fig. 10.

The microscale analysis of the contact line morphology provides a key to understanding the peculiar behaviour of polymer solution drops as compared with water drops. In particular, the liquid filaments left behind by the receding contact line suggest that the conformational change of polymer coils, which originates viscoelastic behaviour is localised near the contact line, while in the rest of the droplet non-Newtonian effects are negligible. In this framework, the reaction force of the stretched polymer coils on the contact line represents an additional contribution to the line

(a)   **(b)**

Fig. 11 Polymer conformation observed on the substrate behind the receding contact line of a dilute polymer solution drop containing fluorescent λ-DNA. **a** Image of stretched λ-DNA molecules collected at a frame rate of 1000 fps with an exposure time of 400 µs; the white reference bar corresponds to the length of a fully stretched DNA molecule. **b** Pictoria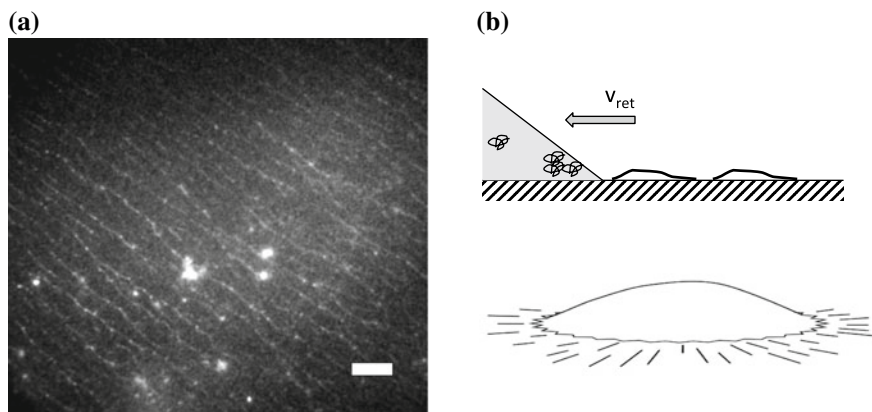l description of the polymer dynamics during drop retraction: as the meniscus recedes, polymer molecules in the liquid wedge are stretched by molecular combing. Copyright (2010) by The American Physical Society

tension, which causes the reduction of the apparent dynamic contact angle during drop recoil, as discussed above.

Polymer conformation near the contact line The nature of the dissipative phenomena arising near the contact line during drop retraction was revealed by visualisation experiments aiming at the direct observation of the polymer conformation as well as the contact line morphology at the microscopic scale (Smith and Bertola 2010a; Bertola 2013; Biolè and Bertola 2015c).

To investigate the dynamics of polymer molecules during drop retraction, and its potential effect on the velocity of the receding contact line, fluorescent λ-DNA (a linear biopolymer with a random coil conformation, a diameter of about 1.4 µm, a stretched length of about 22 µm, and thus visible using a fluorescent microscope) was added to the impacting drop and observed through an optical microscope equipped with image intensifier (Smith and Bertola 2010a, b). After the passing of the contact line, stretched DNA molecules can be observed on the substrate, oriented in the direction perpendicular to the contact line, as shown in Fig. 11a. Independent experiments on forced dewetting showed that polymer deposited on the substrate results in a velocity-dependent force at the contact line (Smith and Sharp 2014). This bears strong similarities with other DNA stretching methods, such as molecular combing or air blowing techniques (Kim et al. 2007); in these techniques, DNA molecules are stretched using combination of hydrodynamic and surface forces arising when a liquid meniscus moves on a solid surface. For example, in molecular combing such meniscus is created by slowly pulling out a plate from a solution containing DNA. The same conditions occur when an impacting droplet retracts on the target surface
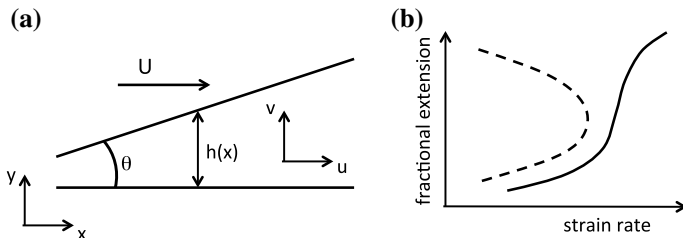
Fig. 12 Schematic of the liquid wedge near the contact line (**a**) and schematic of supercritical coil–stretch transition (de Gennes 1974) (**b**)

after maximum spreading, the only difference being that this process is orders of magnitude faster than molecular combing, where the typical velocity of the meniscus is 0.2 mm/s. This mechanism is illustrated qualitatively in Fig. 11b, and can be easily modelled as a supercritical coil–stretch transition induced by the shear flow in the liquid wedge near the contact line (de Gennes 1974).

The hydrodynamics of the liquid wedge near the contact line can be modelled as the flow between a fixed horizontal surface (the substrate) and a plate inclined at an angle θ (corresponding to the instantaneous value of the apparent dynamic contact angle), moving at velocity U, as shown schematically in Fig. 12a. The minimum thickness of the liquid film, h_0, must be no less than the unperturbed size of the polymer coils, R_0; for polyethylene oxide molecules in water, one finds $R_0 = 0.0888M^{0.5} = 178$ nm, where M is the molecular weight (Brandrup et al. 2005), and hence one can take an order of magnitude $h_0 \approx 0.2$ μm. Polymer coils are subject to hydrodynamic interaction with the solvent, with a characteristic Zimm time $\tau_0 \approx 0.2\eta_s R_0^3/k_B T = 0.27$ ms and a Rouse time $\tau_R \approx 2R_h\eta_s R_0^2/\pi k_B T = 0.41$ ms, where η_s is the solvent viscosity.

At this point, it is important to note that the magnitude of U, i.e. the main parameter of the process, is not necessarily equal to the contact line velocity during drop retraction. Previous works (Bertola 2013; Smith and Bertola 2010a, 2011) show that while in water drops the fluid velocity is the same as the velocity of the receding contact line, in dilute polymer solution drops, the contact line velocity is two or three orders of magnitude smaller than the bulk velocity of the fluid during retraction.

In a reference frame originating on the contact point, the velocity components parallel and perpendicular to the substrate during drop retraction are, respectively, $u \approx Uy/h(x)$ and $v \approx \xi(\theta)x$, where $h(x) \approx \theta x$ is the liquid film thickness and $\xi(\theta)$ is a positive function of the apparent contact angle (see Fig. 12a). The velocity gradient of this flow field can be split into its symmetrical part, $A = \frac{1}{2}(u_y + v_x) = \frac{1}{2}(U/h + \xi)$, associated with a pure deformation, and its anti-symmetrical part $\omega = \frac{1}{2}(u_y - v_x) = \frac{1}{2}(U/h - \xi)$, associated with a pure rotation. Since $\xi(\theta) > 0$, $\omega/A < 1$, therefore it is possible to have strong distortions of the polymer coils, even in the absence of elongational flow (Lumley 1973). This corresponds to a second-order transition from coil to stretch conformation state, i.e. with a constantly positive slope

of the stretching ratio, $l = r/L$, where r is the polymer elongation and L is the length of the fully stretched chain, with respect to the order parameter $\xi(\theta)$ (i.e. $dl/d\xi > 0$), as illustrated schematically in Fig. 12b (de Gennes 1974).

Following the classical finite extensibility approach Peterlin (1966), the stretching ratio is related to the velocity gradient as

$$l = \frac{3}{Z\mathcal{L}^{-1}(l)} \left\{ 1 + \frac{1}{6} \frac{\left(\frac{U}{h} + \xi\right)^2 \tau^2}{\frac{9l^2}{[\mathcal{L}^{-1}(l)]^2} - \frac{U}{h}\xi\tau^2} \right\} \tag{12}$$

where τ is the relaxation time, which is given by de Gennes (1974)

$$\tau(l) \approx \frac{\tau_R}{1 + \frac{1}{l}} \tag{13}$$

and $\mathcal{L}^{-1}(l)$ is the inverse Langevin function, which can be estimated, for example, using Kroger's approximation Kroger (2015):

$$\mathcal{L}^{-1}(l) = \frac{3l - (l/5)(6l^2 + l^4 - 2l^6)}{1 - l^2} \tag{14}$$

The resulting recall force of a stretched polymer coil is

$$F = \frac{k_B T L}{R_0^2} \mathcal{L}^{-1}(l) \tag{15}$$

The ensemble of polymer molecules stretching as the drop edge sweeps the surface provides the dissipative force necessary to slow down the displacement of the contact line. This can be interpreted, from a macroscopic point of view, as an additional, dissipative force acting on the contact line and opposed to its movement, or an effective contact line friction. This also explains the reduction of the dynamic contact angle observed in experiments: to overcome the action of polymer molecules on the contact line, the horizontal component of the surface force driving the droplet retraction must be larger than in a Newtonian fluid, and therefore the apparent dynamic contact angle must be smaller.

2.2 Impact on Heated Surfaces

Early studies about the impact of viscoelastic drops on heated surfaces focused primarily on dilute polymer solution drops and found significant differences with respect to the impact morphology of Newtonian drops (Bertola 2004); in particular, it was observed that adding small amounts of a flexible polymer to the aqueous phase, secondary atomisation can be suppressed completely (Bertola and Sefiane 2005), and

droplet rebound in the Leidenfrost regime, i.e. when a stable vapour film separates the drop from the impact surface, is significantly enhanced (Bertola 2009b). More recently, it was shown that Leidenfrost rebounds are only weakly affected by the polymer concentration (i.e. by the fluid rheology) (Bertola 2014), but can be related to the symmetry of the rebound process (Chen and Bertola 2016b).

Since the fluid properties (surface tension, viscosity and relaxation time), and consequently the dimensionless parameters, are strongly dependent on temperature, it is necessary to estimate the drop temperature accurately. In particular, the drop temperature depends on nature of the liquid–surface interface and on the contact duration. If the liquid wets the surface for a sufficiently long time, it can reach the boiling point, after which temperature remains constant; vice versa, if the contact time is very short and the liquid does not wet the surface, the drop heating can be negligible.

Suppression of secondary atomisation and splashing The most evident effect of the fluid viscoelasticity on the morphology of drops impacting on heated surfaces is perhaps the suppression of secondary atomisation and the significant limitation of the range of experimental conditions where drop breakup occurs (Bertola 2004). Figure 13 shows an example of comparison between the impact morphology of a water drop and a dilute polymer solution (200 ppm PEO in water) drop having the same diameter and impacting with the same Weber number on a surface kept at constant temperature; while the water drop exhibits breakup with secondary atomisation upon impact, the polymer solution drops exhibit only a small rebound without any liquid mass loss.

In Newtonian drops, secondary atomisation can also be observed during drop rebound (see Sect. 1); for a given value of the impact Weber number, dry rebound (i.e. without secondary atomisation) occurs only above a certain temperature, which is often referred to as *dynamic Leidenfrost temperature* (Wang et al. 2000); its value has been shown to increase with the Weber number (Yao and Cai 1988).

It should be observed that both the inhibition of drop breakup and the suppression of secondary atomisation cannot be explained only with the increase of the Ohnesorge number, because the shear viscosity of these polymer solutions is only 20–50% higher than the viscosity of the solvent. Thus, their origin must be related at least partially to the fluid elasticity. In particular, one can identify three independent mechanisms that affect either drop breakup or secondary atomisation, or both. First, the elongational viscosity is known to change substantially the breakup dynamics of free-surface flows and their decay into drops (Bazilevskii et al. 1981; Rozhkov 1983); thus, elongational viscosity opposes the scattering of secondary droplets from the free surface of the impacting drop, as well as the detachment of satellite drops from the rim during corona splashing. Second, polymer additives improve the stability of the surface between the drop and the surrounding atmosphere and, in case of Leidenfrost drops, also the surface in contact with the vapour cushion that separates the drop from the hot wall; this reduces the chances that the liquid may locally touch the wall and start boiling. Third, even in cases when the liquid makes contact with the wall with consequent bubble nucleation, the presence of the polymer can significantly affect
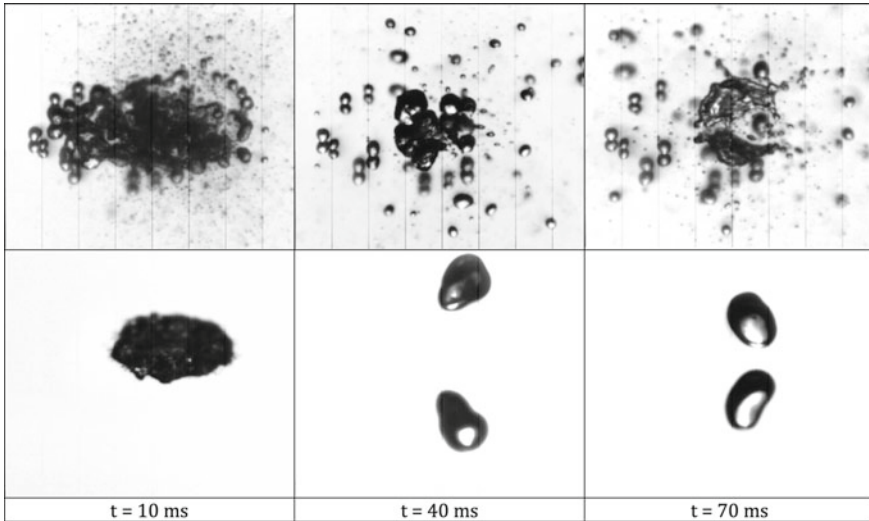
Fig. 13 Comparison between the impacts of a water drop (top) and PEO solution (concentration: 200 ppm; molecular weight: 4 MDa) drop (bottom) impacting on a polished copper surface at T = 160 °C and We = 220

the process of growth, detachment and rise of vapour bubbles (Hartnett and Hu 1986; Kim et al. 2004), and hence prevent their bursting on the drop free surface.

If one accepts the current definition of dynamic Leidenfrost temperature (the minimum temperature to observe dry rebound without secondary atomisation), one must conclude the dynamic Leidenfrost temperature of viscoelastic drops is significantly lower than that of Newtonian drops of similar viscosity.

Figure 14 compares the dynamic Leidenfrost temperatures, determined by experimental observation (Bertola and Sefiane 2005), of a water and a polymer solution drops with $D_0 \approx 3.8$ mm impacting on a polished aluminium surface. The dynamic Leidenfrost temperature of the polymer solution drop is significantly lower than that of the water drop, and is a weakly growing function of the impact Weber number; in addition, extrapolating experimental data to the limit $We \rightarrow 0$ one finds the conventional value of Leidenfrost temperature for sessile water drops on polished aluminium (Bernardin and Mudawar 2002).

As a conclusive remark, it should be observed that in the case of viscoelastic fluids, the definition of a dynamic Leidenfrost temperature is less significant than in case of simple liquids. In fact, for drops of pure water, secondary atomisation actually disappears when a continuous and stable vapour cushion prevents the drop from making contact with the hot surface, which is indeed analogous to the Leidenfrost phenomenon in sessile drops. This is no longer true when polymer additives are dissolved into the impacting drop: in fact, even if the film is unstable and the liquid locally touches the hot wall, there are other physical mechanisms that prevent scattering of satellite droplets from the free surface of the liquid, as discussed above.
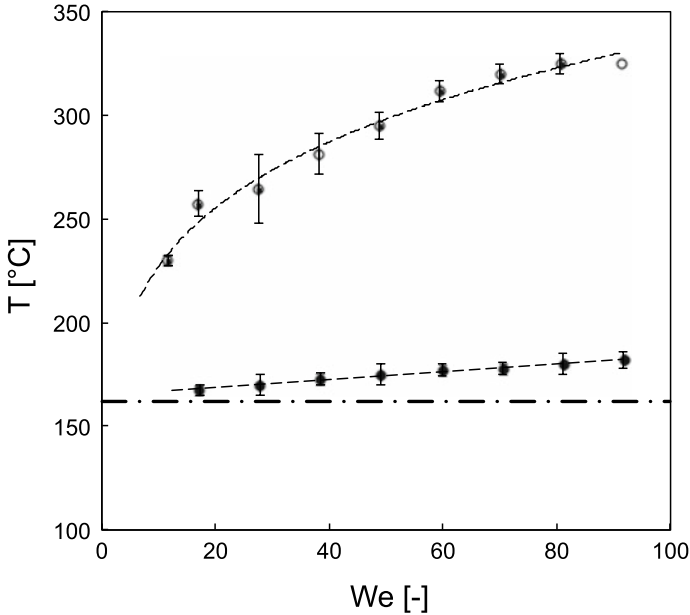
Fig. 14 Dynamic Leidenfrost temperature of water (open symbols) and 200 ppm polyethylene oxide solution (filled symbols) drops with $D_0 \approx 3.8$ mm impacting on a polished aluminium surface. The horizontal dash-dot line indicates the Leidenfrost temperature of sessile water drops on polished aluminium ($T_{L0} = 162\,^\circ$C)

In this case, the expression 'dynamic Leidenfrost temperature' may be misleading, because it suggests the impacting drop never wets the surface, whereas wetting might occur without the development of secondary atomisation.

Viscoelastic Leidenfrost drops Above the dynamic Leidenfrost point, the vapour film between the drop and the hot surface is stable, and therefore the liquid is not in contact with the wall; thus, one can neglect the effects of wetting and wall friction (Bertola 2009b, 2014; Black and Bertola 2013). A rough estimate of the average temperature of the drop can be obtained from a lumped capacitance energy balance; neglecting the heat exchange between the liquid drop and the surrounding plume of hot air, i.e. considering only the conduction heat flux from the surface to the liquid through the liquid film, the energy balance equation can be written as

$$mCdT = \frac{\pi D^2 k_v}{4\delta}(T_S - T)dt \tag{16}$$

where m is the drop mass, C is the specific heat of water, D is the diameter of the drop bottom, δ is the thickness of the vapour layer, k_v its thermal conductivity, T_S is the surface temperature and T the average temperature of the drop. Integration of Eq. (16) allows one to estimate the time required for the drop to reach a certain average

temperature. The most favourable heating conditions occur when the heated surface is largest (i.e. the drop is at maximum spreading, where $D \approx 3D_0$) and the vapour film thickness is minimum ($\delta_{\min} \approx 10\mu m$) (Rein 2003); under these assumptions, the time necessary to heat a drop up to a certain temperature T is

$$t_{\min} = \frac{2\rho D_0 C \delta_{\min}}{27 k_v} ln \frac{T_S - T_{amb}}{T_S - T} \tag{17}$$

According to Eq. (17), a 3 mm diameter water drop would reach the saturation temperature in 87 ms, which is a significantly longer time than the maximum duration of the contact observed experimentally, which is around 20 ms (Bertola 2009b). If Eq. (16) is solved with respect to temperature, one can also estimate the average drop temperature after a certain time; in particular, after 20 ms, the temperature increase of a 3 mm drop is only 10 °C. Thus, one can use the fluid properties calculated at ambient temperature without introducing significant errors.

The main macroscopic quantities that characterise the impact of Leidenfrost drops are the maximum diameter at the end of inertial spreading, the drop retraction velocity after maximum spreading and the maximum height reached by the drop centre of mass during rebound. The maximum spreading diameter indicates how much of the initial impact kinetic energy is stored as surface energy as the drop is deformed, while the maximum bouncing height indicates how much energy remains after the impact or, alternatively, can give a measure of the total energy dissipation during impact when subtracted from the impact kinetic energy.

Simple drop impact models on dry surfaces based on energy conservation show that the maximum spreading diameter scales with the Weber number as $D_{\max}/D_0 \sim We^{1/2}$ or, more precisely (Rein 2003):

$$\frac{D_{\max}}{D_0} = \sqrt{\frac{\alpha^2}{6} We + 2} \tag{18}$$

where $\alpha = v_i/v_r$ is the ratio between the rebound and the impact velocities (restitution coefficient). An alternative approach suggests that for $We > 1$ and negligible viscous dissipation, the momentum equation combined with volume conservation yields $D_{\max}/D_0 \sim We^{1/4}$ (Clanet et al. 2004; Biance et al. 2006). However, the latter approach implicitly assumes that upon impact, the drop deforms like a disc, ignoring the formation of a central lamella surrounded by a toroidal rim, which is observed already at moderate Weber numbers.

The maximum diameter of water and polyethylene solution drops at different concentrations after the inertial spreading is plotted in Fig. 15 as a function of the impact Weber number. As expected, the maximum spreading diameter grows monotonically with the Weber number; however, neither Eq. (18) nor the momentum conservation approach ($D_{\max}/D_0 = We^{1/4}$) provides an accurate prediction of experimental data, although they indeed suggest some scaling when plotted in logarithmic scale (Fig. 15b).
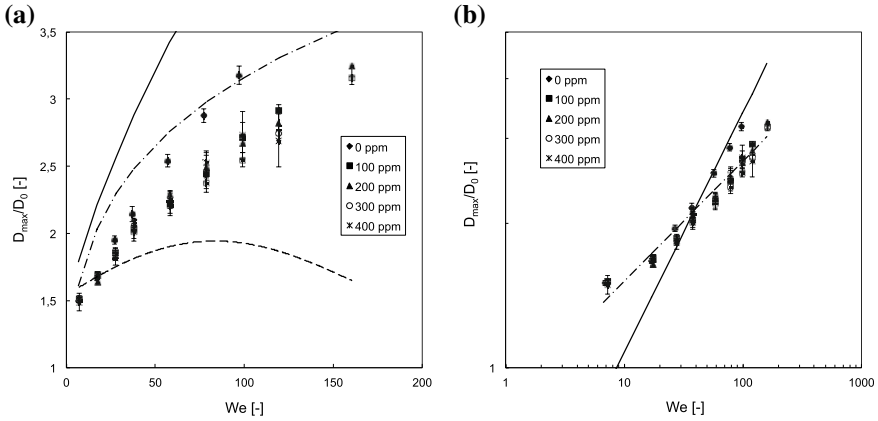
Fig. 15 Maximum spreading diameter of water and polyethylene oxide solution drops at different concentrations with $D_0 \approx 3$ mm impacting on a polished aluminium surface at 400 °C. **a** Linear scale; the dash-dot line corresponds to $D_{max}/D_0 = We^{1/4}$, while the solid and dashed lines correspond to Eq. (18) with $\alpha = 1$ (no energy dissipation) and $\alpha = v_i/v_r$, respectively. **b** Logarithmic scale; the dash-dot line corresponds to $D_{max}/D_0 = 0.85We^{1/4}$, while the solid line corresponds to $D_{max}/D_0 = 0.34We^{1/2}$

For $We \gtrsim 20$, the maximum spreading diameter of viscoelastic drops is systematically smaller than that of water drops having the same impact Weber number, i.e. the fraction of impact kinetic energy (which is proportional to the Weber number) converted into surface energy (which is proportional to the area of the drop surface at maximum spreading) is also smaller. Since the viscosity of polymer solutions is higher than the viscosity of the solvent (in this case, water), the viscous dissipation during the inertial spreading stage is higher in polymer solution drops, hence the observed reduction of the maximum spreading diameter. However, this does not exclude that the surface energy difference between Newtonian and viscoelastic drops at maximum spreading may be stored (at least partially) elsewhere, for example, as elastic energy.

The total energy dissipation during impact and rebound can be obtained from the difference between the drop release height, $H_0 = v_i^2/2mg$, and the maximum bouncing height, $H_{max} = v_r^2/2mg$. During rebound, surface energy is converted back to kinetic energy and propels the drop off the surface; thus, the maximum height of the drop centre of mass allows one to calculate the fraction of surface energy recovered as mechanical energy during rebound. Figure 16 shows that for $We \gtrsim 40$, the maximum bouncing height of viscoelastic drops is significantly larger than that of Newtonian drops, irrespective of the polymer concentration (Bertola 2014) and of the drop diameter (Bertola 2009b), whereas for $We \lesssim 40$ differences are not significant. This shows viscoelastic drops can recover a higher fraction of the initial impact kinetic energy even if they store less in the form of surface energy.

Although these results are consistent with a scenario where the fluid elasticity causes higher rebounds in polymer solution drops, a comparison with shear-thinning
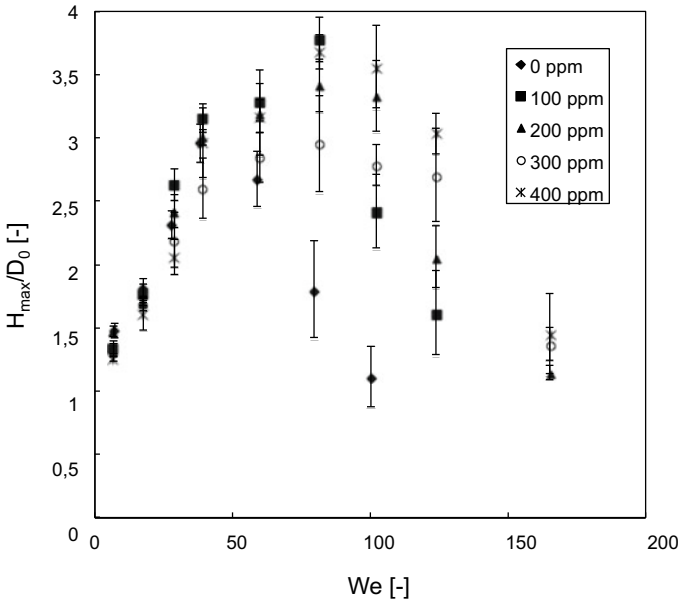
Fig. 16 Maximum bouncing height of water and polyethylene oxide solution drops at different concentrations with $D_0 \approx 3$ mm impacting on a polished aluminium surface at 400 °C

drops, where the fluid elasticity is negligible, demonstrated this interpretation is not correct. In fact, shear-thinning drops bounce much higher than polymer solution drops, even when they have a larger shear viscosity, as shown in Fig. 17 (Black and Bertola 2013).

A more systematic comparison of Newtonian, shear-thinning and viscoelastic drops with matching flow curves revealed that high rebounds (i.e. high restitution coefficients) are axisymmetric throughout the process, while low bouncing heights are observed whenever the rebound is not axisymmetric (Chen and Bertola 2016b). Examples of the drop morphology during rebound for the three fluids considered are displayed in Fig. 18a–c, which shows that while the higher viscosity viscoelastic and shear-thinning drops preserve axisymmetry during rebound, the lower viscosity water drop exhibits non-axisymmetric oscillations. The symmetry breaking observed in lower viscosity water drops is related to the formation of finger-like protrusions on the rim during impact (Fig. 18d), which indicate the onset of the well-known rim instability eventually leading to splashing (Rein 1993; Yarin 2006). These protrusions grow during the inertial spreading stage, and form an axisymmetric crown at maximum spreading; however, at the onset of recoil one can observe that some of the protrusions coalesce to create bigger fingers during retraction, while others do not. Thus, the mass distribution in the retracting droplet becomes non-uniform, which induces asymmetries both in the drop shape and in the internal flows, and eventually causes the drop to rotate around its centre of mass during rebound.
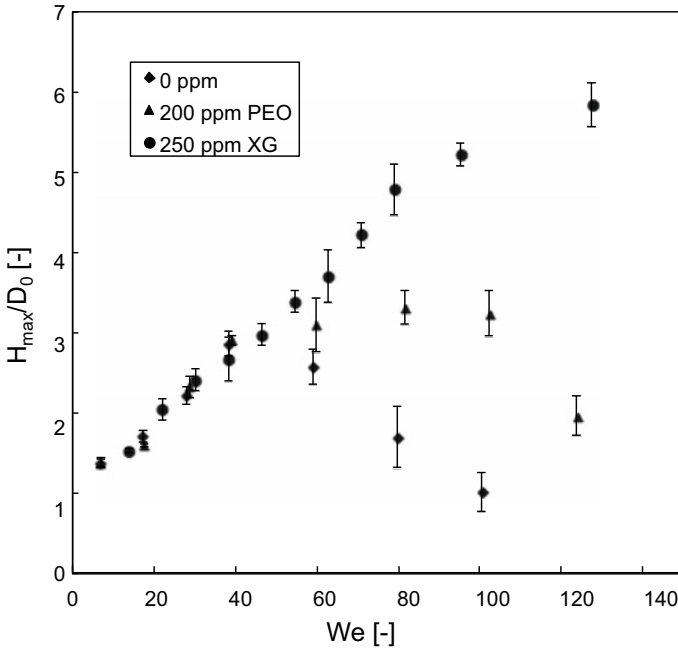
Fig. 17 Comparison of the maximum bouncing heights of water, polyethylene oxide (PEO) solution and xanthan gum (XG) solution drops with $D_0 \approx 3$ mm impacting on a polished aluminium surface at 400 °C
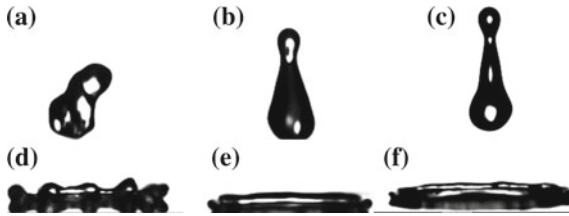
Fig. 18 Rebound morphology of **a** water, **b** 200 ppm polyethylene oxide solution, and **c** 250 ppm xanthan gum solution drops with $D_0 \approx 3$ mm impacting on a polished aluminium surface at 400 °C. The symmetry breaking during the water drop rebound is related to the formation of a crown during impact, which is not observed for the other fluids (**d**–**f**)

When drops exhibit axisymmetric oscillations during rebound (Fig. 18b, c), their kinetic energy converts periodically into surface energy and vice versa, with some dissipation depending on the fluid viscosity. However, if oscillations are not axisymmetric and the drop rotates around its centre of mass (Fig. 18a), a significant part of the kinetic energy is used to sustain the rotation reducing the maximum bouncing height. The rotational kinetic energy of tumbling drops can be estimated as follows:

$$E_{rot} = \frac{1}{2} I \omega^2 \tag{19}$$

where I is the moment of inertia; assuming the elongated drop can be approximated as a cylinder, one obtains

$$I = m \left(\frac{R^2}{4} + \frac{l^2}{12} \right) = \frac{1}{72} \pi \rho D_0^5 \left(\frac{1 + 2k^3}{2k} \right) \tag{20}$$

where $l = k D_0$ is the cylinder length, measured from images, and R is the cylinder radius, calculated imposing volume conservation.

Since the rotational kinetic energy is not recoverable as potential energy, its value per unit weight must correspond to the bouncing height reduction observed in tumbling drops with respect to drops with the same rheology (viscosity, flow curve) that remains axisymmetric during rebound:

$$\frac{\Delta h}{D_0} = \frac{E_{rot}}{mgD_0} = \frac{D_0 \omega^2}{24g} \left(\frac{1 + 2k^3}{2k} \right) \tag{21}$$

where ω denotes the mean angular velocity and g denotes the gravity acceleration.

Figure 19 compares the maximum bouncing heights of Newtonian, shear-thinning and viscoelastic drops of fluids with matching flow curves. In particular, the viscosity of Newtonian fluids corresponds to the infinite-shear rate and the zero-shear rate viscosities of the non-Newtonian fluids, obtained by fitting the flow curve with the Carreau–Yasuda model (Chen and Bertola 2016b). The bouncing heights of non-Newtonian drops and of the Newtonian drop with viscosity equal to the zero-shear rate viscosity are almost identical, while the bouncing height of the Newtonian drop

Fig. 19 Maximum bouncing height of Newtonian drops (glycerol solutions), shear-thinning drops (100 ppm xanthan gum solution), viscoelastic drops (80 ppm polyacrylamide solution) with $D_0 \approx 3$ mm impacting on a polished aluminium surface at $400\,°C$: **a** measured heights; **b** measured heights corrected for the rotational kinetic energy (Eq. 21)
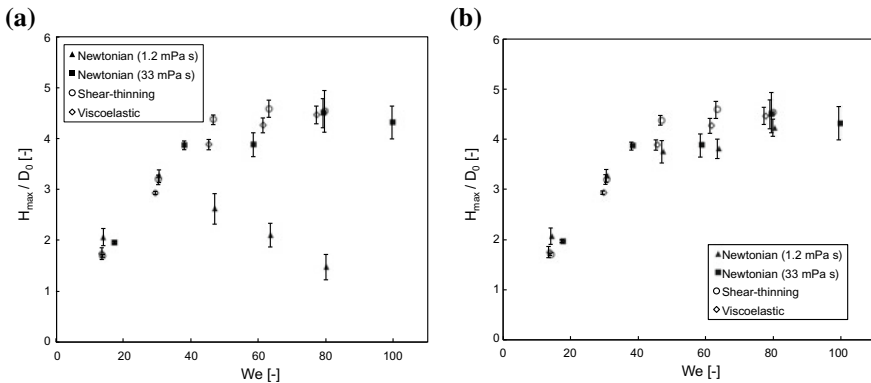
with viscosity equal to the infinite-shear rate viscosity is significantly smaller, similar to water drops in Figs. 16 and 17. However, when the bouncing height of the low-viscosity drop is corrected adding the contribution of the rotational kinetic energy (Eq. 21), it becomes almost identical to the bouncing heights of non-Newtonian drops, as shown in Fig. 19b.

This suggests that the maximum bouncing height (i.e. the restitution coefficient), corresponding to the fraction of the impact kinetic energy recovered after impact, is not affected by non-Newtonian effects, but depends essentially on the zero-shear rate viscosity (i.e. on the viscous dissipation) and on the drop symmetry during rebound. In particular, tumbling drops cannot recover the rotational kinetic energy, and therefore display a significantly smaller bouncing height.

Other impact regimes Besides the conventional impact regimes observed in Newtonian drops (Bertola 2015), dilute polymer solution drops may exhibit other impact morphologies, depending on the Weber number, the impact surface temperature, the polymer concentration and molecular weight. At low polymer concentrations, there is a range of Weber numbers where a single satellite drop separates in the vertical direction during rebound, shortly after the drop has bounced off the surface; this drop is tethered to the main drop body by a thin liquid filament, which is subject to uniaxial stretching, and does not break up until the two droplets re-coalesce into a single drop, as shown in Fig. 20. The diameter of the single satellite drop is between 40 and 50% of the equilibrium drop diameter, D_0; this means that the mass of the satellite drop is about 10 of the total mass of the drop, and therefore the equivalent drop diameter of the drop after the satellite droplet separation is about 96% of the initial equilibrium diameter.
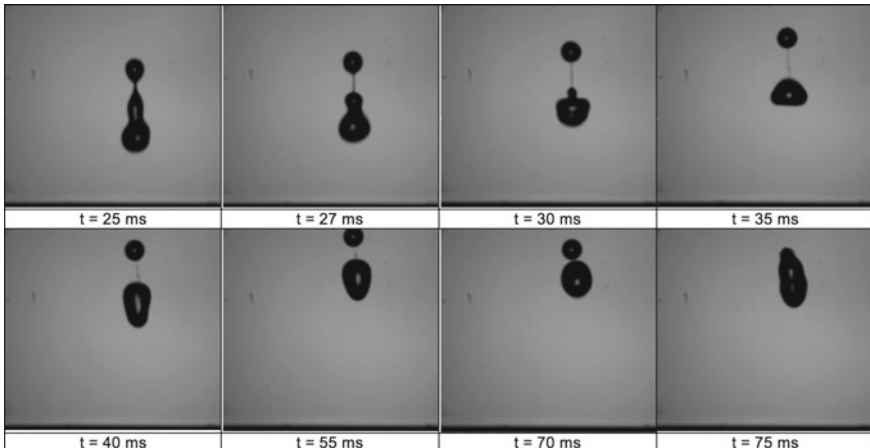

Fig. 20 Single satellite drop morphology observed during the impact of a PEO solution drop (concentration: 100 ppm; molecular weight: 4 MDa) impacting on a surface at T = 400 °C with We = 80; the time origin is the moment of impact

Fig. 21 Semi-splash morphology observed during the impact of a PEO solution drop (concentration: 300 ppm; molecular weight: 4 MDa) impacting on a surface at time origin is the moment of impact

A second impact morphology peculiar of polymer solution drops can be observed at high Weber numbers. When the drop reaches maximum spreading, satellite droplets are formed around the disc perimeter due to the rim instability; in Newtonian drops, this instability eventually evolves into drop splashing. In the case of polymer solutions, a liquid bridge prevents the separation of the satellite droplets from the lamella, as shown in Fig. 21; although the stretching of the liquid bridge is less than in the case of the single satellite drop filament, its elasticity is sufficient to recall the satellite droplets and prevents splashing or breakup. This impact morphology is not observed in Newtonian drops, and can be labelled as *partial splashing* (or *semi-splashing*).

The formation of liquid bridges preventing the separation of satellite droplets also affects the secondary atomisation regime, as shown in Fig. 22. In this case, satellite droplets are sprayed out of the spreading drop free surface due to the bursting of vapour bubbles produced at nucleation sites on the impact surface; however, shortly after their ejection, all satellite droplets forming the spray are pulled back into the main drop, and hence this morphology can be labelled *semi-spray*. The phenomenon has an overall duration of a few milliseconds, and therefore it is very difficult to detect and analyse.

Figure 23 shows the impact regime map relative to a dilute PEO solution with concentration of 200 ppm and molecular weight of the PEO of 4 MDa. In the range of parameters considered, the impact regimes observed are secondary atomisation (SA), rebound with secondary atomisation (RSA), dry rebound (R) and semi-spray (R*). Thus, the map is significantly different with respect to the map obtained for drops of pure water (Bertola 2015); the dominant impact morphology, observed for most combinations of surface temperature and Weber number, is dry rebound, meaning that the polymer additive strongly inhibits both secondary atomisation and splashing.

The effect of polymer concentration is clearly seen upon comparing the map in Fig. 23 with the impact regime maps for a molecular weight of 4 MDa and PEO concentrations of 100 and 400 ppm, displayed in Fig. 24. Reducing the polymer concentration increases the number of different impact morphologies, while for the
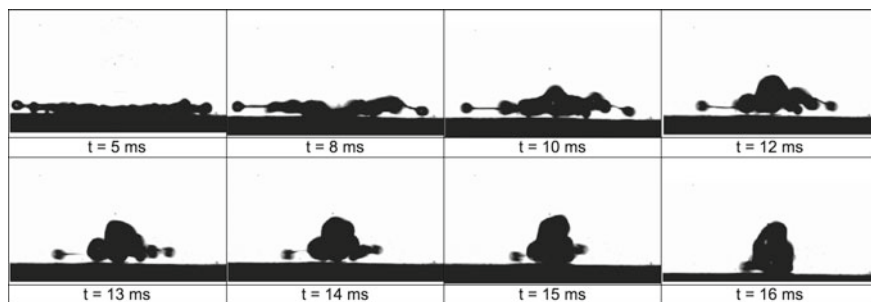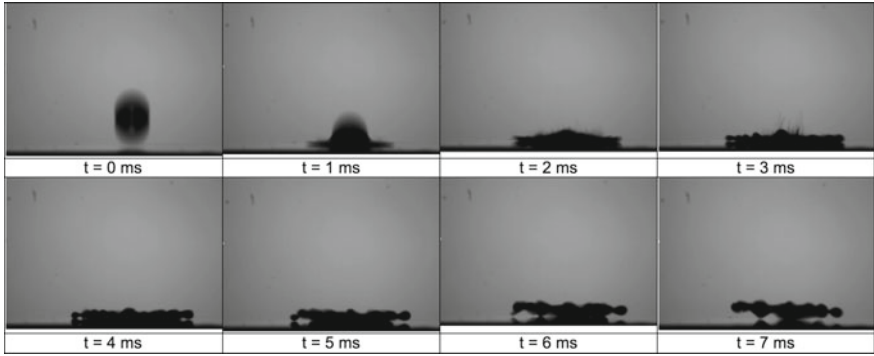
Fig. 22 Semi-spray morphology observed during the impact of a PEO solution drop (concentration: 200 ppm; molecular weight: 4 MDa) impacting on a surface at T = 250 °C with We = 100; the time origin is the moment of impact
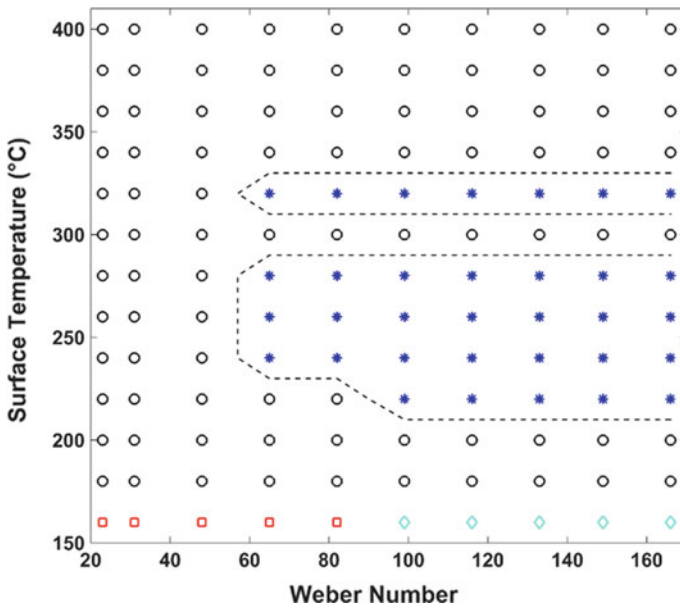
Fig. 23 Impact regime map obtained for a concentration of 200 ppm and a molecular weight of 4 MDa; regimes shown: SA ($\square$), RSA ($\diamond$), R ($\circ$) and R* ($*$)

higher polymer concentration, dry rebound is observed almost everywhere, with the semi-spray regime confined to a small region. Upon keeping the molecular weight constant at 4 MDa and gradually increasing the concentration from 100 to 200 ppm, all breakup and splashing are completely overcome; with the exception of small-scale secondary atomisation which is prevalent at a surface temperature of 160 °C. However, upon increasing the concentration to 400 ppm, no secondary atomisation
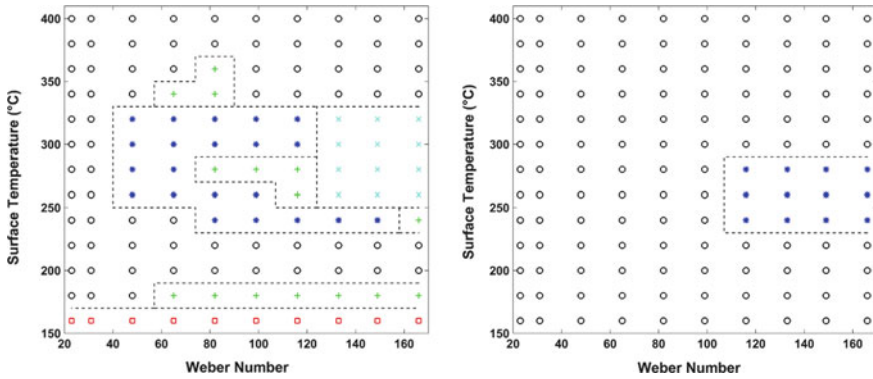
Fig. 24 Impact regime maps obtained for a molecular weight of 4 MDa at concentrations of 100 ppm (left) and 400 ppm (right); regimes shown: SA (□), B (+), R (○), R* (∗) and S (×)
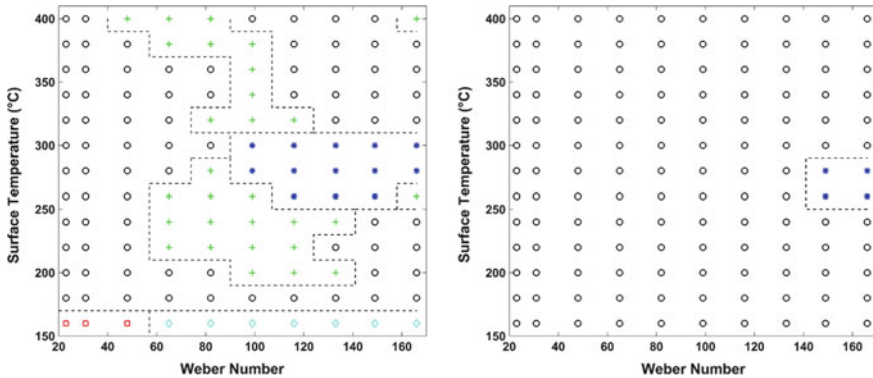
Fig. 25 Impact regime maps obtained for a concentration of 200 ppm and molecular weights of 2 MDa (left) and 8 MDa (right); regimes shown: SA (□), B (+), R (○), R* (∗) and S (×)

is observed even at surface temperature of 160 °C. For all surface temperatures considered, rebound is the primary impact outcome.

Similarly, the effect of the molecular weight of the polymer can be seen upon comparing the map in Fig. 23 with the impact regime maps for a concentration of 200 ppm and molecular weights of 2 MDa and 8 MDa, displayed in Fig. 25. Within the 2 MDa (200 ppm) impact regime map, secondary atomisation (SA), rebound with secondary atomisation (RSA), rebound (R), semi-spray (R*) and drop breakup (B) regimes are observed. Upon gradual increase of molecular weight from 2 MDa to 4 MDa, the breakup regime is completely suppressed; however, some secondary atomisation is still present at a surface temperature of 160 °C. Increasing the molecular weight to 8 MDa, all secondary atomisation is completely suppressed.

Thus, from a qualitative standpoint, the effect of molecular weight is similar to that of the polymer concentration; low molecular weights enable the development of

different impact morphologies, while increasing the molecular weight progressively suppresses secondary atomisation and breakup/splashing, until only the dry rebound regime can be observed.

The similarity between the effects of the molecular weight and of the polymer concentration on the impact morphology is justified because both of these parameters affect the relaxation time of polymer solutions (Kalashnikov and Askarov 1989). When the relaxation time is shorter than the characteristic hydrodynamic timescales corresponding to the various impact morphologies, the effect of the polymer additive is negligible; however, when the relaxation time and the hydrodynamic timescales are of the same order, the behaviour of polymer solutions becomes significantly different from that of the pure solvent.

3 Impact of Viscoplastic Drops on Solid Surfaces

3.1 Impact on Homothermal Surfaces

Although viscoplastic (or yield stress) fluids have been studied for about one century, and despite their relevance in several applications, the first investigation of yield-stress drops was published only recently (Nigen 2005). This work studies the impact of a model viscoplastic fluid (Vaseline) on a plexiglass surface, for different impact velocities. The rheological behaviour of the fluid was described using a Cross model, modified to include a yield-stress component. The variation of the final drop shape with respect to the impact velocity was characterised with respect to the Bingham number, $Bm = \tau_0 D_0 / \mu_0 v_i$, where v_i is the impact velocity and μ_0 is the zero-shear rate viscosity; however, such definition is not well posed because whilst the Bingham number characterises the ratio of viscous to yield-stress forces, viscous dissipation only occurs during fluid motion, and therefore the Bingham number definition given above is only valid at zero-shear rate, i.e. when the drop is at maximum spreading.

Because surface forces play an important role in all drop impact phenomena, it is interesting to observe what happens when the yield-stress magnitude is comparable with the capillary (Laplace) pressure. This leads to the definition of a capillary regime and a viscoplastic regime, which can be characterised through the Bingham-capillary number (Bertola 2009a):

$$\check{B} = \frac{\tau_0 D_0}{\sigma} \tag{22}$$

Whilst in the capillary regime, the impact morphology is qualitatively similar to that of simple liquids, in the viscoplastic regime, one can sometimes observe permanent deformations that do not disappear upon impact or under the action of surface forces. For example, if drops are produced from a capillary nozzle, the prolate shape that is created during the fluid extrusion (Coussot and Gaulard 2005; German and Bertola 2009a, 2010a, b) remains partly visible after impact, as shown in Fig. 26,
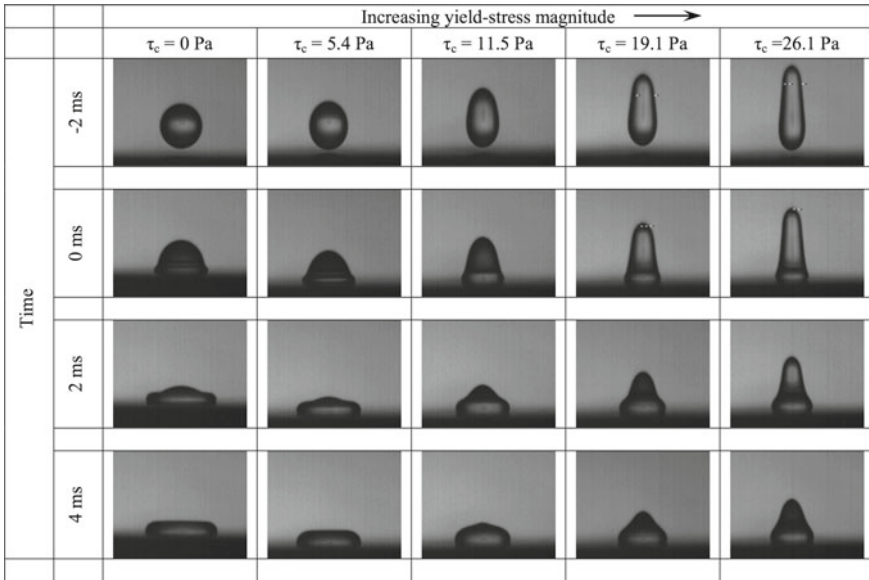
Fig. 26 Base diameter and dynamic contact angle of commercial hair gel (Carbopol gel) drops with different magnitudes of the yield stress and $D_0 \approx 2.5 \div 3$ mm impacting on a hydrophobic surface (Parafilm) from a fall height of 25 mm

which displays the impact morphology of hair gel-water drops for different yield-stress magnitudes. This phenomenon is also influenced by inertia, and becomes less and less pronounced at higher impact Weber numbers. The droplets symmetry can be improved significantly if the dispensing nozzle has a very small diameter (Saïdi et al. 2010); however, for high yield-stress magnitudes and low impact velocities, drops still preserve the initial shape they have after detachment from the capillary.

In viscoplastic drops, the maximum spreading diameter at the end of inertial spreading decreases linearly with the yield-stress magnitude (German and Bertola 2009a), while in Newtonian drops, the same quantity depends on viscosity according to a power law (Rein 1993; Chandra and Avedisian 1991; German and Bertola 2009b), as shown in Fig. 27.

The influence of surface wettability on viscoplastic drop impacts is only noticeable after the end of the inertial expansion stage. In the viscoplastic regime ($\check{B} > 1$), drops impacting on hydrophobic surfaces exhibit only small retractions similar to those observed for high-viscosity Newtonian fluids; impacts on hydrophilic surfaces show no significant retraction, and slow capillary-driven spreading follows directly on from the fast spreading of inertial expansion at low impact velocities. At higher Weber numbers, drop diameters remain nearly constant after maximum spreading (German and Bertola 2009a). These results are substantially confirmed by a more detailed study of the effect of surface wettability and roughness on viscoplastic drop impacts (Saïdi et al. 2011), which compares two smooth substrates with distinct surface energies

(a) **(b)**
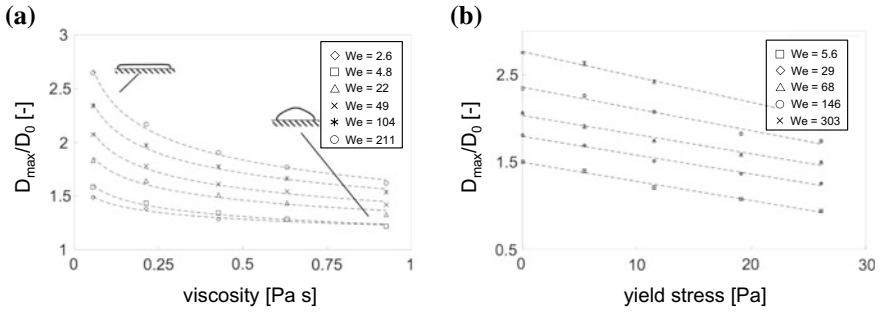
Fig. 27 Maximum spreading diameters of Newtonian glycerol–water mixture (**a**) and viscoplastic commercial hair gel (Carbopol gel) drops (**b**) impacting on a hydrophobic surface (Parafilm). Adapted from German and Bertola (2009a)

and three substrates with similar surface energy but different roughness. The same work also attempts at a quantification of the effects of apparent wall slip (Bertola 2009a; Barnes 1995) on drop impact, however without being conclusive since it was not possible to disentangle the effects of wall slip and surface wettability during experiments. It is speculated that at low inertia, where a gravitational subsidence is observed, the creeping movement amplitude is governed by interfacial effects rather than wall slip, while at high impact velocities, wall slip effects become appreciable only in the last moments of the recoil, when shear rates become very low.

When the drop radius is much larger than the capillary length, $a = \sqrt{\sigma/\rho g}$, surface tension effects can be neglected in comparison with those of gravity; furthermore, large diameters also imply large Weber numbers, so that impacts are dominated by inertia and by the rheological properties of the fluid only. Such experimental conditions are explored in a recent work, which describes the impact of relatively large bits (characteristic sizes between 10 and 30 mm) of various viscoplastic fluids, with yield-stress magnitudes ranging from 4 to 124 Pa, and capillary lengths of the order of a few millimetres (Luu and Forterre 2009). Although these fluids include many aqueous Carbopol dispersions, it must be observed that their yield-stress magnitudes are significantly smaller than the values reported in the open literature for Carbopol dispersions with the same concentrations (Rogers and Barnes 2001). This suggests the Carbopol dispersions used in that work were not prepared following the standard protocol which prescribes fluid neutralisation to ensure it has the highest yield-stress magnitude.

By comparing impacts on a glass surface and on a superhydrophobic surface (contact angle of nearly 180°), these experiments confirm that the maximum spreading diameter of viscoplastic drops is weakly dependent on the surface wettability, and smaller than the capillary limit as defined by Saïdi et al. (2011); unfortunately, similar results are also obtained with high-viscosity Newtonian fluids (German and Bertola 2009b), so that it is not possible to establish whether the yield stress has an independent influence. The most interesting finding of this work is the strong and rapid recoil, which may even be followed by a complete rebound, observed after

the spreading phase of Carbopol drops impacting on the superhydrophobic surface. Since both a recoil driven by surface tension and a purely elastic rebound (the flow threshold corresponds to a shear deformation of about 25%, whereas deformations during impact vary between 100 and 500%) must be ruled out, it is suggested that at such high velocity gradients ($We \approx 1400$) Carbopol dispersions may exhibit a viscoelastic behaviour: during the rapid spreading phase, the flow is faster than the fluid relaxation time, resulting in giant elastic deformations on short timescales. This conjecture is supported by the comparison of experimental results with a minimal model of elasto-viscoplastic inertial spreading, where elasticity is tentatively accounted for by the storage modulus measured below the flow threshold (indeed, a very rough approximation). However, it appears that in order to obtain independent evidence in support of this picture, dynamic rheometric tests with characteristic frequency comparable with the inverse of the impact timescale are necessary.

3.2 Impact on Heated Surfaces

The study of viscoplastic drops impacting on heated surfaces is limited to the case of Leidenfrost drops (Chen and Bertola 2016a). In this context, the Leidenfrost drop impact represents a model system to investigate the behaviour of a viscoplastic fluid where the yield stress is of the same order of magnitude as the Laplace pressure in the absence of wetting.

At the end of the inertial spreading following impact, the liquid lamella is static (i.e. there is no inertial force); thus, retraction results from the competition between the driving surface tension forces (or the Laplace pressure) and the resisting yield stress, and can be expressed in terms of the Bingham-Capillary number, $\check{B}$, defined in Eq. (22). At low values of the Bingham-capillary number ($\check{B} < 1$), the Laplace pressure exceeds the yield stress, and therefore the drop recoils to restore the spherical shape minimising the surface energy; however, for $\check{B} \gtrsim 1$, the surface tension can no longer overcome the yield stress, and causes only little retraction resulting in
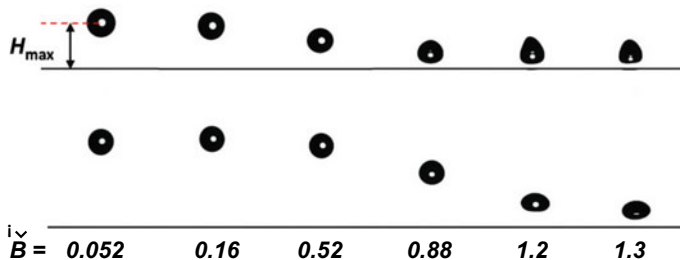
Fig. 28 Images of Carbopol gel drops with $D_0 \approx 3$ mm at maximum bouncing height after impacting on a polished aluminium surface at 400 °C, for different magnitudes of the yield stress and **a** $We \approx 15$ and **b** $We \approx 110$
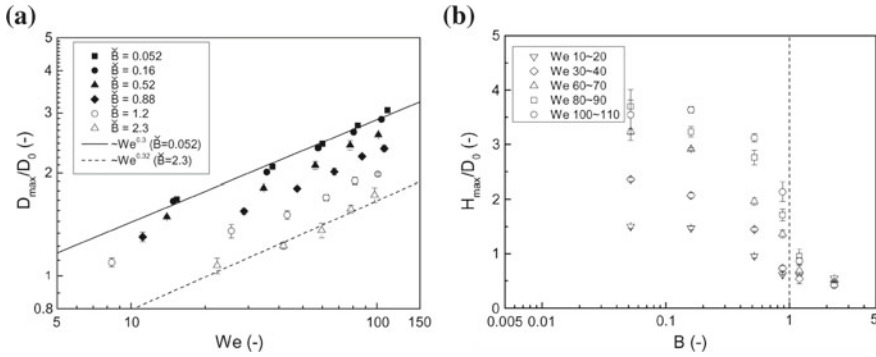
Fig. 29 Maximum spreading diameter (**a**) and maximum bouncing height (**b**) of viscoplastic drops with $D_0 \approx 3$ mm impacting on a polished aluminium surface at $400\,°C$, for different magnitudes of the yield stress and different impact Weber numbers (Chen and Bertola 2016a)

an oblate drop shape. Consequently, rebound is possible only when $\check{B} < 1$, and not when $\check{B} \gtrsim 1$, as shown in (Fig. 28), which displays images of viscoplastic drops at maximum bouncing height for different values of $\check{B}$, for the same impact Weber number.

The maximum spreading diameter, which is proportional to the surface energy of the drop at the end of spreading, hence it can be used to estimate the energy dissipation during the spreading process for a given initial kinetic energy of the drop, which is displayed in Fig. 29a as a function of the impact Weber number. For a given magnitude of the yield stress (i.e. for a given $\check{B}$), the maximum spreading diameter scales approximately as $D_{\max}/D_0 \sim We^{1/3}$, which is in between the scalings resulting from energy conservation ($D_{\max}/D_0 \sim We^{1/2}$) and momentum conservation ($D_{\max}/D_0 \sim We^{1/4}$). The maximum spreading diameter decreases monotonically with respect to the Bingham-capillary number since larger values on the yield stress cause larger viscous dissipation of energy.

The maximum bouncing height of the drop centre of mass during rebound, which indicates how much of the initial impact kinetic energy remains after the impact, hence it can be used to calculate the total energy dissipation during impact when subtracted from the impact kinetic energy, which is displayed in Fig. 29b as a function of the Bingham-capillary number. For drops with a relatively low yield stress ($\check{B} = 0.052$; $\check{B} = 0.16$; $\check{B} = 0.52$), the rebound behaviour is similar to high-viscosity Newtonian drops. When the yield stress is larger than the Laplace pressure ($\check{B} = 1.2$; $\check{B} = 2.3$), the rebound behaviour of drops becomes totally different from the others, and the maximum bouncing height is equal to $0.5D_0$ within experimental error; in addition drops keep a permanent deformation resulting into an oblate shape.

Although the rebound of Leidenfrost drops is usually explained as a consequence of the rapid release of the surface energy stored during inertial spreading, similar to drop rebound on non-heated, hydrophobic surfaces, where there is no vapour film, some authors suggest that the rebound is also due to the formation of a high-pressure

vapour layer between the liquid and solid surface during impact, which acts as an elastic cushion which contributes to propelling the drop off the surface (Rein 2003). However, according to the above results, drops do not rebound when surface forces cannot restore the spherical shape, and therefore one must conclude the contribution of the vapour cushion to rebound is negligible.

4 Atomisation of Non-Newtonian Fluids

In many technical applications, fluids atomised are non-Newtonian in their response to deformation. Examples are paints used for coating purposes and polymer solutions in spray drying processes for polymer powder production. Other fields of application are crop spraying in agriculture, where polymeric compounds are used to suppress the formation of very small drops (anti-drift agents), and rocket propulsion, where solid propellants are being replaced by gel-like fluids. The advantage of such propellants is that they are similarly shelf-stable as solids, while thrust is controllable, which is not the case with solid propellants. In all cases, it is important to predict the drop size spectrum produced by the atomisation process, which depends both on the atomiser and its state of operation, and on liquid material properties. In most cases, the viscous or elastic properties of the liquid depend on the rates of deformation, where viscoelastic liquids may exhibit a memory effect, so that their material properties may additionally depend on the deformation history.

In this section, we first present a review of published research on spray formation from non-Newtonian liquids (Brenn and Plohl 2017).

4.1 Non-Newtonian Jet Breakup and Spray Formation

We first discuss the breakup of laminar jets of non-Newtonian liquids. Mun et al. (1998) showed that in laminar capillary jet breakup, both the breakup length of the jet and the size of the main and satellite drops formed are functions of the concentration and the molecular weight of the polymer in the solution. The authors investigated solutions of poly(ethylene oxide) (PEO) in mixtures of water and glycerol. The composition of the solvent was designed so as to maintain a constant shear viscosity of 5 mPa·s for all the experiments. The extensional viscosity of the liquids, represented by the Trouton ratio, was determined with an opposing-jets rheometer. The experiments showed that, at low molecular weight of the order of 8–100 kDa and low concentration of the polymer between 0.1 and 1 wt%, the jet may be destabilised by the dissolved substance. At higher molecular weight, the jet breakup length increases with the polymer concentration and reaches a plateau. These results explain the different trends in jet breakup length found by Kroesser and Middleman (1969) and by Goldin et al. (1969). Drop size measurements show that the formation of satellites is suppressed only when the jet breakup length increases due to the dissolved polymer.

The increase of drop size due to the polymer is explained by the formation of fewer drops with fluids showing larger breakup lengths.

The breakup of laminar viscoelastic liquid jets was further studied by Christanti and Walker (2001). The jets are produced by a Spraying Systems twin-fluid atomiser without an airflow, essentially using the cylindrical tube in the atomiser for liquid supply to the orifice. The liquid flow rate was kept constant throughout the experiments, with a jet velocity of about 2 m/s and a jet diameter of about 500 μm. The liquids were the glycerol–water mixtures with dissolved PEO of Mun et al. (1998), where three different molecular weights of the polymer and mass fractions up to 0.3% were studied. The extensional viscosity of the solutions was again characterised by an opposing-jets rheometer. The jet breakup experiments show that the polymer content delays the onset of jet surface deformation and, due to the formation of the beads-on-a-string structure, raises the breakup length considerably, up to more than a factor of two as compared to the Newtonian case. Drop size distributions show that the main and satellite drop sizes on average agree with predictions by Rayleigh (1878) and by Bousfield et al. (1986), respectively. Drop size spectra do not change significantly as the concentration of PEO with the molecular weight of 300 kDa is increased from 0.1% to 0.33%. Drop formation from solutions of two different molecular weight PEOs shows to be dominated by the PEO with the higher molecular weight. The smaller PEO helps to suppress the formation of small-size drops. The stretching rates are attempted to be estimated but do not lead to a characterisation of the drop sizes formed as functions of characteristic numbers involving the stress relaxation time.

Christanti and Walker (2002) studied the breakup of laminar jets of PEO solutions investigated by Christanti and Walker (2001), going to higher molecular weights of the PEO up to 5000 kDa and applying defined disturbances to the jet. The focus is on the formation of satellite droplets in the jet breakup. Relaxation times of the solutions were determined from the rates of thinning of filaments formed between the main drops in the breakup process. For dilute solutions, the results agree with the prediction from the Zimm model. Satellite droplet formation may be suppressed due to the polymer action, even at small disturbance amplitudes. The drop size distribution may be controlled by the molecular weight of the polymer. The parameter determining the drop formation process is the product of liquid stress relaxation time to the disturbance growth rate.

Teske and Bilanin (1994) investigated sprays produced from Newtonian liquids by various types of atomisers, representing a non-dimensional drop size by means of characteristic numbers. The authors account for the influences from the velocity ratio between liquid and ambient air, the spraying angle, as well as the Reynolds number $Re = U_j D_j \rho / \mu$ (jet velocity and diameter U_j and D_j, liquid density and dynamic viscosity ρ and μ), the ratio of rotary and axial velocities in rotary atomisation, the liquid Weber number $We = U_j^2 D_j \rho / \sigma$ (surface tension σ of the liquid against the ambient air), as well as the liquid Deborah number, which is defined as the ratio $De = \tau_n U_j / D_j$ of time scales of stress relaxation and flow, τ_n and D_j / U_j, and ratio of elastic to viscous stresses $\Pi_s = c_n D_j / (\mu U_j)$ (stress relaxation amplitude c_n, viscous stress $\mu U_j / D_j$). For water sprays, three non-dimensional

characteristic sizes of the cumulative drop size spectrum are represented as functions $A + B \, Re \, We^b$. This correlation is different for rotary atomisation. The values of A and B are found different (A even with different sign) in the different sprays studied, while the exponent b is constant for each atomiser type ($b = 0.42$ for flat-fan and $b = 0.38$ for pressure-swirl atomisers. The correlation is different for every atomiser geometry, represented by the spray opening angle.

A pressure-drop-based method for measuring the extensional viscosity of dilute polymer solutions was presented by Dexter (1996). The solution to be characterised flows through a packed bed of screens, driven by varying pressure difference. The extensional viscosity is derived directly from the ratio of applied pressure difference to the resulting liquid volume flow rate. The pressure drop is assumed to be due to contributions from shear, elongation and inertia. The equation for the extensional viscosity of the polymer solution derived and evaluated by the measurements does not claim to provide accurate values, but rather a measure for it. A correlation between this quantity and the median drop size in the sprays from a Spraying Systems TeeJet flat-fan atomiser shows that the median drop size increases by a factor of 5 due to a tenfold increase of the extensional viscosity. At the same time, the percentage of drops smaller than 102 μm drops from 30 to 1.

Zhu et al. investigated the effectiveness of anti-drift agents used in agricultural pesticide formulations for suppressing small drop size fractions in pesticide sprays (Zhu et al. 1997). In order to simulate the process of liquid flow through atomisers for agricultural applications, the liquids were exposed to shear. Aqueous solutions of different polymers with different molecular weights and anionicities were studied at different concentrations. The high-shear dynamic and extensional viscosities of liquid samples were determined after different numbers of passes through the test piping. The apparatus used for extensional rheometry was the one by Dexter (1996). The liquids were then atomised by a flat-fan pressure atomiser and drop sizes measured with a phase-Doppler anemometer. The liquid rheometry showed a significant decrease in the shear viscosity against the fresh solution after 11 passes through the apparatus. At that state of the liquid, the drop size $D_{v0.5}$ of the cumulative volume distribution in the sprays decreased by 25%. The authors concluded from this finding that formulations containing polymers of the kinds studied increase in susceptibility to drift as the solution passes several times through the sprayer. This effect is partially suppressed with anionic poly(acrylamide)s by increasing the polymer concentration. Increasing the concentration, however, does not help with non-ionic polymers. The reason for this difference is seen in the different conformations of the molecules in the solution.

Mun and co-workers investigate the atomisation of dilute solutions of PEO for four different molecular weights in the same mixtures of glycerol and water as above (Mun et al. 1999). The solutions were supplied at a constant pressure to several Spraying Systems full jet and cone jet nozzles allowing for a constant liquid volume flow rate. The liquids were characterised for their shear and extensional viscosities, as in Mun et al. (1998), and for the surface tension against air. The volume mean drop size in the sprays increases by a factor of 4 due to 0.095 wt% of 600 kDa PEO in the solution. The exact value depends on the atomiser geometry. At the same time,

the content of drops smaller than 105 µm in the sprays decreases by a factor of 5 or more. From these, follow implications on liquid characterisation, agricultural chemical formulation and atomiser design.

The effect of polymer rigidity and concentration on the atomisation of aqueous polymer solutions by a pressure-swirl atomiser was studied by Harrison et al. (1999). The focus of the study is on the opening angle of the spray cone as a function of the concentration of the polymers. The non-monotonous behaviour of the spray cone angle with varying polymer concentration for flexible (poly(acrylamide)), semi-rigid (CMC) and rigid polymers (Xanthan gum) is related to the extensional viscosity of the solutions. The spray cone formation and sheet breakup are enhanced at low polymer concentrations and retarded with increasing concentration. The drop sizes produced are not reported.

Romagnoli et al. (2000) study the spraying of solutions of PEO and hydroxypropyl guar gum (HPG) in water and in aqueous solutions of poly(ethylene glycol). Atomisers were flat-fan TeeJet nozzles from Spraying Systems. The liquid extensional viscosity was rheologically characterised, and their surface tension was measured. Drop sizes were measured with a Malvern instrument at a constant distance from the atomiser orifice. Drop size spectra in sprays from two solutions with very similar extensional viscosities, but surface tensions differing by 17%, are found to be very different. This finding allows for the conclusion that, in the cases investigated, the extensional viscosity is not the most important factor determining the drop size.

In their experiments on viscoelastic fluids atomisation, Thompson and Rothstein (2007) used solutions containing worm-like micelles of CTAB, with sodium salicylate at the same molarity. The nozzles were flat-fan and pressure-swirl atomisers from the company McMaster-Carr. Oscillatory and steady shear rheometry revealed the shear viscosity as a function of the shear rate and the storage and loss moduli as functions of the oscillation frequency. Zero-shear viscosities up to 68 Pa s are reached, accompanied by stress relaxation times of the order of 30 s. For the flat-fan atomisers, the authors present a chart for the pairing of the Weber and elasticity numbers, We and El, of regimes of stable sheet or sheet breakup mechanisms where the elasticity number is defined as $El := \lambda_1 \nu_0 / R^2$ (stress relaxation time λ_1, zero-shear rate liquid kinematic viscosity ν_0, jet radius R) and is $O(10^6)$ in the study. The regimes seem very similar for two atomisers with opening angles differing by a factor of 2. As a dominant breakup mechanism, the formation of perforations in the fan-shaped sheets is found. The corresponding nomogram for the pressure-swirl atomiser accounts for the various shapes of liquid systems formed for varying Weber and elasticity numbers from a jet to a ruptured cone. Drop size dependencies on liquid properties and setting of atomiser operation are not reported.

Williams et al. (2008) investigated the influence of different poly(acrylamide)s dissolved in water at various concentrations on the Sauter-mean drop size in sprays of the solutions produced by an agricultural spray nozzle from Lurmark. The polymers were non-ionic, anionic or cationic. A characterisation of the solutions included shear and extensional rheometry, as well as tensiometry. The Sauter-mean drop size in the sprays was measured with a Malvern Spraytec RS instrument. Bouncing of 1 mm drops impacting an inclined plant leaf at a set velocity was characterised by

the bouncing distance. The polymer solutions exhibited shear-thinning and strain-hardening behaviour. The shear viscosities at low shear rates reported are O(1 Pa s) at polymer concentrations O(0.07 wt%). The flow curves exhibit a hump around shear rates of 500 s^{-1}. The strain hardening is seen by an increase of the apparent extensional viscosity with the Hencky strain. The thinning curves of the filament diameter in the extensional rheometry show a transition from a viscoelastic to a Newtonian behaviour, as seen in other studies also (Stelter et al. 2002a). Spray Sauter-mean drop sizes increase by approximately 10% while the extensional viscosity of the liquid increases by a factor of four.

Park and Harrison (2008) studied the effects of elasticity of the liquid on the performance of the spray produced with a Spraying Systems Turbo TeeJet nozzle. The context is spraying of pesticide formulations and spray painting. An increased extensional viscosity raises the breakup lengths of sheets. In the sheet breakup, filaments connecting the nascent drops are formed. The stability of these filaments leads to increased drop sizes and suppresses the fine droplet fractions in the sprays. The polymer employed was PEO. The solvents used were different mixtures of water and glycerol, and the largest polymer mass fraction in the solutions was 0.6 wt%. The resulting shear viscosity was around 5 mPa for all the solutions studied. The extensional characteristics of the solutions are not reported. The volumetric mean drop diameter in the sprays increases by 40% as 0.6 wt% of PEO with a molecular weight of 100 kDa are added to the Newtonian solvent.

Negri and Ciezki (2015) investigated the spraying behaviour of 13 Boger fluids, with an impinging-jet injector. The application is rocket propulsion with gelled propellants. The formation of spray drops by breakup of liquid sheets formed by the mutual impact of two inclined cylindrical liquid jets is ligament mediated. For characterising the ligaments, the authors defined a thread parameter as the ratio of the sum of the third powers to the sum of the second powers of the major axis lengths of the filaments visualised in the process. The definition, therefore, is analogous to that of a Sauter-mean drop diameter. It is assumed that the thread parameter is relevant for quantifying the drop size distribution in the spray. The data show that the thread parameter is correlated with the stress relaxation time of the Boger fluids. It is shown that the elasticity number $El = \lambda_1 \nu / D_j^2$ (liquid kinematic viscosity ν, jet diameter D_j), representing the ratio of the stress relaxation time to a viscous diffusive timescale, correlates well with the thread parameter. The thread parameter itself, however, is presented in dimensional form.

The group of Keshavarz et al. (2015) studied the formation of drops in an air-assisted spraying process of aqueous PEO solutions with dynamic shear viscosities around 3 m Pa s, polymer mass fractions between 0.01 and 0.1% and small molecular weights between 300 and 1000 Da. Careful extensional rheometric characterisation of the solutions includes the presentation of a jet-thinning-based method originally proposed by Schümmer and Tebel (1983), now called ROJER. This method allows the stress relaxation time even of dilute solutions to be measured, where the limitations of the CaBER method do not allow this. Findings by Marmottant and Villermaux (2004), as well as estimates on time to breakup of a filament producing the drops and a time scale characteristic for the influence from the atomising air, lead to a

correlation of the mean drop size with the influencing characteristic numbers We, Oh and De. Here, $Oh = \mu/(\sigma D \rho)^{1/2}$ is the Ohnesorge number, representing a ratio of a capillary to a viscous timescale. The accuracy of predictions of this model remains to be verified. We name this paper despite the twin-fluid atomisation process since it presents a mean drop size model.

In the following, we discuss the instability of liquid jets and sheets formed for producing sprays by well-known types of atomisers. For reasons of relevance for the application, we then go into the details of spray formation by sheet breakup.

4.2 Instability of Non-Newtonian Jets and Sheets

Due to the instability of jets and sheets in contact with an ambient gaseous medium, deformations of the free surface of the liquid system, which are caused by dynamic influences, may grow either in space or time, or both. The deformations, therefore, lead to the breakup of the system into drops. The mechanism of instability may be either capillary (the Rayleigh mechanism), due to a tangential acceleration of the gas–liquid interface (the Kelvin–Helmholtz mechanism), or due to a normal acceleration of the interface (the Rayleigh–Taylor mechanism), or due to more than one of these mechanisms. For jets, we concentrate our discussion on the capillary instability, while for sheets, we look at the Kelvin–Helmholtz mechanism. We discuss details of the linear stability analysis of jets and sheets in a vacuum and in a gaseous ambient medium, respectively.

Linear stability analysis of a laminar liquid jet We sketch the linear temporal capillary instability analysis of a liquid jet. The jet is assumed to be axisymmetric around the z-axis of the cylindrical coordinate system. The liquid is treated as incompressible and linearly viscoelastic. Dynamic influences from an ambient medium, as well as body forces, are not accounted for.

The jet surface in Fig. 30 is described as $r_s(z, t) = a + \eta(z, t)$, where η is the deformation against the undisturbed cylinder of radius a. The variables and equations of change are non-dimensionalised with the undeformed jet radius a, the capillary timescale $(\rho a^3/\sigma)^{1/2}$, the capillary pressure σ/a and the reference stress
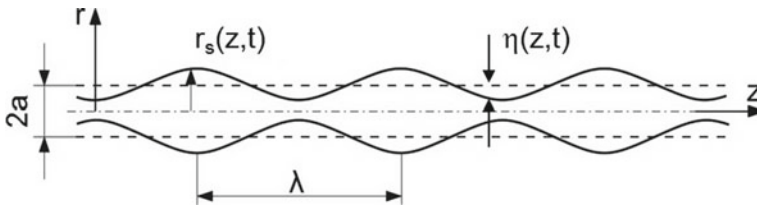

Fig. 30 Surface of an axially symmetric capillary jet with sinuous deformation of wavelength λ

$\mu_0(\sigma/\rho a^3)^{1/2}$ for length, time, pressure and extra stress, respectively. Here, ρ is the liquid density, σ is the surface tension and μ_0 is the liquid zero-shear viscosity.

For the problem at hand, the linearised equation of continuity and the two linearised components of the momentum equation in the radial (r) and axial (z) directions read

$$\frac{1}{r}\frac{\partial}{\partial r}(ru_r) + \frac{\partial u_z}{\partial z} = 0 \tag{23}$$

$$\frac{\partial u_r}{\partial t} = -\frac{\partial p}{\partial r} + Oh_0\left[\frac{1}{r}\frac{\partial}{\partial r}(r\tau_{rr}) - \frac{\tau_{\theta\theta}}{r} + \frac{\partial\tau_{rz}}{\partial z}\right] \tag{24}$$

$$\frac{\partial u_z}{\partial t} = -\frac{\partial p}{\partial z} + Oh_0\left[\frac{1}{r}\frac{\partial}{\partial r}(r\tau_{rz}) + \frac{\partial\tau_{zz}}{\partial z}\right] \tag{25}$$

where $Oh_0 = \mu_0/(\sigma a\rho)^{1/2}$. As the rheological constitutive equation (RCE), we use the linearised form of the Oldroyd-B model, which reads

$$\tau + De_1\frac{\partial\tau}{\partial t} = 2\left(D + De_2\frac{\partial D}{\partial t}\right) \tag{26}$$

where the symbols τ and D denote the extra-stress and the rate-of-deformation tensors, respectively. De_1 and De_2 are the Deborah numbers corresponding to the stress relaxation and deformation retardation times, λ_1 and λ_2, respectively.

This set of equations is solved subject to linearised boundary and initial conditions. The first boundary condition is the kinematic condition that the radial rate of deformation of the jet surface equals the radial velocity component evaluated at the position of the undeformed cylindrical jet. The second condition is the dynamic condition stating that there is no transfer of shear stress across the jet surface. The third condition is the dynamic condition that the (r, r) component of the total stress tensor must be zero. The two latter conditions imply that the dynamic influence from an ambient medium is disregarded. The three boundary conditions, which are to be evaluated at $r = 1$, read

$$u_r = \frac{\partial\eta}{\partial t} \tag{27}$$

$$\tau_{rz} = 0 \tag{28}$$

$$-p + Oh_0\tau_{rr} - \left(\eta + \frac{\partial^2\eta}{\partial z^2}\right) = 0 \tag{29}$$

The term in the last equation depending on the deformation η represents the linearised jet surface curvature. Furthermore, the initial conditions are

$$\eta(0, z) = \cos kz \quad \text{and} \quad \frac{\partial\eta}{\partial t}(0, z) = 0 \tag{30}$$

indicating that the jet is initially deformed from the cylindrical shape according to a cosine function, and that the surface is initially at rest.

These equations describe the linear problem. They exhibit solutions which are well known from the literature (Goldin et al. 1969; Brenn et al. 2000). For finding the solutions of the equations of motion, we first solve the RCE. All the flow field variables depend on time as per the exponential function $\exp(-\alpha t)$. The quantity α in the exponent of this function is a complex angular frequency which may reduce to a growth or damping rate of the jet surface deformation in aperiodic cases. Given this time dependency, we find for the extra-stress tensor, the solution

$$\tau = 2\frac{1 - De_2\alpha}{1 - De_1\alpha}D =: 2\beta D \tag{31}$$

This means that the extra-stress tensor of the linear viscoelastic fluid differs from the form for a Newtonian material just by a frequency-dependent factor β in front of the rate-of-deformation tensor. This fluid is, therefore, formally identical to a Newtonian one, so that all the results obtained for Newtonian liquids may be transcribed immediately to the present linear viscoelastic case, just with the Ohnesorge number Oh of the Newtonian case replaced by $Oh_v := \beta Oh_0$. The velocity field in the jet due to the deformation reads

$$u_r = \hat{\eta}Oh_v\left[(l_v^2 + k^2)\frac{I_1(kr)}{I_1(k)} - 2k^2\frac{I_1(l_vr)}{I_1(l_v)}\right]\exp(ikz - \alpha t) \tag{32}$$

$$u_z = i\hat{\eta}Oh_v\left[(l_v^2 + k^2)\frac{I_0(kr)}{I_1(k)} - 2kl_v\frac{I_0(l_vr)}{I_1(l_v)}\right]\exp(ikz - \alpha t) \tag{33}$$

where $l_v^2 = k^2 - \alpha/Oh_v$ defines a modified wave number and $\hat{\eta}$ is the deformation amplitude. In all complex solutions of the real differential equations, we mean the real parts of the solutions only. For the pressure field, we obtain

$$p = \hat{\eta}\frac{\alpha}{k}\left(2k^2Oh_v - \alpha\right)\frac{I_0(kr)}{I_1(k)}\exp(ikz - \alpha t) \tag{34}$$

The dispersion relation of the jet is found by introducing the velocity and pressure fields in the jet into the dynamic zero normal stress boundary condition (29). The result is the well-known relation

$$\alpha^2 - 2\alpha k^2 Oh_v\left[1 - \frac{1}{k}\frac{I_1(k)}{I_0(k)} - \frac{2kl_v}{l_v^2 + k^2}\frac{I_1(k)}{I_0(k)}\left(\frac{I_0(l_v)}{I_1(l_v)} - \frac{1}{l_v}\right)\right] =$$
$$= k\left(1 - k^2\right)\frac{I_1(k)}{I_0(k)}\frac{l_v^2 - k^2}{l_v^2 + k^2} \tag{35}$$

which was first presented by Goldin et al. (1969) and for the Newtonian liquid by Rayleigh (1892). For zero liquid viscosity ($Oh_v \to 0$), this relation reduces to the Rayleigh (1878) result for the inviscid jet in a vacuum.
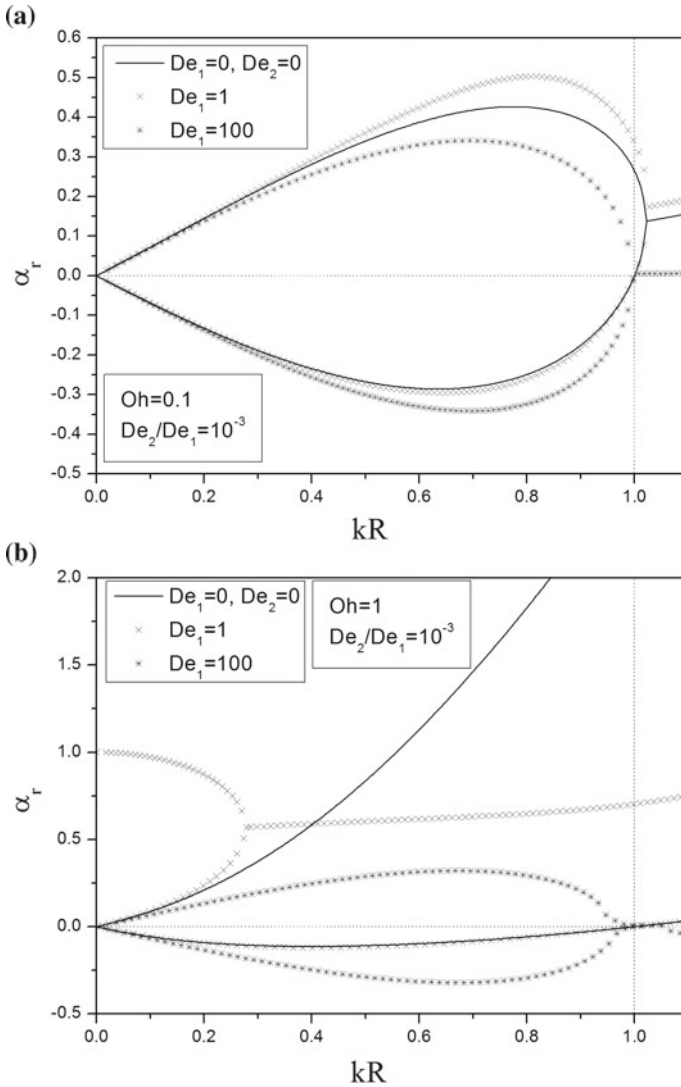
Fig. 31 Dispersion relations of Newtonian and linear viscoelastic jets for varying De_1 at **a** $Oh = 0.1$ and **b** $Oh = 1$. The ratio $De_2/De_1 = 10^{-3}$ is kept constant

The dispersion relation (35) emerging from the linear stability analysis is depicted in Fig. 31 for viscoelastic jets together with the corresponding curves for the Newtonian jet with the same value of Oh. For the ratio De_2/De_1, we set the value of 10^{-3}, corresponding to findings by Brenn and Plohl (2015). This value deviates by several orders of magnitude from the ones often used in the literature. It was found to be the correct value following from oscillating drop experiments for measuring the deformation retardation time.

For disturbance wave numbers $0 \leq k \leq 1$ and for Newtonian fluid, the relation has two real solutions, one positive and one negative. Due to the formulation of the time dependency by the exponential function with a minus sign in front of the exponent αt, the unstable behaviour of the jet is associated with the negative value. For wave numbers $k > 1$, the relation has two complex conjugate solutions with a positive real part. The two values of α represent two waves on the jet surface travelling in different directions and with different phase velocities. In contrast to this, for the linear viscoelastic fluid, the structure of the solutions may be different. At the smaller Oh in Fig. 31a, we find two real solutions with different signs for the viscoelastic case as well as for the Newtonian. At the higher Oh in Fig. 31b, however, the real solutions are replaced by complex ones at $k \geq 0.28$ already. This is an important finding for the viscoelastic jet stability behaviour.

It is seen in Fig. 31 that, at a given Oh, for both De_1 depicted, the viscoelastic jets exhibit larger growth rates of disturbances than their Newtonian counterparts. This would mean that we expect the viscoelastic jet to break up more rapidly than a corresponding Newtonian jet, which is in clear contradiction to the experimental observation showing beads-on-a-string structures with filaments of long lifetime. This discrepancy can be explained by the nonlinear nature of the formation of the latter structure. A description of the dynamics of that phenomenon, therefore, requires a nonlinear stability analysis with account for the strain-hardening behaviour of the liquids.

Linear stability analysis of a sheet The corresponding analysis for a plane liquid sheet is analogous to the analysis for the jet. The geometry of a sheet, however, suggests formulation of the equations of motion in Cartesian coordinates. Furthermore, in the description of the sheet surface deformation, the possibility of the formation of two different shapes of the sheet surface must be accounted for: the deformation may be sinuous or varicose, depending on the relative phases of the wave-like deformations of the two surfaces. The sinuous case is sketched in Fig. 32. We look at this deformation only, since in terms of the order of magnitude of disturbance growth, it is the more 'dangerous' case for the sheet. The resulting dispersion relation for the sinuous sheet deformation reads

$$Oh_{vs}^2 \left[(l^2 + k^2)^2 \tanh k - 4k^3 l \tanh l \right] + \alpha^2 \frac{\rho_g}{\rho} + k^3 = 0 \qquad (36)$$

where the Ohnesorge number for the viscoelastic sheet

$$Oh_{vs} = \frac{\mu_0}{(\sigma H \rho)^{1/2}} \frac{1 - (\alpha - ikU_0)\lambda_2}{1 - (\alpha - ikU_0)\lambda_1} \qquad (37)$$

and, in contrast to the jet, the length scale for non-dimensionalisation is the half thickness H of the sheet and ρ_g is the density of the gas ambient to the liquid sheet. The dispersion relation is depicted for five different combinations of Ohnesorge, Deborah and gas Weber number in Fig. 33. It is seen that high Deborah and Weber numbers enhance the sheet instability. Comparing the disturbance growth rates predicted
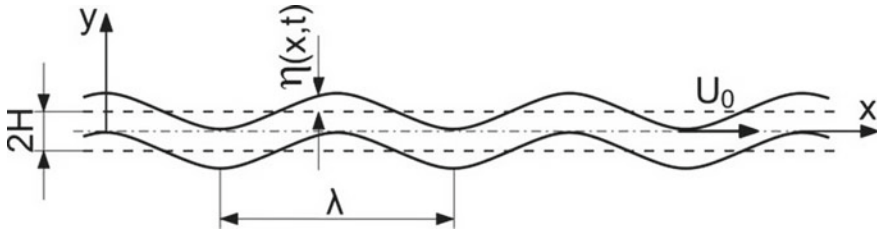
Fig. 32 Surface of a plane liquid sheet with sinuous deformation of wavelength λ
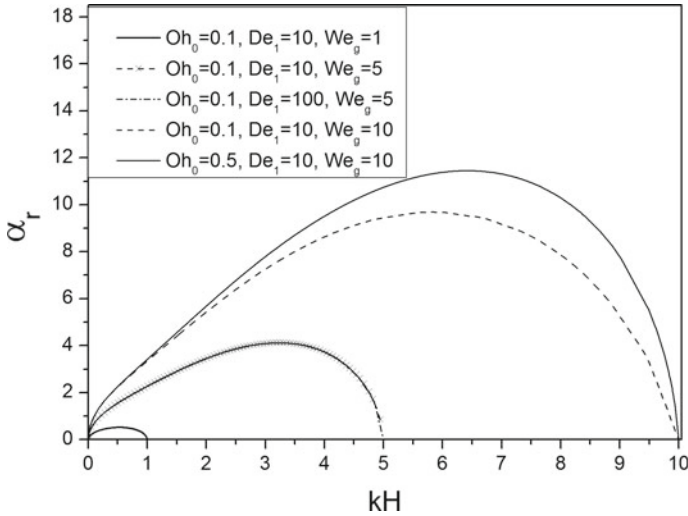
Fig. 33 Dispersion relation of linear viscoelastic sheets for sinuous surface deformation. The ratio $De_2/De_1 = 10^{-3}$

by these data, it is seen that, corresponding to the Kelvin–Helmholtz instability mechanism, the gas Weber number has the strongest influence on the destabilisation of the sheet. While for a given set of parameters, the increase of De_1 by one order of magnitude has a very small influence only, and increasing the gas Weber number from 1 to 5 destabilises the sheet significantly.

In the following section, we discuss experimental studies on the breakup of liquid jets.

4.3 Experimental Studies on Jet Breakup

Experiments on the breakup of laminar jets show marked differences between Newtonian and viscoelastic liquids: while Newtonian jets exhibit the well-known behaviour of spatial and/or temporal growth of surface deformation amplitudes until drops pinch

off, viscoelastic, in particular, strain-hardening liquids form the so-called 'beads-on-a-string' structure, exhibiting drops connected by fine filaments which can live very long and retard the pinch-off of drops.

In drop formation by viscoelastic liquid jet breakup, the importance of stress relaxation in the liquid jet and its timescale were quantified in the literature. As mentioned in Sect. 4.1, Christanti and Walker (2001) investigated the breakup of laminar liquid jets into drops via the beads-on-a-string structure, using solutions of poly(ethylene oxide) (PEO) of varying molecular weight in different mixtures of glycerol and water. The solutions were designed to keep the dynamic viscosity of 5 mPa·s throughout. Drop sizes were measured by image analysis. The drop size spectra measured exhibit bimodal shapes, as depicted in Fig. 34. The size spectrum for the solutions of low molecular PEO exhibits peaks at the size predicted by Rayleigh's inviscid, linear stability analysis (Rayleigh 1878) (the main drops), and at a size smaller by a factor 3 than the main drops (satellite droplets) in agreement with the computational results for inviscid liquid by Bousfield et al. (1986). Given the small Ohnesorge number $O(10^{-2})$ of the jets in these experiments, the good match of the experimental findings with inviscid analytical and computational results is not surprising. The experiments with higher molecular weight of the dissolved polymer in Fig. 34b, however, show that the peak at the smaller size in the drop size spectrum may be suppressed if, at the polymer concentrations at hand, the molecular weight exceeds a value around 10^3kDa. This finding is explained by the stress relaxation time λ_1 of the liquid, which increases with the molecular weight of the polymer in a given solvent. The values of λ_1 of the test liquids presented by Christanti and Walker (2002) are derived from the Zimm model and the Flory–Fox equation and accurate enough to relate their non-dimensional equivalent, the Deborah number $De_1 = \lambda_1(8\sigma/\rho d^3)^{1/2}$, to the suppressed satellite droplet formation. The result is that, for $De_1 \gg 1$, satellite droplets are suppressed (Christanti and Walker 2002).

For the reason of this phenomenon, the related jet breakup length is difficult to predict. An experimental study by Stelter (2001) showed that the relation found by Kroesser and Middleman (1969) may be generalised by forming the Ohnesorge number with an elongational viscosity. The scaling behaviour of this quantity is derived from the elongational characterisation of the liquid.

4.4 Rheological Characterisation of Viscoelastic Liquids

For the evaluation of deformation and breakup models for liquid jets and sheets for spray formation, viscoelastic liquids must be characterised rheologically so as to account for their viscous and elastic behaviour. In many applications, the polymer content is low, so that the shear viscosity does not appreciably deviate from the viscosity of the solvent. The elongational viscosity caused by the deformation of the polymer macromolecules in the solvent, however, may nonetheless be substantially higher than the Trouton viscosity of the Newtonian solvent in uniaxial elongational flow, which is three times the shear viscosity.
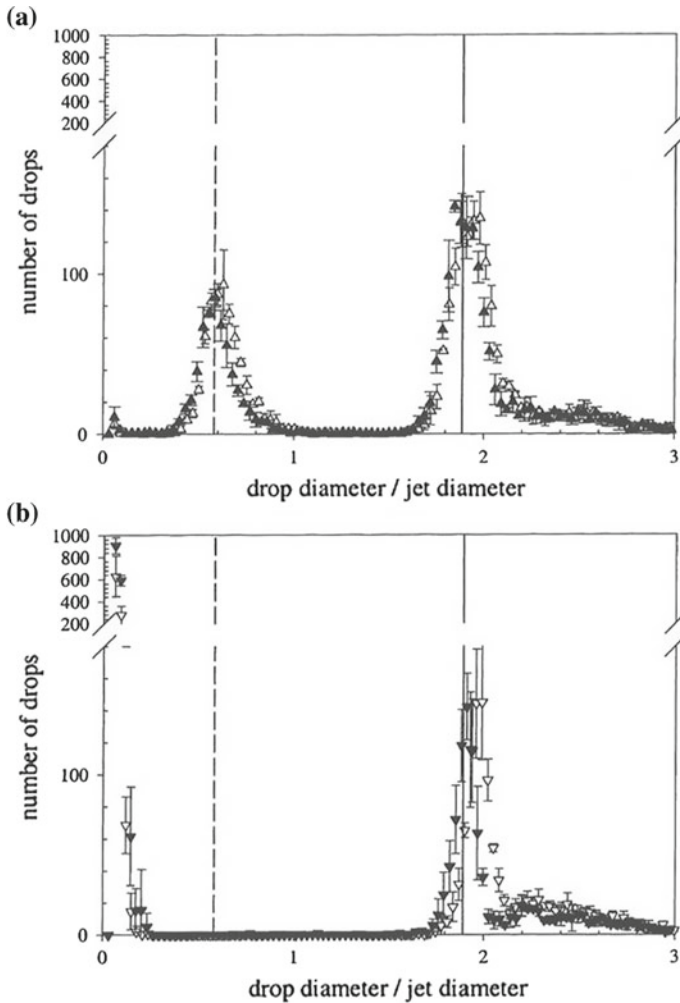
Fig. 34 Drop size spectra measured by image processing in viscoelastic jet breakup (Christanti and Walker 2001). **a**—100 kDa PEO at 0.3%wt. (open triangles) and 1%wt. (filled triangles); **b**—1000 kDa PEO at 0.05%wt (open triangles down) and 0.14%wt. (filled triangles down). Reprinted from Christanti and Walker (2001) with permission from Elsevier

Complex fluids with a polymeric dissolved component at an appreciable concentration may exhibit shear-thinning behaviour, i.e. their shear viscosity decreases with increasing shear rate. This material property is measured in the steady flow of a shear rheometer. Furthermore, viscoelastic liquids exhibit a viscosity which is formulated as a complex conjugate quantity $\mu^* = \mu' - i\mu''$, where the real part corresponds to a viscosity, and the imaginary part to an elasticity. This material property relates an extra stress to a rate of deformation. An alternative for describing

the viscoelastic behaviour of a material at small deformations is to relate the extra stress to a deformation. The material property in this relation is a complex modulus $G^* = G' + iG''$, where G' is the storage and G'' is the loss modulus. The former quantifies elasticity and the latter the viscous loss. Consequently, in a deformation varying harmonically with time at the angular frequency α, complex viscosity and modulus are related as per $G^* = i\alpha\mu^*$. Comparing the real and imaginary parts of the two quantities G^* and μ^*, the storage modulus is related to the imaginary viscosity (the elasticity) as per $G' = \alpha\mu''$ and the loss modulus is $G'' = \alpha\mu'$.

Sufficiently elastic liquids may be characterised by analysing liquid filaments in a filament-stretching elongational rheometer, now termed as the CaBER-type instrument. This device forms a filament between two plates by a step-strain process and measures the thinning of the filament with time. The drainage flow in the filament flow corresponds closely to the actual filament thinning flow in liquid jet and sheet breakup, so that liquid characterisation on the basis of this process is appropriate for spray formation modelling and produces liquid properties relevant to atomisation.

The thinning of the filament is predicted theoretically. Assuming that inertia and body forces are unimportant in this flow, the balance equations of mass and of momentum in the direction of the symmetry (z) axis of the filament are integrated over the filament cross section to obtain a quasi-one-dimensional description of the slender system at hand. The rheological constitutive equation (RCE) of the viscoelastic liquid for formulating the axial normal extra stress is taken from a micro-rheological approach (Yarin 1993). The result is the set of equations

$$\frac{\partial a^2}{\partial t} + \frac{\partial V a^2}{\partial z} = 0 \tag{38}$$

$$0 = \frac{\partial}{\partial z}\left\{\sigma_{zz}a^2 + 2\sigma a\left[1 + \left(\frac{\partial a}{\partial z}\right)^2\right]^{-1/2}\right\} \tag{39}$$

where a is the filament radius and V is the axial velocity component. In viscoelastic liquid filaments, the axial normal stress

$$\sigma_{zz} = \sigma/a \tag{40}$$

is of the order of the stress imposed by the capillary pressure. The axial normal stress is composed of a capillary and a polymeric contribution. Using a microscopic material model relying on macromolecular deformations, we may write

$$\sigma_{zz} = -\sigma/a + ckA_{zz} \tag{41}$$

where c is the concentration of the polymer molecules in the solution, k is the elastic constant of the coiled molecules in the solution and A_{zz} is the zz-component of the orientation–deformation tensor (Stelter et al. 2000; Yarin 1993). The stress is, therefore, related to the deformation of the polymer molecules in the solution. In

the present uniaxial stretching flow, the deformation is dominated by the tensor component A_{zz}, which in the material model is governed by the equation

$$\frac{dA_{zz}}{dt} = 2A_{zz}\frac{\partial V}{\partial z} - \frac{A_{zz}}{\lambda_1} \tag{42}$$

From Eqs. (40) and (41), it follows that $A_{zz} = 2\sigma/cka$. Substituting this result into (42), we obtain the differential equation

$$\frac{d}{dt}\left(\frac{1}{a}\right) = -\frac{4}{a^2}\frac{da}{dt} - \frac{1}{a\lambda_1} \tag{43}$$

for the filament radius $a(t)$. The solution representing the evolution of the diameter $d(t) = 2a(t)$ of a viscoelastic filament with time reads

$$d(t) = d_0 \exp\left(-t/3\lambda_1\right) \tag{44}$$

The analogous analysis for the Newtonian fluid is based on the composition of the stress σ_{zz} in a Newtonian filament

$$\sigma_{zz} = -\frac{\sigma}{a} + 3\mu\frac{\partial V}{\partial z} \tag{45}$$

from the capillary pressure σ/a and the viscous normal stress governed by the Trouton viscosity 3μ. Assuming that this stress is zero in a Newtonian filament (Stelter et al. 2000; Entov and Hinch 1997), the differential equation for the Newtonian filament diameter emerging from Eq. (45) has the solution

$$d_N(t) = d_0 - \frac{\sigma}{3\mu}t \tag{46}$$

This equation, however, bases on the assumption that the filament diameter does not depend on the z-coordinate. It therefore predicts the wrong filament diameter evolution if the filament is not cylindrical. An image like Fig. 35 shows that this may be the case in a viscous, Newtonian liquid filament (Stelter 2001). For this case, Papageorgiou (1995) developed a self-similar description of the jet surface shape, from which he derived the corrected filament diameter evolution with time

$$d_{N,P}(t) = d_0 - 0.4254\frac{\sigma}{3\mu}t \tag{47}$$

The filament diameter evolution reveals the straining rate

$$\dot{\epsilon} \equiv \frac{\partial V}{\partial z} = -\frac{2}{a}\frac{da}{dt} \tag{48}$$

Fig. 35 Filament of the Newtonian silicon oil Wacker W1000 ($\sigma = 21.2$ mN/m, $\mu = 970$ mPas) in a CaBER-type filament-stretching elongational rheometer (Stelter 2001)

The elongational viscosity in uniaxial straining flow follows from the relation

$$\sigma_{zz} = \mu_{el}\dot{\epsilon} \tag{49}$$

For the viscoelastic liquid, the viscoelastic elongational viscosity is

$$\mu_{el}(t) = \frac{3\sigma\lambda_1}{d_0} \exp\left(t/3\lambda_1\right) \tag{50}$$

while for the Newtonian fluid in uniaxial elongational flow, the elongational viscosity is certainly the Trouton viscosity

$$\mu_{el,N} = 3\mu \tag{51}$$

The corresponding strain rate in the viscoelastic case is obtained as

$$\dot{\varepsilon} = \frac{2}{3\lambda_1} \tag{52}$$

and in the Newtonian case

$$\dot{\varepsilon}_N(t) = \frac{2\sigma}{3\mu d(t)} \tag{53}$$
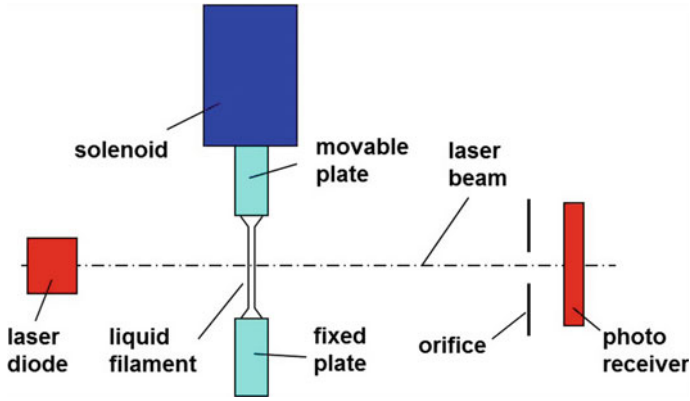
Fig. 36 Setup of an elongational rheometer of the CaBER type (Stelter et al. 2002b)
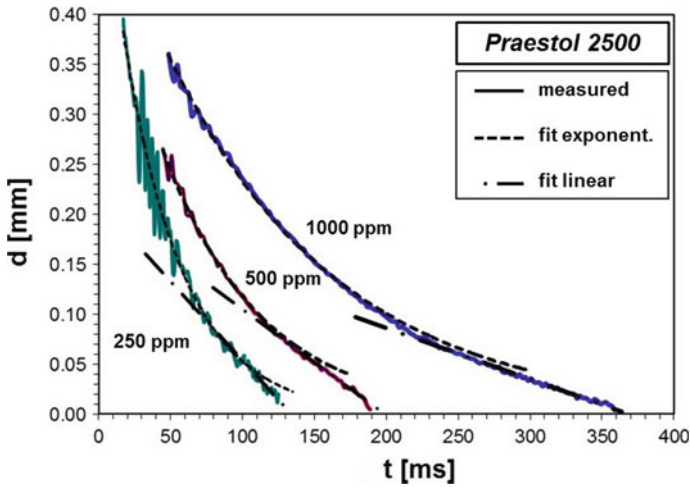
Fig. 37 Data $d(t)$ from the elongational rheometer in Fig. 36 for aqueous Praestol 2500 solutions of three different polymer concentrations (Stelter 2001)

It is interesting to note that, in contrast to the Newtonian liquid, the strain rate of the viscoelastic liquid does not depend on time. The Deborah number $De_1 = \lambda_1 \dot{\varepsilon}$, therefore, exhibits the constant value of $2/3$, which is in favour of a comparability of results from various experiments with this technique.

The experimental realisation of this characterisation technique yields a device as presented by Stelter et al. (2002b) and sketched in Fig. 36. Measurements of the filament diameter as a function of time with aqueous various polymer solutions, such as shown in Fig. 37, showed that the viscoelastic filament thinning does not follow the predicted exponential law throughout its lifetime, but changes its behaviour before pinching. The reason is that the stretching of the polymer macromolecules in the
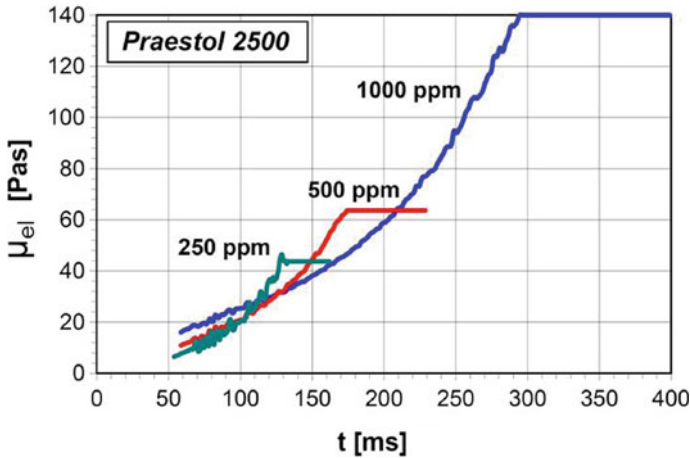
Fig. 38 Elongational viscosity of the filaments shown in Fig. 37 for aqueous Praestol 2500 solutions of three different polymer concentrations (Stelter 2001)

solutions is limited by a maximum achievable molecular deformation (Yarin 1990). From the instant on when this state of maximum deformation is reached, the liquid behaves no longer as elastic, but as a Newtonian fluid with a very high elongational viscosity termed as the 'steady terminal elongational viscosity' (STEV), as shown in Fig. 38. These curves correspond to the data shown in Fig. 10 of Tirtaatmadja and Sridhar (1993), which also show an increase of the elongational viscosity with time and a limitation of the increase by a terminal value. At this state, the thinning of the filament turns from exponential to linear, i.e. the liquid dynamic response upon deformation turns from fully elastic to viscous, Newtonian. This is seen clearly in the measurement data in Fig. 37. In the thinning of liquid filaments in the course of a ligament-mediated spraying process, this same process occurs, so that we may assume that drop formation is dominated by this terminal viscosity.

A systematic study of the steady terminal elongational viscosity (STEV) of solutions of flexible and rigid, rod-like polymers in various solvents was carried out by Stelter et al. (2002a). It was seen that, for a given polymer in its solvent, the value of this material property increases with the polymer concentration. The same trend is seen for the stress relaxation time λ_1. It is an evident option now to depict the former material property of the solutions as a function of the latter in a diagram. This diagram is shown in Fig. 39. In this study, the mass fraction of Praestol 2500 in water, in ethylene glycol and in a methanol–water mixture varied between 62.5 and 500 ppm, and in two different glycerol–water mixtures between 50 and 500 ppm. The mass fractions of poly(ethylene oxide) (PEO) in water were 25 and 50 ppm, and of the copolymer of carboxy-methylcellulose with poly(acrylamide) varied between 1000 and 4000 ppm. For the hydrolysed Praestol 2540 and two poly(acrylamides) named Sedipur (BASF), the mass fraction in water varied between 31.25 and 500 ppm, and for xanthan gum between 1000 and 4000 ppm (Stelter et al. 2002a). The STEV of
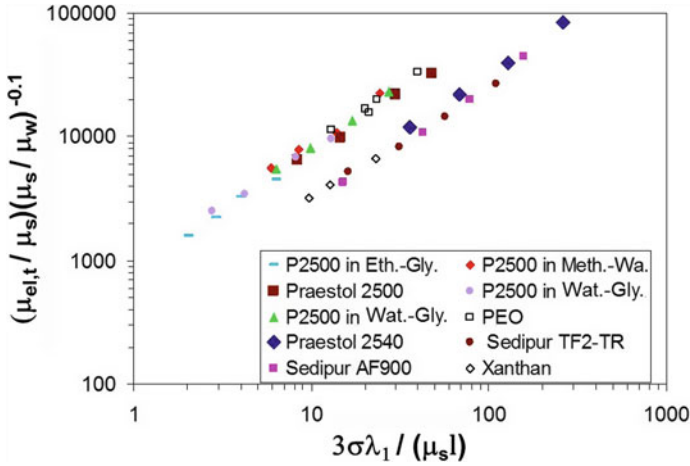
Fig. 39 Non-dimensional steady terminal elongational viscosity of solutions of polymers in various solvents. The data collapse into two groups, one for the flexible and another for the rigid, rod-like polymers (Stelter et al. 2002a)

PEO solutions at higher concentrations could not be measured due to the formation of beads-on-a-string structures which prevent the measurement of the filament thinning in the late stages of the draining. It is interesting to note that there exists a dependency of the steady terminal elongational viscosity on the stress relaxation time of the liquid. One other finding is that the flexible and the rigid, rod-like polymers behave differently in the stretching process of filament thinning. All the data group along two different lines in the diagram, where the upper line is formed by the flexible and the lower one by the rigid, rod-like polymers. The two terminal elongational viscosities for the aqueous solutions are given as functions of the stress relaxation time by the equations

$$\mu_{el,t,flex} = 3074.9\lambda_1 + 0.003 \tag{54}$$

$$\mu_{el,t,rigid} = 1288.1\lambda_1 + 0.003 \tag{55}$$

where the elongational viscosities are obtained in Pa·s if the stress relaxation time is entered in s (Stelter et al. 2002b). The ratio of the factors in front of λ_1 flexible to rigid exhibits the value of 2.39. This empirical value will gain big importance for the characterisation of spray formation processes from solutions of flexible or rigid, rod-like polymers in water, as will be pointed out later.

Forming non-dimensional numbers with this viscosity to characterise drop formation may be a promising approach to a universal description of ligament-mediated drop formation from Newtonian and viscoelastic liquids.

4.5 Non-Newtonian Sprays

For the design of sprays, the description of their formation should include a prediction of the drop size appropriate for the application, either in a spectral, local or in an integral, global manner. Due to the complicated liquid breakup and flow processes producing the spray drops, the most promising approach is to formulate a normalised mean drop size of the spray as a function of a product of powers of non-dimensional numbers relevant to the process. The correct representation, i.e. the correct set of non-dimensional numbers, follows from a dimensional analysis and turns out to be, e.g., of the form $D_{32}/d = f(Re_{el}, We)$. In this function, the Reynolds number Re_{el} formulated with an equivalent elongational viscosity turns out crucial for a universal representation of the formation of sprays from Newtonian and non-Newtonian viscoelastic liquids.

Mechanical degradation of polymers in strong flows Molecular properties of macromolecular compounds may be subject to changes under strong mechanical loads. Strong straining and shearing flows tend to deform the macromolecules of (flexible) polymeric substances and to turn the molecules of rigid, rod-like polymers. Flexible macromolecules are uncoiled and stretched in straining and shearing flows (de Gennes 1974). The mechanical strength of the molecules is limited. Strong straining and shearing flows may, therefore, lead to mechanical degradation of the polymer in the solution, breaking the macromolecules into smaller pieces. This reduction of the molecular weight of the polymer changes the stress relaxation time. Since this material property is important in the modelling of the rheological material behaviour of the polymer solutions, the potential of the flows through the atomisers for breaking the macromolecules was investigated. Varying the flow rate through various flat-fan atomisers, the strain and shear rates in the nozzle flow were varied (Stelter et al. 2002b). Liquid samples were taken from the sprays and allowed to rest long enough so that foam and air bubbles in the liquid disappeared. Measuring the liquid stress relaxation time of these sprayed liquid samples revealed values which were systematically less than the relaxation times of the fresh solutions. The results for aqueous solutions of four different polymers at varying mass fraction are shown in Fig. 40, where λ_1 and $\lambda_{1,0}$ are the stress relaxation times of the sprayed and of the fresh solution, respectively. The independent variable

$$De^* = \lambda_{1,0} \frac{U}{d_e} \frac{d_{\min}}{d_{\max}} \qquad (56)$$

is a modified convective Deborah number accounting for the contraction of the cross section in the atomiser and for the flow rate through the nozzle. The diameters characterising the bore geometries of the flat-fan atomisers used in the present study are listed in Table 1. The fact that the time elapsed between the spraying of the test liquids and the measurements of the relaxation time indicates that the molecular process reducing the relaxation time led to a permanent change of the molecular properties of the dissolved polymer. This is seen in contrast to the (reversible) break
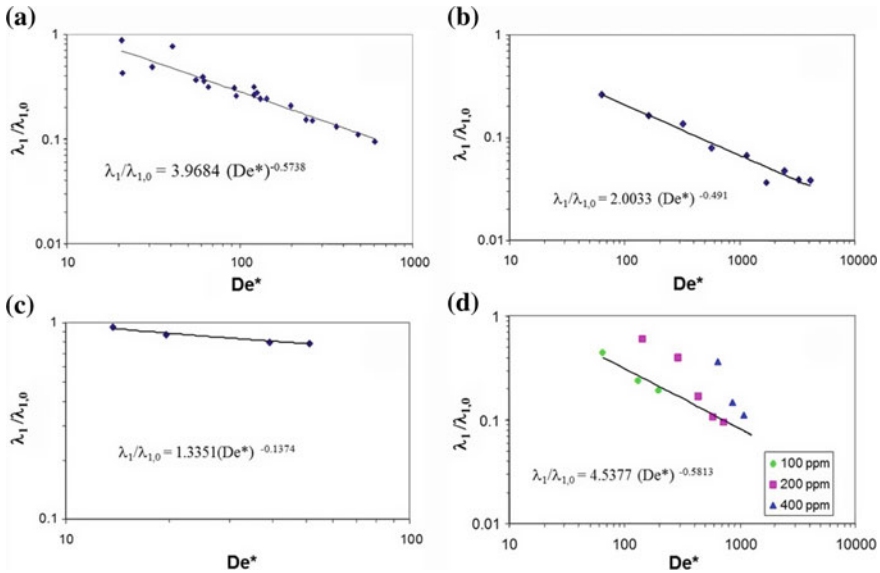
Fig. 40 Decrease of the stress relaxation time λ_1 against the values of the fresh solution due to mechanical degradation of the polymers in the nozzle flow. Aqueous solutions of **a**—Praestol 2500 at 200 ppm wt., **b**—PEO at 100 ppm wt., **c**—CMC-g-PAM at 1500 ppm wt., **d**—Praestol 2540 at the mass fractions in the legend (Stelter et al. 2002b)

down of micelles in micellar solutions by straining or shearing. The micelles are re-established after some time when the solution is kept at rest. This is not the case in the present polymer solutions.

Sprays from flat-fan sheet breakup Pressure atomisers of the flat-fan type are used in many fields, among them for pesticide spraying in agriculture. The shape of the bore in the atomiser produces a flat-fan liquid sheet at the atomiser exit. The sheet is Kelvin–Helmholtz unstable and develops waves on its surface, which are unstable and break the sheet into ligaments. The ligaments finally break down into the spray drops (Dombrowski and Johns 1963). Spray formation by flat-fan pressure atomisers is, therefore, ligament mediated and belongs to the group of processes we presently discuss.

Figure 41 shows a flat-fan sheet of a 100 ppm wt. aqueous poly(acrylamide) solution Praestol 2500 produced by an atomiser Lechler 632.304 at the flow rate of 40 l/h. The zoom-in photograph shows beads-on-a-string structured ligaments and drops which clearly indicates the importance of the ligament-thinning process found in the rheometric characterisation above in the formation of drops. The approach to represent drop formation by properties of the ligament in its late stages of thinning, in particular, by its steady terminal elongational viscosity, is therefore promising. For developing this universal characterisation of the atomisation result, series of drop size measurements in flat-fan sprays were carried out with a phase-Doppler
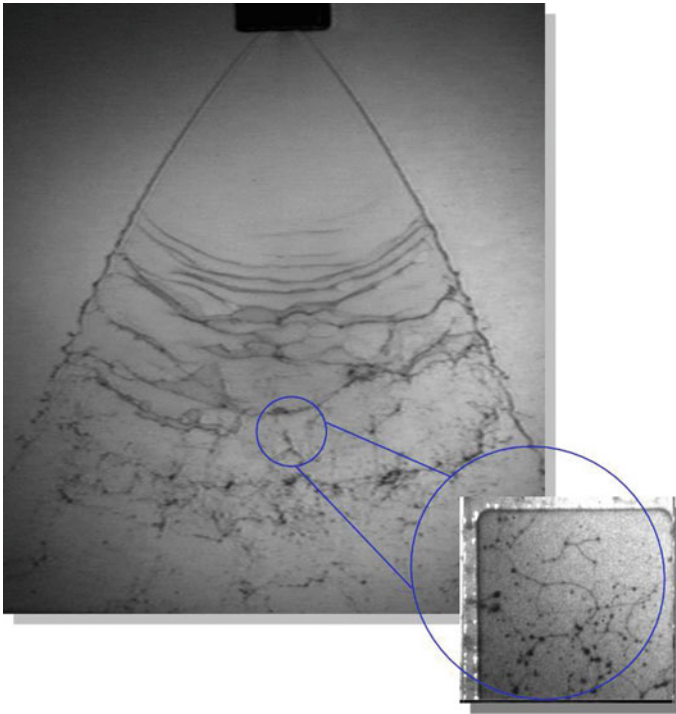
Fig. 41 Flat-fan-shaped sheet of a 100 ppm wt. aqueous Praestol 2500 solution from the flat-fan atomiser Lechler 632.304 (Stelter 2001). The zoom-in shows that the sheet breakup goes along with the formation of beads-on-a-string structures originating from ligament thinning

anemometer (PDA) by Stelter et al. (2002b). The measurements were carried out in a spray region close to the breakup zone so as to characterise the primary atomisation result without influence from drop–drop interactions and evaporation. Global mean drop sizes are derived from the measured local drop sizes, weighted by the local spray cross-sectional areas and the local drop number fluxes. In this manner, the global mean Sauter-mean drop size of a spray characterised by phase-Doppler measurements may be deduced from the local measurement data as per

$$D_{32} = \frac{\sum\limits_{j=1}^{J} \sum\limits_{i=1}^{I} d_{i,j}^3 \dot{n}_{i,j} \Delta A_j}{\sum\limits_{j=1}^{J} \sum\limits_{i=1}^{I} d_{i,j}^2 \dot{n}_{i,j} \Delta A_j} \tag{57}$$

In this equation, $d_{i,j}$ is the drop size and $\dot{n}_{i,j}$ is the number flux of drops of size class i detected at position j in the spray and ΔA_j is the partial area of the spray cross section represented by the local measurements at position j.

Table 1 Properties of flat-fan atomisers and test liquids in the experiments of Fig. 42

#	Nozzle type	d_e [mm]	d_{min} [mm]	d_{max} [mm]	Flow rates [l/h]	Polymer mass fraction [ppm]
1	Spraying systems TEEJET 80015	0.76	0.5	1.16	20–55	0–400 P2500, P2540
2	Spraying systems TEEJET 80015	0.74	0.4	1.16	30–50	0
3	Lechler 632.301	0.7	0.52	0.93	30–41	0–400 P2500

Table 1 lists the geometrical properties of the three flat-fan atomisers used in the study, together with the flow rates covered by these experiments and the polymers with the range of their mass fractions in the aqueous solutions.

In physical processes as complicated as spray formation, dimensional analysis is a way to find a universal representation of the dependencies of the process result on the various influencing parameters. For a dimensional analysis of the atomisation process, we start from the list of relevant parameters, which is the global mean Sauter-mean drop diameter D_{32}, a length scale d of the atomiser, for which we take the area-equivalent orifice diameter, the volume flow rate-equivalent liquid velocity U as well as the liquid properties σ, ρ and $\mu_{el,eff}$, where the latter is an effective elongational viscosity which we formulate as $De_d k \sigma \lambda_1/d$, with the convective Deborah number $De_d = \lambda_1 U/d$ and the empirical factor k allowing for the representation of the spray property at hand. Given the three basic dimensions involved in the problem, this list of six relevant parameters results in three non-dimensional numbers characterising the spray formation process, which are $Re_{el}=Ud\rho/\mu_{el,eff}$, $We=U^2 d\rho/\sigma$ and D_{32}/d. We therefore seek to represent the normalised global mean Sauter-mean diameter of the spray drops as a function $D_{32}/d=f(Re_{el}, We)$ (Stelter et al. 2002b).

In doing so, we start from the representation of the normalised D_{32} of pure solvent, i.e. water sprays, by a function $D_{32}/d = C Re_{el}^m We^n$. Fitting the function to the experimental data means determining the parameters C, m and n. The next step is to fit the data for the solutions of flexible polymers in water to those of the water sprays by appropriately selecting the empirical factor k, while keeping C, m and n constant. We arrive at a universal representation of these two groups of sprays by selecting $k = k_{flexible} = 1/1500$. In doing the same for the data from the rigid, rod-like polymers dissolved in water, we find that the empirical factor $k_{flexible}$ must yield a ratio to $k = k_{rigid}$ for these polymers of 2.39, which equals the ratio of $(d\mu_{el,t}/d\lambda_1)_{flexible}/(d\mu_{el,t}/d\lambda_1)_{rigid}$ from the rheometric characterisation. This finding applies to the representation of all the spray properties investigated here. The factor k for the solutions of rigid polymers, therefore, is $k_{rigid} = 1/3581$ (Stelter et al. 2002b).

The diagram in Fig. 42 shows the non-dimensional global Sauter-mean drop size of sprays of water, together with aqueous solutions of flexible and of rigid, rod-like polymers produced by flat-fan atomisers. Given the three different atomiser geometries
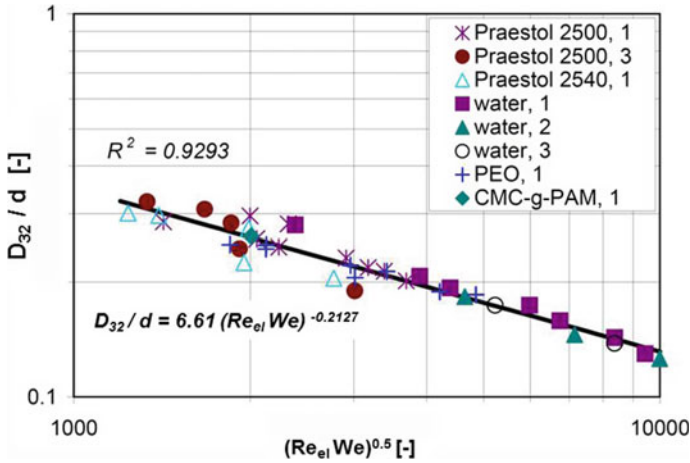
Fig. 42 Normalised global Sauter-mean drop size of water and polymer solution sprays from three different flat-fan atomisers (Stelter et al. 2002b)

and the four different polymers plus the water sprays involved, the universality in the representation of the mean drop size is excellent. This approach is, therefore, promising for a universal representation of drop sizes in sprays of viscoelastic liquids produced by flat-fan pressure atomisers. The data show the expected effect that a decrease of the characteristic number $Re_{el} We$ makes the mean Sauter-mean drop size in the flat-fan sprays increase. This is plausible and observed in Newtonian sprays also, where an increase of, e.g., the liquid velocity makes mean spray drop sizes decrease and vice versa. It is interesting to note that, for the viscoelastic sprays, the Reynolds number newly defined with the effective elongational viscosity $\mu_{el,eff}$ turns equivalent to the inverse of a capillary Deborah number squared as per $Re_{el} = 1/(kDe_c^2)$ with $De_c = \lambda_1/(\sigma/\rho d^3)^{1/2}$. The characteristic number determining the global mean Sauter-mean drop size in the flat-fan sprays, therefore, rather corresponds to a ratio We/De_c^2. The convective influence on the sheet breakup is represented by the Weber number, where the thermodynamic state of the ambient air was not varied in the above experiments, so that it does not appear in the analysis, despite its influence through the Kelvin–Helmholtz instability (Stelter et al. 2002b).

In the experimental study discussed here, the above-presented characterisation of sprays from flat-fan atomisers was found to hold for spectral properties of the spray drop ensembles also. The design of liquids to be atomised, e.g., for crop spraying in agriculture, aims to minimise the formation of small drops in the atomisation process, which are transported by wind to undesired places and may harm cultures. The polymeric compounds used for this purpose are called 'anti-drift agents'. It is, therefore, desirable to predict the influence of polymeric ingredients in the liquid recipes on the drop size spectra. In investigating this potential of the present characterisation method, the data in Fig. 43 were found.
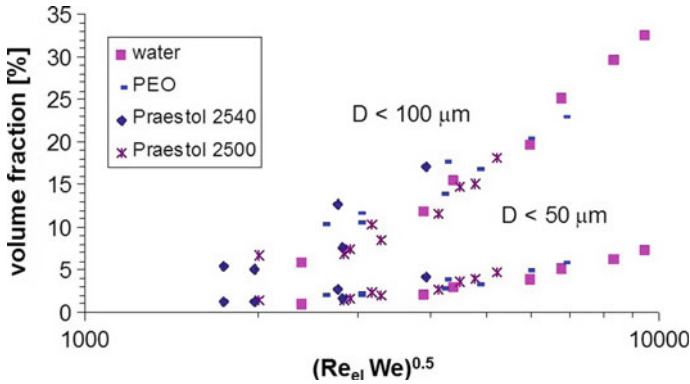
Fig. 43 Volume fractions of drops with sizes less than 100 and 50 µm in the global drop size spectra of various sprays from flat-fan spray atomiser 1 (Stelter et al. 2002b)

Table 2 Properties of pressure-swirl atomisers and test liquids in the experiments of Fig. 44

Atomiser #	Atomiser type	d_e[mm]	Flow rates [l/h]	Polymer mass fraction [ppm]
1	Schlick model 121 V	0.45	6–14	0–100 P2500, PEO
2	Schlick model 121 V	0.72	10–22	0–100 P2500, PEO

Sprays from hollow-cone sheet breakup Pressure atomisers producing sprays of the hollow-cone type, called pressure-swirl atomisers, are used in many applications, among them spray drying and spray painting. The atomiser type stands out for the production of fine droplets at a moderate liquid flow rate. This is due to the formation of a conical liquid sheet at the atomiser exit with an air core. The sheet thins downstream and due to its Kelvin–Helmholtz instability, it develops waves on the surface which grow and break the sheet into ligaments. The ligaments finally break down into the spray drops. The sheet differs geometrically from the flat-fan case in that it is closed in the circumferential direction, thus avoiding the formation of a free rim at a sheet edge since this does not exist. Spray formation by pressure-swirl atomisers is ligament mediated and belongs to the group of processes we presently discuss. A series of experiments with PDA drop size measurements were carried out using various aqueous polymer solutions for this atomiser type also. Table 2 lists the geometrical properties of the two pressure-swirl atomisers used in the study, together with the flow rates covered by these experiments and the polymers with the range of their mass fractions in the aqueous solutions.

The dimensional analysis of the atomisation process by a pressure-swirl atomiser differs from the flat-can case in that the liquid sheet thickness at the atomiser orifice is an additional parameter, which is fixed by the atomiser bore geometry in flat-fan atomisers. This additional parameter is represented by quantifying the ratio of the pressure drop across the atomiser to the kinetic energy (or dynamic pressure)
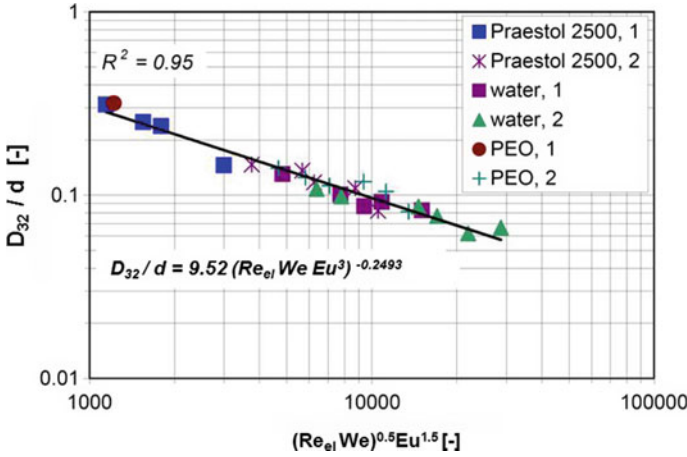
Fig. 44 Normalised global Sauter-mean drop size of water and aqueous polymer solution sprays from two different pressure-swirl atomisers (Stelter et al. 2002b)

of the liquid produced, which is called the Euler number Eu. This number adds to the set of numbers found for flat-fan atomisation. The non-dimensional numbers representing the atomisation process with pressure-swirl atomisers are, therefore, $Re_{el}=U D\rho/\mu_{el,eff}$, $We=U^2 d\rho/\sigma$, $Eu = \Delta p/\rho U^2$ and D_{32}/d. We seek to represent the normalised global Sauter-mean diameter of the spray drops as a function $D_{32}/d = f(Re_{el}, We, Eu)$.

The diagram in Fig. 44 shows the non-dimensional global Sauter-mean drop size of sprays of water and aqueous polymer solutions produced by pressure-swirl atomisers (Stelter et al. 2002b). For spray formation by pressure-swirl atomisers, solutions of flexible polymers were investigated only. Given the two different atomiser geometries and the two different aqueous polymer solutions plus the water sprays involved, the universality in the representation of the mean drop size is excellent. This approach is promising for a universal representation of drop sizes in sprays of viscoelastic liquids produced by pressure atomisers.

4.6 Concluding Remarks

The study on spray formation from viscoelastic liquids presented shows that, for the modelling of spray formation by viscoelastic liquid sheet breakup, an appropriate characterisation of the liquid rheological behaviour upon deformation is needed. For spray formation by pre-filming atomisers, which break down to form the spray drops, mediated by ligaments, the property of particular importance is the behaviour in uni-axial elongational flow. In measurements of the elongational viscosity, it turns out that the ligament lifetime and the final drop size formed by their breakup are determined

by a steady terminal value of the elongational viscosity, which we managed to relate to the stress relaxation time of the liquid. Further research in this field will replace the empiricism of the model presented by fundamental knowledge about the molecular deformation and alignment processes in the filament-stretching flow.

References

Attané P, Girard F, Morin V (2007) An energy balance approach of the dynamics of drop impact on a solid surface. Phys Fluids 19(1):012101

Barnes HA (1995) A review of the slip (wall depletion) of polymer solutions, emulsions and particle suspensions in viscometers: its cause, character, and cure. J Non-Newton Fluid Mech 56(3):221–251

Barnes AC, Neilson GW, Enderby JE (1995) The structure and dynamics of aqueous solutions containing complex molecules. J Mol Liq 65–66:99–106

Bartolo D, Boudaoud A, Narcy G, Bonn D (2007) Dynamics of non-newtonian droplets. Phys Rev Lett 99(17)

Bazilevskii AV, Voronkov SI, Entov VM, Rozhkov AN (1981) On orientational effects at breakup of jets and threads of dilute polymer-solutions. Dokl Akad Nauk SSSR 257(2):336–339

Bechtel SE, Bogy DB, Talke FE (1981) Impact of a liquid drop against a flat surface. IBM J Res Dev 25(6):963–971

Bergeron V, Martin J-Y, Vovelle L (1998) Interaction of droplets with a surface: impact and adhesion. In: Fifth international symposium on adjuvants and agrochemicals memphis, Tennessee, USA, 17–21 Aug 1998

Bergeron V, Bonn D, Martin J-Y, Vovelle L (2000) Controlling droplet deposition with polymer additives. Nature 405:772–775

Bergeron V, Martin J-Y, Vovelle L (2003) Use of polymers as sticking agents. US Pat 6:534–563

Bernardin JD, Mudawar I (2002) A cavity activation and bubble growth model of the leidenfrost point. J Heat Transf 124(5):864–874

Bertola V (2004) Drop impact on a hot surface: effect of a polymer additive. Experiments in fluids 37(5):653–664

Bertola V (2009a) Wicking with a yield stress fluid. J Phys Condens Matter 21(3)

Bertola V (2009b) An experimental study of bouncing leidenfrost drops: comparison between newtonian and viscoelastic liquids. Int J Heat Mass Transf 52(7):1786–1793

Bertola V (2010) Effect of polymer additives on the apparent dynamic contact angle of impacting drops. Colloids Surf A: Physicochem Eng Asp 363(1–3):135–140

Bertola V (2013) Dynamic wetting of dilute polymer solutions: the case of impacting droplets. Adv Colloid Interface Sci 193–194:1–11

Bertola V (2014) Effect of polymer concentration on the dynamics of dilute polymer solution drops impacting on heated surfaces in the leidenfrost regime. Exp Therm Fluid Sci 52:259–269

Bertola V (2015) An impact regime map for water drops impacting on heated surfaces. Int J Heat Mass Transf 85:430–437

Bertola V, Sefiane K (2005) Controlling secondary atomization during drop impact on hot surfaces by polymer additives. Phys Fluids 17(10):108104

Bertola V, Wang M (2015) Dynamic contact angle of dilute polymer solution drops impacting on a hydrophobic surface. Colloids Surf A: Physicochem Eng Asp 481:600–608

Biance A-L, Chevy F, Clanet C, Lagubeau G, Quéré D (2006) On the elasticity of an inertial liquid shock. J Fluid Mech 554(1):47–66

Biolè D, Bertola V (2015a) The fuzzy interface of a drop. Comput Vis Sci 17(1):19–32

Biolè D, Bertola V (2015b) A goniometric mask to measure contact angles from digital images of liquid drops. Colloids Surf A: Physicochem Eng Asp 467:149–156

Biolè D, Bertola V (2015c) The role of the microscale contact line dynamics in the wetting behaviour of complex fluids. Arch Mech 67(5):401–414

Biolè D, Wang M, Bertola V (2016) Assessment of direct image processing methods to measure the apparent contact angle of liquid drops. Exp Therm Fluid Sci 76:296–305

Black K, Bertola V (2013) Non-newtonian leidenfrost drops. At Sprays 23(3):233–247

Bonhoeffer B, Kwade A, Juhnke M (2017) Impact of formulation properties and process parameters on the dispensing and depositioning of drug nanosuspensions using micro-valve technology. J Pharmaceut Sci 106(4):1102–1110

Borodin O, Smith GD (2000) Molecular dynamics simulations of poly(ethylene oxide)/lii melts. 2. dynamic properties. Macromolecules 33(6):2273–2283

Bousfield DW, Keunings R, Marrucci G, Denn MM (1986) Nonlinear analysis of the surface tension driven breakup of viscoelastic filaments. J Non-Newton Fluid Mech 21:79–97

Brandrup J, Immergut EH, Grulke EA, Abe A, Bloch DR (2005) Polymer handbook, 4th edn. Wiley

Brenn G, Plohl G (2015) The oscillating drop method for measuring the deformation retardation time of viscoelastic liquids. J Non-Newton Fluid Mech 223:88–97

Brenn G, Plohl G (2017) The formation of drops from viscoelastic liquid jets and sheets—an overview. At Sprays 27:285–302

Brenn G, Liu ZB, Durst F (2000) Linear analysis of the temporal instability of axisymmetrical non-newtonian liquid jets. Int J Multiph Flow 26:1621–1644

Chandra S, Avedisian CT (1991) On the collision of a droplet with a solid surface. Proc R Soci Lond A: Math Phys Eng Sci 432:13–41

Chandrasekhar S (1961) Hydrodynamic and hydromagnetic stability. International series of monographs on physics. Clarendon Press

Chen L, Wang Y, Peng X, Zhu Q, Zhang K (2018) Impact dynamics of aqueous polymer droplets on superhydrophobic surfaces. Macromolucles 51(19):7817–7827

Chen S, Bertola V (2016a) The impact of viscoplastic drops on a heated surface in the leidenfrost regime. Soft Matter 12:7624–7631

Chen S, Bertola V (2016b) Jumps, somersaults, and symmetry breaking in leidenfrost drops. Phys Rev E 94(2)

Chibowski E (2003) Surface free energy of a solid from contact angle hysteresis. Adv Colloid Interface Sci 103(2):149–172

Chibowski E (2007) On some relations between advancing, receding and Young's contact angles. Adv Colloid Interface Sci 133(1):51–59

Christanti Y, Walker LM (2001) Surface tension driven jet break up of strain-hardening polymer solutions. J Non-Newton Fluid Mech 100:9–26

Christanti Y, Walker LM (2002) Effect of fluid relaxation time of dilute polymer solutions on jet breakup due to a forced disturbance. J Rheol 46:733–748

Clanet C, Béguin C, Richard D, Quéré D (2004) Maximal deformation of an impacting drop. J Fluid Mech 517:199–208

Coussot P, Gaulard F (2005) Gravity flow instability of viscoplastic materials: the ketchup drip. Phys Rev E 72:031409

Crooks R, Cooper-White J, Boger DV (2001) The role of dynamic surface tension and elasticity on the dynamics of drop impact. Chem Eng Sci 56:5575–5592

de Gennes PG (1974) Coil-stretch transition of dilute flexible polymers under ultrahigh velocity gradients. J Chem Phys 60(12):5030–5042

de Gennes PG (1985) Wetting: statics and dynamics. Rev Mod Phys 57(3):827–863

Dexter RW (1996) Measurement of extensional viscosity of polymer solutions and its effects on atomization from a spray nozzle. At Sprays 6:167–191

Dombrowski N, Johns WR (1963) The aerodynamic instability and disintegration of viscous liquid sheets. Chem Eng Sci 18:203–214

Dussan EB (1985) On the ability of drops or bubbles to stick to non-horizontal surfaces of solids. Part 2. small drops or bubbles having contact angles of arbitrary size. J Fluid Mech 151:1–20

Eggers J (1997) Nonlinear dynamics and breakup of free-surface flows. Rev Mod Phys 69:865–930

Eggers J, Fontelos MA, Josserand C, Zaleski S (2010) Drop dynamics after impact on a solid wall: theory and simulations. Phys Fluids 22(6):062101

Entov VM, Hinch EJ (1997) Effect of a spectrum of relaxation times on the capillary thinning of a filament of elastic liquid. J Non-Newton Fluid Mech 72:31–53

Ford RE, Furmidge CGL (1967) Impact and spreading of spray drops on foliar surfaces. Soc Chem Ind Monogr 25:32–417

Fujimoto H, Oku Y, Ogihara T, Takuda H (2010) Hydrodynamics and boiling phenomena of water droplets impinging on hot solid. Int J Multiph Flow 36(8):620–642. ISSN 0301-9322

German G, Bertola V (2009a) Impact of shear-thinning and yield-stress drops on solid substrates. J Phys: Condens Matter 21(37):375111

German G, Bertola V (2009b) Review of drop impact models and validation with high-viscosity newtonian fluids. At Sprays 19(8)

German G, Bertola V (2010a) The free-fall of viscoplastic drops. J Non-Newton Fluid Mech 165(13–14):825–828

German G, Bertola V (2010b) Formation of viscoplastic drops by capillary breakup. Phys Fluids 22(3):033101

Goldin M, Yerushalmi J, Pfeffer R, Shinnar R (1969) Breakup of a laminar capillary jet of a viscoelastic fluid. J Fluid Mech 38:689–711

Gottfried BS, Lee CJ, Bell KJ (1966) The leidenfrost phenomenon: film boiling of liquid droplets on a flat plate. Int J Heat Mass Transf 9(11):1167–1188

Harrison GM, Mun R, Cooper G, Boger DV (1999) A note on the effect of polymer rigidity and concentration on spray atomisation. J Non-Newton Fluid Mech 85:93–104

Hartnett JP, Hu RYZ (1986) Role of rheology in boiling studies of viscoelastic liquids. Int Commun Heat Mass Transf 13(6):627–637. ISSN 0735-1933

Josserand C, Thoroddsen ST (2016) Drop impact on a solid surface. Ann Rev Fluid Mech 48(1):365–391

Kalashnikov VN, Askarov AN (1989) Relaxation time of elastic stresses in liquids with small additions of soluble polymers of high molecular weights. J Eng Phys Thermophys 57(2):874–878

Keshavarz B, Sharma V, Houze EC, Koerner MR, Moore JR, Cotts PM, Threlfall-Holmes P, McKinley GH (2015) Studying the effects of extensional properties on atomization of weakly viscoelastic solutions using rayleigh ohnesorge jetting extensional rheometry (rojer). J Non-Newton Fluid Mech 222:171–189

Kim KY, Kang SL, Kwak H-Y (2004) Bubble nucleation and growth in polymer solutions. Polym Eng Sci 44(10):1890–1899

Kim JH, Shi W-X, Larson RG (2007) Methods of stretching dna molecules using flow fields. Langmuir 23(2):755–764

Kroesser FW, Middleman S (1969) Viscoelastic jet stability. AIChE J 15:383–386

Kroger M (2015) Simple, admissible, and accurate approximants of the inverse langevin and brillouin functions, relevant for strong polymer deformations and flows. J Non-Newton Fluid Mech 223:77–87

Lefebvre A (1988) At Sprays. Combustion (Hemisphere Publishing Corporation). Taylor & Francis. ISBN 9780891166030

Lin SP, Reitz RD (1998) Drop and spray formation from a liquid jet. Ann Rev Fluid Mech 30(1):85–105

Lindner A, Vermant J, Bonn D (2003) How to obtain the elongational viscosity of dilute polymer solutions? Physica A 319:125–133

Lumley JL (1973) Drag reduction in turbulent flow by polymer additives. J Polym Sci: Macromol Rev 7(1):263–290

Luu L-H, Forterre Y (2009) Drop impact of yield-stress fluids. J Fluid Mech 632:301–327

Mao T, Kuhn D, Tran H (1997) Spread and rebound of liquid droplets upon impact on flat surfaces. AIChE J 43(9):2169–2179

Marmottant P, Villermaux E (2004) Fragmentation of stretched liquid ligaments. Phys Fluids 16:2732–2741

Moreira ALN, Moita AS, Panao MR (2010) Advances and challenges in explaining fuel spray impingement: how much of single droplet impact research is useful? Prog Energy Combust Sci 36(5):554–580

Mun RP, Byars JA, Boger DV (1998) The effects of polymer concentration and molecular weight on the breakup of laminar capillary jets. J Non-Newton Fluid Mech 74:285–297

Mun RP, Young BW, Boger DV (1999) Atomisation of dilute polymer solutions in agricultural spray nozzles. J Non-Newton Fluid Mech 83:163–178

Mundo C, Sommerfeld M, Tropea C (1995) Droplet-wall collisions: experimental studies of the deformation and breakup process. Int J Multiph Flow 21(2):151–173

Negri M, Ciezki HK (2015) Effect of elasticity of boger fluids on the atomization behaviour of an impinging jet injector. At Sprays 25:695–714

Nigen S (2005) Experimental investigation of the impact of an apparent yield-stress material. At Sprays 15:103–117

Oliveira MSN, Yeh R, McKinley GH (2006) Iterated stretching, extensional rheology and formation of beads-on-a-string structures in polymer solutions. J Non-Newton Fluid Mech 137(1):137–148. Extensional Flow

Papageorgiou DT (1995) On the breakup of viscous liquid threads. Phys Fluids 7(7):1529–1544

Park GY, Harrison GM (2008) Effects of elasticity on the spraying of a non-newtonian fluid. At Sprays 18:243–271

Pasandideh-Fard M, Qiao YM, Chandra S, Mostaghimi J (1996) Capillary effects during droplet impact on a solid surface. Phys fluids 8(3):650–659

Pedersen CO (1970) An experimental study of the dynamic behavior and heat transfer characteristics of water droplets impinging upon a heated surface. Int J Heat Mass Transf 13(2):369–381. ISSN 0017-9310

Peterlin A (1966) Hydrodynamics of linear macromolecules. Pure Appl Chem 12(1–4):563–586

Plateau J (1867) Lettre au sujet de la transformation spontanée d'un cylindre liquide en sphères isolées. Comptes Rendus des Séances de l'Académie des Sciences 65:290–291

Quéré D (2013) Leidenfrost dynamics. Ann Rev Fluid Mech 45:197–215

Rayleigh L (1878) On the instability of jets. Proc Lond Math Soc 10:4–13

Rayleigh L (1879) On the capillary phenomena of jets. Proc R Soc Lon Ser A Math Phys Sci 29:71–97

Rayleigh L (1892) On the instability of a cylinder of viscous liquid under capillary force. Philos Mag 34:145–154

Rein M (1993) Phenomena of liquid drop impact on solid and liquid surfaces. Fluid Dyn Res 12(2):61–93

Rein M (ed) (2003) Drop-Surface interactions, CISM courses and lectures no. 456. Springer, Wien-New York

Rogers GP, Barnes HA (2001) New measurements of the flow-curves for carbopol dispersions without slip artefacts. Rheologica Acta 40:499–503

Roisman IV (2009) Inertia dominated drop collisions. ii. An analytical solution of the navierstokes equations for a spreading viscous film. Phys Fluids 21(5):052104

Roisman IV, Berberović E, Tropea C (2009) Inertia dominated drop collisions. i. On the universal flow in the lamella. Phys Fluids 21(5):052103

Romagnoli V, Felton P, Prudhomme RK (2000) Control of drop size by rheology. In: Proceedings of the eighth international conference on liquid atomization and spray systems (ICLASS), Pasadena (CA, USA), pp 34–38

Rozhkov AN (1983) Dynamics of threads of diluted polymer solutions. J Eng Phys 45(1):768–774

Rozhkov AN, Prunet-Foch B, Vignes-Adler M (2003) Impact of drops of polymer solutions on small targets. Phys Fluids 15:2006–2019

Saidi A, Martin C, Magnin A (2010) Influence of yield stress on the fluid droplet impact control. J Non-Newton Fluid Mech 165:596–606

Saïdi A, Martin C, Magnin A (2011) Effects of surface properties on the impact process of a yield stress fluid drop. Exp Fluids 51(1):211–224

Schiaffino S, Sonin AA (1997) Molten droplet deposition and solidification at low weber numbers. Phys Fluids 9(11):3172–3187

Schümmer P, Tebel KH (1983) A new elongational rheometer for polymer solutions. J Non-Newton Fluid Mech 12:331–347

Smith MI, Bertola V (2010a) Effect of polymer additives on the wetting of impacting droplets. Phys Rev Lett 104(15)

Smith MI, Bertola V (2010b) The anti-rebound effect of flexible polymers on impacting drops. In: Proceedings of the 23rd European conference on liquid atomization and spray systems, Brno, Czech Republic, 6–8 Sept 2010

Smith MI, Bertola V (2011) Particle velocimetry inside newtonian and non-newtonian droplets impacting a hydrophobic surface. Exp Fluids 50(5):1385–1391

Smith MI, Sharp JS (2014) Origin of contact line forces during the retraction of dilute polymer solution drops. Langmuir 30:5455–5459

Stelter M (2001) Das Zerstäubungsverhalten nicht-Newtonscher Flüssigkeiten (The atomization behaviour of non-Newonian liquids - in German). Phdthesis, Friedrich-Alexander University Erlangen-Nürnberg

Stelter M, Brenn G, Yarin AL, Singh RP, Durst F (2000) Validation and application of a novel elongational device for polymer solutions. J Rheol 44:595–616

Stelter M, Brenn G, Yarin AL, Singh RP, Durst F (2002a) Investigation of the elongational behavior of polymer solutions by means of an elongational rheometer. J Rheol 46:507–527

Stelter M, Brenn G, Durst F (2002b) The influence of viscoelastic fluid properties on spray formation from flat-fan and pressure-swirl atomizers. At Sprays 12:299–327

Stow CD, Hadfield MG (1981) An experimental investigation of fluid flow resulting from the impact of a water drop with an unyielding dry surface. Proc R Soc Lond A: Math Phys Eng Sci 373(1755):419–441

Tadmor R (2011) Approaches in wetting phenomena. Soft Matter 7:1577–1580

Teske ME, Bilanin AJ (1994) Drop size scaling analysis of non-newtonian fluids. At Sprays 4:473–483

Thompson JC, Rothstein JP (2007) The atomization of viscoelastic fluids in flat-fan and hollow-cone spray nozzles. J Non-Newton Fluid Mech 147:11–22

Tirtaatmadja V, Sridhar T (1993) A filament stretching device for measurement of extensional viscosity. J. Rheol 37:1081–1102

Wachters LHJ, Westerling NAJ (1966) The heat transfer from a hot wall to impinging water drops in the spheroidal state. Chem Eng Sci 21(11):1047–1056

Wang A-B, Lin C-H, Chen C-C (2000) The critical temperature of dry impact for tiny droplet impinging on a heated surface. Phys Fluids 12(6):1622–1625

Wang Y, Minh D-Q, Amberg G (2017) Impact of viscoelastic droplets. Journal of Non-Newtonian Fluid Mechanics 243:38–46

Weber C (1931) Zum zerfall eines flssigkeitsstrahles. ZAMM—J Appl Math Mech/Zeitschrift für Angewandte Mathematik und Mechanik 11(2):136–154

Williams PA, English RJ, Blanchard RL, Rose SA, Lyons L, Whitehead M (2008) The influence of the extensional viscosity of very low concentrations of high molecular mass water-soluble polymers on atomisation and droplet impact. Pest Manag Sci 64(5):497–504

Worthington AM (1876) On the forms assumed by drops of liquids falling vertically on a horizontal plate. Proc R Soc Lond 25(171–178):261–272

Yao S-C, Cai KY (1988) The dynamics and leidenfrost temperature of drops impacting on a hot surface at small angles. Exp Therm Fluid Sci 1(4):363–371. ISSN 0894-1777

Yarin AL (1990) Strong flows of polymeric liquids. Part 1. Rheological behaviour. J Non-Newton Fluid Mech 37:113–138

Yarin AL (1993) Free liquid jets and films—hydrodynamics and rheology. Longman Sci Tech

Yarin AL (2006) Drop impact dynamics: splashing, spreading, receding, bouncing. Annu Rev Fluid Mech 38:159–192

Zhu H, Dexter RW, Fox RD, Reichard DL, Brazee RD, Ozkan HE (1997) Effects of polymer composition and viscosity on droplet size of recirculated spray solutions. J Agric Eng Res 67:35–45

Advanced Particle-Based Techniques for Complex Fluids and Multiscale Flow Processes

Marco Ellero

Abstract Particle-based methods represent a general multiscale framework to study complex flow problems at different space- and timescales. Whereas they rely on a general set of Newton's equations of motion for a system of interacting elements, the very concept of 'particle' can assume different physical realizations depending on the targeted level of description and the physics of interest. At microscopic scales, particles can represent real molecules/atoms interacting with conservative classical potentials; at the mesoscale, a 'particle' represents a thermodynamic system containing potentially thousands of atoms/molecules and its dynamics is governed by a set of ordinary stochastic differential equations where the interaction forces are of conservative, dissipative and random nature. Finally, at the continuum macroscopic scales, it is possible to derive a suitable set of Newton's equations such that the corresponding particle configurations represent an adaptive Lagrangian discretization of arbitrary sets of partial differential equations (e.g. Navier–Stokes), that is, a computational fluid dynamics technique. All the different levels can be integrated in a general thermodynamic framework for discrete systems which satisfies basic physical laws such as energy conservation, entropy increase or—in the case of Brownian systems—the fluctuation–dissipation theorem at the very discrete level. In this chapter, we review the use of mesoscopic and macroscopic particle techniques for the modelling and simulation of complex fluids such as polymer or particle suspensions. It will be shown how complex microstructural properties can be incorporated in different ways, i.e. from micro-mechanical to field-based equations, depending on the available information and computational requirements. The development of hybrid particle methods coupling simultaneously dynamics occurring at different scales will be also discussed in relation to the problem of cellular transport/adhesion in biofluidics.

M. Ellero (✉)
Basque Center for Applied Mathematics (BCAM), Bilbao, Spain
IKERBASQUE, Basque Foundation for Science, Bilbao, Spain
e-mail: M.Ellero@swansea.ac.uk

361

1 Introduction

Numerical modelling and simulation of complex fluid dynamics and soft matter represent an established field in computational science, often denoted as *computational rheology* (Owens and Phillips 2002). To this class belong simulation tools specifically addressing the dynamics of so-called complex liquids, that is, all those fluids which do not follow the standard Newtonian approximation, i.e. a simple proportionality between stress and velocity-gradient tensors. These fluids are, therefore, denoted as non-Newtonian and their simulation poses an entirely new class of challenges both in theory and numerics. From a modelling point of view, the search of suitable continuum closures for the dynamical evolution of the stress field in non-Newtonian fluids (e.g. viscoelastic, plastic, etc.) is a long-standing issue in rheology (Bird et al. 1987). The classical approach consists in deriving suitable field evolution in the form of partial differential equations and their discretizations using conventional finite differences (FD), finite volumes (FV), finite elements (FE) methods used in computational fluid dynamics (CFD) (Ferziger and Perić 1999). This top-down pathway represented, and still represents to date, the major modelling/simulation approach in the field.

In recent years, however, following the theoretical progress and numerical development made in mesoscopic techniques, a different paradigm has been proposed, whereas, instead of solving continuum macroscopic PDEs, the microstructure defining the complexity of these liquids is solved directly at the mesoscopic level, with the complex hydrodynamic behaviour emerging naturally at the macroscopic scale. From a modelling point of view, this bottom-up approach represents an appealing strategy as direct mesoscopic modelling allows to bypass the needs of approximated continuum closures. Moreover, the mesoscopic simulation framework takes directly into account non-continuum effects which generally limit the validity of PDE-based models, especially under microflow conditions where the size of external geometries can be of the same order of the real mesoscopic units. On the other hand, bottom-up mesoscopic approaches are computationally demanding and, therefore, are currently limited to study the dynamics of small liquid samples and/or for complex fluid rheometrical characterizations under simple viscometric conditions.

In this chapter, an overview of some of the most popular particle methods for the description of complex fluids is offered. They include, both, bottom-up mesoscopic particle techniques and top-down macroscopic particle discretizations of prescribed sets of PDEs. A detailed discussion on the two approaches will be given together with prototypical applications in the area of complex fluids, i.e. polymeric/particle suspensions. Finally, possible hybrid strategies to couple different levels of description in particle-based methods will be discussed within the general framework of multiscale simulation of blood flow.

2 Mesoscopic and Macroscopic Particle Methods

In this section, we outline the so-called dissipative particle dynamics (DPD) method and its refinements—i.e. the smoothed dissipative particle dynamics (SDPD)—for the simulation of mesoscopic fluid flows as well as macroscopic particle techniques for the solution of partial differential equations. In Sect. 1, the methods are critically reviewed. In Sect. 2, an overview of applications in the area of complex fluid's modelling is offered. In particular, bottom-up mesoscopic, top-down macroscopic, as well as hybrid multiscale approaches are discussed.

2.1 *The Dissipative Particle Dynamics Method*

As many other numerical techniques specifically designed for mesoscopic flows (such as Brownian Dynamics (Ermak and McCammon 1978), Lattice Boltzmann (Ladd and Verberg 2001) or multi-particle collision dynamics (Ripoll et al. 2005), in the classical **Dissipative Particle Dynamics** (DPD) (Hoogerbrugge and Koelman 1992; Koelman and Hoogerbrugge 1993; Español and Warren 1995, 2017), thermal noise is incorporated in the equations of motion of particles in order to model Brownian fluctuations, crucial to recover the correct physics at the mesoscopic scales. DPD represents a grid-off method in which the fluid is modelled by means of interacting particles which represent coarse-grained elements of fluids containing potentially thousands of atoms/molecules. An illustrative sketch is shown in Fig. 1. Real constituents are lumped into few fluid elements (DPD particles) which interact via special conservative, dissipative, stochastic forces. The evolution equations for DPD particles follow Newton's equations of motion:
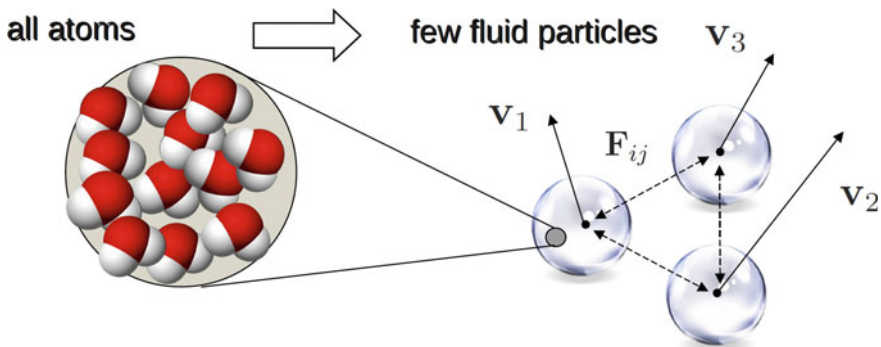

Fig. 1 Mesoscopic fluid description. Real molecules/atoms are lumped into few fluid elements (DPD particles) which interact via special conservative, dissipative, stochastic forces $\mathbf{F}_{ij}$ defined in Eq. (2). Arrows denote velocity vectors

$$\dot{\mathbf{r}}_i = \mathbf{v}_i$$
$$m\dot{\mathbf{v}}_i = \sum_j \mathbf{F}_{ij} \qquad (1)$$

where $\mathbf{r}_i$ and $\mathbf{v}_i$ are, respectively, the position and velocity of the centre of mass of particle i and $\mathbf{F}_{ij}$ are pairwise interactions between particles i and j. Unlike Molecular Dynamics, where particles represent real molecules and conservative interaction is modelled by specific potentials (e.g. Lennard-Jones type) (Allen and Tildesley 1987), in DPD, the 'coarse' fluid particles interact via a combination of soft conservative, dissipative and stochastic forces, the latter ones being originated by the reduction of degrees of freedom when moving from a detailed microscopic description towards a coarse-graining one. Moreover, dissipative and stochastic forces need to be connected by a fluctuation–dissipation theorem (FDT) in order to guarantee the correct thermodynamic equilibrium of the system (Español and Warren 1995).

More specifically, in classical DPD, we have

$$\mathbf{F}_{ij}^C = a_{ij}\omega^C\left(r_{ij}\right)\mathbf{e}_{ij}$$
$$\mathbf{F}_{ij}^D = \gamma\omega^D\left(r_{ij}\right)\left(\mathbf{e}_{ij}\cdot\mathbf{v}_{ij}\right)\mathbf{e}_{ij}$$
$$\mathbf{F}_{ij}^R = \sigma\omega^R\left(r_{ij}\right)\xi_{ij}\mathbf{e}_{ij} \qquad (2)$$

Here a_{ij} is the strength of the repulsive potential, γ is a friction coefficient, σ is the strength of the thermal noise and ξ_{ij} is a normally distributed random number with zero mean and unit variance, $\mathbf{e}_{ij} = \mathbf{r}_{ij}/r_{ij}$ is the unit vector joining particles i and j, whereas $\mathbf{v}_{ij} = \mathbf{v}_i - \mathbf{v}_j$ is the particle velocity difference. $\omega^C\left(r_{ij}\right)$ is a compact support weighting function for the conservative force, whereas $\omega^D\left(r_{ij}\right)$ and $\omega^R\left(r_{ij}\right)$ are two additional weighting functions. In order for the thermal noise to satisfy exactly the FDT, the input parameters must be constrained, in particular, they need to satisfy $\sigma^2 = 2\gamma k_B T$ and, at the same time, the weighting functions need to be chosen such that $\omega^D\left(r_{ij}\right) = [\omega^R\left(r_{ij}\right)]^2$ (Español and Warren 1995). It was shown that hydrodynamic behaviour is recovered on larger spatio-temporal scales, that is, by applying arguments of kinetic theory, the governing equations approximating the dynamics of a Newtonian fluid with specific transport coefficients (viscosity, compressibility, etc.) related to DPD model parameters can be obtained (Español 1995).

The advantage of this bottom-up approach to hydrodynamics is that no specific reference to any set of partial differential equations is needed. An approximately Newtonian solvent with incorporated Brownian fluctuations is recovered, which provides the hydrodynamic basis of more complex fluid models (see Sect. 2).

Although this set of equations (Eq. 2) are very appealing, the price to pay for this simplicity is that no direct connection exists between the DPD model parameters and the physical parameters of the liquid system one tries to simulate. As mentioned above, in order to define the fluid transport coefficients, one needs to rely on kinetic theory (Marsh et al. 1997) or map and calibrate the parameters in ways that are

not always systematic (Backer et al. 2005; Qiao and He 2008). Moreover, transport coefficients have a complex dependence on the DPD model parameters in such a way that a precise and independent definition of hydrodynamic regimes is a challenging task. Perhaps, the most serious problem is the lack of a thermodynamics particle volume entering into the equations of motion (Eq. 2) and the resulting inability to specify the spatial scale at which a DPD simulation operates. The same issue poses also some difficulties on the separate identification of resolution and finite-size effects in the output results (Vázquez-Quesada et al. 2009b; Español and Warren 2017). In other words, there is no concept of numerical convergence in DPD and it is difficult to assess the dependence of the number of computational particles on the simulated dynamics (Ellero and Español 2018).

The previous drawbacks in modelling liquids have been addressed and solved in a modification of the DPD method denoted as **Smoothed Dissipative Particle Dynamics** (SDPD) (Español and Revenga 2003; Ellero et al. 2003). The new particle model is entirely embedded in the GENERIC framework (general equation for non-equilibrium reversible–irreversible coupling) (Grmela and Öttinger 1997; Öttinger and Grmela 1997; Öttinger 2005), and therefore it maintains the thermodynamic consistency of the original DPD method, but in addition allows for a direct specification of the transport coefficients as input parameters. In fact, it has been shown that SDPD can be interpreted as a generalization of the well-known **Smoothed Particle Hydrodynamics** method (SPH) (Español and Revenga 2003; Vázquez-Quesada et al. 2009b) which is a Lagrangian meshless Navier–Stokes solver proposed by Monaghan (Gingold and Monaghan 1977; Monaghan 2005), albeit with consistent introduction of thermal fluctuations. Let us see in detail how the new SDPD particle model works and in what it differentiates from the classical DPD.

2.2 The 'Smoothed' Dissipative Particle Dynamics method

SDPD is a Lagrangian particle method for the numerical solution of thermal flow problems able to address both the macroscale *and* the mesoscale. Roughly, the mesoscale involves timescales from 1 ns to 10^6 ns and space scales from 10 nm to 10^4 nm. In SDPD, a set of fluid particles $i = 1, .., N$ are distributed homogeneously over the domain and move according to forces estimated from their local neighbourhood. The set of ordinary stochastic differential equations for the particle positions, velocities follows the same equation of motion (Eq. 2) with a modified definition of the inter-particle interactions. In SDPD, they read (Ellero and Español 2018)

$$\dot{\mathbf{r}}_i = \mathbf{v}_i$$

$$m\dot{\mathbf{v}}_i = -\underbrace{\sum_j \overbrace{\left(\frac{P_i}{d_i^2} + \frac{P_j}{d_j^2}\right) W'_{ij}\mathbf{e}_{ij}}^{\mathbf{F}^C_{ij}}}_{(\nabla p/\rho)_i} + \underbrace{\frac{5\eta}{3}\sum_j \overbrace{\frac{W'_{ij}}{d_i d_j r_{ij}}\left[\mathbf{v}_{ij} + \left(\mathbf{e}_{ij}\cdot\mathbf{v}_{ij}\right)\mathbf{e}_{ij}\right]}^{\mathbf{F}^D_{ij}}}_{\eta\nabla^2\mathbf{v}_i + (\eta/3)\,\nabla(\nabla\cdot\mathbf{v}_i)}$$

$$+ \sum_j \overbrace{A_{ij}\frac{d\hat{\boldsymbol{\xi}}_{ij}}{dt}\cdot\mathbf{e}_{ij}}^{\mathbf{F}^R_{ij}} \tag{3}$$

Here, the mass density is calculated as $\rho_i = m_i/\phi_i$, where $\phi_i = 1/d_i$ is the volume associated to a SDPD fluid particle i and $d_i = \sum_j W_{ij}$ is the local number density. Here, $W_{ij} = W(r_{ij}, r_c)$ is a kernel function with compact support r_c, $W'_{ij} = \partial W(r)/\partial r|_{r=r_{ij}}$ its derivative. $\hat{\boldsymbol{\xi}}_{ij} = (1/2)[\boldsymbol{\xi}_{ij} + \boldsymbol{\xi}_{ij}^T]$ is the symmetric part of $\boldsymbol{\xi}_{ij}$ which is a matrix of independent increments of the Wiener process. Each component may be simulated as $\xi_{ij}(\Delta t)^{1/2}$ with ξ_{ij} being, as in the DPD equation (Eq. 2), an independent Gaussian random number and Δt the numerical time step. A_{ij} represents the strength of thermal noise which is constrained by the FDT. The remaining notation is the same as in standard DPD. More importantly, $P_i = P(\rho_i, T_i)$ is a given pressure associated (by using an input equation of state) to the particle i and η is the input shear viscosity of the simulated fluid. If we neglect the last stochastic term in Eq. (3), it can be shown that the previous equations represent a Lagrangian discretization of the Navier–Stokes equations (NSE) using the so-called Smoothed Particle Hydrodynamics (SPH) interpolation (Liu and Liu 2010; Violeau and Rogers 2016; Ellero et al. 2010; Ellero and Adams 2011). In other words, the overall conservative force can be interpreted as an SPH discretization of the pressure gradient in the NSE, whereas the dissipative force approximates the Laplacian of the velocity (Litvinov et al. 2009). Finally, the last random term $\mathbf{F}^R_{ij}$ is constructed in such a way that the fluctuation–dissipation theorem (FDT) is also exactly satisfied at the discrete level. This is guaranteed by the fact that the model is GENERIC compliant (Öttinger 2005).

As it can be seen, although the structure of the SDPD equations is very similar to DPD, their physical interpretation is different. The SDPD method represents a proper stochastic extension of the deterministic continuum SPH method to the regime of fluctuating hydrodynamics (Landau and Lifshitz 1987). Thanks to the clear connection to the underlying set of partial differential equations describing the fluid flow (e.g. the NSE in the case of Newtonian fluids), SDPD enables a direct specification of the fluid transport coefficient as input parameters and a proper numerical resolution study as in standard computational fluid dynamics (CFD) techniques, albeit with a thermodynamically consistent incorporation of Brownian fluctuations. In addition, by enabling an input choice of the pressure equation of state and speed of sound, SDPD allows to handle liquid's incompressibility in a better way compared to clas-

sical DPD (Alizadehrad and Fedosov 2018). Finally, SDPD allows also to connect naturally the classical bottom-up DPD technique (defined in the mesoscopic realm) with specific top-down discretization of partial differential equations using SPH meshless interpolations (Ellero and Español 2018).

3 Modelling Complex Fluids with Particle Methods

In this section, we will describe several possibilities to incorporate microstructural complexity in fluids simulated using either DPD or SDPD approaches. To illustrate the problems, we will consider several classes of non-Newtonian fluids, such as polymeric or particle suspensions, and show how their relevant complex features can be modelled at different levels.

Complex non-Newtonian fluids are characterized by the presence of supramolecular structures suspended in a simple solvent liquid. As a result, in many cases (but not all), the solvents can be generally described by a Newtonian fluid model. On the other hand, the dispersed complex mesostructure can be represented, for example, by suspended solid/soft particles, high molecular weight flexible polymers, deformable cells or droplets. The essential feature shared by all these complex fluid systems is that the typical spatial scale of the suspended mesostructure is generally orders of magnitude larger than the size of the solvent molecular constituents (e.g. in the case of water molecules ≈ 0.2 nm), see Fig. 2. Not only this, relaxation timescales
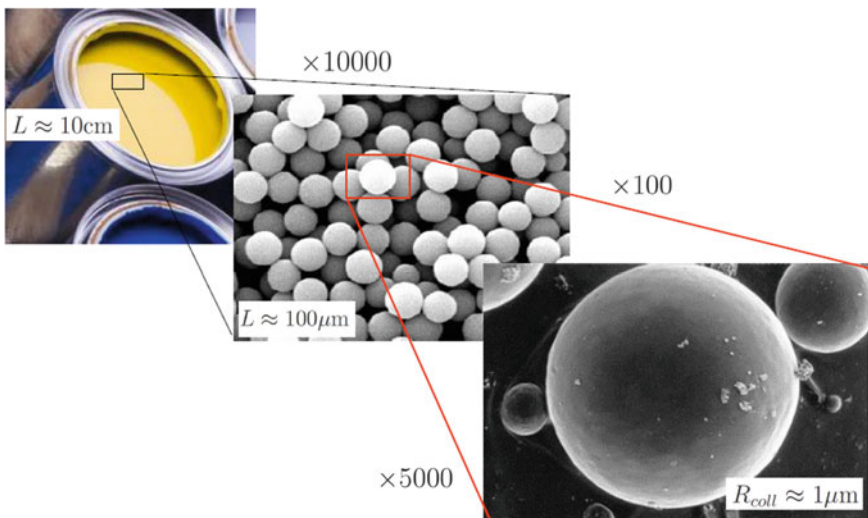

Fig. 2 Multiple spatial scales involved in a complex liquid. Paints, for example, are formed by a concentrated suspension of colloidal particles (pigments and other fillers) responsible for the opacity, colour and anti-corrosive properties

for the mesostructure can be also in the order of seconds or larger for many complex fluids, in such a way that the mesoscopic dynamics occur on temporal scales much slower than the microscopic ones characterizing the solvent medium. This makes the use of direct microscopic simulation techniques, such as molecular dynamics (Allen and Tildesley 1987), unpractical to capture the slow mesodynamics and the resulting hydrodynamics behaviour. Mesoscopic methods, such as (S)DPD, allow to bypass the microscopic details lumping them into a coarse-graining/hydrodynamics description of the solvent. This allows to focus, from a numerical point of view, on an efficient model for the mesostructure defined *uniquely* on the spatio-temporal scales of physical interest.

There is another possible differentiation within this coarse-graining description of complex fluids. As it will be seen in the next section, whereas in classical DPD, the only way to model fluid complexity is by direct model of the suspended mesostructure and analysing *a posteriori* the 'output' complex hydrodynamic response (see Sect. 2.1), in SDPD also the inverse approach is possible. In fact, thanks to the established link to proper set of partial differential equations (PDEs), it is possible to use the Lagrangian meshless formalism of SDPD (and SPH) to discretize general constitutive equations (see Sect. 2.2). Provided that an accurate continuum constitutive equation for the complex fluid can be formulated in the framework of PDEs, the classical top-down CFD approach can be also considered.

In the next section, we will consider examples of several complex fluids modelling by using, both, bottom-up and top-down particle-based descriptions.

3.1 Bottom-Up Mesoscopic Approach

In this approach, the mesostructure is *directly* modelled. This can be done in a number of ways depending on the nature of the suspended objects. In the following part of this section, we will discuss two prototypical examples for complex suspensions, which are the case of polymer molecules and rigid particles suspended in a liquid.

3.1.1 Polymeric Fluids

Flexible polymer molecules (see Fig. 3) have been modelled in DPD and SDPD by means of coarse-graining spring-bead chain models. The polymer beads have the same mass and interact hydrodynamically with each other in the same way as the fluid particles, i.e. via Eqs. (1)–(3). The effect of the chemical bonds between monomers is taken into account through an additional potential acting only between neighbouring polymer beads (Fan et al. 2006; Litvinov et al. 2008).

Spring-bead models range from simple harmonic chain to Gaussian chain, Rouse chain, etc. A popular model to simulate a realistic polymer molecule is the finite extensible nonlinear elastic (FENE) potential (Bird et al. 1987), which reads
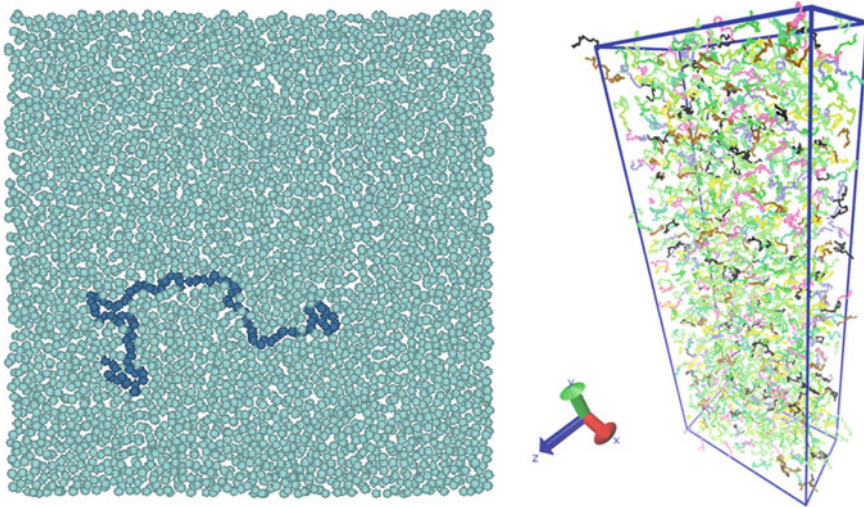
Fig. 3 Mesoscopic (S)DPD polymer model. Left: single flexible polymer chain suspended in a Newtonian thermal solvent. Reproduced with permission from S. Litvinov, M. Ellero, X. Hu, N.A. Adams, 'Smoothed dissipative particle dynamics model for polymer molecules in suspension' Physical Review E 77 (6), 066703 (2008). © 2008 American Physical Society. Right: bottom-up mesoscopic model of a concentrated polymer solution/melt. Reproduced with permission from S. Litvinov, Q. Xie, X. Hu, N. Adams, M. Ellero, 'Simulation of individual polymer chains and polymer solutions with smoothed dissipative particle dynamics', Fluids 1 (1), 7 (2016)

$$U_{FENE}(r) = -\frac{1}{2}kR_0^2 \ln\left[1 - \left(\frac{r}{R_0}\right)^2\right], \tag{4}$$

where $r = \|\mathbf{r}_{ij}\|$ is the distance between neighbouring beads of the polymer chain, R_0 is the maximum allowed spring length and k is the effective spring constant. In this model, since the solvent is also represented by (S)DPD particles, the hydrodynamic interactions within the polymer are included explicitly by means of the interacting forces acting between the solvent particles (light blue points in Fig. 3, left) and the polymer beads (dark blue points in Fig. 3, left). Moreover, the correct Brownian fluctuations on the polymer beads are guaranteed by the presence of the random terms in Eqs. (1)–(3) which satisfy the FDT. Therefore, in DPD/SDPD mesoscopic models, the dynamics of the polymer bead i reads

$$m_i \frac{d\mathbf{v}_i}{dt} = \mathbf{F}_i^{hydro} + \mathbf{F}_{i,i_1}^{FENE} + \mathbf{F}_{i,i_2}^{FENE}, \tag{5}$$

where m_i is the mass of the bead i, $\mathbf{F}_i^{hydro}$ is the total sum of the resulting (S)DPD forces acting on particle i given in Eqs. (1–3) and i_1, i_2 are the next two neighbouring beads of i in the polymer chain which interact via the non-hydrodynamic elastic forces derived by the potential (Eq. 4), i.e.

$$\mathbf{F}_{ij}^{FENE} = \frac{k\mathbf{r}_{ij}}{1 - (r/R_0)^2} \tag{6}$$

The static and dynamic conformational properties of a single polymer suspended in a Brownian Newtonian medium modelled via SDPD have been validated in Litvinov et al. (2008, 2016). The effect of confinement on the conformational properties of the polymer molecule was also investigated by considering a microchannel with gap H varying between 1 and 5 μm, for a polymer with average free gyration radius of comparable size, leading to results in agreement with the de Gennes' theory (de Gennes 1979). In Litvinov et al. (2010), simulation of a polymer tethered to a planar wall undergoing shear flow was also studied. Depending on the magnitude of the imposed shear flow, the polymer aligns and stretches in the flow direction. Provided that an amorphous model for the SDPD solid wall is used, excellent results for the average polymer extension in the flow direction compared to experimental data for a tethered DNA are obtained.

In Litvinov et al. (2016), it was shown that the mesoscopic model can be extended to capture the collective dynamics of diluted and concentrated polymer solutions and rheology of an entangled network, i.e. a polymer melt.

Bottom-up derived hydrodynamics of polymers liquids and/or melts can be obtained by considering a large sample of polymer molecules (Fig. 3, right). This approach allows to bypass the choice of any approximate constitutive model for the polymeric liquid, where the only simulation input to be specified is the effective intra-monomer elastic interaction, Eq. (6). On the other hand, the computational load of this bottom-up simulation approach becomes significant as it scales with the number of suspended molecules, which in turn are typically made of several computational fluid particles. With this approach, it might be indeed difficult to reach numerically macroscopic spatial scales, i.e. much larger than the size of the single molecular constituent. However, in flow situations where the ratio between the size of the external geometry and the polymer length (e.g. in the order of tens of μm for a DNA or stretched PAA molecules) is not too large, the present approach represents a valuable option.

An application is represented by **microfluidics** where a single or a collection of molecules are actuated by accurate control of very small amounts of liquid ($<$1 ml) flowing through complex micro-devices. A challenging aspect in the modelling of high molecular weight polymer liquids on these micro-scales ($\ll$1 mm), in fact, is that no more scale separation exists between the size of the microstructure and that of the device (i.e. channel width), in such a way that a homogenization assumption for the complex fluid cannot be made and, consequently, no continuum model can be used. As a specific example, the complex fluid dynamics and microstructural changes in a polymeric fluid flowing through a microfluidics-based rheometer (Fig. 4) have been simulated using mesoscopic models in Litvinov et al. (2014). In its classical version, these microfluidics rheometers are essentially represented by a microchannel which is used to characterize the rheological properties of complex liquids flowing through it (Pipe and McKinley 2009). Steady rheology of complex biofluids (e.g. the non-Newtonian viscosity $\eta(\dot{\gamma})$) can be easily experimentally assessed by measuring
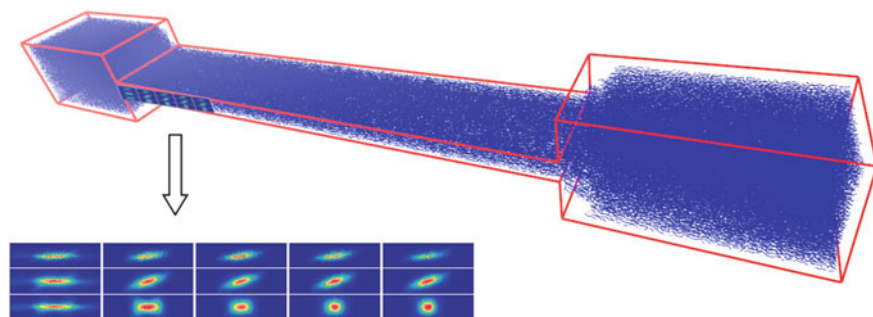
Fig. 4 Setup of the microfluidic channel. A preliminary contraction flow forces the suspended polymers to enter the straight square channel in an initially stretched configuration. Their microstructural configuration relax downstream in the purely shearing part of the flow and provides a spatial decay mechanism for the macroscopic velocity profile

the fully developed velocity profile (e.g. via PIV techniques) and fitting it with an analytical one derived by a power-law model. It is, however, unclear whether micro-rheometers can provide accurate information also on the dynamical properties of the liquid sample, e.g. relaxation times. In Klessinger et al. (2013), a preliminary extensional flow in the micro-device was considered, forcing the polymer molecules to uniformly pre-stretch before entering the following straight channel. The idea is that an externally induced out-of-equilibrium initial configuration for the polymer liquid at the channel entry will relax and will affect the flow downstream. From the PIV measurement of the spatially relaxing velocity profile, the longest relaxation time of polymer solution could be, therefore, inferred. Recent mesoscopic simulations performed in this microfluidic setup (Fig. 4) allowed to clarify the link between the relaxation time of the macroscopic velocity profile with the specific heterogeneous relaxation processes of the flowing molecules (the inset of Fig. 4). In particular, it was observed that the shape of the velocity profile varies along the channel, from an almost parabolic at the entry region to classical centre-flattened type typical of shear-thinning fluids. The fully developed velocity profile downstream in the channel is accurately described by the Carreau–Yasuda rheological model and can serve as accurate tool for the characterization of the steady-state rheology (Litvinov et al. 2014). Moreover, the decay length for the profile shape leads to a specific timescale which is equal to the largest relaxation time of the polymer extension in the flow direction, and therefore it justifies the application of the above-mentioned microfluidics devices for transient rheometry.

3.1.2 Colloidal Suspensions

Accurate prediction of the dynamics and mechanical properties of micro/nanoparticle suspensions interacting with simple and complex media and under complex microflow conditions is critical for many industrial processes. Also, in this case, direct modelling
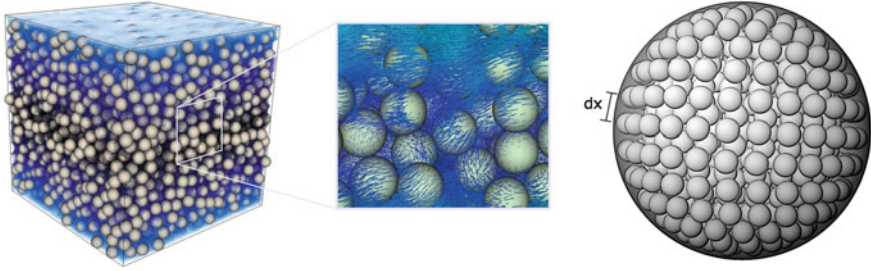
Fig. 5 SPH/SDPD Lagrangian model for a particle suspension. Left: rigid (grey) particles are suspended in a liquid discretized by small (blue) fluid particles which explicitly mediate long-range hydrodynamic interactions (inset) (Vázquez-Quesada et al. 2015; Vázquez-Quesada and Ellero 2016a). Right: scheme of the location of the boundary particles (white spheres) within a solid grey region. The resolution depicted is five boundary particles per sphere's radius corresponding roughly to 500 computational elements per solid sphere. Reproduced with permission from A. Vázquez-Quesada, M. Ellero, 'Rheology and microstructure of non-colloidal suspensions under shear studied with smoothed particle hydrodynamics' Journal of Non-Newtonian Fluid Mechanics 233, 37–47 (2016). Elsevier © 2016

of the mesostructure (i.e. the dispersed solid phase) by means of mesoscopic techniques can allow to improve our understanding of the macroscopic rheological properties of complex suspensions as well as their dynamics. Moreover, mesoscopic simulations of particulate systems can allow also to develop more accurate continuum PDE-based models which can be efficiently applied on macroscopic scales.

Here, we are interested in hard particles suspended in simple Newtonian solvents. Solid inclusions of arbitrary shape can be modelled using boundary particles located inside the solid region (Bian et al. 2012) (Fig. 5, right). Boundary particles interact with fluid particles by means of the same forces described in Eq. (3). No-slip boundary condition at the liquid–solid interface is enforced during each interaction between fluid particle i and boundary particle j by assigning an artificial velocity to the boundary particle j, which satisfy zero interpolation at the interface (Ellero and Tanner 2005). The same approach is also used to model any arbitrary wall. Once all the forces acting on every numerical boundary particle j belonging to a solid sphere (labelled by Greek indexes α) are calculated, the total force $\boldsymbol{F}_\alpha^{\mathrm{sph}}$ and torque $\boldsymbol{T}_\alpha^{\mathrm{sph}}$ exerted by the surrounding fluid (modelled by SPH/SDPD) on the solid sphere can be obtained as

$$\boldsymbol{F}_\alpha^{\mathrm{sph}} = \sum_{j \in \alpha} \boldsymbol{F}_j, \qquad \boldsymbol{T}_\alpha^{\mathrm{sph}} = \sum_{j \in \alpha} \left(\boldsymbol{r}_j - \boldsymbol{R}_\alpha \right) \times \boldsymbol{F}_j \qquad (7)$$

where $\boldsymbol{R}_\alpha$ is the centre of mass of the solid suspended particle α (grey spheres, Fig. 5, left). When properly integrated, $\boldsymbol{F}_\alpha^{\mathrm{sph}}$ and $\boldsymbol{T}_\alpha^{\mathrm{sph}}$ allow to obtain the new linear velocity $\boldsymbol{V}_\alpha$, angular velocity $\boldsymbol{\Omega}_\alpha$ and position of the solid inclusion. Positions of boundary particles inside a solid sphere α are finally updated according to a rigid
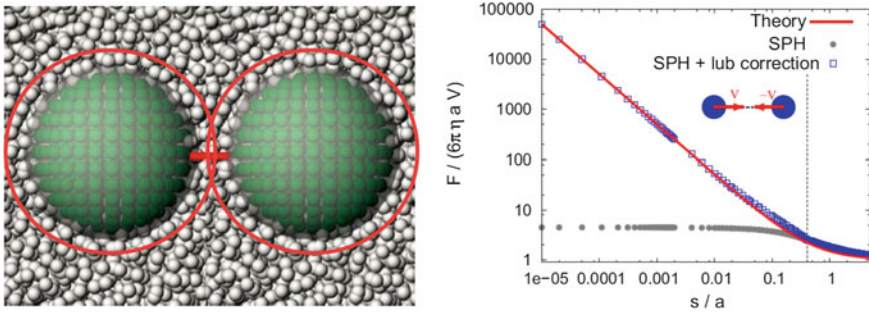
Fig. 6 Sketch of the inter-particle short-range lubrication model. Below a specific resolution-dependent inter-particle distance s_c, HIs mediated by the solvent are poorly represented. At distances smaller than s_c (red circles—left and vertical dotted line—right), exact lubrication corrections are considered. Reproduced with permission from A. Vázquez-Quesada, M. Ellero, 'Rheology and microstructure of non-colloidal suspensions under shear studied with smoothed particle hydrodynamics' Journal of Non-Newtonian Fluid Mechanics 233, 37-47 (2016). Elsevier © 2016

body motion (Vázquez-Quesada et al. 2015; Vázquez-Quesada and Ellero 2016a). The present SPH/SDPD model captures accurately the long-range hydrodynamic interactions (HIs) between solid particles (Bian et al. 2012).

As discussed in detail in Bian and Ellero (2014) and Vázquez-Quesada and Ellero (2016a), when two solid particles (e.g. α and β) get very close to each other, the HIs mediated by the SPH/SDPD fluid are poorly represented. This is due to the limited number of particles used to discretize the NSE in the vanishing gap s between two solid spheres and it needs to be corrected. In particular, when simulating two spheres approaching each other with constant velocity, the normal hydrodynamic force acting on them and computed uniquely from the SPH/SDPD discretization of the suspending fluid deviates from the divergent behaviour predicted by the Stokes theory. This typically occurs at a gap distance s_c in the order of the cutoff radius r_c of the weighting function in Eq. (3) (i.e. few fluid particles sizes) and remains approximately constant at smaller distances (see Fig. 6, right). Analytical normal/tangential lubrication forces can be, therefore, used at distances below s_c, by properly removing the residual force contribution obtained from the explicit description of the fluid. This allows to obtain a well-defined and accurate transition between the far/short-range HIs. The normal/tangential lubrication correction forces read, therefore (Vázquez-Quesada and Ellero 2016a),

$$
\begin{aligned}
\boldsymbol{F}_{\alpha\beta}^n(s) &= f_{\alpha\beta}(s)\boldsymbol{V}_{\alpha\beta}\cdot\boldsymbol{e}_{\alpha\beta}\boldsymbol{e}_{\alpha\beta} \\
\boldsymbol{F}_{\alpha\beta}^t(s) &= g_{\alpha\beta}(s)\boldsymbol{V}_{\alpha\beta}\cdot\left(\boldsymbol{1}-\boldsymbol{e}_{\alpha\beta}\boldsymbol{e}_{\alpha\beta}\right)
\end{aligned}
\tag{8}
$$

where the scalar functions $f_{\alpha\beta}(s)$ and $g_{\alpha\beta}(s)$ are defined as

$$f_{\alpha\beta}(s) = -6\pi\eta \left[\left(\frac{a_\alpha a_\beta}{a_\alpha + a_\beta} \right)^2 \frac{1}{s} + a_\alpha \left(\frac{1 + 7\frac{a_\beta}{a_\alpha} + \left(\frac{a_\beta}{a_\alpha}\right)^2}{5\left(1 + \frac{a_\beta}{a_\alpha}\right)^3} \right) \ln\left(\frac{a_\alpha}{s}\right) \right]$$

$$g_{\alpha\beta}(s) = -6\pi\eta a_\alpha \left[\frac{4\frac{a_\beta}{a_\alpha}\left(2 + \frac{a_\beta}{a_\alpha} + 2\left(\frac{a_\beta}{a_\alpha}\right)^2\right)}{15\left(1 + \frac{a_\beta}{a_\alpha}\right)^3} \right] \ln\left(\frac{a_\alpha}{s}\right) \tag{9}$$

For comparison, the merged theoretical solution between the close and far-field approaches calculated in Jeffrey and Onishi (1984) is used. As it can be seen, the correct normal HIs (red line, Fig. 6, right) are reproduced at every inter-particle distance.

Short-range lubrication forces correct, therefore, the poor description of the HIs between solid particles when they are located at relative distances s comparable to the numerical resolution used for the discretization of the solvent. Figure 6 (left) shows an illustrative picture of the problem. Red circles represent the range of activation of the lubrication correction for the two spheres. Outside that region, hydrodynamics is fully captured by the explicit description of the SPH/SDPD solvent. It should be remarked that the lubrication range depends on the resolution used to describe the solvent. In the limiting case of *fully resolved* simulation, no lubrication would be needed. This is, however, practically difficult to achieve in simulations (especially for dense particle systems) as near contacts can occur frequently.

It should be also borne in mind that, due to the singular dependence on $1/s$ in Eq. (8), the lubrication forces acting between approaching or departing particles under nearly touching conditions can be very large and the numerical problem becomes stiff. Effective implicit-splitting techniques have been recently developed which allows to bypass the strict time-step limitation associated to these diverging lubrication contributions (Bian and Ellero 2014).

Using similar models, it is possible to incorporate also more refined lubrication expression which is not restricted to a constant viscosity Newtonian solvent. Novel analytical expressions for the short-range lubrication interactions between spheres suspended in complex *shear-thinning* (Vázquez-Quesada and Ellero 2016b) or *shear-thickening* fluids (Vázquez-Quesada et al. 2018) have been recently derived. These lubrication models can in principle enable the simulation of dense particulate systems suspended in complex non-Newtonian media.

Rheological data for mesoscopic simulation of complex suspensions can be obtained by applying steady or oscillatory shear flows and determining their mechanical response (i.e. the viscometric functions) by measuring overall forces exerted on the plates of a virtual rheometer. These have been studied for particulate systems under constant shear flow with Newtonian matrices (e.g. glycerol-based liquids) (Vázquez-Quesada and Ellero 2016a), weakly shear-thinning matrices (e.g. low molecular weight silicon oils) (Vázquez-Quesada et al. 2016, 2017a) and highly elastic polymer matrices (e.g. Boger liquids) (Vázquez-Quesada et al. 2019), obtaining excellent comparison with experimental data for these systems. Figure 7 shows
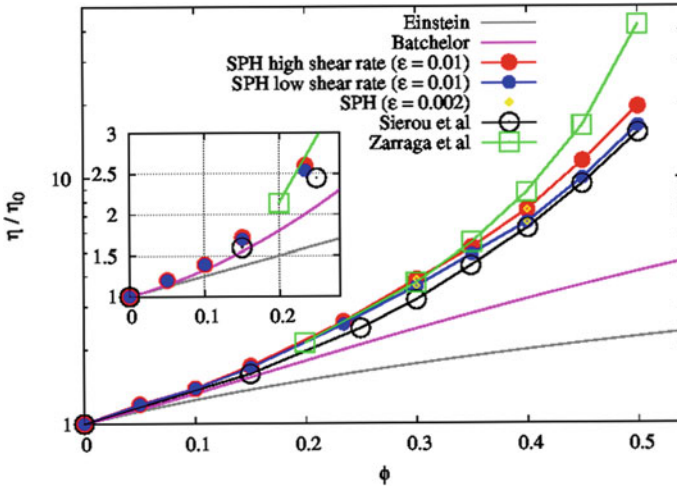
Fig. 7 Relative viscosity versus volume fraction. Results of SPH/SDPD are compared with the experiments by Zarraga et al. (2000) (□). and the simulations by Sierou and Brady (2002) (○). Low-shear rate (●) and large-shear rate (●) SPH viscosities. Einstein and Batchelor solutions (Einstein 1906; Batchelor and Green 1972) valid in the dilute/semi-dilute regimes are shown in the inset. Reproduced with permission from A. Vázquez-Quesada, M. Ellero, 'Rheology and microstructure of non-colloidal suspensions under shear studied with smoothed particle hydrodynamics' Journal of Non-Newtonian Fluid Mechanics 233, 37–47 (2016). Elsevier © 2016 (Color figure online)

the comparison of the relative suspension viscosity using the SDPD/SPH Newtonian method with the Einstein theory in the dilute regime (i.e. for solid volume fraction $\phi \ll 0.1$—grey line (Einstein 1906)), higher order Batchelor theory in the semi-dilute regime (i.e. $\phi \leq 0.2$—pink line (Batchelor and Green 1972)), previous numerical calculations using Stokesian Dynamics (SD) simulations (Sierou and Brady 2002) and experimental data from Zarraga et al. (2000) (green line). The particle model captures very well the theoretical/experimental data in the dilute and semi-concentrated regime, i.e. for solid volume fractions $\phi \leq 0.4$. In the concentrated regime—above 45% solid volume fraction—purely hydrodynamic models (both SD or SDPD) are not able to reach the large suspension viscosity values observed in experiments. In order to obtain them, additional inter-particle contact friction forces are necessary (Seto et al. 2013).

Starting from validated mesoscopic particle models for colloidal and non-colloidal fluids, one can explore the possibility to perform virtual design of new particle formulations, that is, by precise characterization of their input microstructure (particle shape, suspending medium rheology, non-hydrodynamic inter-particle interactions, etc.) to study the corresponding bulk mechanical response. Complex-shape solid particles, for example, can be modelled by filling specified interior regions with boundary SPH/SDPD particles (see Fig. 8) and estimating the overall drag force/torque exerted by the surrounding fluid in a similar way to what discussed for the spheres. More attention, however, should be paid to the definition of solid–liquid interface. Enforcement
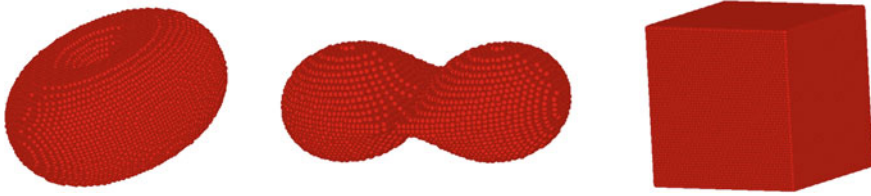
Fig. 8 Complex-shape solid particles can be modelled by filling specified interior regions with boundary SPH/SDPD particles and estimating the overall drag force/torque exerted by the surrounding fluid in a similar way to what discussed for the spheres

of no-slip boundary condition must be generalized in the case of a known predefined interface exist, for example, using techniques for the artificial-velocity assignment developed in Adami et al. (2012). Alternatively, frozen boundary particles inside solid regions with no artificial-velocity prescription could be used, but the resulting hydrodynamic interface should be estimated a posteriori by analysing the decay of the velocity field near the suspended particle. Moreover, a refined modelling of lubrication interaction should be linked to the local interface curvature (Bertevas et al. 2009).

This bottom-up numerical approach reduces at minimum the number of physical approximation used in the model characterization, and therefore can allow to explore the rheological and dynamical behaviours of complex suspensions in a realistic and controlled way. On the other hand, as already mentioned previously, direct simulation of the mesostructure limits the size of the overall simulated sample, and therefore large-scale particulate systems are hindered by finite computational resources. In order to bypass these limitations, an alternative is to mathematically derive *continuum* models for complex fluids based on a set of partial (or integral) differential equations and use CFD numerical schemes to solve them on a discrete space. This alternative strategy represents the top-down approach. In the next section, we outline a popular particle-based model for the discretization of continuum PDEs for complex fluids.

3.2 Top-Down Continuum Approach

Mathematical derivation of constitutive equations for complex fluids in the form of partial differential equations is a subject of long-standing investigation (Bird et al. 1987). For many complex fluids, derivation of accurate closure relations can be a hard task, whereas exact solutions can be found only in a limited set of cases. On the other hand, being aware of the physical assumptions involved in the derivation of continuum PDE-based models and of the related limitations, one can use efficient top-down discretization techniques to solve them accurately and target continuum large-scale flow problems in a natural way. In the following of this section, different

continuum non-Newtonian models are reviewed in connection to top-down particle-based discretizations of PDEs.

Inelastic Non-Newtonian Models In the simplest case of inelastic non-Newtonian fluids, the general hydrodynamic behaviour based on the Navier–Stokes equations can be retained (for example, the discrete Eq. 3), where the viscosity coefficient η is no longer a constant but it is allowed to vary as a function of the local velocity gradient $\dot{\gamma}$. Here, we have two general behaviours: (1) complex fluids characterized by a *decreasing* viscosity with increasing shear rate are denoted as *shear-thinning fluids*: this behaviour describes reasonably well the hydrodynamics of polymer solutions, melts, emulsions, etc.; (2) complex fluids characterized by an *increasing* viscosity with increasing local shear rate are denoted as *shear-thickening fluids*; these models describe well some particulate systems undergoing liquid–solid transitions and jamming (Mewis and Wagner 2011).

As an example, in the following, a continuum model for the so-called *discontinuous shear-thickening (DST) fluid* is discussed. Although complex models for DST fluids exist (Singh et al. 2018), a simplified inelastic framework for DST fluids can be used based on an *'inverse' bi-viscous matrix* with the viscosity coefficient in the NSE (e.g. Eq. 3) defined as

$$\eta(\dot{\gamma}) = \begin{cases} \eta_0, & \text{if } \dot{\gamma} \leq \dot{\gamma}_c - \delta\dot{\gamma} \\ m\dot{\gamma} + n, & \text{if } \dot{\gamma}_c - \delta\dot{\gamma} < \dot{\gamma} \leq \dot{\gamma}_c + \delta\dot{\gamma} \\ \eta_1, & \text{if } \dot{\gamma} > \dot{\gamma}_c + \delta\dot{\gamma} \end{cases} \tag{10}$$

where $\dot{\gamma}$ is the local shear rate, $\dot{\gamma}_c$ is a critical shear rate defining the viscous transition and $\delta\dot{\gamma}$ determines the width of the range of shear rates where the viscosity changes smoothly from η_0 to η_1. In contrast to the standard bi-viscous model, $\eta_1 > \eta_0$ is considered here. The liquid/solid-like transition observed in DST fluids at high shear rates is modelled by a linear liquid–liquid transition between two regimes characterized by a large viscosity ratio occurring over a small but finite range of shear rates with thickness $\Delta = \delta\dot{\gamma}/\dot{\gamma}_c \ll 1$ (see Eq. 10). For $\delta\dot{\gamma} \rightarrow 0$, the singular discontinuous model is obtained.

By introducing the discrete viscosity function, $\eta_i = \eta(\dot{\gamma}_i)$, in the SPH-SDPD equations (Eq. 3), a Lagrangian meshless discretization of the generalized NSE for inelastic shear-thickening fluids is recovered. Here, $\dot{\gamma}_i = \|\dot{\gamma}_i\| = (1/2)(\dot{\gamma}_i : \dot{\gamma}_i)^{1/2}$ and the local particle shear rate tensor $\dot{\boldsymbol{\gamma}}$ is estimated on each fluid particle i as (Vázquez-Quesada et al. 2017b)

$$\dot{\boldsymbol{\gamma}}_i = -\frac{1}{d_i} \sum_j W'_{ij} \boldsymbol{e}_{ij} \boldsymbol{v}_{ij}. \tag{11}$$

The inverse bi-viscous model (Eq. 10) is therefore used to calculate the local particle viscosity η_i.

The hydrodynamic behaviour of the DST model fluid is shown in Fig. 9. Here, different steady-state velocity profiles in a two-dimensional Poiseuille-like channel
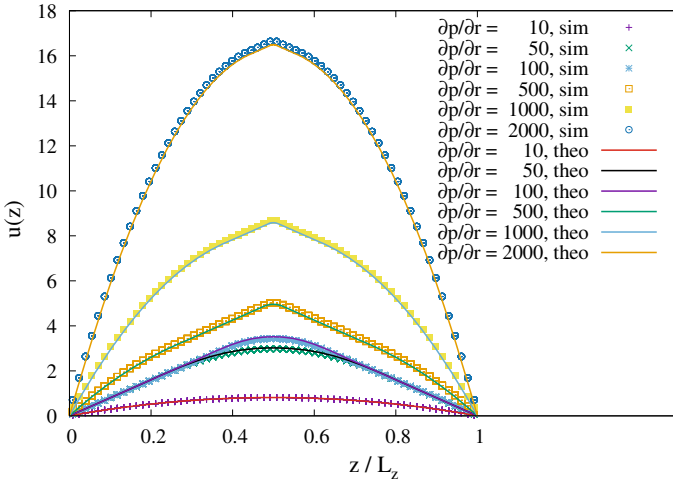
Fig. 9 Comparison of the theoretical velocity profiles (lines) with the SPH simulations (points) for a DST fluid flowing in a channel at different pressure gradients. Only steady-state velocity profiles are shown. Reproduced with permission from A. Vázquez-Quesada, N.J. Wagner, M. Ellero, 'Planar channel flow of a discontinuous shear-thickening model fluid: Theory and simulation' Physics of Fluids 29(10), 103–104 (2017). © 2016 AIP Publishing

flow are reported. Comparison of the converged SPH simulations (i.e. SDPD without stochastic terms) with analytical theories shows excellent agreement. Note that at low applied pressure gradient, the DST model essentially exhibits Newtonian-like behaviour at low-viscosity η_0 and, correspondingly, the classical parabolic profile is obtained. At larger pressure gradient, a transition to the thickened state ($\rightarrow \eta_1 \gg \eta_0$) is triggered, and the velocity field exhibits a complex shape with a non-parabolic (i.e. nearly linear) profile towards the centre of the channel with the classical cusp in the middle at $z = L_z/2$ (Vázquez-Quesada et al. 2017b). At larger pressure gradients, almost the entire fluid (except in a very narrow central region) undergoes shear rates $\dot{\gamma} \geq \dot{\gamma}_c$ and the velocity profile is again parabolic nearly everywhere with viscosity η_1. As in the case of a DST fluid, different inelastic models can be considered within the Lagrangian particle-based discretization framework of Eq. (3). Provided that a given viscosity function $\eta(\dot{\gamma})$ accurately match experimental data, SDPD/SPH models can be used to describe the corresponding liquid's dynamics under complex flow conditions where no analytical results are available (Martys et al. 2010).

Viscoelastic Models The previous non-Newtonian continuum model incorporates complexity through the unique use of a non-constant viscosity function $\eta(\dot{\gamma})$. The framework is the same as the NSE and, as a result, the viscous stress reacts *instantaneously* to an applied deformation. In particular, stress is a temporal point-wise function of the local velocity gradient, and no memory effects are present. In this sense, these fluids are inelastic or also called memory-less. In many complex fluids, this represents, however, a crude approximation of their hydrodynamic behaviour. In
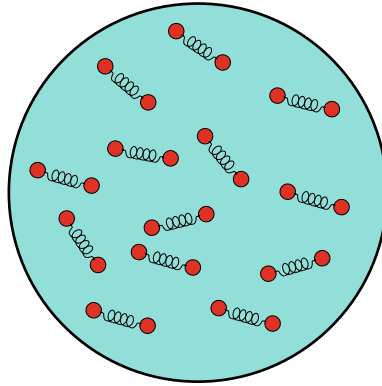
Fig. 10 SDPD/SPH modelling of polymer suspension (Vázquez-Quesada et al. 2009a). The whole blue sphere represents an SDPD particle containing many polymer molecules. $\mathbf{c} = \sum_\alpha \mathbf{q}_\alpha \mathbf{q}_\alpha$ is the *conformation tensor* which represents the average state (elongation and orientation) of the polymer molecules inside a SDPD particle. Reproduced with permission from A. Vázquez-Quesada, M. Ellero, P. Español, 'Smoothed particle hydrodynamic model for viscoelastic fluids with thermal fluctuations' Physical Review E 79(5), 056707 (2009). © 2009 American Physical Society

fact, polymeric liquids or suspensions are generally characterized by a stress depending on its entire past flow history along the Lagrangian trajectory, where memory can persist over large macroscopic temporal windows. In order to introduce memory effects, viscoelasticity must be considered in non-Newtonian continuum models.

In the context of polymeric fluids, for example, a popular continuum viscoelastic model is represented by the so-called Oldroyd-B fluid. This is a coupled set of PDEs involving macroscopic flow velocity field (and its gradients), pressure field and, in addition, an average coarse-graining tensor $\mathbf{c} = \sum_\alpha \mathbf{q}_\alpha \mathbf{q}_\alpha$ (denoted as *conformation tensor*). The latter tensor represents the average state (elongation and orientation) of the polymer molecules ($\mathbf{q}_\alpha$ is the end-to-end vector of polymer molecule α) suspended within a given continuum element of fluid (Fig. 10).

The conformation tensor is governed by an additional partial differential equation which is coupled to the momentum conservation equation as follows. In particular, the discrete SPH/SDPD form reads Vázquez-Quesada et al. (2009a, 2012)

$$\dot{\boldsymbol{c}}_i = \underbrace{\left(-\sum_j \frac{1}{d_j} \boldsymbol{v}_{ij}\, \boldsymbol{e}_{ij}\, W'_{ij} \right)}_{\boldsymbol{\kappa}_i = (\nabla \boldsymbol{v})_i^T} \cdot \boldsymbol{c}_i + \boldsymbol{c}_i \cdot \underbrace{\left(-\sum_j \frac{1}{d_j} \boldsymbol{v}_{ij}\, \boldsymbol{e}_{ij}\, W'_{ij} \right)^T}_{\boldsymbol{\kappa}_i^T = (\nabla \boldsymbol{v})_i} + \qquad (12)$$

$$+ \frac{1}{\lambda}\,(\mathbf{1} - \boldsymbol{c}_i)$$

where λ is a model parameter representing the longest polymer relaxation time, i.e. quantifying the memory of the fluid. It can be showed that the resulting momentum equation is the same as Eq. (3), where the isotropic pressure tensor P_i on a given fluid particle is replaced by a general anisotropic viscoelastic tensor taking into account the additional contribution due to the presence of the polymers, i.e. the conformation tensor $\mathbf{c}_i$, in the form

$$P_i \mathbf{1} \longrightarrow \boldsymbol{\pi}_i = P_i \mathbf{1} - \frac{\eta_p}{\lambda} \left(\boldsymbol{c}_i - \mathbf{1} \right) \tag{13}$$

The first two terms in Eq. (12) take into account local flow-induced stretching effects on the polymer molecules, the third term is an irreversible relaxation contribution. A last random term can be present in the case of *fluctuating viscoelasticity* (not shown here) which is connected to the Brownian motion of the polymer molecules contained in an SDPD fluid particle (Fig. 10). Here, η_p is the polymeric contribution to the total fluid viscosity (in addition to the solvent viscosity η considered in Eq. (3)). The deterministic part of Eq. (12) can be interpreted as a specific SPH discretization of the classical Oldroyd-B constitutive model for a dilute suspension of Hookean dumbbells. Generalization to more complex polymeric models, such as finitely extensible nonlinear elastic springs, with the proper introduction of thermal fluctuations is straightforward (Vázquez-Quesada et al. 2009a).

The viscoelasticity contained in the evolution of the conformation tensor allows to incorporate memory effects in the polymeric fluid model. For example, in a start-up channel flow for an Oldroyd-B fluid, stress will not depend temporally point-wise on the instantaneous gradient of the velocity (as in the NSE framework), but on all its past values in a temporal range consistent with its relaxation time λ. An example of dynamical evolution of the velocity field in a start-up channel flow is given in Fig. 11. Numerical results are spatially converged. Analytical time-dependent reference results for the Oldroyd-B fluid are obtained in Waters and King (1970). The agreement with the analytical solution is good as it is confirmed by the comparison of the time-dependent peak velocity at the centreline. Figure 11 left (top/bottom) shows results for an Oldroyd-B fluid with a finite solvent viscosity η in the momentum (Eq. 3). Figure 11 right (top/bottom) shows results with a vanishing solvent viscosity $\eta = 0$ in the momentum (Eq. 3). In the latter resulting viscoelastic model—denoted as Upper Convected Maxwell (UCM)—the effective viscous contribution η_p is, therefore, due only to the polymer-stress model governed by Eq. (13). As a consequence, in mathematical terms, the corresponding momentum equation changes type passing from a parabolic (in the case of a Newtonian or an Oldroyd-B fluid, i.e. $\eta \neq 0$) to a hyperbolic partial differential equation and the resulting fluid model is called *purely elastic*. As discussed in detail in Xue et al. (2004), the UCM fluid introduces remarkable difficulties for its numerical simulation under transient conditions. Indeed, it is generally acknowledged that the absence of an explicit dissipation term in the momentum equation is responsible for the growth of small numerical subgrid fluctuations, producing instabilities and divergent results. In the last decade, many techniques for steady-state calculations have been proposed which are able to sta-

bilize the simulations without affecting the accuracy of the steady results. Most of these numerical strategies (e.g. BSD, EVSS, AVSS (Xue et al. 2004)) aim at enforcing the parabolic character of the momentum equation by suitable introduction of an elliptic operator. However, it has been noticed that, if one is interested not only in the final steady state, but also in an accurate representation of the transient regime, such measures lead to falsely diffuse dynamics with the consequent production of fictitiously smooth fields and spurious diffusion. The proper way to proceed is, therefore, only through an exact treatment of the hyperbolic character of the equations. In particular, in the context of the start-up channel flow of a UCM fluid, it has been shown that the correspondent problem is described by a wave equation for the polymer stress. The presence of a discontinuity in the velocity field at the boundary at the initial time $t = 0$ is recognized as source of shear waves propagating from the wall towards the centreline. An accurate description of the wave-like character of this problem cannot be obtained through the use of standard stabilizing techniques based on the introduction of elliptic operators. These indeed act as damping out numerically dangerous high-frequency oscillations from the hydrodynamics but, at the same time, over-smoothing the results with consequent loss of accuracy (Ellero and Tanner 2005).

The results for the velocity profile obtained using the fully Lagrangian SPH-UCM model are shown in Fig. 11 (right-top) for different times and compared with the relative analytical solution. The results are interesting to evaluate the level of accuracy of the present method. Indeed, it is possible to see how accurately the SPH method captures the discontinuity in the gradient of velocity. Although the numerical solution for the velocity field is a little smeared out as effect of the numerical smoothing kernel W (Eq. 12) active on size comparable to particle spacing, a satisfactory agreement with the theory is obtained. Better results can be obtained by refining the particle discretization in the cross-stream direction.

The numerical solution reproduces well the analytical theory as it is confirmed also from the evolution of the centreline velocity plotted in Fig. 11 (right-bottom). Here, the behaviour of the fluid near the first two peaks is also shown in enlarged scale. Compared to the case of an Oldroyd-B fluid, the evolution of the centreline velocity exhibits here stronger under-damped oscillations. Oppositely, in that case, the additional viscous term in the momentum equation contributes to *physically* over-damp the velocity field with a factor inversely proportional to the Weissenberg number producing a monotonic decay for the velocity.

As an application of the current simulation framework, SPH Lagrangian viscoelastic models have been recently used to simulate the flow of highly elastic fluids through a modulated microchannel (Vázquez-Quesada and Ellero 2012; Grilli et al. 2013). In this flow process, nonlinear instabilities of the polymeric material might appear at sufficiently large values of the Weissenberg number (Wi $= \lambda \dot{\gamma}$ quantifying the fluid elasticity), leading to a drastic change of its flow dynamics and, eventually, onset of a chaotic unsteady state even in absence of inertia (zero Reynolds number): a phenomenon denoted as *elastic turbulence* (Groisman and Steinberg 2000). In the area of biomicrofluidics, elastic instabilities triggering micro-turbulence have been recently exploited for the design of novel mixing devices operating with biological
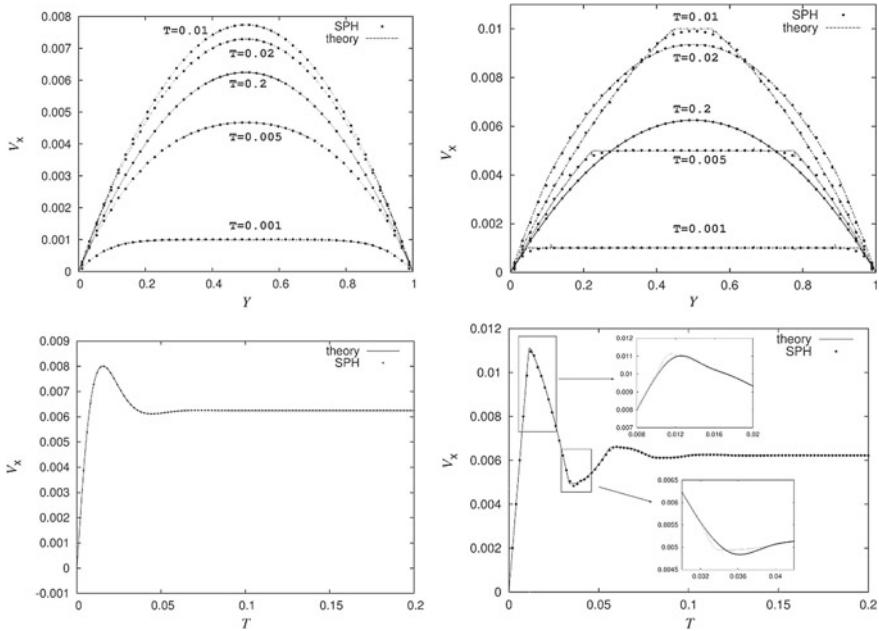
Fig. 11 Left: Velocity profile $V_x(Y)$ for the Oldroyd-B fluid with finite solvent viscosity η (top); evolution of the centreline velocity and comparison with analytical results (bottom). Right: Velocity profile $V_x(Y)$ for the upper convected Maxwell fluid with zero solvent viscosity η (top); evolution of the centreline velocity and comparison with analytical results (bottom). Reproduced with permission from M. Ellero, R.I. Tanner, 'SPH simulations of transient viscoelastic flows at low Reynolds number' Journal of Non-Newtonian Fluid Mechanics 132 (1-3), 61–72 (2005). Elsevier © 2005

liquids (Pathak et al. 2004; Gan et al. 2007), whereas in manufacturing engineering (e.g. polymer extrusion) elastic instabilities represent a source of artefacts to be avoided (Meulenbroek et al. 2003).

Despite the large technological importance of the problem, the flow of highly elastic liquids through complex geometries has been investigated in the past with controversial results (Talwar and Khomami 1995; Chmielewski and Jayaraman 1993; Arora et al. 2002; Howe et al. 2015). The main issue is related to a typical sudden large increase in the flow resistance and unsteadiness which cannot be predicted based on existing models. In Vázquez-Quesada and Ellero (2012) and Grilli et al. (2013), the continuum flow of a polymeric liquid around a linear micro-array of cylinders was considered using the above-mentioned Lagrangian particle technique for the solution of viscoelastic partial differential equations (e.g. Oldroyd-B models). Evidence of unsteady elastic behaviour and enhanced resistance was proven, in quantitative agreement with experimental observations (Arora et al. 2002) and theoretical predictions of the energy spectrum (Fouxon and Lebedev 2003). Simulations indicate also that for a sufficiently large level of fluid elasticity, a chaotic self-sustained state corresponding to inhomogeneous near-wall structures of polymer over/under-extension
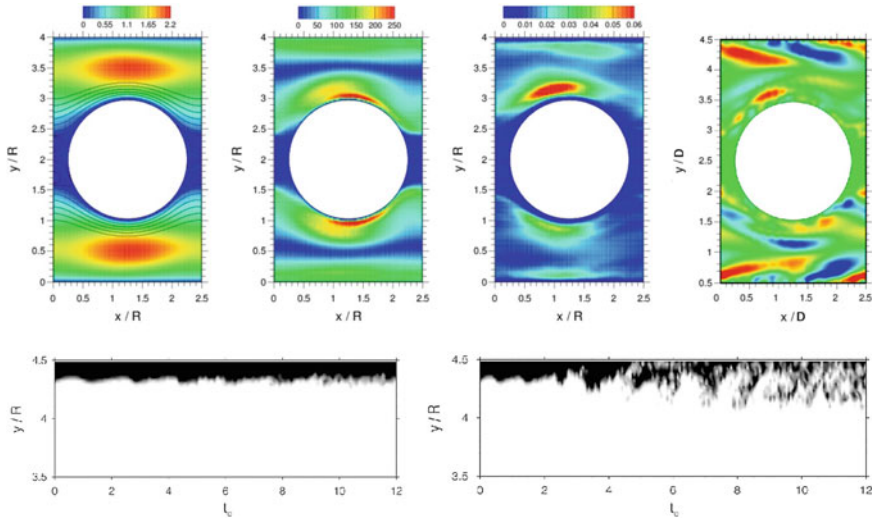
Fig. 12 Viscoelastic flow through a periodic array of cylinders. Top: **a** steady mean velocity field (streamwise direction x); **b** steady mean polymer conformation tensor (xx-component); **c** Reynolds stress (xx-component); **d** snapshot main unsteady mode conformation tensor (xx-component) obtained via dynamic mode decomposition analysis. Bottom: space–time diagram of mass mixing in the top near-wall layer with no elastic instability (left) and with instability (right). Reproduced with permission from M. Grilli, A. Vázquez-Quesada, M. Ellero, 'Transition to turbulence and mixing in a viscoelastic fluid flowing inside a channel with a periodic array of cylindrical obstacles', Physical Review Letters 110(17), 174501 (2013). © 2013 American Physical Society

(Fig. 12, top) can be established where enhanced mixing of mass takes place (Fig. 12, bottom).

Elastic instabilities and micro-turbulence in biological liquids might be particularly relevant to optimize devices involving transport of solute under microflow conditions where passive mixing is strongly hindered by the slow molecular diffusion. The study of passive strategies to control *micro-mixing* based on fluid elasticity is an active current area of research in computational rheology.

3.3 Multiscale Particle Approach

In the previous section, the potential use of different particle-based schemes for the description of hydrodynamic flow occurring in separate spatio-temporal scales, i.e. mesoscopic to macroscopic, has been discussed. In this section, possible hybrid particle-based approaches are considered in which the aforementioned different scales are handled altogether within a simulation. As a prototype multiscale problem, the case of cellular transport/adhesion in the macro-vasculature is considered.

A popular topic in cardiovascular CFD is based around the modelling of complex cellular dynamics and biofluidics. Blood, for example, is a multi-component mixture of cellular elements suspended in plasma. The latter represents approximately 55% of the entire volume occupied by blood and can be approximately considered as a Newtonian fluid. The remaining part is represented by the suspended cells which include red blood cells (RBCs), white blood cells (WBCs) and platelets.

In many biological processes, it is critical to predict accurately the cellular transport and deposition close to vessel walls in presence of a complex, unsteady flow. This is important to control drug delivery but also for the understanding of several cardiovascular diseases. As an example, atherosclerosis is a degenerative disease of the arterial wall that is thought to be initiated due to inflammation of the arterial endothelium, promoting the over deposition of white blood cells (WBCs). This anomalous WBC accumulation is site specific and can lead to initial stage lesions or, on a long-term timescale, atherosclerotic plaques.

Due to their flexibility in handling complex transient flow processes and fluid–structure interactions, particle methods have been frequently used to simulate blood flow, either at continuum macroscopic level (e.g. via SPH) (Shahriari et al. 2012; Caballero et al. 2017) or at the mesoscopic level by direct modelling (e.g. via SDPD) of the suspended cells (Ye et al. 2016; Fedosov et al. 2014), in a similar way to what is discussed in Sect. 2 for particulate systems. In these approaches, however, either the exact microscopic cellular information is missed (macro-level) or the large-scale separation existing between biological components (order of microns) and typical vessel size in the macrovascular network (order of cm) prevents the use of detailed mesoscopic particle methods (mesolevel) for realistic blood samples. To study these problems in full fashion, a *multiscale transport model for leukocytes* (Gholami et al. 2015) has been developed and coupled to an endothelial cell receptor binding model in order to link the transport and surface biology. The multiscale Lagrangian particle tracking (LPT) strategy proposed in Gholami et al. (2014) is based on a continuum viewpoint coupled with a discrete representation of the leukocytes as 'test particles' rather than real cells. Leukocyte dynamics is handled based on a continuum advection–diffusion equation for a concentration field in the bulk domain (i.e. far from arterial walls), whereas discrete cells interacting with precise hydrodynamic and biological adhesion-mediated forces are considered only in proximity of the vessel walls. In particular, the following three levels of description are considered (Fig. 13).

3.3.1 Macroscopic Continuum Bulk-Flow Modelling:

The hydrodynamic equations for a Newtonian fluid are described by the discrete SPH Navier–Stokes equations discussed in Sect. 2. In addition, transport of small tracers suspended in the bulk (the WBCs) can be modelled on a continuum basis by using a bulk concentration field $C(\mathbf{r}, t)$. The SPH discrete advection–diffusion equation therefore reads
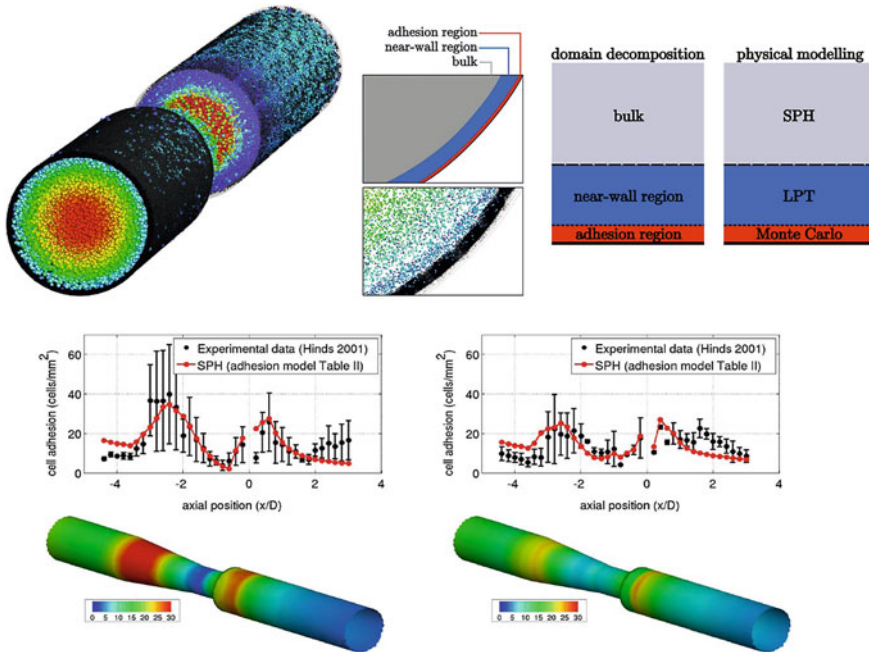
Fig. 13 Multiscale Lagrangian particle tracking (LPT) scheme for leukocytes in flow: leukocyte dynamics in the bulk is described by a continuum concentration field governed by an advection–diffusion equation; near-wall layer is filled with test particles undergoing detailed LPT with realistic lubrication and biologically derived adhesion forces. The new model allows for the simulation of clinically significant numbers of leukocytes as encountered in macroscopic arteries. Reproduced with permission from B. Gholami, A. Comerford, M. Ellero, 'SPH simulations of WBC adhesion to the endothelium: the role of haemodynamics and endothelial binding kinetics', Biomechanics and Modeling in Mechanobiology 14 (6), 1317–1333 (2015). © 2015 Springer

$$\dot{N}_i = 2D \sum_j \frac{W'_{ij}}{d_i d_j} \frac{1}{r_{ij}} \left(N_i d_i - N_j d_j \right) \tag{14}$$

where N_i is the number of cells contained within a SPH fluid particle and $C_i = N_i/\phi_i$, ϕ_i being the fluid particle volume (see Eq. 3).

3.3.2 Mesoscopic Discrete Near-Wall Modelling

Transport of WBCs in blood is governed by significantly smaller timescales ($\tau_p = \rho_p d_p^2/18\eta$) compared to that of the bulk blood flow ($\tau_{\tt flow} = d/U$), with ρ_p and d_p being tracers density and diameter, d the diameter of the artery, U the flow velocity and η the liquid's viscosity. As a result, a discrete definition of tracers only in the near-wall region is required where, due to the complex tracer–wall interactions, a

continuum description based on evolution equations for a concentration field is not
feasible. A standard LPT scheme can be used to model dynamics of discrete tracers
in the near-wall regions. Within each SPH fluid iteration step dt_{sph}, the equations of
motion for each tracer k are integrated with an appropriately smaller time step dt in
the range of τ_p:

$$\dot{\mathbf{u}}_k = \mathbf{f}_{k,drag} + \mathbf{f}_{k,lubr} + \mathbf{f}_{k,lift} + \mathbf{f}_{k,coll} \tag{15}$$

$$\dot{\mathbf{x}}_k = \mathbf{u}_k \tag{16}$$

where $\mathbf{f}_{k,drag}$ is the Stokes drag acting on the leukocyte and $\mathbf{f}_{k,lubr}$ is the wall drag
modification in the limit of $\mathrm{Re}_p = \rho_p U d_p / \mu \ll 1$ (Cox and Brenner 1967; Goldman
et al. 1967a, b; Loth 2000). $\mathbf{f}_{k,lift}$ is Saffman particle lift (Saffman 1965) and $\mathbf{f}_{k,coll}$ is
a stochastic force which takes into account collisions with red blood cells. Derivation
of each of these terms is explained in detail in Gholami et al. (2014).

Consistency of the global solution is guaranteed by coupling of quantities at
the near-wall interface to enforce conservation of mass. Several continuum-particle
hybrid coupling methods have been developed during the past decades (Koumout-
sakos 2005; Delgado-Buscalioni and Coveney 2003; De Fabritiis et al. 2006; Fedosov
and Karniadakis 2009), many of which have received significant attention. This cou-
pling scheme is based on communication of tracer concentration data at the near-wall
interface, which is highly efficient while staying dynamic and well tuned for a range
of realistic vascular setups. Full details of the implementation are given in Gholami
et al. (2014).

3.3.3 Microscopic Stochastic Adhesion Modelling

Adhesion behaviour of WBC changes significantly under different flow conditions,
e.g. disturbed flow conditions (Chiu and Chien 2011). Furthermore, different cell
types in blood exhibit specific adhesion characteristics. In this way, an overly simple
adhesion criterion, based on cell-endothelium separation distance, does not capture
the realistic receptor–ligand adhesion behaviour. Therefore, a more physiologically
realistic model needs to be adopted in order to reproduce findings of in vitro studies. A
number of cell adhesion models take coupling of mechanical and chemical quantities
into account through definition of association rate, k_f, and dissociation rate, k_r as a
function of dislodging force (Bell 1978; Evans et al. 1991). These coefficients define
the rate of formation and breakage of bonds between a pair of receptor–ligand. The
overall tendency of the pair to be in the bound state is called binding affinity and is
defined as the ratio of formation to breakage rates, i.e. $K_a = k_f / k_r$. In more advanced
models, the binding affinity is proposed by Bell et al. (1984) and Piper et al. (1998)
to be

$$K_a \left(\frac{f}{n} \right) = K_a^0 \left[1 + c \left(\frac{af}{n k_B T} \right)^d \right]^{-1} exp \left[- \left(\frac{af}{n k_B T} \right)^b \right], \tag{17}$$

where K_a^0 is the ratio of association to dissociation rates in absence of force and n is the number of bonds between two cells. $k_B T/a$ serves as a reference scale for force term f. Parameters b and c are used to determine a power law (Evans et al. 1991) or exponential law (Bell 1978), and parameter d is associated with flexibility of formed bonds. Equation (17) links the likelihood of cell–cell bond formation due to mechanical quantities such as hydrodynamic force.

Findings from a number of experimental studies, such as Florin et al. (1994) and Alón et al. (1995), suggest that the formation of a single bond, regardless of the overall number of adhesions, is significant in determining the dynamics of the cell (Piper et al. 1998), making the adhesion process a stochastic phenomenon on small scales (Chesla et al. 1998; Zhu 2000). Hence, a probabilistic model based on the attaching/detaching kinetic equation developed by Piper et al. (1998) is targeted. In particular, a straightforward modification of the deposition criterion for WBCs can be been considered for the steady-state attachment probability distribution. In this way, instead of considering a deposition event certain (attachment probability $P_a = 1$ for all WBCs within a sub-layer of one cell diameter from the wall), a Monte Carlo acceptance–rejection method can be used to reproduce the following distribution:

$$P_a = 1 - \left[1 + \sum_{n=1}^{\infty} \frac{1}{n!} \prod_{m=1}^{n} m_r m_l A_c K_a \left(\frac{f}{m} \right) \right]^{-1}, \tag{18}$$

which is the probability of having at least one bond. Parameters m_r (density of receptors), m_l (density of ligands) and A_c contact area are regarded as phenomenological fitting parameter. The model has been validated against experimental data from Hinds et al. (2001) where the deposition profiles have been measured for the steady gravity-driven flow of U937 cells in an E-selectin-coated geometry (see Fig. 13 bottom).

The multiscale SPH approach allows particle methods for hemodynamics simulations to be achieved in a tractable manner. As an example, Longest et al. (2004) use a maximum of 500,000 tracers in full domain in a realistic femoral anastomosis geometry to reach convergence. Considering the normal concentration of leukocytes in blood, approximately $10^4/mm^3$, and typical size of large vessels, a fully converged near-wall profile would require computation of trajectories for hundreds of millions of tracers. In contrast, the number of simulated tracers is reduced through specific tracking of leukocytes only in close vicinity of walls. The reduced number of tracked test particles which can be achieved by distributing them within a thin near-wall region only (Fig. 13 top) allows considerable speed-up of simulation for these systems, preserving the accuracy of the deposition profiles (Gholami et al. 2014).

In summary, the Lagrangian nature of SPH particle solver automatically takes into account WBC concentration advection in the bulk region, whereas in the near-wall region a microscopic LPT dynamics including lubrication as well as biological adhesion effects is considered. The multiscale method is not restricted to leukocyte dynamics but it could be applied to model a wide range of problems in biomedical

engineering characterized by large spatial separation between flow scales and sub-micron constituent size, where the relevant physical processes occur only in specific regions of space.

4 Conclusions

In this chapter, we have reviewed a class of advanced particle-based methods for the multiscale simulation of the rheology and hydrodynamics of complex fluids. All methods rely on a particle framework based on a general set of Newton's equations of motion for a system of interacting particles. This general framework allows to describe discrete systems of 'particles' defined at very different spatio-temporal levels ranging, in principle, from the classical Molecular Dynamics methods for atomistic systems interacting via realistic potentials, to mesoscopic coarse-graining methods—such as Dissipative Particle Dynamics and its refined versions at the mesoscopic realm, up to Lagrangian particle discretizations of sets of continuum partial differential equations, such as the popular Smoothed Particle Hydrodynamics method. Upon proper definition of interaction potentials and particle variables (as well as their discrete evolution equations), it is possible to describe the hydrodynamic of complex fluids at different scales in a very efficient way, depending on the physics of interest, from micro-mechanical models until macroscopic continuum models where microstructural relaxation processes are governed by field equations. We have critically assessed the advantages/limitations of each of this description in the context of modelling of complex non-Newtonian fluids, such as those represented by polymeric or particulate systems. A set of applications has been also discussed with particular emphasis on multiscale hybrid approaches in the context of cellular transport processes and biofluids.

References

Adami S, Hu XY, Adams NA (2012) A generalized wall boundary condition for smoothed particle hydrodynamics. J Comput Phys 231(21):7057–7075

Alizadehrad D, Fedosov DA (2018) Static and dynamic properties of smoothed dissipative particle dynamics. J Comput Phys 356:303–318

Allen MP, Tildesley DJ (1987) Computer simulation of liquids. Clarendon Press, Oxford

Alón R, Hammer DA, Springer TA (1995) Lifetime of the p-selectin-carbohydrate bond and its response to tensile force in hydrodynamic flow. Nature 374(6522):539–542

Arora K, Sureshkumar R, Khomami B (2002) Experimental investigation of purely elastic instabilities in periodic flows. J Non-Newtonian Fluid Mech 108(1):209–226

Backer JA, Lowe CP, Hoefsloot HCJ, Iedema PD (2005) Combined length scales in dissipative particle dynamics. J Chem Phys 123(11):114905

Batchelor GK, Green J-T (1972) The determination of the bulk stress in a suspension of spherical particles to order c^2. J Fluid Mech 56(3):401–427

Bell GI (1978) Models for the specific adhesion of cells to cells. Science 200(4342):618

Bell GI, Dembo M, Bongrand P (1984) Cell adhesion. Competition between nonspecific repulsion and specific bonding. Biophys J 45(6):1051–1064

Bertevas E, Fan X, Tanner RI (2009) Simulation of the rheological properties of suspensions of oblate spheroidal particles in a Newtonian fluid. Rheologica Acta 49(1):53–73

Bian X, Ellero M (2014) A splitting integration scheme for the SPH simulation of concentrated particle suspensions. Comput Phys Commun 185(1):53–62

Bian X, Litvinov S, Qian R, Ellero M, Adams NA (2012) Multiscale modeling of particle in suspension with smoothed dissipative particle dynamics. Phys Fluids 24(1):012002

Bird RB, Curtiss CF, Armstrong RC, Hassager O (1987) Dynamics of polymeric liquids, vol II. Wiley, New York, US

Caballero A, Mao W, Liang L, Oshinski J, Primiano C, McKay R, Kodali S, Sun W (2017) Modeling left ventricular blood flow using smoothed particle hydrodynamics. Cardiovascular Eng Technol 8(4):465–479

Chesla SE, Selvaraj P, Zhu C (1998) Measuring two-dimensional receptor-ligand binding kinetics by micropipette. Biophys J 75(3):1553–1572

Chiu J-J, Chien S (2011) Effects of disturbed flow on vascular endothelium: pathophysiological basis and clinical perspectives. Physiol Rev 91(1):327–387

Chmielewski C, Jayaraman K (1993) Elastic instability in crossflow of polymer solutions through periodic arrays of cylinders. J Non-Newtonian Fluid Mech 48(3):285–301

Cox RG, Brenner H (1967) The slow motion of a sphere through a viscous fluid towards a plane surface-II Small gap widths, including inertial effects. Chem Eng Sci 22(12):1753–1777

De Fabritiis G, Delgado-Buscalioni R, Coveney PV (2006) Multiscale modeling of liquids with molecular specificity. Phys Rev Lett 97(13):134501

de Gennes P-G (1979) Scaling concepts in polymer physics. Cornell University Press

Delgado-Buscalioni R, Coveney PV (2003) Continuum-particle hybrid coupling for mass, momentum, and energy transfers in unsteady fluid flow. Phys Rev E 67(4):046704

Einstein A (1906) Eine neue bestimmung der moleküldimensionen. Annalen der Physik 324(2):289–306

Ellero M, Adams NA (2011) SPH simulations of flow around a periodic array of cylinders confined in a channel. Int J Numer Methods Eng 86(8):1027–1040

Ellero M, Español P (2018) Everything you always wanted to know about SDPD (but were afraid to ask). Appl Math Mech 39(1):103–124

Ellero M, Tanner RI (2005) SPH simulations of transient viscoelastic flows at low Reynolds number. J Non-Newtonian Fluid Mech 132(1–3):61–72

Ellero M, Español P, Flekkøy EG (2003) Thermodynamically consistent fluid particle model for viscoelastic flows. Phys Rev E 68:041504

Ellero M, Español P, Adams N (2010) Implicit atomistic viscosities in smoothed particle hydrodynamics. Phys Rev E 82(4):1–6

Ermak DL, McCammon JA (1978) Brownian dynamics with hydrodynamic interactions. J Chem Phys 69(4):1352–1360

Español P (1995) Hydrodynamics from dissipative particle dynamics. Phys Rev E 52:1734–1742

Español P, Revenga M (2003) Smoothed dissipative particle dynamics. Phys Rev E 67:026705

Español P, Warren P (1995) Statistical mechanics of dissipative particle dynamics. EPL (Europhys Lett) 30(4):191

Español P, Warren PB (2017) Perspective: dissipative particle dynamics. J Chem Phys 146:150901

Evans E, Berk D, Leung A (1991) Detachment of agglutinin-bonded red blood cells. I. forces to rupture molecular-point attachments. Biophys J 59(4):838–848

Fan XJ, Phan-Thien N, Chen S, Wu XH, Ng TY (2006) Simulating flow of DNA suspension using dissipative particle dynamics. Phys Fluids 18:063102

Fedosov DA, Karniadakis GE (2009) Triple-decker: interfacing atomistic-mesoscopic-continuum flow regimes. J Comput Phys 228(4):1157–1171

Fedosov DA, Peltomäki M, Gompper G (2014) Deformation and dynamics of red blood cells in flow through cylindrical microchannels. Soft Matter 10:4258–4267

Ferziger JH, Perić M (1999) Computational methods for fluid dynamics, 2nd edn. Springer, Berlin

Florin E-L, Moy VT, Gaub HE (1994) Adhesion forces between individual ligand-receptor pairs. Science 264(5157):415–417

Fouxon A, Lebedev V (2003) Spectra of turbulence in dilute polymer solutions. Phys Fluids 15(7):2060–2072

Gan H, Lam Y, Nguyen N, Tam K, Yang C (2007) Efficient mixing of viscoelastic fluids in a microchannel at low Reynolds number. Microfluidics and Nanofluidics 3:101–108

Gholami B, Comerford A, Ellero M (2014) A SPH multiscale particle model of the near-wall dynamics of leukocites in flow. Int J Num Meth Biomed Eng 30:83–102

Gholami B, Comerford A, Ellero M (2015) SPH simulations of WBC adhesion to the endothelium: the role of haemodynamics and endothelial binding kinetics. Biomech Model Mechanobiol 14(6):1317–1333

Gingold RA, Monaghan JJ (1977) Smoothed particle hydrodynamics-theory and application to non-spherical stars. Monthly Notices Royal Astron Soc 181:375–389

Goldman AJ, Cox RG, Brenner H (1967a) Slow viscous motion of a sphere parallel to a plane wall-I motion through a quiescent fluid. Chem Eng Sci 22(4):637–651

Goldman AJ, Cox RG, Brenner H (1967b) Slow viscous motion of a sphere parallel to a plane wall-II Couette flow. Chem Eng Sci 22(4):653–660

Grilli M, Vázquez-Quesada A, Ellero M (2013) Transition to turbulence and mixing in a viscoelastic fluid flowing inside a channel with a periodic array of cylindrical obstacles. Phys Rev Lett 110:174501

Grmela M, Öttinger HC (1997) Dynamics and thermodynamics of complex fluids. I. Development of a general formalism. Phys Rev E 56:6620–6632

Groisman A, Steinberg V (2000) Elastic turbulence in a polymer solution flow. Nature 405(6782):53–55

Hinds MT, Park YJ, Jones SA, Giddens DP, Rita Alevriadou B (2001) Local hemodynamics affect monocytic cell adhesion to a three-dimensional flow model coated with e-selectin. J Biomech 34(1):95–103

Hoogerbrugge PJ, Koelman JMVA (1992) Simulating microscopic hydrodynamic phenomena with dissipative particle dynamics. EPL (Europhys Lett) 19(3):155

Howe AM, Clarke A, Giernalczyk D (2015) Flow of concentrated viscoelastic polymer solutions in porous media: effect of MW and concentration on elastic turbulence onset in various geometries. Soft Matter 11:6419–6431

Jeffrey DJ, Onishi Y (1984) Calculation of the resistance and mobility functions for two unequal rigid spheres in low-Reynolds-number flow. J Fluid Mech 139:261–290

Klessinger UA, Wunderlich BK, Bausch AR (2013) Transient flow behavior of complex fluids in microfluidic channels. Microfluidics and Nanofluidics 15(4):533–540

Koelman JMVA, Hoogerbrugge PJ (1993) Dynamic simulations of hard-sphere suspensions under steady shear. EPL (Europhys Lett) 21(3):363

Koumoutsakos P (2005) Multiscale flow simulations using particles. Ann Rev Fluid Mech 37:457–487

Ladd AJC, Verberg R (2001) Lattice-boltzmann simulations of particle-fluid suspensions. J Statist Phys 104(5):1191–1251

Landau LD, Lifshitz EM (1987) Fluid mechanics. Course of theoretical physics. Butterworth-Heinemann, 2 edn

Litvinov S, Ellero M, Hu X, Adams NA (2008) Smoothed dissipative particle dynamics model for polymer molecules in suspension. Phys Rev E 77:066703

Litvinov S, Ellero M, Hu X, Adams NA (2009) Self-diffusion coefficient in smoothed dissipative particle dynamics. J Chem Phys 130(2):021101

Litvinov S, Ellero M, Hu X, Adams NA (2010) Particle-layering effect in wall-bounded dissipative particle dynamics. Phys Rev E 82:066704

Litvinov S, Hu X, Ellero M, Adams N (2014) Mesoscopic simulation of the transient behavior of semi-diluted polymer solution in a microchannel following extensional flow. Microfluid Nanofluidics 16(1–2):257–264

Litvinov S, Xie Q, Hu X, Adams N, Ellero M (2016) Simulation of individual polymer chains and polymer solutions with smoothed dissipative particle dynamics. Fluids 1(1):7

Liu MB, Liu GR (2010) Smoothed particle hydrodynamics (SPH): an overview and recent developments. Arch Comput Methods Eng 17(1):25–76

Longest P, Kleinstreuer C, Buchanan J (2004) Efficient computation of micro-particle dynamics including wall effects. Comput Fluids 33(4):577–601

Loth E (2000) Numerical approaches for motion of dispersed particles, droplets and bubbles. Progress Energy Combust Sci 26(3):161–223

Marsh CA, Backx G, Ernst MH (1997) Fokker-planck-boltzmann equation for dissipative particle dynamics. EPL (Europhys Lett) 38(6):411

Martys NS, George WL, Chun B-W, Lootens D (2010) A smoothed particle hydrodynamics-based fluid model with a spatially dependent viscosity: application to flow of a suspension with a non-newtonian fluid matrix. Rheol Acta 49(10):1059–1069

Meulenbroek B, Storm C, Bertola V, Wagner C, Bonn D, van Saarloos W (2003) Intrinsic route to melt fracture in polymer extrusion: A weakly nonlinear subcritical instability of viscoelastic poiseuille flow. Phys Rev Lett 90:024502

Mewis J, Wagner NJ (2011) Colloidal suspension rheology. Cambridge University Press, 2011. Cambridge Books Online

Monaghan JJ (2005) Smoothed particle hydrodynamics. Reports Progress Phys 68(8):1703

Öttinger HC (2005) Complex fluids. pp 97–156. John Wiley Sons, Inc

Öttinger HC, Grmela M (1997) Dynamics and thermodynamics of complex fluids. ii. illustrations of a general formalism. Phys Rev E 56: 6633–6655

Owens RG, Phillips TN (2002) computational rheology. World Scientific

Pathak JA, Ross D, Migler KB (2004) Elastic flow instability, curved streamlines, and mixing in microfluidic flows. Phys Fluids 16(11):4028–4034

Pipe CJ, McKinley GH (2009) Microfluidic rheometry. Mech Res Commun 36(1):110–120, 2009. Recent Advances in Microfluidics

Piper JW, Swerlick RA, Zhu C (1998) Determining force dependence of two-dimensional receptor-ligand binding affinity by centrifugation. Biophys J 74(1):492–513

Qiao R, He P (2008) Mapping of dissipative particle dynamics in fluctuating hydrodynamics simulations. J Chem Phys 128(12):126101

Ripoll M, Mussawisade K, Winkler RG, Gompper G (2005) Dynamic regimes of fluids simulated by multiparticle-collision dynamics. Phys Rev E 72:016701

Saffman PG (1965) The lift on a small sphere in a slow shear flow. J Fluid Mech 22(02):385–400

Seto R, Mari R, Morris JF, Denn MM (2013) Discontinuous shear thickening of frictional hard-sphere suspensions. Phys Rev Lett 111:218301

Shahriari S, Kadem L, Rogers BD, Hassan I (2012) Smoothed particle hydrodynamics method applied to pulsatile flow inside a rigid two-dimensional model of left heart cavity. Int J Numer Methods Biomed Eng 28(11):1121–1143

Sierou A, Brady JF (2002) Rheology and microstructure in concentrated noncolloidal suspensions. J Rheol 46(5):1031–1056

Singh A, Mari R, Denn MM, Morris JF (2018) A constitutive model for simple shear of dense frictional suspensions. J Rheol 62(2):457–468

Talwar KK, Khomami B (1995) Flow of viscoelastic fluids past periodic square arrays of cylinders: inertial and shear thinning viscosity and elasticity effects. J Non-Newtonian Fluid Mech 57:177–202

Vázquez-Quesada A, Ellero M (2012) SPH simulations of a viscoelastic flow around a periodic array of cylinders confined in a channel. J Non-Newtonian Fluid Mech 167168:1–8

Vázquez-Quesada A, Ellero M (2016a) Rheology and microstructure of non-colloidal suspensions under shear studied with smoothed particle hydrodynamics. J Non-Newtonian Fluid Mech 233:37–47. Papers presented at the Rheology Symposium in honor of Prof. R. I. Tanner on the occasion of his 82nd birthday, in Vathi, Samos, Greece

Vázquez-Quesada A, Ellero M (2016b) Analytical solution for the lubrication force between two spheres in a bi-viscous fluid. Phys Fluids 28(7):073101

Vázquez-Quesada A, Ellero M, Español P (2009a) Smoothed particle hydrodynamic model for viscoelastic fluids with thermal fluctuations. Phys Rev E 79:056707

Vázquez-Quesada A, Ellero M, Español P (2009b) Consistent scaling of thermal fluctuations in smoothed dissipative particle dynamics. J Chem Phys 130(3):034901

Vázquez-Quesada A, Ellero M, Español P (2012) A SPH-based particle model for computational microrheology. Microfluidics and Nanofluidics 13(2):249–260

Vázquez-Quesada A, Bian X, Ellero M (2015) Three-dimensional simulations of dilute and concentrated suspensions using smoothed particle hydrodynamics. Comput Part Mech, 1–12

Vázquez-Quesada A, Tanner RI, Ellero M (2016) Shear thinning of noncolloidal suspensions. Phys Rev Lett 117:108001

Vázquez-Quesada A, Mahmud A, Dai S, Ellero M, Tanner RI (2017a) Investigating the causes of shear-thinning in non-colloidal suspensions: experiments and simulations. J Non-Newtonian Fluid Mech 248:1–7

Vázquez-Quesada A, Wagner NJ, Ellero M (2017b) Planar channel flow of a discontinuous shear-thickening model fluid: theory and simulation. Phys Fluids 29(10):103104

Vázquez-Quesada A, Wagner NJ, Ellero M (2018) Normal lubrication force between spherical particles immersed in a shear-thickening fluid. Phys Fluids 30(12):123102

Vázquez-Quesada A, Español P, Tanner RI, Ellero M (2019) Shear-thickening of a non-colloidal suspension with a viscoelastic matrix. J Fluid Mech. in press

Violeau D, Rogers BD (2016) Smoothed particle hydrodynamics (SPH) for free- surface flows: past, present and future. J Hydraul Res 54:1–26

Waters ND, King MJ (1970) Unsteady flow of an elastico-viscous liquid. Rheol Acta 9(3):345–355

Xue S-C, Tanner RI, Phan-Thien N (2004) Numerical modelling of transient viscoelastic flows. J Non-Newtonian Fluid Mech 123(1):33–58

Ye T, Phan-Thien N, Lim CT (2015) Particle-based simulations of red blood cellsa review. J Biomech 49 (11):2255–2266. Selected Articles from the International Conference on CFD in Medicine and Biology (Albufeira, Portugal August 30th - September 4th, 2015)

Zarraga IE, Hill DA, Leighton DT (2000) The characterization of the total stress of concentrated suspensions of noncolloidal spheres in newtonian fluids. J Rheol 44(2):185–220

Zhu C (2000) Kinetics and mechanics of cell adhesion. J Biomech 33(1):23–33